CENTRAL RESEARCH LIBRARY
DOCUMENTS COLLECTION

MARTIN MARIETTA ENERGY SYSTEMS LIBRARIES

3 4456 0285924 4

ORNL-4470
UC-25 – Metals, Ceramics, and Materials

cy 1

METALS AND CERAMICS DIVISION
ANNUAL PROGRESS REPORT
FOR PERIOD ENDING JUNE 30, 1969

OAK RIDGE NATIONAL LABORATORY
operated by
UNION CARBIDE CORPORATION
for the
U.S. ATOMIC ENERGY COMMISSION

Printed in the United States of America. Available from Clearinghouse for Federal Scientific and Technical Information, National Bureau of Standards, U.S. Department of Commerce, Springfield, Virginia 22151
Price: Printed Copy $3.00; Microfiche $0.65

LEGAL NOTICE

This report was prepared as an account of Government sponsored work. Neither the United States, nor the Commission, nor any person acting on behalf of the Commission:

A. Makes any warranty or representation, expressed or implied, with respect to the accuracy, completeness, or usefulness of the information contained in this report, or that the use of any information, apparatus, method, or process disclosed in this report may not infringe privately owned rights; or

B. Assumes any liabilities with respect to the use of, or for damages resulting from the use of any information, apparatus, method, or process disclosed in this report.

As used in the above, "person acting on behalf of the Commission" includes any employee or contractor of the Commission, or employee of such contractor, to the extent that such employee or contractor of the Commission, or employee of such contractor prepares, disseminates, or provides access to, any information pursuant to his employment or contract with the Commission, or his employment with such contractor.

ORNL-4470

Contract No. W-7405-eng-26

METALS AND CERAMICS DIVISION ANNUAL PROGRESS REPORT

for Period Ending June 30, 1969

J. H Frye, Jr., Director
J. E. Cunningham, Associate Director

Section Heads

G. M. Adamson, Jr.
B. S. Borie
W. O. Harms
C. J. McHargue
P. Patriarca
J. R. Weir, Jr.

Compiled and Edited by Sigfred Peterson

OCTOBER 1969

MARTIN MARIETTA ENERGY SYSTEMS LIBRARIES

3 4456 0285924 4

OAK RIDGE NATIONAL LABORATORY
Oak Ridge, Tennessee
operated by
UNION CARBIDE CORPORATION
for the
U. S. ATOMIC ENERGY COMMISSION

Reports previously issued in this series are as follows:

ORNL-28	Period Ending March 1, 1948
ORNL-69	Period Ending May 31, 1948
ORNL-407	Period Ending July 31, 1949
ORNL-511	Period Ending October 31, 1949
ORNL-583	Period Ending January 31, 1950
ORNL-754	Period Ending April 30, 1950
ORNL-827	Period Ending July 31, 1950
ORNL-910	Period Ending October 31, 1950
ORNL-987	Period Ending January 31, 1951
ORNL-1033	Period Ending April 30, 1951
ORNL-1108	Period Ending July 31, 1951
ORNL-1161	Period Ending October 31, 1951
ORNL-1267	Period Ending January 31, 1952
ORNL-1302	Period Ending April 30, 1952
ORNL-1366	Period Ending July 31, 1952
ORNL-1437	Period Ending October 31, 1952
ORNL-1503	Period Ending January 31, 1953
ORNL-1551	Period Ending April 10, 1953
ORNL-1625	Period Ending October 10, 1953
ORNL-1727	Period Ending April 10, 1954
ORNL-1875	Period Ending October 10, 1954
ORNL-1911	Period Ending April 10, 1955
ORNL-1988	Period Ending October 10, 1955
ORNL-2080	Period Ending April 10, 1956
ORNL-2217	Period Ending October 10, 1956
ORNL-2422	Period Ending October 10, 1957
ORNL-2632	Period Ending October 10, 1958
ORNL-2839	Period Ending September 1, 1959
ORNL-2988	Period Ending July 1, 1960
ORNL-3160	Period Ending May 31, 1961
ORNL-3313	Period Ending May 31, 1962
ORNL-3470	Period Ending May 31, 1963
ORNL-3670	Period Ending June 30, 1964
ORNL-3870	Period Ending June 30, 1965
ORNL-3970	Period Ending June 30, 1966
ORNL-4170	Period Ending June 30, 1967
ORNL-4370	Period Ending June 30, 1968

Contents

SUMMARY xv

PART I. FUNDAMENTAL PROGRAMS

1. CRYSTAL PHYSICS 1
   - Ferrite Crystal Growth for Neutron Beam Control 1
   - Internal Centrifugal Zone Growth 1
   - Morphologies of Rod and Lamellar Tungsten in Unidirectionally Solidified UO_2-W Eutectic 2
   - Growth of Graphite Crystals 2
   - High-Temperature Solution Growth of Single-Crystal Neptunium Dioxide 3
   - Single-Crystal Growth of $HfSiO_4$ Doped with Tb^{4+} or Yb^{3+} 3
   - Growth of $SrCl_2$ Crystals Doped with ^{241}Am, ^{244}Cm, or ^{245}Cm 3
   - Growth of Pure and Doped CeO_2 and ThO_2 Single Crystals 3
   - Hydrothermal Synthesis 3
     - Preliminary Studies on the Hydrothermal Synthesis of Sulfides 3
     - Infrared Spectrum of Quartz Growth in RbOH 4
   - Magnetic Study of NpO_2 Single Crystals 4

2. DEFORMATION AND ANNEALING OF METALS 5
   - Texture Inhomogeneities in Cold-Rolled Niobium 5
   - Texture Development in an Nb–40% V Alloy 5
   - The Recrystallization Characteristics of Moderately Deformed Aluminum 6
   - The Recovery Characteristics of Niobium and Nb–40% V 6

3. DEFORMATION OF CRYSTALLINE SOLIDS 7
   - Plastic Deformation of Rhenium 7
   - Precipitation Hardening in Body-Centered Cubic Alloys 8
   - Characteristics of Stress and Dilatation Fields of Straight Dislocations in Anisotropic Crystals 8
   - Structural and Elastic Properties of Zonal Twin Dislocations in Anisotropic Crystals 10
   - Structural Changes Produced by the Deformation of Nonrandom Alloys 10

4. DIFFUSION IN SOLIDS 12
   - Cation Self-Diffusion in UO_2 12

Diffusion of ^{233}U in UO_2 12
Cation Self-Diffusion in UN_{1+x} 12
Tracer Diffusion in Tungsten 12
Effects of Short-Circuiting Paths on Diffusion Coefficient Measurements 13
Combined Surface and Grain Boundary Diffusion 13
Oxidation Kinetics and its Influence on the Near-Surface Effect in Diffusion 13
Residual Activity Methods for Determination of Lattice Diffusion Coefficients 13

5. ELECTRON MICROSCOPY 14
High-Fluence Neutron Irradiation Damage in Aluminum 14
High-Neutron-Fluence Damage in an Aluminum Alloy 14
Quenching Defects in Aluminum 15
Thermal Rejection and Growth of Gas Bubbles in Electrodeposited Nickel 15
Phase Instability in Hastelloy N 15
Autoradiographic Study of ^{14}C in Hastelloy N 16
Recrystalization of Nickel 270 16
The Energy Relations in the Room-Temperature Deformation of Aluminum Single Crystals 16
The Energy Stored in a Gold-Silver Alloy 16
Orientation Determination from Dodecahedral Etch Pits 17

6. FUNDAMENTAL CERAMICS RESEARCH 18
Electronic Band Structure Calculations for Paramagnetic Uranium Mononitride 19
Low-Temperature Thermal Conductivity 20
Chemical Analysis for Carbon and Nitrogen by Proton Reaction Analysis 21

7. MÖSSBAUER STUDIES OF ALLOYS 23
Mössbauer Spectroscopy with ^{61}Ni In Compounds and Transition Metal Alloys 23
Final Positions of Low-Energy ^{57}Fe Recoil Atoms in Body-Centered Cubic Iron-Aluminum Alloys 24
Experiments 24
Results 25
Discussion 26

8. PHYSICAL CERAMICS STUDIES 28
Deformation of Uranium Dioxide Single Crystals 28
"Desintering" 28
Compressive Creep of Uranium Mononitride 28
Some Observations on Activation Energy in Sintering 29
Topology of Sintering 29
Diffusion of Thorium in ThO_2 29

9. PHYSICAL PROPERTIES . . . 30

Electronic Heat Transport . . . 30
Electrical Resistivity of Tentalum to 2600°K . . . 30
Electrical Heating Method . . . 31
Physical Properties of Gold . . . 31

Lattice Heat Transport . . . 32
Thermal Conductivity of ThO_2 and UO_2 . . . 32
Thermal Conductivity of LiF . . . 32

Calorimetric Studies . . . 33
Components of Specific Heat Capacity of Nickel, Iron, and Ni_3Fe . . . 33
Physical Properties of Ordered and Disordered Ni_3Fe . . . 33

Related Studies . . . 33
Uranium Nitride . . . 33
Thorium Nitride . . . 33

10. SPECTROSCOPY OF IONIC MEDIA . . . 34

Liquid Systems . . . 34
A Spectroscopic Study of Interactions Between $NiCl_4^{2-}$ and Outer-Shell Cations in CsCl-Rich Melts of CsCl-$ZnCl_2$ and CsCl-$MgCl_2$ . . . 34
Coordination Chemistry of Nickel(II) in Liquid Mixtures of Zinc and Cesium Chlorides . . . 34
Coordination Equilibria of Chloronickelate(II) Complexes in $CsAlCl_4$ . . . 35
Electrical Conductivities of Systems Containing Aluminum Halides . . . 35
Spectra of Dilute Solutions of Bismuth Metal in Molten Bismuth Trihalides. The Bi-$BiBr_3$ System . . . 35
The Determination of Successive Equilibrium Constants . . . 36
The Equilibrium Constants for the Ni(II)-Cl^-, I^- System in Dimethyl Sulfone at 125°C . . . 36

Molten Fluoride Spectroscopy . . . 36
Diamond-Windowed Cell for Molten Fluoride Spectroscopy . . . 36
Salt Purification for Fluoride Spectroscopy . . . 38
MoF_3 Solution Spectra . . . 38
Vapor Phase Studies Over MoF_3 Solutions . . . 39

Solid Systems . . . 39
The Electronic Structure of the Nickel(II) Ion in Doped LiCl Crystals . . . 39
The Electronic Structure of Nickel Ions in Cs_3NiCl_5 and $Cs_3Mg_{1-x}Ni_xCl_5$ . . . 40
Vibrational Structure of the 7000-to-9000 cm^{-1} Band of $Cs_3Mg_{1-x}Ni_xCl_5$ . . . 40
Optical Spectra of the Cobalt(II) Ion at Sites of Approximately Octahedral Symmetry in Several Chloride Crystals . . . 40
K_3MoF_6 Synthesis and Spectrum . . . 41
Structure of the $Al_2X_7^-$ Ion . . . 41
$Ni(AlCl_4)_2$ . . . 41
$Ni(AlBr_4)_2$ and $Ni(AlI_4)_2$ . . . 41
Titanium Aluminum Chlorides . . . 42

11. SUPERCONDUCTING MATERIALS . . . 43

Flux Pinning by Grain Boundaries in Superconducting Niobium-Zirconium Alloys . . . 43

Superconductivity in Niobium Containing Ferromagnetic Gadolinium or Paramagnettic Yttrium Dispersions . . . 43

Phase Transformations Associated with the Samarium-Type Structure in Intra-Rare-Earth Alloys . . . 43

12. SURFACE REACTIONS OF METALS . . . 45

Refractory Metal Studies . . . 45
Stress Development During Oxidation . . . 45
Anodic-Film Sectioning Technique . . . 45

X-ray Diffraction Studies of Thin Oxide Films . . . 46

Oxidation of Uranium Alloy . . . 48

13. THEORETICAL RESEARCH . . . 50

The Protinic Structure of Molecules . . . 50

Rigid-Band Behavior of Solvent Atom Knight Shifts in Noble Metal Alloys . . . 50

Calculations Pertaining to the Thermopower of Copper . . . 51

Electronic States in Disordered Systems . . . 51

14. X-RAY DIFFRACTION . . . 52

Routine Analysis . . . 52

Crystal Structures of Transition Phases Formed in U–16.60 at. % Nb–5.64 at. % Zr Alloy . . . 53

Thermal Motion in Highly Oriented Graphite . . . 55

Small-Angle X-Ray Scattering Investigation of Aqueous Solutions of Tetraalkylammonium Halides . . . 56

Simple Method for Estimating the Gas-Amplification Factor in a Proportional Counter . . . 56

Mechanism and Kinetics of Omega Transformation in Ti–25 at. % Nb . . . 56
Small-Angle X-Ray Scattering . . . 56
High-Angle X-Ray Scattering . . . 57

An Alignment Procedure for the Kratky Camera . . . 57

PART II. HIGH-TEMPERATURE MATERIALS

15. PHYSICAL AND MECHANICAL METALLURGY OF REFRACTORY ALLOYS . . . 58

Basic Physical Metallurgy Studies . . . 58
Interactions of Refractory Metals with Active Gases in Vacuum and Inert Gas Environment . . . 58
Solubility, Diffusivity, and Permeability of Interstitials in Refractory Alloys . . . 58
Development of Age Hardenable Alloys . . . 59

Long-time High-Temperature Mechanical Properties of Commercial Refractory Alloys . . . 59

Welding and Brazing Development . . . 60
Brazing Alloy Development . . . 60
Welding of T-111 Alloy Forced Circulation Loop (FCLLL-1) . . . 61

Thermal Conductivity of Tungsten Alloys . . . 61

16. TUNGSTEN METALLURGY . . . 63

Effect of Extrusion Conditions on the Structure of Extruded Tungsten . . . 63

Chemical Vapor Deposition of Tungsten and Tungsten-Rhenium Alloys 63
Chemical Vapor Deposition of Vanadium 64
The Ductile-to-Brittle Transition Temperature of CVD W–5% Re Sheet 65
Formation of Gas Bubbles in CVD Materials 65
Gas Porosity and Hot Cracking in Fusion Welds in Tungsten 66
Creep-Rupture Properties of Tungsten Alloys 66

17. ALKALI-METAL CORROSION OF HIGH-TEMPERATURE MATERIALS 68
Mass Transfer of Interstitial Impurities Between Vanadium Alloys and Sodium 68
Effect of Oxygen in Sodium on Vanadium and Vanadium Alloys 68
Interstitial Effects on Mechanical Properties of Vanadium Alloys 69
Mass Transport of Interstitial Impurities Between 300 Series Stainless Steels and Vanadium Alloys 69
Compatibility of Stainless Steel and Insulation in LMFBR Systems 69
Corrosion of Refractory Alloys by Lithium 71
Thermal-Convection Loop Tests 71
Forced-Circulation Lithium Loop 71
Compatibility of Boiling Potassium with Refractory Alloys 72
Capsule and Natural-Circulation Loop Tests 72
Forced-Circulation Boiling Potassium Loop 73
Effect of Oxygen on the Compatibility of Refractory Metals with Alkali Metals 74
Alkali Metal Penetration 74
Effect of Oxygen on Dissolution of Refractory Metals in Alkali Metals 75

18. NITRIDE FUELS DEVELOPMENT 76
Synthesis, Fabrication, and Characterization 76
Synthesis and Fabrication of UN 76
Synthesis and Fabrication of $U^{15}N$ 77
Synthesis and Fabrication of (U,Pu)N 77
Particle Size Distribution Measurements of UN Powders 78
Nitride Powder Morphology 78
Quantitative Chemical Analysis of Uranium Nitride 78
Conversion of UO_2 and $(U,Pu)O_2$ to Carbonitride Fuels 79
Direct Conversion of Sol-Gel $(U,Pu)O_2$ to Carbonitride 79
Kinetic Studies of Fuel-Producing Reactions 79
Compatibility of Cladding with Nitride Fuels 80
Effects of Oxygen Contamination in (U,Pu)N 80
Temperature Gradient Effects on Ceramic Fuels 81
Chemical Effects of Nuclear Burnup on Ceramic Fuels 81
Compatibility of Vanadium Alloys with UN 81
Thermodynamic Studies 81
The U-V-C Phase Diagram and the Thermodynamic Properties of UVC_2 81
Thermodynamic Investigations of V(C,N) Solutions and the Formation of Active Carbon 81
Irradiation Performance of Nitride Fuels 82
LMFBR Applications 82
Irradiation Behavior of UN 82
Thermal Contact Resistance 84

19. MATERIALS DEVELOPMENT FOR ISOTOPIC POWER PROGRAMS 85
Curium Program 85
Sublimation of W–25% Re in Low-Pressure Oxygen 85
Effect of Low-Pressure Gases on the Creep Properties of Refractory Metals 86
Mechanical Properties of Capsule Materials 86
Compatibility 86
Welding Development for Compatibility Program 87
Brazing Alloy Development 87
Chemical Vapor Deposition of Test Components 87
Fluid-Bed Coating for Isotopic Fuel Particles 88
Cladding Materials Program 89
Mechanical Properties of Haynes Alloy No. 25 89
Interaction of Stress and Vacuum on Properties of Superalloys at Elevated Temperatures 90
Evaporation of Superalloy Capsule Materials in Vacuum 91
Development of Improved Alloys 91
Strontium Program Compatibility Studies 92
SNAP-21 and SNAP-23 Programs 92
Capsule Welding 92
Nondestructive Testing 92
Thermoelectric Conversion Systems for the Isotope Kilowatt Program 93

PART III. GENERAL FUELS AND MATERIALS RESEARCH

20. FUEL ELEMENT FABRICATION DEVELOPMENT 94
Irradiation Performance of Aluminum-Base Fuel Dispersions 94
Influence of Void Volume on the Irradiation Damage in Dispersion Fuel Plates 94
Effect of Fuel Fines on the Irradiation Performance of Dispersion Fuel Plates 95
Postirradiation Examination of a HFIR Fuel Element 95
Fuel Plate Fabrication 99
Nonuniform Deformation in Simulated Fuel Plates 99
Effect of Fuel Fines on the Fabrication of Fuel Plates 102
Characterization of Sol-Gel U_3O_8 103
Influence of Cladding Strength on the Void Volume and Dogboning of Composite Fuel Plates 105
Fit of Fuel Compact to Frame Cavity 105
Compatibility of Burned U_3O_8 and Aluminum Matrix During Fabrication 106
Characterization of Electrolessly Deposited Nickel Coatings 107
Plate Surface Studies 107
Joining of Fuel Element Components 110
Fuel-Plate-to-Side-Plate Electron-Beam Welding Development 110
Spacer Attachment By Explosive Welding 110
Development of Ductile Dispersion-Strengthened Aluminum 111
21. JOINING RESEARCH ON NUCLEAR MATERIALS 112
Heat Affected Zone Studies 112
Ductility at High Temperatures 112
Ductility at Intermediate Temperatures 113

Weld Metal Studies 114
The Effect of Minor Elements on the Hot Cracking of Inconel 600 114
Studies on 18% Cr–8% Ni Stainless Steels 114
Effect of Defects on the Mechanical Properties of Weldments 116

22. NONDESTRUCTIVE TEST DEVELOPMENT 118

Electromagnetic Inspection Methods 118
Analytical Studies 118
Experimental Studies 118

Ultrasonic Test Methods 119
Fabrication of References 119
Optical Visualization of Ultrasound 119
Frequency Analysis 120

Penetrating Radiation Inspection Methods 120
Radiation Attenuation Studies 120
Radiation Scattering Studies 120

23. RESEARCH REACTOR CORE IMPROVEMENT AND PROCUREMENT ASSISTANCE 121

Preparation of UAl_x Fuel Particles 121

Roll Bonding of Unclad 6061 Aluminum 122

Fabrication Development of More Economical HFIR Fuel Plate Fuel 122

Fabrication of ATR Fuel Plates 123

Development of Nondestructive Inspection Techniques 123
Scanner Calibration Studies 123
Radiographic Densitometry 125

Cost Effectiveness Study on Modifications to HFIR Fuel Elements 125

HFIR Fuel Element Manufacture 125

Procurement Assistance 126

High Flux Isotope Reactor Control Rod Modification 126

24. SOL-GEL FAST REACTOR OXIDE FUELS 127

Development of Fabrication Processes 127
Sphere-Pac Development 127
Pellet Development 128
Capsule Fabrication 128

Characterization of $(U,Pu)O_2$ Fuels 130
Chemical Analysis 130
Thermal Conductivity 130
Deformation 130

Thermodynamics of Mixed Oxide Fuels 132
Thermodynamic Applications to $(U,Pu)O_{2\pm x}$ Fuel Systems 132
A Model for the Low-Temperature Heat Capacity of UO_2 132
Standard Samples of UO_2 for Oxygen Determination 134

Irradiation Behavior 134
Uninstrumented Tests 134
ORR Instrumented Tests 135

Transient Irradiation Tests 137
Fast Flux Irradiation Tests 137

Mathematical Analysis of Irradiation Experiments 138
Reactor Physics Analyses 138
Heat Transfer Analyses 138
Comparison of Thermal-Flux and Fast-Flux Thermal Gradients 139

25. ZIRCONIUM METALLURGY 141

Experimental Fabrication of Zircaloy-4 Tubing 141

Texture Development and Control in Zircaloy Tubing 141

Annealing Textures in Zircaloy Tubing 142

Plastic Yielding of Highly Textured Zircaloy Tubing 143

PART IV. REACTOR DEVELOPMENT SUPPORT

26. DESALINATION 145

Evaluation of UMBR Fuel Element Performance and Fabrication 145

Physical Properties of Thorium-Uranium Alloys 146

Metal-Fueled PWR 147

27. GAS-COOLED REACTOR PROGRAM 148

Coated Particle Bonding Development for HTGR Fuels 148

Irradiation of Bonded Beds 149

Irradiation of Pyrolytic Carbon Coatings 150

Concrete for Reactor Pressure Vessels 153

Steam Corrosion of Advanced Steam Generator Alloys 153

Gas-Cooled Fast Reactor Fuel Element Development 154
GCFR Fuel Development 154
Cooperative Irradiation Test Capsules 157

28. HEAVY SECTION STEEL TECHNOLOGY 160

Characterization of Heavy Section Steel Weldments 160

Evaluation of Discontinuities in HSST Plate 01 160

29. HIGH FLUX ISOTOPE REACTOR TARGET DEVELOPMENT 163

TRU Target Fabrication 163

HFIR Target Performance 164
Status of Targets in HFIR 164
Analysis of Target Performance 165

Irradiation Effects on Mechanical Properties of Cladding 166

Density Changes in Aluminum Alloys as a Result of Irradiation 167

30. LMFBR CLADDING AND STRUCTURAL MATERIALS 168

Fabrication Development for LMFBR Fuel Cladding 168
Fabrication of Small-Diameter Stainless Steel Tubing 168

Effect of Process Variation on the Texture of Titanium-Modified Type 304L Stainless Steel Tubing . . . 168
Texture of Drawn and Planetary-Swaged Tubes of Titanium-Modified Type 304L Stainless Steel . . . 169
Electron Microscopy of Cold-Worked Tubes of Titanium-Modified Type 304L Stainless Steel . . . 170
Effect of Boron on the Hot Ductility of Type 316 Stainless Steel . . . 172
Inspection of Tubing for LMFBR Fuel Cladding . . . 172
Biaxial Creep-Rupture Properties of Titanium-Modified Type 304L Stainless Steel Tubing . . . 173

Effects of Irradiation on LMFBR Cladding and Structural Alloys . . . 173
Irradiation Damage to Annealed Type 316 Stainless Steel . . . 173
Transmission Electron Microscopy of Irradiated Austenitic Stainless Steel and Nickel 270 . . . 174
Creep-Rupture of Aged Titanium-Modified Type 304L Stainless Steel Containing Cyclotron-Injected Helium . . . 176
Production of Displacement Damage by Light Ions . . . 176
Irradiation Effects in Incoloy 800 . . . 177
Electron Microscopy of Vanadium and V–20% Ti Irradiated in EBR-II . . . 178

Welding Development for LMFBR Vessels and Components . . . 179

31. MILITARY REACTOR FUEL ELEMENT PROCUREMENT ASSISTANCE . . . 181

32. MOLTEN-SALT REACTOR PROGRAM . . . 182

MSRE Surveillance . . . 182
Specimen Removal and General Observations . . . 182
Properties of Hastelloy N Surveillance Samples . . . 183
Postirradiation Welding of Hastelloy N . . . 184

MSBR Development . . . 184
Effect of Titanium and Carbon on Fracture of Nickel Alloys . . . 184
Comparison of the Thermal Stability of Titanium-Modified Hastelloy N at 650 and 760°C . . . 186
Electron Microscopy . . . 187
Development of a Modified Hastelloy N for Future MSBR's . . . 188
Corrosion Studies . . . 189
Residual Stress Measurements in Hastelloy N Welds . . . 190
Evaluation of New Materials . . . 191
X-Ray Studies . . . 192
Graphite Irradiation in HFIR . . . 193
Microstructure of Graphite . . . 195
Gas Impregnation of Graphite with Carbon . . . 195
Graphite-to-Hastelloy N Transition Joints . . . 197
Physical Properties of Graphites . . . 198

33. REACTOR EVALUATION . . . 199

Computer Program Development for Cost Analysis . . . 199
Fuel Fabrication Costs . . . 199
Optimization of Fabrication Capacity Expansion . . . 200
Recycle DELAY Code . . . 200

Fuel Fabrication Cost Analysis . . . 200
Fuel Recycle Task Force . . . 201

Guide for Reactor Evaluation 201
Fuel Fabrication Costs for a Conceptual (U,Pu) Metallic-Fueled PWR 201
Comparative Cost Evaluation for Sphere-Pac Fuel Rods 201

Fuel Performance Model Development 202

Fission-Gas Release From $(U,Pu)O_2$ Fuel During Fast Flux Irradiation 203

34. THORIUM UTILIZATION 204

Thorium-Uranium Recycle Facility 204
Status of TURF 204
Preparation of ^{233}U Fuel for the MSRE 205

Fuel-Graphite Development 205
Particle Handling 205
Particle Coating 205
Particle Inspection 205
Bonding of Fuel Particles 206

Coating of $(^{233}U–Th)O_2$ Fuel 206

Irradiation of Thoria-Base Oxide Fuels 206

35. WATER REACTOR SAFETY 208

Fuel Rod Failure Program Coordination 208

High-Temperature Properties of Zircaloy Cladding 209

PART V. OTHER PROGRAM ACTIVITIES

36. ABSORBER MATERIALS FOR SO_2 FROM FLUE GASES 211

37. ARMY PULSED RADIATION FACILITY REACTOR ASSISTANCE 212

Core Alloy Development 212

Alloy Evaluation 212

38. METALLOGRAPHY 213

Alpha Metallography Facility 213

Electron Microprobe Analysis 213

The Shielded Electron Microprobe Analyzer 216

Quantitative Television Microscopy 216

Heating Stage Microscopy 217

Equipment and Techniques in Metallography 217

39. NERVA PROGRAM METALLURGICAL SUPPORT 218

Nondestructive Inspection of Coolant Channels in Beryllium Reflector Components 218
Detection of Defects 218
Measurement of Misalignment 219

Effects of Space Environment on NERVA Materials 219
Outgassing of NERVA Fuel Elements 219
Adhesion of NERVA Materials 221

40. MISCELLANEOUS STUDIES 222
Low-Temperature Ductility and Hydrogen Embrittlement of Uranium – A Literature Review 222
The Effect of Alloy Additions and Heat Treatments on the Mechanical Properties of U–0.5% Ti Alloy 222

PAPERS AND PUBLICATIONS

PAPERS AND ORAL PRESENTATIONS 223

PUBLICATIONS 231

ORGANIZATION CHART 243

Summary

PART I. FUNDAMENTAL PROGRAMS

1. Crystal Physics

Crystals of refractory materials are being grown by internal centrifugal zone growth, from molten salt solvents, by temperature-gradient zone melting, from supercritical aqueous systems, and by the general Verneuil method. Some have been used by researchers of several disciplines. Manganese gallium ferrite crystals were grown and found favorable as a neutron beam polarizer, but improvement of crystal perfection is needed. Improving our internal centrifugal zone growth technique has increased the size of our UO_2 crystals to 1.3 cm in diameter X 2.2 cm long. To study the morphological and epitaxial characteristics of the UO_2-W eutectic structure, we developed a technique for selectively etching away the UO_2 matrix. This study is now in progress using a scanning electron microscope and x-ray techniques. Graphite crystals were grown in the carbon-nickel system by the temperature-gradient zone melting method. Single crystals of $^{237}NpO_2$ were grown up to 2 X 2 X 3 mm in size. For electron spin resonance studies crystals were grown of $HfSiO_4$ doped with Tb^{4+} or Yb^{3+}; $SrCl_2$ doped with ^{241}Am, ^{244}Cm, or ^{245}Cm; and ThO_2 doped with ^{151}Eu, ^{153}Eu, ^{241}Am, ^{243}Am, or Tl. Conditions favorable for the epitaxial growth of PbS were determined. We are analyzing infrared spectra of quartz crystals grown in RbOH solvent. The temperature dependence of the magnetic susceptibility of NpO_2 single crystals was measured from 77 to 800°K. An unexplained change of slope was observed near 300°K.

2. Deformation and Annealing of Metals

The unique surface texture and the zone at intermediate depths lacking certain of the strong orientations usually present in body-centered cubic metals appear to be associated with high frictional forces and fabricating under "high" body rolling conditions respectively. Despite differences in dislocation substructure and other deformation characteristics, the cold-rolled center texture of an Nb–40% V alloy was identical to that of pure niobium. Isothermal recrystallization of moderately deformed aluminum was studied by quantitative metallography and found quantitatively consistent with a proposed edge-nucleated, growth-controlled model. The kinetics of recovery of x-ray line broadening in niobium and Nb–40% V are being analyzed in terms of dislocation behavior.

3. Deformation of Crystalline Solids

Current work covers the nature of slip and twinning in rhenium single crystals, precipitation in refractory alloys of the hafnium-niobium type, the changes in structure during deformation of nonrandom alloys, and the characterization of dislocations and zonal twin dislocations in anisotropic crystals.

4. Diffusion in Solids

Cation self-diffusion coefficients have been measured by use of the tracer ^{233}U and the alpha-energy degradation method for the nuclear fuels UO_2 and UN_{1+x}. We carefully considered the relative importance of lattice and short-circuit diffusion in these fuels and also in refractory metals, including tungsten. Lattice diffusion coefficients for three tracers in tungsten were measured over the range 1300 to 2400°C and obeyed Arrhenius relations very accurately. A mathematical analysis was made for combined surface and grain boundary diffusion. The possible influence of oxidation on the previously observed near-surface effect was explored and found capable of explaining this effect. Residual activity methods for measurement of diffusion coefficients were critically examined with data obtained by use of the highly precise anodizing-and-stripping technique.

5. Electron Microscopy

Changes in microstructure of highly irradiated aluminum and aluminum alloys are described. In addition to voids and dislocation loops resulting from displacement processes, gas bubbles and a solid precipitate believed to contain transmutation-produced silicon are observed. Complementary studies of quenching defects in aluminum are summarized. Precipitation phenomena in Hastelloy N are reported, and observations on the recrystallization behavior of nickel 270 and the formation of gas bubbles in electrodeposited nickel are presented. Measurements of the stored energy induced in aluminum single crystals and gold-silver alloy polycrystals by room temperature tensile deformation are described.

6. Fundamental Ceramics Research

A multidisciplinary program of basic research focused on uranium mononitride and related actinide, hard-metal type compounds has begun to yield significant results. These results include electronic band structure calculations, transport property measurements, cation self-diffusion determination as a function of temperature and nitrogen pressure, and a new method of chemical analysis of nitrogen and carbon by proton reaction. The program involves work both at ORNL and also at several other laboratories using specimens supplied by ORNL.

7. Mössbauer Studies of Alloys

Mössbauer spectra taken at 4°K with ^{61}Ni in ionic compounds containing Ni^{2+} and Ni^{4+} ions led, after subtraction of second-order Doppler shift, to an approximate value for the difference of the nuclear radius of ^{61}Ni in the first excited state and the ground state. With this result, the measured isomer shifts in copper-nickel alloys could be interpreted in terms of changes of the electronic configuration of nickel upon alloying: nickel as impurity in copper has at most 5% of a 4*s* electron less or 25% of a 3*d* electron more than in pure nickel, in contradiction to predictions of a rigid-band model.

The results of Mössbauer experiments with ^{57}Fe following neutron capture in bcc iron-aluminum alloys were interpreted in terms of a collision model, by which we estimated the fraction of ^{57}Fe recoil atoms that come to rest at a lattice site, the number of point defects, and the distribution of iron and aluminum atoms in the immediate neighborhood of their final positions. Preliminary estimates of the influence of point defects on hyperfine fields were deduced from the experimental data in conjunction with the model results.

8. Physical Ceramics Studies

Analysis of dislocation behavior during deformation of single-crystal UO_2 specimens is being extended to hyperstoichiometric crystals. Activation energies determined during short-term sintering tests are not compatible with a diffusion-controlled process, suggesting material transport by a mechanism not diffusion controlled. The cause of loss of density in sintered specimens during long heating periods is being studied. The deformation of polycrystalline UN under controlled nitrogen pressure is being investigated.

9. Physical Properties

Accurate measurement and theoretically based analyses of related physical properties of solids provided guidelines for understanding of their electronic and lattice heat transport. A diversity of solids are under study. Electrical resistivity measurements on tantalum were completed to 2600°K to provide data for thermal conductivity extrapolations. The Lorenz function of gold was shown to be similar to that of copper from 80 to 400°K. Thermal conductivity studies on ThO_2 and UO_2 showed their Debye temperatures to be nearly equal. Measurements on LiF revealed a strong radiation component that supplements lattice conduction above 450°K. Calorimetric studies on nickel and iron revealed specific heat capacity discontinuities at their Curie temperatures. Studies are in progress on UN and ThN.

10. Spectroscopy of Ionic Media

Absorption spectra of molten salts are giving details about the structures of ionic entities in melts. Results concern the nature of nickel complexes and bismuth species in molten halides, methods for studying molten fluorides, and observations on related solids.

11. Superconducting Materials

The effect of the magnetic nature of a precipitate particle on its ability to pin superconducting fluxoids was investigated by dispersing yttrium and dysprosium metals in niobium and testing the composites at low temperatures. Both additions drastically increased the superconducting critical current density and magnetic hysteresis of the niobium at all fields and temperatures in the superconducting state but did not change the limiting fields and temperatures for the occur-

rence of superconductivity. The ability of a planar defect to pin fluxoids was investigated by examining the grain size dependence of the critical current density in Nb–33% Zr. When the effective grain or cell size was varied from 0.25 μ to 1.5 mm, the apparent critical current density, at constant applied field and temperature, decreased by more than two orders of magnitude.

12. Surface Reactions of Metals

Our interest in the role of stress in the oxidation of metals and alloys has continued. Our research efforts have been divided between studies of stress effects in the oxidation of refractory metals and in a uranium-base alloy, diffusion measurements in tungsten, and a further refinement of our method for deducing strain and thickness for thin oxide films from their x-ray line shapes.

Oxidation rate measurements for tantalum confirmed rate reversal with increasing temperature between 650 and 800°C. We are using our "flexure" technique in investigating the role of stress in this phenomenon. The effect of stress was also evident in the surface morphology of the oxide formed on U–7.5% Nb–2.5% Zr. Oxidation rate measurements between 160 and 275°C are reported as well as the results of a hot-stage-microscope study of the oxidation of the alloy at 800°C. Diffusion data for Nb, Ta, and W in tungsten were obtained from about 1300 to 2500°C. The importance of short-circuit diffusion modes was emphasized in this work. A reassessment of the methods of x-ray line shape analysis for thin oxide films showed that our experimental data suffered from a "hook effect," which has led to errors in thickness estimates by this technique. Corrections for this error have been developed.

13. Theoretical Research

Previously developed band theory programs were used to investigate the thermopower of copper and the Knight shifts of copper and some of its alloys. A recently developed technique for investigating the electronic states in disordered systems was tied in with a method that was developed earlier, and the experience already gained with the older method has been used to elucidate the newer. The motion of protons in molecules has been investigated, showing that the protons are more delocalized in such systems than has usually been assumed.

14. X-Ray Diffraction

Routine diffraction work during the reporting period is summarized. Crystal structures of $RbBrO_4$ and two forms of $Ti(AlCl_4)_2$ were studied. A computer program for plotting stereographic projections of lattice plane normals and directions was prepared. Metastable phases formed on quenching and aging a certain "gamma-stabilized" uranium alloy were shown to have structures based on systematic atom displacements rather than on chemical ordering as previously reported.

Thermal diffuse x-ray scattering from samples of highly oriented graphite was analyzed to give a detailed model of the transverse and longitudinal vibration modes of the lattice. Good agreement is obtained with previous estimates of total rms displacements and with inelastic neutron scattering measurements.

Small-angle x-ray scattering from aqueous solutions of salts of aliphatic quaternary ammonium halides demonstrated that polymolecular clusters of organic cations (or micelles) probably do not exist at the concentrations studied. Small-angle scattering from Ti–25 at. % Nb alloys, aged after beta quenching so as to form the metastable omega phase, has been analyzed to yield quantitative size and qualitative distribution parameters for the omega particles; this work has been complemented by high-angle diffraction studies of single crystals of the same alloy in several aged conditions.

PART II. HIGH-TEMPERATURE MATERIALS

15. Physical and Mechanical Metallurgy of Refractory Alloys

Details of the interactions of refractory metals with active gases in vacuum between 600 and 1200°C were reviewed; the extent and kinetics are governed by the deviation of the interstitial concentrations from equilibrium. The solubility, diffusivity, and permeability of nitrogen in tungsten were determined and compared with published data and with other metals. The permeability of nitrogen through tungsten is several orders of magnitude lower than through other refractory metals. The precipitation kinetics of Nb-Hf alloys within the miscibility gap are controlled by excess vacancies. Modulated structures have not been observed. The creep-rupture properties to 1000 hr of Nb-, Ta-, and Mo-base alloys are sensitive to the pretest annealing temperatures. The data are being correlated with the microstructures.

Brazing alloys based on Ti-Zr-Ge and Ti-V-Cr are suitable for joining refractory metals, ceramics, and

graphite to themselves and to each other. About 80 gas tungsten-arc welds were used to construct a complex T-111 forced-circulation loop. Three field welds were made in a portable inert-atmosphere welding device. Theoretically based analyses of the effects of temperature and alloying on the electronic and lattice components of thermal conductivity of metals were used to extrapolate accurate low-temperature data to 1700°K. Calculated values of the thermal conductivity of tungsten alloys at high temperature were within 10% of measured values where available.

16. Tungsten Metallurgy

In our extrusion development program we have determined the effect of prior metallurgical structure and extrusion temperature between 1150 and 1700°C on the structure of duplex tube-shell extrusions of powder-metallurgy tungsten at an extrusion ratio of 3. With the extrusion conditions investigated, a wrought duplex structure was obtained only by extruding a recrystallized starting structure at 1150°C.

Large quantities of high-purity chemically vapor-deposited (CVD) tungsten sheet were produced for mechanical property measurement, but deposition of large sheets of W–5% Re was handicapped by nodule formation and gradients in deposit thickness and rhenium composition. Uniform rhenium alloying was obtained by maintaining the deposition temperature above 700°C. Uniform deposit thicknesses were obtained by raising the deposition pressure from 10 to 50 torr, but this also reduced the rhenium deposition efficiency. Periodic reversal of the gas flow to minimize gas phase depletion resulted in a layered structure with fine interlayer porosity. Fully dense deposits of vanadium were obtained by the hydrogen reduction at 1000 to 1200°C of three different feed materials – VCl_3 powder entrained with argon, VCl_4 gas chlorinated in situ, and VF_5 gas.

Bend tests of CVD W–5% Re sheet showed a minimum in the ductile-to-brittle transition temperature of 150°C after annealing 1 hr at 2200°C. Lower annealing temperatures were not sufficient to sinter fine grown-in porosity in the as-deposited material.

Gas bubble formation in annealed CVD materials was correlated with the fraction of the absolute melting point (T_m) at which the material was deposited. In materials deposited below about $0.3T_m$ a large supersaturation of vacancies can be produced during deposition and their coalescence with gaseous impurities during annealing results in the nucleation and growth of gas bubbles.

Intergranular hot cracking of fusion welds in several grades of tungsten was examined by electron fractography. From these observations a mechanism of hot cracking was proposed based on the growth and coalescence of pores into grain boundary cracks by the stress-induced diffusion of vacancies.

In a comparison of the creep-rupture properties of arc-melted (AM) and powder-metallurgy (PM) W–25% Re at 1650 and 2200°C, the PM material exhibited shorter rupture lives and much lower ductilities than the AM material. Based on 1000-hr stress-rupture data for arc-melted tungsten alloys between 1650 and 2200°C the W–5% alloy is the strongest, followed by unalloyed W, W–26% Re, and W–25% Re–30% Mo.

17. Alkali-Metal Corrosion of High-Temperature Materials

Examination of published oxidation results for vanadium-titanium and vanadium-aluminum alloys in sodium showed that the reaction kinetics is consistent with an internal oxidation model in which solid-state diffusion of oxygen into the alloys controls the rate of oxide precipitation.

At 550°C unalloyed vanadium picked up oxygen at 0.5 ppm/hr at 2×10^{-6} torr O and 0.1 ppm/hr at 2×10^{-7} torr. In static capsule tests at 600 and 800°C, sodium (50–1300 ppm O) did not penetrate vanadium containing up to 1900 ppm O. The vanadium gettered oxygen from the sodium, indicating a large equilibrium distribution coefficient.

We are measuring the mass transfer of carbon and nitrogen from stainless steel to vanadium in a sodium environment using bimetallic thermal convection loops.

The compatibility of thermal insulation with stainless steel from 700 to 815°C in moist air was determined. We found (1) no catastrophic oxidation of type 316 stainless steel, (2) type 304L stainless steel superior to type 316 in scaling resistance, (3) temperature cycling effects on scaling depending on the thickness of the scale, and (4) more scaling with asbestos-diatomaceous silica insulation than with alumina-silica "blanket" insulation.

Hafnium, oxygen, and nitrogen were transported from hot-leg specimens in a T-222 thermal convection loop operated with lithium. Thermal aging and nitrogen pickup reduced room-temperature ductility in specimens exposed at 1270 to 1300°C.

Fabrication of a T-111 forced-circulation lithium loop was completed and shakedown operations began. Weld tests of T-111 and T-222 conducted in conjunction with loop assembly showed no breakdown in corrosion

resistance even at 500 ppm O contamination; however, weld heat treatment at 1300°C was required to eliminate base metal corrosion.

Oxygen-induced attack of CVD niobium and arc melted W–25% Re was found in refluxing potassium capsule tests at 1200°C. No attack of TZM or FS-85 was found in boiling potassium natural-circulation loops at 1250°C. Slight mass transfer was observed in the nozzle-turbine blade test section of a D-43 forced-circulation boiling potassium loop after 10,000 hr at a maximum temperature of 1200°C. Boiler and condenser regions of the loop showed negligible corrosion.

The threshold oxygen concentrations in Nb or Ta for penetration by K, Na, and Li at 600°C were determined. Solution interaction parameters were used to characterize the effect of oxygen in Na and K on the dissolution of Nb and Ta.

18. Nitride Fuels Development

We are developing nitride fuels for space-nuclear and liquid-metal fast breeder reactors (LMFBR). Properly designed (U,Pu)N LMFBR fuel pins can operate at significantly higher linear heat ratings and power densities than can mixed oxides. Nitride fuels also appear more fabricable and more compatible with cladding alloys than are carbides. Our program includes synthesis, fabrication, characterization, thermodynamic studies, compatibility studies, and irradiation testing.

We continued to develop processes for fabricating a variety of sizes and shapes, develop powder characterization procedures, and upgrade equipment. Specimens of $U^{15}N$ were prepared for irradiation and other tests. Synthesis and fabrication of mixed (U,Pu)N began.

Conversion of sol-gel oxide to carbonitride was greatly enhanced when carbon was incorporated in the sol. The kinetics of sol-gel conversion reactions are studied in detail to optimize efficiency.

Our compatibility and thermodynamic studies deal primarily with vanadium-base LMFBR cladding alloys. We are concerned with the effects of oxygen contamination, temperature gradients, and nuclear burnup on compatibility. Oxygen contamination may be desirable in nitride fuels because it can reduce twenty-fold the nitrogen pressure in $UN\text{-}U_2N_3$ and thus might prevent reaction with the cladding. We confirmed the existence of UVC_2 and found evidence for a more active form of carbon in the V-C-N system.

To determine its basic irradiation behavior under LMFBR conditions UN was irradiated at central fuel temperatures of 1200 to 1400°C to a burnup of 1.8 at. %. Cladding restraint significantly reduced fuel swelling. We continue to investigate thermal contact resistance associated with the fuel-cladding interface, since this may limit fuel performance.

19. Materials Development for Isotopic Power Programs

Research and development on materials for encapsulation of isotopic power fuels is being carried out for space and terrestrial (including undersea) applications.

Tungsten was preferentially lost from W–25% Re as a volatile oxide in the thermionic range of 1650 to 1950°C and 10^{-7} to 10^{-4} torr O_2, pressures expected from Cm_2O_3 fuel. Similar oxygen pressures drastically increased creep rates of tungsten and W–50% Mo, and stress enhanced sublimation. We developed an analytical model to predict failure time of nonvented capsules containing alpha-emitting isotopes from conventional creep data. Compatibility of capsule material with $^{244}Cm_2O_3$ is being tested at temperatures representative of various energy conversion devices. Tests for 1000 hr at 1650 and 1850°C were completed. We developed several alloys for brazing tungsten for service at 1650°C under vacuum. Intricate tungsten test components and coated microspheres were prepared by chemical vapor deposition.

We obtained creep-rupture data for welds and tensile data for aged specimens of Haynes alloy No. 25. Welds were comparable to wrought material although failures were predominantly at the fusion line. We uncovered a highly embrittling aging reaction at about 700°C, probably due to precipitation of β-Co_3W. The creep strength decreased in vacuum, particularly for thin specimens. Less volatile and more oxidation-resistant alloys are being investigated; they have ordered structures and high concentrations of noble metals.

Type 316 stainless steel, Haynes alloy No. 25, and Hastelloy C capsules were compatible with nonradioactive $SrTiO_3$ and Sr_2TiO_4 up to 1100°C. Further investigation of these alloys with SrO is seeking the nature of an observed interaction.

We developed and successfully used electron-beam welding and ultrasonic inspection techniques for the SNAP-21 and SNAP-23 capsules.

For the Isotope Kilowatt Program, we reviewed thermoelectric conversion systems and conceptual design studies on a 3-kw thermoelectric converter. A pellet-type converter using direct heat transfer from a tungsten fuel block shows the highest conversion efficiency of about 8%.

PART III. GENERAL FUELS AND MATERIALS RESEARCH

20. Fuel Element Fabrication Development

Irradiation testing of UAl_x and burned U_3O_8 powders as dispersion fuels was extended to higher loadings and burnups. No evidence of potential failure was noted at conditions proposed for advanced HFIR cores. Significantly less swelling was noted for the burned U_3O_8 fuels than for high-fired U_3O_8 or UAl_x. The amount of swelling may be predicted from the initial void volume in the plates and the burnup.

A second irradiated HFIR fuel element was examined in the hot cells. It was in even better condition than the first one, with no significant dimensional changes or metallographic evidence of incipient failure. The oxide deposit was much more uniform and was thinner.

Formation of the dogbone shape during rolling of fuel plates was shown by the use of high-speed motion pictures. During much of the rolling, voids are present at both ends of the core. Techniques for reduction of the amount of dogboning are proposed. The volume of fabrication voids in such plates depended on both the type and concentration of the U_3O_8. Conditions reducing dogboning also reduce the void volume. Sol-gel U_3O_8 offers excellent possibilities for increasing the void volume. The fit between the fuel cores and the frames before rolling was not as critical as previously expected.

Miniature fuel plates electrolessly coated with nickel-phosphorus alloy have been placed within the reactor. On samples, the coating resisted spalling from thermal shock and treatment at 300°C but spalled completely after being held at 500°C. We developed anodic films that protected pure aluminum against corrosion in static tests but not aluminum alloys under dynamic conditions with high heat fluxes.

Suitable electron-beam welds were made with either type 6061 or 2219 aluminum in HFIR joint geometries. While adequate penetration was achieved, the strengths are slightly lower than desired. Explosive welding techniques were developed for attaching spacers to HFIR fuel plates. While only intermittent bonds have been achieved in the preliminary tests, the technique appears to be adaptable but expensive.

For applications below about 200°C, the tensile strength of dispersion-strengthened aluminum can be enhanced by dissolved magnesium. The room and high-temperature strengths and ductility of $Al\text{-}Al_2O_3$ dispersions can be improved by use of atomized alloy powders containing Fe, Mo, Zr, Ti, and Cr.

21. Joining Research on Nuclear Materials

We are concerned with the weldability of materials applicable to the fabrication of nuclear power plants. Our initial studies are centered on the weldability of alloys containing nickel ranging from the low percentages used in stainless steels to the large amounts represented by Inconel 600. Our concern is with both weld metal and heat-affected zones.

Sulfur in high-nickel alloys decreased hot ductility and drastically impaired recovery of ductility in the heat-affected zone after exposure to a peak temperature of 2450°F. Manganese did not improve the hot ductility but appeared somewhat detrimental. Phosphorus was not detrimental. Work on intermediate-nickel Incoloy 800 class of material has concentrated on intermediate temperatures (1400 to 1600°F). The presence of titanium is necessary if elevated-temperature ductility is to be restored after the alloy has undergone a ductility minimum. Titanium mainly enhances the propensity toward recrystallization.

Both sulfur and phosphorus increased the hot-cracking sensitivity of weld metal in the high-nickel alloys of the Inconel 600 class. Adding Si, Mn, Al, or Ti decreased the propensity toward cracking. Minor variations in chemical composition affected the amount and distribution of ferrite in stainless steel welds, particularly for the chemical compositions tailored to provide specific ferrite percentages.

The investigation of the effect of defects on the mechanical properties of weldments has begun. We are developing weld discontinuities that simulate, both in size and location, those found in actual welds.

22. Nondestructive Test Development

We continued analytical studies of eddy-current phenomena, deriving new equations, refining old derivations, and writing computer programs to use the equations to study cases of interest. Improved eddy current coils were designed and made. An infrared microscope was developed on a subcontract at the University of Tennessee.

Fabrication and measurement studies are continuing on reference standards for ultrasonic inspection. The schlieren system was improved and used in preliminary work on welds. We improved the system for frequency analysis and applied it to the study of frequency effects related to several variables in ultrasonic testing.

Computer programs were prepared to aid the development of graphical plots for data from x-ray attenuation experiments. Work has begun on the use of Compton

backscattered radiation for the examination of coatings or claddings on reactor components.

23. Research Reactor Core Improvement and Procurement Assistance

Providing technical assistance to the AEC Division of Reactor Development and Technology with managing the procurement of research reactor fuel elements was continued. Techniques were developed to roll crush UAl_x fuel in yields of 85 to 90% usable material, compared to 69% by other processes. As another aid to production we showed that chemical cleaning could enable bonding of type 6061 aluminum to itself, meeting present nonbond specifications.

Fuel plates of HFIR geometry were successfully fabricated with a 125% loading of both high-fired and burned U_3O_8. With the modified conditions, inspection problems were encountered. Full-size ATR fuel plates 8 and 19 were fabricated to study dogboning. Dogboning was reduced most effectively by enlarging and weakening the core by adding more aluminum.

The calibration curves for the x-ray attenuation homogeneity scanner were extended to higher uranium concentrations and to the use of the burned U_3O_8 fuels. An extensive study of the effects of the processing variables on the sensitivity of radiographic film for determining variations in fuel content has continued.

A cost effectiveness plan for determining the total cost of a project similar to increasing the loading of the HFIR fuel element was developed. This computer technique takes into account the various probabilities for success. With HFIR, savings of $3,500,000 or more are predicted.

HFIR fuel element production at Metals and Controls has continued on schedule with a minimum of problems. Fuel plate yields for the year were 92.45%, a slight improvement over last year. Waivers are still being required on most fuel elements.

We began to assist Phillips Petroleum Company with purchasing fuel elements for the Power Burst Facility. Specifications, procurement documents, drawings, and potential contractors have been reviewed.

24. Sol-Gel Fast Reactor Oxide Fuels

The objective of this program is to obtain an economically optimized $(U,Pu)O_2$ fuel cycle for a Liquid Metal Fast Breeder Reactor (LMFBR) by extending the performance capability and advancing the fabrication technology for oxide fuels. Primarily, we use structures derived from sol-gel processed material. With the Sphere-Pac process, we loaded a variety of irradiation capsules containing $(U,Pu)O_2$ microspheres. We developed methods for fabrication of pellets from sol-gel-derived material with controlled densities ranging from 80 to 93% of theoretical and with an adjusted oxygen-to-metal ratio of 1.98. We designed and fabricated two instrumented capsules for testing fuel under power transient conditions in TREAT. We fabricated five doubly encapsulated sodium bonded fuel pins for irradiation in EBR-II; these capsules are performing satisfactorily.

Uninstrumented irradiations in the ETR to 5 at. % burnup and instrumented tests in ORR confirmed that Sphere-Pac fuels will perform in reactors comparably to pelletized fuels of similar smear density. In instrumented tests Sphere-Pac fuels showed thermal conductivities similar to those for pelletized fuels of comparable density. Our work on mathematical analysis of irradiation experiments was directed toward the verification of the accuracy of our reactor physics and heat transfer analyses. Correlations between experimental results and calculations show that the calculations are quite accurate and reliable for extrapolation of the probable performance of fuel pins in thermal reactor environments.

25. Zirconium Metallurgy

Most of the mechanical and physical properties of zirconium alloys depend strongly on crystallographic texture. For many applications, therefore, a particular texture is desired. Our studies of the fabrication and resulting textures in Zircaloy tubing have enabled us to predict the texture produced by any fabrication sequence, to specify procedures to yield a given texture, and to design the dies and mandrels to most easily effect control of texture. To determine factors influencing the development of texture during fabrication, we examined texture after each step in fabricating tubing by a variety of methods and variations. Parameter charts that interrelate up to seven fabrication variables facilitate prediction and control of texture. In addition, annealing, when required, may be useful in tailoring texture. Finally, the biaxial yield behavior of Zircaloy tubing has been examined as a function of texture, and a method of predicting this behavior from texture data has been developed.

PART IV. REACTOR DEVELOPMENT SUPPORT

26. Desalination

Metallurgical assistance to the Desalination Program was directed at both the Unclad Metal Breeder and a

uranium-metal-fueled pressurized water reactor. Literature surveys on the materials problems were made for both projects.

The Th–20 wt % U alloy for UMBR can be cast into a configuration containing sharp corners without cracking. Excellent structures of a type desirable for good irradiation performance were achieved. Physical property measurements were also completed on such alloys produced by various techniques. The powder metallurgy alloys varied widely in electrical resistivity.

27. Gas-Cooled Reactor Program

All-ceramic nuclear fuels consisting of $(Th,U)O_2$ or $(Th,U)C_2$ particles with composite coatings of pyrolytic carbon and SiC offer considerable advantages as fission-product-retaining fuel for high-temperature gas-cooled reactors. Much of our support for the Program consisted of the preparation and irradiation testing, to high fast fluence, of coated particles and simulated bonded-bed fuel elements. Testing to fast fluences near the design maximum for HTGR's demonstrated good performance of particles that had isotropic outer coatings with densities between 1.7 and 1.9 g/cm^3, as predicted by our mathematical model. However, fast-neutron irradiation of injection-bonded coated particles resulted in complete debonding or coating breakage. Efforts are now concentrated on preparation of stable fuel elements by careful selection of raw materials and use of other fabrication methods. We also investigated the corrosion properties in steam at 1100 and 1200°F of nickel alloy weldments proposed for advanced HTGR steam generators. We characterized the aggregates and cast concrete bodies of three mixes being used in mechanical properties studies at other laboratories. A significant new activity in the Program supports the development of fuel elements for a gas-cooled fast breeder reactor (GCFR). We are investigating the compatibility between fuel and cladding materials at the temperatures and heat ratings proposed for a GCFR and participating in the design, fabrication, and examination of irradiation experiments on GCFR fuel pins.

28. Heavy Section Steel Technology

The Metals and Ceramics Division is actively involved in the Heavy Section Steel Technology (HSST) Program as consultants and experimentalists. Our studies on heavy section steel submerged-arc weldments showed that the fracture toughness of the weld metal is superior to that of the quenched and tempered 12-in.-thick Mn-Mo-Ni steel base plate. A coordinated effort between this Division and the Inspection Engineering Department showed that entrapped slag is responsible for the indications nondestructively disclosed in HSST plate 01.

29. High Flux Isotope Reactor Target Development

The Transuranium Project is producing quantities of the heavier transuranium elements for research by successive neutron captures in plutonium, americium, and curium. The irradiations are carried out in the High Flux Isotope Reactor. Target elements are removed periodically and reprocessed to obtain the product actinides and to recycle target actinides to the HFIR.

We design, fabricate, and evaluate the performance of target elements, fabricate special target assemblies and sources, and monitor the performance of these elements in the HFIR. The remote fabrication line and encapsulation equipment were operated to produce targets, hydraulic rabbits, and sources containing ^{242}Pu, ^{244}Cm, ^{253}Es, and ^{252}Cf. Some minor difficulties were encountered with the remote equipment, but suitable improvements were made to meet the necessary schedules and performance standards. Targets containing ^{242}Pu that had been irradiated in only the HFIR performed satisfactorily for 17 full cycles in the HFIR, accumulating fluences ranging from 8.2 to 9 $\times$ 10^{22} neutrons/cm^2 (>0.81 Mev) and attaining 42 to 46% FIMA at the midplane. This is both a higher level of burnup and fast flux exposure than was experienced by the targets that failed after irradiation in both Savannah River and HFIR. We continued seeking the causes of low-ductility failures in the HFIR targets and alloys more suitable for cladding use.

Our failure model predicts the target life will be extended with more porosity available in the pellets. At present, seven targets in the HFIR have been irradiated for over two years. Six low-density targets have achieved a burnup of approximately 62% FIMA. One of the original targets that had not been irradiated in Savannah River Reactor has been irradiated to 70.5% FIMA without failure.

30. LMFBR Cladding and Structural Materials

This work is directed at both short- and long-term LMFBR applications in three general areas: (1) cladding fabrication, (2) effects of irradiation on cladding and structural alloys, and (3) welding for vessels and components.

As the result of studies on the effect of drawing and interpass annealing schedules, we produced small-diameter tubing of type 316 stainless steel with an

ASTM grain size of 12 that otherwise met the specifications for FFTF fuel cladding. Tubes fabricated from titanium-modified type 304L stainless steel by a schedule involving 10 to 15% reduction per pass exhibited less preferred orientation than those undergoing 20 to 30% reduction per pass; the differences in texture between drawn and planetary-swaged tubing also was established. The morphology of ϵ- and α'-phases produced during cold working of titanium-modified type 304L stainless steel was determined. Boron contents greater than 10 ppm were detrimental to the hot ductility of type 316 stainless steel. Ultrasonic and dye-penetrant techniques were developed for nondestructive evaluation of LMFBR fuel cladding. The ductility of titanium-modified type 304L stainless steel tubing in biaxial creep-rupture tests was comparable to that of commercially available unmodified alloy.

The elevated-temperature mechanical properties of type 316 stainless steel were determined after irradiations at 550, 650, and 750°C to a thermal fluence of 9×10^{20} neutrons/cm^2. The short-time tensile ductility at 550 to 750°C was lowered in all cases and varied inversely with the test temperature. Increases in yield strength after irradiation at 650 and 750°C resulted from thermal aging and not from the effects of irradiation. At 650°C the creep rate increased and the ductility and rupture life decreased with increasing irradiation temperature. The increase in creep rate was the result of thermal aging and not of irradiation. The effect of irradiation temperature in the range of 370 to 525°C and fast neutron fluence (>0.1 Mev) to 9×10^{22} neutrons/cm^2 on the microstructure as revealed by electron microscopy was investigated for types 304 and 304L stainless steels. Irradiation-induced voids approached a limiting size, which increased with irradiation temperature. Specimens of titanium-modified type 304L stainless steel containing 20 ppm of cyclotron-injected helium exhibited significantly higher ductility than comparable helium-injected specimens of standard type 304L stainless steel. An analytical study showed that while ion bombardment in cyclotrons cannot precisely simulate neutron-induced damage, it may serve as a useful supplement to neutron damage studies. Additions of 0.1% Ti increased the creep ductility of Incoloy 800 at 700 and 760°C; this effect was apparently independent of carbon content in the range 0.03 to 0.12%. Unalloyed vanadium irradiated at approximately 600°C to a maximum total neutron fluence of 1.7×10^{22} neutrons/cm^2 in the EBR-II contained 5×10^{15} voids/cm^3 with an average diameter of 120 A. No voids were observed in V–20% Ti irradiated under comparable conditions.

The effects of welding processes and conditions on the properties of thick-plate weldments in type 304 stainless steel were determined.

31. Military Reactor Fuel Element Procurement Assistance

During this year, assistance in standardization of specifications, review of technical requirements, and participation in fuel procurement and quality control audits was associated with the Type 4 core for the Navy's PM Reactor in Antarctica, two half-cores for the Army's MH1A Reactor, and 116 ETR-type fuel assemblies for the Air Force reactor at Wright-Patterson Field (AFNETR). Accomplishments include expediting prompt delivery of a PM core but rejection of defective control assemblies, improvement of MH1A specifications, and cost reduction for AFNETR fuel.

32. Molten-Salt Reactor Program

The MSRE has been critical for 15,425 hr (June). Surveillance samples of graphite and Hastelloy N have been removed periodically for examination. The samples were mechanically sound and showed no evidence of corrosion. The mechanical properties of the Hastelloy N were measured and the fracture strain was reduced.

Advanced molten-salt reactors require improvements in the materials of construction. The addition of small amounts of Ti, Hf, and Nb improve the resistance of Hastelloy N to embrittlement by irradiation, probably through formation of a very fine MC-type precipitate. Our corrosion work has focused on the compatibility of Hastelloy N with the new coolant salt, sodium fluoroborate. The higher corrosion rate of this salt is attributed partially to impurities.

The dimensional changes of graphite under neutron irradiation pose some problems to advanced reactors. We have irradiated samples of most commercial graphites and find that available materials satisfy the requirements for our first reactor. Coupling the dimensional measurements with x-ray anisotropy measurements showed that growth rates of the crystallites depend solely upon orientation. We are developing graphites that are dimensionally more stable under irradiation. Techniques were developed for carbon impregnation of graphite with gaseous reactants to achieve the very low gas permeability required for an advanced system.

33. Reactor Evaluation

We continued to assist the AEC by developing computer codes for the analysis of the economics

involved in fuel cycle and codes for the analysis of fuel element performance. A fuel performance model and computer code for pin-type fuel elements are being developed to more effectively coordinate our present performance evaluations with radiation experiments being conducted at ORNL and elsewhere. The computer code development for economic analyses is being done to incorporate more detailed analysis of individual steps involved in fuel element fabrication and to model the management decisions required in a growing nuclear economy. In addition to these efforts, we assisted in the evaluation of several reactor concepts during the year and continued the assistance to the AEC aimed at updating the *Civilian Nuclear Power, a Report to the President – 1962.*

34. Thorium Utilization

The thorium utilization program is concerned with the use of thorium to economically produce electric power by the thorium-^{233}U fuel cycle. Before the thorium-^{233}U fuel will be practical, new fabrication processes and equipment must be developed to handle the highly radioactive recycle fuel and demonstrated by irradiation in power reactors of fuel fabricated by them. In line with this objective, we are developing processes and designing equipment for the remote refabrication of thorium-^{233}U-bearing High-Temperature Gas-Cooled Reactor fuels, to be demonstrated in the recently completed Thorium Uranium Recycle Facility. This facility has already been used for preparing 63 kg of ^{233}U-bearing salt for the Molten Salt Reactor Experiment. We also prepared 32 kg of Th-^{233}U oxide fuel for the High-Temperature Lattice Test Reactor.

35. Water Reactor Safety

The coordination of all AEC-sponsored programs on the failure of light-water reactor fuel rods during a loss-of-coolant accident has been undertaken at the Oak Ridge National Laboratory. We give briefly the reasons for concern over fuel rod failure and outline the scope of the coordinating effort. Tests to evaluate the effects of environmental and material variables on the mode of failure of the fuel cladding are also described.

PART V. OTHER PROGRAM ACTIVITIES

36. Absorber Materials for SO_2 from Flue Gases

Pollution control studies of the reaction of SO_2 with $NaAlO_2$ granules and subsequent regeneration in H_2 showed that cyclic phase transformations did not cause breakup of the spheres. Extensive breakup was observed on heating if the $NaAlO_2$ was allowed to absorb moisture.

37. Army Pulsed Radiation Facility Reactor

In seeking an improved core alloy over U–10% Mo for pulse reactor service, we determined the toughness properties of several uranium-molybdenum alloys containing small additions of Al, Cr, Nb, Ta, or Ti. After aging at the maximum embrittlement temperature of 475°C, at least one alloy showed a clear superiority in notch toughness at all aging times to 64 hr.

38. Metallography

The alpha metallography facility has operated satisfactorily for almost a year. Photomacrography attachments have been added to our metallograph. Two glove boxes have been added to provide low-power photomacrography and microhardness testing. Electron microprobe analysis continues to be a prime research tool. A shielded electron microprobe analyzer has been installed in the High Radiation Level Examination Laboratory for the analysis of highly radioactive specimens. Our Quantimet Image Analyzing Computer has been of great help in quantitative metallography. A proper setting of the threshold control, correct choice of magnification, and the selection of a sufficient number of fields are very important for analyzing minute microstructural features. Hot-stage microscopy has been used to a definite advantage, and a résumé was issued on new equipment and techniques in the field.

39. NERVA Program Metallurgical Support

Several eddy-current probes have been designed, built, and tested for nondestructive inspection of coolant channels in beryllium reactor components. These probes have demonstrated the feasibility and usefulness of the inspection techniques and may be used as prototypes for quality control instruments. Outgassing of NERVA fuel elements is being measured under conditions similar to those expected in space operations; the rates for 11 different gases can be determined semicontinuously during each test run, and the results can be analyzed and plotted as a function of time and temperature with the aid of a computer. The emphasis of the adhesion studies has been shifted to the effects of shear motion on adhesion in controlled vacuum environments.

40. Miscellaneous Studies

Literature was surveyed on the effects of several factors on the ductile-to-brittle transition in uranium and on the hydrogen embrittlement of uranium.

We determined the effects of several ternary additions and heat treatment on the tensile properties of U–0.5% Ti.

Part I. Fundamental Programs

1. Crystal Physics

G. W. Clark

We are primarily concerned with the growth of crystals of high-melting-point refractory materials. Crystals are often required to characterize physical properties uniquely. Very specific crystals (phase, composition, purity, perfection, etc.) are frequently required in technical devices for their operation. Since suitable crystals are often difficult to obtain, we are conducting a continuing program to provide crystals needed in research, to devise and improve methods of crystal growth, and to develop increased understanding of crystal growth processes and kinetics. Crystals are being grown by several methods: by internal centrifugal zone growth, from molten-salt solvents, by temperature-gradient zone melting, from supercritical aqueous systems, and by the general Verneuil method. Some of these crystals have been used by other researchers in investigations of electron spin resonance; optical, magnetic, and elastic properties; deformation; fission gas release; diffusion; radiation damage; thermal conductivity; and a possible neutron-beam chopper, monochromator, or polarizer. Also, we are investigating selected physical properties, both those related to the crystal-growth process and those important for characterizing new compounds.

FERRITE CRYSTAL GROWTH FOR NEUTRON BEAM CONTROL

G. W. Clark

The use of a ferrite crystal as a neutron-beam polarizer was proposed by Mook.[1] By adjusting the chemical composition of a magnetic crystal whose spins are all parallel and antiparallel to the direction of magnetization, the condition[2] can be found where the sum of the magnetic scattering from one sublattice just balances the sum of the nuclear scattering. Then the neutrons scattered from the other sublattice will be polarized. On this basis, Mook suggested a manganese gallium ferrite. We have successfully grown several boules by the Verneuil method, using an oxyhydrogen flame, and obtained conditions favoring the growth of oriented single crystals, free of any second phase. The results from our first crystal test specimen are most encouraging. Its measured figure of merit as a neutron monochromator and its absorption and reflection factors are most favorable when compared to the presently commonly used Co–8% Fe crystals. However, some improvement of crystal perfection is needed. The reflected beam was 95% polarized, which is just less than the usual 96 to 97% obtained from Co–8% Fe crystals. This work will continue.

INTERNAL CENTRIFUGAL ZONE GROWTH

J. C. Wilson G. W. Clark
K. W. Boling[3] A. T. Chapman[4]

We are progressively improving our internal centrifugal zone growth technique.[5] In this technique, a preheated ceramic or cermet rod moves slowly through

[1] Private communication from H. A. Mook, Solid State Division.

[2] P. A. Egelstaff, *Thermal Neutron Scattering,* Academic Press, New York, 1965, p. 36.

[3] Mechanical Properties Group.

[4] Consultant from Georgia Institute of Technology, Atlanta, Ga.

[5] A. T. Chapman and G. W. Clark, *Metals and Ceramics Div. Ann. Progr. Rept. June 30, 1965,* ORNL-3870, pp. 3–4.

a radio-frequency induction coil, causing progressive melting (2500 to 3300°C) and recrystallization inside of its solid shell. Thermal gradients favorable to the formation of a single crystal or a eutectic matrix along the rod axis are promoted by rotation of the rod and centrifugally casting the internal melt against the inner rod wall under specific conditions. This year we grew our largest, apparently crack-free UO_2 crystal – 1.3 cm in diameter X 2.2 cm long.

Crystals of UO_2 for research were furnished to at least eight different experimenters at ORNL and other laboratories during the year.

The ICZG technique was extended to ThO_2-UO_2 mixtures containing more than 60 wt % ThO_2 by using rf-power at a frequency of 26 MHz in place of the previous 4 MHz. The results of tests are now being evaluated.

MORPHOLOGIES OF ROD AND LAMELLAR TUNGSTEN IN UNIDIRECTIONALLY SOLIDIFIED UO_2-W EUTECTIC

A. T. Chapman[4] R. J. Gerdes[6] G. W. Clark

Eutectic structures result from ICZG in a pressed bar containing a mixture of UO_2 and from 5 to 15 wt % tungsten. The unidirectional solidification inherent in our process yielded pronounced alignment of tungsten rods or lamellae in the UO_2 matrix. We developed a technique for selectively etching away the UO_2 matrix uniformly and leaving the tungsten structure exposed for study. The morphologies of the tungsten rods and lamellae, their crystalline perfection, and the epitaxial relations between the tungsten and UO_2 are now being studied with a scanning electron microscope and x-ray techniques. Figure 1.1 shows an example of exposed tungsten rods above the UO_2 matrix. The tungsten rods are close to 1 μ in diameter in this observed area.

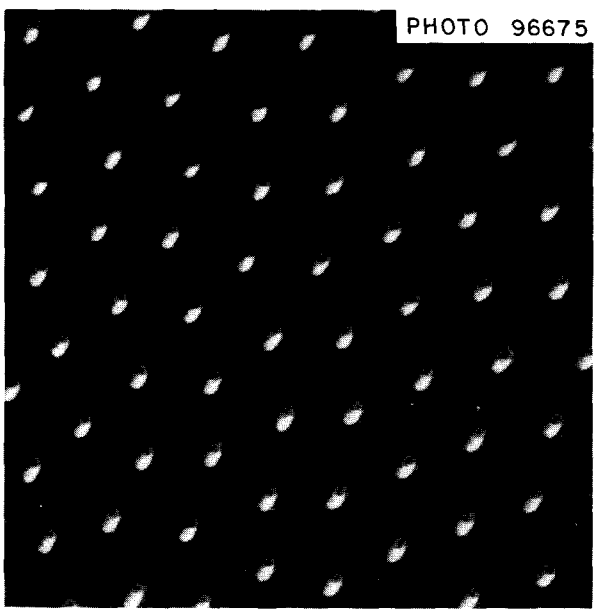

Fig. 1.1. Scanning Electron Micrograph of 1-μ-Diam Tungsten Rods Protruding from Uranium Dioxide Single-Crystal Matrix. Uranium dioxide was selectively chemically etched to expose the rods. 2100X. Photo by R. J. Gerdes, Georgia Institute of Technology.

GROWTH OF GRAPHITE CRYSTALS

J. C. Wilson G. W. Clark

We investigated the feasibility of growing large graphite crystals in the carbon-nickel system by the method: "temperature gradient zone melting" (TGZM).[7] An axial temperature gradient of about 25°C/mm was produced in a pair of 17-mm-diam cylinders of grade AUC graphite separated by a 0.1-mm-thick disk of nickel. The graphite-nickel interfaces were held at 1450°C (well above the carbon-nickel eutectic temperature[8] of 1314°C) for 2 hr in a nitrogen atmosphere.

Examination of the lower (cooler) C-Ni interface disclosed that graphite crystals had grown to a thickness of a few tenths of a millimeter. The surface of the grown graphite was distorted, probably by differential contraction stresses between the graphite and the nickel, since pressure ridges were visible on the surface, along with numerous twins. The surface showed no optical anisotropy under polarized light (except at the twins), and the angles between twins were multiples of 60°; therefore, the surface viewed was {0001} and the crystal growth up the temperature gradient occurred along the *c* axis. Because of the surface deformation the size of the individual crystals could not be accurately estimated, but the crystals must have been several millimeters across. The experiments will be continued with a moving temperature gradient to grow larger crystals.

---

[6] Electron Microscopist at Georgia Institute of Technology, Atlanta, Ga.

[7] W. G. Pfann, *Zone Melting,* Wiley, New York, 1959.

[8] H. M. Strong and R. E. Hanneman, "Anomalous Behavior in the Crystallization of Diamond and Graphite," pp. 579–83 in *Crystal Growth,* ed. by H. S. Peiser, Pergamon, New York, 1967.

HIGH-TEMPERATURE SOLUTION GROWTH OF SINGLE-CRYSTAL NEPTUNIUM DIOXIDE

C. B. Finch G. W. Clark

Single crystals of $^{237}NpO_2$ were grown up to 2 X 2 X 3 mm from (1) PbF_2-B_2O_3-NpO_2 and (2) Li_2O-MoO_3-NpO_2 solutions at 1200 to 1350°C. Magnetic susceptibility, x-ray diffraction, and chemical analysis data indicate that crystals grown from either solvent are near stoichiometric. Crystals grown from (1) contain as solvent impurities 200 ppm boron, 1000 ppm lead, and an undetermined amount of fluorine; those from (2) contain only 10 ppm molybdenum and 2 ppm lithium. The growth parameters for NpO_2 approximately parallel those previously reported for the isostructural CeO_2 and ThO_2 from the same solvents. Crystal perfection, judged from external appearance, appears best in crystals grown at a linear velocity less than 1 mm/week.

SINGLE-CRYSTAL GROWTH OF $HfSiO_4$ DOPED WITH Tb^{4+} OR Yb^{3+}

C. B. Finch G. W. Clark

A thermal gradient method[9] was used to grow $HfSiO_4$ single crystals up to 2 X 2 X 3 mm in size, each doped with less than 1 wt % $Tb^{3+,4+}$ or Yb^{3+}. The crystals will be used in future electron spin resonance studies.

GROWTH OF $SrCl_2$ CRYSTALS DOPED WITH ^{241}Am, ^{244}Cm, OR ^{245}Cm

C. B. Finch M. M. Abraham[10]

The Bridgman method was successfully used to grow $SrCl_2$ single crystals up to 0.5 cm diam X 1 cm, each doped with approximately 0.1 wt % ^{241}Am, ^{244}Cm, or ^{245}Cm. The crystals grew in a 0.5-cm-ID conical-bottom, evacuated quartz ampule (charged with $SrCl_2$ and transuranic chloride), which was lowered about 10 cm at 1 cm/hr through a zone varying from 900 to 600°C. The curium-doped $SrCl_2$ emits a blue phosphorescence and turns progressively lavender with time. The americium-doped crystals emit no such phosphorescence and are an unchanging pale yellow. The crystals were examined by ESR methods, and their transuranic dopant spectra were characterized.

[9] M. M. Abraham, G. W. Clark, C. B. Finch, R. W. Reynolds, and H. Zeldes, *J. Chem. Phys.* **50**, 2057 (1969).

[10] Solid State Division.

GROWTH OF PURE AND DOPED CeO_2 AND ThO_2 SINGLE CRYSTALS

C. B. Finch G. W. Clark

Single crystals of CeO_2 and ThO_2 were grown up to 2 X 2 X 2 mm from the high-temperature solvents $Na_2O \cdot B_2O_3$ and $PbO \cdot B_2O_3$. Crystals of ThO_2 were grown (as octahedra up to 3 mm on edge) from the Li_2O-$2WO_3$–2 wt % B_2O_3 solvent, each doped with less than 1 wt % of ^{151}Eu, ^{153}Eu, ^{241}Am, ^{243}Am, or Tl. Crystals with each dopant were studied by electron spin resonance before and after electron irradiation.

HYDROTHERMAL SYNTHESIS

Preliminary Studies on the Hydrothermal Synthesis of Sulfides

O. C. Kopp[11] G. W. Clark

Galena (PbS) was chosen as the initial compound to be investigated because of its relatively high solubility in water, ready availability, and stable character. Experiments to determine the best growth conditions were performed in 14-mm-OD pencil bombs and the 19-mm split bomb.[12] Various solvents, including sulfur-bearing compounds, chlorides, and alkali hydroxides were used. The alkali hydroxides were further studied to determine the effect of alkali ion, solvent normality, pressure, and temperature. In terms of both size and external crystal perfection, the effect of alkali ion at comparable normality (0.5 *N*) from best to poorest appears to be RbOH $\geqslant$ CsOH > KOH $\approx$ NaOH. For any given solvent, the effect of increasing solvent normality on growth was judged to be favorable up to normalities of 0.5 or 1.0 *N*. Above 2.5 *N* reaction between nutrient, solvent, and the container reduces PbS to lead, preventing crystal growth of PbS.

The best conditions determined thus far are: solvent, 0.5 *N* RbOH; growth temperature, approximately 400°C; gradient, 2 to 6°C/cm; pressure, about 1 kilobar. Self-nucleated crystals to 1 X 2 X 5 mm have been obtained, and epitaxial growth on galena seeds has been accomplished.

[11] Consultant from the University of Tennessee, Knoxville.

[12] O. C. Kopp and G. W. Clark, *Rev. Sci. Instr.* **37**, 372–73 (1966).

Infrared Spectrum of Quartz Grown in RbOH

O. C. Kopp[11] P. A. Staats[13]

Detailed analysis of the infrared spectra of quartz crystals grown with RbOH solvent is in progress. Several absorption bands have been observed in the important region 3200 to 3600 cm^{-1}. Broad peaks at 3200 and 3300 cm^{-1} appear to be independent of crystal orientation and impurity effects and are considered to be overtone and/or combination bands. Peaks at 3350, 3395, 3436, and 3580 cm^{-1} are attributed to O–H stretching vibrations influenced by nearby impurities. Minor peaks were also observed for specific crystals, some of which are attributed to absorption bands of the seed crystal or occlusions at the seed-crystal interface; however, the nature and source of some of the minor inconsistent peaks are still not clear.

MAGNETIC STUDY OF NpO_2 SINGLE CRYSTALS

H. M. Smith G. W. Clark

The magnetic properties of NpO_2 single crystals grown by the flux method from two different solvents, PbF_2 and $Li_2O \cdot 2MoO_3$, have been studied with our Faraday apparatus. The results for crystals from the two growth systems closely agree over the entire range 77 to 800°K. Below 300°K, the magnetic moment of the Np^{4+} ion was 3.02 Bohr magnetons, and the Weiss constant θ was 125°K. The magnetic moment is in close agreement with previous work done on NpO_2 powder by Ross and Lam.[14] In the interval 300 to 800°K, the magnetic properties of NpO_2 single crystals from both solvents differ from those in the low-temperature region. The relationship of inverse susceptibility to temperature is linear in this region also, but the magnetic moment of the Np^{4+} ion and θ are different, being 3.23 Bohr magnetons and 181°K respectively. Single crystals of ruby were used to check the behavior of the Faraday apparatus over the entire temperature range. No anomaly appeared, so the change in the magnetic properties of NpO_2 crystals is believed to be real. We are trying to interpret and understand this behavior.

---

[13] Physics Division.

[14] J. W. Ross and D. J. Lam, *J. Appl. Phys.* 38, 1451–53 (1967).

2. Deformation and Annealing of Metals

R. A. Vandermeer

Our deformation studies have been aimed at a better understanding of the characteristics of materials undergoing gross strain. The evolution of texture and texture inhomogeneity in body-centered cubic materials have been areas of concern during the past years. We are also engaged in a diversity of annealing studies in an effort to quantify certain aspects of recovery and recrystallization. We are seeking to understand the stability of various microstructural configurations, the manner in which defect concentrations and arrangements change, the nature of nucleation sites for recrystallization, and the mobility of grain boundaries.

TEXTURE INHOMOGENEITIES IN COLD-ROLLED NIOBIUM[1]

R. A. Vandermeer J. C. Ogle

Two distinct types of depth-dependent variations in texture have been observed in niobium cold-rolled various amounts up to 99.5% reduction in thickness. These nonuniformities are thought to be the results of nonhomogeneous plastic deformation during rolling. The first type is characterized by a zone at intermediate depths that lacks certain strong orientations that are present in the surface and center layers of the rolled stock. This type of texture modification is associated with "high" body rolling and may be related to the shape of the zone of deformation in rolling. The second type of texture inhomogeneity involves the formation of a unique texture in the surface layers of heavily rolled strip. High friction forces between workpiece and rolls appear to be needed to generate and maintain this texture. We believe that this unique surface texture results from a shear mode of deformation in the surface layers.

TEXTURE DEVELOPMENT IN AN Nb–40% V ALLOY[2]

R. A. Vandermeer J. C. Ogle

We investigated by the Schulz x-ray reflection technique the evolution of rolling texture in a polycrystalline Nb–40% V alloy rolled at room temperature in amounts up to 98% reduction in thickness. The (110) and (200) pole figures were obtained at the rolling surface and at various depths through the specimen. The results are compared with our earlier findings for pure niobium.

Unlike in unalloyed niobium, profuse twinning occurred during the initial stages of rolling in this alloy. Transmission electron microscopy showed that a dense, uniformly distributed dislocation configuration formed in this alloy, in striking contrast to the well-known cell structure in niobium. In spite of these structural differences we could detect no difference in texture or in the sequence of texture development at the strip interior. We conclude, therefore, that microstructural changes need not reflect texture changes. These results also cast serious doubt on the validity of the present cross-slip theory of texture development when applied to body-centered cubic materials.

The unique surface texture found in niobium after heavy deformation was not seen in the alloy. However, a skin effect was observed after reductions of at least 90% and could be interpreted as the initial stage of a developing surface texture.

[1] Abstracted from *Trans. Met. Soc. AIME* **245**, 1511–18 (1969).

[2] Abstract of paper to be presented at the 1969 Fall Meeting of The Metallurgical Society of AIME, Philadelphia.

THE RECRYSTALLIZATION CHARACTERISTICS OF MODERATELY DEFORMED ALUMINUM[3]

R. A. Vandermeer

The isothermal recrystallization of moderately deformed polycrystalline alloys of zone-refined aluminum containing 20 and 45 at. ppm gold has been studied by quantitative metallography. Using systematic point counting procedures, the basic structural parameters X_v, the volume fraction recrystallized, and S_v, the grain boundary area per unit volume, were measured on specimens annealed for different times at specific temperatures in the range 80 to 187°C. Both the maximum, G_m, and the average, $\overline{G}$, growth rates of the recrystallizing grains were also determined.

In the early stages, the kinetics of recrystallization could be described by the expression

$$X_v = 1 - \exp(-Bt^2) , \qquad (1)$$

where t is the annealing time and B is a temperature-dependent constant. The increase of the largest recrystallized grain with time was approximately linear (i.e., G_m was constant). All rate parameters displayed an Arrhenium-type temperature dependence with the activation energies $Q_{\overline{G}} = Q_{G_m} = \frac{1}{2}Q_B = 25.7$ kcal/mole. At constant X_v, $\overline{G}$ was proportional to $1/t$. These observations together with the general appearance of the recrystallized grains on the plane of polish suggested that recrystallization started with a site-saturated, matrix grain edge nucleation followed by two-dimensional growth perpendicular to the nucleated edge.[4] Therefore, the recrystallized colonies (a group of contiguous grains strung out along a matrix grain edge) could be represented as a constant number, N_v, per unit volume of ideal cylinders of average length l and radius r embedded in a three-dimensional matrix.

Based on this phenomenological model, the following equation relating S_v to X_v was derived

$$S_v = I_c X_v^{1/2} + K X_v , \qquad (2)$$

Where I_c and K are constants. Over the range $0.003 \leqslant X_v \leqslant 0.20$, Eq. (2) fits the experimental data quite well. Deviations at $X_v < 0.003$ are believed to arise because not all the nucleated colonies were large enough to be resolved by the metallographic technique. Deviations at $X_v > 0.2$ were due to impingements between colonies.

Because $\overline{G}$ and G_m differed (i.e., some colonies grew faster than others), a distribution of colony sizes must have existed. The data revealed that the fraction having radii between r and $r + dr$ could be represented by

$$f(r)\, dr = cr^{-4}\, dr , \qquad (3)$$

where c is a constant. Other characteristics of recrystallization were: $N_v = 5730$ cm^{-3}, $l = 0.023$ cm, $G_m/\overline{G} = 2.6$, $\overline{G}$ decreased approximately 30% as X_v went from 0.003 to 0.10, and the ratio of the minimum effective colony radius to the maximum was 0.27. All of the experimental findings were quantitatively consistent with the proposed edge-nucleated, growth-controlled model for recrystallization.

THE RECOVERY CHARACTERISTICS OF NIOBIUM AND Nb–40% V

P. V. Guthrie[5]

Recovery studies of cold-rolled niobium and Nb–40% V have continued using x-ray diffraction, electron microscopy, and hardness as the principal tools of investigation. Initial x-ray diffraction studies of lightly deformed niobium indicated that considerable deformation inhomogeneity was present, leading to the choice of a severely cold-rolled (~90%) bulk material as the prestrained reference state. The pure metal and alloy offer two distinctly different dislocation substructures for subsequent recovery studies. Room-temperature deformation of niobium produces the well-known dislocation cells, whereas deformation of Nb–40% V at room temperature forms a dense, more or less uniform array of dislocations. Even though the method, temperature, and amount of deformation are the same, the deformation parameters as determined by the Warren-Averbach method of multiple-order x-ray diffraction differ considerably. The as-cold-rolled effective particle sizes for niobium and Nb–40% V in the ⟨200⟩ direction are 600 and 200 A, respectively, while the rms strain values at 100 A are 0.00121 and 0.00267 respectively.

Recovery of niobium as measured by the particle size, rms strain, hardness, and line breadth takes place at all temperatures investigated in the range 400 to 800°C. As would be expected, the rate of recovery of each of the above parameters increases with increasing temperature. In addition, the change in each of the above parameters appears to be a linear function of the logarithm of time. On the other hand, the recovery of Nb–40% V is small at 500°C, while at 800°C the initial rate of recovery is much greater than that for niobium.

To complete the study we plan to correlate the recovery measurements with the changes in the dislocation substructure as observed by transmission electron microscopy.

---

[3] An extended abstract of a paper to be presented at the International Conference on Quantitative Relations Between Properties and Microstructure to be held in Haifa, Israel July 27–August 1, 1969.

[4] R. A. Vandermeer and P. Gordon, *Trans. Met. Soc. AIME* **215**, 577 (1959).

[5] ORAU Fellow.

3. Deformation of Crystalline Solids

R. O. Williams

The group is primarily interested in the deformation of metals and alloys, specifically how the mechanical stress required for deformation is related to structure and the nature of the changes in structure that accompany deformation.

PLASTIC DEFORMATION OF RHENIUM

R. W. Carpenter

Rhenium single crystals of relatively high purity were strained at room temperature to determine the work-hardening behavior and slip stress. The c/a ratio is 1.62, a bit less than that of magnesium and slightly larger than that of zirconium or titanium. The crystals tested were made by electron-beam float zone refining from powder-metallurgy round bar stock. Chemical analysis of the resulting single crystals after three-pass zone melting showed the total metallic impurity content to be approximately 31.5 ppm by weight; major impurities were 4 ppm W, 4 ppm Al, and 3 ppm each Cr, Si, and Ta. Interstitial content was 56 ppm total; carbon and oxygen were present in the amounts of 32 and 25 ppm respectively. The resistance ratio of the starting material was 265 and increased to 4300 after three-pass zoning.

All the crystals examined so far were strained in compression. The stress axis in all cases was within 7.5° of a $\{2\bar{1}\bar{1}0\}$ close-packed direction. In general, the initial flow stress was low, and the work-hardening rate was initially high and an increasing function of strain up to about 2% plastic strain, after which it became constant through a total plastic strain of 4%, where the tests were terminated. The yield stress was about 940 g/mm^2. Surface slip trace analysis showed the primary slip plane to be prism I type, $\{1\bar{1}00\}$. If the active dislocations are assumed to be "a" type, the critical resolved shear stress is about 460 g/mm^2. The secondary slip plane was also shown by trace analysis to be prism I type. Twinning occurred after about 2% plastic strain and continued up to 4% plastic strain. The active twin planes were $\{11\bar{2}1\}$ type. The critical resolved twinning stress for the first $\{11\bar{2}1\}$ type twin to occur was about 950 g/mm^2. Interpretation of the stress-strain curve is complicated by the initiation of twinning to about 2% plastic strain, since this is the region in which the rising work-hardening rate becomes nearly constant.

Transmission electron microscope investigations of the deformation substructure have shown arrays of long straight dislocations on the active prism slip plane that appear to be "a" dipoles and some small loops. The distribution of these dipole groups is very patchy, with some quite large regions having no visible dislocations. Sections normal to the active prism slip plane show dislocation pairs nearly parallel to the foil normal. Twins observed in transmission were of the $\{11\bar{2}1\}$ type and quite thin, varying from a maximum of about 2 μ to small fractions of 1 μ in thickness. Several instances of dislocation pileups against twin boundaries were observed.

The critical resolved shear stress (CRSS) for prism slip in rhenium is low, lower in fact than the currently accepted values for magnesium, titanium, or beryllium.[1] The CRSS for prism slip found in this work (460 g/mm^2) is also very much lower than the 1700 g/mm^2 reported by Jeffery and Smith.[2] The origin of the high work-hardening rate remains unresolved. It is not a result of an undetermined dislocation-twin interaction, since the high work-hardening rate is well established before twinning occurs. Churchman[3] long ago speculated that it may be due to a low stacking-fault energy on the prism I planes, but no such faults were observed in the present work.

This work will be continued with primary emphasis on the analysis by transmission electron microscopy of deformation substructure, developed under a variety of experimental conditions.

---

[1] P. G. Partridge, *Met. Rev.* **12**, 169 (1967).

[2] R. A. Jeffery and E. Smith, *Phil. Mag.* **13**, 1163 (1966).

[3] A. T. Churchman, *Trans. AIME* **218**, 262 (1960).

PRECIPITATION HARDENING IN BODY-CENTERED CUBIC ALLOYS

R. W. Carpenter C. T. Liu[4] P. G. Mardon[5]

Several binary refractory metal alloy systems, such as niobium-hafnium, tantalum-hafnium, and niobium-zirconium, exhibit stable or metastable miscibility gaps in the solid state. The strengthening effect of a precipitation reaction within the gap region is of fundamental interest, since a very high volume fraction of precipitate is produced and the reaction is expected to be homogeneous.

Two alloys of the niobium-hafnium system were selected for an initial investigation of the strengthening in concentrated body-centered-cubic alloys: Nb–38 at. % Hf and Nb–54 at. % Hf. Specimens were homogenized in vacuum and drop-quenched into an oil bath to retain the single-phase body-centered-cubic solution stable at 1850°C. The homogenizing treatment resulted in relatively large equiaxed-grained polycrystals. X-ray diffraction and transmission electron microscopy established that both alloys are segregated in the as-quenched condition. No precipitate structure is visible optically in this condition. The yield stress of both alloys was about 107,000 psi in the quenched condition.

Aging experiments were conducted at temperatures ranging from 600 to 1300°C. In general the yield stress of alloys decreased from the value corresponding to the quenched condition at all aging temperatures above 600°C. Both alloys exhibited hardening upon aging at 600°C. The largest response occurred in the 54 at. % Hf alloy: after 4 and 136 hr aging the yield stress was 138,000 and 155,000 psi respectively.

Initial transmission electron microscope investigation of the structure responsible for the hardening showed that after 136 hr aging at 600°C the hexagonal α-hafnium-rich phase was present. This result was confirmed by x-ray diffraction. The alpha morphology was plate-type and relatively coarse; plate thickness was about 250 A and length about 2000 A. The platelet volume fraction was very high. Precipitate morphology after aging 4 hr at 600°C also appeared platelike but very fine; platelets were approximately 100 A long. Again the precipitate density was very high, but the diffraction effects after this aging treatment are not completely resolved. X-ray diffraction shows simply a strained beta body-centered cubic lattice, but a significant amount of diffuse streaking is present; the same is true of selected area diffraction. This structure apparently results from coarsening the segregated regions observed in quenched specimens and is the progenitor of the still coarser alpha observed after aging 136 hr at 600°C.

This work is continuing, with primary emphasis on experimental elucidation of the structures developed during aging, which are responsible for the observed increase in strength.

[4] Physical Metallurgy Group.

[5] X-ray Diffraction Group.

CHARACTERISTICS OF STRESS AND DILATATION FIELDS OF STRAIGHT DISLOCATIONS IN ANISOTROPIC CRYSTALS[6]

M. H. Yoo B. T. M. Loh[7]

Elastic properties of a straight dislocation situated perpendicular to a symmetry plane in an anisotropic crystal have been calculated numerically with the procedures developed by Stroh.[8] A complete set of expressions for the stress components and the dilatation is given explicitly for both edge and screw dislocations. The elastic solution for a mixed dislocation is obtained by a superposition of the solutions for the edge and the screw dislocations.

Some typical dislocations considered are edge dislocations of $\{11\bar{2}2\}\frac{1}{3}\langle 11\bar{2}\bar{3}\rangle$ slip systems in hexagonal close-packed metals, $\frac{1}{2}\langle 110\rangle$ screw dislocations in face-centered cubic metals, and edge zonal twin dislocations of 15 compound twin systems in structures ranging from cubic to orthorhombic crystal system. The numerical results are obtained for the following metals, which cover the essential range of observed elastic anisotropies in metals: Al, Ni, Cu, and α-brass of face-centered cubic; Li, Nb, W, Fe, and β-brass of body-centered cubic; Zn, Mg, Re, Zr, Ti, and Be of hexagonal close-packed; In, β-Sn, Bi, Hg, and α-U.

The results of the stress and the dilitation fields are presented by contour plots as shown in Fig. 3.1 for α-iron. By extending Chou's analysis,[9] the degree of asymmetry of the elastic fields is characterized in terms of the parameters that are related to the elastic constants. Some direct physical consequences of these asymmetric elastic fields of dislocations on mechanical properties of anisotropic materials are discussed.

[6] Abstract of paper to be presented at the 1969 Fall Meeting of the Metallurgical Society of AIME, Philadelphia, Oct. 13–16, 1969.

[7] Electron Microscopy Group.

[8] A. N. Stroh, *Phil. Mag.* **3**, 625 (1958).

[9] Y. T. Chou, *J. Appl. Phys.* **34**, 429 (1963).

ORNL-DWG 69-3005

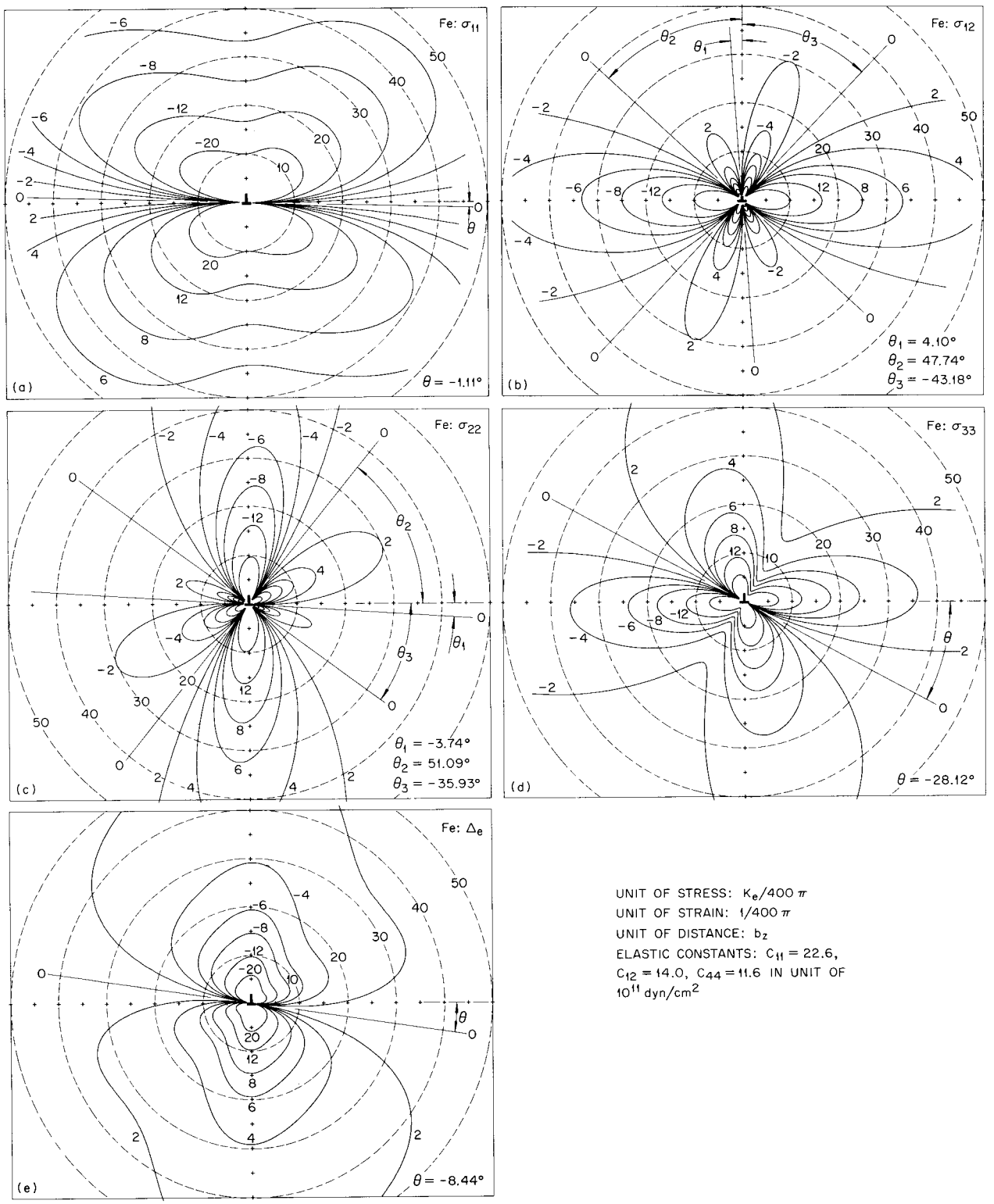

Fig. 3.1. Stress Fields (σ_{11}, σ_{12}, σ_{22}, and σ_{33}) and Dilatation Field (Δ_e) of an Edge Twin Dislocation of $\{112\}\langle 11\bar{1}\rangle$ Twin in α-Fe.

STRUCTURAL AND ELASTIC PROPERTIES OF ZONAL TWIN DISLOCATIONS IN ANISOTROPIC CRYSTALS[10]

M. H. Yoo B. T. M. Loh[7]

A descriptive definition of zonal twin dislocations is given for compound twin systems with the well-defined rational elements, K_1, K_2, η_1, and η_2. The Burgers vector of a zonal twin dislocation can be defined as

$$\mathbf{b}_z = \frac{e}{2}\eta_1$$

where e is a numerical factor that depends on twin system and crystal structure. The expressions for e have been derived for the 15 compound twin systems in metallic structures. Geometric characteristics of zonal twin dislocations are thoroughly discussed, such as the periodicity of twin interface structure and of atom shuffling, relationships between slip and twin dislocations, and zonal twin dislocations in fully ordered structures.

Interaction forces between two parallel edge twin dislocations are obtained directly from the stress components of a dislocation. Based on this result, equilibrium positions of a group of edge twin dislocations that constitute a stable incoherent twin boundary have been calculated numerically for various values of number of dislocations, N, and applied stress, τ_a. The effects of independent variations of N and τ_a on the equilibrium positions of the dislocations are examined, and the asymmetry of oblateness in the stable twin shape is correlated to the anisotropic stress field of a dislocation.

Short-range structural properties of zonal twin dislocations are discussed in terms of a Peierls-Nabarro model. The Peierls-Nabarro stress, the stress necessary to move a zonal twin dislocation along the twin interface, can be estimated. The product of two elastic coefficients, $K_e S_{66}$, is introduced as an anisotropic parameter of energetic criteria for operative twin modes. In a wide range of temperatures, the calculated parameters correctly predict the more active mode between a conjugate pair of crystallographically nonequivalent compound twin systems.

[10] Abstract of paper to be published in the Proceedings of an International Conference on "Fundamental Aspects of Dislocation Theory," April 21–25, 1969, National Bureau of Standards, Gaithersburg, Maryland.

STRUCTURAL CHANGES PRODUCED BY THE DEFORMATION OF NONRANDOM ALLOYS

R. O. Williams

It is widely appreciated that deformation necessarily tends to make nonrandom solid solutions more random, this being the origin of one component of alloy strengthening.[11] It is less widely appreciated that this randomization is not isotropic and directional properties are developed; this effect is very apparent[12] in the magnetic properties of deformed Ni_3Fe. Approximate treatments of these effects are known, but we have shown that if the deformation is precisely described then the changes are exactly defined by an unbounded set of differential equations.

For the face-centered cubic lattice the changes in the Warren order parameter, α_{hkl}, for sites related by the vector **hkl** is given as

$$\frac{d\alpha_{hkl}}{d\gamma} = 3^{-1/2}\,(\mathbf{hkl}\cdot\mathbf{LMN})\,(\alpha_{hkl-RST} - \alpha_{hkl})\,, \quad (1)$$

when the increment of slip on the $[RST]$ (LMN) systems produces a strain increment of $d\gamma$ and where

$$\alpha_{hkl} = 1 - P_{AB}/X_B\,. \quad (2)$$

The probability of finding a B atom at the end of vector **hkl** when an A is at its origin is P_{AB}, and X_B is the fraction of B atoms. The unit cell is taken to have an edge of 2.0 so that the vectors **hkl** and **RST** have integral components.

Each operating slip system adds an additional term to this expression. One solves this collection of differential equations numerically; the results are specific for the structure and the particular combination of slip systems.

In the following figures we give the calculated results for the atoms in the first two shells for the Cu_3Au type structure for certain combinations of slip systems. Figure 3.2 shows that a single slip system produces a very marked change in two of the first 12 neighbors but no change whatsoever for the six neighbors that lie in the slip plane. Elongation in the [111] direction produces a rapid mixing as indicated in Fig. 3.3. Figures 3.4 and 3.5 show that (010)[100] and (011)[$9\bar{2}\bar{2}$] rolling produces more complex results.

[11] J. C. Fisher, *Acta Met.* 2, 9 (1954).

[12] G. Y. Chin, *J. Appl. Phys.* 36, 2915 (1965); G. Y. Chin, E. A. Nesbitt, and J. H. Wernick, *J. Appl. Phys.* 38, 2623 (1967).

The magnetic anisotropy can be calculated from the population of the neighbors in the first shell.[12] The maximum magnetic anisotropy that can be produced in the ordered Ni_3Fe structure (same as the Cu_3Au structure) for the above modes of deformation is listed in Table 3.1.

The calculated anisotropy will surely exceed that which can be actually developed, but the above values are 25 times what has been observed.[12] One might expect that significantly higher values can be realized, and the present analysis can be used as a guide as to how the processing is to be done.

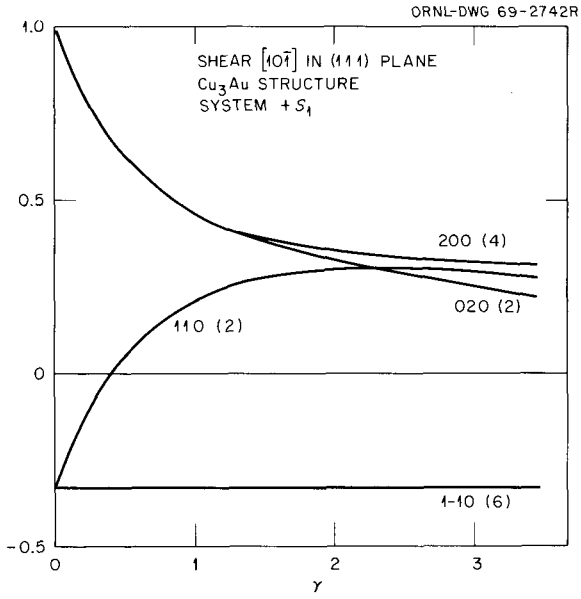

Fig. 3.2. The Change in the Warren Order Parameters for the Atoms in the 110 and 200 Type Shells Produced by the Operation of a Single Slip System. The number in the parentheses indicates how many atoms change according to the curve.

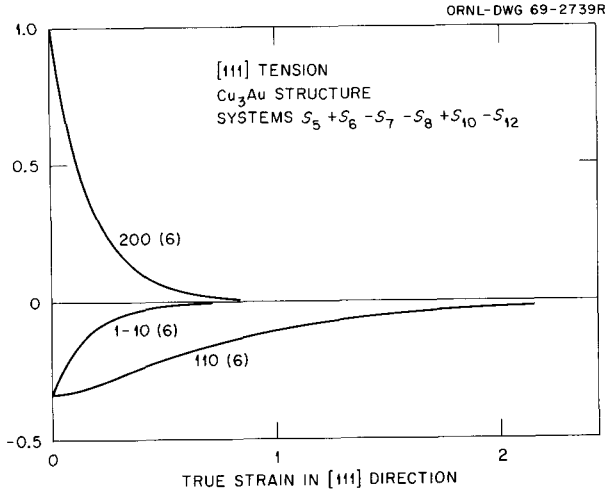

Fig. 3.3. The Changes Produced by [111] Tension, Six Systems Operating.

Table 3.1. Maximum and Minimum Magnetic Energy Density Produced in Ni_3Fe for Certain Kinds of Deformation (Calculated)

Deformation	Magnetic Energy Density (ergs/cm^3)		Direction of Easy Magnetization
	Minimum	Maximum	
	$\times 10^6$	$\times 10^6$	
[1$\bar{1}$0](111) Shear	0.2	12.4	[1$\bar{1}$0]
[111] Tension	2.3	8.4	[111]
(101)[100] Rolling	0.7	10.3	[001]
(011)[9$\bar{2}\bar{2}$] Rolling	2.6	11.8	[4$\bar{5}\bar{5}$]

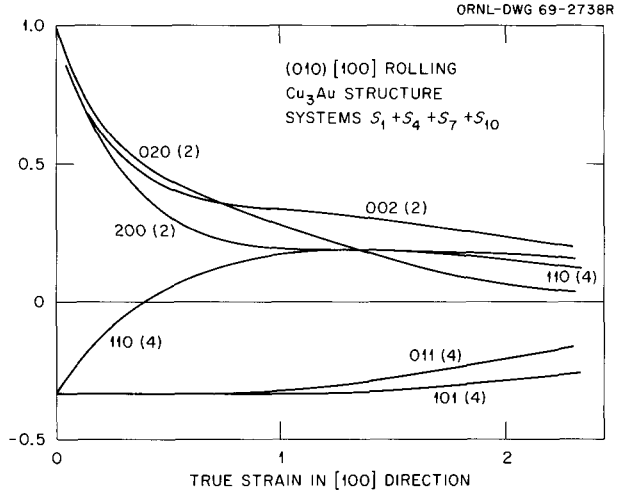

Fig. 3.4. The Changes Produced by (101) [100] Rolling, Four Systems Operating.

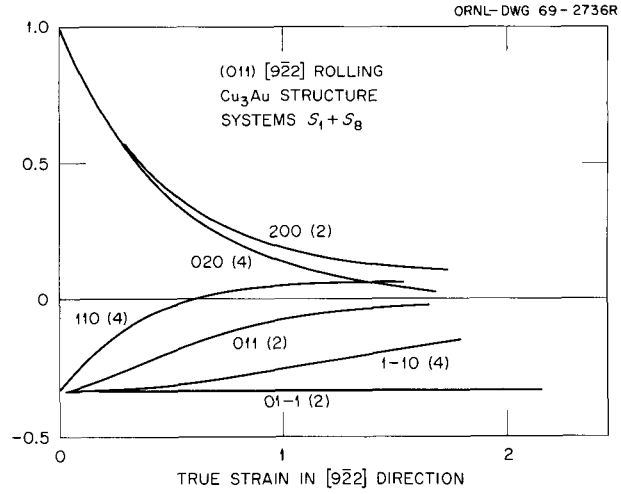

Fig. 3.5. The Changes Produced by (011) [9$\bar{2}$2] Rolling, Two Systems Operating.

4. Diffusion in Solids

T. S. Lundy

Our interest encompasses the entire subject of atomic migration in metals and ceramics, including the relationships that exist between diffusion and nearly all high-temperature solid-state processes. During this reporting period we concentrated our research efforts on measurement of diffusion coefficients of ^{233}U in the nuclear fuels UO_2 and UN_{1+x}, the diffusion of various tracers in monocrystalline tungsten, the effects of short-circulating influences on measured diffusion coefficients, and the near-surface effect. The work on diffusion in tungsten was conducted jointly with the Reactions at Metal Surfaces Group.

CATION SELF-DIFFUSION IN UO_2 (Ref. 1)

D. K. Reimann[2] T. S. Lundy

The alpha-energy degradation technique was used to examine self-diffusion of ^{233}U in monocrystalline and large-grained polycrystalline UO_2 prepared by the floating-zone technique.[3] All previously reported diffusion coefficients for this system were too large relative to the true lattice diffusion coefficients by as much as several orders of magnitude. Short-circulating influences may have played a major role in determining the previously measured D values.

DIFFUSION OF ^{233}U IN UO_2 (Ref. 4)

D. K. Reimann[2] T. S. Lundy

The diffusion of ^{233}U in nominally stoichiometric UO_2 single crystals was studied by the alpha-energy degradation method from 1620 to 2010°C. The results can be summarized by

$$D = 6.8 \times 10^{-5} \exp(-98{,}300/RT)\ \mathrm{cm^2/sec}\ .$$

The activation energy of 98.3 ± 8 kcal/mole agrees with some of the previously reported values; however, the actual diffusion coefficients are as much as three orders of magnitude smaller. Polycrystalline specimens of the same composition clearly showed preferential grain boundary diffusion.

CATION SELF-DIFFUSION IN UN_{1+x} (Ref. 5)

D. K. Reimann[2] T. S. Lundy

Diffusion coefficients of ^{233}U in arc-cast UN_{1+x} were determined as functions of both temperature and nitrogen pressure by use of the alpha-energy degradation method. The lack of analytical data prevented direct correlation with stoichiometry. However, the diffusion coefficients at 1600 and 1760°C depended markedly on nitrogen pressure. At low pressures the dependence was consistent with an interstitial mechanism of diffusion, but at high pressures the dependence could not be described by the usually defect calculations. Some qualitative explanations based on the phase diagram for the uranium-nitrogen system are given.

TRACER DIFFUSION IN TUNGSTEN[6]

R. E. Pawel[7] T. S. Lundy

The lattice diffusion coefficients for Nb, Ta, and W isotopes in tungsten were measured from 1300 to 2400°C by standard tracer methods in combination

[1] Abstracted from *J. Nucl. Mater.* **28**, 218–19 (1968).

[2] Temporary noncitizen employee from Germany.

[3] A. T. Chapman and G. W. Clark, *J. Am. Ceram. Soc.* **48**, 494–95 (1965).

[4] Abstracted from paper accepted by *Journal of the American Ceramic Society.*

[5] Abstract from paper in preparation.

[6] Abstracted from paper accepted for publication in *Acta Metallurgica.*

[7] Reactions at Metal Surfaces Group; see Chap. 12.

with anodic-film sectioning techniques. The Arrhenius relation was obeyed over the entire temperature range, and the following analytical expressions were obtained:

$$D(\mathrm{Nb}) = 3.01 \exp(-137{,}600/RT)\ \mathrm{cm}^2/\mathrm{sec}\ ,$$

$$D(\mathrm{Ta}) = 3.05 \exp(-139{,}900/RT)\ \mathrm{cm}^2/\mathrm{sec}\ ,$$

$$D(\mathrm{W}) = 1.88 \exp(-140{,}300/RT)\ \mathrm{cm}^2/\mathrm{sec}\ .$$

The characteristics exhibited by the penetration profiles of both mono- and polycrystalline specimens emphasized the need for sensitivity and completeness in the data used for the determination of both lattice and short-circuit diffusion parameters. When measuring lattice diffusion coefficients, even in single crystals, we found that the section thickness must be kept smaller than $\sqrt{Dt}$ to minimize the effects of short-circuit paths. Conversely, in the region of the profile governed by short-circuit effects, extensive sets of data could not be described in terms of a simple model leading to a unique diffusion coefficient.

EFFECTS OF SHORT-CIRCUITING PATHS ON DIFFUSION COEFFICIENT MEASUREMENTS[8]

T. S. Lundy R. E. Pawel[7]

Effects of short-circuiting paths on observed diffusion behavior in real crystalline systems are considered. Experimentally measured diffusion coefficients may vary widely from values associated with true lattice diffusion to those appropriate for short-circuiting paths alone, depending upon the conditions of the experiment and the sensitivity and completeness of the data.

COMBINED SURFACE AND GRAIN BOUNDARY DIFFUSION[9]

J. P. Stark[10]

A mathematical analysis for the accumulation of tracer as diffused through a thin metallic slab by grain boundary diffusion is presented. Boundary conditions on the side where the tracer is deposited describe a small depletable source, and the grain boundary concentration is enhanced by surface diffusion. Because of the mathematical difficulty associated with boundary conditions for combined grain boundary and surface diffusion, two cases are studied: zero and infinite surface diffusivity combined with finite grain boundary diffusivity. The difference between the accumulated tracer for the two cases is similar to the contribution from lattice diffusion only. Thus, for relatively short diffusion time, grain boundary diffusion analyses without surface diffusion complications are adequate.

OXIDATION KINETICS AND ITS INFLUENCE ON THE NEAR-SURFACE EFFECT IN DIFFUSION[11]

D. K. Reimann[2] J. P. Stark[10]

Kinetic equations are derived to describe the effect of thermal fluctuations upon tracer oxides at the surface of diffusion specimens. The rate of metal oxide reduction during such fluctuations was consistent with observations on the near-surface effect (NSE) of diffusion. In particular, the theory explains the NSE for diffusion of ^{60}Co in Ag, ^{72}Ga in Ga, and ^{65}Zn in Cu; furthermore, experimental confirmation was found for the diffusion of ^{233}U in Au.

RESIDUAL ACTIVITY METHODS FOR DETERMINATION OF LATTICE DIFFUSION COEFFICIENTS[12]

T. S. Lundy R. E. Pawel[7]

Residual activity methods (including the Gruzin method) for determining lattice diffusion coefficients in various metals and ceramics are being used with increasing frequency. These methods have certain inherent advantages, most of which are associated with ease of experimentation. However, pronounced dangers in their indiscriminate use arise from the large likelihood of misinterpretation of the data when multiple mechanisms of diffusion exist. These dangers were discussed in terms of information gathered from experiments performed by the highly precise anodizing-and-stripping technique for the purpose of evaluation of the Gruzin method.

---

[8] Abstracted from *Trans. Met. Soc. AIME* **245**, 283–86 (1969).

[9] Abstracted from paper to be published in *Journal of Applied Physics.*

[10] ORAU Research Participant at the ORNL during the summer of 1968 from the University of Texas at Austin.

[11] Abstracted from paper to be published in *Acta Metallurgica.*

[12] Abstract of paper presented at the 1969 Spring Meeting of The Institute of Metals Division of The Metallurgical Society of AIME in Pittsburgh, Pa., May 12–15.

5. Electron Microscopy

J. O. Stiegler

The aim of the Electron Microscopy Group is a closer understanding of the mechanical properties of metals in terms of their microstructures. A major portion of our current effort centers around holes that develop in metals under service conditions, namely voids and gas bubbles that form under neutron irradiation, cavities and cracks that develop during creep, and hot cracks that occur in welds. We are working closely with the LMFBR and Aluminum Irradiation Damage programs in these areas, but are supplementing our studies with work on voids produced in high-purity aluminum by both irradiation and quenching and with examination of other materials containing holes.

We are also examining high-temperature deformation processes and precipitation reactions in the complex Hastelloy N alloy used in the Molten Salt Reactor Experiment. The more basic aspects of the elevated-temperature ductility problem common to nickel-base alloys and stainless steels are being investigated in nickel and some dilute nickel alloys.

At lower temperatures we are studying the relationships between the energy stored by a metal during plastic deformation and its corresponding microstructure. Since the orientation of the crystals is frequently important in deformation studies, we have developed a simple technique for orientation determination in suitable materials.

In the following pages we report briefly on some aspects of our work that were completed this year. Other contributions by members of the Electron Microscopy Group appear in Chaps. 3, 16, 30, and 32 of this report.

HIGH-FLUENCE NEUTRON IRRADIATION DAMAGE IN ALUMINUM[1]

J. O. Stiegler C. K. H. DuBose
K. Farrell R. T. King[2]

Structural damage occurring in 99.9999% aluminum and in 99%-pure commercial aluminum as a result of high-fluence neutron irradiation has been examined by transmission electron microscopy. Both displacement damage and impurities produced by nuclear transmutations were observed. In the high-purity aluminum, octahedral voids and many dislocation loops were created by a fast fluence of 3.5×10^{20} neutrons/cm^2 (>0.82 Mev) at 50°C. A contrast analysis of some of the larger loops showed them to be vacancy type. The distribution of the voids and loops was nonuniform, areas containing large voids usually having small loops and vice versa, suggesting that most of the loops were probably of vacancy character. The heterogeneous disposition of the voids is interpreted in terms of an association of voids with dissolved impurities. The only radiation damage observed in the commercially pure aluminum after exposure to 3.5×10^{20} neutrons/cm^2 at 50°C was a few prismatic dislocation loops around grown-in dislocations; loops of both vacancy and interstitial types were identified. Commercially pure material irradiated to fast and thermal fluences in excess of 10^{22} neutrons/cm^2 at 45°C contained a uniform distribution of cubic voids and dislocations and a fine precipitate of silicon.

Postirradiation annealing caused the voids to disappear at a temperature in the range 230 to 315°C, and the silicon precipitate in the highly irradiated impure aluminum coarsened markedly. Annealing at 455°C caused gas bubbles to form on grain boundaries and dislocations in the heavily irradiated impure aluminum.

HIGH-NEUTRON-FLUENCE DAMAGE IN AN ALUMINUM ALLOY[3]

R. T. King[2] J. O. Stiegler
E. L. Long, Jr.[4] K. Farrell

A cold-drawn Al–1% Ni alloy irradiated to 1×10^{22} fast neutrons/cm^2 and more than 2×10^{22} thermal neutrons/cm^2 at 60°C in aqueous environment dis-

[1] Abstract of paper presented at the IAEA Symposium on Radiation Damage in Reactor Materials, Vienna, June 2–6, 1969.

[2] Mechanical Properties Group.

[3] Abstract of paper submitted to *Journal of Nuclear Materials.*

[4] Metallography Group.

played several forms of irradiation damage, namely polyhedral voids up to 600 A in diameter at concentrations of approximately $10^{15}/cm^3$ and a fine solid precipitate of transmutation-produced silicon. Post-irradiation annealing for 1 hr above 220°C caused the voids to disappear; cold pressing the specimens through a 65% reduction in thickness also eliminated most of the voids. The irradiation-induced precipitate coarsened with increasing annealing temperature. After a 400°C anneal, many barely resolvable gas bubbles were observed and the silicon precipitate was quite coarse. These bubbles may be responsible for increasing the recrystallization temperature from approximately 210 to 540°C. Growth of the bubbles on annealing at 530°C and above caused significant swelling.

Irradiation increased the tensile strength of the alloy at test temperatures up to about 300°C. Significant ductility losses were observed over a broad temperature range below 300°C, with the greatest ductility loss at 175°C. Postirradiation annealing before testing at 175°C caused complete recovery of the ductility to the level of unirradiated material only after recrystallization at 540°C; concurrently strength was only partially recovered. These effects are explained in terms of the response of the irradiation-induced microstructural features to annealing and to plastic strain during testing.

QUENCHING DEFECTS IN ALUMINUM

A. Wolfenden

Defect configurations similar to those produced by neutron irradiation can sometimes be induced into aluminum by quenching it from a high temperature into a relatively cold medium. Voids and dislocation loops have been observed in three-pass zone-refined aluminum quenched from about 600°C into a variety of media, but the quenching procedure and the prior treatments were important in determining the types and concentrations of defects produced. Both void and loop formation appear to be favored by pretreatments that might introduce gaseous impurities. To clarify the role of dissolved gases in void nucleation, quenching experiments are in progress with aluminum bombarded by protons and helium ions and with aluminum pre-annealed in argon and hydrogen.

THERMAL REJECTION AND GROWTH OF GAS BUBBLES IN ELECTRODEPOSITED NICKEL[5]

K. Farrell J. T. Houston

An electrolytic nickel rod softened rapidly during annealing, even at low temperatures. This was followed by a slower softening process during which tiny gas bubbles were first observed after anneals at 500°C. Many of the bubbles were associated with kinks on dislocations. Most of the hydrogen was evolved from the specimens before or during the formation of the tiny bubbles. With increasing annealing treatment, slow softening continued, the gas bubbles coarsened, large grain-boundary bubbles developed, and significant swelling occurred. Swelling and softening ceased at about 6% swelling during a 1000°C anneal in air, and simultaneously equiaxed grains formed. These observations are discussed in terms of gas bubble nucleation and growth in a material containing dissolved gas and initially supersaturated with lattice vacancies. We concluded that the slow softening data may be a measure of the removal of dislocation pinning points within the grains as bubble coarsening proceeds.

PHASE INSTABILITY IN HASTELLOY N (REF. 6)

R. E. Gehlbach H. E. McCoy, Jr.[2]

Although Hastelloy N is basically a solid-solution alloy, various thermomechanical treatments change its mechanical properties and microstructure. Since it is intended for use up to 850°C and is now used in molten fluoride reactor systems, we must understand the nature of the precipitation processes and the effect on mechanical behavior.

Identifying and characterizing the precipitates involved several complementary techniques: optical metallography, transmission electron microscopy, extraction replication, x-ray diffraction, and electron-probe microanalysis. In addition, chemical analysis with a microprobe attachment for the electron microscope and electron diffraction were employed to identify individual particles, agglomerates, and grain-boundary films on extraction replicas without interference from the matrix. These techniques help resolve differences in precipitates and relate the microstructure to mechanical properties.

The microstructure is characterized by stringers of massive primary precipitate particles of the Ni_3Mo_3C type. Exposure between 500 and 1000°C results in precipitation of particles of the Ni_2Mo_4C type in the

[5] Abstract of paper submitted for publication.

[6] Abstracted from pp. 346–66 in *International Symposium on Structural Stability in Superalloys, Seven Springs, Pennsylvania, September 4–6, 1968,* vol. II. Available from Dr. John Radavich, AIME High-Temperature Alloys Committee, Micromet Laboratories, West Lafayette, Ind.

grain boundaries. In air-melted heats that contain approximately 0.6% Si, the carbide-type precipitates are enriched in silicon; they are not dissolved at high annealing temperatures but melt and transform to a noncarbide phase. In vacuum-melted heats with low silicon contents, carbides go into solid solution.

The only precipitates that form in air-melted alloys at temperatures as high as 1180°C are complex pseudocarbides of the $Ni_3(Mo,Cr)_3(C,Si)$ and $Ni_2(Mo,Cr)_4(C,Si)$ types. The amount and behavior of precipitates are highly silicon dependent; this impurity stabilizes the particles, preventing their being taken into solid solution at high annealing temperatures and causing them to transform to the high-temperature phase. This latter phase is a silicide with an M_6C structure and is probably responsible for the increased embrittlement at high annealing temperatures.

AUTORADIOGRAPHIC STUDY OF ^{14}C IN HASTELLOY N (REF. 7)

R. E. Gehlbach M. D. Allen[4] J. D. Braun[8]

The carbon distribution in Hastelloy N was studied by autoradiographic techniques. The radioisotope ^{14}C was introduced into the molten alloy, and the resulting distribution and microsegregation of carbon in and around precipitate particles were followed as functions of heat treatment.

Autoradiographic emulsions discussed include stripping film and NTB-2, NTB-3, and NTE liquid emulsions made by Kodak. Methods of liquid emulsion application, precautions with the emulsions, sample preparation, sources of errors, artifacts, and interpretation are discussed.

Carbide and noncarbide phases are easily distinguished by autoradiographic techniques. Supplementary techniques permit thorough identification of phases present. A high-temperature noncarbide phase was involved in the transformation from silicon-rich M_6C-type carbides to an intermetallic silicide phase.

[7]Abstracted from pp. 113–18 of *Proceedings, First Annual Technical Meeting, International Metallographic Society, Inc., November 11, 12, and 13, 1968 – Denver, Colorado, U.S.A.*, ed. by K. A. Johnson and J. H. Bender, International Metallographic Society, Inc., Los Alamos, N.M., 1969.

[8]Mound Laboratory, Monsanto Research Corporation, Miamisburg, Ohio.

RECRYSTALLIZATION OF NICKEL 270 (REF. 9)

J. T. Houston K. Farrell

Nickel 270, a commercially pure nickel, when cold worked through reductions-in-area of 10 to 94%, displays slight recovery hardening after annealing in the range 200 to 300°C. The 30-min recrystallization temperatures are in the range 290 to 400°C and decrease linearly with increasing degree of prior cold work. The time dependence of recrystallization in specimens deformed 94% yields an apparent activation energy of about 40 kcal/mole, which is in better agreement with that for zone-refined nickel than with that for substantially less pure nickel.

THE ENERGY RELATIONS IN THE ROOM-TEMPERATURE DEFORMATION OF ALUMINUM SINGLE CRYSTALS[10]

A. Wolfenden

The energy relations involved in the room-temperature tensile deformation of aluminum single crystals have been measured with a single-step calorimeter as functions of strain and initial specimen orientation. Both the expended and dissipated energy of plastic deformation showed orientation-dependent trends. The extremely small values of the stored energy had relatively large errors. The orientation dependence (if any) of the energy stored in the range of strains investigated was small and not resolved by the calorimetric technique. The results are compared with previous data for this metal and for copper and silver single crystals.

THE ENERGY STORED IN A GOLD-SILVER ALLOY[11]

A. Wolfenden

As part of a series of experiments on the determination of the stored energy of cold work, a single-step calorimeter was used to measure the energy relations involved in the room-temperature tensile deformation of the Au–27.8 at. % Ag alloy of two grain sizes (32 and 446 μ). The rate of energy storage was initially low and then became almost linear with increasing strain in the range of strains used. The effects of grain size on

[9]Abstract of paper submitted to *Transactions of the American Society for Metals.*

[10]Abstract of paper submitted to *Scripta Metallurgica.*

[11]Abstracted from paper accepted for publication in *Scripta Metallurgica.*

the stored energy were evident only at low strains. The incremental rate of storage ($\Delta E_s/\Delta E_w$) increased at low strains reaching about 0.3 at a logarithmic strain of about 0.03 and then decreased slowly with increasing strain. The stored energy was proportional to the square of the flow stress, with the constant of proportionality apparently independent of grain size.

ORIENTATION DETERMINATION FROM DODECAHEDRAL ETCH PITS[12]

B. T. M. Loh

A simple, rapid, and accurate method was developed for determining the crystal face orientation of cubic metals from dodecahedral etch pits. The few procedures involved in the method can be summarized as follows: (1) measuring the two diagonal ratios of a (four-sided) pit, (2) looking up two angles that define the orientation of the crystal from graphs that plot their angles as a function of the diagonal ratios, and (3) plotting the two angles as a stereographic projection. The method is restricted to systems that allow four-sided pits to be formed from one family of planes.

[12] Abstract from paper submitted to *Metallography*.

6. Fundamental Ceramics Research

W. Fulkerson

For the past several years we have been developing a multidisciplinary program of basic research on uranium mononitride and related actinide refractory hard-metal type compounds of interest for fast reactor fuels. By concentrating on one member of this class of materials we hope to get a more fundamental understanding of the whole class. At the same time, we are contributing specific knowledge about UN, which has been useful support to the Nitride Fuels Development Program (Chap. 18 of this report). In turn we receive most of our research specimens from this nitride development program.

The research now in progress is listed in Table 6.1. The studies are being made by eight groups in the Metals and Ceramics Division and by the Physics, Solid State, and Health Physics Divisions. We have also initiated work on UN at other laboratories by supplying suitable specimens. This includes nuclear magnetic resonance measurements on $U^{15}N$ at Argonne National Laboratory, very low-temperature thermal conductivity

Table 6.1. Fundamental Studies on UN and Related Compounds

Study	Investigator	Division or Affiliation
Electronic Band Structure Calculations	H. L. Davis	Solid State
Low-Temperature Specific Heat	J. O. Scarbrough	Metals and Ceramics
Elastic Moduli and Debye Temperature	H. L. Whaley	Metals and Ceramics
Optical Reflectivity and Photoelectric Effect	R. G. Lye	Research Institute for Advanced Studies, Martin-Marietta Corporation.
	E. T. Arakawa	Health Physics
Transport Properties	J. P. Moore	Metals and Ceramics
Thermal Conductivity	D. L. McElroy	Metals and Ceramics
Electrical Resistivity		
Seebeck Coefficient		
Low-Temperature Thermal Conductivity	W. S. Williams	University of Illinois
	L. G. Radosevich	University of Illinois
Self Diffusion of ^{233}U in UN	D. K. Reimann	Metals and Ceramics
	D. Kroeger	Metals and Ceramics
	T. S. Lundy	Metals and Ceramics
Compressive Creep	C. S. Yust	Metals and Ceramics
Elastic Neutron Diffraction	W. C. Koehler	Solid State
Magnetic Susceptibility	H. M. Smith	Metals and Ceramics
Nuclear Magnetic Resonance	M. Kuznietz	Argonne National Laboratory
Electron Spin Resonance	M. M. Abraham	Solid State
Chemical Analysis by Proton Reaction	J. H. Gibbons	Physics
	R. L. Macklin	Physics
	R. Jaszczak	Physics
Single Crystal Growing	W. Fulkerson	Metals and Ceramics
	J. Y. Chang	Metals and Ceramics

measurements at the Materials Research Laboratory of the University of Illinois, and visible and vacuum ultraviolet reflectivity measurements at the Research Institute for Advanced Studies (RIAS) of the Martin-Marietta Corporation.

Significant progress has been made this year in a number of these studies, and some of the results are briefly abstracted below. In addition, very interesting results of the self diffusion of ^{233}U in UN are given in Chap. 4 of this report. Preliminary work indicates that for a given temperature (at least in the measured range, 1600 to 1860°C) there is a minimum in the diffusion coefficient as a function of nitrogen pressure. Further work is in progress to verify the existence of this minimum, which probably indicates a change in the rate-controlling mechanism for diffusion as the stoichiometry is changed in the single-phase region. Also, on the high pressure side of the minimum the diffusion coefficient is independent of temperature if the pressure is held constant because, apparently, the stoichiometry adjusts in such a way as to offset the change in the mobility of the defects responsible for diffusion. This behavior may lead to interesting effects in the compressive creep of UN (see Chap. 8 of this report) since the kinetics of creep is often diffusion controlled.

ELECTRONIC BAND STRUCTURE CALCULATIONS FOR PARAMAGNETIC URANIUM MONONITRIDE

H. L. Davis[1]

Some results from a preliminary attempt at the calculations of the electronic band structure of uranium nitride are presented in Fig. 6.1, which is a conventional plot of $E_{\mathbf{k}}$ vs **k** behavior along two symmetry directions in the Brillouin zone. These results were obtained using the nonrelativistic Korringa-Kohn-Rostoker (KKR) method for band-structure calculations. The one-electron muffin-tin potentials used in the calculation were obtained from the lattice superposition of free atom charge densities.[2]

Calculations were also performed along other symmetry directions in the Brillouin zone besides the two expressed in Fig. 6.1. In addition, to calculate the integrated density of states for several energies in the range 1.0 to 1.2 rydbergs, constant energy surfaces were obtained by the KKR method coupled with constant-energy-search techniques. These procedures led to a

[1] Now in Solid State Division.

[2] The necessary atomic wave functions were calculated by T. C. Tucker of the Mathematics Division.

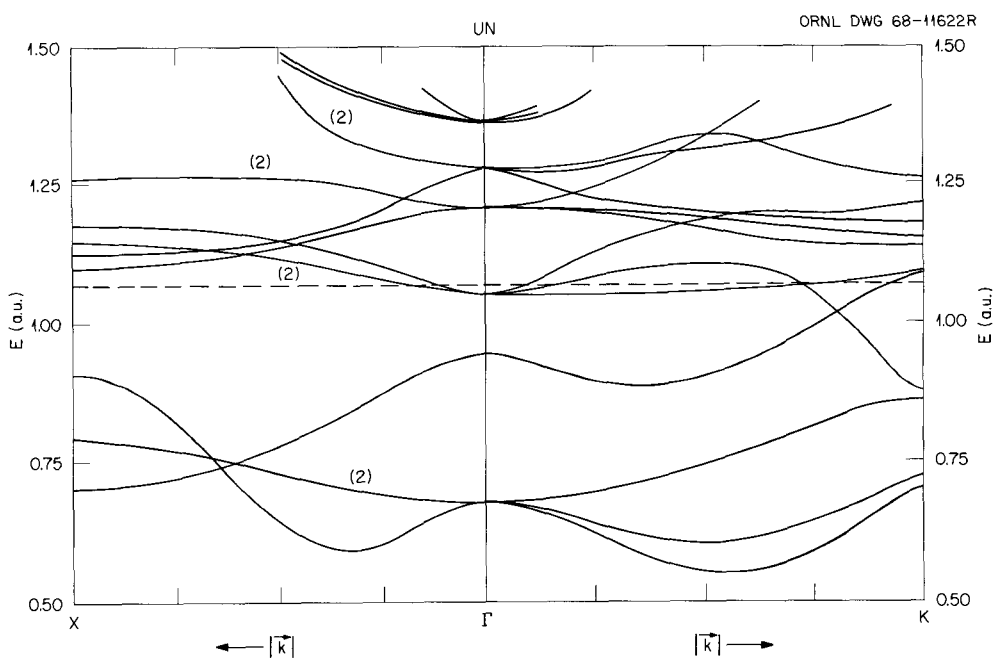

Fig. 6.1. Band Structure of UN Along Two Symmetry Directions in the Brillouin Zone. The energy unit is the rydberg, and energy is measured relative to the average value of the potential between the touching muffin-tin spheres centered about the U and N sites in the lattice. The bands designated "(2)" are doubly degenerate, and the other bands are nondegenerate.

calculated Fermi energy of 1.073 rydbergs. We calculated the electronic density of states at the Fermi energy, which gives a theoretical estimate of 15.1 millijoules mole^{-1} °K^{-2} for UN's unenhanced low-temperature electronic specific heat. This is reasonable agreement for a first-attempt calculation with the experimental value[3] of 49.6 millijoules mole^{-1} °K^{-2}, since various many-body effects may increase the bare band structure value.

Besides the E_k vs k behavior, the band-structure wave functions were calculated at several representative points in the Brillouin zone. The wave functions were expressed in the form

$$\psi_k(\mathbf{r}) = \sum_{lm} C^U_{lm} R_l(r_U) Y_{lm}(\theta_U, \phi_U)$$

if **r** inside U muffin-tin sphere

$$\psi_k(\mathbf{r}) = \sum_{lm} C^N_{lm} R_l(r_N) Y_{lm}(\theta_N, \phi_N)$$

if **r** inside N muffin-tin sphere

$$\psi_k(\mathbf{r}) = \sum_j F_j \exp[i(\mathbf{K}_j + \mathbf{k}) \cdot \mathbf{r}]$$

if **r** outside both muffin-tin spheres.

The C^U_{lm}, C^N_{lm}, and F_j are expansion coefficients depending on the E_k and k of interest. The $R_l(r_U)$ and $R_l(r_N)$ are the radial components of the wave function, which satisfy the conditions

$$\int_0^{R^U_{mt}} [R_l(r_U)]^2 r_U^2 \, dr_U = \int_0^{R^N_{mt}} [R_l(r_N)]^2 r_N^2 \, dr_N = 1 \, .$$

Here, R^U_{mt} and R^N_{mt} are the respective muffin-tin sphere radii. The C^U_{lm} and C^N_{lm} coefficients for two representative (E_k,k) points are expressed in Table 6.2.

Although this work is still in progress, the completed calculations do allow a few qualitative comparisons of the present band-structure model with some physical properties of UN. As is illustrated by Fig. 6.1 and Table 6.2, a Fermi energy of 1.073 rydbergs will intersect a narrow *d-f* band. This Fermi energy leads to a calculated topology for the Fermi surface with large "hole" regions. This usually implies a positive sign for the thermoelectric power, as has been measured for UN. On the other hand, because the Hall coefficient at low temperatures is negative[4] the situation is not straightforward.

[3] J. O. Scarbrough, H. L. Davis, W. Fulkerson, and J. O. Betterton, Jr., *Phys. Rev.* **176**, 666–71, (1968).

[4] M. A. Kanter, *Bull. Am. Phys. Soc.* **13**, 125 (1968).

Table 6.2. Electronic Wave Function Expansion Coefficients for Two Band-Structure Points of a Theoretical Model for Uranium Nitride

l	for k = (0.2, 0.3, 0.4) E = 1.07 rydbergs		for k = (0.2, 0.3, 0.4) E = 0.60 rydberg	
	$\Sigma\lvert C^U_{lm}\rvert^2$	$\Sigma\lvert C^N_{lm}\rvert^2$	$\Sigma\lvert C^U_{lm}\rvert^2$	$\Sigma\lvert C^N_{lm}\rvert^2$
0	0.0000	0.0003	0.1090	0.0011
1	0.0101	0.0011	0.0747	0.4731
2	0.1779	0.0107	0.2378	0.0017
3	0.7996	0.0003	0.1020	0.0005

The present calculations provide some insight into a possible reason for the strong binding of UN. As is illustrated in Table 6.2, the electrons occupying the *s-p* band in the 0.55–0.90 rydberg range distribute themselves nearly evenly around the U and N sites in the crystal. This type of behavior strongly resembles that of a covalent molecular bond, which could imply a strong contribution to the binding. We thus postulate that the strong binding of UN is due to some of the electrons from the free atoms rearranging themselves in the solid to form a covalent *s-p* band a few electron volts below the Fermi energy.

We anticipate that, as experiment leads to more quantitative information concerning UN's band structure, the present calculations will be further refined. Such refinements will involve changing the one-electron potentials used in these calculations and also considering all relevant relativistic efforts.

LOW-TEMPERATURE THERMAL CONDUCTIVITY

W. S. Williams[5] L. G. Radosevich[5]

The thermal conductivity of a 98%-dense pressed-and-sintered rod of UN supplied by ORNL was measured between 2 and 83°K. The results, after being corrected to theoretical density, agreed almost perfectly at 80°K with those obtained by Moore *et al.*[6] for a similar specimen. Both sets of data are shown in Fig. 6.2, in which the ORNL results are shown only as smoothed values. Significantly, no anomaly in the thermal conductivity appears in the vicinity of the Néel

[5] The authors are, respectively, Professor of Physics and Ceramic Engineering and a postdoctoral fellow in physics at the University of Illinois.

[6] J. P. Moore, W. Fulkerson, and D. L. McElroy, "Thermal Conductivity, Electrical Resistivity, and Seebeck Coefficient of Uranium Mononitride," paper submitted to the *Journal of the American Ceramic Society.*

point (approximately 53°K), which is in sharp contrast to the behavior of the electrical resistivity.[6] If we assume that the Lorenz number L for UN is the Sommerfeld value L_0 at all temperatures and use the electrical resistivity values of Moore *et al.*, measured on our specimen, we find a minimum in the electronic portion of the thermal conductivity near the Néel point but no anomaly in the lattice contribution (see Fig. 6.2).

We are not able to say at this time whether this separation of the thermal conductivity into electronic and lattice portions using L_0 is valid over the entire temperature range. However, at low temperatures (below 10°K) where elastic scattering of the current carriers by crystal defects is predominant (see Chap. 9 of this report) L_0 is the theoretically correct Lorenz number, and in this temperature range the thermal conductivity is almost entirely electronic.

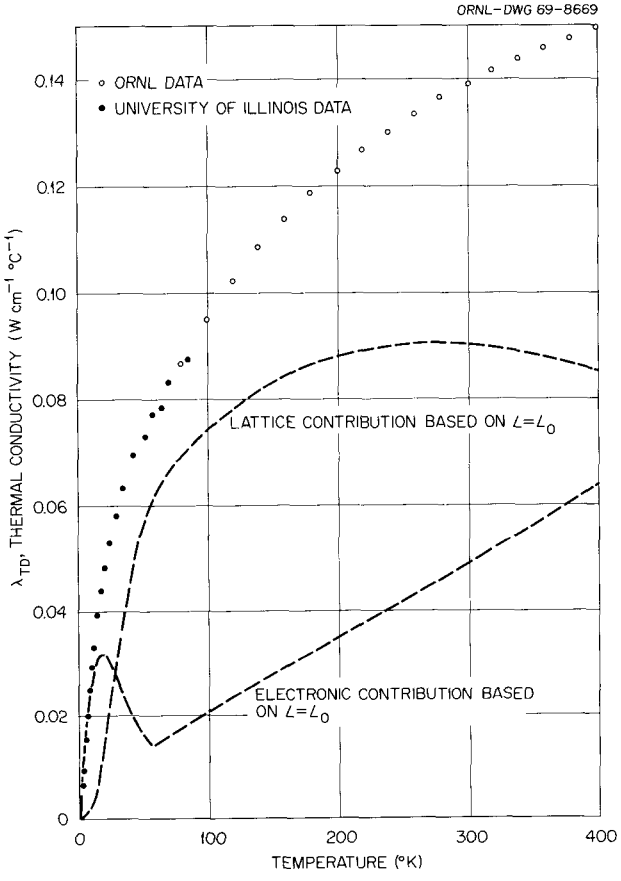

Fig. 6.2. The Thermal Conductivity of UN as Measured by ORNL from 80 to 400°K and by the University of Illinois from 2 to 82°K. The electronic portion of the thermal conductivity was obtained using the Sommerfeld value of L_0 and ORNL electrical resistivity values. The lattice component was obtained by difference.

CHEMICAL ANALYSIS FOR CARBON AND NITROGEN BY PROTON REACTION ANALYSIS

J. H. Gibbons[7] R. L. Macklin[7]
R. Jaszczak[7] W. Fulkerson

Encouraging preliminary experiments indicate that proton reaction analysis[8] may provide a sensitive, nondestructive method for determining contents of nitrogen and carbon in UN and U(C,N). Conventional chemical analytical techniques have been very unreliable. The new method involves irradiating unknown specimens and known standards in vacuum with a sharply focused beam of protons from the ORNL 3-Mv Van de Graaff machine. The resulting spectra produced are measured and quantitatively compared. The most promising proton reactions are $^{15}N(p,\alpha\gamma)^{12}C$ and $^{12}C(p,\gamma)^{13}N$, which produce gamma quanta with characteristic energies of 4.43 and 2.28 Mev respectively. With proton energies of about 1.9 Mev or greater, the ^{12}C reaction is swamped by the ^{15}N reaction,[9] but at lower energies the ^{15}N reaction is sufficiently suppressed that carbon can be clearly distinguished. This is shown in Fig. 6.3, which presents gamma spectra for a specimen of U(C,N) containing about equal amounts of carbon and nitrogen. The two spectra show how the nitrogen and carbon relative intensities change as the proton energy is varied from 0.7 to 1.26 Mev. Measurements can be made on porous specimens, and there is no reason why the method could not be applied to LMFBR fuel material containing plutonium. The technique can also be used on radioactive specimens.

[7]Physics Division.

[8]R. L. Macklin, J. H. Gibbons, E. Ricci, T. Handley, and D. Cuneo, "Proton Reaction Determination of Lithium and Fluorine in Molten Salt Reactor Graphite," *Nucl. Appl.* 5, 269–74 (1968).

[9]In naturally occurring nitrogen ^{15}N is present to the extent of 0.36 at. %, but this amount is easily detected by this method.

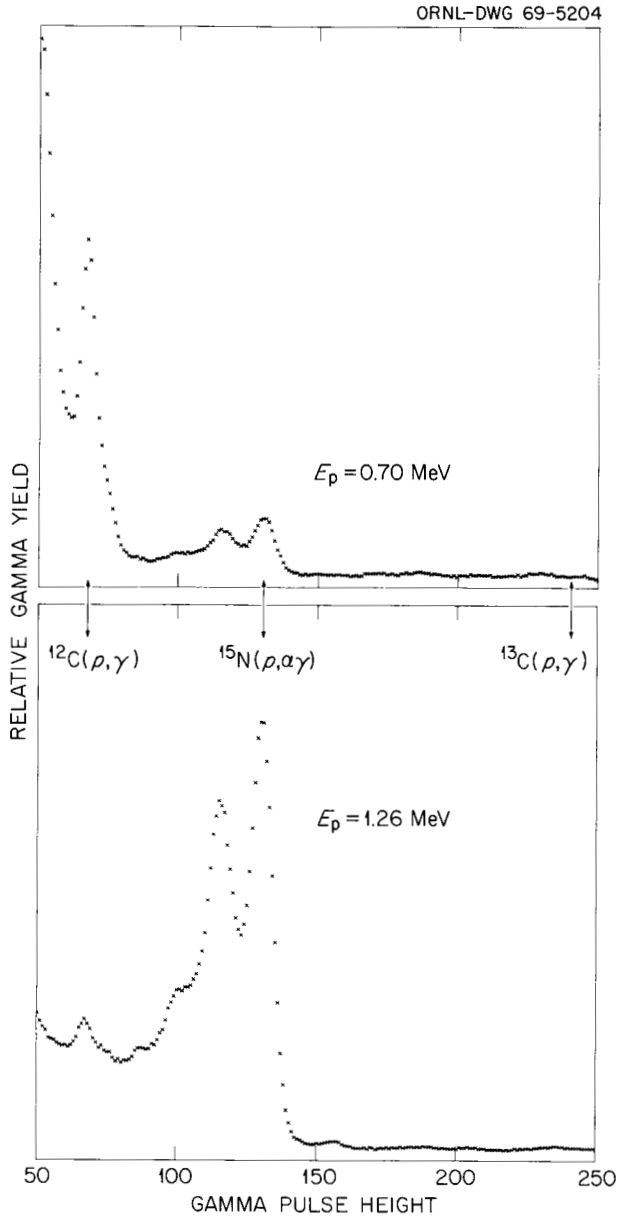

Fig. 6.3. Gamma Spectra Produced by the Reaction of 1.26- and 0.7-Mev Protons with a U(C,N) Alloy Containing Approximately Equal Atomic Percentages of Carbon and Nitrogen. The ^{12}C and ^{15}N peaks are indicated.

7. Mössbauer Studies of Alloys

B. S. Borie

Two major lines of research are pursued in the Mössbauer experiment program. One is the investigation of magnetic and other properties related to the electronic structure of transition metal alloys with Mössbauer spectroscopy of ^{61}Ni. The second objective is the study of irradiation effects in metallic solids with on-line Mössbauer spectroscopy of nuclei excited in a nuclear reaction.

MÖSSBAUER SPECTROSCOPY WITH ^{61}NI IN COMPOUNDS AND TRANSITION METAL ALLOYS

J. C. Love[1] F. E. Obenshain[2]
G. Czjzek

The Mössbauer resonance of the 67.4-kev gamma transition of ^{61}Ni has been observed for Cu-Ni, Co-Ni, and Fe-Ni alloys and for several nickel compounds. The nonmagnetic source was ^{61}Co in a ^{64}Ni–14 at. % V matrix, in which the ^{61}Co was produced in situ by the reaction ^{64}Ni$(p,\alpha)^{61}$Co, using 22-Mev protons. Most of the data were obtained with both source and absorber at 4.2°K.

The second-order Doppler shift due to zero-point motion of the nickel nucleus was estimated for several absorbers and subtracted from the observed energy shift in each case to give a true isomer shift, which is proportional to the electronic charge density at the nucleus. Relativistic Direc-Slater wave functions were calculated in the Wigner-Seitz approximation for several electronic configurations of nickel. The calculated charge densities and the isomer shifts observed between nickel metal and Ni^{2+} (0.072 mm/sec) and between Ni^{2+} and Ni^{4+} (–0.144 mm/sec) yield the following limits on the fractional change in charge radius $\Delta R/R$ of the ^{61}Ni nucleus: $-2.6 \times 10^{-4} < \Delta R/R < -0.9 \times 10^{-4}$.

The isomer shift of dilute ^{61}Ni in copper is $(2.5 \pm 2.8) \times 10^{-3}$ mm/sec relative to nickel metal, corresponding to a *loss* of less than 5% of a 4*s* electron or the addition of less than 25% of a 3*d* electron. This result contradicts the rigid band model of these alloys which predicts the transfer *to* the nickel site of about 40% of a 4*s* electron.

The magnetic moment of the first excited state of ^{61}Ni was determined to improved precision: $\mu_{ex} = -(0.642 \pm 0.008)\mu_{gnd} = +(0.481 \pm 0.006)\mu_N$, using Drain's[3] value of $\mu_{gnd} = -0.74868\mu_N$. The effective hyperfine field at ^{61}Ni in Fe-Ni, Co-Ni and Cu-Ni alloys was found to have a Slater-Pauling type dependence on the electron-to-atom ratio of the alloy; it is approximately described by the function $H_{eff}(^{61}\text{Ni}) = 87.3\ \bar{\mu}(\text{alloy}) + 39.3\ \bar{\mu}(\text{Ni})$. The hyperfine fields at ^{61}Ni in NiF_2 (45 kilooersteds), $KNiF_3$ (65 kilooersteds) and NiO (100 kilooersteds) are compared with the core-polarization field for Ni^{2+} ($H_{CP} = -275$ kilooersteds) calculated by Watson and Freeman[4] from Hartree-Fock wave functions and with estimated orbital fields based on experimental *g* values, and surprisingly good agreement is found if the measured fields are assumed to be negative.

Recoilless fractions and effective Debye temperatures were derived for the Cu-Ni alloys and Ni compounds from the area under the Mössbauer resonance. The results show that the coupling of an impurity nickel atom in a copper lattice is equal to the Cu-Cu coupling to within 2%.

[1] ORAU fellow from Ohio State University, now at Yale University, New Haven, Conn.

[2] Physics Division.

[3] L. E. Drain, *Phys. Letters* **11**, 114 (1964).

[4] R. E. Watson and A. J. Freeman, *Phys. Rev.* **120**, 1134 (1960).

FINAL POSITIONS OF LOW-ENERGY ^{57}Fe RECOIL ATOMS IN BODY-CENTERED CUBIC IRON-ALUMINUM ALLOYS[5]

G. Czjzek W. G. Berger[6]

One of the open problems in radiation damage theory concerns the final position of primary recoil atoms. The question has been studied extensively theoretically,[7,8] but direct experimental evidence is sparse. Observing the Mössbauer effect following neutron capture[9-11] offers a means for direct experimental investigation.

Neutron capture populates a highly excited level (6 to 8 Mev) of the product nucleus. The capture level is de-excited by emission of gamma rays, which impart recoil energies of a few hundred electron volts to this nucleus. The nucleus is displaced from its lattice position and comes to rest in the lattice within about 10^{-13} sec. The dominant mechanism of energy loss in this energy range is by elastic collisions with other lattice atoms. These may in turn be displaced, and the final position of the recoiled atom is likely to be disturbed.

Neutron capture in ^{56}Fe populates a level in ^{57}Fe at 7.643 Mev (ref. 12). In about half the capture events the de-excitation leads to the 14.4-kev level in ^{57}Fe, and the Mössbauer effect can be observed with 14.4-kev gamma rays emitted by these nuclei.[11] The recoil energies due to high energy gamma emission range between about 10 and 549 ev. The mean lifetime of the Mössbauer level (1.4×10^{-7} sec) is very long compared to the flight time of approximately 10^{-13} sec.

Earlier (n,γ)-Mössbauer experiments with pure iron targets[11] showed no detectable influence of the recoil event on the hyperfine interactions of the nuclei. Strong effects were found in ionic crystals, where both lattice disturbances and electronic aftereffects have strong but difficult-to-separate influences on the hyperfine interactions. In metallic systems electronic aftereffects can be neglected, and if recoil effects on the hyperfine interactions are observed they can be ascribed uniquely to lattice disturbances.

Since hyperfine interactions at an iron atom in Fe-Al alloys are strongly influenced by the distribution of atoms in the first few coordination shells of the sensing nucleus,[13-15] such alloys should be well suited for the observation of recoil effects.

Experiments

The experiments were performed at the Karlsruhe FR2 reactor with a bismuth-filtered neutron beam of about 3×10^7 neutrons cm^{-2} sec^{-1}. The Mössbauer spectrometer consisted of a conventional loudspeaker system as velocity drive in connection with a multichannel analyzer operated in the time mode. We detected the 14.4-kev gamma rays with a proportional counter with an anticoincidence shield described previously.[9] The (n,γ)-Mössbauer spectra were taken with a single-line absorber of $Na_4Fe(CN)_6 \cdot 10H_2O$ containing 1 mg/cm^2 ^{57}Fe. With every sample we also took an absorption spectrum using a source of ^{57}Co in Cu and the alloy targets as absorbers. Comparison of these two spectra revealed directly the difference between the hyperfine interaction of the ^{57}Fe nuclei in an undisturbed lattice position and in a position reached after recoil.

Alloy samples ranged from about 26 to 52 at. % Al. The lattice structure of the alloys is body-centered cubic. The equilibrium order[16] at room temperature is of Fe_3Al type for alloys containing about 25 to 33 at. % Al and of CsCl type from about 33 to 54 at. % Al, as shown in Fig. 7.1. At deviations from stoichiometric composition surplus atoms of one kind are randomly substituted in the sublattice of the other atoms.

---

[5] Based on experiments performed in Karlsruhe while G. Czjzek was on a one-year research assignment at Kernforschungszentrum Karlsruhe, Institut für Angewandte Kernphysik, Karlsruhe, Germany.

[6] Kernforschungszentrum Karlsruhe, Institut für Angewandte Kernphysik.

[7] C. Erginsoy, G. H. Vineyward, and A. Shimizu, *Phys. Rev.* 139, A118 (1965).

[8] P. H. Dederichs, C. Lehmann, and H. Wegener, *Phys. Status Solidi* 8, 213 (1965).

[9] D. W. Hafemeister and E. Brooks Shera, *Phys. Rev. Letters* 14, 593 (1965).

[10] J. Fink and P. Kienle, *Phys. Letters* 17, 326 (1965).

[11] W. G. Berger, J. Fink, and F. E. Obenshain, *Phys. Letters* 25A, 466 (1967).

[12] L. V. Groshev *et al.*, *Nucl. Phys.* 58, 465 (1964).

[13] M. B. Stearns and S. S. Wilson, *Phys. Rev. Letters* 13, 313 (1964).

[14] L. Cser, J. Ostanevich, and L. Pal, *Phys. Status Solidi* 20, 581, 591 (1967).

[15] G. P. Huffman and R. M. Fisher, *J. Appl. Phys.* 38, 735 (1967).

[16] M. Hansen, *Constitution of Binary Alloys*, McGraw-Hill, New York, 1958.

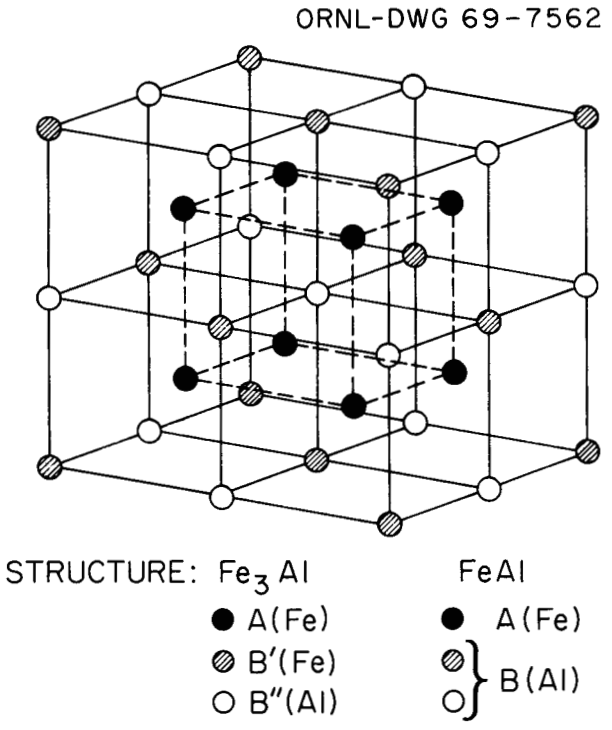

Fig. 7.1. Lattice structure and order of Fe-Al alloys (25 to 54 at. % Al).

We prepared samples with FeAl order (25 to 52 at. % Al) by vacuum melting high purity iron and aluminum powder. The solidified buttons were homogenized, crushed, and annealed 24 hr at 700°C. All samples were analyzed chemically and by x-ray diffraction. The Fe_3Al samples and one FeAl specimen (35.5 at. % Al) were kindly provided by Prof. V. Gerold (Max-Planck Institut für Metallforschung, Stuttgart). The preparation has been described by Lütjering and Warlimont.[17]

Results

Alloys with FeAl structure (35 to 52 at. % Al). – These alloys are paramagnetic above 20°K, and the Mössbauer absorption spectrum at room temperature consists of one broadened line. We fitted such spectra with a single line of Lorentz shape. The overall fit is not good, but the center of the line can be determined accurately. The resulting shifts relative to the center of a pure iron spectrum are shown in Fig. 7.2 as a function of aluminum concentration. (The positive sign of the shift means that the resonance is centered at a higher energy than in iron). The dependence of the observed shifts on aluminum concentration can be explained by assuming that the spectra consist of several overlapping lines, each shifted by an amount $S = n_1 \Delta I_1 + n_2 \Delta I_2$, where n_k is the number of aluminum atoms in the kth coordination shell of the absorbing iron nucleus, and ΔI_k, the shift caused by an aluminum atom in the kth shell, is independent of the aluminum concentration (Fig. 7.2, curve 1).

The (n,γ)-Mössbauer spectra obtained at room temperature also show only one line. The center shifts relative to iron, determined in the same way as for the absorber spectra, are much smaller than those of the absorber lines (Fig. 7.2) for the same aluminum concentration.

With Fe–48.3 at. % Al we took (n,γ)-Mössbauer spectra at four different temperatures between 80 and 770°K to test the stability of the final positions of the recoil atom. For defects with an activation energy of migration Q the characteristics of the Mössbauer spectrum will change at a temperature at which the jump frequency $n_j \approx \nu_0 \exp(-Q/kT)$ (ν_0

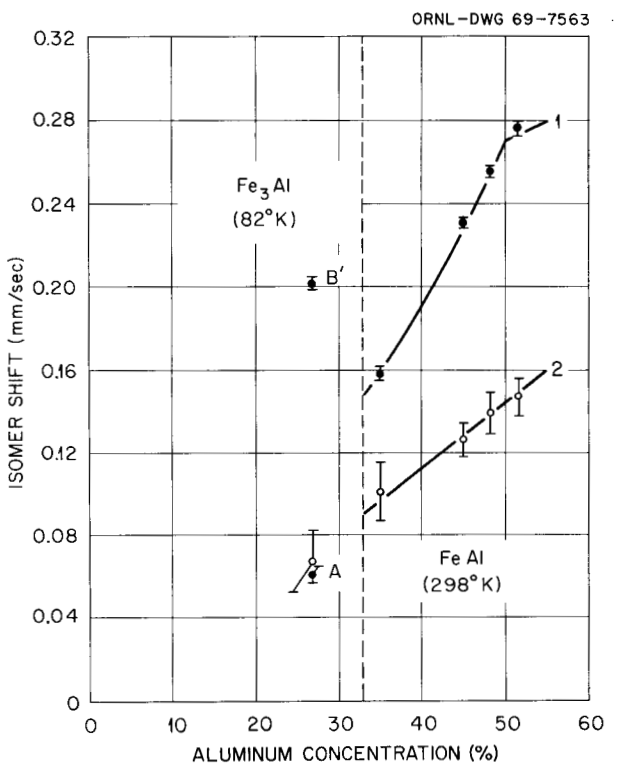

Fig. 7.2. Line shifts in Fe-Al alloys relative to metallic iron. ● absorber spectra. ○ (n,γ)-spectra. The points marked A and B′ correspond to the two different iron sites in Fe_3Al.

[17] G. Lütjering and H. Warlimont, *Z. Metallkunde* **56**, 1 (1965).

$\sim 10^{13}$ sec^{-1}) becomes larger than the inverse of the mean lifetime (1.4×10^{-7} sec) of the 14.4-kev level of ^{57}Fe.

Between room temperature and 570°K the shift between absorber and (n,γ) line was reduced by 10% of the total. The activation energy, Q, deduced from the temperature region of this change is 0.4 ± 0.1 ev, a value expected for interstitials. The smallness of the change indicates a very minor occurrence of recoil atoms in interstitial sites or of interstitials near the recoil atom.

Fe_3Al Sample (26.75 at. % Al). – This sample is ferromagnetic with a Curie temperature of 800°K. The Mössbauer absorption spectrum obtained at 80°K with the ^{57}Co in Cu source is shown in Fig. 7.3(*a*) and is similar to reported spectra.[14] The general interpretation of the spectrum is that iron nuclei on lattice sites A (4 nearest Al neighbors) see a smaller hyperfine field than iron nuclei on sites B′ (no Al atoms in the first neighborhood shell).[18] The (n,γ)-Mössbauer spectrum for the same sample at 80°K is displayed in Fig. 7.3(*b*). Comparison shows clearly that at most a small fraction of the recoiled nuclei can be in positions equivalent to normal iron lattice sites in Fe_3Al.

Discussion

To interpret the observed effects we performed calculations with a simple collision model, extending the methods of Dederichs and co-workers.[8] We use the approximation of elastic hard-sphere collisions to estimate the probability of direct replacement collisions – after a collision with a lattice atom the recoil atom retains less energy than the displacement threshold energy, E_d, transfers an energy larger than E_d to the struck atom – and the probability of indirect replacements – the recoil atom creates a vacancy in a collision with a lattice atom, and is itself stopped in the next collision with a first, second, or third neighbor of the vacancy. The recoil atom then forms an unstable interstitial and will reunite within about 10^{-9} sec with the vacancy.

By similar processes vacancies are created near the final position, either by a replacement collision of the recoil atom in the neighborhood of a vacancy created in a previous collision with a lattice atom, or by a nearby collision of the atom that has been replaced by the recoil atom. Other local processes calculated are the stopping of the replaced atom, which then becomes an interstitial in the vicinity of the recoil atom, and exchange collisions of the replaced atom leading to a disturbance of the lattice ordering near the final site of the recoil atom. Simple arguments show that these local processes dominate the contribution to defects near the final position of the recoil atom.

The model calculations were performed for pure iron and for iron-aluminum alloys with Fe_3Al and FeAl structures. Some results for Fe_3Al are: 80% of the recoil atoms come to rest on a lattice site – 44% on an A site, 21% on a B′ site, and 15% on a B″ site; 20% of the recoil atoms end in an interstitial position; 23% have a vacancy in the first coordination shell; 12% have a vacancy in the second coordination shell; 6% have an iron interstitial in the

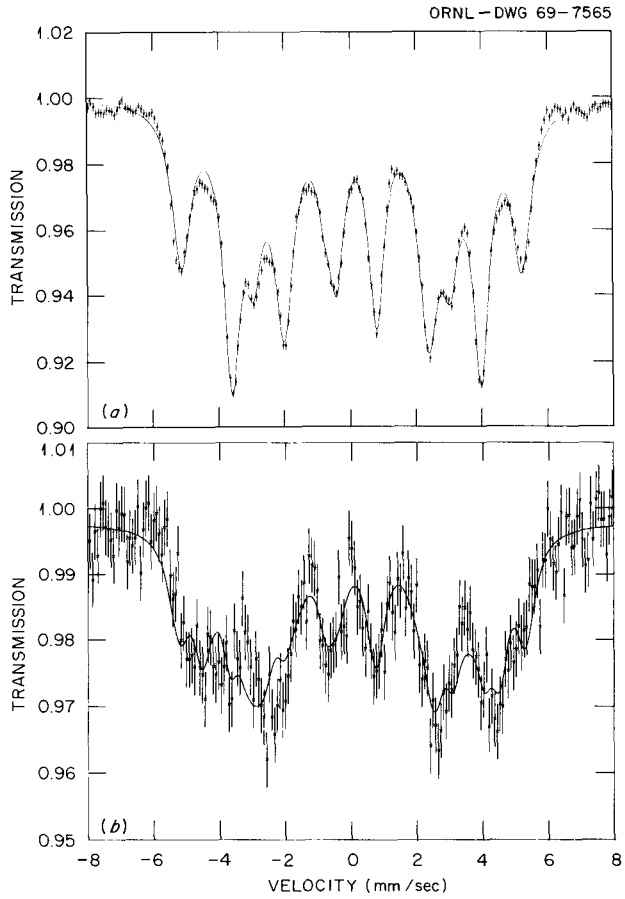

Fig. 7.3. Mössbauer Spectra of Fe_3Al (26.75 at. % Al) at +82°K. (*a*) Absorber spectrum. (*b*) (n,γ) spectrum.

[18] We deduce from the spectrum the influence of aluminum neighbors on the shift and on the magnetic hyperfine field in the same way as outlined above for the FeAl-structure alloys.

neighborhood; 2% have an aluminum interstitial in the neighborhood. The average number of aluminum atoms in the first coordination shell is 2.2; in the second it is 1.6.

Using detailed results on the atomic distribution near the final positions of the recoil atom and the influence of aluminum neighbors deduced from the absorber spectrum, we can fairly well reproduce the observed Mössbauer spectrum following neutron capture in Fe_3Al [continuous line in Fig. 7.3(*b*)] if we assume that a vacancy in the first neighborhood shell reduces the magnetic hyperfine field at the site of the ^{57}Fe recoil atom by 16% and contributes an isomer shift of –0.03 mm/sec. The same reduction of the field but zero isomer shift is assumed for a ^{57}Fe recoil atom at an interstitial site. Vacancies in the second coordination shell and nearby iron interstitials are neglected. The effect of aluminum interstitials is taken to be the average of aluminum atoms in lattice sites in the first and second coordination shell. With the same assumptions we calculate the shifts expected for (n,γ) Mössbauer spectra in FeAl structure alloys shown by curve 2 in Fig. 7.2.

The results, especially the shifts and field changes due to defects, should be considered as qualitative indicators of trends rather than as quantitative estimates since they are derived from a crude model with several shortcomings. The most serious one is presumably the neglect of energy losses to lattice vibrations. Comparison with detailed calculations[7] shows that a more realistic model should result in a much smaller fraction of interstitial sites for the recoil atom positions.

8. Physical Ceramics Studies

C. S. Morgan

These studies are aimed at improving the basic understanding and practical technology of solid state processes in ceramics through investigation of the mechanisms of material transport in deformation and sintering. We emphasize analyzing dislocation generation and propagation. Studies of the microstructure of graphite and deformation of sol-gel UO_2 are reported in Chaps. 32 and 24 respectively.

DEFORMATION OF URANIUM DIOXIDE SINGLE CRYSTALS

C. S. Yust C. J. McHargue

The study of the deformation of uranium dioxide single crystals is being extended to include hyperstoichiometric crystals. Hyperstoichiometric uranium oxide is known to deform at lower stress at a given temperature and strain rate than stoichiometric material, and our intent is to study the effects of excess oxygen on dislocation generation and propagation during deformation. To date we have demonstrated that the composition of uranium dioxide crystals can be adjusted to a desired oxygen-to-uranium ratio in the creep system and subsequently reduced to $UO_{2.00}$. Electron micrographs of material exposed to such a cycle of oxidation and reduction are essentially the same as those of the source uranium dioxide, indicating that this cycle of operations does not alter the dislocation structure of the specimen.

"DESINTERING"

K. H. McCorkle[1] C. S. Morgan

It is well established that a sintering ceramic powder compact will often lose density, or "desinter," if the annealing temperature is too high and is maintained a sufficient time. This phenomenon, which is normally attributed to pressure of entrapped gas, usually limits the density obtainable in sintering. The occurrence and causes of this desintering are being investigated in sol-gel ThO_2 specimens. Thoria chunks of very high initial density are obtained by carefully evaporating and sintering at 1150°C.

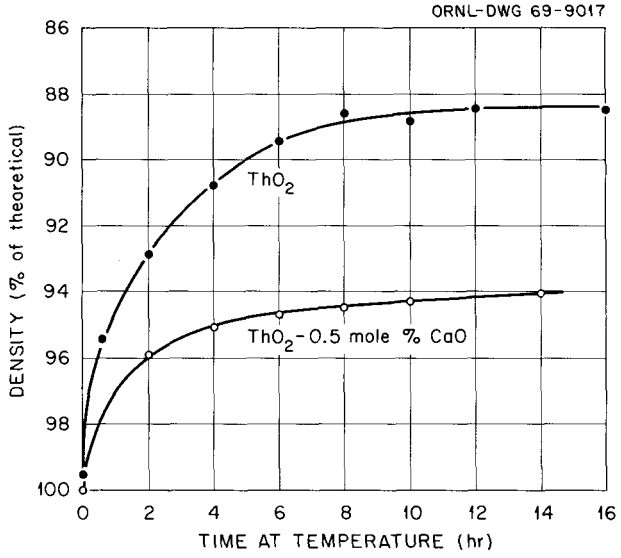

Fig. 8.1. Desintering of ThO_2 and ThO_2–0.5 mole % CaO Sol-Gel Specimens at 1800°C.

Figure 8.1 compares the desintering of a pure ThO_2 specimen with the sharply reduced extent of the desintering process in a specimen containing about 0.5 mole % CaO. The interrelation of pore structure, crystallite size, and crystal face energies are being studied in an effort to elucidate the cause and mechanism of desintering.

COMPRESSIVE CREEP OF URANIUM MONONITRIDE

C. S. Yust L. L. Hall

The high-temperature compressive creep characteristics of polycrystalline UN are being investigated. The

[1]Chemical Technology Division.

specimens used are 95% dense and have a grain size of about 10 μ. Preliminary results in Ar–4% H_2 atmosphere covering a range of 1150 to 1600°C were somewhat irregular. A new test system allowing deformation under a wide range of carefully controlled nitrogen pressures is being prepared. This will permit determination of the effect of stoichiometry on the creep process in UN. Nitrogen pressure drastically affects the diffusion of uranium in UN, and this should be reflected in the creep behavior of this material.

SOME OBSERVATIONS ON ACTIVATION ENERGY IN SINTERING[2]

C. S. Morgan L. L. Hall

For a number of years we have been concerned with the densification kinetics during early sintering of highly active ceramic powders. The densification of ThO_2, for example, is characterized by an initial rapid rate during the time a compact is being heated to a preselected study temperature. This initial rapid densification appears to have a temperature-dependent end point, is unaffected by the heating rate, and is followed by much slower isothermal changes in density. Evidence has been presented to show that the densification kinetics during the initial step cannot be accounted for by a diffusion-controlled process, and it has been argued that plastic flow by dislocation generation and motion plays a significant role. Indeed, the kinetics of this densification has many features similar to that of primary creep of metals under stress. In the current work the variation of the sintering activation energy with changes in the initial heating conditions is reported and analyzed.

Small, highly sinterable ThO_2 powder compacts were heated rapidly at a uniform rate and held various times at an initial temperature T_1. The densification rates were determined during short incremental heating times at T_1 and at temperatures T_2 30°C above or below T_1. The activation energy, Q, was determined from the Arrhenius equation,

$$\ln \frac{k_1}{k_2} = \frac{Q}{R}\left(\frac{1}{T_2} - \frac{1}{T_1}\right) ,$$

where k_1 and k_2 are the densification rates at temperatures T_1 and T_2 are R is the gas constant.

Tests in which the initial heating time was long, for example 1 hr, gave activation energies that approximated the activation energy for self-diffusion of thorium in ThO_2. However, when short heating times were used the activation energies were as high as 391 kcal/mole and were always higher when determined from densification rates obtained on raising the temperature than on lowering it. We think that the experimental densification rates yield such high values for the activation energy when substituted in the Arrhenius equation because one is actually comparing densification rates caused by different transport mechanisms, rather than the same process affected only by the temperature change. A possible explanation is that after a short hold at one temperature the dislocations move easily when the temperature is raised but dislocation motion becomes more difficult when the temperature is dropped. This results in unreasonable activation energies because the densification from fast dislocation motion caused by the temperature rise is being compared with densification effected by diffusion-controlled dislocation motion and/or by other diffusion-controlled transport processes.

This work demonstrates the importance of considering the possibility of material transport by dislocation motion in evaluating a sintering problem.

TOPOLOGY OF SINTERING

L. K. Barrett[3] C. S. Yust

Efforts are continuing to formulate a mathematical model for sintering incorporating topological aspects of the sinter body. Experiments are being conducted to assess the shape of the void-solid interface in typical ceramics. A series of sections in a 92%-dense ZnO body showed that appreciable connectivity still exists in the void of such a specimen. This agrees with the result previously determined in a pure copper sinter body. The studies of the change of shape of the void-solid interface with change in density will serve as the basis for the formulation of a mathematical model of sintering.

DIFFUSION OF THORIUM IN ThO_2

L. E. Poteat[4] C. S. Morgan

Additional tests of penetration of ^{230}Th in ThO_2 specimens were made to further check the temperature effect on single-crystal diffusion and to cover more grain sizes in polycrystalline specimens. An attempt to determine the influence of increasing the number of dislocations present on the ^{230}Th penetration profile failed. This investigation is now completed and will be prepared for publication.

[2] Abstrated from a note to be published in the *Journal of the American Ceramic Society*.

[3] Consultant from the University of Tennessee.

[4] Consultant from Clemson University, Clemson, S.C.

9. Physical Properties

D. L. McElroy

We are studying heat transport and related physical properties of solids over a broad temperature range. Carefully selected and well-characterized solids are chosen to investigate periodic trends and the effects of intentional changes. These data are analyzed using existing theories in a search for the limits of theory and for a practical understanding of heat transport. For instance, this experimental approach may allow reliable thermal conductivity λ predictions of metals and alloys beyond the range of available λ data by using electrical resistivity ρ data. An obvious shortcoming of this approach is the dilemma when theory fails. Our previous measurements have shown that existing transport theory is inadequate in many cases. We feel a fuller experimental demonstration of these failures will probably stimulate further theoretical work in transport phenomena. Hence, this past year most of our efforts were devoted to developing and upgrading property measurement methods of broad applicability and high accuracy.

Coordinated programs are being conducted in several applied research areas and other sections of this report include results of our studies on UN, a Th-U alloy, MSRE graphites, sol-gel powders, W-Re alloys, and thermal contact resistance in Chaps. 6, 26, 32, 34, 15, and 18 respectively. In addition we are constructing equipment of proven design to allow measurements on plutonium-bearing materials and on irradiated graphites.

ELECTRONIC HEAT TRANSPORT

Electrical Resistivity of Tantalum to 2600°K

R. K. Williams

Using an ultrahigh-vacuum furnace, we obtained electrical resistivity data for tantalum between 300 and 2600°K. Pressures were held at 5×10^{-8} torr or less during all of the tests, and ρ at room temperature of the electron-beam-melted specimen actually decreased by about 0.05 μohm-cm during the run. Temperatures were measured with Pt–10% Rh vs Pt thermocouples ($T \leqslant 1700$°K) and an automatically balancing optical pyrometer ($T \geqslant 1100$°K), and the two methods agreed to ±3° at temperatures below 1700°K.

Approximately 90 data points were obtained, and their repeatability and determinate errors were comparable to results obtained in our lower temperature apparatus.[1] However, the temperature measurements became increasingly uncertain at high temperatures, and this error could amount to as much as ±15° at 2600°K. The graphically smoothed results, corrected for thermal expansion,[2] can be described to a standard deviation of 0.029 μohm-cm by the equation $\rho = -1.89325 \times 10^2/T + 4.84500 \times 10^{-2}\ T - 5.69237 \times 10^{-6}\ T^2 + 5.98696 \times 10^{-10}\ T^3$, where ρ is in μohm-cm and T is in °K. Over the whole range $d^2\rho/dT^2$ is negative, but it becomes smaller at higher temperatures and appears to approach zero. This behavior for ρ has been previously reported[3] for Ta, Nb, Pd, and Pt.

The development of this equipment represents a major measurement capacity expansion, which is needed[4] to obtain reliable data on refractory metals and alloys for heat transport analysis and data extrapolation. These studies require knowledge of the Lorenz function and lattice component behavior. A number of

[1] W. Fulkerson, J. P. Moore, and D. L. McElroy, "Comparison of the Thermal Conductivity, Electrical Resistivity, and Seebeck Coefficient of a High-Purity Iron and Armco Iron to 1000°C," *J. Appl. Phys.* 37, 2639–53 (June 1966).

[2] J. B. Conway and A. C. Losekamp, "Thermal Expansion Characteristics of Several Refractory Metals to 2500°C," paper presented at the Fifth Conference on Thermal Conductivity, University of Denver, 1965.

[3] H. H. Potter, *Proc. Phys. Soc.* 53, 695 (1941).

[4] R. K. Williams and W. Fulkerson, "Separation of the Electronic and Lattice Contributions to the Thermal Conductivity of Metals and Alloys," pp. 389–456 in *Thermal Conductivity, Proc. 8th Conf., held at Purdue University, West Lafayette, Indiana, October 7–10, 1968,* ed. by C. Y. Ho and R. E. Taylor, Plenum Press, New York, 1969.

pure metal and dilute alloy samples representative of the group VB and VIB elements were obtained for determination of these characteristics.

Electrical Heating Method

K. H. Bode J. P. Moore
R. K. Williams R. S. Graves

We are attempting to perfect an electrical heating method for obtaining λ and ρ data on small diameter rods to 1500°K since small samples of a variety of materials, including refractory metals and their alloys, are more readily available than are the large 3-in.-diam disks required for radial heat flow measurements. This method centers around a current-carrying rod with controlled boundary conditions to allow comparisons to various existing solutions to this heat conduction problem.[5] Construction, testing, and assembly of the apparatus are nearly complete. Initial measurements will use an Nb–10% W alloy for which we previously measured λ from 80 to 1300°K using our radial heat flow apparatus[6] and our absolute longitudinal method.

Two Nb–10% W alloy specimens were measured by our absolute longitudinal method between 80 and 400°K to aid in establishing a "standard" specimen. One was machined from a disk used in our radial heat flow experiment[6] to 1300°K. The other came from the extruded and swaged material used for fabricating a long specimen for the direct heating experiment. The λ and ρ data from these two samples agreed within 1% from 80 to 410°K and with the high-temperature data from the radial apparatus to within 1% over the temperature range of overlap. This material will make an acceptable standard since the transport properties are insensitive to fabrication details and are reasonably well known.

Physical Properties of Gold

J. P. Moore R. S. Graves
D. L. McElroy

A study of the transport properties of high-purity gold indicated a behavior similar to that of copper reported previously.[7] If we assume that the lattice conduction in these two simple metals is negligibly small, the ratio $\lambda\rho/TL_0$ (L_0 is the Sommerfeld value 2.443×10^{-8} $v^2/°K^2$) is the same for Cu and Au to within 0.4% for all reduced temperatures, T/θ, from 0.26 to 2.4 when Debye temperatures θ for copper and gold of 320 and 169°K, respectively, are used.[8] In contrast with our results for some transition elements,[4] Fig. 9.1 shows that the ratio approaches 1.0 with increasing T/θ, as would be expected from theory for elastic scattering of electrons by phonons in simple

[5] K. H. Bode, "Possibilities to Determine Thermal Conductivity Using New Solutions for Current-Carrying Electrical Conductors," pp. 317–37, *Thermal Conductivity, Proc. 8th Conf., held at Purdue University, West Lafayette, Indiana, October 7–10, 1968,* ed. by C. Y. Ho and R. E. Taylor, Plenum Press, New York, 1969.

[6] J. P. Moore and R. S. Graves, *Metals and Ceramics Div. Ann. Progr. Rept. June 30, 1966,* ORNL-3970, p. 79.

[7] J. P. Moore, D. L. McElroy, and R. S. Graves, "Thermal Conductivity and Electrical Resistivity of High-Purity Copper from 78 to 400°K," *Can. J. Phys.* **45**, 3849–65 (1967).

[8] K. A. Gschneider, Jr., "Physical Properties and Interrelationships of Metallic and Semimetallic Elements," *Solid State Phys.* **16**, 275 (1964).

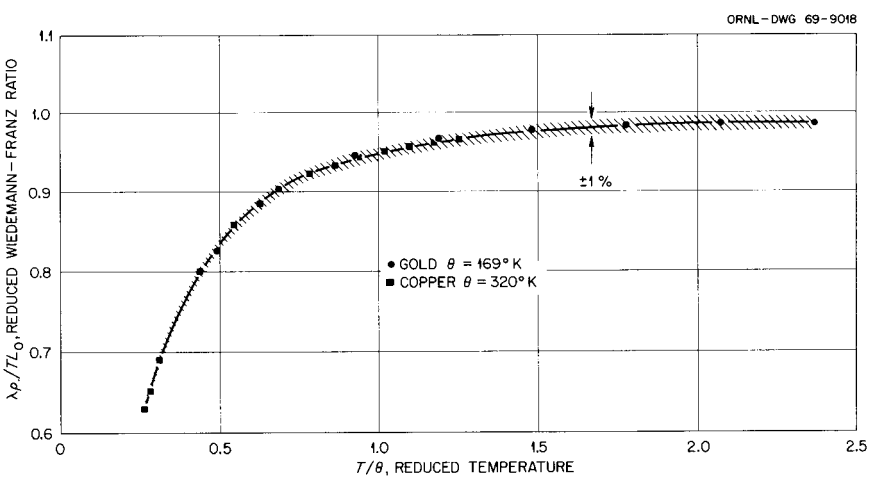

Fig. 9.1. Reduced Wiedemann-Franz Ratio as a Function of Reduced Temperature for Gold and Copper.

metals. The high precision of the gold λ data led to discovery and correction of small errors in our Chromel-P vs constantan thermal emf tables.

LATTICE HEAT TRANSPORT

Thermal Conductivity of ThO_2 and UO_2

J. P. Moore R. S. Graves
D. L. McElroy

Low-temperature results by others[9,10] using longitudinal systems and our radial heat flow results on UO_2 differ by a factor of 2 below 300°K. To resolve this and to improve our knowledge of phonon scattering by spin disorder in UO_2, we measured λ of single-crystal and polycrystalline UO_2 from 80 to 400°K. The results are in excellent agreement with our previous high-temperature results[11] above 300°K but indicate some error in the previous data from 225 to 300°K. The λ results are smooth over the entire temperature range and indicate significant errors in the results of Bethoux[9] and Aring and Seivers[10] above 100°K.

We attempted to obtain λ data on 98%-dense UO_2 specimens supplied by the AEC-sponsored round-robin UO_2 program, but the specimen crumbled to powder at 450°K due to the presence of second-phase uranium metal. Fabrication changes have been made, and new specimens are ready for λ measurements.

Measurements of λ from 80 to 1400°K were completed on 93%-dense ThO_2, a λ standard proposed by the U.S. Air Force. The thermal resistivity, $1/\lambda$, was a linear function of temperature from 400 to 1400°K, with a slope within 2% of that found for UO_2 from 500 to 1200°K. If this high-temperature linear region is indicative of three-phonon Umklapp scattering, the modified Liebfried-Schlömann equation would predict that the Debye temperature of ThO_2 and UO_2 are the same within 7%. The linearity of $1/\lambda$ with T from 400 to 1400°K and the different linearity also observed from 200 to 400°K are difficult to interpret in terms of phonon processes. The behavior is quite similar to that previously reported for silicon.[12] The stability of the 93%-dense ThO_2 and the linearity of $1/\lambda$ with T over wide temperature ranges make it quite an attractive λ standard.

Thermal Conductivity of LiF

P. H. Spindler J. P. Moore
R. S. Graves

Thermal conductivity measurements were completed from 80 to 1100°K on single-crystal and polycrystalline LiF (NaCl structure, mp 1115°K) to ascertain thermal radiation conduction and the effects of vacancy formation on lattice conduction. This analysis is difficult in most translucent materials since these phenomena occur at temperatures so high that measurement accuracy is poor. However, both effects occur in LiF at comparatively low temperatures at which the radial heat flow apparatus is capable of accurate results. We noted a linear temperature dependence for the thermal resistivity from 80 to 450°K, $1/\lambda_L = 0.033\ T - 2.83$ (where λ_L is in w cm^{-1} $°K^{-1}$, T in °K). Above 450°K an enhancement of λ was noted and may be interpreted as thermal radiation conduction. The deviation from the $1/\lambda_L$ curve at 1100°K was about 30%. The total thermal conductivity is being analyzed with the so-called Rosseland approximation,

$$\lambda = \lambda_L + 16\sigma n^2 T^3/3k_R ,$$

where σ is the Stefan-Boltzmann constant, n is the refractive index, and k_R is the Rosseland mean absorption coefficient. Vacancy formation effects will be calculated and compared to any difference between this prediction and the measured λ values.

CALORIMETRIC STUDIES

Components of the Specific Heat Capacity of Nickel, Iron, and Ni_3Fe

T. G. Kollie

The specific heat capacity, C_p, of nickel, iron, and the alloy Ni_3Fe were investigated. Discontinuities of C_p of about 35% were noted for nickel and iron at the Curie temperatures, indicating that these Curie transformations are second-order. The contributions to C_p due to

[9] O. Bethoux, *Réalisation d'un Appareil Pour la Measure de la Conductibilité Thermique a Basse Température, Avant et Après Irradiation Neutronique. Application au Dioxyde d'Uranium,* CEA-R-2372 (September 1963).

[10] K. Aring and A. J. Sievers, "Thermal Conductivity and Far-Infrared Absorption of UO_2," *J. Appl. Phys.* **38**, 1496–98 (1967).

[11] T. G. Godfrey, W. Fulkerson, T. G. Kollie, J. P. Moore, and D. L. McElroy, "Thermal Conductivity of Uranium Dioxide from −57 to 1100°C by a Radial Heat Flow Technique," *J. Am. Ceram. Soc.* **48**, 297–305 (1965).

[12] W. Fulkerson, J. P. Moore, R. K. Williams, R. S. Graves, and D. L. McElroy, "Thermal Conductivity, Electrical Resistivity, and Seebeck Coefficient of Silicon from 100 to 1300°K," *Phys. Rev.* **167**, 765–82 (1968).

the changes of energy states of electrons and phonons of these elements and of ordered and disordered states of the Ni_3Fe alloy are being analyzed.[13] A new digital voltmeter recorder-computer system is being interfaced with a new pulse heating calorimeter.[14] This computer system acquires data at an effective rate and with an accuracy about equal to that of the old recorder, but it processes data during a run, yielding on-line C_p results within minutes of a run completion (instead of the previously required three days). Final data analysis will still be done with the large computer by means of compatible magnetic tape data transfer. This processing includes a data smoothing and temperature-rate-of-change calculating program, which should be applicable to other experiments.[15]

Physical Properties of Ordered and Disordered Ni_3Fe

J. P. Moore R. S. Graves

Transport properties (λ, ρ, and S) of two Ni_3Fe samples similar to the C_p specimens have been measured between 80 and 410°K. One sample had been quenched from 1400°K and was highly disordered ($\rho_{4.2°K}$ = 4.3 μohm-cm). The other had been annealed below the critical point for 30 days and was comparatively ordered ($\rho_{4.2°K}$ = 2.8 μohm-cm). The measurements indicate a significant lattice component to the thermal conductivity at low temperatures, but this appears to become negligibly small above 300°K. Between 200 and 410°K, the ratio $\lambda\rho/T$ is within ±2.5% of the Sommerfeld value for both samples. The slight difference in this ratio for the two specimens could be associated with the large difference in the electronic density of states for the ordered and disordered structures, noted in specific heat capacity measurements between 1.2 and 4.2°K.

RELATED STUDIES

Uranium Nitride[16]

W. Fulkerson J. P. Moore
D. L. McElroy

Electrical resistivity measurements were made between 2.2 and 77°K for a polycrystalline uranium mononitride specimen. The resistivity was separated into magnetic, defect, and phonon scattering contributions. Below the Néel point (~53°K) the phonon contribution was less than 1%. The magnetic contribution increased as $T^{1.91}$ between 2 and 13°K and as $T^{2.38}$ between 20°K and the Néel point. There was no evidence of a negative exponential factor in the electrical resistivity, as might be expected if there were a significant gap in the spin-wave spectrum. The absence of a gap would explain the observed difference between the value of the Debye temperature derived from low-temperature specific heat measurements and that obtained from the velocity of sound.

Thorium Nitride

S. C. Weaver[17] D. L. McElroy

A physical properties study was initiated on the ThN-UN system to identify the electronic and lattice components of heat transport in ThN, to show the effect of alloying on the magnetic transition in UN, and to explore practical applications of such fuels. Arc-casting in nitrogen atmospheres yielded coarse-grained specimens of more than 98% ThN, with less than 2% Th metal as second phase.

---

[13] T. G. Kollie, *The Contributions to Specific Heat Capacity of Ni, Fe, and Ni_3Fe,* Ph.D. Thesis, University of Tennessee, in preparation (1969).

[14] T. G. Kollie, M. Barisoni, and D. L. McElroy, "A Pulse Calorimeter Using a Digital Voltmeter for Data Acquisition," to appear in the proceedings of the European Conference on Thermophysical Properties of Solid Materials at High Temperatures, Nov. 11–13, 1968, Baden-Baden, West Germany; ORNL-4380 (February 1969); and submitted to High-Temperatures-High Pressures.

[15] T. G. Kollie, D. L. McElroy, and C. R. Brooks, *Convolute Method of Smoothing or Calculating the Time Derivatives of a Signal Recorded in Digital Form on Equal Time Intervals,* ORNL-TM-2517 (April 1969).

[16] Abstract submitted for presentation at the American Ceramic Society, Basic Science Section, Ottawa, Canada, 1969.

[17] Ceramics Technology Group.

10. Spectroscopy of Ionic Media

G. P. Smith

The objective of this research is information on the structure and behavior of ionic entities in molten salts, especially those entities formed by transition and posttransition metal ions. The primary method of study is optical absorption spectroscopy. A supportive line of research is the spectroscopy of transition metal ions in crystals to help identify the melt entities. Measurements of nonspectroscopic properties, such as crystal structure and electrical conductivity, provide auxiliary information.

LIQUID SYSTEMS

A Spectroscopic Study of Interactions Between $NiCl_4^{2-}$ and Outer-Shell Cations in CsCl-Rich Melts of $CsCl\text{-}ZnCl_2$ and $CsCl\text{-}MgCl_2$

W. E. Smith[1] J. Brynestad
G. P. Smith

Optical absorption spectra (5 to 25 $\times$ 10^3 cm^{-1}) are reported for dilute solutions of $NiCl_2$ in molten $CsCl\text{-}ZnCl_2$ mixtures containing up to 45 mole % $ZnCl_2$ at temperatures up to 1000°C and in molten $CsCl\text{-}MgCl_2$ mixtures containing 25 and 40 mole % $MgCl_2$ at 550 to 900°C. Under all these conditions Ni(II) is coordinated to four chlorides with an approximately tetrahedral geometry, but the spectrum of the $NiCl_4^{2-}$ chromophore depends on the presence or absence of a divalent solvent cation in the outer shell. The fraction of $NiCl_4^{2-}$ entities having divalent solvent cations in their outer shells is small for up to 25 mole % divalent chloride but increases rapidly from 25 to 40 mole % divalent chloride. This behavior is treated in terms of a model of interionic interactions from which we conclude that $NiCl_4^{2-}$ is a little more basic than $ZnCl_4^{2-}$ in chlorozincate melts.

[1] Presently at Department of Chemistry, University College of London, England.

Coordination Chemistry of Nickel(II) in Liquid Mixtures of Zinc and Cesium Chlorides[2]

W. E. Smith[1] J. Brynestad
G. P. Smith

The equilibrium coordination chemistry of dilute solutions of nickel(II) in liquid mixtures of $ZnCl_2$ with up to 50 mole % CsCl was investigated by optical absorption spectrophotometry in the range 5000 to 27,000 cm^{-1}. The measurements covered temperatures from near the liquidus up to 600 to 900°C depending on the solvent composition. At temperatures near the liquidus, nickel(II) has well-defined coordination geometries. In solvents containing about 50 to 20 mole % CsCl tetrahedrally and octahedrally coordinated entities are in equilibrium. The equilibrium shifts in favor of the four-coordinate entities with increasing temperature or CsCl content. Both entities are associated with chlorozincate polymer molecules. In solvents containing from no CsCl to about 10 mole % a different pair of tetrahedrally and octahedrally coordinated entities are in equilibrium. The equilibrium shifts in favor of the six-coordinate form as the CsCl content increases. These entities are associated with the chlorozincate network. In the four-coordinate form nickel(II) occurs at network-forming sites, but in the six-coordinate form it occurs at network-modifying sites. With increasing temperature the coordination geometries become increasingly disordered. At 800°C there is substantial disorder. With further increases in temperature small chloronickel(II) molecule ions are formed.

[2] Abstract of paper being prepared for publication.

Coordination Equilibria of Chloronickelate(II) Complexes in $CsAlCl_4$

J. Brynestad G. P. Smith

Nickel(II) forms discrete chloro complexes in $CsAlCl_4$ with a well-defined dependence on the free chloride ion concentration. The species $NiCl_4^{2-}$, $NiCl_3^-$, $NiCl^+$(solvated), and Ni^{2+}(solvated) have been observed. At 600°C the equilibrium quotient for $NiCl_4^{2-} \rightleftharpoons NiCl_3^- + Cl^-$ was $[Cl^-]\ [NiCl_3^-]/[NiCl_4^{2-}] = 0.065 \pm 0.005$. The various coordination equilibria in this system continue to be investigated, and quantitative information on equilibrium quotients and heats of reaction will be available shortly.

Electrical Conductivities of Systems Containing Aluminum Halides

C. R. Boston

Studies of electrical conductivity of alkali halide-aluminum halide mixtures have been completed. The systems measured were pure $AlCl_3$ (ref. 3), $AlCl_3$-KCl (ref. 4), and $AlBr_3$-NaBr. Conductivities were determined as functions of both temperature and composition. The experimental conditions were rather severe, requiring temperatures up to 1080°C and pressures in excess of 100 atm. The systems were considered as consisting of the two binary systems, MX-$MAlX_4$ and $MAlX_4$-Al_2X_6. The results for the MX-$MAlX_4$ mixtures indicate large differences in polarizabilities for X^- and AlX_4^-, whereas the compositional effects for $MAlX_4$-Al_2X_6 mixtures are attributed to basic changes in melt structure.

Spectra of Dilute Solutions of Bismuth Metal in Molten Bismuth Trihalides. The Bi-$BiBr_3$ System

C. R. Boston

Previous studies[5,6] indicated two subvalent bismuth species in dilute solutions of bismuth in $BiCl_3$, obeying the equilibrium

$$4Bi^+ \rightleftharpoons Bi_4^{4+}. \quad (1)$$

Electrochemical measurements[7,8] also support this equilibrium. Recent measurements[9,10] in acidic solvents such as $AlCl_3$-NaCl eutectic showed Bi^+, Bi_5^{3+}, and Bi_8^{2+}.

Absorption spectra of Bi-$BiBr_3$ solutions were quite similar to those observed[5,6] for Bi-$BiCl_3$ and consisted of a single intense band at 16,300 cm^{-1}. At low bismuth concentrations Beer's law was obeyed, indicating that essentially only Bi^+ was present, but above 0.15 *M* large deviations indicated other species (presumably Bi_4^{4+}). Similar changes occur in the Bi^+ spectrum as chloride is replaced by bromide to those in NaX-AlX_3 solvent;[9,11] the bands shift to lower energies and become somewhat more intense. The most striking difference is in the intensities, which are ten times greater in BiX_3 than in NaX-AlX_3 mixtures. The high intensity in BiX_3 probably arises from interaction between Bi^+ and Bi^{3+}, as has been suggested[9] for these ions in NaCl-$AlCl_3$.

Mass action constants for reaction (1) calculated from our spectrophotometric data compare reasonably well with the equilibrium constant obtained by Topol and Osteryoung[8] from emf measurements, as shown below:

Solvent	Mass Action Constant from Spectra	Equilibrium Constant from emf
$BiCl_3$ at 264°C	3.8×10^6	2.7×10^6
$BiBr_3$ at 240°C	2.4×10^4	1.9×10^4

These results show that the replacement of chloride by bromide favors the formation of Bi^+. Electrical conductivity measurements[12] indicate that this trend continues for the iodide. The buildup of polymeric species increases with decreasing temperature and increasing acidity of the melt.

---

[3] Reported in paper accepted for publication in *Journal of Chemical Physics.*

[4] Reported in paper submitted for publication to *Journal of Chemical Physics.*

[5] C. R. Boston and G. P. Smith, *J. Phys. Chem.* **66**, 1178–81 (1962).

[6] C. R. Boston, G. P. Smith, and L. C. Howick, *J. Phys. Chem.* **67**, 1849–52 (1963).

[7] L. E. Topol, S. J. Yosim, and R. A. Osteryoung, *J. Phys. Chem.* **65**, 1511 (1961).

[8] L. E. Topol and R. A. Osteryoung, *J. Phys. Chem.* **66**, 1587 (1962).

[9] N. J. Bjerrum, C. R. Boston, and G. P. Smith, *Inorg. Chem.* **6**, 1162–72 (1967).

[10] N. J. Bjerrum and G. P. Smith, *Inorg. Chem.* **6**, 1968–72 (1967).

[11] N. J. Bjerrum, H. L. Davis, and G. P. Smith, *Inorg. Chem.* **6**, 1603 (1967).

[12] L. F. Grantham, *J. Chem. Phys.* **43**, 1415 (1965).

The Determination of Successive Equilibrium Constants

L. R. Lieto[13]

The determination of equilibrium constants involving very similar inseparable entities is difficult. The simultaneous presence of more than two species that affect an observable property has, in the past, imposed considerable effort on extracting properties of the individual species in a mixed system.

We developed a mathematical model equating observable quantities to sums of functions of concentrations of the species present. We then wrote and checked an algorithm to solve the equations for the equilibrium constants in systems where the number of observations exceeds the number of species. The algorithm provides least-squares estimates of the equilibrium constants and some idea of the reliability of each constant. The model chosen and the method of calculation yield reliable results regardless of the relationship between constants, their absolute values, or the numbers of species simultaneously present.

The Equilibrium Constants for the Ni(II)-Cl^-, I^- System in Dimethyl Sulfone at 125°C

L. R. Lieto[13]

The calculational procedure described above was used to determine the four equilibrium constants resulting when NiI_4^{2-} is converted to $NiCl_4^{2-}$ by the stepwise replacement of I^- with Cl^-. This system was examined at 125, 137, and 150°C in dimethyl sulfone. Data were obtained spectrophotometrically at various concentration ratios of LiI to LiCl and analyzed with computers. From the spectra of NiI_4^{2-} and $NiCl_4^{2-}$ measured with only one halide present and spectra of the mixture present at 15 different chloride-to-iodide ratios, we calculated spectra of NiI_3Cl^{2-}, $NiI_2Cl_2^{2-}$, and $NiICl_3^{2-}$ within about ±10%. The equilibrium constants at 125°C are:

$$NiI_4^{2-} + Cl^- \rightleftharpoons NiI_3Cl^{2-} + I^-, k_1 = 8.60 \pm 0.50;$$

$$NiI_3Cl^{2-} + Cl^- \rightleftharpoons NiI_2Cl_2^{2-} + I^-, k_2 = 5.65 \pm 0.30;$$

$$NiI_2Cl_2^{2-} + Cl^- \rightleftharpoons NiICl_3^{2-} + I^-, k_3 = 2.30 \pm 0.20;$$

$$NiICl_3^{2-} + Cl^- \rightleftharpoons NiCl_4^{2-} + I^-, k_4 = 2.50 \pm 0.25.$$

[13] AEC Postdoctoral Fellow from Arizona State University.

MOLTEN FLUORIDE SPECTROSCOPY

L. M. Toth[14] G. P. Smith

The establishment of a molten fluoride absorption spectroscopy program has been essentially completed and is being turned over to the Reactor Chemistry Division. It includes the development of a diamond-windowed spectrophotometric cell, which is unreactive to molten fluorides, and the production of fluoride solvents and solutes of the purity required for spectroscopy. Spectroscopic measurements on fluoride systems during this period have been designed both to assist other programs and to spot-check areas for future research.

Diamond-Windowed Cell for Molten Fluoride Spectroscopy[15]

L. M. Toth[14] J. P. Young[16]
G. P. Smith

Until now the windowless container has been used extensively for measuring absorption spectra of ions in molten-fluoride solvents. However, a container or cell with fixed transparent windows is needed to provide a fixed and easily determined path length, the facility to bubble the melt with reactive gases, and better containment of volatile species. The problem has been to find windows transparent in the range 200 to 250 mμ and resistant to the extremely corrosive molten fluorides. Initially we tried silica, platinum-coated silica, and fluoride salt crystals as window materials, but none were satisfactory.

Because diamond has long been recognized as perhaps the most ideal window material for molten fluorides, a diamond-window spectrophotometric cell, shown in Fig. 10.1, was fabricated and has satisfied the above design requirements. Except for the diamond windows, the cell is made entirely of graphite. It consists of a cell body, two retainers for the diamonds, a sleeve to hold the retainers in place, and a nut to secure the sleeve. The optical path length is 1.0 cm. The windows are approximately 5 × 5 × 1 mm type IIa plates.

A horizontal groove on the body fixes the vertical position of the window, and a vertical groove in the retainer fixes the horizontal position. The depth of each groove is one-half the window thickness. The windows

[14] On loan from the Reactor Chemistry Division.

[15] From a paper published in *Anal. Chem.* **41**, 683–85 (1969).

[16] Analytical Chemistry Division.

ORNL-DWG 68-9074

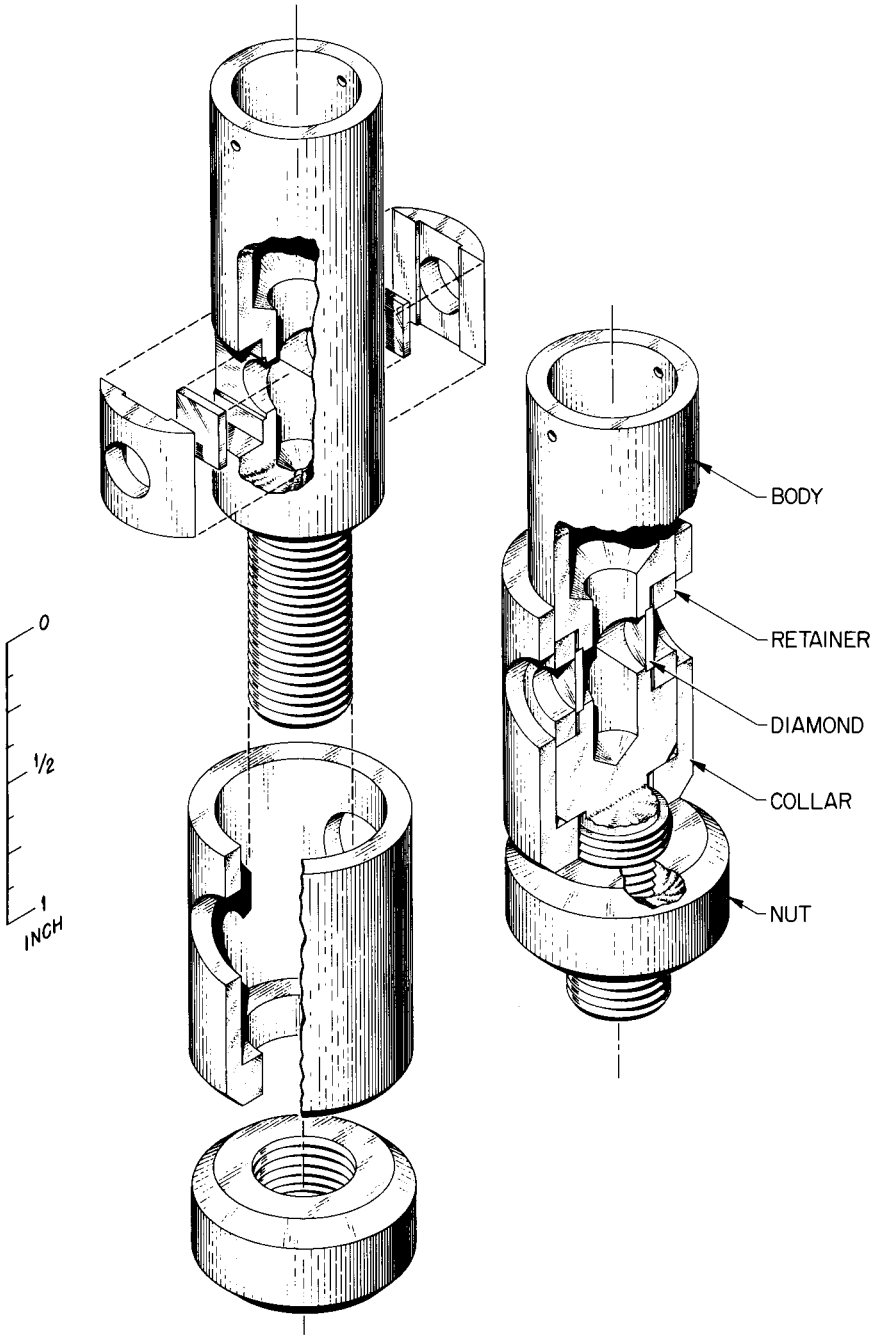

Fig. 10.1. Two Views of the Diamond Windowed Cell.

are not sealed gastight to the cell body but merely fit flush to the body with a force of a few grams exerted upon them. Fluid does not leak around the windows because most molten fluoride salts do not wet graphite. The advantages of this arrangement are simplicity of design, ease of assembly and disassembly, and no significant danger of window breakage due to loading stresses.

This cell was successfully used in a number of tests. A spectrophotometric base line for LiF–34 mole % BeF_2 and the spectra of NiF_2 and UF_4 in this solvent were recorded. Because of the reproducibility of the base line achieved with the diamond cell, a broad peak centered at 2.06 μ in the UF_4 spectrum, shown in Fig. 10.2, was identified for the first time in a molten fluoride system. This peak has been seen in noncorrosive systems.

Operating experience with the diamond cell has been acquired during the past year. The availability of pure solutions (described below) has enabled use of the automatic data handling systems presently available on commercial spectrometers. In particular, we can now record spectra on paper tape and either combine them with others or subtract components from composite spectra with the computer. It represents an improvement in speed and quality of output that has never been available for molten fluoride data handling.

Salt Purification for Fluoride Spectroscopy

L. M. Toth[14]

Melts that are both low in oxide content and free of suspended matter are a prerequisite for spectroscopy of dilute species in fluoride solvents. Even small amounts of solute that react with the soluble oxides and leave solution cause problems, either by remaining suspended and scattering light or by precipitating on the windows of the cell.

The salts are best purified as individual components instead of as the mixed salts. We use the customary approach of subliming volatile fluorides and sparging nonvolatile fluorides with HF.

In the past, volatile fluorides have been sublimed so rapidly that impurities are entrained. Baffle plates partially remedied the entrainment. However, using low sublimation rates at 10^{-4} to 10^{-5} torr eliminated the need for baffles and produced much better results. Some very crude salts (such as ZrF_4) required a second sublimation. At these low rates we have been able to purify up to 50 g of salt in 2 to 3 days. The results on some of these fluoride salts are listed in Table 10.1.

MoF_3 Solution Spectra

L. M. Toth[14] J. P. Young[16]
G. P. Smith

Spectra of dilute solutions of MoF_3 in molten Li–34 mole % BeF_2 (hereafter referred to as "L_2B") were studied to demonstrate both the valence state and coordination of the molybdenum species. Peaks at 472 and 353 mμ with molar absorptivities of about 8 and 12 liter mole^{-1} cm^{-1}, respectively, were observed. The positions of these two transitions are consistent with predictions from the spectrochemical series. We conclude that MoF_3 in L_2B is present as Mo^{3+} ions that

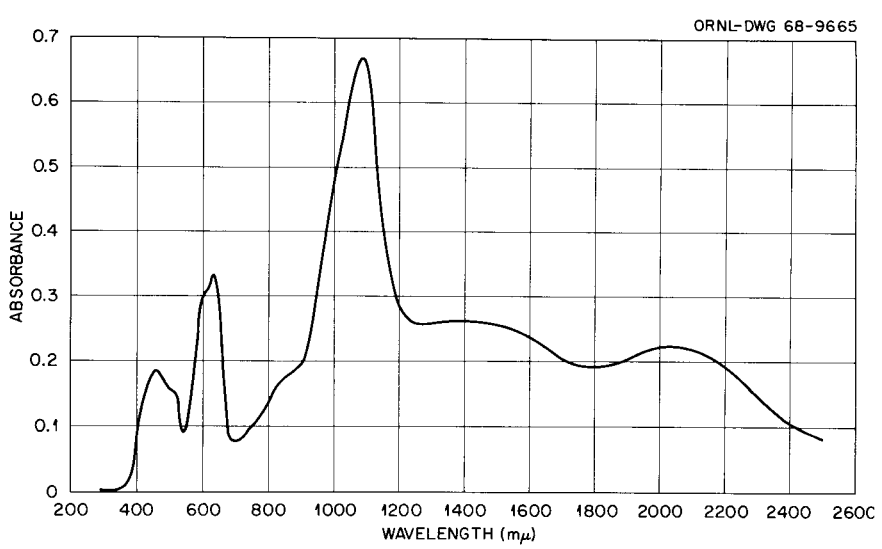

Fig. 10.2. Absorption Spectrum of a Dilute Solution of UF_4 in Molten LiF–34 mole % BeF_2 at 650°C.

Table 10.1. Results of Purification of Fluorides

Salt	Purification Process			Average Crystal Weight[a] (g)	Oxide Content[b] (ppm)
	Method	Temperature (°C)	Time		
ZrF_4	2 sublimations	590–600	3 days each	0.25	70
NbF_5	Sublimation	100	5 days	0.50	<50
LiF	HF sparging	900	1 hr		<50

[a]In all cases transparent single crystals were formed.
[b]Determined by $KBrF_4$ method.

are octahedrally coordinated to fluoride ions to form MoF_6^{3-}.

For these studies the melts have been contained in windowless cells made from graphite, platinum, molybdenum, or copper. The variety of container materials was used in an unsuccessful effort to maintain stable MoF_3 solutions. Molybdenum was invariably lost from solution after 24 hr at 700°C by an unexplained mechanism. Experience with the system has led us to believe that impurity reactions were involved.

Vapor Phase Studies Over MoF_3 Solutions

L. M. Toth[14] J. P. Young[16]

Previously it was proposed that MoF_3 disappears from L_2B solutions by disproportionation:[17]

$$2MoF_3 \rightleftharpoons Mo + MoF_6 .$$

We sought to support this argument by measuring the spectrum of MoF_6 in the gas phase over a solution of MoF_3 in L_2B. MoF_6 has a strong charge transfer absorption in the 200-mμ region ($\epsilon = 10^3$ liter mole^{-1} cm^{-1}) with vibrational structure that provides a "fingerprint" for identification.

Initial attempts to measure MoF_6 spectra directly over the melt in a windowless container at 550 to 700°C revealed nothing. Because we knew neither our sensitivity limits nor the reason for losses of molybdenum from the MoF_3-L_2B solutions, we refined our approach in the following manner.

We simply maintained an L_2B solution of MoF_3 at 700°C or greater in an appendix tube attached to the 10-cm path-length gas cell fitted with quartz windows. The gas cell was kept at room temperature and fitted into the sample compartment of a Cary model 14 spectrometer. Any MoF_6 generated in the hot appendix tube was then expected to diffuse into the gas cell, where its spectrum could be measured.

The second-order rate constant data of Weaver, Hess, and Friedman[18] indicates that 1000 ppm MoF_3 in L_2B would have an equilibrium pressure of at least 1 torr. A calibration of our system with MoF_6 gas showed that we could detect it at pressures as low as 0.020 torr.

First, MoF_6 was introduced to demonstrate that pressures as low as 0.020 to 0.050 torr were stable in the system for at least 1 hr. Then solution containing 0.1 to 1.0 wt % MoF_3 in L_2B was fused in the appendix tube and held at 700°C. Under no conditions was MoF_6 evolution from solution observed, not even when the solution temperature was raised to 900°C.

We conclude that MoF_6, within detection limits, does not exist in equilibrium over solutions of MoF_3 in L_2B, and thus we have no basis to say that the above disproportionation occurs.

SOLID SYSTEMS

The Electronic Structure of the Nickel(II) Ion in Doped LiCl Crystals[19]

G. E. Shankle[20]

Single crystals of LiCl doped with $NiCl_2$ exhibit a room-temperature ligand field absorption spectrum characteristic of Ni^{2+} surrounded by an octahedral

[17]C. F. Weaver, D. N. Hess, and H. A. Friedman, *MSR Program Semiann. Progr. Rept. Feb. 29, 1968,* ORNL-4254, p. 133.

[18]Private communication with C. F. Weaver, D. N. Hess, and H. A. Friedman, Reactor Chemistry Division.

[19]Abstract of dissertation presented to University of Tennessee in partial fulfillment of the requirements for the Ph.D. degree, March, 1969; published as ORNL-TM-2514 (July 1969).

[20]AEC predoctoral fellow from the University of Tennessee.

arrangement of chloride ions. Spectra of these crystals at 5°K showed a large amount of well-resolved fine structure, portions of which suggest that the coordination geometry about Ni^{2+} is not perfectly cubic. However, we can rationalize these portions of the fine structure by considering deviations from cubic geometry caused by the association of Ni^{2+} with an Li^{+} vacancy.

The remainder of the fine structure may be organized into several well-defined progressions. Such progressions result from strong coupling of the Ni^{2+} electronic states with vibrational modes of the nearest-neighbor shell of chloride ions, of the LiCl lattice modes, or both. While frequencies for the $NiCl_6{}^{4-}$ complex are not known, no obvious correlation exists between the observed progression frequencies and the frequencies of the LiCl phonon modes. Hence, coupling to pseudolocalized modes appears to be responsible for the observed vibronic fine structures.

The Electronic Structure of Nickel Ions in Cs_3NiCl_5 and $Cs_3Mg_{1-x}Ni_xCl_5$

T. W. Couch[21]

The solid state optical spectra of Cs_3NiCl_5 and $Cs_3Mg_{1-x}Ni_xCl_5$ are reported here and fitted to the empirical ligand field model of intraconfigurational transitions. These materials are isostructural with Cs_3CoCl_5, which crystallizes in the space group I 4/*mcm*. The space groups of the nickel-containing compounds were established at 80 and 5°K by analysis of x-ray diffractometer tracings of finely divided powders. Polycrystalline samples of Cs_3NiCl_5 were grown in the space between an optical cell and an optically polished quartz insert by allowing the melt to cool very slowly. Large crystals of $Cs_3Mg_{1-x}Ni_xCl_5$ were grown from the melt by the Stockbarger method.

To interpret the 5°K spectrum of Cs_3NiCl_5 and the 5°K polarized single-crystal spectrum of $Cs_3Mg_{1-x}Ni_xCl_5$, we wrote a computer program that calculates the energy levels and selection rules for a d^2-d^8 configuration ion in a crystalline field of arbitrary symmetry. The code determined numerical values of the ligand field parameters as applied to the $NiCl_4{}^{2-}$ ion. For $Cs_3Mg_{1-x}Ni_xCl_5$ the parameters are as follows: B, 766 cm^{-1}; C, 3250 cm^{-1}; ζ, −551 cm^{-1}; B_0^2, −2190 cm^{-1}; B_0^4, 2490 cm^{-1}; and B_4^4, 5540 cm^{-1}.

The theory rationalized the spectra of the nickel(II) ion in D_{2d} symmetry in a satisfactory way. Selection rules agreed satisfactorily with the observed polarization properties of the spectra.

Vibrational Structure of the 7000-to-9000 cm^{-1} Band of $Cs_3Mg_{1-x}Ni_xCl_5$

T. W. Couch[21] G. P. Smith

The electronic absorption spectrum of crystalline $Cs_3Mg_{1-x}Ni_xCl_5$ at about 5°K contains in the 7000-to-9000 cm^{-1} range an electronic transition, which consists of approximately 90 sharply defined bands. Using polarization methods we sorted these bands into states of two electronic transitions. Both band systems were built on the progressions of a vibrational mode of 285 cm^{-1}, with very little anharmonic contraction. Within individual steps of the progressions, transitions involving four other vibrational frequencies were found, representing normal modes of an unperturbed $NiCl_4{}^{2-}$ molecule ion with symmetry D_{2d}. Several very weak, low-frequency transitions were found. Some occurred on the hot sides of the electronic origins at frequencies too great to be accounted for by thermal population. The latter are attributed to Ni-Ni interactions, and some of those on the cold sides of the electronic origins are probably lattice frequencies.

Optical Spectra of the Cobalt(II) Ion at Sites of Approximately Octahedral Symmetry in Several Chloride Crystals

F. C. Gilmore[20]

The optical spectra have been obtained for several crystals containing the Co^{2+} ion in an approximately octahedral environment of chloride ions. We studied thin polycrystalline films of $CsCoCl_3$ and $RbCoCl_3$ and doped single crystals of $CsMgCl_3$, $KMgCl_3$, $CsCdCl_3$, $MgCl_2$, $CdCl_2$, and LiCl. The spectra covered the region from 4000 to about 30,000 cm^{-1} and were measured at room temperature, at approximately 80°K, and at approximately 5°K. Spectra of $CsCoCl_3$ were also obtained up to its melting point.

The spectra were interpreted and correlated by ligand field theory. All appear to be consistent with octahedral symmetry about the Co^{2+} ion. Interpreting the previously reported spectrum of $CoCl_2$ in the 650 to 2000 cm^{-1} region we find 420 cm^{-1} for the spin-orbit coupling constant for $CoCl_6{}^{4-}$. A procedure that can be used consistently for all the spectra was developed and used to obtain values of the other three ligand field parameters by least-squares fitting of the observed spectra. The procedure requires assignment of only three spin-orbit levels.

[21] Graduate student from the University of Tennessee.

K_3MoF_6 Synthesis and Spectrum

L. M. Toth[14] G. P. Smith

As an independent demonstration that the melt spectrum of MoF_3 in L_2B was due to octahedrally coordinated Mo^{3+} – that is, MoF_6^{3-} – a spectrum of Mo^{3+} in a known chemical environment was required. We expected K_3MoF_6 to exhibit a cubic structure in which Mo^{3+} ion is coordinated to six fluoride ligands. However, previously reported[22] synthesis of K_3MoF_6 produced an oxyfluoride without the octahedral environment for Mo^{3+}. Therefore, K_3MoF_6 was prepared by mixing stoichiometric quantities of KF and MoF_3 and fusing in a sealed platinum tube at 880°C for 0.5 hr. About 5% yield was obtained in the form of 0.3-mm-diam crystals. These crystals were handpicked and washed with ethanol, acetone, or both.

We measured the density of K_3MoF_6 as 3.23 ± 0.03 g/cm^3 at 25°C, which is consistent with the assumed stoichiometry and measured unit cell dimensions. The crystal structure[23] confirms the formula.

The diffuse reflectance spectrum of K_3MoF_6, shown in Fig. 10.3, has three broad absorption bands with maxima at 262 mμ (38,200 cm^{-1}), 337 mμ (29,700 cm^{-1}), and 425 mμ (23,500 cm^{-1}). The transmission spectrum of the polycrystalline particle had absorption maxima at 337 and 425 mμ, but light scatter at 262 mμ was too severe to permit absorption measurements at this wave length. The spectrum could be analyzed in terms of ligand-field theory and compared with similar analyses for related chlorides and bromides. We conclude that the species present in the MoF_3-L_2B solution is MoF_6^{3-}.

Structure of the $Al_2X_7^-$ Ion

C. R. Boston

A recent report[24] of the congruently melting compound $CsAl_2I_7$ suggests that the structure of the frequently proposed $Al_2X_7^-$ anion could be determined in the solid. High-purity AlI_3 was prepared from 99.9999% Al and 99.99% I_2 by techniques similar to those first developed for the preparation of high-purity $AlCl_3$. The AlI_3 was melted with sublimed CsI in the stoichiometric amounts for $CsAl_2I_7$. Slow cooling

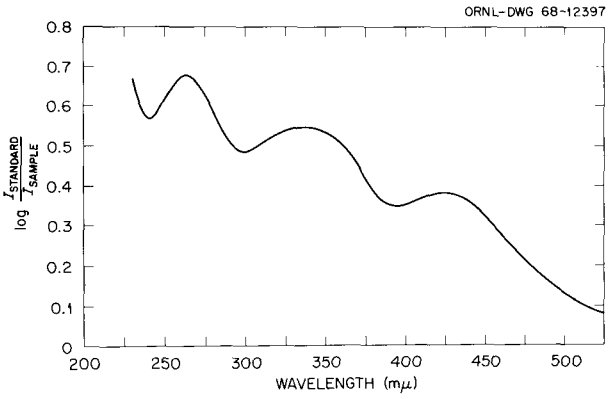

Fig. 10.3. Diffuse Reflectance Spectrum of K_3MoF_6.

produced crystals that melted near 215°C. Iodine and aluminum analyses were within 3% of the theoretical values for $CsAl_2I_7$. We are trying to determine the crystal structure of this compound.

$Ni(AlCl_4)_2$

J. Brynestad H. L. Yakel[25]
G. P. Smith

We prepared $Ni(AlCl_4)_2$ from the reaction between $NiCl_2$ and Al_2Cl_6 despite reports[26] that this reaction does not occur. The compound forms reddish-orange monoclinic needles with the $Co(AlCl_4)_2$ crystal structure.[27] The green nickel compound observed by Belt and Scott[28] must have been something else.

$Ni(AlBr_4)_2$ and $Ni(AlI_4)_2$

L. R. Lieto[29] C. R. Boston

We are trying to prepare the bromo and iodo analogues of $Ni(AlCl_4)_2$. Preliminary experiments indicate that $Ni(AlBr_4)_2$ forms readily when $NiBr_2$ and Al_2Br_6 are mixed at 125°C. The red, crystalline material decomposes at this temperature in the absence of Al_2Br_6 vapor. Solid $Ni(AlI_4)_2$ does not form when NiI_2 and Al_2I_6 are mixed at 210°C. Current efforts are to characterize the $Ni(AlBr_4)_2$ and find other methods or conditions to prepare $Ni(AlI_4)_2$.

---

[22] S. Aleonard, *Compt. Rend.* **260**, 1977 (1965).

[23] L. M. Toth, G. D. Brunton, and G. P. Smith, to be published in *Inorganic Chemistry*.

[24] V. I. Mikheeva, S. M. Arkhipov, and T. V. Revzina, *Zh. Neorgan. Khim.* **13**, 1946–49 (1968).

[25] X-ray Diffraction Group.

[26] T. F. Munday and J. D. Corbett, *Inorg. Chem.* **5**, 1263 (1966).

[27] J. A. Ibers, *Acta Cryst.* **15**, 967 (1962).

[28] R. F. Belt and H. Scott, *Inorg. Chem.* **3**, 1785 (1963).

[29] AEC Postdoctoral Fellow from Arizona State University.

Titanium Aluminum Chlorides

J. Brynestad S. von Winbush[30]
G. P. Smith

We are studying the titanium aluminum chlorides and have prepared $Ti(AlCl_4)_2$ and $TiCl_2 \cdot AlCl_3$. The former is blue and occurs in at least two modifications, one monoclinic and isostructural with $Co(AlCl_4)_2$ and the other orthorhombic. The structure of the latter is under investigation (Chap. 14 of this report). The compound $TiCl_2 \cdot AlCl_3$ has only recently been prepared and is under investigation. Heating in vacuum decomposes it into $TiCl_2$ and $AlCl_3$, but the $TiCl_2$ thus obtained has quite different chemical properties from the usual material prepared by direct reaction at high temperatures.

[30]Consultant from Fisk University, Nashville, Tenn.

11. Superconducting Materials

G. R. Love C. C. Koch

We are studying the effects of metallurgical variables on the properties of superconducting materials. The most highly structure-sensitive superconducting property appears to be current carrying capacity in an applied magnetic field; it is sensitive to mechanical strain, preferred orientation, fabrication and heat-treatment procedures, grain size, and the morphology, composition, and volume fraction of second-phase particles. Meaningful correlation of structure and properties requires detailed knowledge of both. Consequently, much of our effort is devoted to obtaining basic metallurgical information on phase diagrams, transformation kinetics and products, and the microstructures that result from them in systems based upon superconducting materials. The alloys systems of primary interest are those based on niobium and technetium.

The mechanism and kinetics of the omega-transformation in Ti–25 at. % Nb are being studied with the X-Ray Diffraction Group and are reported in Chap. 14.

FLUX PINNING BY GRAIN BOUNDARIES IN SUPERCONDUCTING NIOBIUM-ZIRCONIUM ALLOYS[1]

The influence of grain, subgrain, or dislocation cell size, d, on superconducting critical flux gradient, dB/dr, was investigated in a single-phase Nb–33 at. % Zr alloy. By appropriate heat treatments, d was varied from 0.25 to 1500 μ. A monotonic decrease of more than one hundred-fold in dB/dr accompanied this 6000-fold increase in d. At a given d, the maximum increase in dB/dr obtained from precipitation of a second phase does not exceed a factor of about 30.

SUPERCONDUCTIVITY IN NIOBIUM CONTAINING FERROMAGNETIC GADOLINIUM OR PARAMAGNETIC YTTRIUM DISPERSIONS[2]

Dispersions of gadolinium and yttrium in pure niobium were prepared by solidification from the melt, and the size, shape, and distribution of the particles were determined metallographically. The superconducting critical temperature and critical field of niobium were unaltered by the presence of the dispersions, indicating that neither gadolinium nor yttrium has measurable solubility in solid niobium. Both gadolinium and yttrium dispersions produced large hysteresis in magnetization and large critical current densities. The degree of magnetic hysteresis produced in niobium by these dispersions has been exceeded in niobium only by fast neutron irradiation. Ferromagnetic gadolinium and weakly paramagnetic yttrium appear equally effective as flux pins. We suggest that the nature of the interface between the particle and the superconducting matrix is more important for flux pinning than the bulk magnetic properties of the dispersed phases.

PHASE TRANSFORMATIONS ASSOCIATED WITH THE SAMARIUM-TYPE STRUCTURE IN INTRA-RARE-EARTH ALLOYS[3]

We investigated the nature of phase transformations to the rhombohedral (samarium-type) structure found

[1] G. R. Love and C. C. Koch, *Appl. Phys. Letters* **14**, 250 (April 1969).

[2] Abstract from paper accepted for publication in *Transactions of the Metallurgical Society of AIME*.

[3] Abstract of talk presented at the 1969 Spring Meeting of the Metallurgical Society of AIME, Pittsburgh, Pa., May 12–15, 1969.

in many binary intra-rare-earth alloys. As a typical system, gadolinium-cerium alloys were prepared ranging in composition from 12 to 40 at. % Ce. The critical temperatures for transformation were revealed by measurement of electrical resistance as a function of temperature. The structure and phase morphology were followed by x-ray diffraction and optical and electron microscopy. Two sets of critical temperatures were determined, both having maxima at approximately 30 at. % Ce. The higher temperature set is believed to be responsible for the structural change while the lower one is presumably an atomic "shuffling" process. Long-range diffusion is apparently not required for these transformations. Due to the similarity in morphology and structure the characteristics of the alloy samarium-type phase are being compared to those of pure samarium metal.

12. Surface Reactions of Metals

J. V. Cathcart

Our past research has demonstrated the importance of stress effects, both direct and indirect, in the oxidation processes for metals and alloys. Metals may be divided into two general categories depending on the nature of the stresses developed during oxidation. In systems where oxygen solubility is high or where anion diffusion occurs, stress levels are likely to be very large, leading to gross distortions of the oxidizing metal and rupture of the oxide film. In systems involving cation diffusion, on the other hand, epitaxial effects frequently account for the stresses, which develop in the oxide. In both instances large changes in oxidation rate may result from these stresses. The major goal of our research is the discovery and elucidation of such phenomena.

Specific programs on which we have worked during the past year include a study of stresses developing in tantalum and niobium at high temperatures and relatively high oxygen pressures. Under these conditions the oxide film itself is a major source of strain energy. Our studies of both lattice and short-circuit diffusion phenomena in tungsten were continued; by refining our anodic film sectioning technique, we were able to remove sections no more than 10 A thick from the tungsten diffusion specimens.

We also initiated a study of the oxidation of a uranium alloy. This research included oxidation rate measurements, surface morphology studies, a determination of the magnitude of surface stresses developed during oxidation, and an investigation of the oxidation properties of this alloy at 800°C.

Our interest in the thin film stage of oxidation also continues, and during the past year we have reassessed the analysis previously used in our studies of strain and thickness x-ray line broadening for thin oxide films on copper and nickel.

REFRACTORY METAL STUDIES

R. E. Pawel

Stress Development During Oxidation

We have shown that the thin-film stage of oxidation for tantalum and niobium over a wide temperature range involves the development of significant stress systems in both the oxide film and the substrate metal. Such stresses play an important role in the determination of the oxide morphology and oxidation kinetics for these metals and must be considered in a complete analysis of the reaction characteristics.

During the past year our attention has been centered on the oxidation of tantalum between 500 and 1000°C in oxygen at 1 atm. Under these conditions oxide film formation is a major source of strain energy. Oxidation rate measurements (see Fig. 12.1) showed clearly the unusual reversal in the oxidation rate as temperature increased from 650 to 800°C; the difference in the activation energy for the reaction in the vicinity of these two temperatures is also evident. This behavior points to a significant change in the oxidation mechanism or the properties of the oxide products over the temperature range considered. Measurements of the temperature excursions experienced by thin specimens during the initial moments of oxidation indicated that at least the physical state of the oxide varied over this temperature range, a fact confirmed by metallographic observations. Possible correlations relative to stress generation are being pursued.

Anodic-Film Sectioning Technique

In cooperation with the Diffusion in Solids Group we are continuing to use the highly sensitive and precise

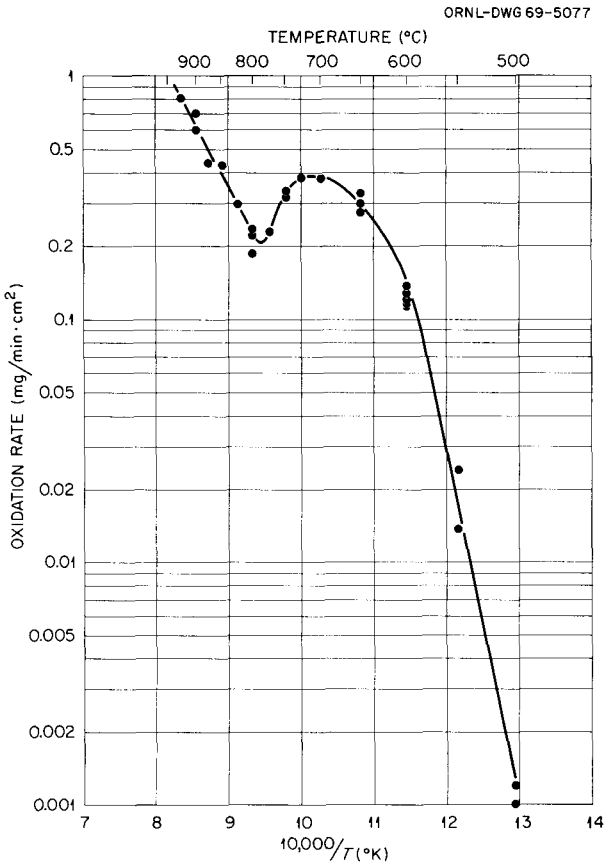

Fig. 12.1. Linear Oxidation Rate Constant For Tantalum Plotted Against Reciprocal Absolute Temperature.

anodic-film sectioning technique to obtain information on mass-transport at low temperatures in body-centered cubic refractory metals. This year we employed the methods for sectioning tungsten[1] to observe the diffusion of niobium, tantalum, and tungsten in single-crystal and polycrystalline tungsten.[2,3] Our lattice diffusion coefficients are compared in Fig. 12.2 with recent literature data. Contrary to the trend of previous data, our results showed that lattice diffusion of these isotopes may be accurately described over the entire temperature range by simple Arrhenius relationships.

At the lowest temperatures of this work, for which the concentration gradients after diffusion were extremely steep, we employed section thicknesses as small as 10 A without appreciable difficulty or loss of consistency in the results. This high degree of sensitivity in determining diffusion profiles is obviously useful for low-temperature diffusion measurements.

Short-circuit modes contributed significantly to the total mass transport in tungsten, particularly at the lower temperatures, and extensive data for the penetration behavior as a result of this mechanism were obtained in both single-crystal and polycrystalline specimens. Theoretical models based on a unique diffusion constant for "grain boundary" or "short circuit" diffusion could not describe our data adequately. We suggest that in real crystals a number of kinds of short circuit paths support a broad spectrum of mobilities. While involving only a small fraction of the total transport, apparent diffusion constants were observed that were at least 10^6 cm^2/sec higher than that for lattice diffusion. The results of these experiments have emphasized the importance of multiple diffusion mechanisms to the overall mass transport process in tungsten. Accumulating information indicates that this is a quite general phenomenon, perhaps responsible for many cases of data misinterpretation in the literature.

X-RAY DIFFRACTION STUDIES ON THIN OXIDE FILMS

J. E. Epperson[4]

A model proposed by Borie[5] for describing the thickness and strain contributions to the diffraction profiles of thin oxide films proved quite adequate for characterizing films formed on the (110) of copper. Although this model has been modified[6] to include the effects of variations in thickness and strain for a given oxide film, this approach has not been completely satisfactory for films formed on other crystallographic planes of copper. We seek to improve the x-ray model and adapt it for wider use.

Anomalously high thickness values obtained when the above model was applied to films formed on the (311) of copper were traced to a "hook effect," an error associated with the premature truncation of the experi-

[1] R. E. Pawel and T. S. Lundy, "The Use of Electrochemical Sectioning in the Study of Diffusion in Tungsten," *J. Electrochem. Soc.* **115**, 233–37 (1968).

[2] T. S. Lundy and R. E. Pawel, "Effects of Short-Circuiting Paths on Diffusion Coefficient Measurements," *Trans. Met. Soc. AIME* **245**, 283–86 (1969).

[3] R. E. Pawel and T. S. Lundy, "Tracer Diffusion in Tungsten," *Acta Metallurgica*, in press.

[4] X-Ray Diffraction Group.

[5] B. S. Borie, *Acta Cryst.* **13**, 542–45 (1960).

[6] C. J. Sparks, Jr., B. S. Borie, and G. V. Czjzek, *Metals and Ceramics Div. Ann. Progr. Rept. June 30, 1964*, ORNL-3670, pp. 60–62.

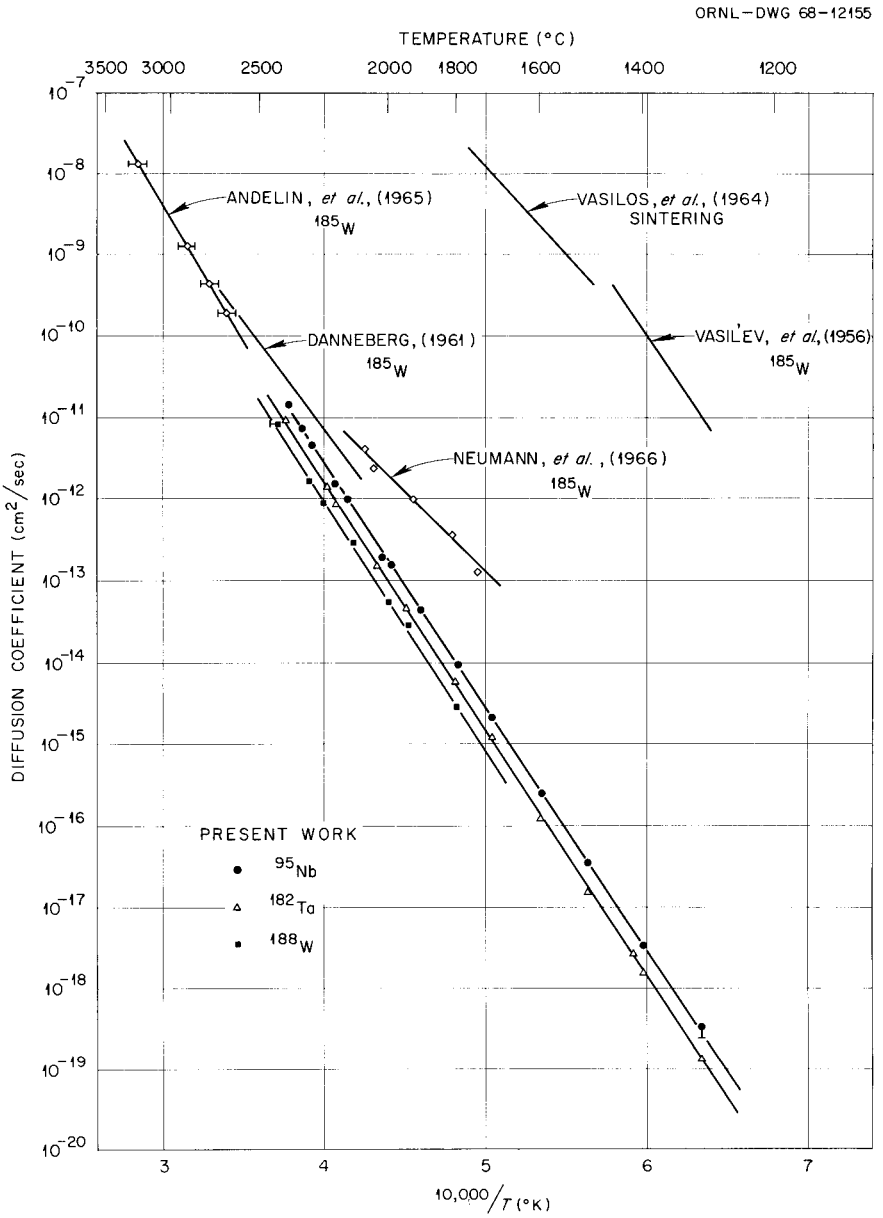

Fig. 12.2. A Comparison of the Present Results for Lattice Diffusion of Nb, Ta, and W in Tungsten with Those from Previous Investigations. References: Andelin, Knight, and Kahn, *Trans. Met. Soc. AIME* **233,** 19 (1965); Danneberg, *Metall* **15,** 977 (1961); Neumann and Hirschwald, *Z. Naturforsch.* **21a,** 312 (1966); Vasilos and Smith, *J. Appl. Phys.* **35,** 215 (1964); Vasil'ev and Chernomerchenke, *Zavodsk. Lab.* **22,** 688 (1956) – AEC-tr-4276.

mental diffraction profiles. We developed a computer simulation program that showed that in the "tail" regions of the diffraction profiles, where truncation normally occurs, the intensity can be represented by

$$I(h) = a/[(h - l)^2 + b(h - l)^4] ,$$

where a and b are constants and l is the order of the reflection. Then, having a rough estimate of the average film thickness, we can determine the Fourier coefficients associated with the truncated portion of the profile.

We also determined that a small hook effect can arise from inhomogeneous strains in the films. However, for the strains encountered in these films the hook effect from this source was negligible.

Application of these corrections to data from a few of the thinner oxide films formed on the (311) of copper indicated that this procedure will be very helpful in future systematic analyses of diffraction profiles.

OXIDATION OF URANIUM ALLOY

J. V. Cathcart G. F. Petersen

We have undertaken a study of the oxidation characteristics of a uranium alloy with a nominal composition of U–7.5 wt % Nb–2.5 wt % Zr. Temperatures investigated included a low range from 160 to 275°C and a high range centered on 800°C. The low-temperature experiments were performed in pure oxygen at 1 atm pressure, whereas at high temperatures we used both air and purified oxygen at pressures no higher than 0.5 torr. This choice of temperatures was dictated in part by the fact that the alloy undergoes a phase transformation near 650°C. Our low-temperature specimens were all annealed 1 hr at 800°C and water quenched to stabilize the high-temperature cubic form of the alloy.

We measured the rate of oxidation of the alloy manometrically at several temperatures between 160 and 275°C. A slow transformation from the stabilized gamma to the alpha phase occurred during oxidation at the higher temperatures in this range, and this transformation appeared to affect the kinetics of oxidation. Nevertheless, the rate curves could be described at all temperatures by an equation of the form

$$\Delta m = kt^{1/n} ,$$

where Δm is the quantity of oxygen comsumed in time t, and k and n are constants. Values of n averaging 1.75 ± 0.25 were obtained, and the variations in n appeared to correlate to some extent with the rate of transformation of the alloy from the gamma to the alpha state.

We employed our flexure technique in an effort to measure the surface stresses generated during oxidation. One side of a narrow strip of the alloy was coated to prevent oxidation; the bending of the specimen during subsequent oxidation was then measured. We estimate the maximum bending stress developed to be of the same order of magnitude as that observed for tantalum, 5000 psi, but we have not yet devised a stress model that would allow us to calculate the actual surface stress on the specimen.

At 800°C the rate of oxidation of the alloy is sufficiently high that a reduced pressure of oxygen is needed to avoid serious self-heating effects during the initial stages. Even at pressures as low as 0.5 torr of air oxidation proceeded readily, and the course of the reaction could be followed with a hot-stage microscope. Within the first few seconds of oxidation the specimen surface distorted substantially. Slip lines were evident, and some of the surface grains tilted. As oxidation progressed cracks also appeared in the surface oxide scale.

As shown in Fig. 12.3, the high-temperature oxide scale consisted of two layers. The surface cracks observed in the hot-stage microscope were concentrated mainly in the outer layer, which was identified as UO_2. The inner layer has not yet been completely identified, but it appeared to consist of at least two phases, one of which may be unoxidized remnants of the alloy. Figure 12.4, shows an electron micrograph of a cross section through the oxide-metal interface. The substructure of the inner layer is clearly visible.

The effects of stress generation during oxidation of this alloy are evident both in the morphology of the oxide scale and in our flexure measurements. However, the sources of these stresses have not yet been identified, and that will be one of our major research goals during the coming year.

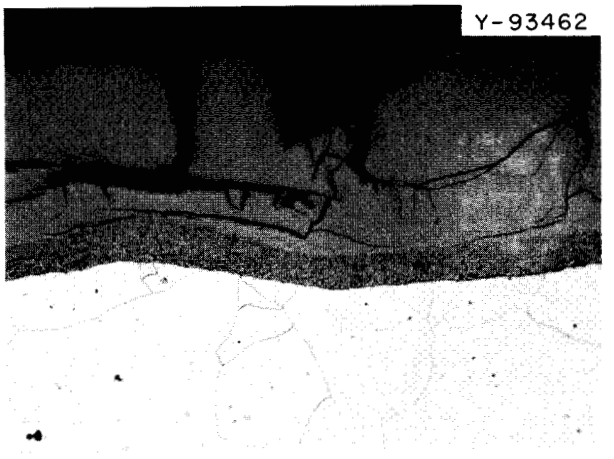

Fig. 12.3. Cross Section of Uranium Alloy Oxidized 2 hr at 800°C and 0.5 torr Air Pressure. 200×.

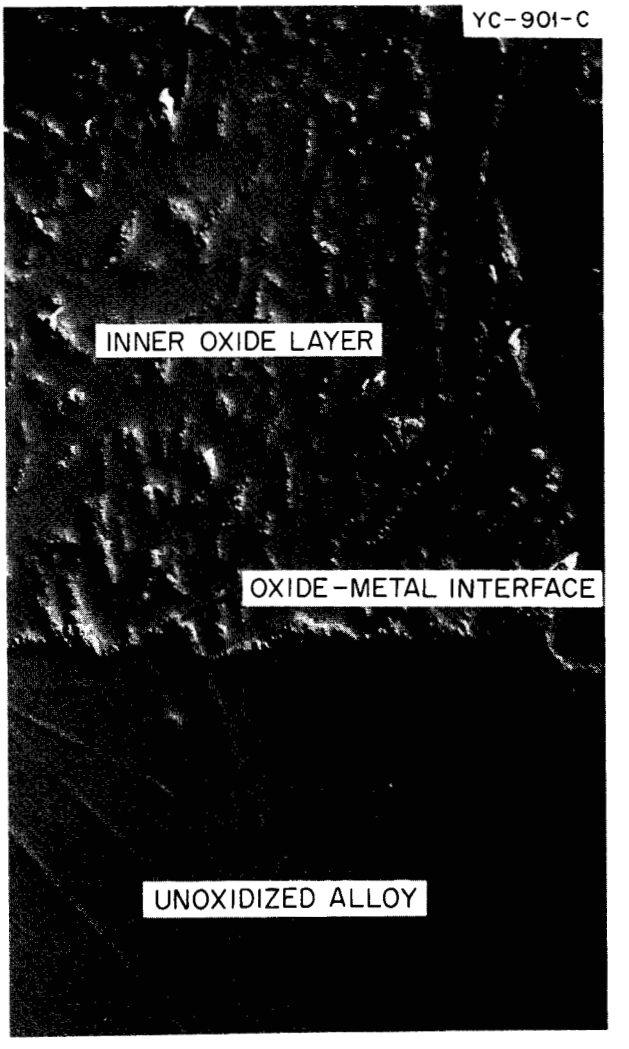

Fig. 12.4. Electron Micrograph of a Cross Section Through the Oxide-Metal Interface of Uranium Alloy Oxidized 2 hr at 800°C and 0.5 torr Air Pressure. 7500×.

13. Theoretical Research

B. S. Borie

THE PROTONIC STRUCTURE OF MOLECULES[1]

I. L. Thomas[2] H. W. Joy

In most theoretical treatments of molecules the constituent atomic nuclei are considered as fixed positive point charges and the Schrödinger equation is separately solved for the electronic motion. The nuclear motion is then found later, using as the potential the electronic charge density distribution obtained previously. In the present work we investigate the effect of removing this approximation by treating the electronic and nuclear motion together and similarly rather than separately and differently.

The molecules CH_4, NH_3, H_2O, and HF are considered. The molecular Hamiltonian operator contains terms to account for the kinetic energy of the protons as well as the usual Coulomb potential energy and electronic kinetic energy terms. An approximate center-of-mass transformation is made and coordinates are chosen relative to the one heavy atom. A standard variational calculation is made, taking the approximate wave function to be a product of an electron part and a proton part. The calculations are done with a modified version of our general-purpose one-center expansion[3] computer program.

The results of the first calculations were unexpected. While the total molecular energies are close to those in the fixed-point proton approximation, the molecular protons are in fact quite delocalized in space, approximately one-third as much as the bonding electrons. Further, the molecules are found to have protonic spectra very similar to their electronic spectra.

Large-basis set calculations are now being made for these and other molecules to establish more firmly the validity of these results and to extend them so as to make understood more fully all of their implications. They have considerable potential for casting new light on many problems in molecular, solid state, and nuclear theory.

RIGID-BAND BEHAVIOR OF SOLVENT ATOM KNIGHT SHIFTS IN NOBLE METAL ALLOYS

H. L. Davis[4]

Recent experimental and theoretical work[5–7] on the Knight shift in noble metals and their alloys has indicated a need for realistic attempts to calculate for these metals the quantity $\langle|\psi_{\mathbf{k}}(0)|^2\rangle$, which represents the electronic probability density at the nucleus averaged over those $\mathbf{k}$ defining the metal's Fermi surface. The Knight shift is directly proportional to $\langle|\psi_{\mathbf{k}}(0)|^2\rangle$. Previously we calculated[8] this quantity for pure copper and obtained excellent agreement with estimates obtained from the experimental shift.

Since Bennett *et al.*[5] have constructed a rigid-band explanation of solvent atom Knight shifts in noble metal alloys, interest has also existed in the rigid-band behavior of $\langle|\psi_{\mathbf{k}}(0)|^2\rangle$. Explicit in their explanation is the requirement that $\langle|\psi_{\mathbf{k}}(0)|^2\rangle$ decrease with an increase in electron-to-atom ratio. In fact, they calculated such a decrease by using simple single orthogonalized plane wave (OPW) models for the band structures of the

[1] Summary of two papers submitted for publication by I. L. Thomas.

[2] Chemical Technology Division.

[3] H. W. Joy, *Metals and Ceramics Div. Ann. Progr. Rept. June 30, 1963,* ORNL-3470, p. 11.

[4] Now in Solid State Division.

[5] L. H. Bennett, R. W. Mebs, and R. E. Watson, *Phys. Rev.* **171**, 611 (1968).

[6] D. O. VanOstenburg and L. C. R. Alfred, *Phys. Rev. Letters* **20**, 1484 (1968).

[7] A. Narath, *Phys. Rev.* **163**, 232 (1967).

[8] H. L. Davis, *Phys. Letters* **28A**, 85 (1968).

noble metals. To check the validity of their rigid-band explanation, we began calculations using more realistic band structure models.

We have completed calculations for copper, based on the best available theoretical model of copper's band structure. They give an increase in $\langle|\psi_{\mathbf{k}}(0)|^2\rangle$ with increase in electron-to-atom ratio. Such an increase makes sense physically, since as the electron-to-atom ratio increases the Fermi energy is further removed from the *d* bands in copper's band structure. One would thus expect the *s* character of the Fermi surface electrons to increase, which then would cause $\langle|\psi_{\mathbf{k}}(0)|^2\rangle$ to increase.

As a result of our calculations, we have concluded that the single OPW models do not give the correct rigid-band behavior of $\langle|\psi_{\mathbf{k}}(0)|^2\rangle$. Thus, the Bennett *et al.*[5] explanation of solvent atom Knight shifts in noble metal alloys cannot be considered a valid description of the experimental results.

CALCULATIONS PERTAINING TO THE THERMOPOWER OF COPPER[9]

R. W. Williams H. L. Davis[4]

Even though the prevailing opinion has been that the electronic contribution to the thermopower of a metal is sensitive to the metal's band structure in the immediate vicinity of the Fermi energy, most previous theoretical attempts to calculate this quantity have relied upon numerical approximations of unknown validity. In particular, some of these approximations have been in the techniques used to calculate the group velocity for Fermi surface electrons. To correct this situation we have modified our existing band structure computer codes to provide for highly accurate calculation of the group velocity of Fermi surface electrons as a function of position on the Fermi surface.

Our first application of these new computer codes pertains to the thermopower of copper. Our interest in copper was motivated by the radically different conclusions obtained by Ziman[10] and Abarenkov and Vedernikov[11] concerning the electronic contribution to copper's thermopower. By calculating the group velocity for copper's Fermi surface electrons in reasonable detail, we showed that Ziman is qualitatively correct, although in error quantitatively. A spin-off from this calculation has been our demonstration that less-exact group velocity calculations can lead to large errors (about 50%) in theoretical estimates of quantities important to the understanding of electron transport in metallic systems. This fact is very nicely demonstrated by comparing our work[9] with the less accurate calculation of Hasegawa and Kasuya.[12]

ELECTRONIC STATES IN DISORDERED SYSTEMS

J. S. Faulkner

An unsolved problem in theoretical solid-state physics concerns the calculation of electronic states for disordered systems such as random alloys or liquid metals. The major steps in the evolution of a theory for such calculations are the Nordheim-Muto theory,[13] average *t*-matrix theories,[14] and the coherent potential theory.[15] We have been able to show that the most advanced of these, the coherent potential theory, when applied to one-dimensional models reduces to a theory that was developed some years ago.[16,17] The experience that we gained with this earlier theory has made it possible to elucidate a number of points concerning the coherent potential theory. In particular, we have been able to define rather clearly the limits of the theory and to show that it is sufficiently complete that it warrants a serious effort to apply it to realistic physical problems.

---

[9] Synopsis of an article published in *Phys. Letters* **28A**, 412 (1968).

[10] J. M. Ziman *Advan. Phys.* **10**, 1 (1961).

[11] I. V. Abarenkov and M. V. Vedernikov, *Soviet Phys. (English Transl.)* **8**, 186 (1966).

[12] A. Hasegawa and T. Kasuya, *J. Phys. Soc. Japan* **25**, 141 (1968).

[13] L. Nordheim, *Ann. Physik* **9**, 607 (1931); T. Muto, *Sci. Papers Inst. Phys. Chem. Research (Tokyo)* **34**, 377 (1938).

[14] J. Korringa, *J. Phys. Chem. Solids* **7**, 252 (1958); J. L. Beeby, *Phys. Rev.* **135**, A130 (1964).

[15] P. Soven, *Phys. Rev.* **156**, 809 (1967); B. Velicky, S. Kirkpatrick, and H. Ehrenreich, *Phys. Rev.* **175**, 747 (1968).

[16] J. S. Faulkner and J. Korringa, *Phys. Rev.* **122**, 390 (1961).

[17] J. S. Faulkner, *Phys. Rev.* **135**, A124 (1964).

14. X-Ray Diffraction

H. L. Yakel

The group's principal objectives continue to emphasize maintenance of general capabilities in x-ray diffraction experimentation and theory of proven utility in metallurgical and ceramic research. We assist other groups in applications of these techniques to their problems of interest and also carry forward basic research programs in selected areas where diffraction methods are likely to be of unique value.

Progress during the past year features the detailed analysis of atomic thermal vibrations in highly oriented graphite, the successful use of small-angle x-ray scattering to study initial stages of precipitation in titanium-niobium alloys, and the reinterpretation of diffraction data from quenched and aged gamma-stabilized uranium alloys in terms of atom displacements rather than chemical ordering.

ROUTINE ANALYSIS

J. E. Epperson L. A. Harris[1] P. G. Mardon[2]
R. M. Steele H. L. Yakel

We present here only a summary of work on the more than 1200 samples submitted to our laboratory for routine x-ray diffraction analysis during the reporting period. Specific results will be found in the reports of other groups. A few highlights of general interest are listed in the following paragraphs.

Crystallographic data were obtained for several alloy phases and compounds that have not been previously reported. A resume of results appears in Table 14.1. The crystal structure of $RbBrO_4$, prepared by Brown, Begun, and Boyd,[3] was determined approximately by comparisons of visually estimated intensities on single-crystal diffraction photographs. The compound $RbBrO_4$ is isostructural with alkali perchlorates and permanganates and, in particular, with $KBrO_4$, the only perbromate whose structure has been quantitatively described.[4]

[1] On temporary assignment to AERE, Harwell, England.

[2] On temporary assignment from AERE, Harwell, England.

[3] L. C. Brown, G. M. Begun, and G. E. Boyd, private communication (1968).

[4] S. Siegel, B. Tani, and E. Appleman, *J. Inorg. Chem.* 8, 1190 (1969).

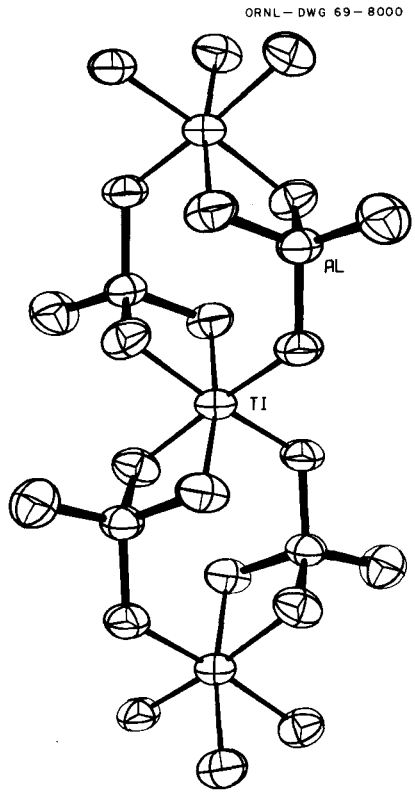

Fig. 14.1. A View of a Portion of an Infinite $Ti(AlCl_4)_2$ Chain with the Crystallographic c Axis Vertical. Atoms are drawn as ellipsoids with major axes proportional to the principal components of thermal vibration.

Table 14.1. Crystallographic Data for New Alloys and Compounds

Composition (at. %)	Crystal System	Lattice Parameters (A)			Remarks
		a_0	b_0	c_0	
26.7 Sc–28.0 La–45.3 Y	Hexagonal	3.637 ± 0.002		11.496 ± 0.005	dhcp[a]
31.8 Sc–22.9 La–45.3 Y	Hexagonal	3.601 ± 0.002		11.395 ± 0.005	dhcp
35.0 Tb–20.86 Sc–14.71 La–29.44 Y	Hexagonal	3.616 ± 0.002		11.375 ± 0.005	dhcp
39.98 Tb–19.26 Sc–13.58 La–27.18 Y	Hexagonal	3.625 ± 0.002		5.723 ± 0.003	hcp[b]
40 Gd–60 Y	Hexagonal	3.647 ± 0.001		5.752 ± 0.004	hcp
50 Gd–50 Sc	Hexagonal	3.525 ± 0.002		5.535 ± 0.004	hcp
95.3 Ni–4.7 Mn	Cubic	3.539 ± 0.001			fcc[c]
93.52 Ni–6.48 Mn	Cubic	3.540 ± 0.001			fcc
90.58 Ni–9.42 Mn	Cubic	3.547 ± 0.001			fcc
85.83 Ni–14.17 Mn	Cubic	3.556 ± 0.002			fcc
94.23 Pd–5.77 Ni	Cubic	3.863 ± 0.001			fcc
95 Ni–5 Cr	Cubic	3.528 ± 0.0005			fcc
$Fe_{0.25}Co_{0.75}S_2$	Cubic	5.519 ± 0.003			FeS_2 type
$Fe_{0.50}Co_{0.50}S_2$	Cubic	5.480 ± 0.001			FeS_2 type
$Fe_{0.70}Co_{0.30}S_2$	Cubic	5.452 ± 0.001			FeS_2 type
$Fe_{0.95}Co_{0.05}S_2$	Cubic	5.423 ± 0.002			FeS_2 type
$RbBrO_4$	Orthorhombic	9.290 ± 0.004	6.060 ± 0.005	7.678 ± 0.010	*Pnma*, $BaSO_4$ type
$Ti(AlCl_4)_2$	Orthorhombic	13.17 ± 0.01	14.99 ± 0.01	5.982 ± 0.003	P·*ab*[d]
$Ni(AlCl_4)_2$	Monoclinic	12.72 ± 0.01	7.67 ± 0.01	11.47 ± 0.02	12/*c*[e]
Te_2AlCl_4	Orthorhombic	10.66 ± 0.02	14.09 ± 0.02	11.83 ± 0.02	*Pbca* Structure unknown

[a] *ABAC* four-layer "double" hexagonal close-packed structure.
[b] *ABAB* two-layer hexagonal close-packed structure (A3 type).
[c] *ABCABC* three-layer face-centered cubic close-packed sturcture (A1 type).
[d] Space groups P*mab* or P2_1*ab* are possible.
[e] Isostructural with $Co(AlCl_4)_2$ and monoclinic $Ti(AlCl_4)_2$. $\beta = 92° 10' \pm 10'$.

The crystal structure of the monoclinic form of $Ti(AlCl_4)_2$ has been derived and refined; it is isostructural with $Co(AlCl_4)_2$ (ref. 5). The sturcture contains regular MCl_6 (M = Ti, Co, Ni) octahedra connected by $AlCl_4$ tetrahedra in infinite chains, as shown in Fig. 14.1. An orthorhombic polymorph of $Ti(AlCl_4)_2$ has also been examined; its unit cell dimensions, listed in Table 14.1, indicate that its structure resembles that of the monoclinic form.

A computer program has been written to plot general stereographic projections of lattice plane normals and directions for any crystal system.[6] The central axis of the projection may be any specified lattice direction or plane normal. Projections of plane normals whose indices lie within chosen ranges or whose interplanar spacings exceed a chosen minimum value may be plotted. Projections of equatorial circles about specified lattice directions or projections of the directions themselves may be drawn. Operations involving plane normals and directions in a given lattice may be interchanged by supplying parameters of the corresponding reciprocal lattice as input data.

CRYSTAL STRUCTURES OF TRANSITION PHASES FORMED IN U–16.60 at. % Nb–5.64 at. % Zr ALLOY[7]

H. L. Yakel

Single-crystal x-ray diffraction studies of the gamma-quenched and aged alloy of uranium with 16.60 at. % (7.5 wt %) Nb and 5.64 at. % (2.5 wt %) Zr reveal two metastable transition phases whose structures are derived from small atom displacements from some of the sites occupied in the A2 γ structure. The phases appear to be identical with those previously reported as having

[5] J. A. Ibers, *Acta Cryst.* 15, 967 (1962).

[6] H. L. Yakel, *Program Stereo: A FORTRAN-Language Program for Plotting Stereographic Projections of Lattice Plane Normals and Directions,* ORNL-TM-2461 (March 1969).

[7] Abstract of paper accepted for publication in the *Journal of Nuclear Materials.*

chemically ordered structures in γ-quenched uranium-molybdenum and uranium-niobium alloys. The first transition structure, γ^s, is formed on γ quenching; it is cubic, space group $I\bar{4}3m$, with a unit cell parameter about twice that of the γ phase. It may be formally described as eight unit cells of the γ structure in which the body-centered atoms have moved in correlated ⟨100⟩ directions. On aging at 150 or 350°C, these movements are further correlated along a particular [001] direction, producing the second transition structure, γ°; it is tetragonal, space group P4/*nmm*, with an atom arrangement similar to that reported for β-

ORNL – DWG 69 – 3151

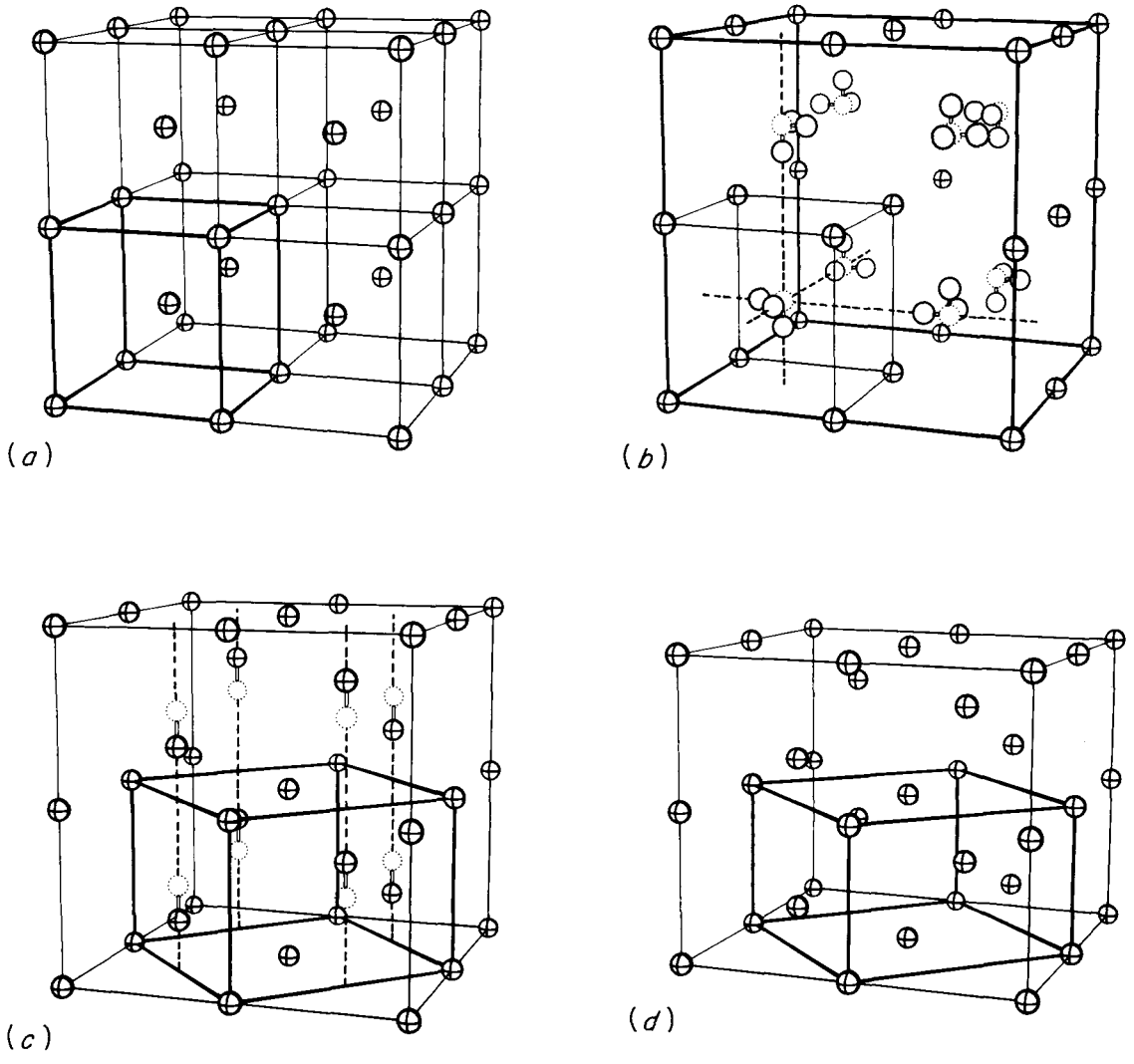

Fig. 14.2. Schematic Drawings of Structures Found in γ-Quenched and Aged Crystals of U–16.60 at. % Nb–5.64 at. % Zr. Atom displacements are deliberately exaggerated for display. Unit cell edges are indicated by heavy lines. (*a*) The ideal high-temperature γ structure. Eight unit cells are shown. (*b*) The γ^s structure found in γ-quenched alloys. Dashed lines are ⟨100⟩ directions through ($\frac{1}{4}$, $\frac{1}{4}$, $\frac{1}{4}$). Original positions of atoms at the centers of the γ cells are dotted and connected to adjacent unmarked spheres that represent the displaced atom in the γ^s structure. (*c*) Fictional structure with γ° atom positions but with $(c/a) = 1/\sqrt{2}$. The c axis of the primitive tetragonal unit cell is vertical. Dashed lines show [001] directions through displaced atoms. Original positions of atoms at the body centers of the γ cells are dotted. They are connected to the adjacent projections of displaced atoms. (*d*) The γ° structure in aged alloys. The c axis of the primitive tetragonal unit cell is vertical; the deviation of the axial ratio (c/a) from $1/\sqrt{2}$ is exaggerated for display.

neptunium.[8] No evidence was found to suggest significant chemical order in either transition structure. The structures are depicted in Fig. 14.2.

THERMAL MOTION IN HIGHLY ORIENTED GRAPHITE

Cullie J. Sparks, Jr. J. E. Epperson

To understand the thermal properties of graphite, it is useful to know the basic elastic behavior associated with lattice vibrations of highly perfect graphite. A simple Debye model of a continuous elastic isotropic medium is questionable because graphite is anisotropic, with weak bonding between the basal planes and strong bonding in them. This has led to a model of the graphite crystal as a system of thin elastic plates with the vibrations separable into two independent parts: bending vibrations of the basal planes and the extensional and shearing vibrations with displacements parallel to the basal planes. This two-dimensional lattice accounts for the dependence of the specific heat on the square of the temperature rather than the cube.

With x-ray diffraction we measured the thermal motion of atoms in graphite to check the validity of this model and to improve it so that calculations of thermal properties may be more reliable. The graphite available to us was hot-pressed pyrolytic material, processed by Union Carbide Corporation, with a mosaic spread of 0.5° FWHM. Integrated intensity measurements of different orders of 00·l reflections were made using various x-ray wavelengths to eliminate extinction effects. These measurements gave an rms displacement $\langle U^2 \rangle^{1/2}$ of 0.11 A at room temperature. Results of integrated intensities at room and liquid-nitrogen temperature on $(10\bar{1}0)$ and $(11\bar{2}0)$ reflections showed less than a 1% change in intensity, verifying the high restoring forces in the plane of the basal sheet.

Measurements to determine the general intensity distribution for diffuse scattering are shown in Fig. 14.3. Here the reciprocal lattice for hot pressed pyrolytic graphite is shown as a plane passing through the hexagonal **c** axis common to the basal planes. The diffuse intensity is strongly concentrated in regions connecting most reciprocal lattice points. The width of the strong diffuse streaks is just the same as the mosaic spread of the basal planes.

The intensity along the **c** axis was integrated over the mosaic spread of the sample, and from this measurement we obtained the velocity of the longitudinal

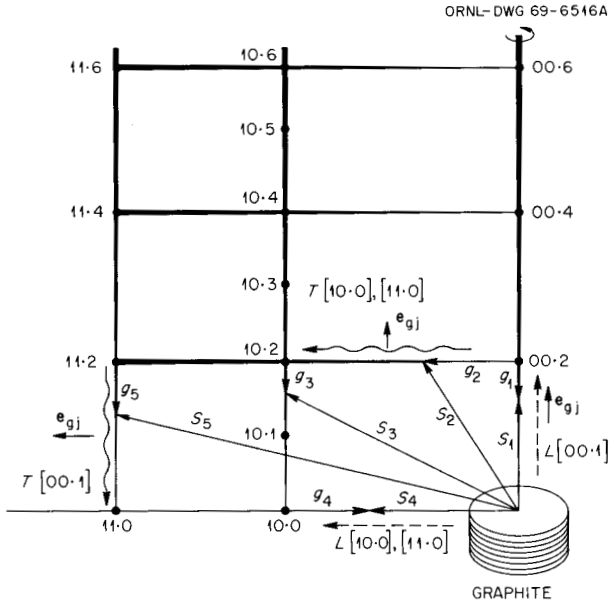

Fig. 14.3. Section of Reciprocal Space Associated with the Graphite Lattice. A complete rotation about the hexagonal axis [00·l] generates the reciprocal lattice for pyrolytic graphite.

mode, $L[00{\cdot}1]$. The value of the modulus of elasticity C_{33} for this longitudinal mode is computed from the maximum velocity to be 3.8×10^{11} dynes/cm^2, in essential agreement with the values of 3.65×10^{11} dynes/cm^2 measured by Blakslee *et al.*[9] and 3.9×10^{11} dynes/cm^2 obtained by Dolling and Brockhouse.[10]

A value of $2M$ associated with the $L[00{\cdot}1]$ mode is obtained from the integrated intensity along the 00·l rod from $l = \frac{1}{2}$ to $\frac{3}{2}$. The corresponding value of $\langle U^2 \rangle^{1/2}$ is 0.022 A, and displacements are coupled over distances of about 12 basal planes (40 A). Thus this longitudinal mode accounts for only about $\frac{1}{5}$ of the total displacement of the carbon atoms out of the basal plane ($\langle U^2 \rangle^{1/2}$ total = 0.1 A). From Fig. 14.3, the transverse [10·0] and [11·0] shear modes are seen to displace the carbon atoms out of the basal plane, and these must be responsible for the remaining large displacements. The narrow width of this mode in the 00·l direction indicates that the displacements are correlated over long distances, probably in excess of 100 basal planes. This is true for the narrow dimension of all the diffuse intensity, although the correlation distances are parallel to the basal plane for the $T[00{\cdot}1]$ mode.

[8] W. H. Zachariasen, *Acta Cryst.* 5, 664 (1952).

[9] O. L. Blakslee, paper presented at the Seventh Conference on Carbon, Cleveland, June 1965.

[10] G. Dolling and B. N. Brockhouse, *Phys. Rev.* 128, 1120 (1962).

For the acoustical modes discussed, the $L[00{\cdot}1]$ mode gives the relative displacement of the entire basal plane acting as a rigid unit, but the transverse shear modes $T[10{\cdot}0]$,$[11{\cdot}0]$ account for the major displacements of the carbon atoms parallel to the hexagonal axis. These modes bend the basal planes and have amplitudes five times larger than $L[00{\cdot}1]$.

SMALL-ANGLE X-RAY SCATTERING INVESTIGATION OF AQUEOUS SOLUTIONS OF TETRAALKYLAMMONIUM HALIDES[11]

R. W. Hendricks S. Lindenbaum[12]

It has been suggested[13,14] on the basis of thermodynamic measurements that tetraalkylammonium halides in aqueous solution form micelles or aggregates. We have examined solutions of Bu_4NBr and $[Bu_3N\text{-}(CH_2)_8\text{-}NBu_3]Br_2$ (Bu = *n*-butyl) in various concentrations up to 7 *m* at 25°C by small-angle x-ray scattering (SAXS). Our results show no micelles or aggregates. Rather, the molecular weight of the solute in solution corresponds to a single associated anion (two anions, in the case of the bolaform electrolyte) and a single cation. This suggests that there is strong anion-cation pairing in these solutions but no appreciable cation-cation or higher-order cluster formation.

SIMPLE METHOD FOR ESTIMATING THE GAS-AMPLIFICATION FACTOR IN A PROPORTIONAL COUNTER[15]

R. W. Hendricks

The gas-amplification factor in a proportional counter was estimated by a comparison technique using an oscilloscope. A known capacitor was put in parallel with the input from the detector at the first group of the preamplifier and a unipolar output signal generated by applying a voltage step from a precision pulse generator. This signal was then matched on the oscilloscope to a similar signal from the main amplifier as created by a monoenergetic x-ray pulse falling on the counter.

To obtain the correct value for the gas-amplification factor, the difference in rise-time between the charge input from the detector and the pulse generator must be considered. This correction was obtained from a calibration chart that had been determined from a computer solution of the differential equations describing the pulse shapes for the pulse generator and the proportional counter at various points in the preamplifier-amplifier system. The calculations are based on a charge-sensitive low-noise preamplifier and a main amplifier having simple RC pulse-shaping networks. Experimental results illustrating the use of the method have been obtained.

MECHANISM AND KINETICS OF OMEGA TRANSFORMATION IN Ti–25 at. % Nb

Small-Angle X-Ray Scattering[16]

R. W. Hendricks G. R. Love[17]
C. C. Koch[17] P. G. Mardon[18]

The early stages of the omega-phase formation in a Ti–25 at. % Nb alloy was investigated by transmission electron microscopy (TEM) and small-angle x-ray scattering. Thin foils, formed by pack rolling, were solution annealed at 1000°C and 10^{-9} torr and quenched in helium. After correction for double Bragg scattering and all other nonsegregation effects, analysis of the SAXS intensity on an absolute basis showed that almost all of the single-phase disorder is retained on quenching. Aging between 325 and 400°C for 1 to 90 min allows the formation of clusters with radii of gyration (R_g) from 10 to 200 A (Fig. 14.4). It is important to note that R_g reaches a constant value for the three lowest aging temperatures but increases continuously for aging at 400°C. Electron diffraction and TEM have confirmed that the clusters have the ω-phase structure. The SAXS patterns indicate a high volume fraction of precipitate with strong interparticle interference effects. Measurements of the integrated intensity as a function of aging time, coupled with the R_g measurements, suggest that either (1) the number of ω nuclei is increasing with aging time, (2) the composition of the ω particles is changing with time, or (3) some combination of both is occurring. Experiments are being performed to differentiate between these possibilities.

---

[11] Abstract of paper presented at American Chemical Society Meeting, Minneapolis, April 1969.

[12] Chemistry Division.

[13] S. Lindenbaum and G. E. Boyd, *J. Phys. Chem.* 68, 911 (1964).

[14] H. E. Wirth, *J. Phys. Chem.* 71, 2922 (1967).

[15] Abstract of paper to be submitted to *Review of Scientific Instruments.*

[16] Abstract of paper presented at the Metallurgical Society of AIME, Pittsburgh, Pa., May 12–15, 1969.

[17] Metallurgy of Superconducting Materials Group.

[18] On temporary assignment from AERE, Harwell, England.

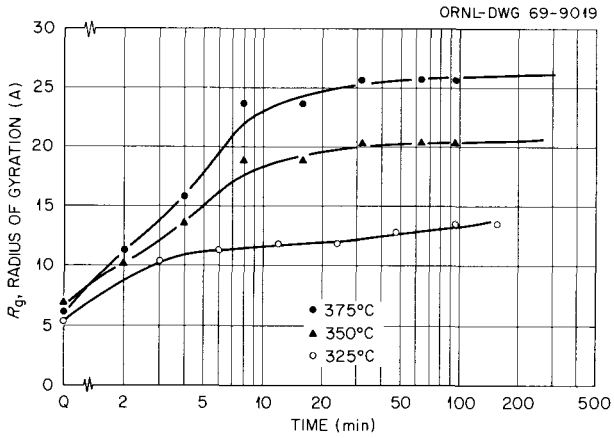

Fig. 14.4. Particle Radius of Gyration, R_g, Versus Time for ω-Phase Formation at Indicated Temperatures.

High-Angle X-Ray Scattering

H. L. Yakel C. C. Koch[17]

We have studied high-angle x-ray scattering by a single crystal of Ti–25 at. % Nb quenched from the β-phase equilibrium field and aged for successive periods at 400°C to form the metastable ω phase. Our principal object was to determine if significant long-range chemical order developed in the ω phase. After 24 hr aging, long-range chemical order was absent, the variable z parameter of atoms in $2d$ positions (space group $P\bar{3}m1$) was 0.50 ± 0.01, c/a for hexagonal ω was 0.614 ± 0.002 (and thus indistinguishable from the ideal ratio of $\sqrt{3}/2\sqrt{2}$ = 0.6124), and the volume per atom in the ω phase was 17.62 ± 0.01 A^3, compared with a volume of 17.64 A^3/atom in the as-quenched β phase.

AN ALIGNMENT PROCEDURE FOR THE KRATKY CAMERA

J. Anderegg[19] R. W. Hendricks
P. G. Mardon[18]

A Kratky camera for small-angle x-ray diffraction studies has been subjected to two major modifications. The first consisted of replacing the balanced filter unit by a diffracted-beam graphite monochromator; the second involved connecting the specimen chamber by bellows seals to the collimation system and the vacuum chamber. The number of windows in the vacuum system was thereby reduced, and a series of air scattering regions along the beam were all eliminated.

These modifications caused us to review the alignment procedure for the camera, and two new auxiliary slits have been made to simplify the technique. The stages involved are now:

1. Pointing of the collimation system at the focal spot by eye and setting the camera angle to 6° to the horizontal. The 20-μ entrance slit and second slit are set to give the required beam geometry in the horizontal lane.
2. Tilting the collimation system to be parallel with the focal spot. The system is not evacuated at this time (the bellows seals are disconnected).
3. Centering of the collimation system on the focal spot in both the vertical and horizontal directions.
4. Adjusting the jaws of the exit slit parallel to each other.
5. Tilting the exit slit to make it parallel to the collimated x-ray beam.
6. Inserting an empty sample holder and tilting it parallel to the beam.
7. Evacuating the camera, removing the sample holder, and repeating stages 2 and 5. After replacing the sample holder, stage 2 is rechecked.
8. Finally, setting the entrance slit to the desired width and rechecking stage 2.

With this procedure the time required for alignment of the camera has been reduced to about two working days.

[19]Molecular Anatomy Program (MAN), ORNL, on leave from Department of Biophysics, University of Wisconsin, Madison.

Part II. High-Temperature Materials

15. Physical and Mechanical Metallurgy of Refractory Alloys

H. Inouye

BASIC PHYSICAL METALLURGY STUDIES

H. Inouye

Interactions of Refractory Metals with Active Gases In Vacuum and Inert Gas Environment[1]

H. Inouye

The state of our knowledge of the interactions of refractory metals with active gases in vacuum and inert gas environments was reviewed. From 600 to 2000°C and 10^{-3} to 10^{-10} torr, contamination, degassing, decarburization, and sublimation reactions occur between the refractory metals and absorbed gases.

The extent and kinetics of these reactions are governed by the deviation of the interstitial concentration in the refractory alloy from the equilibrium concentration dictated by the temperature and pressure of the active gas. The reaction rates in inert gases are equivalent to those in vacuums of approximately 10^{-5} to 10^{-7} torr. These interactions can be reduced by minimizing the surface-to-volume ratio of the metal and minimizing the degree of equilibrium disparity. Added control is gained by the use of barrier foil envelopes and the use of low-pressure CH_4 to neutralize the oxidizing gases.

Solubility, Diffusivity, and Permeability of Interstitials in Refractory Alloys[2]

R. L. Wagner J. E. Spruiell[3]

An ultrahigh-vacuum technique for the determination of solubility, diffusivity, and permeability of gases in metals was applied to the nitrogen-tungsten system. The degassing rate of nitrogen was measured as a function of time from a resistively heated wire specimen, previously equilibrated at 1 to 25 torr N_2, with a mass spectrometer and a known vacuum conductance.

The diffusion constant, D, and the solubility constant, S, between 1000 and 1800°C may be summarized by

$$D = (2.37 \pm 0.43) \times 10^{-3} \exp\left[(-35{,}800 \pm 3900)/RT\right] \text{ cm}^2/\text{sec}$$

and

$$S = (0.21 \pm 0.06) \exp\left[(-17{,}600 \pm 5900)/RT\right] \text{ torr} \cdot \text{liter cm}^{-3} \text{ torr}^{-1/2} .$$

The permeation constants calculated from these results agree within a factor of 2 with directly measured values reported in the literature. The diffusion constants agree within a factor of 3 with literature values, although the activation energies for diffusion (35,800 vs 62,000) are quite different. The solubility obeys Sievert's law and exhibits a positive activation energy for solution. The concentration of nitrogen in tungsten at 1 atm pressure according to the above solubility data is 0.4 ppm at 1000°C and 9.2 ppm at 2000°C.

The permeability of nitrogen through tungsten is one-hundredth that through molybdenum and 10^{-5} times that through niobium or tantalum.

---

[1] H. Inouye, "Interactions of Refractory Metals with Active Gases in Vacua and Inert Gas Environments," pp. 165–95 in *Refractory Metal Alloys Metallurgy and Technology*, ed. by I. Machlin, R. T. Begley, and E. D. Weisert, Plenum, New York, 1968.

[2] Abstracted from R. L. Wagner, *A Technique for Measuring the Diffusivity and Solubility of Gases in Metals with Application to Nitrogen in Tungsten*, M.S. Thesis, the University of Tennessee, ORNL-TM-2584 (in press).

[3] Consultant from the University of Tennessee.

Development of Age Hardenable Alloys[4]

C. T. Liu R. W. Carpenter[5]
H. Inouye

Precipitation phenomena in Nb-Hf alloys have been investigated as a function of composition (30 to 60% Nb), quenching rate, and aging time and temperature. Alloys in this composition range comprise a single-phase body-centered cubic solid solution at high temperature (>1800°C); in the aging temperature range they are inside a miscibility gap in which both equilibrium phases are body-centered cubic.

Optical metallography showed that the precipitation kinetics and morphology are very sensitive to the quenching rate from the homogenization temperature. Rapidly quenched specimens age rapidly; the precipitate is nearly homogeneous and has no distinctive shape. Slowly quenched alloys age much more slowly, and the incoherent precipitate appears as rosettes. For intermediate quenching rates the "homogeneous" and "rosette" modes are both present, the homogeneous becoming dominant at higher quenching rates. X-ray studies of specimens in the early stages of aging showed substantial diffuse scattering at small angles. Side-band structure, indicative of a modulated structure, has not been observed.

These results are discussed in terms of current precipitation theories, particularly the effects of excess vacancies on nucleation and growth. The hardness values of alloys were correlated to the microstructure resulting from different precipitation reactions.

LONG-TIME HIGH-TEMPERATURE MECHANICAL PROPERTIES OF COMMERCIAL REFRACTORY ALLOYS

H. E. McCoy, Jr. R. L. Stephenson

Our objective is to establish the comparative mechanical properties of promising refractory alloys from 1000 to 1650°C. Primary consideration is given to collecting 1000-hr creep-rupture data on materials in typical metallurgical conditions produced by alloy vendors. The program includes studies on the response of these alloys to various heat treatments to establish optimum properties.

The creep-rupture properties of SU-16 (Nb–11% W–3% Mo–2% Hf–0.08% C) and C-129Y (Nb–10% Hf–10% W–0.1% Y) were reported previously.[6] The response of the properties of SU-16 to pretest annealing is shown in Fig. 15.1. Specimens were annealed at various temperatures, then tested at 40,000 psi and 980°C. The times to 1 and 2% creep strain and to rupture decrease to a minimum with a pretest anneal of approximately 1400°C, then increase until approximately 1700°C. To a lesser degree, the strength of C-129Y can also be improved by appropriate pretest annealing. We hope to use transmission electron microscopy and x-ray examination to illuminate the mechanism of such effects in these and similar alloys.

We also studied the effect of pretest annealing temperature on the creep-rupture properties of T-111 (Ta–8% W–2% Hf). The results thus far are shown in Fig. 15.2. The times to 1, 2, and 5% creep strain and to rupture at 35,000 psi and 1205°C decrease with increasing pretest annealing temperature. These data are

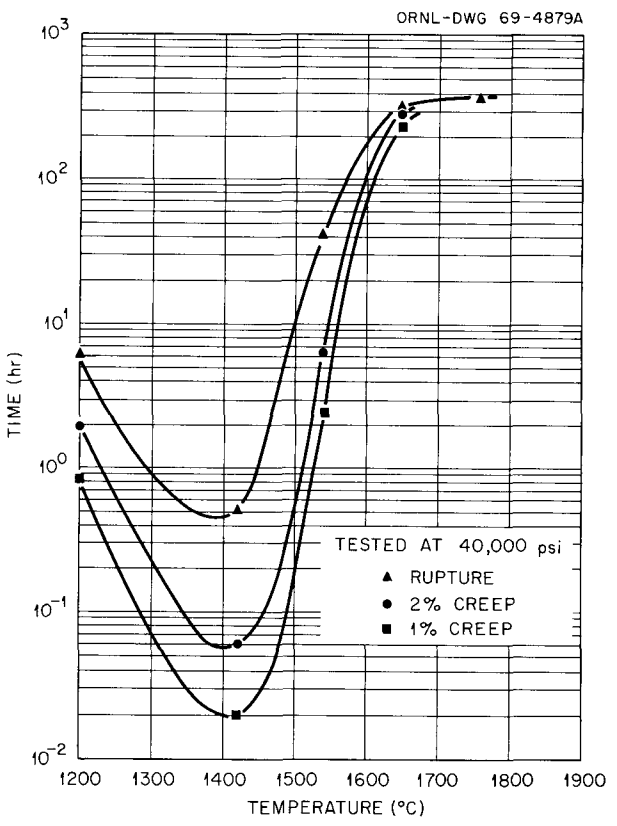

Fig. 15.1. Effect of Pretest Annealing Temperatures on the Creep-Rupture Properties of SU-16 at 980°C.

[4]Abstracted from "Precipitation in Niobium-Hafnium Alloys," paper presented at the Spring Meeting of the Metallurgical Society of AIME, Pittsburgh, Pa., May 12–18, 1969.

[5]Deformation of Crystalline Solids Group.

[6]R. L. Stephenson, *Metals and Ceramics Div. Ann. Progr. Rept. June 30, 1968,* ORNL-4370, p. 60.

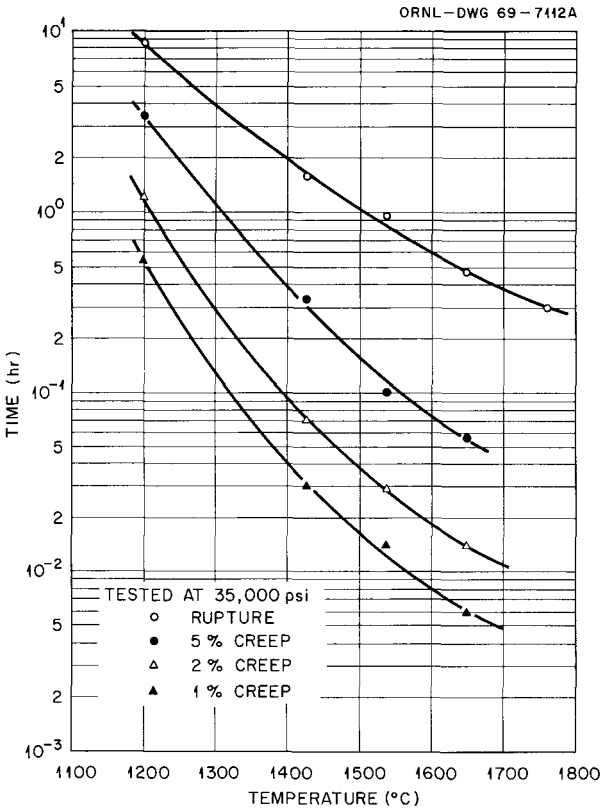

Fig. 15.2. Effect of Pretest Annealing Temperature on the Creep-Rupture Properties of T-111 at 1205°C.

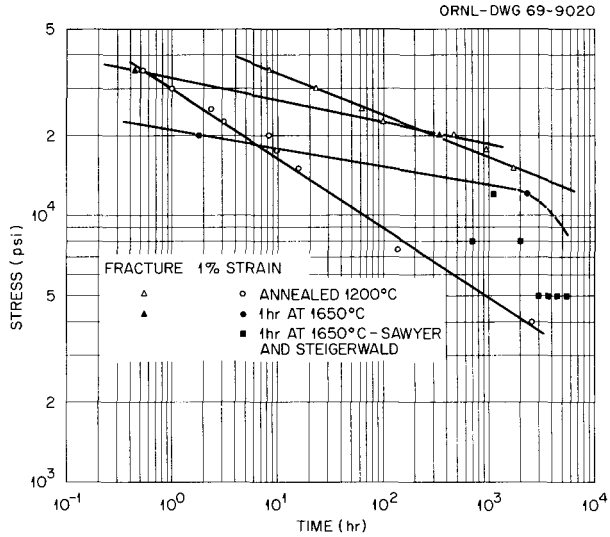

Fig. 15.3. Creep-Rupture Properties of T-111 at 1205°C. Included are results of Sawyer and Stiegerwald, N-68-17372 (June 1967).

in apparent conflict with the data of Sawyer and Steigerwald,[7] who show longer times for material annealed at 1650°C than for material annealed at 1200°C. Upon testing over a broader range of stresses, we found that the stress dependence of material annealed at 1650°C is much different than that of material annealed at 1200°C. Figure 15.3 shows that T-111 annealed at 1650°C is weaker at high stresses but stronger at low stresses, in agreement with the results of Sawyer and Steigerwald.

The effect of fabrication variables on the creep-rupture properties of TZM (Mo–0.5% Ti–0.08% Zr–0.02% C), Cb-TZM (Mo–0.5% Ti–0.08% Zr–0.02% C–1.5% Nb), and TZC (Mo–1.2% Ti–0.25% Zr–0.15% C) have been investigated.[8] We are examining the structures of these alloys by transmission electron microscopy. Materials that show high strengths at moderate temperatures (980°C) have very fine subgrain diameters (about 0.5 μ).

We are also studying the creep-rupture properties of TZM welds. Preliminary data indicate that the rupture life of transverse electron beam welds is virtually identical to that of the base metal at 1650 to 1800°C.

WELDING AND BRAZING DEVELOPMENT

Brazing Alloy Development

Nancy C. Cole D. A. Canonico

Brazing alloy development focused on two ternary systems, Ti-Zr-Ge and Ti-V-Cr, which have proven exceptional for joining refractory metals, ceramics, and graphite to themselves and to each other.[9–12] Several

[7] J. C. Sawyer and E. A. Steigerwald, *Generation of Long Time Creep Data of Refractory Alloys at Elevated Temperatures*, N-68-17372 (ER-7203, NASA-CR-93193) (June 6, 1967).

[8] R. L. Stephenson, "The Effect of Fabrication Variables on the Creep-Rupture Properties of Molybdenum-Base Alloys," *Trans. Met. Soc. AIME* **245**, 997–1001 (1969).

[9] D. A. Canonico, N. C. Cole, and G. M. Slaughter, "Brazing Alloy Development for Graphite and Ceramics," paper presented at American Welding Society Annual Meeting, May 1969.

[10] D. A. Canonico and N. C. Cole, *Fuels and Materials Development Program Quart. Progr. Rept. June 30, 1968*, ORNL-4330, pp. 352–54.

[11] D. A. Canonico and N. C. Cole, *Fuels and Materials Development Program Quart. Progr. Rept. Sept. 30, 1968*, ORNL-4350, pp. 302–5.

[12] D. A. Canonico and N. C. Cole, *Fuels and Materials Development Program Quart. Prog. Rept. Dec. 31, 1968*, ORNL-4390, pp. 284–90.

compositions in the Ti-Zr-Ge system (typified by Ti–20% Zr–15% Ge) possess an outstanding ability for joining graphite to itself and to refractory metals. Their ability to wet and flow into interstices of low-density graphite is impressive. In shear tests of these brazes, failure repeatedly occurs in the graphite.

The Ti-V-Cr system has an interesting flowability pattern on Al_2O_3 and graphite. The composition Ti–21% V–25% Cr joins both materials equally well. Increasing the chromium content favors flow on Al_2O_3, whereas decreasing the chromium content favors flow on graphite.

As-brazed shear strengths of joints brazed with some of our experimental alloys were excellent. For example, Ta–10% W brazed with Ti–46% Zr–8% Ge possessed strengths of 55,000 psi when tested at room temperature and 27,000 psi when tested at 1000°C. The properties of these alloys remained satisfactory after aging in argon for 50 hr at probable service temperatures. Brazes from the Ti-Zr-base systems (with third element additions of Ta, Si, Nb, Ge, Cr, and B) did not lose strength noticeably due to aging. In fact, most of the brazements were stronger. However, the Ti-B-base systems (third element additions of Nb, Mo, and Cr) exhibited somewhat lower shear strengths after aging.

Welding of T-111 Alloy Forced Circulation Loop (FCLLL-1)

L. C. Williams G. M. Slaughter

We successfully welded FCLLL-1, the T-111 forced-circulation loop.[13] This is by far the most complex structure of T-111 ever constructed at ORNL. It incorporated about 80 gas tungsten-arc welds, with all of the joints in the primary piping being of the multipass, full-penetration type. All components were welded in a vacuum-purged argon-atmosphere chamber. The argon before and during welding was constantly monitored by analyzers for oxygen and water vapor and also by making sample welds for subsequent chemical analysis. The final three closure welds were made in place with a portable, rotating, inert-atmosphere welding device developed at ORNL.

[13]L. C. Williams, *Fuels and Materials Development Program Quart. Progr. Rept. Dec. 31, 1968,* ORNL-4390, pp. 290–92.

[14]R. K. Williams, W. Fulkerson, J. P. Moore, and D. L. McElroy, *Metals and Ceramics Div. Ann. Progr. Rept. June 30, 1968,* ORNL-4370, pp. 35–36.

THERMAL CONDUCTIVITY OF TUNGSTEN ALLOYS

R. K. Williams J. P. Moore
W. P. Murray D. L. McElroy

For metals and alloys the thermal conductivity λ is the sum of the electronic and lattice components. We are using theoretically based analyses of the effects of temperature and alloying on these components to extrapolate accurate low-temperature data to high temperatures. Our previous measurements and analyses[14] showed: for Cr, Mo, and W, the Wiedemann-Franz correlation of the electronic component with the easily measured electrical conductivity is inadequate, since the electronic component is 9 to 14% greater than predicted at high temperatures; and for Cr and W the lattice component is substantial, although it is frequently small for metals.

We extended this analysis to dilute alloys that have electronic and lattice components reduced by a solute. Electrical resistivity ρ from 80 to 1700°K and λ from 80 to 350°K on electron-beam-melted tungsten and four tungsten-base alloys were used with our previous λ and ρ data on tungsten to test several increasingly complex estimation methods for predicting λ from 80 to 1700°K for all six materials.[15] The most satisfactory estimation method was derived from two different approaches to separate the electronic and lattice λ components and allows the Lorenz function and lattice portion to be altered by alloying.[16] The calculated λ values as shown in Fig. 15.4 are within 10% for the tungsten alloy measured to high temperatures. Further efforts in this area are aimed toward obtaining more high-temperature λ and ρ data needed to optimize the calculation parameters. Toward this end, two experimental studies reported in Chap. 9 are progressing: (1) development of an electrically heated method for use to 1500°K on small rod samples and (2) use of other materials in an apparatus that has yielded ρ of tantalum to 2600°K.

[15]R. K. Williams, J. P. Moore, and W. P. Murray, *Fuels and Materials Development Program Quart. Progr. Rept. Sept. 30, 1968,* ORNL-4350, pp. 306–9.

[16]R. K. Williams and W. Fulkerson, "Separation of the Electronic and Lattice Contributions to the Thermal Conductivity of Metals and Alloys," *Thermal Conductivity, Proc. 8th Conf., Held at Purdue University, West Lafayette, Indiana, October 7–10, 1968,* ed. by C. Y. Ho and R. E. Taylor, Plenum, New York, 1969.

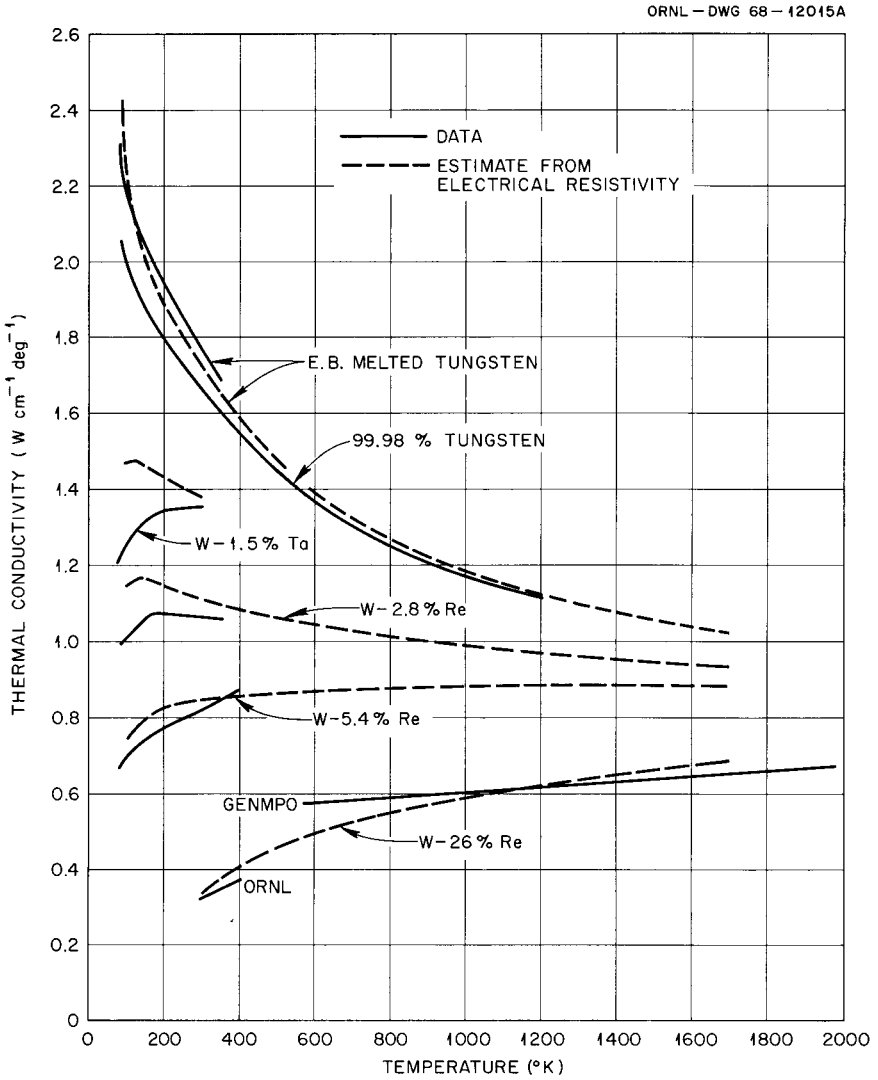

Fig. 15.4. Thermal Conductivity Measurements and Estimates on Tungsten and Several Tungsten-Base Alloys.

16. Tungsten Metallurgy

A. C. Schaffhauser P. Patriarca

Tungsten is of interest for advanced reactor systems employing ultrahigh-temperature liquid-metal-cooled circuits, thermionic conversion, and the Brayton Cycle. This interest stems from the fact that tungsten has a number of attractive properties, including high melting point, good high-temperature strength, high thermal and electrical conductivities, high thermionic emission, and compatibility with many fuel materials and coolants. The goal of this program is to develop economical methods for producing high-quality tungsten and tungsten alloy tubing having good high-temperature creep resistance, microstructural stability, low-temperature ductility, and weldability. The program ecompasses two areas of tubing fabrication – one by modification of conventional techniques based on extrusion, tube reducing, and warm drawing, and the other by direct chemical vapor deposition (CVD) through the hydrogen reduction of heavy-metal halides – and a complete physical-metallurgical evaluation of both. The materials being investigated include unalloyed tungsten, tungsten-rhenium alloy, other solid-solution-strengthened alloys, and dispersion- and precipitation-hardened alloys. All materials are consolidated by arc-casting, powder-metallurgy, or CVD techniques. More basic studies designed to elucidate the mechanisms controlling the metallurgical and mechanical behavior of tungsten and the role of selected alloying elements are included.

Percentage compositions given in this chapter are atomic percentages, as is customary for the tungsten alloys covered.

EFFECT OF EXTRUSION CONDITIONS ON THE STRUCTURE OF EXTRUDED TUNGSTEN

R. E. McDonald W. R. Martin

We are examining the effect of extrusion temperature, reduction ratio, and prior metallurgical structure on the structure of tungsten tube shells extruded by the floating-mandrel extrusion technique.[1] Our intent is to find those extrusion conditions that will optimize the structure and properties of extruded tubing for use as extruded or for subsequent drawing.

In our initial experiments, primary tube-shell extrusions of powder metallurgy tungsten having both wrought and recrystallized starting structures were duplex extruded in molybdenum-alloy billets at a ratio of 3 at preheat temperature between 1150 and 1700°C. We determined the structure and grain size of the primary tube shells, after preheat to the extrusion temperature and after duplex extrusion. From these data we conclude that at extrusion preheat temperatures of 1450°C and higher, wrought structures recrystallized during preheat and the extruded material will have a recrystallized structure. Wrought structures and recrystallized structures are stable during preheat at 1150°C, but an estimated increase in temperature of 150 to 200°C during extrusion due to the deformation is sufficient to cause recrystallization of a wrought starting material during extrusion. However, under the same extrusion conditions, a wrought extruded structure was obtained from a recrystallized starting material because of the lower extrusion force required.

CHEMICAL VAPOR DEPOSITION OF TUNGSTEN AND TUNGSTEN-RHENIUM ALLOYS

J. I. Federer

Tungsten and tungsten-rhenium alloy deposits are being prepared for bend, tensile, and creep-rupture testing. Tungsten sheet stock 0.05 to 0.09 in. thick was deposited by hydrogen reduction of WF_6 on resistance-heated molybdenum substrates at 600 to 650°C and a system pressure of 10 torr. Each deposit provides about

[1] R. E. McDonald and G. A. Reimann, *Floating-Mandrel Extrusion of Tungsten and Tungsten-Alloy Tubing,* ORNL-4210 (February 1968).

55 in.^{2} of sheet stock from which 12 tensile or 50 bend specimens can be machined. The substrate can be dissolved in acid solution at any stage of the specimen preparation process. Metallographic examination of the deposits revealed a typical columnar grain structure with no grown-in porosity. Chemical analysis showed 5 to 10 ppm F.

Efforts to prepare W–5% Re and W–25% Re deposits in the same manner have been less successful. Nodules, which occur frequently in deposits of both alloys, and thickness variations along the deposits decrease the amount of material suitable for specimen preparation. In addition, temperature gradients during deposition result in compositional variations. The latter problem prompted a study of the effect of temperature on compositional uniformity, a relation that was previously known qualitatively. In this study small resistance-heated specimens were exposed to H_2-WF_6-ReF_6 gas mixtures at 600 to 1200°C. Deposits prepared at 10 and 25 torr with a gas mixture containing 3.5% Re were rhenium-rich at 600°C and rhenium-poor in the range 800 to 1200°C. Deposits prepared at 10 torr with a gas mixture containing 20.7% Re were rhenium-rich at 600°C but contained about the same rhenium content as the mixture in the range 700 to 1200°C. The practical significance of these results is that deposits of uniform composition cannot be prepared below about 700°C. Below 700°C, ReF_6 is preferentially reduced, resulting in a rhenium-rich deposit and leaving the gas mixture depleted. At about 700°C neither ReF_6 nor WF_6 is preferentially reduced, so the composition of the deposit should be uniform.

Subsequently, nominal W–5% Re alloys were deposited on resistance-heated sheet-type substrates. Although maintained at 700 to 750°C in the middle portion, the ends of the substrate were cooled by water-cooled power leads, resulting in rhenium-rich deposits on the ends. The substrates were made isothermal by reducing the cross section of the ends. Another difficulty arose in the thicker deposits; the gas mixture becomes depleted in both WF_6 and ReF_6 while flowing along the substrate, resulting in a thicker deposit at the gas inlet end, which lowers the temperature and increases the rhenium content. We attempted to minimize this effect by periodically reversing the gas flow in the deposition chamber. However, this technique caused the deposits to be thicker and rhenium-rich on both ends and resulted in a layered structure with some porosity between the layers.

The effect of deposition pressure on thickness distribution was then investigated. With unidirectional flow and similar deposition conditions, the deposits were thicker on the gas inlet end at 10 torr, thicker on the gas outlet end at 100 torr, and were more uniform over much of the length at about 50 torr. However, rhenium deposition was suppressed at the higher pressures, and the deposits were much more nodular.

Currently, depletion of both WF_6 and ReF_6 is being minimized by using higher flow rates, and nodule formation is being minimized by periodically stopping and starting deposition. The latter technique is intended to refine the grain structure by confining deposition to the fine-grained structure that always occurs at the start of deposition.

CHEMICAL VAPOR DEPOSITION OF VANADIUM

W. C. Robinson, Jr.[2] J. I. Federer

Vanadium and vanadium alloys are potential fuel cladding materials for LMFBR. Chemical vapor deposition of vanadium is being studied as a potential fabrication method for tubing and cladding. In our initial experiments VCl_3 powder was transferred to a heated carbon substrate by entrainment in an argon stream, where it was reduced by hydrogen to metal. Coating thicknesses of 0.001 to 0.005 in. were obtained at 1000, 1100, and 1200°C; deposition below 1000°C appeared impossible.

Subsequently, VCl_4 and VF_5 were prepared to avoid the difficulty of metering entrained VCl_3 powder. Vanadium metal was reacted with chlorine (400°C) or fluorine (250°C) to form the halides. These were transferred into a heated stainless steel tube and reduced with hydrogen at 1200°C. Coatings having thicknesses of 0.001 to 0.015 in. have been prepared in this manner.

The grain structure of deposits prepared from VCl_4 was coarsely columnar, was strongly {110} oriented, and contained precipitate particles at the grain boundaries and within grains. Deposits prepared from VF_5, also coarsely columnar, contained a continuous second-phase precipitate at the grain boundaries and large particles within grains. The deposits contained about 1.2% total interstitial impurities, mostly oxygen and nitrogen, which were probably derived from the reactant gases.

Continuing work will concentrate on improving the purity of the deposits. In addition, deposition of alloys with chromium and titanium will be studied. These will

[2]Present address, Lockheed-California Co., Burbank, Calif. 91503.

be characterized in terms of deposition rate and efficiency, purity, hardness, orientation, and response to heat treatment.

THE DUCTILE-TO-BRITTLE TRANSITION TEMPERATURE OF CVD W–5% Re SHEET

A. C. Schaffhauser

We began bend tests of CVD W–5% Re sheet to determine the ductile-to-brittle transition temperature (DBTT) and effects of heat treatment. The deposition apparatus and conditions are described in a previous section of this chapter. The gas flow was periodically reversed during deposition to help in obtaining uniform thickness along the sheet; however, this also produced a slightly layered microstructure, grown-in porosity between the layers, and a nonuniform microstructure along the deposit. Problems with cracking were encountered during cutting and grinding the as-deposited sheet, but a stress relief anneal of 2 hr at 1100°C significantly increased the specimen yield.

The DBTT for a 90° bend in the 0.030-in.-thick sheet was determined by a standard 4*T* bend test (punch radius four times the sheet thickness). The stress-relieved material had a DBTT greater than 300°C and the data were scattered. Annealing 1 hr at 1600 to 2400°C significantly reduced the DBTT, and the lowest DBTT at 150°C occurred after a 2200°C anneal. A large amount of grain growth occurred during the 2400°C anneal and resulted in a DBTT of 250°C.

Metallographic examination of the bend specimens showed that some sintering and rounding of the fine grown-in porosity occurred during the high-temperature anneals, and this is the most likely reason for the improved ductility after these treatments. These results are encouraging because the DBTT of 150°C is the lowest reported for unworked tungsten or W–5% Re.

FORMATION OF GAS BUBBLES IN CVD MATERIALS

K. Farrell W. C. Robinson, Jr.[2]
J. I. Federer A. C. Schaffhauser

We have continued our studies on the mechanism of gas bubble formation in CVD materials. Previously, the formation and growth of gas bubbles during annealing at high temperatures was correlated[3,4] with the fluorine impurity content in CVD tungsten deposited from WF_6 at 600 to 800°C. But later we found that no gas bubbles developed during annealing tungsten deposited at 1000 to 1200°C from WCl_6 containing fluorine impurities. In our most recent experiments, W containing 2 to 4 ppm fluorine impurities was deposited from WF_6 at 1100 and 1200°C. Some of these deposits were free of grown-in porosity, and no bubble formation was observed by electron microscopy after annealing 1 hr at 2500°C.

Examination of these and other CVD materials after annealing has revealed a correlation between formation of gas bubbles and the fraction of the absolute melting point at which the material was deposited (Table 16.1). Apparently material deposited at temperatures below about 0.3 of the absolute melting temperature ($0.3T_m$) develops gas bubbles during annealing, whereas materials deposited at higher fractions of their melting temperatures remain free of bubbles. Since nucleation and growth of bubbles result from the coalescence of gaseous impurities with lattice vacancies, the probability of nucleation will depend on the amounts of impurities and vacancies. Our interpretation of the evidence in Table 16.1 is that the deposition temperature influences the supersaturation of vacancies pro-

[3] A. C. Schaffhauser and R. L. Heestand, "Effect of Fluorine Impurities on the Grain Stability of Thermochemically Deposited Tungsten," pp. 204–11 in *1966 IEEE Conference Record of the Thermionic Conversion Specialist Conference, Nov. 3 and 4, 1966, Houston, Texas,* The Institute of Electrical and Electronics Engineers, New York, 1966.

[4] J. V. Festa and J. C. Danko, "Some Effects of Fluorine Content on the Properties of Chemically Vapor Deposited Tungsten," p. 349 in *Proceedings of the Conference on Chemical Vapor Deposition of Refractory Metals, Alloys, and Compounds, Gatlinburg, Tennessee, September 12–14, 1967,* ed. by A. C. Schaffhauser, American Nuclear Society, Hinsdale, Ill.

Table 16.1. Formation of Bubbles in Chemically Vapor Deposited Materials

Metal	Volatile Compound	Deposition Temperature (°C)	T_d/T_m Ratio[a]	Presence of Gas Bubbles After Annealing
W	WF_6	600–800	0.24–0.30	Yes
W	WCl_6	1000–1200	0.35–0.40	No
Mo	MoF_6	770–950	0.36–0.42	No
Ta	$TaCl_5$	1000–1200	0.39–0.45	No
Ni	$Ni(CO)_4$	150–250	0.24–0.30	Yes
V	VCl_3	1000–1200	0.50–0.60	No
W	WF_6	1000–1200	0.35–0.40	No
Mo	MoF_6	600–700	0.30–0.34	Not yet determined

[a] Ratio of the deposition temperature to the absolute melting point of the material.

duced during deposition and thus determines the probability of bubble formation during subsequent annealing. During deposition, lattice vacancies are created because the newly deposited atoms do not immediately attain their equilibrium lattice positions. Rearrangement of the atoms and the consequent elimination of vacant sites takes place by diffusion of atoms over the surface. Low temperatures and high rates of deposition will therefore favor a high supersaturation of vacancies, which in turn will ensure bubble formation during subsequent annealing, provided sufficient gases are present. At higher deposition temperatures, surface diffusion is enhanced, and the supersaturation of vacancies is low – and so is the probability of bubble formation.

GAS POROSITY AND HOT CRACKING IN FUSION WELDS IN TUNGSTEN[5]

K. Farrell J. T. Houston
J. W. Chumley

Porosity and intergranular hot cracking occur in fusion welds in tungsten. We have examined these phenomena in full-penetration, bead-on-plate welds in various grades of tungsten, using optical microscopy and electron fractography.

Chemically vapor deposited tungsten displayed hot cracking and extensive but fine intergranular porosity in the heat-affected zone. Two grades of powder metallurgy tungsten developed large pores in the weld bead but appeared to be free of cracks. Another powder metallurgy product and some arc-melted tungsten showed hot cracking and fine porosity in the weld bead. All welds, except those in the arc-melted tungsten, exhibited gross porosity along the fusion lines, but no cracks formed there.

Electron fractographic examination of welds that were broken at room temperature to expose internal pores and hot cracks revealed that the hot cracks were formed by the growth and coalescence of many small pores on grain boundaries. In those welds in which the pores were large and easily visible in the optical microscope the pores were too widely spaced to touch one another and link up into cracks.

The pores are believed to be initiated as gas bubbles. Their location in the welds depends on the prior processing history of the different grades of tungsten and can explain why hot cracks were observed only in the heat-affected zones in chemically vapor deposited tungsten and only in the weld beads in other types of tungsten. Calculations show that during welding suitably arranged pores can grow and coalesce into a grain boundary crack by a mechanism involving stress-induced diffusion of vacancies into the pores. This mechanism of hot crack formation in welds should also apply to other materials.

[5]Summary of paper submitted to *British Welding Journal.*

CREEP-RUPTURE PROPERTIES OF TUNGSTEN ALLOYS

R. L. Stephenson

Our objective is to determine the creep-rupture properties of various tungsten-base materials from 1400

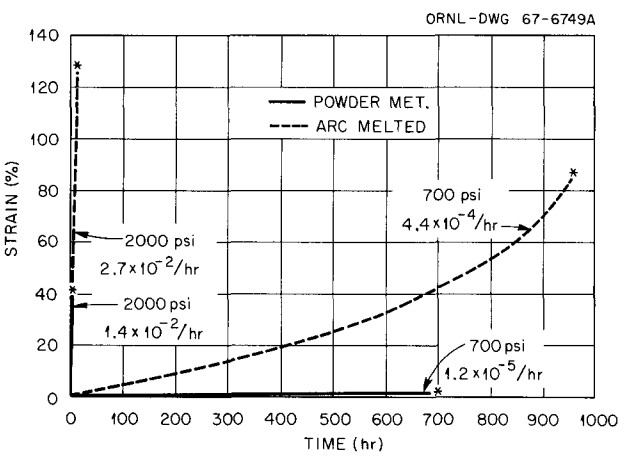

Fig. 16.1. Creep Properties of W–25% Re at 2200°C.

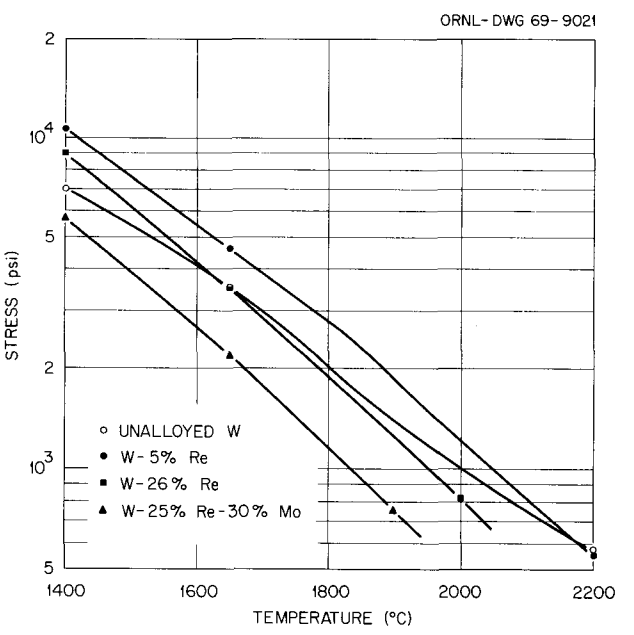

Fig. 16.2. Stress to Produce Rupture in 1000 hr for Arc-Cast Tungsten-Rhenium Alloys.

to 2200°C for times up to 1000 hr. We have compared the properties of arc-melted (AM) and powder-metallurgy (PM) W–25% Re produced from common feed material.[6] Figure 16.1 compares creep curves for each material tested at the same stresses at 2200°C. Rupture times are slightly shorter for the PM material, but the ductility is much lower. Similar but smaller differences in the rupture life and ductility of AM and PM material are observed at 1650°C. Electron microscopy shows that grain boundary voids form in both materials. In the PM material the grain boundaries appear immobile and the voids grow and initiate fracture at low strains. In the AM material fracture seems to be forestalled by the ability of grain boundaries to move.

We are also comparing the properties of arc-melted W, W–5% Re, W–26% Re, and W–25% Re–30% Mo. Figure 16.2 shows the 1000-hr rupture stress as a function of temperature for each of these materials. The data indicate that small additions of rhenium increase the strength for short service times and low temperature but that large additions of lower melting elements (rhenium and molybdenum) reduce the strength at long service times and high temperatures.

[6] R. L. Stephenson, *Comparative Creep-Rupture Properties of W–25% Re Consolidated by Arc Melting and Powder Metallurgy Techniques*, ORNL-TM-2651 (in press).

17. Alkali-Metal Corrosion of High-Temperature Materials

J. H. DeVan A. P. Litman

The purpose of this program is to investigate the chemical and metallurgical effects produced in structural materials during exposure to alkali metals. Our experiments are designed to guide the selection of containment materials for both sodium-cooled fast breeder reactor (LMFBR) systems and lithium-cooled space-power systems in which boiling potassium serves as the Rankine-cycle fluid.

Studies in support of the sodium-cooled fast breeder reactor are designed (1) to determine the effects of interstitial impurities in sodium on the mechanical and corrosion properties of vanadium alloys and (2) to investigate the interactions of 300 series stainless steels, commercial insulation, and sodium in air at 600 to 800°C.

Studies in support of space-power systems are centered around refractory-metal containment materials, in particular, tantalum- and tungsten-base alloys. Our principal objective is to study the conditions affecting thermal-gradient mass transfer to refractory alloys in lithium in the temperature range 1200 to 1650°C. A small effort has been included on boiling potassium systems to bring this portion of the program to an orderly conclusion.

MASS TRANSFER OF INTERSTITIAL IMPURITIES BETWEEN VANADIUM ALLOYS AND SODIUM

As is true for refractory metals as a class, vanadium alloys are highly resistant to dissolutive attack by liquid alkali metals if these liquids remain free of impurities. The presence of oxygen, however, greatly increases the corrosion rate of vanadium alloys in sodium. Oxygen, together with carbon and nitrogen, also may be transferred by the liquid metal to the refractory alloy to cause important mechanical property changes.

Accordingly, we are studying the mechanisms by which vanadium alloys undergo attack in sodium at interstitial impurity levels typical of sodium-cooled reactor systems. Our objectives are (1) to characterize the partitioning behavior of oxygen, nitrogen, and carbon between vanadium alloys and sodium as a function of alloy composition and sodium purity; (2) to determine mechanical property effects produced in vanadium alloys by interstitial impurities acquired from sodium; and (3) to determine the effect of oxygen in vanadium alloys and sodium on the dissolution behavior of the alloys.

Effect of Oxygen in Sodium on Vanadium and Vanadium Alloys

R. L. Klueh

Kinetics of Internal Oxidation. – Vanadium and its alloys readily absorb oxygen from liquid sodium at 600 to 700°C. The kinetics of oxygen absorption differs depending upon the composition of the alloy. Alloys containing titanium and aluminum absorb oxygen with the simultaneous formation of a subsurface hardened zone. The depth of this zone depends on time, temperature, oxygen content of the sodium, and composition of the alloy. Pure vanadium and vanadium containing chromium and niobium absorb oxygen somewhat faster and without the formation of a pronounced hardened zone.

The experimental observations on vanadium-titanium and vanadium-aluminum alloys suggested that these alloys were internally oxidizing in sodium and that the subsurface hardened zone represented a TiO_2 or Al_2O_3 precipitate band. We therefore interpreted the published results for these alloys in terms of an internal oxidation model and showed that the kinetics of the subsurface layer growth was consistent with models proposed by Rapp[1] in which solid-state diffusion of oxygen into the alloy controls the rate of oxide precipitation. We then extended this model to the

[1] R. A. Rapp, *Corrosion* 21, 382 (1965).

consideration of alloy characteristics that would afford maximum nobility in a sodium service environment.

Oxygen Partitioning. – We exposed a series of vanadium capsules and insert specimens to sodium to gain an understanding of the effect of oxygen on the compatibility between vanadium and sodium and to compare these results with similar tests[2] in the niobium-sodium and tantalum-sodium systems.

Tests were conducted[3] at 600 and 800°C with sodium containing from about 50 to 1300 ppm O. In all cases the oxygen was effectively gettered by the vanadium specimen and capsule, indicating a very large equilibrium distribution coefficient. After exposure the sodium contained about 40 and 200 ppm V at 600 and 800°C respectively. In contrast, the niobium-sodium and tantalum-sodium systems exhibit a markedly smaller oxygen distribution coefficient, and the solubility of niobium and tantalum in sodium increases more with increasing oxygen concentration in the sodium. Sodium did not penetrate vanadium that contained as much as 1900 ppm O; tantalum and niobium are penetrated under similar conditions.

Interstitial Effects on Mechanical Properties of Vanadium Alloys

R. L. Wagner

Interstitial contaminants in vanadium and its alloys significantly affect their mechanical properties. We are studying the effect of alloying elements on the nature and rate of interstitial contamination of vanadium and the effect of the contaminants on creep properties.

We measured the contamination of 0.020-in.-thick pure vanadium sheet specimens exposed to oxygen on both sides from 350 to 900°C. The oxygen concentration in the vanadium did not change significantly under a vacuum of 4×10^{-8} torr for 800 hr. Also, in the range 10^{-6} to 10^{-7} torr the oxygen concentration of the vanadium went through a maximum at approximately 550°C. Assuming the reaction rates to be linear in time, the rates for the maximum observed at 550°C were 0.5 and 0.1 ppm/hr at 2×10^{-6} and 2×10^{-7} torr O respectively.

Mass Transport of Interstitial Impurities Between 300 Series Stainless Steels and Vanadium Alloys

J. H. DeVan D. H. Jansen

We are investigating the partitioning of carbon and nitrogen between vanadium alloys and stainless steels in a sodium circuit. Test variables include the relative surface areas and temperatures of stainless steel and vanadium and the chemical composition of the two alloy systems. The tests are being conducted in thermal convection loops designed[4] so that all heated surfaces in contact with sodium are of vanadium, while all isothermal or cooled sections are of stainless steel.

Mass transfer rates and the effect of interstitial transfer on the mechanical properties of the alloys are determined from insert specimens positioned concentrically in the heated and cooled legs of the loop. Loops of types 304 and 321 stainless steel, each incorporating an unalloyed vanadium hot leg section, are currently operating at a 700°C sodium outlet temperature.

We are interested in comparing the rates of interstitial transport in these systems with those in a static, isothermal system and have constructed a series of stainless steel vessels that can accommodate sheet specimens of both vanadium and stainless steel for tensile tests. The relative surface areas of stainless steel and vanadium correspond to the ratios set for our thermal convection loops.

COMPATIBILITY OF STAINLESS STEEL AND INSULATION IN LMFBR SYSTEMS

C. D. Bopp[5] A. P. Litman

Compatibility of insulating materials with stainless steels is an important consideration in the design of LMFBR systems. Accordingly, we are studying the possible reactions between commercial insulating materials and stainless steel.

The first phase of our program is concerned with the interactions of stainless steels and commercial alumina-silica insulation materials between 370 and 760°C. The second phase deals with the effects of sodium leaks in stainless steel systems surrounded by thermal insulation. Small leaks that may be self-sealing at lower temperatures are being investigated by methods similar to those used in the first phase. The effects of large leaks are being studied in heated, pressurized containers with artificial defects incorporated in the container wall.

---

[2] R. L. Klueh, *Metals and Ceramics Div. Ann. Progr. Rept. June 30, 1968,* ORNL-4370, p. 83.

[3] R. L. Klueh, *Fuels and Materials Development Program Quart. Progr. Rept. Sept. 30, 1968,* ORNL-4350, pp. 87–91.

[4] W. O. Harms, J. H. DeVan, and A. P. Litman, *Fuels and Materials Development Program Quart. Progr. Rept. Dec. 31, 1968,* ORNL-4390, pp. 85–86.

[5] On loan from the Reactor Chemistry Division.

We completed a survey[6] of the effects of insulating materials on stainless steel. This included a literature study, a compilation of ORNL experience with thermal insulations, and an examination of pertinent thermodynamic data. This survey indicates that, in the LMFBR temperature range, the oxides of iron, chromium, or nickel on stainless steel should not react with pure alumina or silica, the major components in suitable commercial insulations. However, the presence of low-melting and volatile oxides or of sulfur- or halogen-containing compounds could lead to catastrophic oxidation at the interface between base metal and oxide. We also found disagreement in explaining the details of the acceleration of oxidation by these impurities. Much of the information available is highly empirical and lacking in the areas of long-term, cyclic, and transient effects.

Except for some continuing long-term tests, we have completed our experimental study of the compatibility of insulation with stainless steel in the absence of sodium oxidation products.[7,8] The test results are summarized in Fig. 17.1. When some differences in experimental conditions are allowed for, the scaling kinetics in moist air are similar to those reported for oxygenated superheated steam. The similarity of scaling in moist air and steam was confirmed further by examination of the scale by metallography, elemental analysis, electron microprobe scan analysis, and x-ray diffraction. Our specific test findings were as follows:

1. Catastrophic oxidation (a rapid form of corrosion thought to result from fluxing of the scale by a liquid phase) was not found in tests with type 316 stainless steel to 815°C.
2. Type 304L stainless steel has superior scaling resistance to type 316 stainless steel in moist air in the range 700 to 815°C.
3. Alumina-silica "blanket" insulation did not enhance scaling even under conditions that produced extensive exfoliation of the oxidation products on types 304L and 316 stainless steel. In contrast, scaling was noticeably enhanced by amosite asbestos-diatomaceous silica insulation, probably from interaction of the sodium silicate binder or sulfur impurity with the scale.
4. Temperature cycling increased spalling substantially with relatively thick scales but did not affect the protectivity of the thinner scales formed under less stringent conditions.

[6]C. D. Bopp, *Fuels and Materials Development Program Quart. Progr. Rept. Sept. 30, 1968,* ORNL-4350, pp. 95–102.

[7]C. D. Bopp, *Fuels and Materials Development Program Quart. Progr. Rept. Dec. 31, 1968,* ORNL-4390, pp. 91–92.

[8]C. D. Bopp and A. P. Litman, *Fuels and Materials Development Program Quart. Progr. Rept. March 31, 1969,* ORNL-4420, pp. 92–100.

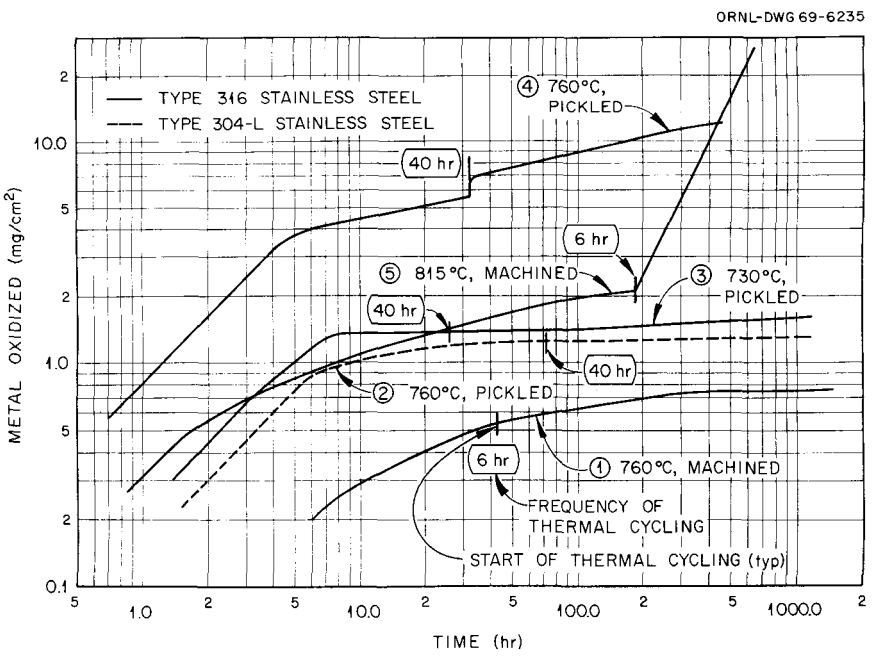

Fig. 17.1. Oxidation of Stainless Steel Against Thermal Insulation in Moist Air.

5. Work hardening by machining gave a temporary improvement in the oxidation resistance of type 316 stainless steel over pickled material, lasting about 100 hr at 815°C and 2000 hr at 760°C.

Work has started on the second phase of this program, which involves the effect of a sodium leak on stainless steel-insulation compatibility.

CORROSION OF REFRACTORY ALLOYS BY LITHIUM

Interest in lithium stems from its attractive properties as a heat-transfer fluid in high-performance nuclear reactor systems. Refractory alloys based on Nb, Ta, W, and Mo have demonstrated low solubilities in lithium, and, by virtue of their superior high-temperature strength, appear ideally suited as container materials. Accordingly, we are investigating the detailed corrosion behavior of refractory metals in lithium from the standpoint of mass transfer resistance and the effects of oxygen on grain-boundary penetration.

Thermal-Convection Loop Tests

J. H. DeVan

The thermal-convection loop affords a convenient means for studying mass transfer properties of liquid metals moving through a temperature gradient. Our current program makes use of the thermal-convection approach for the following purposes: (1) to compare the corrosion resistance of niobium, tantalum, and tungsten alloys in flowing nonisothermal lithium and (2) to measure the magnitude and the time dependence of corrosion reactions governed by solid-state diffusion processes.

The sixth loop in this series, constructed of the tantalum alloy T-222, was examined following operation for 3000 hr at a maximum temperature of 1350°C. Weight change as a function of loop position was analogous to that observed[9] in D-43 and Nb–1% Zr tests at 1200°C, where about two-thirds of the loop surface lost weight and one-third gained weight. Weight losses were relatively small ($\leqslant$0.8 mg/cm^2) and were attributable primarily to the transport of hafnium from the hotter to colder loop regions.[10] The alloy also lost oxygen at all positions and gained nitrogen in the cold regions.[11] A combination of thermal aging and nitrogen pickup significantly reduced room-temperature ductility in specimens exposed at 1270 to 1300°C (ref. 12). This ductility loss was not observed for specimens whose temperature was either higher or lower than 1200°C.

Forced-Circulation Lithium Loop

B. Fleischer

Fabrication of the initial forced-convection lithium loop[9] (FCLLL-1) was completed, and shakedown operations began. Construction required the assembly of 50 T-111 component parts, involving about 75 ft of tubing and machined fittings.[13–15] To join these parts required about 60 inert gas dry box welds and three field welds, which used previously described[16] automatic inert gas equipment. The test section of the loop, shown in Fig. 17.2, contains about 90 T-111 corrosion specimens. This unit is designed so that it can be removed from the test bed loop and replaced with a new test section.

Early results of start-up and shakedown operation have shown that the lithium purification tank performed its task remarkably well. The oxygen and nitrogen contents of the lithium are at the detection limit of the analytical techniques (<5 ppm N and about 17 ppm O).

Before loop fabrication, we corrosion tested[17] a series of T-111 and T-222 weld specimens in lithium at 750 and 1200°C. No attack of weld heat-affected zones was observed in samples containing up to 540 ppm O. However, we found attack to a depth of 0.010 in. in the base metal of these samples unless they had been heat-treated for 2 hr at 1300°C after welding. Lithium

[9] C. E. Sessions, J. H. DeVan, and B. Fleischer, *Metals and Ceramics Div. Ann. Progr. Rept. June 30, 1968,* ORNL-4370, pp. 78–80.

[10] J. H. DeVan, *Fuels and Materials Development Program Quart. Progr. Rept. Sept. 30, 1968,* ORNL-4350, pp. 127–30.

[11] J. H. DeVan, *Fuels and Materials Development Program Quart. Progr. Rept. Dec. 31, 1968,* ORNL-4390, pp. 100–4.

[12] J. H. DeVan, *Fuels and Materials Development Program Quart. Progr. Rept. March 31, 1969,* ORNL-4420, pp. 105–6.

[13] B. Fleischer, *Fuels and Materials Development Program Quart. Progr. Rept. Sept. 30, 1968,* ORNL-4350, pp. 130–35.

[14] D. L. Clark and B. Fleischer, *Fuels and Materials Development Program Progr. Rept. Dec. 31, 1968,* ORNL-4390, pp. 104–9.

[15] D. L. Clark, C. W. Cunningham, and B. Fleischer, *Fuels and Materials Development Program Quart. Progr. Rept. March 31, 1969,* ORNL-4420, pp. 106–13.

[16] E. A. Franco-Ferreira and G. M. Slaughter, *Welding J. (N.Y.)* **45**, 835–42 (1966).

[17] C. E. Sessions, *Fuels and Materials Development Program Quart. Progr. Rept. June 30, 1968,* ORNL-4330, pp. 104–10.

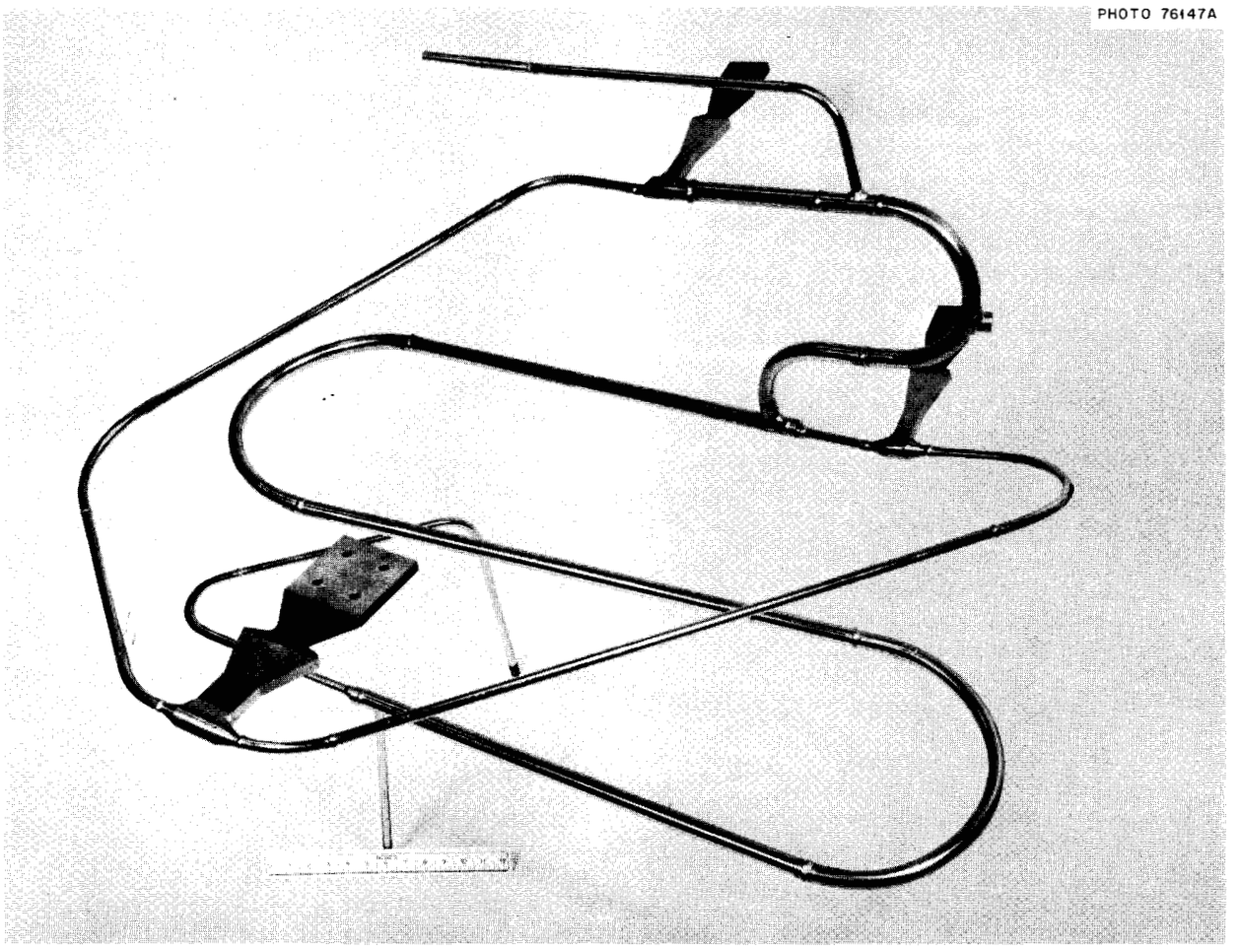

Fig. 17.2. Alloy T-111 Test Section of FCLLL-1 Containing About 90 Specimens.

tests were also conducted on T-111 weld specimens that had been prepared simultaneously with the welding of the T-111 lithium pumped loop described above. Although not heat-treated, these welds showed no evidence of lithium attack.

Procurement of test materials for the replacement section (FCLLL-2) has begun. The test materials ordered include W–25% Re, ASTAR-811C, T-111, and both wrought and CVD tungsten.

COMPATIBILITY OF BOILING POTASSIUM WITH REFRACTORY ALLOYS

This year we concluded the major portion of our investigations[18] of the corrosion of refractory metals by boiling potassium. A few refluxing capsules were conducted to investigate alloys or conditions not covered by our original studies. Also we completed our examination of two engineering-scale forced-circulation loops, which were operated to provide data on the corrosion-erosion resistance of potential nozzle and turbine blade materials.

Capsule and Natural-Circulation Loop Tests

J. R. DiStefano D. H. Jansen

Table 17.1 summarizes the conditions and results of potassium refluxing capsule tests conducted during the past year. An Nb–1% Zr capsule was operated under conditions that minimized the uptake of oxygen from the external environment. Corrosion results, however,

[18] J. R. DiStefano, D. H. Jansen, and B. Fleischer, *Metals and Ceramics Div. Ann. Progr. Rept. June 30, 1968,* ORNL-4370, pp. 76–77.

Table 17.1. Summary of Tests of Compatibility of Boiling Potassium with Refractory Alloys

Material	Temperature (°C)		Test Duration (hr)	Condensing Rate ($g\ min^{-1}\ cm^{-2}$)	Results
	Boiler	Condenser			
			Refluxing Capsules		
W–25% Re[a]		1180	5000	0.30	No evidence of attack
W–25% Re[b]	1250	1210	5000	0.33	Mass transfer of tungsten from boiler to condenser
Nb[c]		1200	5000	0.30	Very heavy attack
Nb–1% Zr	1215	1200	5000	0.29	No evidence of attack
Ta	1250	1205	5000	0.32	Test in progress
			Natural-Circulation Loops		
TZM	1240	1160	4400	0.29	No evidence of attack
FS-85	1250	1200	1300	0.20	20 mg/cm^2 gain in subcooler, stress corrosion in boiler

[a]Powder product.
[b]Arc melted.
[c]Chemically vapor deposited (CVD) inserts in an arc melted capsule.

were similar to those of previous capsules,[19] where small amounts of oxygen entered the system.

An unalloyed niobium capsule, which contained chemically vapor deposited (CVD) niobium inserts, exhibited heavy attack after exposure to potassium, and mass transfer of tungsten from the boiler to condenser region was found[20] in an arc melted W–25% Re capsule. Attack in both these latter capsules appeared to have been oxygen-induced and indicated that locally high oxygen concentrations had been produced at the boiler surfaces as a consequence of the boiling process.

Two natural-circulation boiling potassium loops were also examined after operation under conditions shown in Table 17.1. Neither loop showed any metallographic evidence of attack, and changes in interstitial concentration were relatively minor.[21,22]

[19]J. R. DiStefano, *Refluxing Capsule Experiments with Refractory Metals in Boiling Alkali Metals,* ORNL-4322 (January 1969).

[20]J. R. DiStefano, *Fuels and Materials Development Program Quart. Progr. Rept. Sept. 30, 1968,* ORNL-4350, pp. 103–7.

[21]D. H. Jansen, *Fuels and Materials Development Program Quart. Progr. Rept. June 30, 1968,* ORNL-4330, pp. 84–86.

[22]D. H. Jansen, *Fuels and Materials Development Program Quart. Progr. Rept. Sept. 30, 1969,* ORNL-4350, pp. 107–10.

Forced-Circulation Boiling Potassium Loop

B. Fleischer

A forced-circulation boiling potassium loop fabricated of D-43 was examined after 10,000 hr operation at a 1200°C maximum temperature.[23,24] Inspections of the loop components showed mechanical distortion only in the pump cell. This was apparently caused by excessive temperatures resulting from the economizer effect of the two-pass design used for this pump. The expansion caused continuous loss of pump efficiency, which was reflected by a continuous need to increase pump voltage to maintain design flow during operation.

Examination of internal surfaces of the loop showed no corrosion effects other than in the nozzle-blade test section. The appearance of blade specimens from this section before and after test is illustrated in Fig. 17.3. The slight discolorations noted reflect some slight deposition. The maximum weight change was about 4.6 mg gain on blade 2. This was less than one-third of the

[23]B. Fleischer and C. W. Cunningham, *Fuels and Materials Development Program Quart. Progr. Rept. Sept. 30, 1968,* ORNL-4350, pp. 110–20.

[24]C. W. Cunningham and B. Fleischer, *Fuels and Materials Development Program Quart. Progr. Rept. Dec. 31, 1968,* ORNL-4390, pp. 94–95.

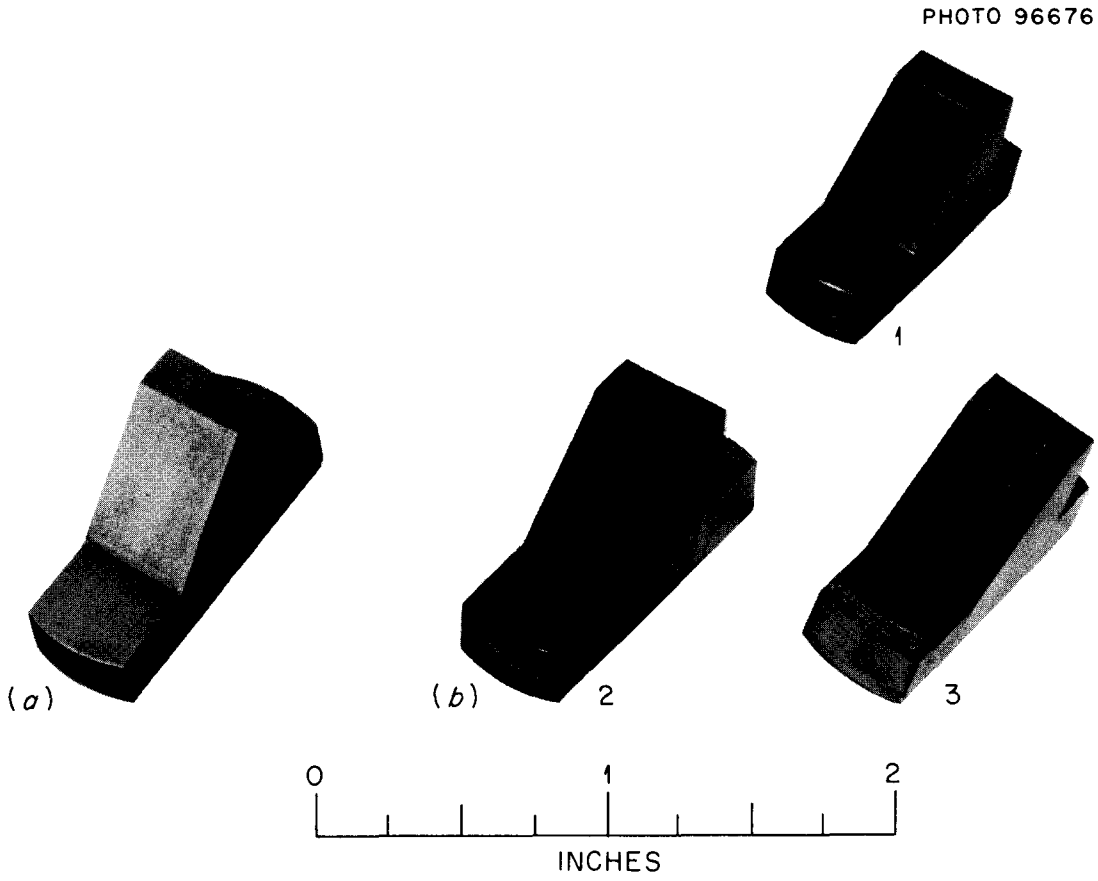

Fig. 17.3. Blade Test Specimens Used in Forced-Circulation Boiling Potassium Loop FCL-8. Loop was fabricated of D-43 and operated 10,000 hr at a 1200°C boiler-condenser temperature. (*a*) Typical specimen before test. (*b*) After 10,000-hr test. Nozzle specimens showed no visible change.

maximum deposition experienced[18] on blades tested in an Nb–1% Zr loop that operated 3000 hr at a maximum temperature of 1090°C.

EFFECT OF OXYGEN ON THE COMPATIBILITY OF REFRACTORY METALS WITH ALKALI METALS

R. L. Klueh

We continued our comparative study[25] of the effect of oxygen on the compatibility of niobium and tantalum with alkali metals (potassium, sodium and lithium) at 600°C. Reaction with oxygen in these systems differs depending upon whether the oxygen is present in the refractory metal or the alkali metal. When the oxygen concentration of the refractory metal exceeds some threshold concentration, the alkali metal penetrates the refractory metal. This effect was studied by making controlled oxygen additions to refractory metal samples and exposing the samples in a static capsule of the same material. When oxygen is in the alkali metal, the effect is to increase the dissolution of the refractory metal. This latter effect was studied by the addition of oxygen to the alkali metal before testing in static capsules.

Alkali Metal Penetration

For penetration to occur, the oxygen concentration of the refractory metal must exceed a critical concentration, which is a function of temperature, the specific alkali metal, and the refractory metal. The effect of temperature has been studied[26] in the systems Nb-O-Li and Ta-O-Li and as well[25] in Ta-O-K. Penetration occurs in two modes, intergranular and transgranular, with each having a different threshold oxygen concentration.

[25] R. L. Klueh, *Metals and Ceramics Div. Ann. Progr. Rept. June 30, 1968*, ORNL-4370, pp. 81–83.

[26] J. R. DiStefano, *Corrosion of Refractory Metals by Lithium*, ORNL-3551 (April 1966).

The penetration of tantalum and niobium by potassium, sodium, and lithium was compared at 600°C. The estimated threshold oxygen concentrations are shown in Table 17.2.

Effect of Oxygen on Dissolution of Refractory Metals in Alkali Metals

The effect of oxygen in the alkali metal was compared for niobium and tantalum in potassium, sodium, and lithium at 600°C. Increasing the oxygen concentration in lithium had no effect on the dissolution of either niobium or tantalum. For potassium and sodium, on the other hand, an increase in the oxygen concentration of the alkali metal led to increased dissolution of the refractory metal. For niobium in potassium[27] and niobium in sodium[28] this effect was attributed to an increase in the solubility of the niobium as a result of interactions between niobium and oxygen dissolved in the alkali metal (i.e., the oxygen decreases the activity coefficient of the niobium in the alkali metal). This interaction was characterized in terms of solution interaction parameters.[28] We now believe that the effect of oxygen in potassium on tantalum can be similarly explained, although the process is more complicated. The concentration of tantalum in sodium again increases with an increase in the oxygen concentration of the sodium. However, as the oxygen concentration of the sodium is increased oxygen migrates from the sodium to the tantalum, which in turn is penetrated by the sodium.

Table 17.2. Estimated Threshold Oxygen Concentrations for Penetration of Refractory Metals by Alkali Metals at 600°C

Corrosion Mode	Oxygen Concentration in Refractory Metal for Penetration by Liquid Metal[a] (ppm O by weight)		
	Potassium	Sodium	Lithium
	Tantalum		
Grain boundary	500	300	150
Transgranular	1400	>1000	500
	Niobium		
Grain boundary	1500	1000	400
Transgranular	>2400	>1600	1300

[a]Values were estimated by metallographic examination and chemical analysis of refractory metals.

[27]R. L. Klueh, *The Effect of Oxygen in Potassium on Niobium-Potassium Compatibility,* ORNL-TM-2476 (February 1969).

[28]R. L. Klueh, "The Effect of Oxygen in Sodium on the Compatibility of Sodium with Niobium," pp. 171–76 in *Proceedings of the International Conference on Sodium Technology and Large Fast Reactor Design November 7–9, 1968,* ANL-7520, Part. I.

18. Nitride Fuels Development

J. L. Scott P. Patriarca

Uranium mononitride is an attractive fuel for nuclear reactors because of its high density, high melting point, good thermal conductivity, and good irradiation stability. These features permit its operation at higher heat ratings and specific power than oxides. The nitride or carbonitride is superior to the monocarbide because of greater ease of control of the chemical activity of the nonmetallic constituent and consequent better quality control and chemical compatibility with claddings. The same properties plus a high breeding gain make mixed (U,Pu)N and (U,Pu)(C,N) attractive as high-performance LMFBR fuels.

Our program involves fuel fabrication, characterization, quality assurance, determination of physical and thermodynamic properties, compatibility studies, and irradiation studies. Close attention is paid to nitrogen, oxygen, and carbon activities because of the sensitivity of the material to variations in these activities. For example, the marked dependence of uranium self-diffusion on nitrogen activity described in Chapter 4 of this report should be noted. Part of the program is directed toward the development of carbonitride fuels. A carbonitride might offer significant advantages over either pure carbide or nitride because of (1) a lower cost fuel cycle involving aqueous processing; (2) a greater plasticity above 600°C, which minimizes effects of fuel swelling; and (3) better control of stoichiometry and fission-product reactivity at high burnups.

Uranium nitride is an interesting material from a fundamental viewpoint, and is being investigated under the Fundamental Ceramics Research Program described in Chapter 6.

SYNTHESIS, FABRICATION, AND CHARACTERIZATION

Synthesis and Fabrication of UN (Ref. 1)

R. A. Potter V. J. Tennery

We continued to synthesize UN powders and fabricated specimens of various sizes and configurations from them. Although we are presently studying the effects of variations in the synthesis process on the powder properties, we continue to follow the same general scheme as previously described[2] for the production of powders used in specimen fabrication. Significant advances were made in machining sintered UN specimens to close dimensional tolerances.

In cooperation with the special materials machine shop, we developed techniques for producing very small pellets for fission-gas release tests. These specimens were 0.040 in. OD × 0.020 in. ID × 0.250 in. long and were machined by electrical discharge from solid sintered UN stock. A cross section of the microstructure of one specimen is shown in Fig. 18.1.

In addition to improving our processes we are continuing to upgrade our facilities and are automating some of the synthesis steps to produce a more uniform and consistent product with less effort. Concurrently we have commissioned a small synthesis apparatus for parametric studies on some facets of the hydride-nitride process and their effects on both the powders and the sintered product. The atmosphere in this equipment is continuously monitored for contamination. With information gained with this small system and from our experience with the large systems, we hope to develop a completely automatic synthesis apparatus that can routinely produce nitride powders with high purity and good fabricability.

Since uranium nitride is extremely susceptible to oxidation, we have installed trace oxygen and moisture analyzers on the large synthesis apparatus and on the glove boxes in which the materials are handled and stored. We have always striven to maintain high-purity atmospheres but have lacked means to detect accidental entry of oxygen. Since the installation of the analyzers,

[1]This work was supported in part by NASA-Lewis Research Center, Cleveland, Ohio.

[2]R. A. Potter, *Metals and Ceramics Div. Ann. Progr. Rept. June 30, 1967,* ORNL-4170, pp. 97–98.

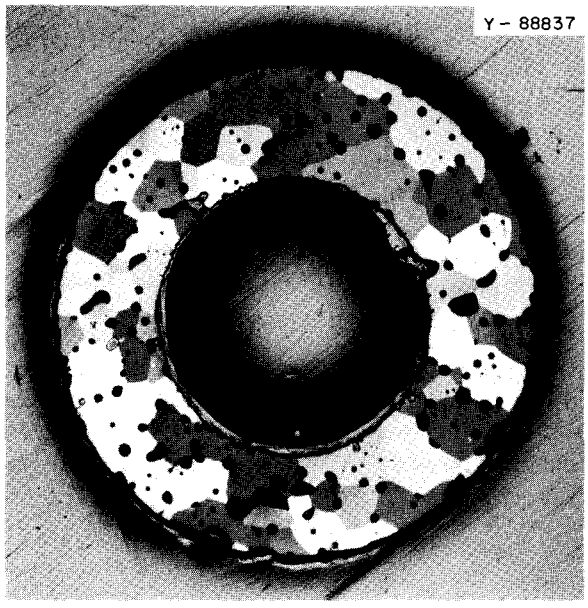

Fig. 18.1. Cross Section of UN Specimen Machined from Solid Sintered Pellet. 75X. Etched with 30 parts concentrated lactic acid, 10 parts concentrated HNO_3, and 1 part concentrated HF. Reduced 22%.

we have found that our systems are normally clean, but on occasions they have experienced impurity increases to several hundred parts per million oxygen. The analyzers have helped us to locate several leaks and optimize some operating procedures. Oxygen and moisture levels of 4 and 1 ppm, respectively, can be maintained in the glove boxes under working conditions, either by argon purging or by a commercial recirculating purifier that we installed on a suite of two boxes.

Synthesis and Fabrication of $U^{15}N$

R. A. Potter T. G. Godfrey

Of concern to the use of nitride fuels for the LMFBR is the generation of helium gas within the fuel through the $^{14}N(n,\alpha)^{11}B$ reaction and the corresponding loss of neutrons. Recently we found that the use of $U^{15}N$ fuel in an LMFBR, with proper recycle of the ^{15}N, may be economically feasible because of the increased neutron economy and reduced fuel inventory.[3] Therefore, high- and low-temperature irradiation experiments to fluences of 2 to 4 X 10^{21} neutrons/cm^2 (>1 Mev) are to be conducted to compare directly the effects of fast neutrons on four candidate fuels: $U^{14}N$, $U^{15}N$, UC, and $UC_{0.5}N_{0.5}$.

We fabricated the $U^{14}N$ and $UC_{0.5}N_{0.5}$ specimens by our usual techniques, cold pressing followed by sintering. The UC specimens are to be arc-cast. The CMF Division of Los Alamos Scientific Laboratory furnished the 99.9%-enriched $^{15}N_2$ necessary for the preparation of the $U^{15}N$ specimens.

The $U^{15}N$ was synthesized, fabricated, and sintered in the usual fashion[2] except that a special gas handling system was constructed to supply the gas to the synthesis apparatus and the sintering furnace and to reclaim the unused gas at the conclusion of the various steps. Because the limited supply of $^{15}N_2$ permitted only one furnace run, a two-tier setter was used and the entire 500-g batch was sintered at once. The sintered pellets were about 95% dense and contained only a small amount of uniformly distributed oxide.

Because of the uniqueness of this material, considerable interest in it has been expressed for other than the intended irradiation experiment. Magnetic susceptibility measurements are to be made, as reported in Chapter 6. In addition, a sample has been supplied to Argonne National Laboratory for NMR studies.

Synthesis and Fabrication of (U,Pu)N

E. S. Bomar Ji Young Chang
J. D. L. Harrison[4]

Additional equipment was installed and placed in operation in the Interim Plutonium Facility during this report period. Also several operational problems were encountered and solved to varying degrees.

We proceeded with the synthesis of both uranium and plutonium nitrides by the hydride-nitride method and have a reserve of 500 g UN and 100 g PuN for fabrication work. Hydriding with an ever-safe Ar–4% H_2 mixture proved impractically slow, so we used pure hydrogen, which on leaving the furnace was diluted with argon to below the combustible limit. Our tube furnaces and gas-distribution system have worked well for synthesis of nitride powder, but the furnace heated too slowly and not to high enough temperatures. After 1 hr at a limiting temperature of 1600°C we obtained sintered densities of 73, 64, and 75% of theoretical for UN, $U_{0.80}Pu_{0.20}N$, and PuN, respectively. The vendor acknowledged an error in estimating the rate of heat loss from the furnaces and made a partial correction

[3] J. L. Scott and W. O. Harms, *Metals and Ceramics Div. Ann. Progr. Rept. June 30, 1966*, ORNL-3970, p. 91.

[4] On assignment from AERE, Harwell, England.

with booster transformers for the power supply. As a consequence we will have to rely principally on a tungsten-resistor furnace for sintering experiments.

The tungsten-resistor furnace was delivered, installed, tested, and found to meet design requirements. The glove box to contain the furnace was also received, but all the glass panels were broken in shipment; completion of the installation awaits replacement of the glass. Meanwhile, the furnace is being used for heat treatment of plutonium-free samples, such as UN and ThN.

With the hot-stage microscope we observed the behavior of individual microspheres of PuO_2 on heating to 1200°C. Photographs taken during the heat treatment showed that the particles were dimensionally stable.

We assembled a console containing instruments for analysis of the atmosphere in several glove boxes for oxygen and water content. It is described elsewhere.[5]

Particle Size Distribution Measurements of UN Powders[1]

V. J. Tennery

A technique was established as being suitable for measuring the particle size distribution of our uranium nitride powders. Gas sedimentation methods were studied as well as the electronic Coulter method. The results were verified by optical and electron microscopy. Using a Micromerograph[6] with nitrogen gas in the settling column gave results essentially identical to those of manual counting, as shown in Fig. 18.2. Agglomeration of the particles was invariably observed with the Coulter Counter,[7] even though 20 dispersion methods were attempted. The distribution curve by the Coulter method was always symmetrically displaced by a factor of 2.5 to 3.5 from the true curve, as shown by the typical result in Fig. 18.2.

Nitride Powder Morphology

V. J. Tennery

A scanning electron microscope was used to determine the actual shape and surface character of the particles of UN produced by the hydride-dehydride-nitride process. These results confirmed the particle size distribution measurements discussed above. A typical group of uranium nitride powder particles is shown in Fig. 18.3. Note the sharp angularity of the particles and the convoluted surfaces. The observed morphology is no doubt the source of many difficulties associated with dry-pressing various shapes from this material.

Quantitative Chemical Analysis of Uranium Nitride[1]

V. J. Tennery

Persistent difficulty in obtaining routine chemical analysis of uranium nitride powders and sintered pieces led to considerable effort to overcome these problems. One approach involved a comparative analysis experiment. Two sets of 16 samples of sintered UN were analyzed at four different sites for U, N, O, and C and

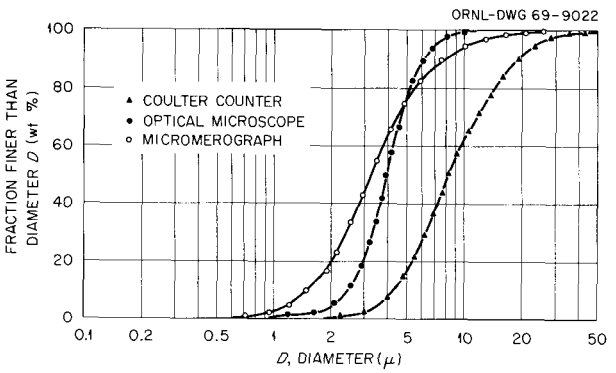

Fig. 18.2. Particle Size Distribution of UN Powder as Determined by Three Methods.

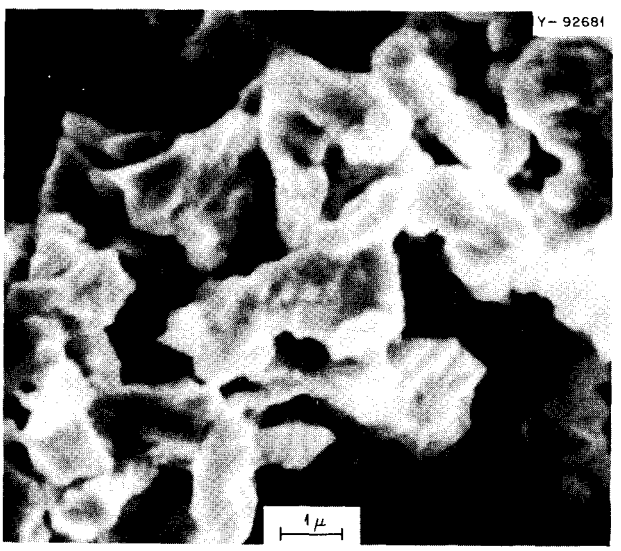

Fig. 18.3. Scanning Electron Micrograph of UN Particles Produced by the Hydride-Dehydride-Nitride Process.

[5] J. D. L. Harrison, *Fuels and Materials Development Program Quart. Progr. Rept. June 30, 1968,* ORNL-4330, pp. 40–41.

[6] Product of Sharples Corp., Philadelphia, Pa.

[7] Product of Coulter Electronics Industrial Division, Hialeah, Fla.

the results compared. The specimens within a set had identical histories. The results from any given laboratory indicated acceptable mass balances for any given sample, but comparisons from different sites indicated significant differences. For reliable analyses of this material a technique for uranium determination must be developed to provide an accuracy of ±0.02% by weight on 1-g or smaller specimens. Nitrogen analyses by the micro-Kjeldahl method are acceptable only when the digestion is performed in sealed containers and the oxidizing agent and the digestion temperatures are selected with extreme care. Oxygen can be determined in the 500 to 2500 ppm range in these materials only when the inert sampling atmosphere is kept very low in oxygen and is continuously monitored. Nitride powder absorbed oxygen from a glove box atmosphere containing 6 ppm O and 1 ppm H_2O. Inert gas fusion techniques using special holders that are loaded in the inert-atmosphere box appear most suitable for this measurement. Quality integrators for the gas chromatographic column are required for reasonable accuracy. The results indicated some problem with the determination of carbon in the 100 to 800 ppm range. Results from a given laboratory were usually consistent, but considerable variation was observed between certain sites.

The analyses of nitride powder containing both the U_2N_3 and UN phases are more difficult because of the difference in the dissolution rates of the two nitrides. We developed a technique that provided reasonable mass balances from powders containing both nitride phases.

CONVERSION OF UO_2 AND $(U,Pu)O_2$ TO CARBONITRIDE FUELS

Because low fuel-cycle cost is an important criterion for an LMFBR fuel, we are investigating the synthesis, fabrication, and performance of carbonitride fuels. Carbonitrides are easier to prepare and, therefore, less expensive than pure nitrides. They are prepared by reaction of oxide fuel powders with an excess of carbon in a nitrogen environment. We are attempting to discover the basic mechanisms of this conversion so that we can optimize its efficiency on a practical scale. Methods for producing both U(C,N) and (U,Pu)(C,N) from sol-gel feed, directly derivable from aqueous processing, are emphasized in this development program.

Direct Conversion of Sol-Gel $(U,Pu)O_2$ to Carbonitride

J. M. Leitnaker K. J. Notz[8]

Several major steps have been taken preparatory to producing (U,Pu)(C,N) from a carbon-bearing sol-gel mixed oxide. Procedures were developed for small-scale preparations of mixed urania-plutonia-carbon sols having atom ratios of U/Pu, 4, and C/(U + Pu), 2.6 to 3.0. The sols are made by mixing 1.3 *M* PuO_2 sol with 1.0 *M* UO_2 sol and then blending carbon black into the mixed sol ultrasonically. The material is processed under conditions that minimize the oxidation of the UO_2 in the sols. Some of the sols have been used to make sol-gel microspheres and shard fragments. The sol-gel material will be converted to carbonitride in a fluidized bed furnace; this furnace has undergone testing and will soon be in service. Several analytical procedures and facilities have also been developed and placed in service for extensive characterization of plutonium-bearing materials.

Kinetic Studies of Fuel-Producing Reactions

T. B. Lindemer J. M. Leitnaker

The kinetics of chemical reactions that produce the uranium carbide or carbonitride fuels have been studied from 1400 to 1700°C. These reactions were studied to determine the mechanisms that control the conversion and included the reaction of N_2 with UC_2, N_2 with UC, and UO_2 with C.

Diffusion of carbon controls the rate of the reaction of UC_2 spheres with nitrogen. In this reaction, studied by quantitative metallography,[9] the carbon diffuses through the U(C,N) product to the nearest free surface. In fully dense spheres, the nearest free surface was the surface of the sphere. But the introduction of a uniform distribution of free carbon or open porosity within the spheres during their manufacture provided additional surfaces for the heterogeneous nucleation of free carbon. Increasing the number of these nucleation sites increased the reaction rate by decreasing the distance the carbon must diffuse to reach a free surface.

---

[8]Chemical Technology Division.

[9]T. B. Lindemer and M. D. Allen, "Technical Note: A Metallographic Method for Studying Reaction Kinetics in Spheres," accepted for publication in *ASM Transactions Quarterly*.

Mathematical analysis of the conversion data showed that the reaction was controlled at or very near the interface between the UC_2 core and the enveloping U(C,N). This indicated that the internal nucleation sites permitted the conversion of UC_2 to U(C,N) at a constant rate during the entire reaction, because the uniform distribution of these sites permitted a constant flux of carbon from the interface.

The reaction of UC with nitrogen takes place in at least three stages. The very rapid first stage produced $UC_{0.8}N_{0.2}$ and UC_2; rejection of carbon by the UC resulted in the formation of UC_2 on a preexisting network of the dicarbide and was favored over the formation of free carbon. The much slower second stage involved the reaction of the UC_2 with nitrogen to form free carbon and additional $U(C_{0.8}N_{0.2})$. The third stage began when the UC_2 had completely reacted; then, more free carbon was produced while the composition of the carbonitride moved toward the more nitrogen-rich equilibrium value. This last stage appeared to be diffusion controlled.

Both the above reactions are controlled by mechanisms that involve solid-state diffusion of material. This type of mechanism also controlled in the reaction of UO_2 and C reported previously.[10,11] These reactions are extremely slow in massive material, even at 1400 to 1700°C. It follows, of course, that conversion should be accelerated significantly when finely divided solids are reacted, as can be done with a sol-gel mixture of UO_2 and C in which the reactants have a size of a few hundred angstroms. Previously reported work[12,13] demonstrated that such a mixture can be reacted rapidly with nitrogen in a fluidized bed to produce U(C,N) if the temperature is below that for appreciable sintering of the solids. Under these conditions the conversion rate appears to be controlled by the removal of carbon monoxide from the system by the fluidizing gas.

[10]T. B. Lindemer, *Metals and Ceramics Div. Ann. Progr. Rept. June 30, 1968*, pp. 87–88.

[11]T. B. Lindemer, J. M. Leitnaker, and M. D. Allen, "Kinetics of the Graphite-Uranium Dioxide Reaction from 1400 to 1756°C," *J. Am. Ceram. Soc.* **52**(5), 233–7 (1969).

[12]R. L. Beatty, J. M. Leitnaker, and K. J. Notz, "Method for Preparation of Carbonitride Nuclear Fuel Materials," patent applied for.

[13]J. M. Leitnaker, R. L. Beatty, K. J. Notz, and K. E. Spear, *Metals and Ceramics Div. Ann. Progr. Rept. June 30, 1968*, pp. 86–87.

COMPATIBILITY OF CLADDING WITH NITRIDE FUELS

The compatibility of nitride fuels with candidate cladding alloys must be thoroughly investigated and understood if these fuel materials are to be considered seriously for use in LMFBR systems. The problem is complicated because of the several multicomponent cladding alloys under consideration and the important effects of burnup on the composition, constitution, and nitrogen activity of the fuel. Our approach is to investigate systematically the thermodynamics and kinetics of those interactions that are pertinent to the compatibility problem. Such interactions involve components of the fuel and the cladding as well as certain fission and transmutation products. A selected number of compatibility-couple experiments are included in this program.

Effects of Oxygen Contamination in (U,Pu)N (Ref. 14)

J. M. Leitnaker R. L. Beatty
K. E. Spear

Oxygen, because of its great chemical affinity for uranium, is a frequent contaminant of uranium nitride and uranium-plutonium nitride fuels and is generally thought to be undesirable. Our recent experiments indicate that the oxygen contamination can be beneficial by providing a sink for excess nitrogen released by fissioning of plutonium.

Two types of experiments have been performed. One demonstrated that the U_2N_3 phase can be formed in the presence of 1 atm N_2 and UO_2 at temperatures much above that believed to be the decomposition temperature. The second demonstrated a large solubility of oxygen in U_2N_3.

The importance of these observations is that a mechanism is available for disposing of excess nitrogen in nitride fuels other than by reaction with the cladding material. In the presence of UO_2 and as the nitrogen pressure increases, a pressure is reached at which oxygen-stabilized U_2N_3 will be formed. At any given temperature, the nitrogen pressure in the UO_2-UN-U_2N_3 three-phase region will be fixed and be $^1/_{20}$ as

[14]Report abstracted from J. M. Leitnaker, R. L. Beatty, and K. E. Spear, "Possible Stabilization of Nitride Fuels by Oxygen," paper presented at the American Nuclear Society National Meeting, Seattle, Wash., June 1969 and J. M. Leitnaker and K. E. Spear, "Oxygen Contamination – An Advantage in UN," submitted to *Nuclear Applications*.

great as in the oxygen-free $UN\text{-}U_2N_3$ two-phase system. This buffering of the nitrogen pressure can prevent reaction with the cladding.

Temperature Gradient Effects on Ceramic Fuels

K. E. Spear J. M. Leitnaker

Effects of temperature gradients on the compatibility of nitride and carbide fuels were considered. We calculated that the assumption of a constant nitrogen pressure leads to the result that a nitride fuel has more potential for nitriding the cladding material in a temperature gradient than it does under isothermal conditions. For carbide fuels, the three assumptions of (1) carbon transport by a $CO\text{-}CO_2$ mechanism, (2) constant CO to CO_2 ratio, and (3) constant total pressure ($P_{CO} + P_{CO_2}$) lead to the result that the carbon activity is greater at the fuel-cladding interface of an operating fuel pin than it is under isothermal conditions.

Chemical Effects of Nuclear Burnup on Ceramic Fuels

K. E. Spear J. M. Leitnaker

The ability to predict and understand the equilibrium chemical interactions of a reactor fuel requires, among other things, a knowledge of the effects of nuclear burnup on the fuel. We calculated these effects for (U,Pu)N and (U,Pu)C fuels and found that the activities of nitrogen and carbon in these fuels increase with burnup. Rand and Markin[15] have similarly shown that the oxygen-to-metal ratios of $(U,Pu)O_{2-x}$ fuels increase with burnup. This effect of burnup on the activities of nonmetals in ceramic fast-reactor fuels can result in compatibility problems not anticipated or encountered with the unirradiated fuel.

Compatibility of Vanadium Alloys with UN

J. D. L. Harrison[16] K. E. Spear

The compatibility of the vanadium alloy V–15% Cr–5% Ti with single-phase UN and with UN containing second-phase UO_2 was investigated by isothermal sandwich experiments at 1000°C for 100 to 500 hr. Both UN compositions reacted at the UN-vanadium alloy interface by 100 hr; the second-phase oxide seemingly had no effect on the reaction. The titanium in the alloy appeared to have reacted with the UN leaving near the interface a metallic layer that was rich in vanadium and chromium and poor in uranium. Uranium diffused about 150 μ into the vanadium alloy in 500 hr and was in the form of a platelet phase containing uranium and titanium. The nitrogen released from the reaction appears to be "fixed" as $(Ti_xU_y)N$ particles with the ratio x/y probably large.

THERMODYNAMIC STUDIES

The thermodynamic properties of high-performance fuels are studied on a continuing basis to help define and solve problems that might arise in advanced concepts of space and civilian power-breeder reactor systems. Thermodynamic analyses of questions concerning stability at high temperatures and compatibility with candidate cladding alloys, including the effects of fission products, not only guide the experimental program but also help interpret experimental results.

The U-V-C Phase Diagram and the Thermodynamic Properties of UVC_2

K. E. Spear J. M. Leitnaker
T. B. Lindemer

The tie-lines in the phase diagram for the ternary U-V-C system were determined by x-ray and metallographic techniques. The existence of a ternary phase UVC_2 was confirmed and its crystal structure was established. This phase was stable at 1200 to 1600°C, but it was never observed in samples quenched from the melt. Reactions in the ternary system were used to determine the thermodynamic properties of UVC_2. In contrast to $UMoC_2$ and UWC_2, UVC_2 is thermodynamically unstable in the presence of carbon; it reacts to form UC_2 and VC.

Thermodynamic Investigations of V(C,N) Solutions and the Formation of Active Carbon[17]

K. E. Spear J. M. Leitnaker

Interest in the V-C-N system is related to possible interactions between fuel and cladding and additions to

[15] M. H. Rand and T. L. Markin, *Some Thermodynamic Aspects of $(U,Pu)O_2$ Solid Solutions and Their Use as Nuclear Fuels,* AERE-R-5560 (August 1967); also pp. 637–50 in *Thermodynamics of Nuclear Materials,* International Atomic Energy Agency, Vienna, 1968.

[16] On assignment from AERE, Harwell, England.

[17] Abstracted from papers: K. E. Spear and J. M. Leitnaker, "Formation of Active Carbon in Twin-Crucible Studies of Vanadium Carbonitride Solutions," *J. Am. Ceram. Soc.* **52**(5), 257–62 (1969) and K. E. Spear and J. M. Leitnaker, "Equilibrium Investigations of Carbon-Rich V(C,N) Solutions," submitted to *High Temperature Science.*

fuels to improve compatibility. Relationships among temperature, pressure, lattice constant, and composition were determined for V(C,N) solutions in equilibrium with carbon and nitrogen gas. The lattice constant variation with composition deviates negatively from Vegard's law. Superstructure lines caused by the ordering of carbon vacancies in the carbon-rich monocarbide were observed in x-ray diffraction patterns of carbonitrides with nitrogen contents less than 10% of the nonmetal atoms. In this same composition region, the (N + C)/V atom ratio is constant at 0.89 ± 0.02; it increases to a value of unity at the VN boundary. The V(C,N) lattice parameter depended on whether the starting material was vanadium carbide or a mixture of vanadium nitride and graphite. This dependence was attributed to the formation of a thermodynamically active form of carbon as a product of the reaction of VC with nitrogen to form carbonitride solutions.

IRRADIATION PERFORMANCE OF NITRIDE FUELS

LMFBR Applications

T. N. Washburn

Mixed nitrides, carbides, and carbonitrides of uranium and plutonium are strong candidates for LMFBR fuel because they afford the potential of fuel pins operating at linear heat ratings to 50 kw/ft and achieving doubling times of less than 10 years. We have initiated irradiation tests to provide the minimum data necessary to establish the relative performance of these advanced LMFBR fuel candidates. One series of tests will be in thermal flux facilities to determine the basic characteristics of fuel swelling and fission-gas release. A second series of tests in the fast flux EBR-II will evaluate their performance under simulated LMFBR conditions. In each series of tests we will determine relative performance of carbides, nitrides formed from metal, nitrides formed by carbothermic reduction of oxides, and carbonitrides. The latter two fuels offer significant promise for an economic fuel cycle. Their performance should be equivalent to that of the more expensive nitride derived from metal, but no data exist yet to support this premise. Our tests are aimed at supplying such data to justify development for LMFBR commercial power station application.

Fabrication of capsule components and fuel specimens was begun for experiments designed for comparative testing of carbides, nitrides, and carbonitrides in thermal flux facilities. In the initial series of tests, a liquid metal bond between fuel and the stainless steel cladding enables high linear heat ratings (25 and 35 kw/ft) without excessive fuel temperatures, but with significant temperature gradients. These tests are an extension of the program for determining the basic irradiation behavior of UN.

Irradiation Behavior of UN

S. C. Weaver

An irradiation test in the Oak Ridge Research Reactor provided very encouraging basic information on the

ORNL-DWG 67-983R

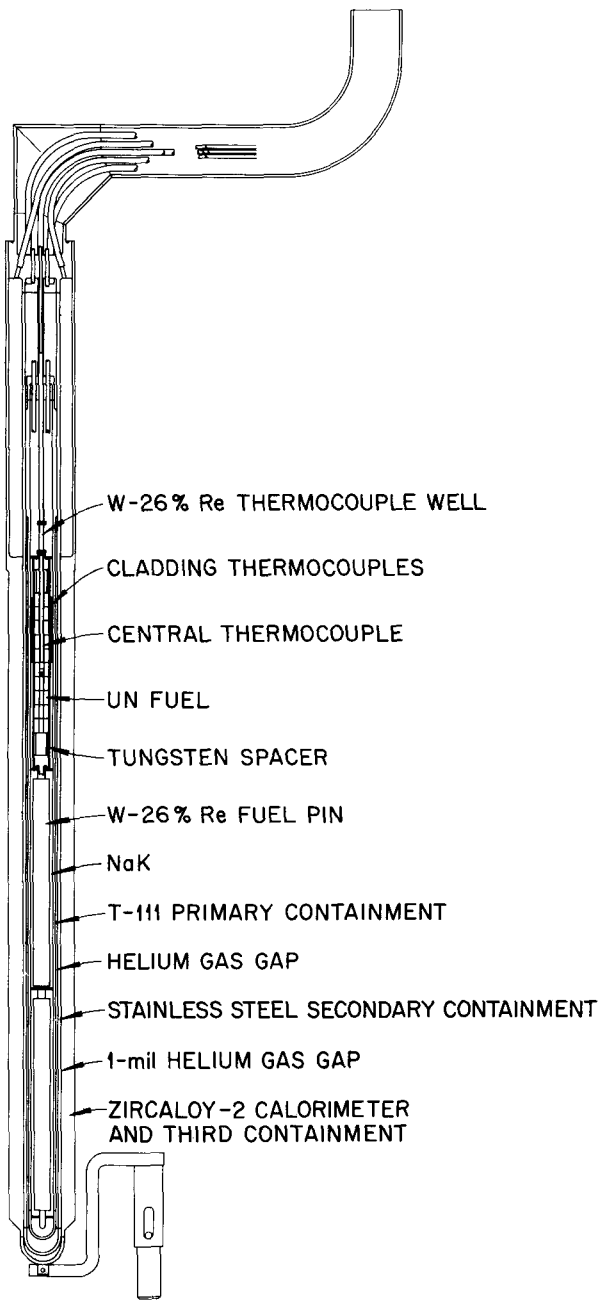

Fig. 18.4. Capsule for Irradiation of UN in the ORR.

irradiation behavior of UN. The capsule, shown in Fig. 18.4, contained three fuel pins with tungsten-rhenium cladding and was irradiated at elevated temperatures and at linear heat ratings up to 8.5 kw/ft. Our design permits us to test UN at temperatures near the peak for fuel in the LMFBR, but without steep temperature gradients. Since cladding temperatures are near the melting point for stainless steel, refractory metals are used instead. The irradiation capsules were of a new, well-instrumented design, which permitted continuous monitoring of the fuel central temperatures, cladding temperatures, and linear heat generation rates. Significantly, burnup values calculated from the capsule calorimeter agreed within 2% with burnups calculated from postirradiation isotopic analyses. One helium-bonded fuel pin contained cold-pressed-and-sintered annular pellets, and the other contained similar solid pellets. The third fuel pin contained both cold-pressed-and-sintered pellets and single crystals and was lithium bonded to provide good heat transfer without restraining swelling. These tests were designed to study the effect of cladding restraint and fuel structure on swelling.

The results, summarized in Table 18.1, showed that pin diameter increases and fission-gas releases were small. Fuel volume increases were about 3% per at. % U burnup except where a central void was present; in that case swelling was somewhat greater. A few fission-gas bubbles (Fig. 18.5) were observed at grain boundaries

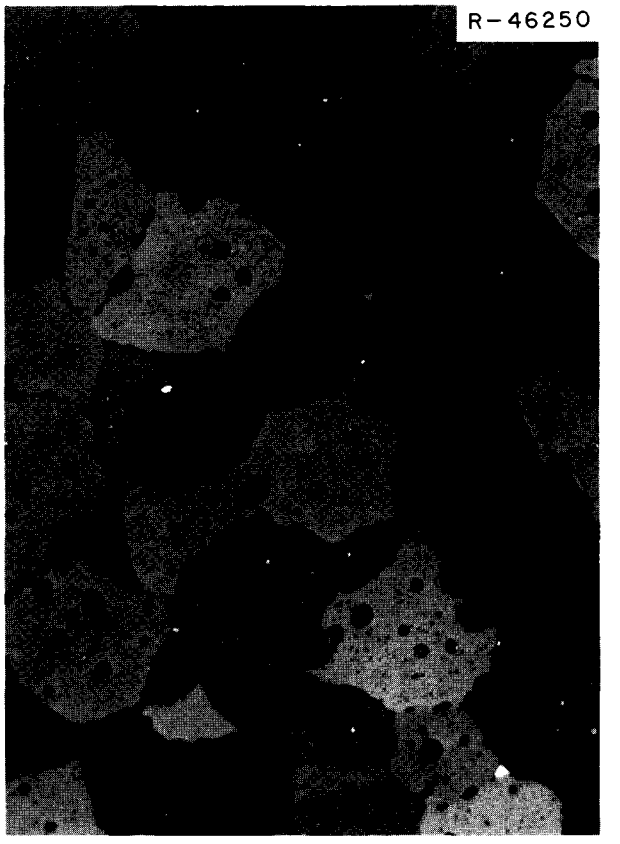

Fig. 18.5. Photomicrograph of UN Irradiated 8155 hr at 1400°C to 1.83 at. % U Burnup. 500X.

Table 18.1. Summary of UN 8155-hr Irradiation Test Results

Fuel Pin	Heat Transfer Bond	Average Cladding Temp. (°C)	Average Central Temp. (°C)	Linear Heat Generation Rate (kw/ft)	Burnup (at. % U)	Fission Gas Release (%)	Fuel Volume Increase (%)	Change in Pin Diameter (%)
Top	Helium	1040	1200	6.37	1.78	0.14	5.45[a] 7.60	<0.08
Middle	Lithium	1100	1250	7.20	2.26[b] 2.45[c]	*d*	*e*	0.38
Bottom	Helium	1200	1400	8.33	1.83	*f*	5.4	0.46

[a]Restrained by central thermocouple well.

[b]Pressed and sintered pellets.

[c]Single crystal pellets.

[d]Gas sample lost during sampling.

[e]Because of the vaporization-condensation effect in these lithium-bonded pellets, volume changes could not be measured accurately.

[f]Fuel pin failed – no gas sample.

and within the grains. Annular pellets, restrained by the strong cladding, swelled into the central void, relieving some of the stress on the cladding. Because the pin containing annular fuel had a central thermocouple well extending halfway down the axis, fuel around the thermocouple well could not swell inward. This provided a direct comparison between swelling of singly and doubly restrained fuel. Measurements of the inside diameters of the annular pellets after irradiation showed that the pellets had indeed swelled into the central void.

One fuel pin failed after 1.83% burnup at 1400°C center-line temperature. The cladding diameter increase was only 0.25% average and 0.46% in the region of failure. The failure is attributed to a loss of ductility of the W–26% Re cladding due to the transmutation of rhenium to osmium, causing the formation of grain boundary sigma phase. This is not to be construed as a detriment to the use of tungsten-rhenium cladding in fast reactors, where the cross section for the transmutation will be considerably less than in these thermal-flux tests.

Of special interest was the comparison of the lithium-bonded single crystal pellets (2.45 at. % U burnup) with the pressed-and-sintered fuel (2.26 at. % U burnup). Voids in the lithium apparently caused both types of fuel to operate very hot, to the extent that UN fuel vaporized from the surface of the pellets and condensed on the relatively cold (1100°C) cladding wall. The pressed-and-sintered pellets showed considerable swelling due to the accumulation of fission gases at grain boundaries, but the single-crystal pellets in the same lithium-bonded pin were still nearly theoretically dense. The lack of swelling in the single crystals is attributed to the absence of grain boundary sites for trapping the fission-gas bubbles, significantly reducing bubble coalescence.

Thermal Contact Resistance

R. K. Williams D. L. McElroy

Thermal contact resistance associated with the fuel-cladding interface can limit the maximum permissible power generation ratings of carbide and nitride fuel elements. The objective of this study is to evaluate the relative importance of a series of variables that are known to affect this important surface property. Thermal contact resistance of several UN-metal interfaces have been studied, including type 302 stainless steel,[18] a V–15% Cr–5% Ti alloy, Mo, Cu, and Al. Data are also being obtained on UN-UN contacts. For all of the interfaces, the thermal contact resistance is quite stress dependent, roughly proportional to the reciprocal of compressive stress. The data also show that at 500°C the type 302 stainless steel, V–15% Cr–5% Ti, and Mo interfaces with UN have nearly identical thermal contact resistances, whereas Cu and Al foils reduce this resistance by a factor of 2 to 3.

---

[18] R. K. Williams, T. E. Banks, and D. L. McElroy, *Metals and Ceramics Div. Ann. Progr. Rept. June 30, 1968,* ORNL-4370, pp. 90–91.

19. Materials Development for Isotopic Power Programs

R. G. Donnelly

Research and development on materials for encapsulation of isotopic power fuels is being carried out for space and terrestrial (including undersea) applications. The space oriented programs are: Curium-244 Isotopic Power Fuels and Materials Development and Cladding Materials for Space Isotopic Heat Sources. The terrestrial power programs include: Strontium-90 Isotopic Power Technology, SNAP-21 System Support – Radioisotope Fuel, SNAP-23 System Support – Radioisotope Fuel, and the Isotope Kilowatt Program.

On the Curium Program, the immediate concern is for thermionic generator applications in the range of 1600 to 2000°C, but we are also interested in high-temperature SiGe thermoelectric and Brayton Cycle conversion applications in the range 900 to 1400°C. Because of the high temperatures involved, we are primarily engaged in testing refractory metals and alloys that might operate in contact with an oxide fuel ($^{244}Cm_2O_3$) and in a space environment.

The Cladding Materials Program is concerned with the evaluation of Haynes alloy No. 25, which has been the capsule material of primary use on low-temperature (<900°C) space thermoelectric generators. In addition, we have undertaken to develop improved encapsulation materials, which meet not only operating requirements but the much more stringent safety criteria that require the fuel capsule to survive the extreme conditions of launch-pad abort, earth reentry, and postreentry.

The purpose of the Strontium Program is to select optimum encapsulating materials and develop capsule sealing techniques for ^{90}Sr-fueled isotopic heat sources designed to power thermoelectric generators. These generators require fuel capsule operation at temperatures to about 1000°C for extended periods of time. Iron-, nickel-, and cobalt-base alloys are the primary candidate encapsulation materials.

The SNAP-21 generators are designed for undersea applications, and the SNAP-23 generators are for on land. Qualified and reproducible welding and inspection procedures are necessary to better ensure the integrity of the fuel containers for both normal and possible accident conditions.

On the Isotope-Kilowatt Program design study, an evaluation of thermal electric converter concepts for large-scale 2 kw(electrical) uses was undertaken. We also provided consultation on materials and fabrication.

CURIUM PROGRAM

Sublimation of W–25% Re in Low-Pressure Oxygen[1]

R. L. Wagner

The alloy W–25% Re is a candidate container material for nuclear oxide fuels. Data on its stability in low-pressure oxygen ($<10^{-4}$ torr) to temperatures approaching 2000°C are desirable to qualify the alloy for thermionic conversion applications.

The sublimation characteristics of 0.040-in. resistively heated W–25% Re wires were determined between 1650 and 1950°C in the pressure range of 10^{-7} to 10^{-4} torr of oxygen. Tungsten is preferentially lost as volatile oxides under all conditions, and at higher pressures a surface layer of the tungsten-rhenium sigma phase is formed.

At a given temperature the sublimation rate increases with pressure; however, at a given pressure the rate exhibits a maximum as a function of temperature. Weight loss data show that container wall removal rates of 2×10^{-5} in./hr are possible at 1850°C and 3×10^{-5} torr of oxygen. This rate is 2½ orders of magnitude greater than in vacuum. The pickup of oxygen is negligible and the exposed wires are bright and free of surface oxide, indicating that oxide vaporized as soon as it was formed.

[1] Abstract of paper to be presented at the AIME Meeting in Philadelphia, October 13–16, 1969.

Effect of Low-Pressure Gases on the Creep Properties of Refractory Metals[2]

H. Inouye

The creep behavior of tungsten and W–50 wt % Mo alloy during their interaction with 10^{-5} and 10^{-6} torr oxygen was determined between 1500 and 2000°C to simulate interaction of cladding with oxide fuel in a thermionic device. The results were compared with their creep behavior at a base pressure of 10^{-8} torr. The creep rates of these metals were up to 4.4 times as high in oxygen as at the base pressure. The reversibility of the creep rates during cycling between the base pressure and in oxygen suggests that the creep degradation results from either dissolved oxygen or an enhanced growth rate of cavities. Stress-induced sublimation and the preferential loss of tungsten were observed.

Mechanical Properties of Capsule Materials

R. W. Swindeman R. L. Stephenson

Creep experiments are usually performed at constant load and temperature. In actual service, materials are usually subjected to varying stresses and temperatures. A capsule containing an alpha-emitting isotope is subjected to an increasing stress as a result of helium release and a decreasing temperature as a result of the decay of the isotope. We need to predict the integrity of such capsules for several half-lives of the isotope to avoid significant activity release. We therefore sought to devise a method of determining from conventional creep data the life of a capsule under predictably varying conditions of stress and temperature.

We developed an analytical model that uses conventional creep data taken at constant load and temperature, to predict failure times under conditions where stress and temperature vary according to simple, monotonic functions of time. The validity of this method has been examined experimentally for T-111 at an initial temperature of 1315°C. The results are shown in Fig. 19.1. The dashed line represents the predicted failure times for a linearly increasing stress and an exponentially decaying temperature.[3] The circles represent experimental determination under these conditions. The solid line was predicted from the same temperature function but a stress that increased at a decreasing rate. (This condition would prevail where complete release of helium from the fuel was observed.) The triangles represent the experimental duplication of these conditions. In both cases, the agreement is gratifying.

Compatibility

J. R. DiStefano

For thermionic applications of $^{244}Cm_2O_3$ heat sources at temperatures of 1650°C and higher the choice of container materials is limited to high-strength refractory metals and alloys. The materials chosen for

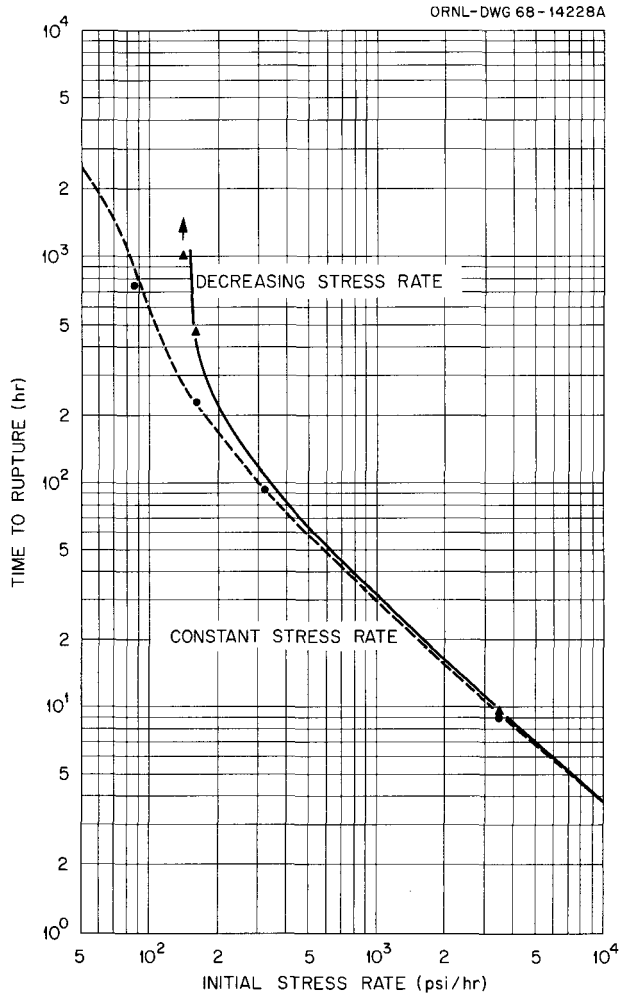

Fig. 19.1. Rupture Life of T-111 as a Function of Initial Stress Rate for a Constant Stress Rate and for a Decreasing Stress Rate. In both cases the temperature is decreased exponentially from 1315°C.

[2]Abstract of paper to be published in the transactions of Vacuum Metallurgy Conference 1969.

[3]R. W. Swindeman and R. L. Stephenson, *Metals and Ceramics Div. Ann. Progr. Rept. June 30, 1968,* ORNL-4370, pp. 92–93.

investigation were Ta, Ta–10% W, T-111, Mo, TZM, W, and W–26% Re, and the test system is shown schematically in Fig. 19.2. Tests have been conducted for 1000 hr at 1650 and 1850°C and evaluated. Now in progress are tests for 10,000 hr at 1650°C and 5000 and 10,000 hr at 1850°C.

For applications of $^{244}Cm_2O_3$ at lower temperatures such as in thermoelectric or Brayton-cycle devices we have also begun to determine the compatibility of potential container materials. Because of the complexity in interpreting tests involving radioactive components, a range of materials including several pure metals that are major components in alloys of interest have also been included as well as some binary systems.

Tests now under way include capsules of Ni, Ni–10% Cr, Ni–20% Cr, Co–10% Cr, Hastelloy C, Hastelloy N, and Haynes alloy No. 25, and these are scheduled to operate for 1000 hr at 750°C. A second series of materials to be tested for 1000 hr at 1200°C includes Nb, Nb–1% Zr, Ta, Ta–10% W, Mo, V, and Zr.

Welding Development for Compatibility Program

G. M. Goodwin R. W. Gunkel

We have successfully developed conditions for seal welding the 750°C, 1000-hr (Hastelloy C, Hastelloy N, Haynes alloy No. 25, Ni, Ni–10% Cr, and Co–10% Cr) and 1200°C, 1000-hr (Zr, V, Nb, Mo, Ta, Ta–10% W, and Nb–1% Zr) compatibility test capsules.

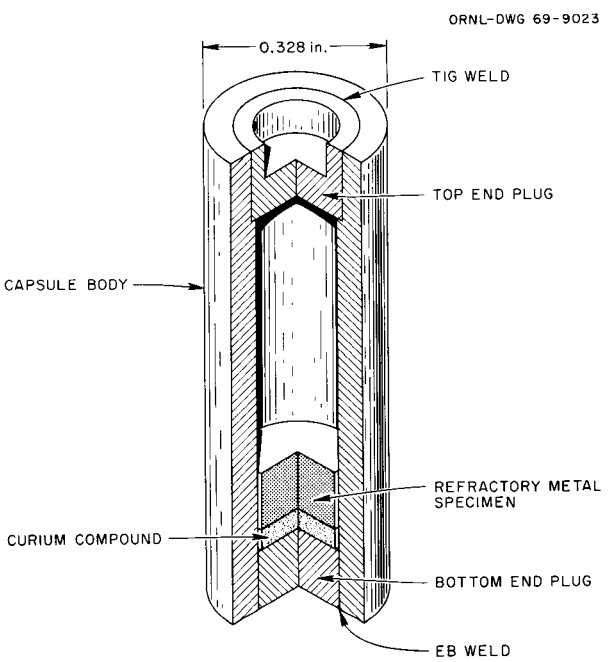

Fig. 19.2. Curium Compatibility Capsule Test System.

We used a program-controlled power supply, ensuring reproducibility of test results with a minimum possibility of operator error. The entire welding sequence, including initial current, upslope time, welding current, welding time, downslope time, and rotational speed, is automatically controlled.

The procedures and conditions developed were used successfully in the glove-box encapsulation of $^{244}Cm_2O_3$ in these materials.

Brazing Alloy Development

N. C. Cole D. A. Canonico

In fabricating an isotopically powered thermionic generator, brazing has several advantages for certain applications.[4] It is ideally suited for joining small parts in regions of limited access. Also, the efficiency of such a generator depends on good heat transfer from the capsule to the emitter. A continuous metallurgical bond, as can be obtained by brazing, enhances this heat transfer. We have developed several braze alloys, listed in Table 19.1, most of which meet the stringent requirement that they wet and flow on tungsten between 2000 and 2400°C. For the joint between the capsule and emitter, stability in vacuum at high temperature is required. A simulated capsule-to-emitter joint brazed with several of these alloys was designed and tested in vacuum at 1650°C for 100 hr. Three brazing alloys (Nb–25% Ir–25% W, Nb–3% Ti–2% Ir, Nb–2% Ti–1% Si) survived the vacuum exposure with no appreciable weight loss from vaporization.

Chemical Vapor Deposition of Test Components

W. C. Robinson, Jr.[5]

Several tungsten components, shown in Fig. 19.3, were prepared by chemical vapor deposition for evaluating the design of heat sources. The capsule in (*a*) measured about 2.5 in. long × 0.7 in. diam × 0.065 in. wall thickness, had an integral tube, and was made for pressure testing. In a first attempt to prepare the capsule, tungsten deposited on a copper substrate cracked during cooling to room temperature because of

[4] N. C. Cole and D. A. Canonico, *Metals and Ceramics Div. Ann. Progr. Rept. June 30, 1968,* ORNL-4370, p. 94.

[5] Present address, Lockheed California Co., Burbank, Calif. 91503.

PHOTO 96677

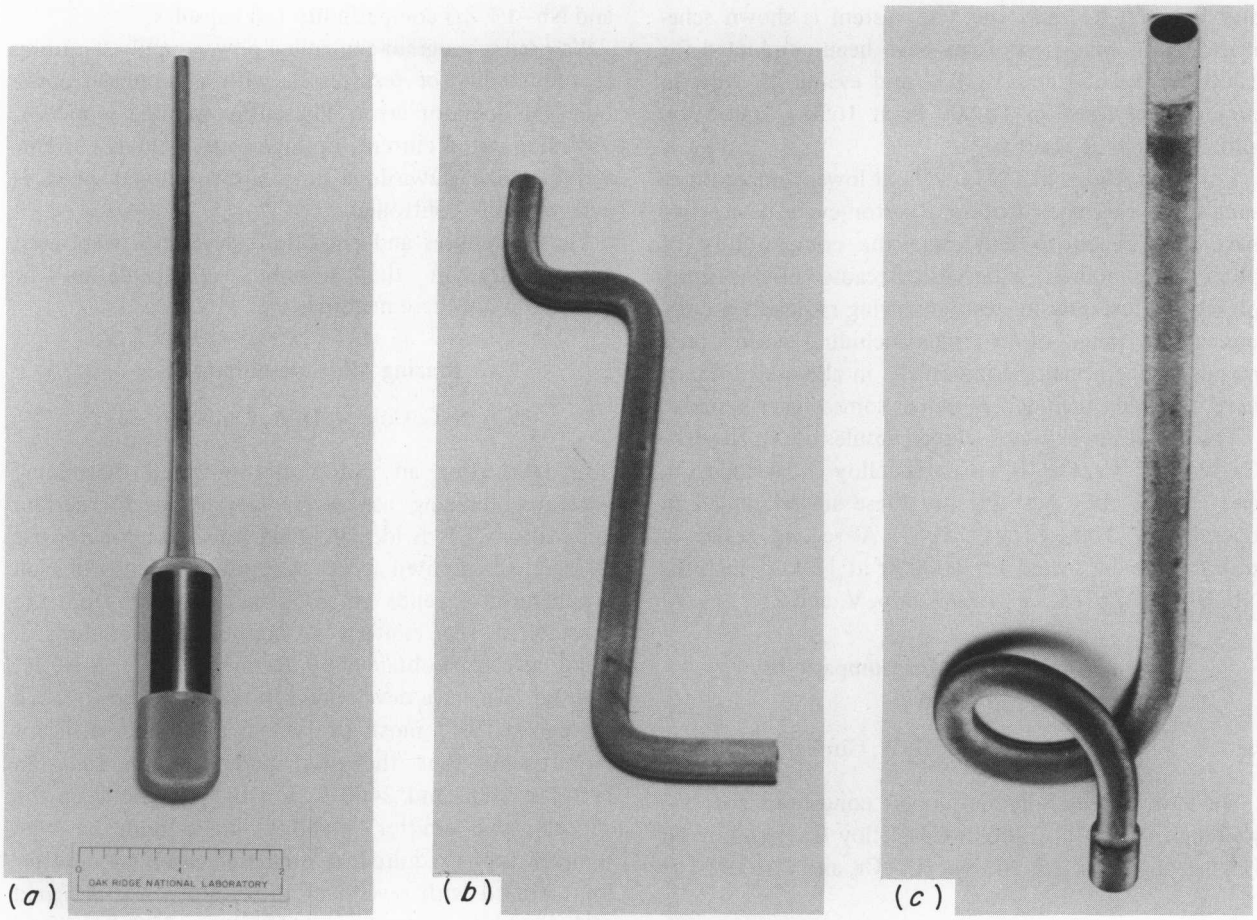

Fig. 19.3. Chemically Vapor Deposited Tungsten Components for Isotope Capsules and Related Studies. (*a*) Capsule with integral pressurizing tube. (*b*) Capsule vent tube. Half size. (*c*) Vapor transport test tube. Full size.

a difference in thermal contraction. The capsule was then successfully deposited on a molybdenum substrate, which was removed by acid dissolution. Creep-rupture testing was conducted at 1650°C by pressurizing with helium. The maximum circumferential strain was 11%.

Five vent tubes (*b*) measuring 0.122 in. ID × about 0.02 in. wall were prepared for a study of problems involved in welding such tubes to capsules and to other materials. Seven loop tubes (*c*) measuring 0.25 in. ID × about 0.025 in. wall were also deposited. After end closures are made the vapor transport of Cm_2O_3 from the loop into the cooled straight section will be studied.

Fluid-Bed Coating for Isotopic Fuel Particles

W. C. Robinson, Jr.[5] J. I. Federer

Metal coatings on isotopic fuel particles could aid in controlling contamination, inhibiting gas release, acting as a binder in pressed compacts, and increasing the thermal conductivity of a fuel form. Coatings are being applied by CVD in a fluidized bed. So far, only tungsten and tantalum coatings have been studied. Sol-gel ThO_2 microspheres were used as a substitute for isotopic fuel particles, such as Cm_2O_3, Pm_2O_3, and $SrTiO_3$. Tungsten coatings 10 to 15 μ thick were

Table 19.1. Experimental Brazing Alloys

Composition (wt %)	Approximate Melting Temperature (°C)
Nb–25Ir–25W	2400
Nb–3Ti–2Ir	2400
Ir–30Pt	2250
Nb–3Ti–1Si	2400
Nb–2Ti–2Si	2400
Nb–2Ti–1Si	2400
Nb–3Ti–2Si	2400
Ir–45Pt–10W	2200
Ir–50Rh	>2400
Mo–25Ir–25W	>2400
Ir–45Rh–10W	>2400
Pt–30W	2300
Pt–15Re–15W	2250
Pt–45Rh–10W	2150
Pt–50Rh	2050

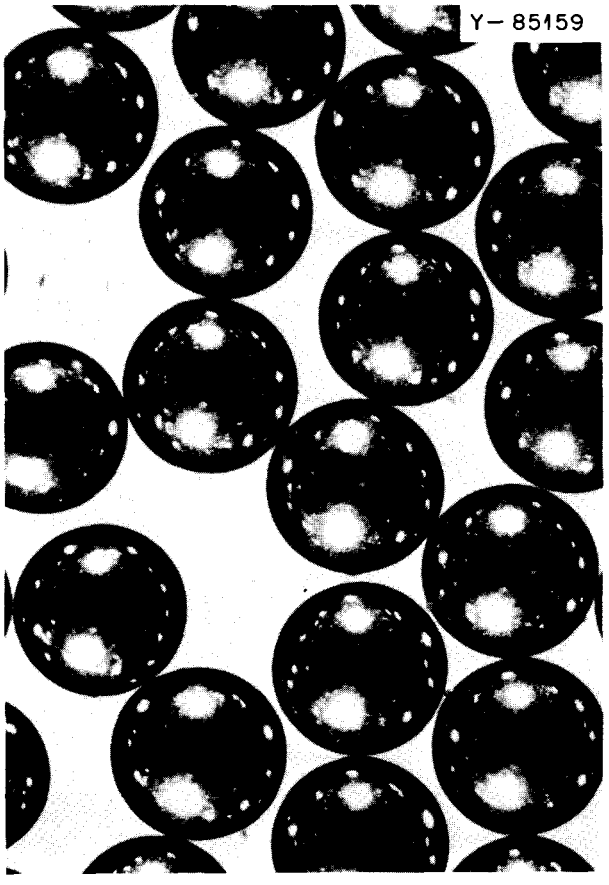

Fig. 19.4. Sol-Gel ThO_2 Microspheres (400 μ in diameter) Coated with 10 to 15 μ Tungsten in a Fluidized Bed. 75X.

successfully applied to ThO_2 microspheres by hydrogen reduction of WF_6 at about 600°C. Typical coated particles are shown in Fig. 19.4. Efforts to apply tantalum coatings by hydrogen reduction of $TaCl_5$ have been less successful. Reduction of $TaCl_5$ requires temperatures in the range 900 to 1000°C to achieve reasonable deposition rates. Only extremely thin or very rough tantalum coatings have been obtained, and gross losses of ThO_2 were observed.

CLADDING MATERIALS PROGRAM

Mechanical Properties of Haynes Alloy No. 25

R. W. Swindeman

Superalloys have potential as canning materials for isotopic heat sources that operate in the 650 to 870°C range. However, the heat source could be exposed to conditions that differ from those of normal operation for superalloys, and some supplementary data are desirable on these materials to assure reliable design. We are collecting short-time creep-rupture data in the range 980 to 1200°C, suitable for use in the safety analyses pertaining to launch pad abort and sub-orbital re-entry situations. Also of interest in this respect are the impact and tensile properties of aged superalloys. We are also concerned with the long-time creep-rupture behavior of weldments at operating temperatures in the 650 to 870°C range.

Creep-rupture data for a cobalt-base superalloy, Haynes alloy No. 25, are summarized in Fig. 19.5. Literature data on five heats of base metal are correlated in (*a*) over the range 650 to 1050°C by the Manson-Haferd parameter. Our data on three heats are compared in (*b*) to the 99% confidence band from (*a*). Weldment data in (*b*) were obtained on sheet specimens that include base metal and a transverse TIG weld in the test section. The weldments apparently are about as strong as the base metal. However, most weldments failed near the fusion line in the 650 to 870°C range.

The effect of aging at several temperatures on the tensile properties of Haynes alloy No. 25 is illustrated in Fig. 19.6. After aging at 700°C for 2000 hr we find an appreciable increase in the yield and ultimate strengths and a corresponding loss of ductility. A less dramatic increase in strength occurs after the 800°C age. Losses in ductility occur at all temperatures. When tensile tests are performed at the aging temperatures, similar changes in strength are apparent. Ductility is a minimum at 700°C and improves at 800 and 850°C.

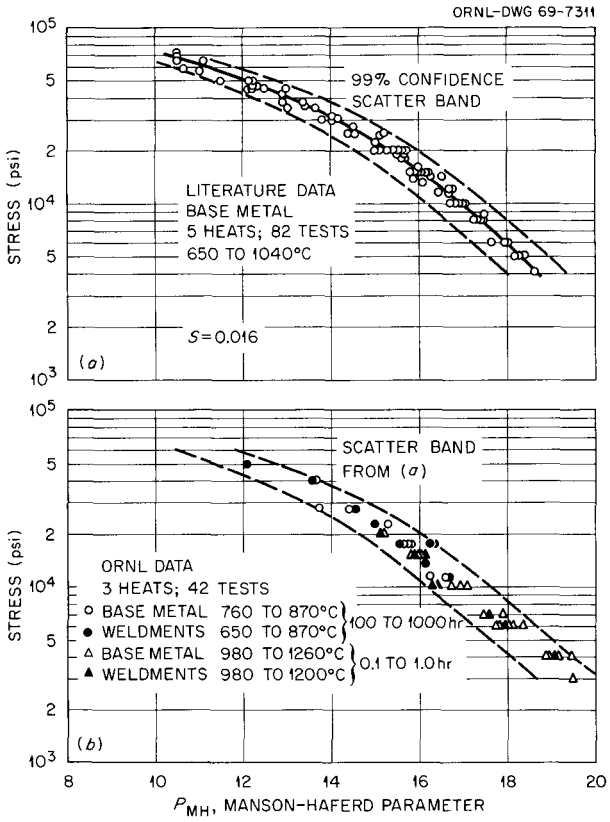

Fig. 19.5. Comparison of the Rupture Strength of Haynes Alloy No. 25 Weldments with the Scatterband Generated by Rupture Tests on Base Metal. Time-temperature correlation is based on the Manson-Haferd parameter, P_{MH} = log time + ST°_{C}.

The properties of aged specimens are affected by the composition and morphology of the precipitating phases. Of these, the precipitation of the Laves phase Co_2W is generally considered[6] to be the embrittling reaction at 800 and 850°C. The pronounced aging response at 700°C is possibly associated with the precipitation of an ordered hexagonal structure,[7] β-Co_3W.

Interaction of Stress and Vacuum on Properties of Superalloys at Elevated Temperatures[8]

D. T. Bourgette

Capsules of Haynes alloy No. 25 for the containment of isotopic oxide fuels in space power devices might be exposed to high vacuum while under stress. High evaporation rates exhibited by this alloy in vacuum necessitate the determination of its creep behavior in this environment in terms of evaporation losses, wall thickness, stress, and temperature. Creep tests were conducted in high vacuum, argon, and air at 785°C and stress levels of 2000 to 15,000 psi on specimens 0.007, 0.012, 0.030, and 0.060 in. thick. Additional tests were conducted with 0.030- and 0.060-in.-thick specimens at 900°C in vacuum and argon. The creep life of this alloy at 785°C in vacuum is improved with an increase in thickness at all stress levels; however, the life in argon and air is greater than in vacuum for thicknesses of

[6] S. T. Wlodeck, "Embrittlement of a Co-Cr-W (L-605) Alloy," *Trans. Am. Soc. Metals*, **56**, 287–303, 1963.

[7] N. Yukawa and K. Sato, "The Correlation Between Microstructure and Stress Rupture Properties of Co-Cr-Ni-W (HS-25) Alloy," *Trans. Japan Inst. Metals Supplement*, **9**, 680–86, 1968.

[8] Abstract of paper to be presented at Fall Meeting of AIME in Philadelphia, Oct. 13–16, 1969.

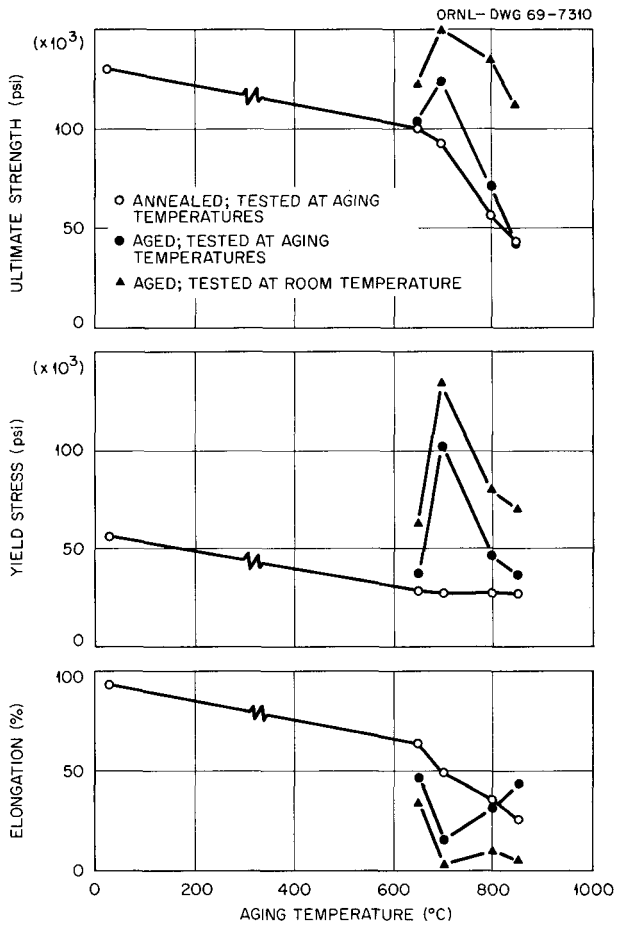

Fig. 19.6. Effect of Aging for 2000 hr on the Tensile Properties of Cobalt-Base Haynes Alloy No. 25.

0.030 in. and less. The creep behavior of 0.060 in. specimens in vacuum and argon is the same at 785°C over a test period of 2000 hr. This behavior indicates that a significant fraction of the specimen volume was affected by evaporation losses in the thinner vacuum-tested specimens. Literature values from creep tests in air and data from current vacuum tests at 900°C indicate that increased evaporation losses decrease the creep life more severely than the 115°C increase in in-test temperature.

Evaporation of Superalloy Capsule Materials in Vacuum[9]

D. T. Bourgette

The evaporation behavior of stainless steels, superalloys, and refractory alloys was studied. Haynes alloy No. 25 and type 316 stainless steel were tested at 760 to 1150°C and 10^{-10} to 10^{-7} torr for times to 3500 hr. The role of composition was determined by comparing the evaporation results and microstructures after 700-hr tests conducted at 870 and 980°C on these alloys and Hastelloy N, Inconel, and types 304 and 446 stainless steel. The evaporation rates increased with increasing chromium and manganese concentrations and temperature, but for any given alloy the rate decreased with time at constant temperature.

Evaporation resulted in surface enrichment of the less volatile elements and bulk changes in alloy composition. The loss of more volatile elements became diffusion-rate dependent. This evaporation mode eventually resulted in subsurface void formation, concentration gradients, and characteristic changes in the microstructure of each alloy.

The creep-rupture properties of a 0.102-cm-thick sheet of type 316 stainless steel tested in argon in the as-received condition were changed significantly after exposure to vacuums of 10^{-7} to 10^{-9} torr for times to 5000 hr at 870°C, but these changes were attributed to precipitation of carbides and *chi* and *sigma* phases. Haynes alloy No. 25 is being tested at 800°C and 10^{-8} torr while under creep stresses of 2500 to 15,000 psi to ascertain the effect of stress on evaporation behavior. Initial results show that (1) evaporation losses increase with stress, (2) the rate of Laves phase precipitation is enhanced, and (3) rupture occurs sooner than for air-tested specimens.

[9]Abstract of paper presented at 1968 AIME Nuclear Metallurgy Symposium on Materials for Radioisotope Heat Sources Oct. 2–4, 1968, Gatlinburg, Tenn.

Tests of evaporation and interstitial stability on second-generation tantalum- and niobium-base alloys in high vacuum at 1200 to 1500°C showed that no serious evaporation problems exist below 1300°C. However, carbon was unstable above 10^{-7} torr and oxygen and nitrogen were unstable at all pressures investigated.

Development of Improved Alloys

C. T. Liu H. Inouye

Alloys for containing radioisotopes in space power devices are being developed to circumvent many of the shortcomings of existing alloys. The evaporation rates of binary alloys of cobalt, nickel, or iron with platinum between 950 and 1050°C at about 10^{-7} torr vacuum decreased as the platinum concentration increased and were one-tenth to one hundredth that of Haynes alloy No. 25. Surface platinum concentration, calculated from the vapor pressure of the alloys and the activity coefficients of the evaporating species, increased due to the preferential evaporation of the solvent (Co, Ni, or Fe). The surface platinum concentration was calculated to be about 100% in CoPt after 500 hr at 1050°C.

Long-range order in Ni_3Co, $(Co,Ni)_3V$, Fe_3Pt, and CoPt increased their tensile strength, yield strength, and hardness and reduced the ductility. In the ordered state, these properties showed little tendency to change when aged at high temperatures. The strongest alloy, $(Co,Ni)_3V$, in the ordered state had the following room-temperature tensile properties: ultimate tensile strength, 183,000 psi; yield strength, 117,000 psi; elongation, 14%; Rockwell "C" hardness, 37. The corresponding values in the disordered state (obtained by water quenching from ~1150°C) were: UTS, 134,000 psi; YS, 67,000 psi; E, 63%; Rockwell "C" hardness, 10. The increase in the tensile strength is attributed to the formation of numerous micro-twins not resolved by the optical microscope.

The creep rates of ordered alloys between 700 and 1000°C were initially very low and steadily increased with time to a steady-state value, a behavior that is opposite to the first-to-second stage creep transition in conventional alloys. The logarithm of strain rate showed a discontinuous change at the critical ordering temperature T_c. Extrapolation of the creep data of the disordered alloys below T_c gave creep rates significantly higher than the measured rates. An activation energy for creep of 85 kcal was calculated for ordered $(Co,Ni)_3V$, compared to 95 kcal for evaporation (assumed to be diffusion controlled). Preliminary creep tests indicate that $(Co,Ni)_3V$ and CoPt are equal in strength or superior to Haynes alloy No. 25 in vacuum.

STRONTIUM PROGRAM COMPATIBILITY STUDIES

J. R. DiStefano

Compatibility of the strontium compounds $SrTiO_3$, Sr_2TiO_4, and SrO with Haynes alloy No. 25, Hastelloy C, and type 316 stainless steel has been determined by exposures of 1000, 5000, and 10,000 hr at 1100°C and 10,000 hr at 900°C. To measure the extent of interaction we determined changes in weight, composition, microstructure, and mechanical properties. Weight and composition changes in the metal specimens were small and insignificant. Metallographic examination showed that all samples exposed to SrO at 1100°C were attacked up to a maximum depth of 0.008 in., primarily along grain boundaries. At 900°C Haynes alloy No. 25 and Hastelloy C were similarly attacked, but type 316 stainless steel was not. Haynes alloy No. 25 and Hastelloy C exposed to $SrTiO_3$ showed subsurface voids, indicating the preferential removal of some element, possibly carbon. Samples exposed to Sr_2TiO_4 appeared similar to those heat treated in argon under similar conditions.

The only significant change observed in the strontium compounds occurred with $SrTiO_3$. A surface reaction zone was found in all the tests involving this compound, and it was identified by microprobe analysis to be a $Cr(Mn)_xTi_yO_z$ phase.

Room-temperature tensile tests showed a drop in yield strength, ultimate tensile strength, and elongation of the metal specimens when heat treated for 1000, 5000, and 10,000 hr at 1100°C and 10,000 hr at 900°C as well as when tested with the strontium compounds. The decline in mechanical properties is, therefore, attributed to increased grain size and phase changes that occur upon heat treatment. Samples exposed to SrO exhibited, on the average, lower tensile strength and elongations than other samples of the same alloy.

These tests have shown that all three superalloys are compatible with both $SrTiO_3$ and Sr_2TiO_4 up to 1100°C. Further investigation of these materials with SrO is being conducted to determine the nature of the interaction.

SNAP-21 AND SNAP-23 PROGRAMS

Capsule Welding

R. W. Gunkel

The SNAP-21 heat source capsule [200 w (thermal) of $^{90}SrTiO_3$ fuel] is a 0.200-in.-wall Hastelloy C-276 tube, 3.200 in. in diameter × 3.310 in. long. The SNAP-23 capsule [1200 w (thermal) of $^{90}SrTiO_3$] is a thick-walled Hastelloy C tube, 5 in. in diameter × 7.860 in. long, with 0.400-in.-thick walls and 0.600-in.-thick end caps.[10] Electron-beam welding was chosen to produce the end-closure joints. The desired depth of defect-free weld[11] was 0.100 in. in the case of SNAP-21 and 0.110 in. for SNAP-23. In each case the edge of the capsule was not to be melted during welding[12] since it serves as a reference for ultrasonic inspection of the weld area.

Acceptable in-cell welds were made in two practice SNAP-21 capsules and six fueled capsules. Subsequently, two dummy-fueled capsules were welded out-of-cell for future pressure testing. Ultrasonic inspection proved all these welds to be acceptable. In addition, a series of electrically heated mockup capsules were successfully constructed. These resemble the regular SNAP-21 fuel capsule except for the flange attachment, which replaces one of the end caps and contains the electrical leads and thermocouple wires.

The SNAP-23 capsule contains a helium atmosphere to ensure good transfer of heat from the fuel to the capsule wall. A helium entrance hole in each capsule is sealed by the gas tungsten-arc process after the electron-beam cap-to-capsule weld has been made. Acceptable in-cell welds were made in both a practice and a fueled capsule. Three additional capsules were also welded out-of-cell for pressure testing.

Nondestructive Testing

K. V. Cook

Nondestructive testing techniques were applied to the SNAP-21 capsule body, the initial bottom end weld (before fueling) and, by remote techniques, the final capsule closure weld. In a similar manner we applied these techniques for the remote inspection of the SNAP-23 capsule final seal weld.

A paper on this subject has been presented and is to be published.[13] The abstract is given below.

---

[10] R. W. Gunkel, *Metals and Ceramics Div. Ann. Progr. Rept. June 30, 1968,* ORNL-4370, pp. 99–100.

[11] R. W. Gunkel, R. G. Donnelly, and G. M. Slaughter, "Electron-Beam Welding of SNAP-21 and SNAP-23 Isotopic Fuel Capsules," paper presented at American Welding Society National Fall Meeting, Cincinnati, Ohio, Oct. 7–10, 1968.

[12] R. W. Gunkel, *Metals and Ceramics Div. Ann. Progr. Rept. June 30, 1968,* ORNL-4370, pp. 97–98.

[13] K. V. Cook, "Remote Ultrasonic Examination of Closure Welds on Isotope Capsules," paper presented at the Seventh Symposium on Nondestructive Evaluation of Components and Materials in Aerospace, Weapons Systems, and Nuclear Applications, sponsored by Southwest Research Institute in San Antonio, Texas, April 23–25, 1969. To be published in the proceedings.

The nondestructive inspection of closure welds on fueled isotope capsules is necessary to ensure high integrity and thus prevent the release of toxic radioactive fuels. We are inspecting closure or seal welds with an ultrasonic pulse-echo technique. This test is performed remotely in a hot cell and has been used on seven strontium-fueled capsules sealed by electron-beam welding. The equipment is discussed along with results of calibration and correlation studies performed before and after hot cell evaluation. Discontinuities as small as 0.015 in. in diameter were detected and recorded. Weld penetration can be determined to an accuracy of 0.010 in. from the *x-y* recordings.

THERMOELECTRIC CONVERSION SYSTEMS FOR THE ISOTOPE KILOWATT PROGRAM

A. C. Schaffhauser

We have completed a review of thermoelectric conversion systems and conceptual design studies on a 2-kw(electrical) thermoelectric converter for the Isotope Kilowatt Program. The objective is to evaluate different systems for conversion of heat from ^{90}Sr and ^{60}Co to electrical power in the range of 1 to 10 kw(electrical) for 2- to 5-year terrestrial and undersea applications.

Conceptual converter designs based on pellet and tubular thermoelectric elements were evaluated for systems using either direct conduction or liquid metal circulation heat transfer from the fuel block. Because of their higher heat flux requirements the tubular converters apply only to systems with direct heat conduction from partially shielded ^{60}Co fuel or the liquid metal heat transfer systems. Based on current thermoelectric technology, a pellet converter using direct heat transfer from a tungsten-shielded fuel block would have the highest conversion efficiency – about 8% net heat input to electrical output – for undersea applications. Advanced thermoelectric materials under development, having 20 to 40% higher material efficiency, could result in conversion efficiencies of 10 to 11%.

Part III. General Fuels and Materials Research

20. Fuel Element Fabrication Development

G. M. Adamson, Jr. W. R. Martin

Program emphasis continued in the direction of improving the performances of existing research reactors by increases in fuel element life, by eliminating production problems, and by reducing production costs. Efforts are on aluminum-base dispersion-type plates containing powdered U_3O_8 or UAl_x as the fuel. During this period, a separately supported development effort aimed at improving the fuel elements for the HFIR was discontinued and combined with this program. This work is closely integrated with other work on research reactor fuel elements reported in Chap. 23.

IRRADIATION PERFORMANCE OF ALUMINUM-BASE FUEL DISPERSIONS

W. R. Martin

We are determining those fabrication factors and basic material characteristics that affect the irradiation performance of these fuels. Reactor fuels generally swell during irradiation as fission products accumulate. In research reactors, this is becoming an operating problem as fuels are being subjected to higher fluxes and doses of neutrons. We have concentrated on two factors: amount of void volume in the fuel core of the rolled plate and fuel fines for several grades of two basic fuels, UAl_x and U_3O_8. In addition, we have examined another irradiated HFIR fuel element to obtain more data on the irradiation performance of the high-fired U_3O_8 fuel under actual operating conditions.

Influence of Void Volume on the Irradiation Damage in Dispersion Fuel Plates

M. M. Martin A. E. Richt

The control of swelling in UO_2 stainless steel cermets by introduction of fabrication voids has been used to explain variations in irradiation performance.[1,2] We applied this concept to aluminum-base dispersion fuel plates and found that their behavior in a reactor also depended significantly upon the amount of voids within the fuel core.

Six miniature test plates, 5¾ in. long × 1¼ in. wide, containing 0.020-in.-thick cores and clad with 0.015 in. type 6061 Al alloy, were irradiated in a pressurized-water loop of the Engineering Test Reactor (ETR) for three cycles at fuel center-line temperatures to 175°C and heat fluxes to 630 w/cm^2. These plates contained fuel loadings of 100 and 125% of that now used in the outer annulus of the HFIR fuel element; the actual values are shown in Table 20.1. The fuel was incorporated in the test plates as dispersions of burned U_3O_8, high-fired U_3O_8, hydride UAl_3, and arc-cast UAl_x in a matrix of Alcoa 101 aluminum.[3]

In general, postirradiation examination indicated all to be in excellent physical condition with no evidence of blistering or gross damage. No incipient cracks were found at the corners of the fuel particles, where failure usually starts.

Typical examples of the microstructure of the fuel plates containing burned and high-fired U_3O_8 dispersions of identical uranium content are shown in Fig. 20.1. The striking difference between their unirradiated appearances results from a higher degree of stringering

[1] J. R. Weir, Jr., *A Failure Analysis for the Low-Temperature Performance of Dispersion Fuel Elements,* ORNL-2902 (May 27, 1960).

[2] M. J. Graber, M. Zukor, and G. W. Gibson, "Superior Irradiation Performance of Stainless-Steel Cermet Fuel Plates Through Use of Low-Density UO_2" *Trans. Am. Nucl. Soc.* **10**(2), 482–83 (November 1967).

[3] M. M. Martin and W. R. Martin, *Metals and Ceramics Div. Ann. Progr. Rept. June 30, 1968,* ORNL-4370, pp. 101–102.

Table 20.1. Summary of Data for Swelling of Fuel Cores in Miniature Aluminum-Based Fuel Plates

Plate Reference Number	Fuel Dispersoid		Initial Fuel Core Density (% of theoretical)	Measured Specimen Burnup (fissions/cm^3)	Fuel Core Volume Change (%)	
	Type	Core Concentration (wt %)			Actual	Predicted
				$\times 10^{20}$		
0-3-893	Burned U_3O_8	44.8	91.1	15.5	+2.0	+0.5
0-56-894	Burned U_3O_8	52.8	89.1	13.6	−1.4	−2.1
0-56-899	High-fired U_3O_8	50.2	96.7	11.7	+1.4	+4.0
0-24-959	Hydride UAl_3	48.6	97.5	16.9	+6.7	+8.1
0-24-964	Arc-cast UAl_x	48.6	95.7	15.7	+4.8	+6.7
0-24-965	Arc-cast UAl_x	48.6	95.7	17.7	+6.0	+8.2

and fragmentation with the burned U_3O_8 particles during fabrication. In the reactor, both oxides reacted extensively with the matrix. The effectively smaller particle size of the burned oxide, however, resulted in complete matrix consumption by the 53% burned U_3O_8. Undoubtedly, this agglomeration of reaction products, fuel, matrix, and fission products is brittle. In contrast, the 45% burned U_3O_8 and 50% high-fired U_3O_8 dispersions still exhibited a continuous network of aluminum matrix after burnups of 15.5 and 11.7 $\times 10^{20}$ fissions/cm^3 respectively.

Figure 20.2 shows the typical microstructure of the arc-cast UAl_x-Al dispersion clad with type 6061 Al. The increased size of the UAl_x particles and the absence of voids after irradiation indicate significant core swelling.

Core swelling was determined from measurements of plate density. As shown in Table 20.1, irradiation induced significantly less swelling in the U_3O_8 dispersions than in the UAl_x dispersions. Core swellings predicted from a rate of 0.63 vol % per 10^{21} fissions/cm^3 and the assumption that the initial void volume is 100% effective in accommodating this growth agreed relatively well with the measured values. We conclude that the lower swelling of the U_3O_8 dispersions in these tests is directly attributable to the greater amounts of voids in the fuel cores as fabricated. More importantly, these data show that one can calculate with reasonable accuracy the amount of swelling that will occur during irradiation at these temperatures.

Sections of the six fuel plates were heat treated after irradiation to determine the breakaway swelling (blistering) temperature of the various types of fuels. All survived a 1-hr exposure at 550°C with no visual indications of blistering. Although voids had been introduced to lower swelling during irradiation, we fully expected the plates to swell at some temperature during postirradiation annealing.[4,5] The absence of a blistering temperature at 550°C or below is not yet understood, but these data do suggest an equilibrium condition between fission products and the aluminum in which they are contained. Clearly, voids introduced in the composite during fabrication can enhance the irradiation performance of dispersion fuel plates.

Effect of Fuel Fines on the Irradiation Performance of Dispersion Fuel Plates

M. M. Martin

Miniature dispersion fuel plates have been prepared to study the influence of powder fines (−325 mesh particles) at concentrations of 10, 25, and 50 wt % on the irradiation performance of both burned and high-fired grades of U_3O_8. Irradiation of eight of these plates (two are instrumented) began in the ETR with cycle 99, but a malfunction in the loop monitoring system during cycle 100 resulted in premature removal after 9200 Mwd. The plates are scheduled for return to ORNL for postirradiation examination during the fall of 1969.

Postirradiation Examination of a HFIR Fuel Element

R. W. Knight A. E. Richt

During the past year we destructively examined a second irradiated fuel element. The examination of a previous element (5-O) was reported previously.[4] The

[4] R. W. Knight and A. E. Richt, *Metals and Ceramics Div. Ann. Progr. Rept. June 30, 1968*, ORNL-4370, pp. 182–86.

[5] G. W. Gibson and M. J. Graber, *Annual Progress Report on Reactor Fuels and Materials Development for FY-1967*, IN-1131 (February 1968).

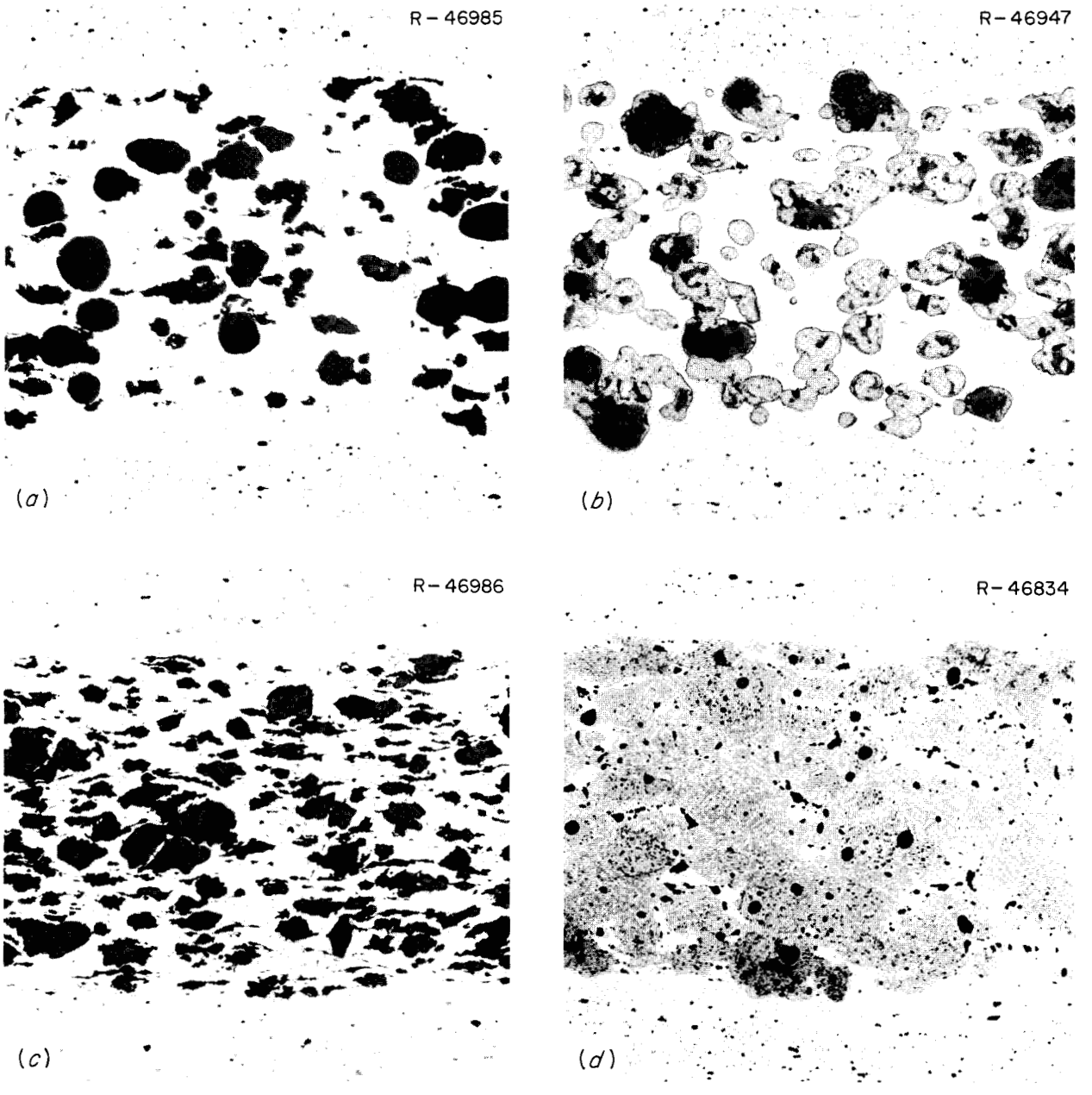

Fig. 20.1. Typical Microstructures of Aluminum-Base U_3O_8 Dispersion Fuel Plates Before and After Irradiation in an ETR Loop. 100×. (*a*) Dispersion of 50 wt % high-fired U_3O_8 as fabricated. (*b*) Same, irradiated to 11.7×10^{20} fissions/cm^3. (*c*) Dispersion of 53 wt % burned U_3O_8 as fabricated. (*d*) Same, irradiated to 13.6×10^{20} fissions/cm^3.

element currently being examined (21-O) differed from 5-O in that it was not subjected to boiling water for 24 hr before being placed in reactor operation.

Both a dimensional and a metallographic examination were made on the element. In general, it appeared to be in better condition than the 5-O assembly. As shown in Fig. 20.3, the element was much brighter in color than the 5-O assembly, indicating that the oxide film was much thinner. Length and diameter were essentially the same as the manufactured dimensions and within the original tolerances. The outside diameter at the horizontal midplane increased 0.009 in. on fuel element 5-O but only 0.002 in. on element 21-O, probably because the pretreatment of element 5-O caused it to operate at a higher temperature.

Channel spacing was measured every ten channels. None was out of specification. Since the oxide had not spalled, a good correlation was possible between channel spacing before and after irradiation, as shown in Table 20.2. While the data are encouraging and do indicate that the channel spacing is still within tolerances, they must be used with care. The two values for the grand average should be comparable, and they indicate no change. Since the surfaces of the used fuel

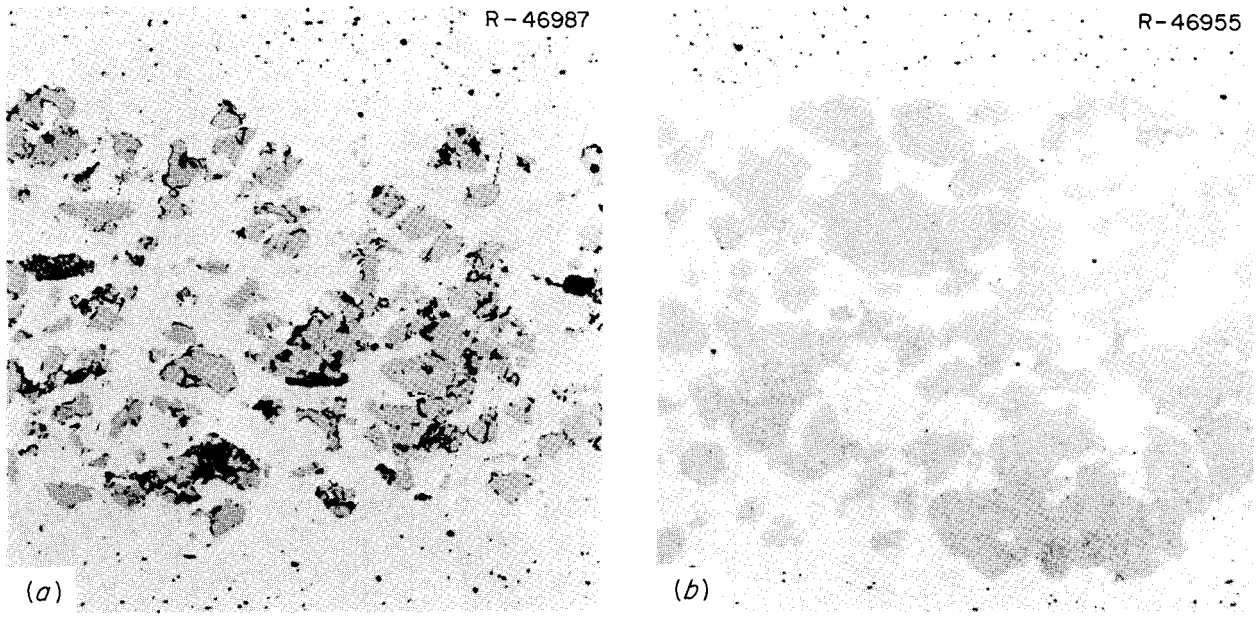

Fig. 20.2. Typical Microstructures of Aluminum-Base UAl_x Dispersion Fuel Plate Before and After Irradiation in an ETR Loop. 100X. As polished. (*a*) As fabricated. (*b*) Irradiated to 15.7 X 10^{20} fissions/cm^3.

Table 20.2. Channel Spacing in HFIR Fuel Element 21-O Before and After Irradiation

	Spacing (in.)			
	Before Irradiation	After Irradiation		
		Position 3	Position 4	Average
Overall grand average	0.0504	0.0505	0.0503	0.0504
Maximum channel average	0.0535	0.0517	0.0514	0.0515
Minimum channel average	0.0485	0.0492	0.0489	0.0491
Maximum spot average	0.055	0.0517	0.0514	0.0515
Minimum spot average	0.046	0.0492	0.0489	0.0491
Maximum local	0.0565	0.0549	0.0531	
Minimum local	0.0400	0.0467	0.0472	

plates contain an oxide layer, we expected that the average spacing would be from 0.001 to 0.0015 in. narrower after exposure, but the differences measured are within the accuracy obtained in comparing values from the two different probes. Values for the maxima and minima are not directly comparable, since many more measurements were made before than after irradiation, thereby increasing the chances of finding greater variations. Because of difficulties in reproducing locations, we made no effort to measure identical locations before and after.

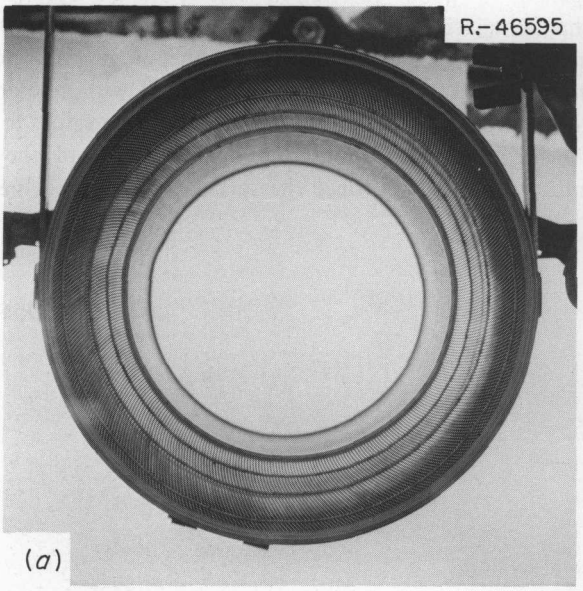

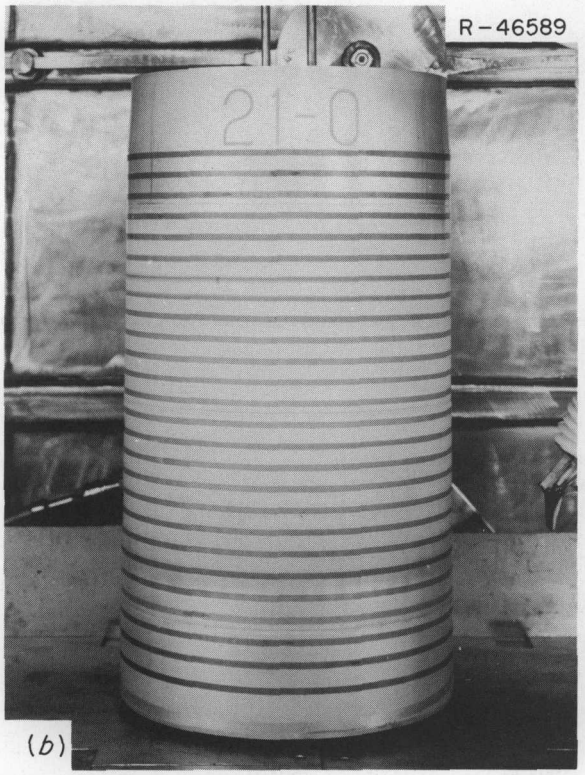

Fig. 20.3. Irradiated HFIR Fuel Element 21-O. (*a*) End view. (*b*) Side view.

Four fuel plates were removed from the 21-O assembly for detailed examination. All appeared to be in excellent condition. No blisters or gross distortion was visible. Gamma scans showed no abnormalities in the burnup distribution, and results of analytical determinations were in excellent agreement with the calculated burnup values. As shown in Fig. 20.4, the oxide film had not spalled from the surfaces of the 21-O fuel plates. As expected, it varied in thickness over the plate surfaces, ranging from 0.0001 in. over the low-temperature regions to 0.0009 in. over the maximum temperature region of the plate. These film thicknesses are slightly greater than that expected from reactor service, indicating an indeterminate growth during storage. However, they are considerably thinner than that found over corresponding regions of plates from the 5-O element.

Metallographic examination of sections of the fuel plates revealed no evidence of blistering, core-cladding separation, or fuel breakup. No incipient cracks were found in the corners of the fuel particles where failure usually starts. The cladding had not corroded excessively; we estimate that less than 0.001 in. of the nominally 0.010-in.-thick cladding was lost. Irradiation-induced swelling of the fuel plates also appeared to be rather insignificant; even in areas of high burnup the fuel cores appeared to increase less than 0.001 in. in thickness. As shown in Fig. 20.5, the extent of reaction between the U_3O_8 particles and the matrix appeared to be about the same at corresponding locations in fuel plates from both elements. Since the oxide thickness on the 21-O fuel plates was considerably thinner than that on the 5-O plates, one would expect that the 21-O plates should have operated at a lower temperature and exhibited lesser reaction. However, the 21-O assembly was fabricated from slightly smaller fuel particles and operated slightly longer. Both these factors could account for the proportionally greater extent of reaction in the 21-O fuel plates.

After irradiation to its expected life, the 21-O fuel element appeared to be in excellent condition with no indications of incipient failure. It appears to be stable both dimensionally and structurally.

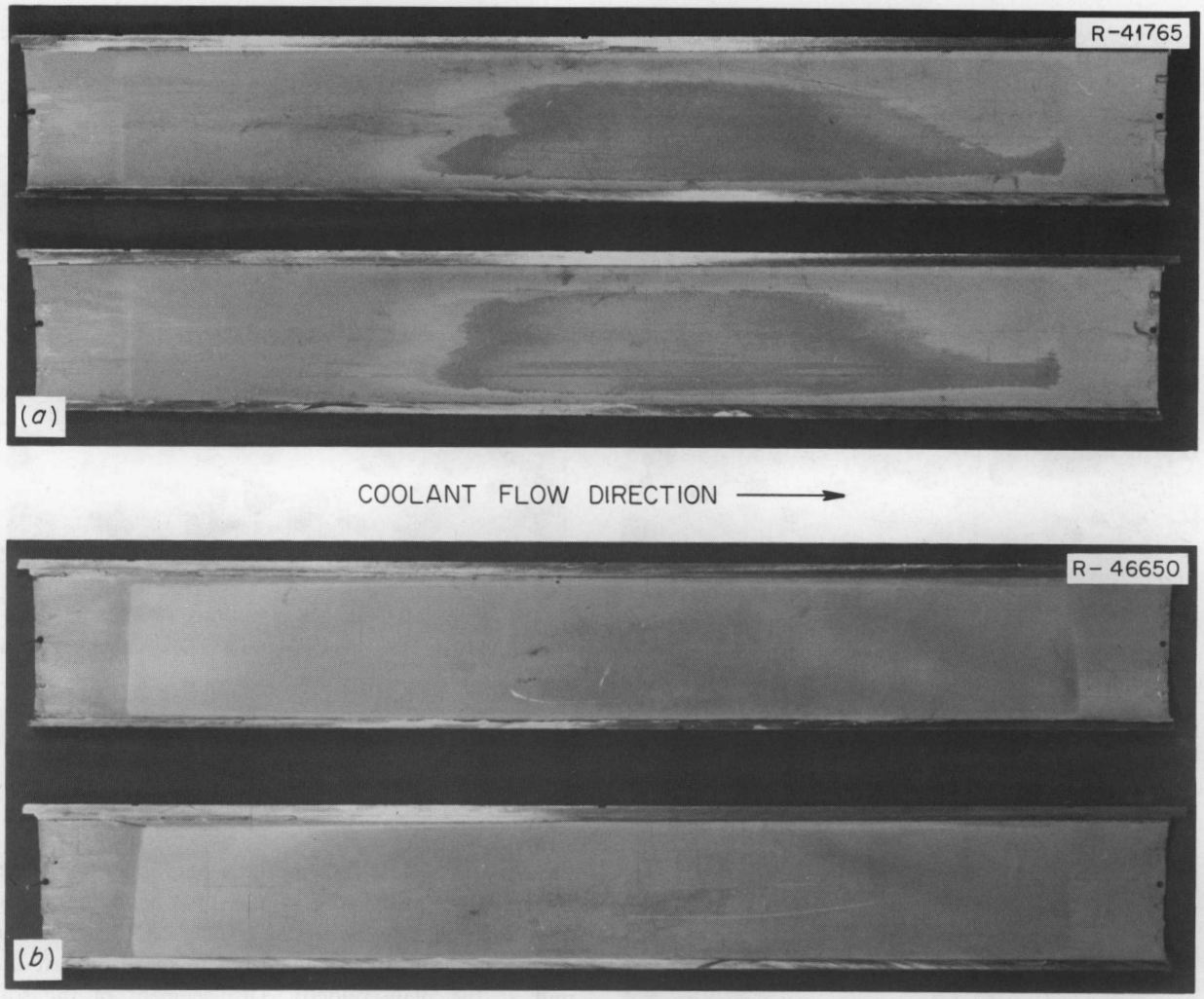

Fig. 20.4. Typical Appearance of Concave Surfaces of Irradiated HFIR Fuel Plates. (*a*) Plates from element 5-O. (*b*) Plates from element 21-O. Regions where the oxide film had spalled from the 5-O plates are delineated by the dark, irregularly shaped areas. Approximately 0.25×.

FUEL PLATE FABRICATION

M. M. Martin J. H. Erwin W. R. Martin

A major part of our effort is directed at a better understanding of dispersion fuel plate fabrication. The present variables being investigated are: (1) fuel loading both at the present HFIR concentration, 1.22 g U/cm^3, and at a 25% higher level, 1.53 g U/cm^3; (2) the effect of the proportion of −325-mesh fines in the fuel powder at levels of 10, 25, and 50 wt % (the lower level corresponds to the present maximum permissible content for HFIR, while the upper typified the normal yield in manufacturing the oxides); (3) types of U_3O_8, including the present high-fired HFIR oxide, a more inexpensive burned U_3O_8, and sol-gel U_3O_8; (4) rolling billet composition and assembly tolerances; and (5) rolling conditions, such as temperature.

Nonuniform Deformation in Simulated Fuel Plates

J. H. Erwin

We used high-speed motion pictures to observe the formation of the "dogbone" shape in simulated fuel plates consisting of X8001 aluminum cladding on 6061 aluminum cores. The 1.25-in.-thick billets were constructed with the core exposed as shown in Fig. 20.6 for viewing as the billet passed through the rolling mill.

The billets were heated to 500°C and reduced at a rate of 0.150 in. per mill pass in a 12-in.-diam by 14-in.-wide two-high mill operating at 26.4 rpm. The

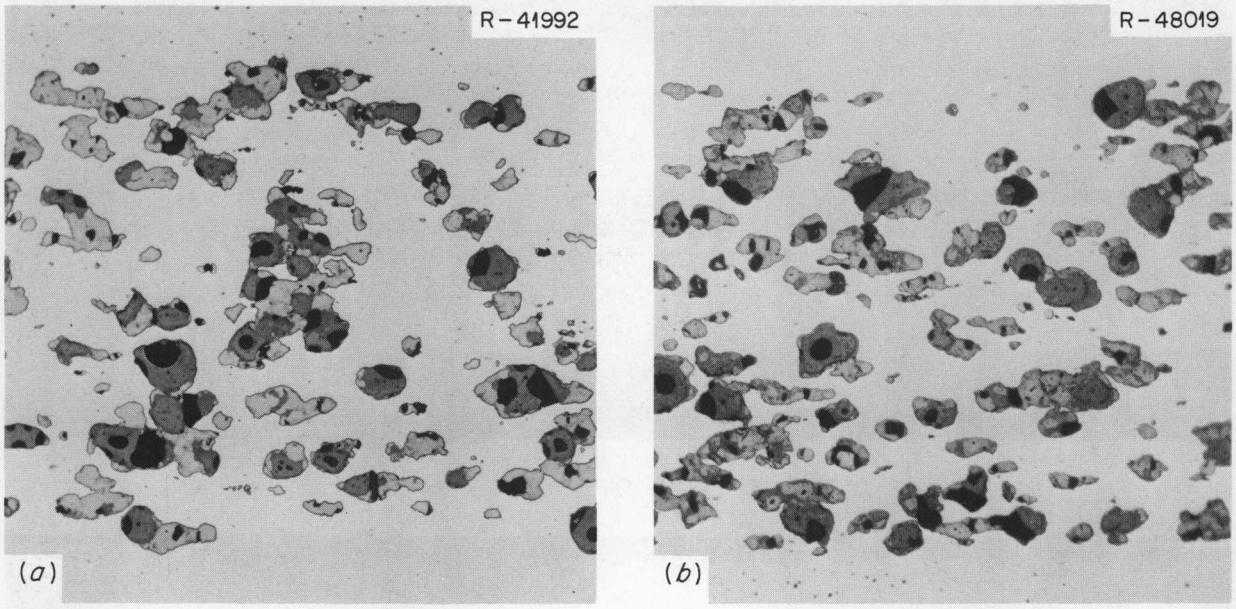

Fig. 20.5. Typical Microstructure of Sections from Irradiated HFIR Fuel Plates. Areas shown are from corresponding regions of plates from elements (*a*) 5-O and (*b*) 21-O. As polished. 100×.

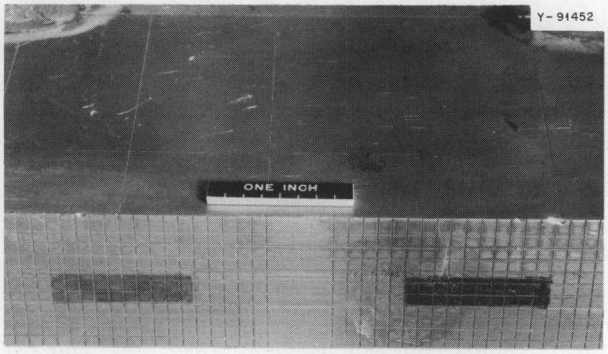

Fig. 20.6. Oblique View of Simulated Fuel Plate Showing Two Cores with Checkered Surface on the Side of the Billet.

billets were reheated and rolled seven passes without changing relationship of the checkered surface with the camera.

Selected frames from the first pass are shown in Fig. 20.7. As noted in these pictures, the frame and core separated as the interface reached the no-slip zone in passing through the rolls. Measurements from the film indicating the degree of deformation within selected locations on the edge of the billet are plotted in Fig. 20.8 to show the abrupt change in deformation rate at the core-frame interface as the separation took place. The midplane of the core, on the other hand, proceeded at a reduced rate until the trailing end reached the no-slip area, and then it increased in speed to leave the mill at the plate velocity. Displacement of the soft cover plate material from both the leading and trailing ends of the hard core allows the formation of the dogbone.

The dogbone formation was previously shown to reach a plateau for the 6061-X8001 aluminum core-cladding combination.[6] Analysis of the film indicates that the dogbone development may be related to the reduction shape factor defined as l/H_{mean} where l is the length of the deformation zone and H_{mean} is the mean of the initial and final billet thickness. When the shape factor is low (<1.5), the midplane of the billet resists deformation in the first section of the deformation zone but begins to deform as it nears the exit point. This is due to stress variations across the thickness of the billet. However, when the shape factor is high (>1.5), the stress is more uniform across the billet thickness and the deformation is more uniform.

[6] J. H. Erwin and W. R. Martin, *Metals and Ceramics Div. Ann. Progr. Rept. June 30, 1968,* ORNL-4370, pp. 107–108.

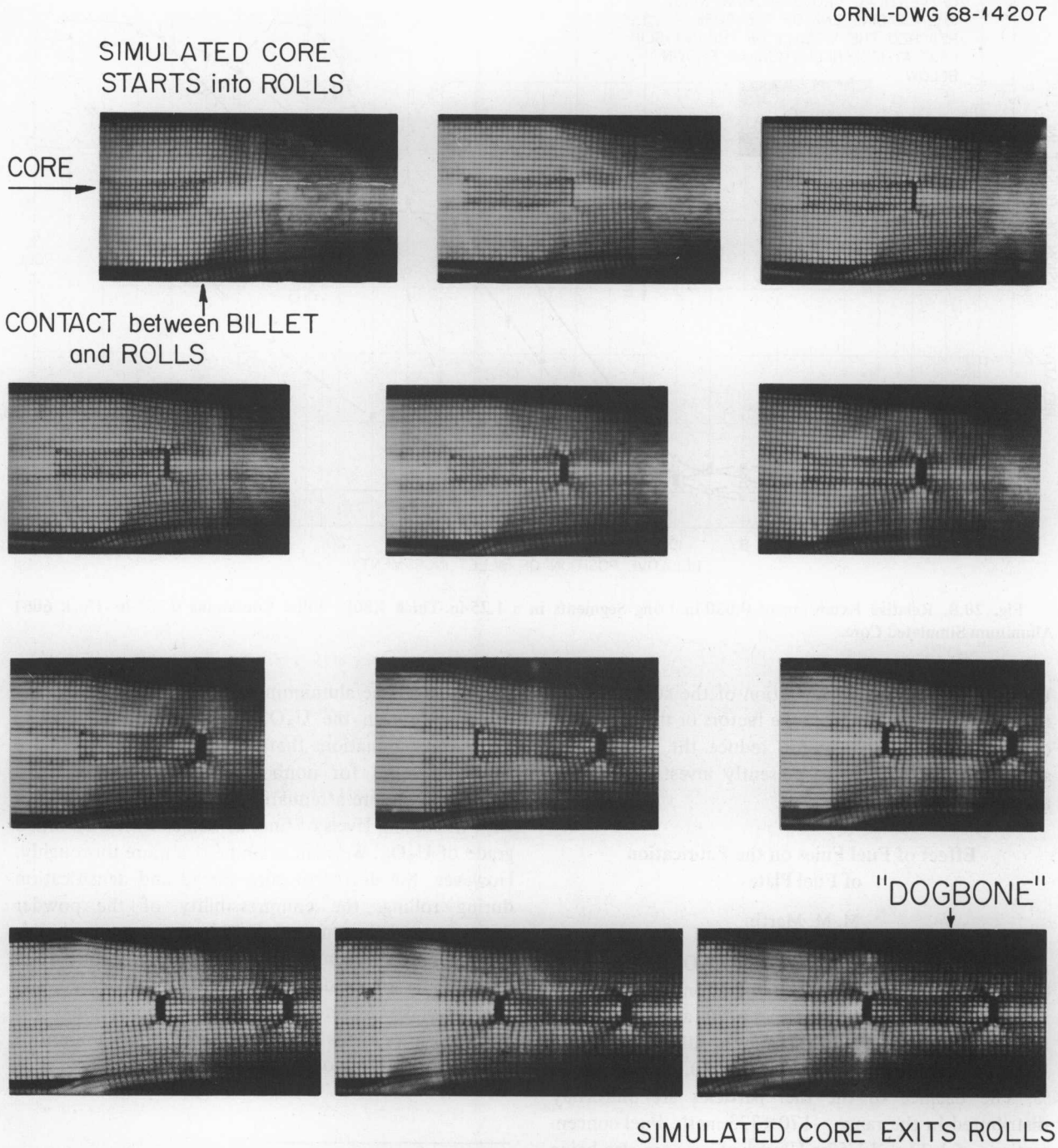

Fig. 20.7. Formation of "Dogbone" During Rolling (0.138 sec) of Simulated Fuel Element at 500°C.

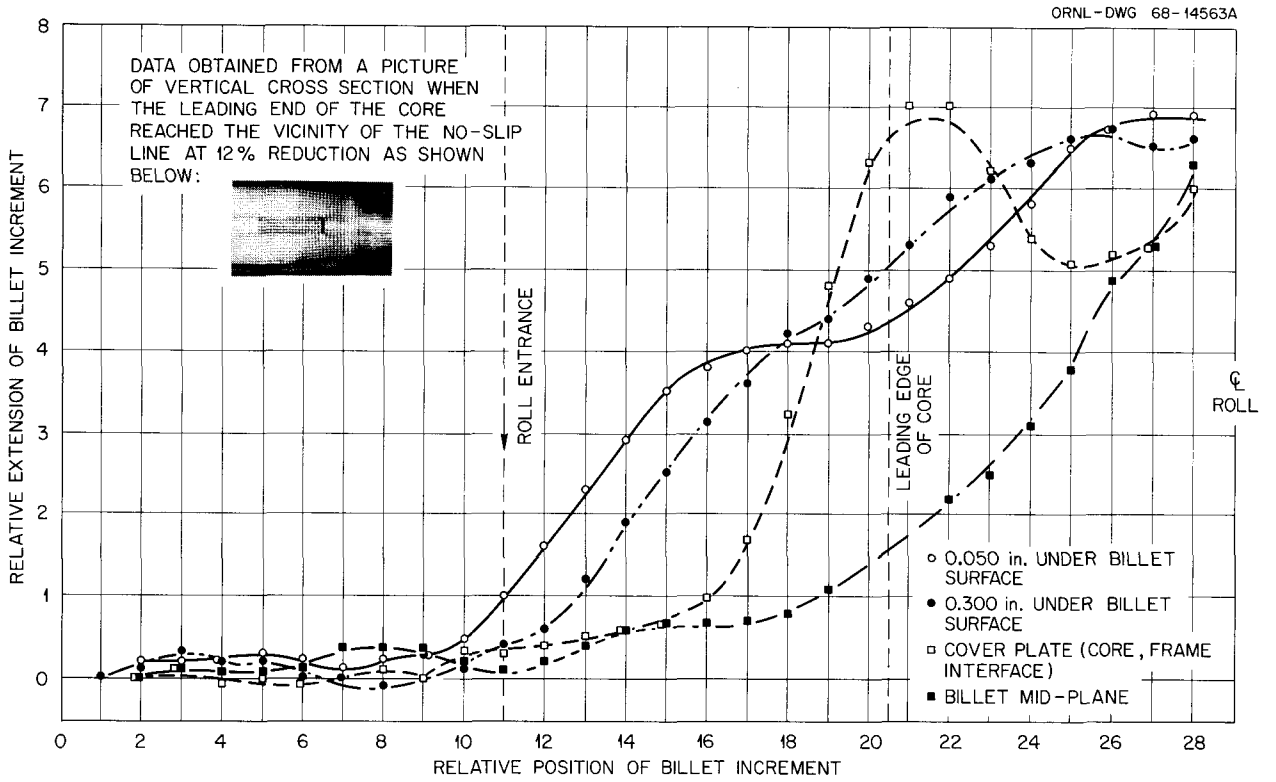

Fig. 20.8. Relative Extension of 0.050-in.-Long Segments in a 1.25-in.-Thick X8001 Billet Containing 0.255-in.-Thick 6061 Aluminum Simulated Core.

We conclude that a redistribution of the stress pattern through the use of larger shape factors or the alteration of the billet geometry could reduce the dogbone to acceptable limits. We are presently investigating both avenues.

Effect of Fuel Fines on the Fabrication of Fuel Plates

M. M. Martin

We are investigating[7] the effect of U_3O_8 powder fines (−325-mesh particles) on the fabrication of burned and high-fired grades of U_3O_8 dispersed in a matrix of 101 aluminum and clad with aluminum alloy 6061. The levels of fines in the experiment are 10, 25, and 50 wt %. The balance of the fuel particles are uniformly distributed in the range −170 +325 mesh. Fuel concentrations of 1.22 and 1.53 g U/cm^3 of core are also being examined. Irrespective of the type and quantity of fuel, identical pressing and rolling conditions were used to fabricate the plates.[8]

Our characterization of 30 miniature plates again showed that the quantity of fabrication voids within the cores depends upon the type and concentration of the U_3O_8 in the aluminum-base dispersions.[9] Also the fines content in the U_3O_8 powders affected nondestructive examinations that use x rays for homogeneity and ultrasound for nonbond inspections. We noted significantly more attenuation of x rays and ultrasound with increasing levels of fines as well as with the burned grade of U_3O_8. We shall examine this more thoroughly. However, the degree of core spread and densification during rolling, the compressibility of the powder mixtures, and the amount of void volume retained after fabrication are all independent of the fines content of both grades of oxides investigated. We conclude that powder-pressing and roll-cladding conditions for U_3O_8-Al dispersions are independent of the amount of fines up to 50 wt % of the U_3O_8.

[7] M. M. Martin and W. R. Martin, *Metals and Ceramics Div. Ann. Progr. Rept. June 30, 1968,* ORNL-4370, pp. 101–102.

[8] M. M. Martin, W. J. Werner, and C. F. Leitten, Jr., *Fabrication of Aluminum-Base Irradiation Test Plates,* ORNL-TM-1377 (February 1966).

[9] M. M. Martin and W. R. Martin, *Metals and Ceramics Div. Ann. Progr. Rept. June 30, 1968,* ORNL-4370, pp. 105–106.

Characterization of Sol-Gel U_3O_8

M. M. Martin

Voids within the fuel core that accommodate particle swelling and fission gases have been shown to influence the irradiation performance of dispersion fuels.[10] We have found that U_3O_8 prepared by the sol-gel process[11] offers the desirable property of more closed porosity within the fuel particles than in the high-fired or burned grades of U_3O_8. Before examining the irradiation performance of this fuel, we characterized the fuel powders and compared sol-gel U_3O_8 to the other grades.

Figure 20.9 shows the as-polished structure of U_3O_8 particles from three methods of preparation. High-fired U_3O_8 is comparable to that being used successfully in HFIR. The burned U_3O_8 is from an earlier stage of the process and is made simply by burning uranium machining chips. The photographs for burned and high-fired oxides show materials both depleted and enriched in ^{235}U. In comparing these, one sees differences of pore size in the two high-fired oxides and agglomeration of fines in the burned oxides. These differences result primarily from a loosening of process control and metal purity requirements with the depleted materials. The sol-gel U_3O_8 contains normal uranium. In contrast to the pores and cracks in high-fired and burned materials, the sol-gel particles have an abundance of uniformly distributed minute voids. The diameter of most of the voids is less than 1 μ.

The sol-gel U_3O_8 came from the Chemical Technology Division. Lines from a Debye-Scherrer powder camera sample were indexed to the orthorhombic form of U_3O_8; two extra lines indicated minor amounts of hexagonal U_3O_8. Spectrographic analysis revealed impurities of Al, B, Fe, Na, and Ni that exceeded the HFIR specification.[12] Closer control of starting materials should reduce these contaminants to an acceptable level. The results of other analyses are given in Table 20.3, which includes for comparison data for high-fired and burned U_3O_8.

Note in Table 20.3 the excellent agreement between the values for toluene density and mercury density determined at 15,000 psi for the sol-gel material. The amount of closed porosity calculated from the toluene and x-ray densities is 12.4 vol %. The mercury and toluene densities for both burned and high-fired materials, however, differ significantly. In fact, the toluene values for high-fired particles are always near

[10] M. M. Martin, J. H. Erwin, and W. R. Martin, "Effect of Type and Concentration of Fuel in the Void Volume in Aluminum Dispersion-Type Fuel Plates," *Trans. Am. Nucl. Soc.* **11**(1), 107 (June 1968).

[11] R. G. Wymer, *Laboratory and Engineering Studies of Sol-Gel Processes at Oak Ridge National Laboratory,* ORNL-TM-2205 (May 1968).

[12] R. W. Knight, J. Binns, and G. M. Adamson, Jr., *Fabrication Procedures for Manufacturing High Flux Isotope Reactor Fuel Elements,* ORNL-4242 (June 1968).

Table 20.3. Characterization of U_3O_8 Materials

	Method of Preparation				
	Burning of Metal Chips	High Firing	Sol-Gel Process	Burning of Metal Chips	High Firing
U concentration, wt %	84.3	84.5	84.7	84.7	85.2
^{235}U assay, wt %	93.2 (enriched)	93.2 (enriched)	0.7 (normal)	0.2 (depleted)	0.2 (depleted)
Mercury density, g/cm^3					
at 29 psig	5.69	6.83	4.90	*a*	*a*
at 15,000 psig	7.06	7.63	7.29	*a*	*a*
Toluene density, g/cm^3	7.64	8.22	7.35	7.92	8.29
Closed porosity, vol %	7.8	0.8	12.4	5.6	1.2
Surface area, m^2/g	0.34	0.05	0.49	0.56	0.06
Major particle size range for property analysis, μ	88–44	88–44	149–44	88–44	88–44
Amount <44 μ, wt %	11	10	27	*b*	3

[a] Not determined.

[b] Analysis generates fines.

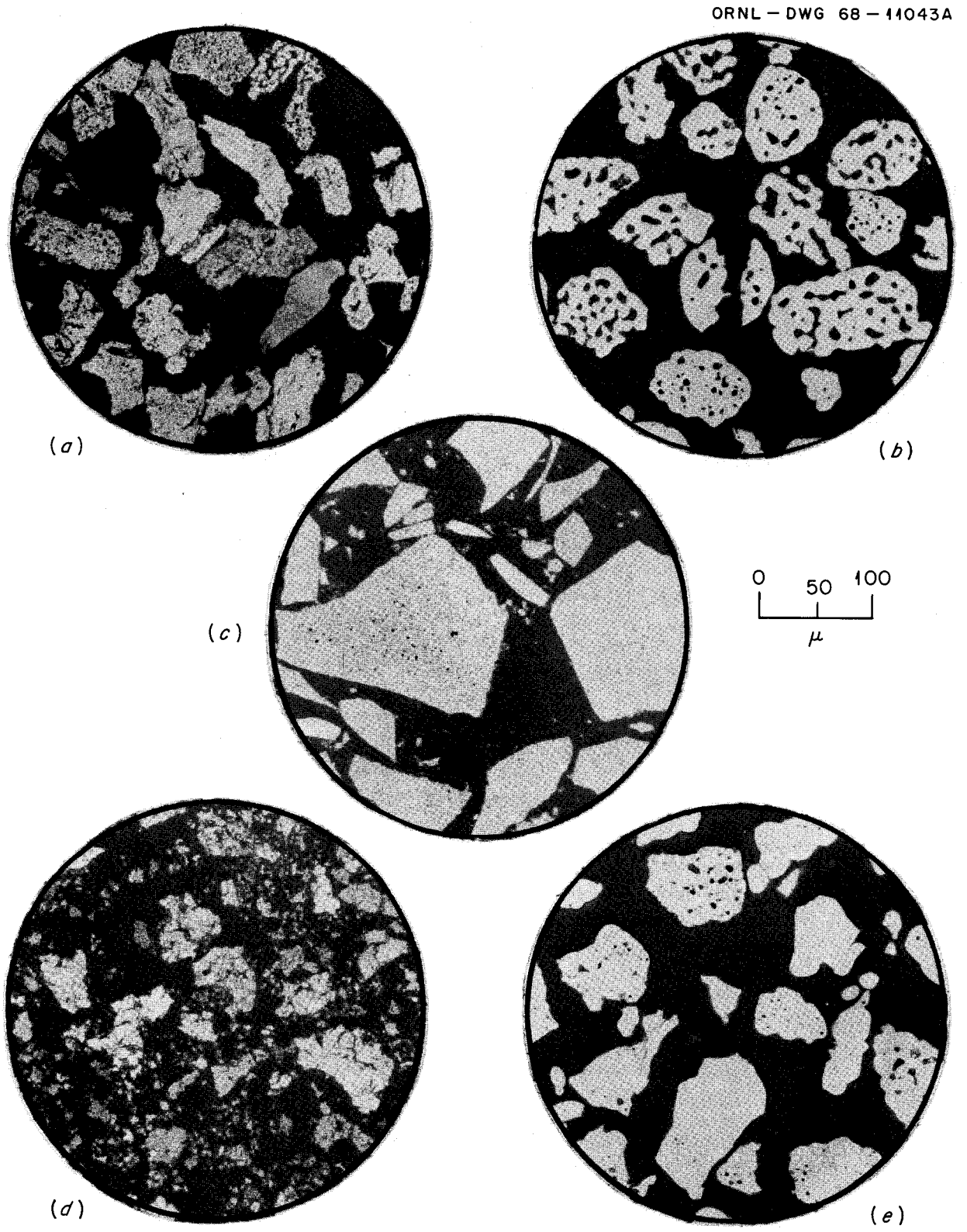

Fig. 20.9. As-Polished Structure of U_3O_8 Particles from Three Methods of Preparation. (*a*) Depleted burned oxide. (*b*) Enriched burned oxide. (*c*) Normal sol-gel oxide. (*d*) Depleted high-fired oxide. (*e*) Enriched high-fired oxide.

that for theoretically dense U_3O_8. We conclude that most of the pores and cracks depicted in Fig. 20.9 for the burned and high-fired materials are open to the surface of the particles. The minute and finely distributed voids in sol-gel U_3O_8, however, are closed.

All the above information gives a reasonably clear picture of sol-gel U_3O_8. The distribution of a relatively large volume of closed porosity appears to be its principal asset, since the material may be able to hold a significant quantity of fission gases. If the pores can be retained during plate fabrication and irradiation, sol-gel U_3O_8 should be an attractive fuel for research reactors. The decision on whether or not it will perform adequately in HFIR must await results from irradiation experiments now being run.

Influence of Cladding Strength on the Void Volume and Dogboning of Composite Fuel Plates

M. M. Martin J. H. Erwin

We found that the type of cladding greatly affects the degree of dogboning and void concentration in the fuel core. Cores of 49 wt % burned U_3O_8 in aluminum were clad and framed with aluminum alloys 1100, 6061, and 2219 and rolled into miniature fuel plates. Average values for these important effects are shown in Table 20.4. The compressive strength of the cladding, shown in the last column of Table 20.4, is related to dogboning.[13] We estimate the compressive strength of the core to be between 2500 and 3100 psi. Dogboning and void concentration increase when weaker cladding materials are used. Thus, replacing type 6061 aluminum with stronger type 2219 on a fuel plate for the ATR, for example, would decrease the degree of dogboning at the core ends. However, since less void volume is available for the accumulation of irradiation-induced growth from gaseous fission products and solid fission fragments, the permissible burnup level may be reduced, as described in an earlier section of this chapter.

[13] J. H. Erwin, M. M. Martin, and W. R. Martin, "The Effect of Fuel Concentration on the Compressive Strength of Core Materials Used in Research Reactor Fuel Plates," *Trans. Am. Nucl. Soc.* 11(2), 490 (November 1968).

Table 20.4. Effect of Type of Cladding on Fabrication Voids and Dogboning in Fuel Plates Containing 49 wt % Burned U_3O_8-101 Al Cores

Aluminum Cladding Alloy	Fabrication Voids (vol %)	Maximum Dogboning[a] (%)	Compressive Strength of Cladding at 500°C for 5% Deformation (psi)
1100	10.9 ± 0.1	130	1000
6061	7.9 ± 0.2	113	1900
2219	6.0 ± 0.2	104	2300

[a]Determined from measurements of x-ray attenuation.

Fit of Fuel Compact to Frame Cavity

M. M. Martin J. H. Erwin W. R. Martin

The dimensional fit between the fuel compact and aluminum frame may be altered by vacuum degassing of compacts after pressing. We investigated the effects of various dimensional misfits on final plate quality and fabrication parameters.

We fabricated dispersion fuel plates containing either 46 wt % U_3O_8 or 52 wt % UAl_3, using the fuel compact dimensions and procedures reported previously.[14] The compacts were clad with type 6061 aluminum by rolling at 500°C to a total reduction in thickness of 89.6% (the last 20% at room temperature). After roll bonding, the plates were annealed at 500°C and then inspected for (1) visual and ultrasonic indications of nonbonds, (2) fuel-core dimensions, and (3) x-ray attenuation indications of excessive fuel concentrations near the core ends. We interpret the latter inspection as an indication of dogboning.

The largest openings between the frame and compact were, respectively, 0.087, 0.106, and 0.013 in. for the length, width, and thickness. Surprisingly, no plate exhibited a blister or ultrasonic nonbond that could be attributed to the misfit between the frame cavity and compact. We conclude that, within the range investigated, blistering in these plates is independent of the degree of fit between the frame cavity and fuel compact.

The x-ray attenuation measurements indicated little fuel-core thickening (dogboning) near the ends of the rolled dispersions. As shown in Table 20.5, the values for plates containing U_3O_8 were consistently less than 15%; one UAl_3-bearing plate exhibited dogboning greater than 30%. The degree of core thickening, however, appeared to decrease with decreasing fit ratios of compact to cavity. Decreases in core thickness decreased the core width but changed core length little. A decrease in core width or length had little effect on

[14] J. H. Erwin and M. M. Martin, *Fuels and Materials Development Program Quart. Progr. Rept. Sept. 30, 1968*, ORNL-4350, pp. 265–70.

Table 20.5. Effect of Fit of Compact to Cavity Upon the Degree of Core Thickening and Spread in U_3O_8- and UAl_x-Bearing Fuel Plates

Variable		Degree of Core Thickening,[a] %		Spread During Rolling, %	
Changed Dimensions	Fit Ratio, Compact/Cavity	46 wt % U_3O_8 Cores	52 wt % UAl_x Cores	46 wt % U_3O_8 Cores	52 wt % UAl_x Cores
Thickness	1.050	0	22	3.8	3.4
	1.000	*b*	18	3.2	3.7
	0.950	*b*	15	2.6	2.1
Length	1.010	15	25	3.8	3.4
	0.995	*b*	18	3.2	3.2
	0.960	*b*	0	3.2	3.3
Width	1.010	*b*	35	3.3	3.0
	0.995	*b*	<15	6.2	5.3
	0.960	*b*	0	6.2	5.3

[a]Based on x-ray attenuation measurements.

[b]Dogboning was always less than 10 to 15%, and exact numbers were not determined.

the opposite dimension, but the spread increased with decreasing width, while the elongation showed little effect from core length variations. As expected from consideration of the volume of matrix available for deformation, the U_3O_8-aluminum compacts widened and elongated slightly more than the UAl_3-aluminum dispersion of similar uranium content. Flaking of fuel particles beyond the core ends, which were essentially square, was not observed in radiographs of the plates.

This study did not slow the blister problem to be singularly dependent upon the misfit between compact and frame. Misfit did affect the degree of core spreading during rolling. Dogboning was less for plates containing U_3O_8 than for plates containing UAl_x and appeared to depend somewhat upon the misfit.

Compatibility of Burned U_3O_8 and Aluminum Matrix During Fabrication

M. M. Martin J. H. Erwin

To further define the fabrication characteristics of burned U_3O_8, we investigated its chemical compatibility with Alcoa 101 aluminum at fabrication temperatures of 500, 525, 550, 575, and 600°C. Individual blends of Al–49 wt % U_3O_8 powders were pressed at 30 tsi to 91%-dense compacts, which were then degassed for 2 hr at their intended fabrication temperatures. The degassing operation caused less than 2% growth in any of the pressed compacts.

After the degassing operation, the compacts were sealed in type 1100 aluminum alloy by roll bonding to a total reduction in thickness of 87.5% at the degassing temperature (the last 20% at room temperature). We chose type 1100 aluminum alloy so that we could examine the compatibility at 550 and 600°C without the eutectic melting that may occur in types 6061 and 2219 alloys. Two final heat treatments at the same temperatures at which each compact was degassed were for 3 and 93 hr in air.

The above fabrication scheme did not densify the degassed compacts. The void volume retained by the core of 10.9 vol % was also independent of the fabrication temperature and duration of the final anneal. Fabrication temperature is probably an insignificant variable because, in the temperature range of these tests, the strength of the type 1100 alloy is very low and does not vary much with temperature.

Sections of the fabricated plates were polished and examined visually and with the aid of an electron probe for evidence of reaction between the fuel and matrix or cladding. The burned U_3O_8 fuel particles were completely compatible with the matrix and cladding at all fabrication temperatures.

After fabrication, the miniature fuel plates appeared sound and showed no evidence of blistering. Metallographic examination of the compatibility sections revealed no evidence of nonbonds between the core and cladding. Interfacial grain growth exceeded 85%. But ultrasonic inspection, in reference to a $^1/_{16}$-in.-diam flat-bottom hole in a HFIR standard, indicated gross nonbonds over the entire area of the core. For this inspection, we feel that the HFIR standard containing high-fired U_3O_8 is a poor reference for plates containing burned U_3O_8. The extensive fragmentation of the burned U_3O_8 fuel particles in conjunction with the increased amount of core void volume in these experi-

mental plates must account for the increased level of ultrasound attenuation.

Characterization of Electrolessly Deposited Nickel Coatings

M. M. Martin J. H. Erwin

Miniature fuel plates electrolessly coated with Ni-P alloy have been fabricated and shipped to the ETR for irradiation testing in the G-12 loop during cycle 102. We are investigating the performance in-reactor of an electroless nickel coating technique for fuel plates clad with both 6061 and 2219 aluminum alloys. Our goal is to reduce the temperature drop that occurs across the 0.001- to 0.002-in.-thick oxide film on aluminum-clad fuel plates. The innovation in the new technique developed at ORGDP is in the procedure for initial cleaning of the aluminum that permits the electroless deposition of a tightly adhering coating of nickel alloyed with 7 to 8 wt % P without a precoating of Zn or Cu. Figure 20.10 shows the as-plated deposit on the two aluminum alloys. Table 20.6 describes the plates to be irradiated. The thickness of Ni-P alloy on each major surface of the plates is 0.0005 to 0.0007 in.

The electrolessly plated nickel is nonmagnetic but becomes magnetic after 72 hr at 300°C. Its electrical resistivity is about 105 ± 5 μohm-cm at 25°C, which corresponds to a calculated electronic thermal conductivity of 0.065 w cm^{-1} $°K^{-1}$. This is a high thermal conductivity in comparison to Griess'[15] value of 0.022 w cm^{-1} $°K^{-1}$ for alumina formed on unirradiated aluminum in corrosion test in hot water. If the Ni-P alloy is stable and remains intact in-reactor, the temperature drop across the alumina film on aluminum-clad fuel plates could be reduced by a factor of 6 with electrolessly deposited nickel coating.

The nickel coatings electrolessly deposited on both 6061 and 2219 aluminum alloys resisted spalling from thermal shock treatments. However, the coating on specimens heat treated 48 hr in argon spalled completely when heated at 500°C but were intact after a similar treatment at 300°C. X-ray diffraction analysis revealed only Al_3Ni_2 on the side of the spalled flakes that had contacted the two aluminum-base alloys. On the opposite side, only NiO was identified. Many diffraction lines from both sides of the flakes, however, have defied identification.

[15] J. C. Griess, H. C. Savage, and J. L. English, *Effect of Heat Flux on the Corrosion of Aluminum by Water. Part IV. Tests Relative to the Advanced Test Reactor and Correlation with Previous Results*, ORNL-3541 (February 1964).

Table 20.6. Miniature Test Plates for Irradiation to Test Nickel Phosphide Coating[a]

Plate Reference Number	Cladding	Average Thickness of Nickel Coating (in.)	
		Calculated[b]	Eddy-Current Techniques
		$\times 10^{-3}$	$\times 10^{-3}$
0-68-1628[c]	6061 Al, Ni coated	0.62	0.61
-1636	6061 Al, Ni coated	0.60	0.64
-1643	2219 Al, Ni coated	0.59	0.66
-1635	6061 Al		
-1630[c]	6061 Al, Ni coated	0.65	0.72
-1638	6061 Al, Ni coated	0.62	0.67
-1642	2219 Al, Ni coated	0.59	0.68
-1633	6061 Al		

[a] All plates contain 2.45 g ^{235}U–49.4 wt %.
[b] Calculated from weight and density change after plating.
[c] Instrumented plates.

When viewed at 500X under bright-field illumination, the spalled flakes of nickel are composed of two layers of single-phase materials. Such layers were not observed in the coatings that were not heat treated or in those heat treated at 300°C, but these coatings also appeared to be single phase. Irrespective of the heat treatments, the electron probe distinguished two layers in the coatings on the two aluminum alloys.

PLATE SURFACE STUDIES

J. V. Cathcart

Corrosion of aluminum-clad fuel elements in HFIR-type reactors is a problem because corrosion product on the surfaces of the fuel elements creates a heat transfer barrier and thereby limits the fuel loading. Our purpose was to develop a thin anodic oxide coating to protect from further corrosion.

Our efforts were divided between isothermal screening tests in static water at 200°C and 225 psi and flowing loop tests with a very high heat flux across the oxide-water interface. The former tests with primarily 99.999% Al specimens were designed in many instances to elucidate reaction mechanisms. The latter tests were made with 6061 or 1100 alloy specimens and were basically engineering tests under simulated reactor conditions.

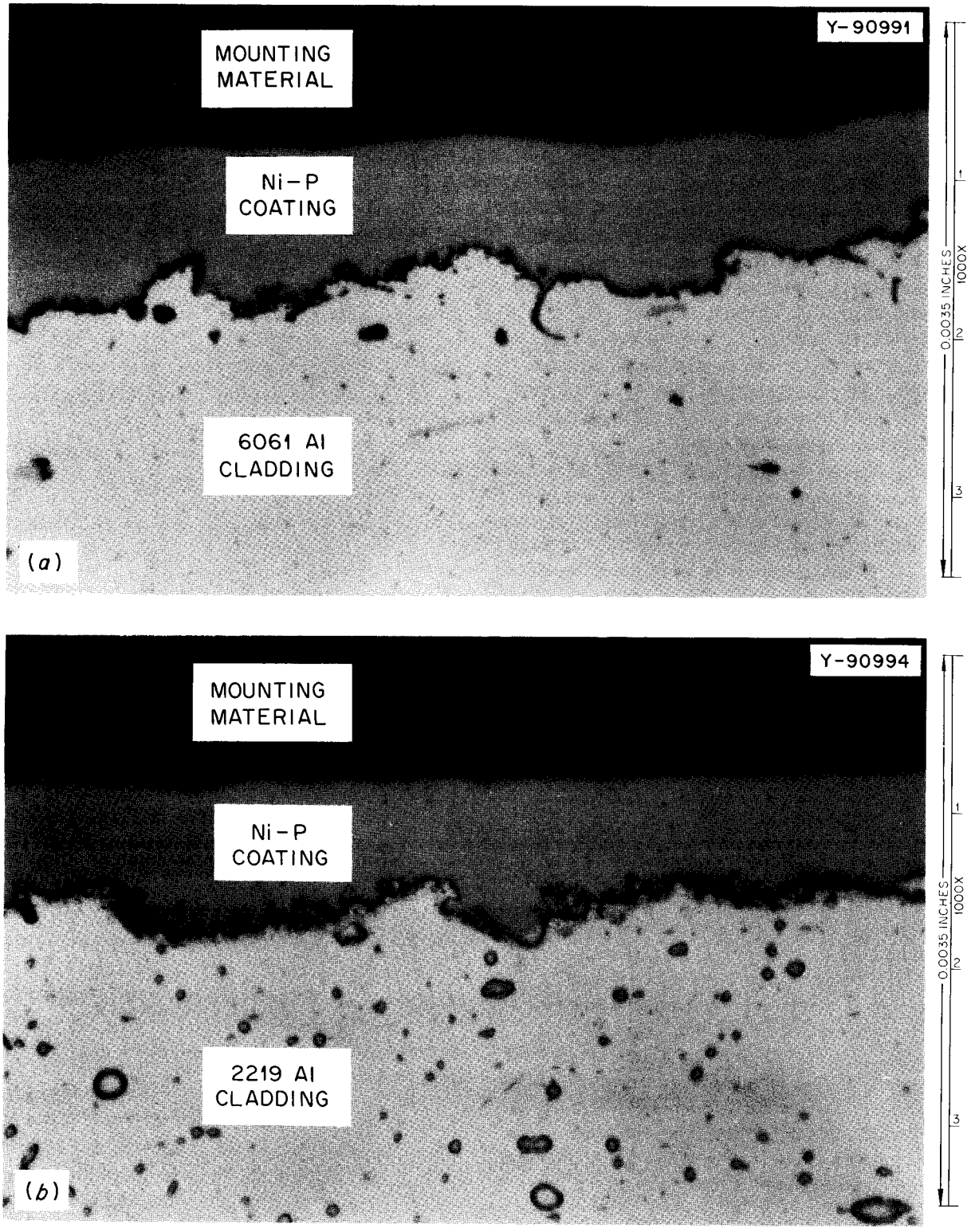

Fig. 20.10. Electrolessly Deposited Nickel-Phosphorus Alloy on (*a*) 6061 and (*b*) 2219 Aluminum Alloys. As polished.

Our previous work[16] showed anodic films formed in oxalic acid baths to protect pure aluminum under the conditions of our screening tests. Also films formed at 4°C were more protective than those produced at room temperature. Further electron microscopy revealed that a probable cause is related to the changes in the shape or distribution of pores that form in the films. Figure 20.11 shows cross-sections of anodic films formed at 4 and 25°C in oxalic acid. Note that the pores in the 25°C film appear longer and more interconnected. Presumably the bottoms of the pores are more accessible in the 25°C film, and, hence, these films are less protective.

We also studied the properties of films formed in an anodizing bath containing 38 g titanium potassium oxalate, 1.2 g citric acid, and 1.0 g oxalic acid per liter of water. They appeared tougher and more elastic than those formed in oxalic acid and hence should better withstand the strain gradients under high heat flux. Static tests showed these films to be at least as protective as low-temperature films formed in oxalic acid. Again, this behavior appears to be tied to the pore structure of the films, the pore spacing being smaller than that for the room-temperature oxalic acid films.

We dynamically tested 6061 and 1100 aluminum in the flowing loop system designed by Griess.[15] The interface was at about 200°C, and the heat flux across it was 10^6 Btu hr^{-1} ft^{-2}. Before testing, the interior of the test section of each of three loops was coated with an anodic film 0.0005 in. thick. The first two loops were anodized in an oxalic acid bath at 16 and 4°C and the third loop was anodized in the titanium potassium oxalate bath described above.

All three loops were operated for about five days. The corrosion rates were essentially the same and indistinguishable from that of an uncoated specimen. Electron microscopy showed only the dense, essentially featureless layer of corrosion product formed during loop operation and no remnant of the anodic film. This fact and the lack of improvement over uncoated loops

[16] J. V. Cathcart, *Metals and Ceramics Div. Ann. Progr. Rept. June 30, 1968,* ORNL-4370, pp. 111–15.

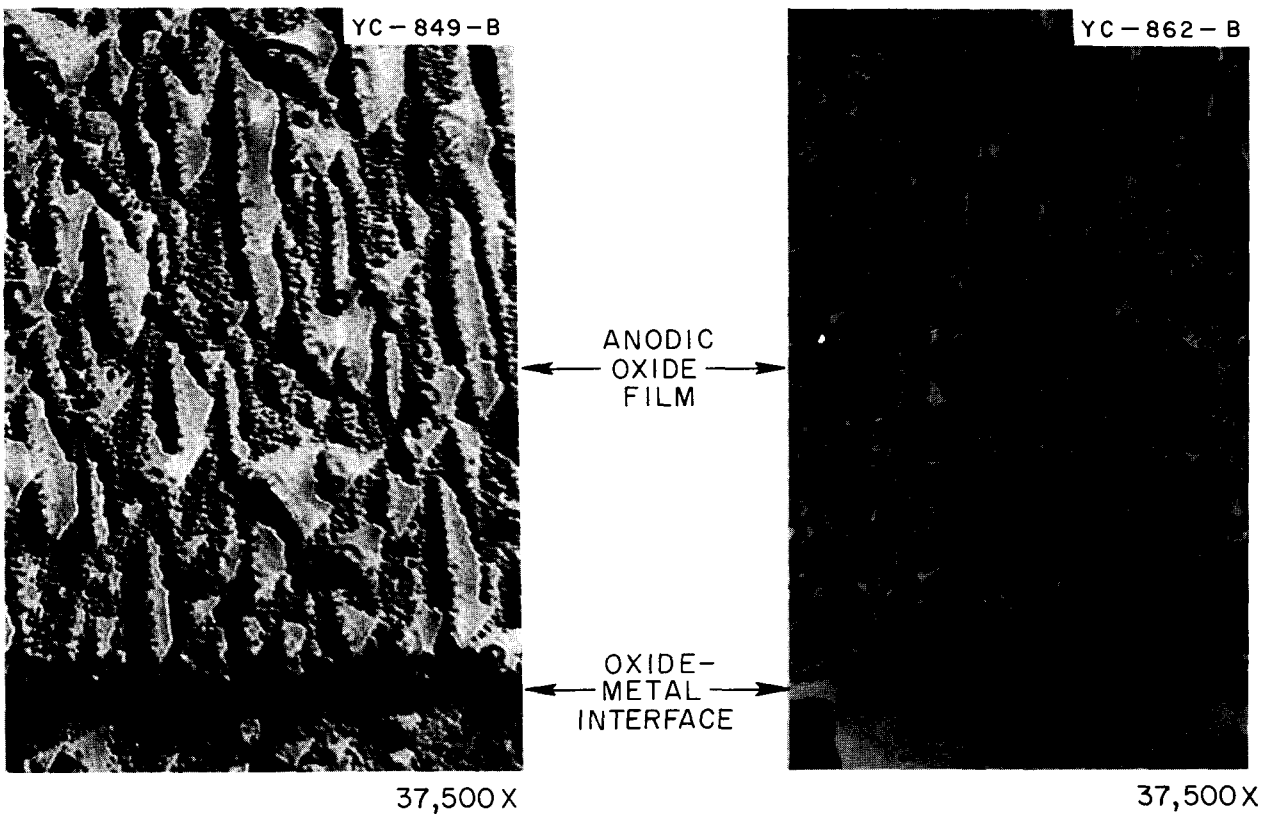

Fig. 20.11. Indirect Replica of Cross Sections Through Anodic Oxide Films Formed on 99.999% Al in 1 wt % Oxalic Acid. (*a*) Formed at 4°C. Note the short, disconnected pores in the film. (*b*) Formed at 25°C. Note the comparatively long, uninterrupted pores in the film.

suggest that the thermal shock accompanying the heating of the loop may have caused the anodic film to spall off early in the test. It is clear, however, that the detailed reasons for the breakdown of the anodic films are still not fully understood.

From these tests, we arrive at the following conclusions. (1) The anodic films tested did not effectively inhibit corrosion of aluminum alloys under dynamic test conditions with a high heat flux across the specimen surface. For this reason this phase of the program had been terminated. (2) Anodic films can protect 99.999% aluminum specimens for periods in excess of 1000 hr under isothermal conditions in static water at 200°C. While lacking engineering applications, the technique could be useful where the protection of high-purity aluminum components is important.

JOINING OF FUEL ELEMENT COMPONENTS

G. M. Slaughter

Fuel-Plate-to-Side-Plate Electron-Beam Welding Development

W. J. Werner R. W. Knight

We are investigating electron-beam welding as an improved method for attaching fuel plates to side plates for aluminum fuel elements. Most of our work had been aimed directly at the HFIR, since it already uses an all-welded element. It should be emphasized, however, that this work is also directly applicable to conventional fuel elements such as for the ETR, ATR, and MTR, since side plate thicknesses, slot depths, and fuel plate thicknesses are much the same as those for the HFIR.

A 30-kv Brad Thompson low-voltage electron-beam welder was obtained for this program and is currently operative. The limited access to the inner side plate of the HFIR inner annulus poses a particularly challenging problem, and as a result our investigations have been conducted with the miniature electron-beam gun especially designed and constructed for this application.[17] Using the abnormally small gun-to-work distance available, we are systematically investigating the effects of variations in welding parameters on weld penetration and geometry. Of particular interest in these studies are: beam voltage, beam current, beam-focus current, and travel speed. The data obtained thus far indicate that suitable weld penetration can be obtained to secure fuel plates to side plates for the HFIR using either type 6061 or 2219 aluminum as the side plate material. Adequate penetration of the weld into the fuel plate is seen in Fig. 20.12. The weld was produced under the following conditions: beam voltage, 18 kv; beam current, 90 ma; focus current, 110 ma; travel speed, 20 in./min. We are now seeking a wider fusion zone at the fuel plate-side plate interface (for strength) by focusing the electron beam either above or below the working surface.

Spacer Attachment by Explosive Welding

A. G. Cepolina[18]

There is incentive to consider the use of spacers for developing longer lived and more advanced fuel elements of the HFIR type or as a possible means of increasing the life of present HFIR fuel elements.

[17] A. G. Cepolina and G. M. Slaughter, *Metals and Ceramics Div. Ann. Progr. Rept. June 30, 1968,* ORNL-4370, pp. 190–91.

[18] Now with Italian Institute of Welding, Genoa.

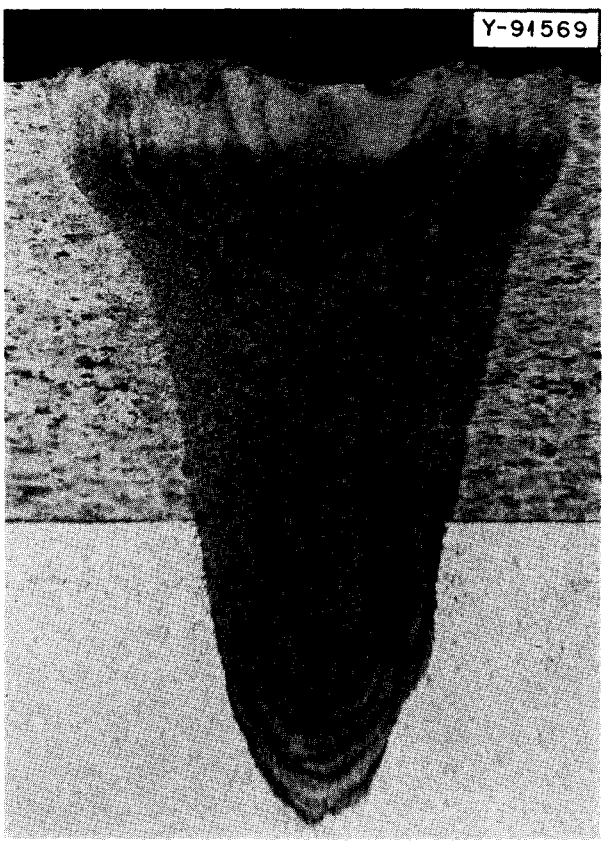

Fig. 20.12. Electron-Beam Weld Showing Adequate Penetration Into the Fuel Plate and Fair Width at the Interface Between Fuel Plate and Side Plate. Etchant: H_2O, HNO_3, HCl, HF. 20X.

Since explosive welding appears to be an attractive means for joining these spacers to the fuel plates, we arranged for Battelle Memorial Institute to make some preliminary feasibility tests. Three experimental samples were made in which 0.050- X 0.050-in. spacer ribs of type 6061 aluminum alloy were joined to 6-in.-long X 0.050-in.-thick fuel plates of type 6061 aluminum alloy.

The ribs were supported in an expendable die of cold-rolled plain carbon steel. The ribs were pressed into grooves so that they protruded 0.005 in. above the ground surface of the die. This protrusion allowed for the slight decrease in the height of the rib as it deformed laterally to fill the tapered side portions of the grooves during explosive welding.

The explosive,[19] Trojan T70C, was positioned over the plate. The assembly of explosive and plate was then positioned at the desired initial separation distance above the exposed surface of the ribs. The explosive was then detonated to drive the aluminum plate against the ribs with enough velocity to produce jetting and bonding between the plate and ribs.

Problems were initially encountered in removing the plate and ribs from the die and fixtures. After modifications, a successful rib-and-plate assembly was made on the third and last attempt. The interface between rib and plate is evident, but there are intermittent areas of bonding. We consider these preliminary results very encouraging and believe that the quality of the bond could be improved by further experimentation. The process looks attractive as a means for joining ribs to full-size plates. Because it appears desirable to use an expendable steel die, it probably would be most economical to perform the welding and plate forming in two separate operations. Of course, a modest development program would be required to scale up the process to production of full-size, composite fuel plates.

DEVELOPMENT OF DUCTILE DISPERSION-STRENGTHENED ALUMINUM

G. L. Copeland

The objective of this work is to improve the high-temperature ductility of dispersion-strengthened aluminum through alloy modifications. We have produced alloys containing the solid-solution strengthener magnesium up to 6% or the compound-forming elements Fe, Mo, Zr, Ti, and Cr up to 8% total. When atomized into water from the melt, the latter elements form small, well-dispersed compounds that contribute to the high-temperature strength. Several alloys were fabricated by ball milling atomized powders to increase the oxide content, consolidating the powder by hot pressing, and then hot forming into rods by extrusion at 30:1 reduction in area. The oxide content varied from less than 0.5 wt % for the atomized powders up to about 12 wt % after ball milling for several hours. Where the strength of the alloy prevented extrusion at 30:1, the alloys were extruded at 10:1 and then hot swaged to the total 30:1 reduction in area.

For alloys consolidated from the atomized powders with no ball milling, the addition of magnesium increased the strength markedly below about 200°C. Above this temperature, strength and elongation increased slightly. The alloys containing Fe, Mo, Zr, Ti, and Cr exhibited appreciably greater strengths even up to 450°C while maintaining good ductility. For instance, these alloys are about three times as strong at 300°C as the wrought alloy 6061 in the T6 condition.

For alloys consolidated from powder ball milled for 2 hr and containing 2 to 4% oxide, the magnesium additions increase the strength at temperatures up to about 200°C; above this temperature, both the strength and elongation are reduced somewhat. The alloys containing Fe, Mo, Zr, Ti, and Cr show increased strengths at all temperatures. The ductility is also improved at the higher temperatures. Both strength and total elongation at 450°C are about 50% higher for these alloys than for unalloyed aluminum of the same oxide content.

At oxide contents around 8.5 wt % the trends are the same. The strength and ductility increases due to the alloying elements are less dramatic at this strength.

For applications below about 200°C, the tensile strength of dispersion-strengthened aluminum can be enhanced by the solid-solution strengthening by magnesium addition. The room- and high-temperature strengths of $Al\text{-}Al_2O_3$ dispersions can be improved by using atomized alloy powders containing Fe, Mo, Zr, Ti, and Cr. The ductility for a given strength level is improved by these additions.

[19] A nitrostarch-ammonium-nitrate-base powder explosive manufactured by the Trojan Powder Company, Allentown, Pa.

21. Joining Research on Nuclear Materials

G. M. Slaughter

This program is concerned with obtaining a basic understanding of the weldability of materials commonly used in the fabrication of nuclear power plants. We have concentrated on nickel-containing alloys, since they have exhibited a strong tendency to crack during welding. Difficulties during welding have been encountered in weld metal and in heat-affected base metal, both at high temperatures (near the solidus) and at intermediate temperatures (about 650°C). The nickel contents under study vary from low percentages (about 8 to 10%) representative of stainless steels to high percentages (about 70 to 80%) representative of Inconel 600.

Our primary effort has been to determine the effects of minor quantities of such elements as C, S, P, Ti, Al, Mn, and Si on weldability. The effects of defects on the mechanical properties of weldments are also being investigated.

HEAT AFFECTED ZONE STUDIES

Ductility at High Temperatures

D. A. Canonico W. J. Werner

With the Duffer's Gleeble, we are studying the effects of small amounts of S, P, and Mn on the hot ductility of high-nickel alloys represented by the Inconel 600 class of material. Base-line compositions for this study are a ternary (Ni–16% Cr–8% Fe) and a "nominal commercial analysis" (Ni–16% Cr–8% Fe–0.03% C–0.04% Cu–0.20% Mn–0.20% Si). Neither composition contained intentionally added sulfur or phosphorus. We prepared 13 additional compositions containing sulfur to 0.012%, phosphorus to 0.015%, and manganese (in the presence of 0.009% S) to 0.84%. Hot ductility data were obtained during both heating and cooling for all 15 alloys. In addition to conventional exposure of the alloys to a peak temperature equal to their zero ductility temperature (ZDT), we also exposed them to a peak temperature of 2450°F, which is the ZDT of the nominal composition. The results of this study are summarized in Table 21.1. The results show that sulfur has a deleterious effect on the ZDT and on ductility, during both heating and cooling. Recovery of ductility is significantly impaired by >0.01% S.

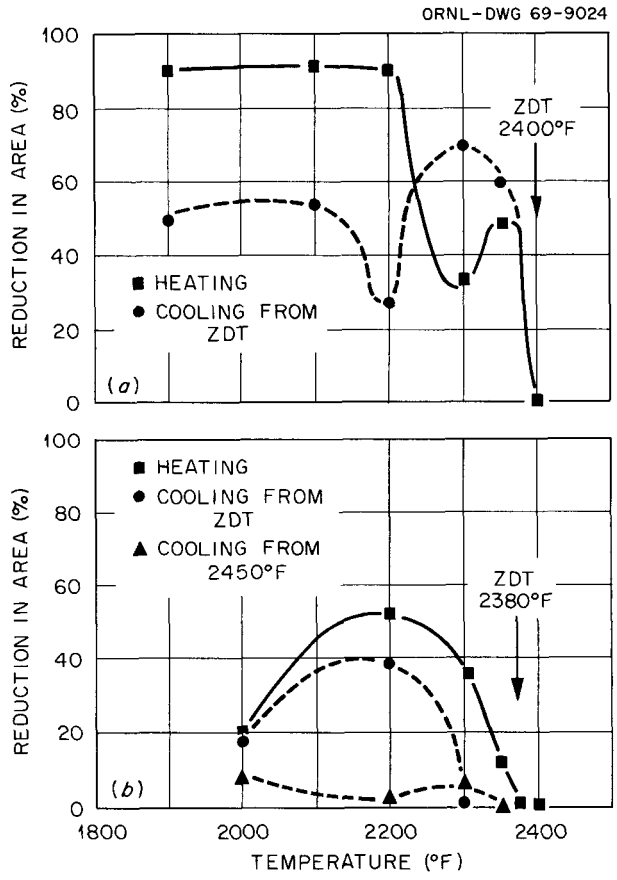

Fig. 21.1. Comparison of the Hot-Ductility Behavior of Two Nickel-Bearing Alloys with Similar Sulfur Contents. (*a*) Intermediate nickel alloy (800-11), Fe–33% Ni–21% Cr–0.31% Ti–0.015% S. (*b*) High-nickel alloy (600-5), Ni–16% Cr–8% Fe–0.012% S.

Previously, we reported[1] that sulfur (up to 0.015%) in the presence of 0.3% Ti did not have a detrimental effect on the ZDT of carbon-free alloys with intermediate nickel content (representative of Incoloy 800 class of material). This surprising fact was attributed to a titanium-sulfur association. Figure 21.1 compares previous data to those recently observed. The influence of sulfur in the presence of titanium in the Incoloy 800 class of alloy is minor; however, it is quite deleterious in the titanium-free Inconel 600 alloy. The sulfur is particularly detrimental in the Inconel 600 composition if the specimens are exposed to a peak temperature in excess of its ZDT. In the latter case, ductilities less than 10% exist at temperatures as low as 2000°F.

Phosphorus had only a minor effect on ductility of the high-nickel alloys, during both heating and cooling. The recovery of the composition containing 0.015% P was only slightly impaired. Compositions containing less phosphorus recovered ductility immediately, and the ZDT of alloy 600-7 was slightly increased.

Surprisingly, manganese in an alloy containing 0.009% S was not beneficial; indeed, a deleterious effect was indicated. Increasing manganese from 0.15% (alloy 600-4) to 0.84% (alloy 600-14) decreased the ZDT measurably and noticeably affected the alloy's ability to recover ductility, particularly after exposure to a 2450°F peak temperature. Addition of phosphorus to an alloy containing 0.008% S and 0.80% Mn (alloy 600-15) did not affect the recovery.

Ductility at Intermediate Temperatures[2]

W. J. Werner

Nickel-rich materials usually lose ductility in the temperature range 1400 to 1600°F. Since this condition can contribute to the cracking propensity of a weldment, we have undertaken a study of the effect of exposure to this temperature range.

A series of special Incoloy 800 alloys were prepared and tensile-tested to determine the effects of two intentionally added alloying elements, titanium and aluminum, and two residual elements, sulfur and phosphorus. The mechanical properties results were complemented by optical microscopy, transmission electron microscopy, and scanning electron microscopy.

On the basis of the tensile results shown in Fig. 21.2, the alloys were divided into two types. One type – containing titanium – exhibited an intermediate-temperature ductility minimum and was characterized by recrystallization and recovery of ductility at elevated

[1] D. A. Canonico and W. J. Werner, *Metals and Ceramics Div. Ann. Progr. Rept. June 30, 1968,* ORNL-4370, pp. 151–55.

[2] Based on M.S. Thesis, University of Tennessee, December 1968.

Table 21.1. Results of Hot-Ductility Tests on High-Nickel Alloys Representing the Inconel-600 Class of Material

Experimental Alloy	Amount of Minor Element (wt %)			ZDT (°F)	Ductility at 2300°F (%)		
					During Heating	During Cooling	
	S	P	Mn			From ZDT	From 2450°F
600-1	0.003	0.001	0.007	2450	96	99	99
600-2	0.002	0.002	0.11	2450	87	99	99
600-3	0.006	0.001	0.11	2450	87	94	94
600-4	0.010	0.002	0.15	2450	35	81	81
600-5	0.012	0.002	0.12	2380	37	0	6
600-6	0.002	0.006	0.23	2450	100	100	100
600-7	0.002	0.011	0.20	2500	100	15	91
600-8	0.002	0.015	0.17	2450	100	76	76
600-9	0.003	0.004	0.16	2475	85	88	99
600-10	0.003	0.006	0.17	2475	90	0	81
600-11	0.006	0.008	0.17	2450	76	70	70
600-12	0.009	0.002	0.32	2425	50	55	49
600-13	0.009	0.002	0.48	2425	53	9	9
600-14	0.009	0.002	0.84	2400	53	15	0
600-15	0.008	0.007	0.80	2400	40	8	33

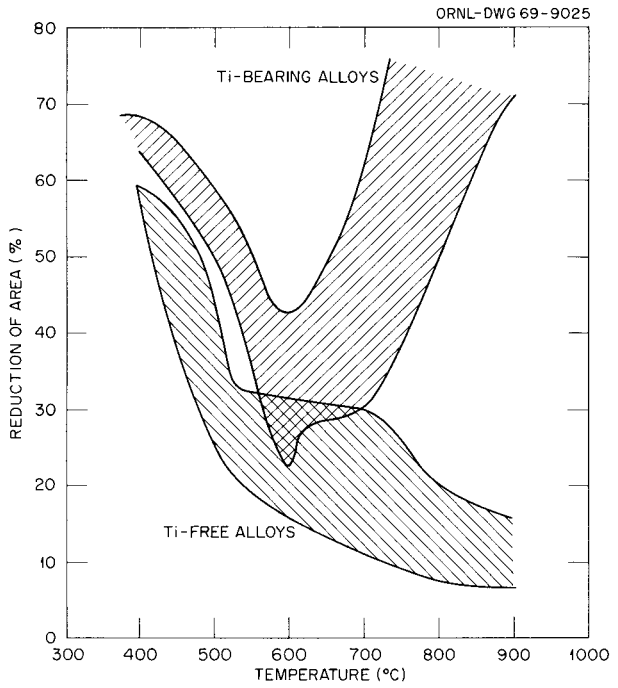

Fig. 21.2. Ductility of the Special Incoloy 800 Alloys as a Function of Testing Temperature.

temperatures. The other type – not containing titanium – exhibited a continuous decrease in ductility with increasing test temperature. It was characterized by (1) intergranular failure at temperatures of 600°C and above due to the propagation and linking of sharp, cracklike voids and (2) lack of recrystallization at all test temperatures.

The microscopy studies indicated that grain-boundary shear played a major role in the deformation of the second type of alloys, as can be seen in Fig. 21.3. In all cases the observations on intergranular void formation were consistent with Gifkins'[3] model for the nucleation of voids at jogs or offsets in sliding boundaries. Furthermore, the restoration of ductility in the titanium-bearing alloys at elevated temperatures can be attributed to the annihilation of jogs by recrystallization. The data suggest that one or more of the residuals present in the titanium-free alloys could have formed a grain-boundary film that impeded recrystallization or solution-hardened the grains to such an extent that insufficient grain deformation occurred to provide the driving force for recrystallization. Redistribution of the detrimental species by titanium compound formation appears to be responsible for the enhanced ductility of the titanium-bearing alloys at elevated temperatures.

[3]R. C. Gifkins, "A Mechanism for the Formation of Intergranular Cracks When Boundary Sliding Occurs," *Acta Met.* 4, 98 (1956).

WELD METAL STUDIES

The Effect of Minor Elements on the Hot Cracking of Inconel 600 (Ref. 4)

G. M. Goodwin

This investigation was undertaken to determine the effect of six minor elements, S, P, Si, Mn, Ti, and Al, on the hot-cracking propensity of Inconel 600. Utilizing a newly developed weldability evaluation test, the "TIGMAJIG," and a technique allowing the preparation of a large number of laboratory-scale specimens of systematically varied composition, the main effects and all interaction effects of the six intentionally added minor elements were measured in a full factorial experiment.

Sulfur and phosphorus were highly detrimental to hot-cracking sensitivity. The effect of these elements was attributed to a high degree of segregation and a subsequent reduction in the effective solidus and liquidus, coupled with a decrease in the solid-liquid interfacial energy, permitting wetting of the grain and subgrain boundaries and the subsequent formation of grain-boundary films.

Manganese and silicon both reduced the detrimental effect of sulfur, because, at least in part, of an increase in the solid-liquid interfacial energy. Also, both titanium and aluminum had beneficial effects on hot-cracking propensity. The effect of these two elements and, in part, the effect of manganese and silicon could be due to their excellent deoxidizing capabilities.

Studies on 18% Cr–8% Ni Stainless Steels

W. J. Werner D. A. Canonico

The preparation of special alloys for inclusion in this study has been discussed previously.[5] Our efforts have been centered on the preparation of stainless steel compositions in which the major element (Fe-Ni-Cr) contents have been suitably adjusted to produce weld-

[4]Work performed on subcontract under the direction of W. F. Savage, Department of Materials Engineering, Rensselaer Polytechnic Institute, Troy, N.Y. presented as Ph.D. dissertation, Rensselaer Polytechnic Institute, Troy, N.Y.

[5]W. J. Werner and D. A. Canonico, *Fuels and Materials Development Program Quart. Progr. Rept. Sept. 30, 1968,* ORNL-4350, pp. 252–54.

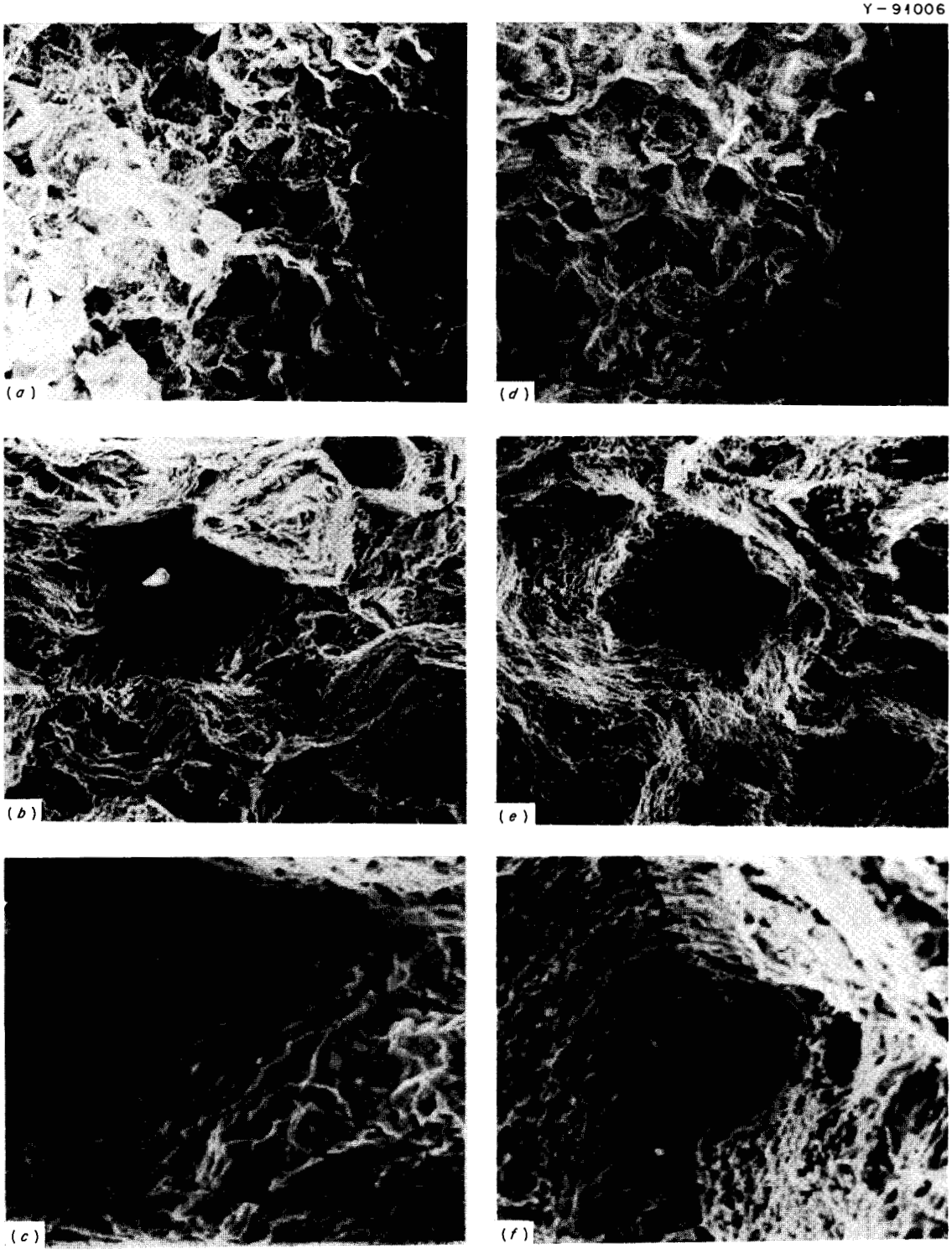

Fig. 21.3. Scanning Electron Micrographs of the Actual Fracture Surfaces of Representative Titanium-Free Alloys Tensile Tested at Approximately 700°C. Sulfur-bearing alloy; consecutive micrographs of the same field at (*a*) 100X, (*b*) 300X, and (*c*) 1000X. Ternary alloy; consecutive micrographs of the same field at (*d*) 100X, (*e*) 300X, and (*f*) 1000X.

metal microstructures containing various percentages of ferrite (for the prevention of hot cracking) in an austenite matrix. The alloy compositions were selected to provide ferrite levels from 0% (100% austenite) to nearly 40% using the Schaeffler diagram[6] as a guide.

These alloys (type 308L stainless steel) have been melted and fabricated into $\frac{1}{8}$-in.-thick sheet. Excellent control was obviously maintained in melting these alloys since the nominal and actual chromium and nickel equivalents (which determine ferrite content) are very close (Table 21.2).

The quantitative television microscope (QTM) was employed to determine the ferrite content in wrought and welded samples of each composition. Weld metal samples consisted of gas tungsten-arc bead-on-plate fusion welds (no filter metal addition) made at a welding current of 150 amp with a $\frac{1}{8}$-in.-diam electrode, an electrode-to-work distance of $\frac{1}{8}$ in., and a travel speed of 9 in./min. We found significant differences in the amount of δ-ferrite between that predicted by the Schaeffler Diagram and the actual wrought and weld metal samples. The measured and predicted ferrite values are included in Table 21.2.

Further studies will seek to relate measured ferrite contents with the microstructures of the welds and the role of minor elements on weldability.

Effect of Defects on the Mechanical Properties of Weldments

C. D. Lundin[7]

This task was started to determine when a discontinuity becomes unacceptable. Discontinuities generally exist in structural components. The objective of this study is to characterize various discontinuities and establish their effect on the mechanical properties of the material being joined.

The program has been directed toward (1) production of discontinuities in weldments, (2) effect of welding parameters on the occurrence of discontinuities, (3) the nondestructive location and evaluation of discontinuities, (4) the characterization of discontinuities by surface topography with the scanning electron microscope, and (5) the mechanical testing of specimens containing discontinuities.

Discontinuities have been produced by electron-beam welding in Inconel 600 and type 310 stainless steel. The

[6]A. L. Schaeffler, "Selection of Austenitic Electrodes for Welding Dissimilar Metals," *Welding J. (N.Y.)* **26**, 601-s–20-s (November 1947).

[7]Consultant from The University of Tennessee.

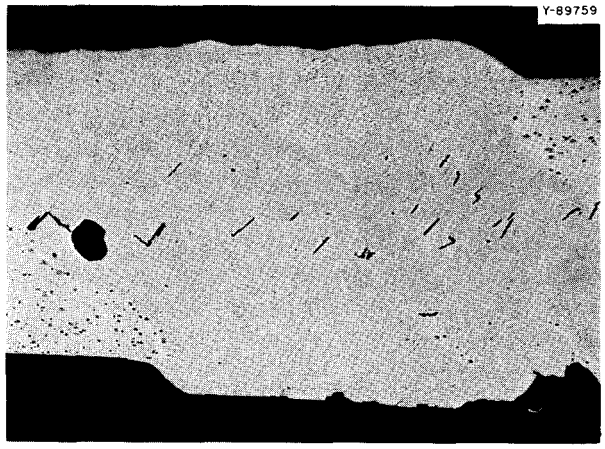

Fig. 21.4. Discontinuities in Multipass Inconel Electron Beam Weld. Etchant: HCl, H_2O_2. 26X. Reduced 48%.

Table 21.2. Chromium and Nickel Equivalents and Ferrite Contents of the Experimental Alloys

Alloy	Chromium Equivalent (%)		Nickel Equivalent (%)		Ferrite Contents (%)		
	Nominal	Actual	Nominal	Actual	Predicted[a]	Wrought	Weld Metal
1	19.5	19.3	9	9.1	13	3.7	2.4
2	19.7	19.5	13.2	12.5	4	7.7	10.2
3	23.7	23.2	13.2	12.9	13	15.2	9.7
4	23.2	23.2	9	9.1	38	16.4	5.1
5	19.5	19.5	9.9	9.6	12	8.1	2.4
6	21.2	20.4	9	8.6	30	7.8	7.8
7	20.8	20.4	13.2	12.8	6	8.0	9.9
8	23.0	23.2	9.9	9.8	30	11.7	3.0

[a]From Schaeffler diagram and actual chromium and nickel equivalents.

orientation of the discontinuities can be varied by changing the angle at which the electron beam penetrates the material. Figure 21.4 shows discontinuities produced at high welding speeds in $^1/_8$-in. Inconel 600 alloy. The electron beam was oriented at 45° to the sheet surface in this case. Discontinuities were also produced in type 310 stainless steel under the identical welding conditions, but none were found in the type 304 stainless steel welds. As the welding speed was decreased (larger weld), the incidence of discontinuities decreased.

The welds were inspected by x-ray and ultrasonic nondestructive techniques. The x-ray characterization of the discontinuities requires that the rough as-welded face and root of the weld be removed. Even then, the specimen must be oriented properly with respect to the x-ray beam. The ultrasonic testing will be completed shortly.

Characterization of the discontinuities by surface topography is in progress. Several significant findings have been made in the area of determining the mechanism of discontinuity formation.[8]

Specimens are being machined for mechanical test studies. These specimens will be examined before testing by whatever nondestructive technique proves to reveal the most information.

---

[8]C. D. Lundin, *Fuels and Materials Development Program Quart. Progr. Rept. Mar. 31, 1969,* ORNL-4420, pp. 209–10.

22. Nondestructive Test Development

R. W. McClung

This program is designed to develop new and improved methods of examining reactor materials and components. To achieve this we study the pertinent physical phenomena, develop instrumentation and other equipment, devise application techniques, and design and fabricate reference standards. Among the subjects being actively pursued are electromagnetics (with major emphasis on eddy currents), ultrasonics, and penetrating radiation.

ELECTROMAGNETIC INSPECTION METHODS

C. V. Dodd — J. W. Luquire[1]
W. E. Deeds[1] — W. G. Spoeri

We continued research and development of electromagnetic inspection methods on both analytical and empirical bases, with major emphasis on eddy currents.

Analytical Studies

We continued our analytical studies of eddy-current phenomena by deriving new equations, refining some of our older derivations, and writing computer programs to solve problems involving these phenomena and to study various cases of particular interest.[2,3] We wrote two reports[4,5] giving detailed derivations of a number of coil and conductor configurations, computer programs, and instructions on their use. The various configurations analyzed and computer codes written are summarized in Table 22.1.

We are applying these programs to study eddy-current problems of special interest, such as the response of eddy currents to defects in tubes, and determining the optimum conditions for maximum sensitivity to a defect.[6,7] In addition we are performing experimental measurements to verify and aid in our study of defects.[8]

We are also using these programs to improve the performance of the phase-sensitive eddy-current instrument by determining optimum operating conditions for maximum sensitivity and minimum lift-off effect.[8]

Experimental Studies

We continue to develop better eddy-current probe coils. We have developed probes as small as 0.032 in. in diameter[7] and probes to operate from room temperature to 350°F with only small thermal drift.[6]

We are studying infrared methods of nondestructive testing, with most of the work being performed under a small subcontract with the University of Tennessee. A

[1] Consultant from the University of Tennessee.

[2] C. V. Dodd, W. E. Deeds, and J. W. Luquire, "Integral Solutions to Some Eddy Current Problems," paper at the 8th Symposium on Physics and Nondestructive Testing, Schiller Park, Ill., Sept. 24–26, 1968. To be published in proceedings of the meeting.

[3] C. V. Dodd, W. E. Deeds, J. W. Luquire, and W. G. Spoeri, "Analysis of Eddy-Current Problems with a Time-Sharing Computer," paper presented at the 28th Annual Conference of the American Society for Nondestructive Testing, Detroit, Mich., Oct. 14–17, 1968, and to be published in *Materials Evaluation.*

[4] C. V. Dodd, W. E. Deeds, J. W. Luquire, and W. G. Spoeri, *Some Eddy-Current Problems and Their Integral Solutions,* ORNL-4384 (April 1969).

[5] J. W. Luquire, C. V. Dodd, W. E. Deeds, and W. G. Spoeri, *Computer Programs for Some Eddy-Current Problems,* ORNL-TM-2501 (report in preparation).

[6] C. V. Dodd, J. W. Luquire, W. E. Deeds, and W. G. Spoeri,. *Fuels and Materials Development Program Quart. Progr. Rept. Dec. 31, 1968,* ORNL-4390, pp. 177–81.

[7] C. V. Dodd, J. W. Luquire, W. E. Deeds, and W. G. Spoeri, *Fuels and Materials Development Program Quart. Progr. Rept. March 31, 1969,* ORNL-4420, pp. 188–92.

[8] C. V. Dodd, J. W. Luquire, W. E. Deeds, and W. G. Spoeri, "Electromagnetic Inspection Methods," in *Fuels and Materials Development Program Quart. Progr. Rept. June 30, 1969,* ORNL-4440 (in preparation).

Table 22.1. Computer Programs Written for Solution of Equations of Eddy-Current Coil and Conductor Configurations

Configuration	Program Calculation
Coil in air	Coil inductance
Coil above a two-conductor plane	Normalized coil impedance Defect sensitivity factor for a defect in the cladding material Defect sensitivity factor for a lattice of defects in the cladding material Defect sensitivity factor for a defect in the base material Net eddy-current force exerted on a conductor
Reflection-type coil above a two-conductor plane	Magnitude and phase of induced voltage Phase shift of induced voltage with "lift-off" set Phase of induced voltage for a range of cladding thickness values with "lift-off" automatically set Change in magnitude and phase of induced voltage due to a defect in the cladding material Change in magnitude and phase of induced voltage due to lattice of defects in the cladding material Change in phase of induced voltage due to a lattice of defects in the cladding material with the "lift-off" set Change in magnitude and phase of induced voltage due to a defect in the base material
Through-transmission coils	Magnitude and phase of the induced voltage Change in magnitude and phase of induced voltage due to a defect in the plate between the coils
Coil between two conducting planes	Normalized coil impedance
Coil encircling a two-conductor rod	Normalized coil impedance Defect sensitivity factor for a defect in the outer material Defect sensitivity factor for a lattice of defects in the outer material Defect sensitivity factor for a differential coil system for a lattice of defects Defect sensitivity factor for a defect in the inner material
Coil inside a two-conductor tube	Normalized coil impedance Defect sensitivity factor for a defect in the inner material Defect sensitivity factor for a lattice of defects in the inner material Defect sensitivity factor for a defect in the outer material

recent paper from this program described the development of an infrared microscope.[9]

ULTRASONIC TEST METHODS

K. V. Cook H. L. Whaley

Fabrication of References

A major problem in inspecting materials is the establishment of realistic reference discontinuities. Our work with electrical discharge machining (EDM) is promising to be a reliable method for machining the necessary reference notches and holes in most of the materials we encounter. Thus, we are continuing to determine machining characteristics and reference curves as materials are made available. However, there are materials in which difficulties have been noted.[10] For instance, EDM generates microcracking in molybdenum-base alloys. We feel that microcracking in these materials may be minimized or eliminated by EDM in a controlled temperature environment. Therefore, we have designed, in cooperation with the General Engineering Division, a system that should allow EDM at various temperatures.

Silicone rubber replicas, measured by the differential-focusing optical method, continue to provide our most accurate method of establishing dimensions for internal reference notches or holes. However, it takes at least 4 hr for the rubber to harden. We wanted to observe the flatness of flat-bottomed holes without this delay and did so by using a dental impression compound,[11] which hardens in minutes. This work on fabrication of references has been partially funded by the High-Temperature Materials Program.

Optical Visualization of Ultrasound

We tested our mirror-type schlieren system[12] and confirmed expected improvements in operating characteristics. An ultrasonic research tank was designed and

[9] W. A. Simpson, C. C. Cheng, W. E. Deeds, and C. V. Dodd, "An Infrared Microscope System for the Detection of Internal Flaws in Solids," paper presented at the Spring meeting of the American Society for Nondestructive Testing, Los Angeles, March 10–13, 1969, and submitted for publication to *Materials Evaluation.*

[10] K. V. Cook and H. L. Whaley, *Metals and Ceramics Div. Ann. Progr. Rept. June 30, 1968,* ORNL-4370, pp. 129–31.

[11] Regular Permlastic, Kerr Manufacturing Company, Detroit, Mich.

[12] K. V. Cook and H. L. Whaley, *Fuels and Materials Development Program Quart. Progr. Rept. Sept. 30, 1968,* ORNL-4350, pp. 245–48.

fabricated for use with the system. This tank has improved optical characteristics and permits reproducible mechanical positioning of the samples.

Plans were formulated to apply the system to study the ultrasonic inspection of welds. Model welds with simulated defects were fabricated in Plexiglas, but problems have been encountered with poor adhesion in the "weld zone." Butt welds containing intentional defects are being fabricated from aluminum and steel plate for this study. We are investigating improved methods for recording the data to be obtained from the study of these samples.

Frequency Analysis

We applied our frequency analysis technique to study the radiation patterns of flat, focused, and collimated transducers of various frequencies and sizes. The results agree well with the Fresnel-zone theory and allow determination of several factors, including optimum transducer-to-specimen distance, location of focal points, effective transducer element size, and degree of symmetry of the radiation pattern. The system was also applied to study the frequency dependence of some important ultrasonic test variables, and an abstract of a report[13] on this investigation follows.

To increase our understanding of frequency effects in ultrasonic testing, we have developed a system to analyze the frequency content of reflected or transmitted ultrasonic pulses. The system is composed of commercially available electronic equipment and can be used with conventional ultrasonic instruments operating in either a contact or immersion mode. We have applied the system to examine the frequency effects of the following ultrasonic test variables: transducer type, instrument type, transducer positioning, tuning devices, and collimation.

PENETRATING RADIATION INSPECTION METHODS

B. E. Foster S. D. Snyder
T. Eck[14]

Radiation Attenuation Studies[15]

In our development of x-ray attenuation as well as in our studies of radiographic densitometry, it was often quite difficult to determine the correct curve for the many data points. We developed computer programs to provide representative curves in fifth-degree polynomial form by a least-squares fit.[16,17]

Radiation Scattering Studies

B. E. Foster S. D. Snyder

We have begun preliminary investigations into the use of Compton backscattered radiation from a 0.5-curie ^{241}Am source for measuring the thickness of the coatings or claddings on reactor components. The studies involve an on-axis unfocused collimator, shielding, detector, and associated instrumentation.[16-18]

---

[13] H. L. Whaley and K. V. Cook, "Ultrasonic Frequency Analysis," proposed paper for the 29th National Conference of the American Society for Nondestructive Testing, October 13–15, 1969, Philadelphia, and an ORNL-TM report is in preparation.

[14] Summer student sponsored by Oak Ridge Associated Universities.

[15] These studies are partially funded by the Aluminum Technology programs.

[16] B. E. Foster, S. D. Snyder, and T. Eck, *Fuels and Materials Development Program Quart. Progr. Rept. Dec. 31, 1968,* ORNL-4390, pp. 186–88.

[17] B. E. Foster and S. D. Snyder, *Fuels and Materials Development Program Quart. Progr. Rept. Mar. 31, 1968,* ORNL-4420, pp. 196–97.

[18] B. E. Foster and S. D. Snyder, "Penetrating Radiation and Holographic Inspection Methods," in *Fuels and Materials Development Program Quart. Progr. Rept. June 30, 1969,* ORNL-4440 (in preparation).

23. Research Reactor Core Improvement and Procurement Assistance

G. M. Adamson, Jr.

This program is aimed at assisting the AEC Division of Reactor Development and Technology in their management and procurement of fuel elements for research reactors. The program is divided into three tasks: (1) direct technical assistance to RDT, (2) adapting nondestructive testing techniques to dispersion-type fuel elements and understanding the application, and (3) solving technical or production problems encountered by the fuel element fabricators. This task adapts technical developments made under other programs to use with the specific geometries of the present large test reactors.

This program is closely integrated with related work on dispersion fuel elements reported in Fuel Element Fabrication Development, Chap. 20. During the year, some of the effort formerly supported under a HFIR fuel element development program was transferred to this task.

PREPARATION OF UAl_x FUEL PARTICLES

G. L. Copeland

The Advanced Test Reactor (ATR) specifications for UAl_x (a mixture of UAl_2, UAl_3, and UAl_4) fuel particles call for a particle size distribution of −100 mesh containing a maximum of 25 wt % −325 mesh. The uranium concentration is specified as 69 ± 3 wt %. The present production process involves arc-casting, breaking the cast buttons between the platens of a press, and then further comminuting with a jaw crusher, sometimes followed by a hammer mill. A significant cost factor is the fact that this process yields approximately 50 wt % −325 mesh material in the −100-mesh fraction, so approximately 33% of the finished product must be completely recycled.

We investigated several crushing methods in an attempt to improve the yield. The commonly used crushing devices such as ball mill, rod mill, hammer mill, jaw crusher, disk pulverizer, and even a hand mortar and pestle all yield about 50 wt % fines (−325 mesh) in the −100-mesh product. A fluid energy mill also did not work well on this material. The only device that improved yields is the roll crusher. We experimented with a crusher having two smooth 12-in.-diam rolls. Our initial experiments with UAl_x containing 69 wt % U yielded a −100-mesh product containing only 16% fines. However, this device revealed inhomogeneities in the as-cast material. Areas rich in aluminum were malleable and rolled into flakes that would not pass through the 100-mesh screen. Chemical analysis showed the uranium concentration to be 68.17, 70.01, and 69.75 wt %, respectively, for the +100, −100, +325, and −325 mesh fractions. An anneal at 600°C for 72 hr in argon homogenized the material and greatly decreased the amount of flakes produced. The uranium content was 69.04, 69.10, and 69.30 wt %, respectively, for the same size fractions. The resulting size distribution is shown in Table 23.1. About one-third of the flake material can be reduced to the usable size range by a hammer mill. This results in an overall process yield of 90%, and the 10% requiring recycle is oversize rather than undersize.

The amount of material that flakes can be reduced by increasing the uranium content. Table 23.1 shows that roll crushing UAl_x containing 73 wt % U gave only 80% usable material, with the 20% requiring recycle being excess fines. Further work indicates that the yield of 80% is typical of roll crushing UAl_x with uranium contents of 65 to 73 wt %. Yields of 85% and higher have been achieved only for recycle material that has been crushed, consolidated, and remelted, which was the case for the 69 wt % material in Table 23.1. The better yield for recycle material may be due to better homogeneity. The impurity contents do not appear to differ significantly from the original material. The greater typical yield of usable material justifies con-

Table 23.1. Results of Roll Crushing UAl_x

U.S. Standard Mesh	Size Distribution[a] (wt %)	
	69 wt % U[b]	73 wt % U
+100	14.82	2.58
−100 +140	23.48	23.41
−140 +200	24.92	21.12
−200 +325	16.30	16.30
−325	20.47	36.57
Total	99.99	99.98
Usable material for ATR[c]	85.2	81.1
Usable material after further crushing[c]	5.0	1.5
Total yield[c]	90.2	82.6
Amount of material for recycle	9.8	17.4

[a]Sieved 15 min on Ro-Tap.
[b]Material manufactured by consolidating and remelting previously crushed particles.
[c]Material passing 100 mesh with a maximum of 25 wt % passing 325 mesh.

sideration of the roll crusher for production of UAl_x fuel particles.

ROLL BONDING OF UNCLAD 6061 ALUMINUM

J. H. Erwin

Since it is becoming increasingly difficult to obtain type 6061 sheet and plate clad with type 1100 aluminum, we investigated chemical cleaning as a surface preparation in the roll bonding of 6061 aluminum. Plates 1/8 and 1/4 in. thick × 5 in. wide × 8 1/2 in. long were cleaned by a 2-min submersion in a 75°C bath of Oakite 160 followed by neutralization in cold 42% HNO_3 and rinsing in cold water. Five of the cleaned plates were stacked together and welded as an individual billet. Five such billets were heated to 500°C and rolled to reductions ratios of 4, 6, 10, 14, and 18. The bond produced at each reduction was evaluated by measurement of the interfacial grain growth found in the four interfaces of both transverse and longitudinal sections. The data are summarized in Table 23.2.

We conclude that bonds equal to the present reactor requirements can be accomplished with a 6:1 hot reduction of the chemically cleaned 6061 aluminum. However, the inconsistency shown by the bond obtained in the one interface at 18:1 reduction most likely represents an insufficient control over the cleaning process. We are presently investigating the limitations of the standardized cleaning procedure.

Table 23.2. Interfacial Grain Growth in Five-Ply Billets of Type 6061 Aluminum Rolled to Five Different Reduction Ratios[a]

	Interfacial Grain Growth (%)				
	4:1	6:1	10:1	14:1	18:1
Transverse view of interfaces[b]	84.6	91.4	91.9	99.3	96.2
	79.4	86.8	89.4	98.3	96.1
	67.3	73.2	85.8	90.8	95.5
	59.9	69.4	84.0	88.7	60.0
Longitudinal view of interfaces[b]	80.6	88.7	93.3	97.9	98.1
	75.8	88.5	90.6	97.2	94.8
	45.7	88.1	78.8	95.9	93.4
	43.4	70.5	77.8	93.7	62.9

[a]All billets were reduced 25% per mill pass at 500°C.
[b]Percentages for the four interfaces in each five-ply billet are arranged in vertically descending order, from maximum to minimum values.

FABRICATION DEVELOPMENT OF MORE ECONOMICAL HFIR FUEL PLATE FUEL

M. M. Martin J. H. Erwin
R. W. Knight

We are investigating the fabricability of HFIR fuel plates containing increased fuel loadings to 25% for the outer annulus and 35% for the inner annulus with an ultimate goal to produce a fuel element that will have a longer operating life. Along with this increased loading, we are investigating the use of high-fired and burned U_3O_8 with varying particle size distributions; this is reported in Chap. 20. Burned U_3O_8 costs about one-half as much as high-fired, and if one is able to increase the permitted amount of −325-mesh material a further reduction in cost may be realized.

We have manufactured 48 full-size HFIR fuel plates; of these, 16 were fabricated using present materials and processes, 8 using burned U_3O_8 with present process loading, 16 with 125% loading of high-fired U_3O_8, and 8 with 125% loading of burned U_3O_8. The plates were divided equally between inner- and outer-annulus types. They were manufactured by the Metals and Controls, Inc., reference HFIR process. Pertinent data concerning these plates are shown in Table 23.3. Note that the void space is an average of 3% vol greater in the burned U_3O_8 plates and the average spread is 1% greater.

Although no problems were encountered during the fabrication of these plates, considerable work remains to be done with them before a manufacturing process can be established. New homogeneity standards must be made to inspect either the higher loaded fuel plates or

Table 23.3. Pertinent Attributes of Fuel Plates with Advanced Loading and Burned U_3O_8 Compared with Reference Process

Type of Plate	Location	Type of U_3O_8	Loading (g ^{235}U)	Spread (%)	Void (vol %)
Standard	Inner	Burned	15.19	4.0	5.2
		High fired	15.18	3.0	3.0
Advanced	Inner	Burned	20.28	3.9	6.7
		High fired	18.98	3.5	3.8
Standard	Outer	Burned	18.47	4.0	7.2
		High fired	18.44	2.2	4.2
Advanced	Outer	Burned	23.10	3.8	9.1
		High fired	23.05	3.3	5.4

any burned oxide fuel plates. New ultrasonic standards must be made for plates of comparable loading in fuel quantity and particle size to determine machine calibration and quality levels to which the plates can be inspected. Finally, plates of each kind must be formed to determine their forming characteristics and capabilities.

FABRICATION OF ATR FUEL PLATES

R. W. Knight M. M. Martin
J. H. Erwin

Fuel plates of ATR types 8 and 19 were fabricated to illustrate the effects of several variables on dogbone. The normal core specifications for these plates and reference data on dogbone have been reported.[1] All fuel plates were hot bonded at a 20% reduction per pass and cold rolled 20%.

Results of measurements of the dogbone in sections of the rolled plates and the plate variables are shown in Table 23.4. It appears that the best solution to reducing dogbone is to add aluminum to the core to reduce its strength. The thicker cores in the type 19 plates reduced dogbone. The addition of the 2219 aluminum insert gave a reduction in dogbone that may be beneficial, particularly on the type 19 plate. The effect of inserts on the type 8 plate may be insignificant. The use of inserts also reduced the average core thickness near the plate ends. The use of 2219 aluminum cover plates did little to reduce dogboning in the type 8 plate but appears to have reduced dogboning in the type 19 plate. Figure 23.1 shows sections taken from the middle of each end of each plate examined. Fuel plates that have the 2219 alloy cover plates developed cores with the fishtail shape, but no flaking was found.

DEVELOPMENT OF NONDESTRUCTIVE INSPECTION TECHNIQUES

B. E. Foster S. D. Snyder

Scanner Calibration Studies

We are establishing calibration curves of x-ray attenuation for various amounts of U_3O_8 in HFIR fuel plates and studying the effects of particle size on these calibrations. We have also investigated the use of x-ray energies slightly higher than our normal 50-kv constant potential to improve our sensitivity to fuel changes in plates with increased uranium loadings.[2] We have

[1] M. M. Martin, J. H. Erwin, and W. R. Martin, *Metals and Ceramics Div. Ann. Progr. Rept. June 30, 1968,* ORNL-4370, p. 162.

[2] B. E. Foster and S. D. Snyder, *Fuels and Materials Development Program Quart. Progr. Rept. Sept. 30, 1968,* ORNL-4350, pp. 287–89.

Table 23.4. Comparison of Core End Thickness with Average Core Thickness

Plate	Average Thickness (in.)	Maximum Thickening of Core (in.)	Maximum Thickening of Core (%)	Average Core End Thickness (in.)	Plate Characteristic
	0.0192	0.0301	157		Reference type 8 plate
973-1-8	0.0194	0.0268	138	0.0253	Cover plates one-half of normal thickness
975-3-8	0.0178	0.0268	155	0.0220	2219 Al inserts 0.203 X 2.060 X 0.206 in. at each end of core
975-4-8	0.206	0.0304	148	0.0265	2219 Al cover plates
	0.0201	0.0404	201		Reference type 19 plate
977-1-19	0.0337	0.0365	108	0.0349	Core twice normal thickness
976-3-19	0.0169	0.0212	125	0.0196	22.19 Al inserts 0.279 X 0.250 X 2.071 in. at each end of core
976-4-19	0.0202	0.0268	133	0.0238	2219 Al cover plates

PHOTO 96678

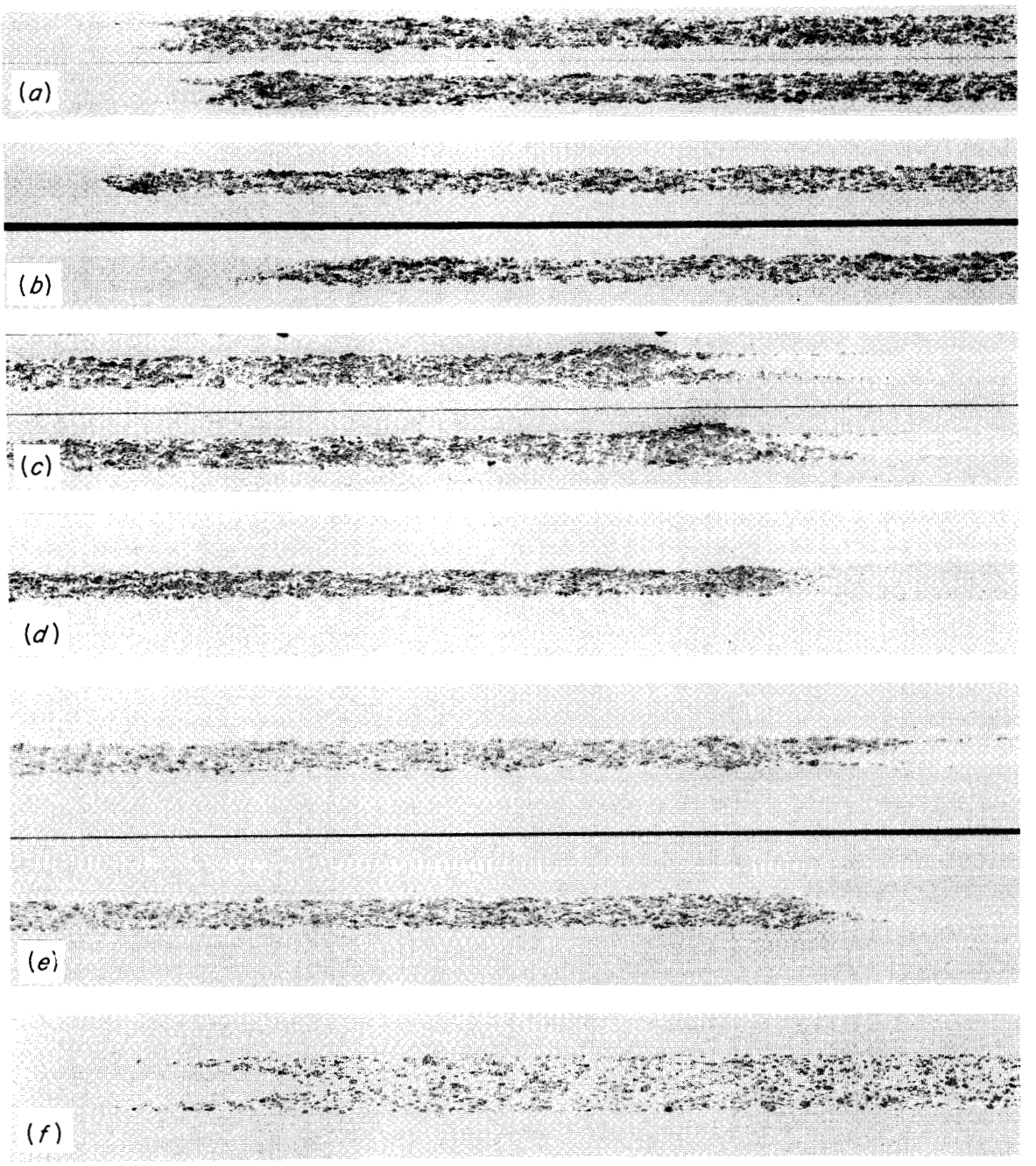

Fig. 23.1. Sections of Fuel Plates Showing End Effects from Different Billet Parameters: (*a*) Plate 973-1-8, (*b*) Plate 975-3-8, (*c*) Plate 975-4-8, (*d*) Plate 976-3-19, (*e*) Plate 976-4-19, and (*f*) Plate 977-1-19. 10X.

continued the efforts to resolve the original calibration of x-ray attenuation (uranium content related to attenuation) and present-day chemical analysis for uranium.[3–5]

Radiographic Densitometry

We continued our extensive study on the use of radiography and densitometry to determine the qualitative and quantitative capabilities and limitations of these techniques for detecting and measuring fuel inhomogeneity in fuel plates with dispersion cores. Much of our effort has been devoted to examining the many variables that can affect the density of radiographic film; for example, x-ray energy, exposure time, distance from film to focal spot, x-ray scattering, film processing, fog factor, densitometer-aperture size, and repeatability.[2,3] A report is being prepared including the data and conclusions of this work.

COST EFFECTIVENESS STUDY ON MODIFICATIONS TO HFIR FUEL ELEMENTS

J. I. Federer M. M. Martin

The cost effectiveness of increasing the loading of the HFIR fuel element from 9.4 to 12.0 kg ^{235}U was studied. This change would extend the element lifetime about 14 days to a total of about 37 days. As a result, the number of cores required for one year's operation would decrease from 14 to about 9. The savings in fuel element procurement, reprocessing, and increased production due to less refueling time would be about $400,000 per year. Nonrecurring costs involve fabrication development, criticality testing, and reactor testing of the first advanced element. Estimated savings of $3,500,000 to $4,000,000 would be obtained over a 15-year period if the advanced element were successfully developed. The time period includes about four years for development and for consumption of current elements in stockpile.

[3]B. E. Foster and S. D. Snyder, *Fuels and Materials Development Program Quart. Progr. Rept. Dec. 31, 1968,* ORNL-4390, pp. 259–66.

[4]B. E. Foster, S. D. Snyder, and R. W. McClung, *Fuels and Materials Development Program Quart. Progr. Rept. Mar. 31, 1969,* ORNL-4420, pp. 237–40.

[5]B. E. Foster, S. D. Snyder, and R. W. McClung, "Determination of Homogeneity in Fuel Plates," *Fuels and Materials Development Program Quart. Progr. Rept. June 30, 1969,* ORNL-4440 (in preparation).

The fabrication development involves simultaneous development of fuel and poison (B_4C) plates. Fabrication and irradiation testing of miniature fuel and poison plates would, if successful, be followed by fabrication development of full-size plates. The probabilities for success and failure and the related times and costs of the fabrication development were evaluated by means of the DECIDE computer program.[6]

HFIR FUEL ELEMENT MANUFACTURE

R. W. Knight

Assistance to Metals and Controls, Incorporated,[7] has continued throughout the past year. To date, 77 fuel assemblies have been delivered. Table 23.5 shows fuel element rejections by groups. None of the 77 fuel assemblies met all the specifications; however, it is significant that during this year four assemblies had no dimensional rejections. The fuel plate yields for plates in groups are presented in Table 23.6. These results show an improvement in yield of 0.35% over last year's total.

During the year, 57 approval requests were processed; of these 11 were submitted for fuel plate waivers. Waivers on 226 fuel plates were requested, 155 were approved for a yield of 68.58%; 32 approval requests were submitted for routine process and drawing changes, all were approved. Two approval requests were submitted requesting permission to try a process change on a limited number of fuel plates and two were

[6]F. T. Snyder, W. C. Stoddart, and P. E. Scott, *DECIDE, a Computer Solution of Probabilistic Networks to Aid Decision Making Involving Uncertainty,* ORNL-TM-2096 (January 1968).

[7]A division of Texas Instruments, Inc., Attleboro, Mass.

Table 23.5. Total Fuel Element Rejections by Groups

Group	Type	Numbers	Elements with Deviations	Total Deviations
1	Outer	1–12	12	88
	Inner		11	48
2	Outer	13–24	12	74
	Inner		12	35
3	Outer	25–36	12	92
	Inner		9	13
4	Outer	37–48	12	37
	Inner		7	18
5	Outer	49–60	11	35
	Inner		2	2
6	Outer	61–72	12	36
	Inner		3	3

Table 23.6. Fuel Plate Yield for FY-1968 and 1969

Reasons for Rejection	Plates Rejected[a]			
	FY-1968		FY-1969	
	Number Rejected	Percent	Number Rejected	Percent
Compacts	80	0.50	47	0.57
Surface	305	1.89	117	1.42
Bond defects	1713	10.61	483	5.85
Core location	155	0.96	69	0.84
Homogeneity	438	2.71	165	2.00
Dimensions	23	0.14	32	0.39
Form	1	0.01	2	0.02
Miscellaneous	24	0.15	22	0.26
Total	2739	16.97	937	11.35
Accepted on waiver	1520	9.42	343	4.15
Total rejected	1219	7.55	594	7.20

[a]During FY-1968 16,138 fuel plates were manufactured and during FY-1969 8256.

submitted giving the results of the process change. Four requests were submitted for major process changes: (1) to remove combs, (2) to increase the scratch depth from 0.001 to 0.003 in. on the fuel side of the fuel plate, (3) to increase the tolerance of troublesome fuel element dimensions in the unrestrained condition, and (4) to accept without waiver fuel plates with −12% homogeneity rejections. Of the four requests, (1) and (2) originated at ORNL and were approved by Reactor Operations, (3) was approved in part, and (4) was disapproved. The remaining approval requests were submitted for information only; one request for material certification and three requests to purchase items.

Approximately 225 kg of U_3O_8 was manufactured this year to provide material for continuing production of fuel elements. A second lot of 25 kg of burned U_3O_8 was manufactured to provide a research quantity of this cheaper material in hopes that it may eventually be used in HFIR fuel elements.

PROCUREMENT ASSISTANCE

R. J. Beaver G. M. Adamson, Jr.

A program was initiated in this fiscal year to assist the Phillips Petroleum Company, Idaho Falls, Idaho, in reviewing specification and procurement documents and assist in surveillance of the vendor selected to fabricate approximately 3000 fuel rods for the Power Burst Facility (PBF) and for the accompanying core structural components. This fuel consists of the pelletized mixture, 30 wt % UO_2 in stabilized ZrO_2, contained in tight-fitting stainless steel tubes. NUMEC, Apollo, Pennsylvania, was awarded the contract. Initial production is anticipated in August 1969. Assistance and review are also being provided in design and fabrication problems.

During the year we made several visits to both National Lead and to United Nuclear to assist AEC in reviewing progress on their ATR and ETR production contracts.

ORNL sponsored a two-day meeting to acquaint companies fabricating research reactor fuel elements with results of the development programs at Idaho Nuclear Company and ORNL. Seven companies or institutions, with 40 representatives, attended in addition to AEC, INC, and ORNL personnel.

Similar efforts for military reactors are reported in Chap. 31.

HIGH FLUX ISOTOPE REACTOR CONTROL ROD MODIFICATION

J. H. Erwin

Plates 122 through 131-0 were fabricated for HFIR outer control rods 10 and 11. These plates differ from the previous plates in that the billet assembly changes involving the tantalum region and the cover plate material[8] were incorporated. The unclad cover plate material produced blister-free plates that exhibited better than 60% interfacial grain growth between the cover plates and frame. The unbroken joints at the tantalum compact interfaces were not bonded sufficiently during rolling to avoid a loss of sound transmission in the nonbond inspection.

Radiant heating applied to the control plate after preforming stripped this plate free of the epoxy resin and back-up plate used for support during preforming. The clean separation obtained by radiant heating eliminated the laborious removal of epoxy from the outer surface of the control rod plates.

[8]J. H. Erwin, *Metals and Ceramics Div. Ann. Progr. Rept. June 30, 1968,* ORNL-4370, pp. 191–92.

24. Sol-Gel Fast Reactor Oxide Fuels

A. L. Lotts

The objective of this program is to obtain an economically optimized $(U,Pu)O_2$ fuel cycle for a liquid-metal fast breeder reactor (LMFBR) by extending the performance capability and advancing the fabrication technology of oxide fuels. These fuels have the most advanced technology and greatest potential for reliable operation in first-generation LMFBR's. They have been tested in fast-flux environments but have not yet been exposed under actual prototypic conditions. Currently, the burnup and heat rate are limited to about 50,000 Mwd/MT and 16 kw/ft, respectively, based on irradiation experiments with fuels that are not necessarily optimized for thermal, chemical, and mechanical performance.

The capability of oxide fuels can possibly be improved by adjusting structures or void distribution in the fuels. We emphasize irradiating fuels derived from the sol-gel process with thoroughly characterized structures and void distributions different from those of the oxide fuels irradiated heretofore. These include fuels fabricated by Sphere-Pac, vibratory compaction, extrusion, and pelletization. We compare the performance of these with that of reference fuels, such as pellets derived from mechanically blended powders and coprecipitated material. The development of mathematical methods to analyze test results and predict the performance of a fuel rod is integrated with the test program.

This is a joint program with the Chemical Technology Division, which prepares the sol-gel-derived fuel.

DEVELOPMENT OF FABRICATION PROCESSES

J. D. Sease

Fast reactors operating at high specific power will require fuel pins of small diameter with fuel ranging from 80 to 90% of theoretical density and a high fissile loading. Our work is to develop procedures for Sphere-Pac, methods for pelletizing and extruding, and procedures for fabricating irradiation capsules. This year the Sphere-Pac process was used with sol-gel fuel for a number of irradiation tests, and an engineering assessment of the Sphere-Pac process was begun. Methods for fabricating pellets with controlled density were developed and procedures for making irradiation capsules derived.

Sphere-Pac Development

W. L. Moore

The Sphere-Pac process involves the sequential loading of sol-gel microspheres into cladding. The principles of this process have been discussed previously.[1-3] Work this year has mainly involved setting up equipment for loading $(U,Pu)O_2$ fuel and the loading of capsules for irradiation in EBR-II, ORR, ETR, and TREAT. The binary particle beds for these experiments contained approximately 73% 420 to 590-μ coarse microspheres and 27% $<$ 44-μ fine microspheres. Smear densities ranged from 80 to 85% of theoretical. The fuel was 20% PuO_2 with either depleted or enriched UO_2. More details on the loadings are reported below under Irradiation Behavior.

We began an engineering evaluation of the Sphere-Pac process. Equipment for performing detailed time and motion studies of the process has been set up, and experimentation is now in progress.

---

[1] R. B. Fitts, A. R. Olsen, and J. Komatsu, *Metals and Ceramics Div. Ann. Progr. Rept. June 30, 1968,* ORNL-4370, p. 142.

[2] R. B. Fitts, A. R. Olsen, and J. Komatsu, "Sphere-Pac Fabrication of Sol-Gel Nuclear Fuels," Paper presented at the American Ceramic Society Nuclear Division Fall Meeting, Oct. 6–9, 1968, Pittsburgh, Pa.

[3] F. G. Kitts, R. B. Fitts, and A. R. Olsen, "Sol-Gel Urania-Plutonia Microsphere Preparation and Fabrication into Fuel Rods," *Intern. Symp. Plutonium Fuel Technol., Scottsdale, Ariz. 1967, Nucl. Met.*, vol. 13, 195–210 (1968).

Pellet Development

R. A. Bradley

The objective of this work is to develop methods of pelletizing sol-gel-derived $(U,Pu)O_2$ with controlled densities of 80 to 93% of theoretical and with an adjusted oxygen-to-metal ratio of 1.98.

Sol-gel pelletization begins by blending UO_2 and PuO_2 sols to obtain the desired ratio of plutonium to uranium.[4,5] The blended UO_2-PuO_2 sol is dried to a gel at 100°C and ground to −325 mesh. The powder particles, which have a porosity of about 50% and a surface area of 40 to 60 m^2/g, are tightly bonded agglomerates of intimately mixed UO_2 and PuO_2 crystallites. In this form, the powder contains about 5 to 7 wt % H_2O, excess oxygen, and small amounts of residual nitrate and formate. Although this powder can be used to make pellets, its very high surface area, high volatile content, and variable oxygen-to-metal ratio make it very difficult to consistently fabricate crack-free pellets of controlled density.[5] Therefore, we calcine the powder at 500 to 600°C to eliminate the volatiles, reduce the surface area to 5 to 20 m^2/g, and adjust the oxygen-to-metal ratio to about 2.2.

Properly selecting the calcining conditions leads to powder suitable for making either high- or low-density pellets.[6] To make low-density pellets, we calcined the powder by heating to 520°C in Ar–4% H_2, preserving the agglomerated nature of the material. To make high-density pellets, we oxidize the powder by heating to 520°C in air and then reduce it in Ar–4% H_2. This treatment breaks up the agglomerates, producing a powder that will yield 91%-dense pellets. In either case, the final step stabilizes the oxygen-to-metal ratio at about 2.2 by holding in CO_2 at 520°C for about 1 hr.

The powder is formed into pellets by uniaxially pressing without a binder at 25,000 to 50,000 psi. Pellets are sintered by heating in argon or Ar–4% H_2 at 300°C/hr to 1450°C and holding for 10 hr. The oxygen-to-metal ratio is adjusted to 1.98 by equilibrating in dry Ar–4% H_2 at 1450°C during the final 4 hr of the sintering cycle. We have had considerable difficulty in adjusting the oxygen content, but it can be done if the furnace system is tight enough to provide a sufficiently low water-to-hydrogen ratio in the furnace atmosphere.

We have prepared solid $U_{0.8}Pu_{0.2}O_{1.98}$ pellets for two TREAT irradiation capsules and are presently fabricating dished-end annular pellets for another capsule.

Next year we expect to investigate methods of fabricating pellets with controlled pore size, pore distribution, and grain size. We will also fabricate pellets for additional irradiation experiments.

Capsule Fabrication

R. B. Pratt M. K. Preston
W. L. Moore

We are fabricating capsules for fast fuels irradiation in ETR, EBR-II, TREAT, and ORR. This year we made five encapsulated sodium-bonded fuel pins for EBR-II and designed and fabricated two instrumented capsules for transient testing in TREAT.

The EBR-II capsule is shown schematically in Fig. 24.1. The most difficult step in fabricating these capsules was the sodium bonding of the fuel pin to the outer jacket. Procedures were developed for loading sodium containing less than 20 ppm O into the 0.040-in. gap, with voids and bubbles less than $^1/_{16}$ in. Details of the fabrication procedures and data are reported elsewhere.[7,8]

A TREAT capsule, depicted in Fig. 24.2, is instrumented, 3 in. in diameter × 9 ft long overall, and consisting of four primary components: fuel rod, inner capsule, heater, and pressure vessel. The fuel rod contains up to three ¼-in.-diam fuel sections for comparative testing. The inner capsule surrounds the fuel rod and contains an aluminum heat sink instrumented with six thermocouples and bonded with sodium to the fuel rod. The tubular heater, consisting of wire wound on a 1⅛-in.-diam stainless steel tube and insulated with fiber, contains six thermocouples and is used to bring the fuel cladding to simulated operating temperature before the power transient. The pressure vessel, made of AISI type 4130 steel, consists of a long cylindrical container with squared flanges and a short nosepiece that contains all necessary leads for power and thermocouples. During the next several years, we

[4] W. L. Moore and R. A. Bradley, *Fuels and Materials Development Program Quart. Progr. Rept. June 30, 1968,* ORNL-4330, pp. 7–8.

[5] R. A. Bradley, *Fuels and Materials Development Program Quart. Progr. Rept. Sept. 30, 1968,* ORNL-4350, pp. 5–7.

[6] R. A. Bradley, "Pellet Development," *Fuels and Materials Development Program Quart. Progr. Rept. June 30, 1969,* ORNL-4440 (in preparation).

[7] R. B. Pratt, M. K. Preston, R. A. Bradley, and W. L. Moore, *Fuels and Materials Development Program Quart. Progr. Rept. March 31, 1969,* ORNL-4420, pp. 7–10.

[8] J. D. Sease, W. L. Moore *et al., Fabrication of Sol-Gel Sphere-Pac Capsules for EBR-II,* report in preparation.

plan to fabricate a number of TREAT capsules. Initially, two capsules (TREAT I and II) were fabricated for irradiation testing this summer. More details of the TREAT capsule fabrication are reported elsewhere.[7,9]

The fuel element portions of ORR instrumented capsule SG-2 were fabricated and sent to the Y-12 Plant for insertion into the irradiation capsule. The fuel elements consist of two 3-in.-long annular pins clad in $^3/_8$-in.-OD titanium-modified type 304 stainless steel with a $^1/_8$-in.-diam central thermocouple well of W–26%

[9] M. K. Preston, R. B. Pratt, W. L. Moore, and R. A. Bradley, "TREAT Capsules," *Fuels and Materials Development Program Quart. Progr. Rept. June 30, 1969,* ORNL-4440 (in preparation).

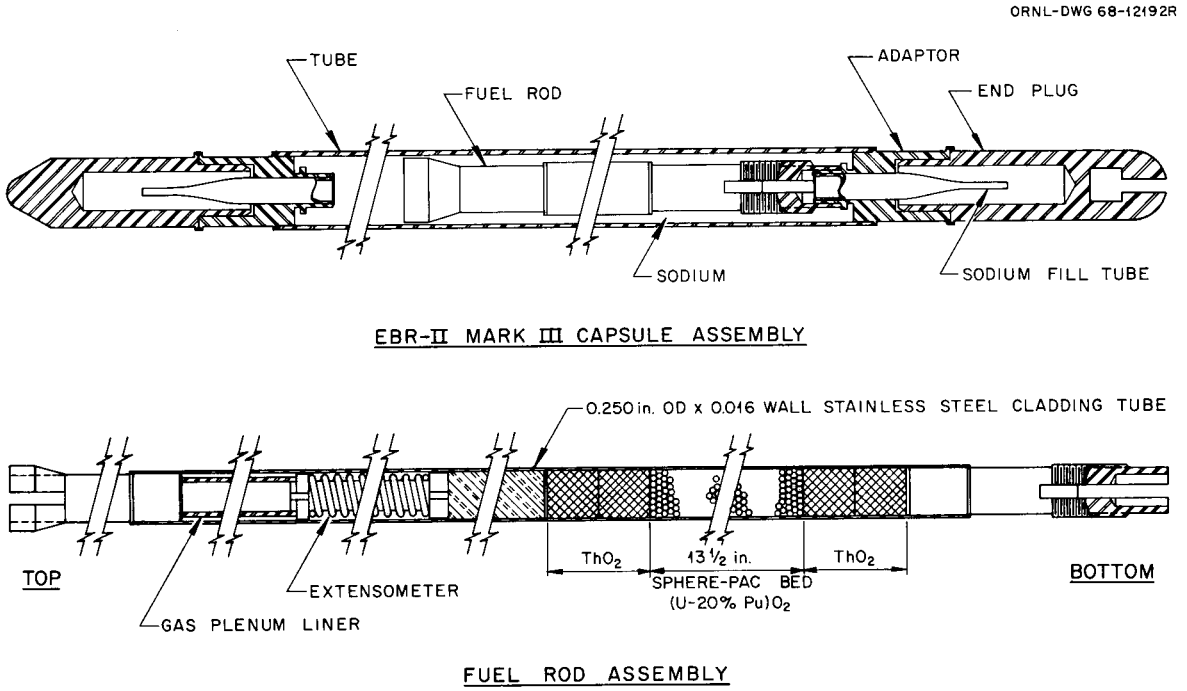

Fig. 24.1. Fuel Rod Assembly for Series I ORNL Oxide Fuels Tests in EBR-II.

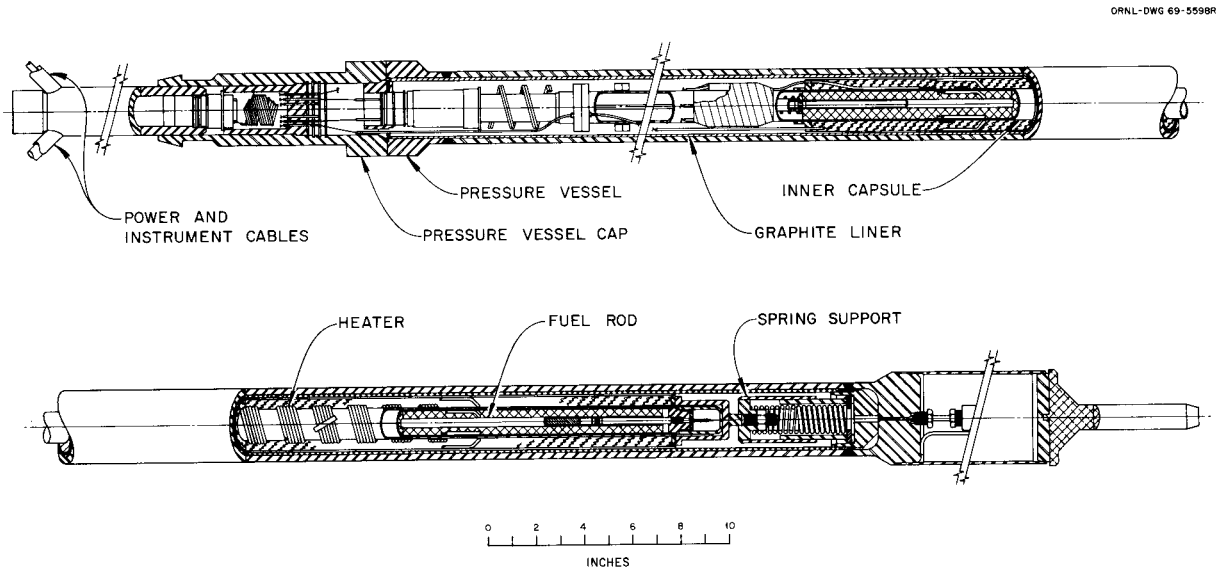

Fig. 24.2. Capsule Assembly for ORNL Transient Experiments in TREAT.

Re. The fuel used in the elements was nominal $U_{0.8}Pu_{0.2}O_2$ with an adjusted oxygen-to-metal ratio of 1.99. It was loaded by Sphere-Pac to 80.7% of theoretical density in the top element and to 82.5% of theoretical density in the bottom element. The elements were fabricated without difficulty.

CHARACTERIZATION OF $(U,Pu)O_2$ FUELS

W. H. Pechin

The preirradiation characterization of a fuel material is absolutely necessary in understanding the fabrication processes and in the interpretation of irradiation results. Characterization is divided into the examination of the fuel material as produced and the determination of basic properties of the material.

Chemical Analysis

W. H. Pechin

The analyses being used on the sol-gel mixed oxide fuel are listed in Table 24.1. The major impurities in the sol-gel material have been C, 20 to 120 ppm; Fe, 50 to 100 ppm; and Si, 75 to 100 ppm. The only impurity that has exceeded desirable levels was fluorine; one batch contained 28 ppm. The desired maximum content is 25 ppm.

The major efforts this year have been on measurement of oxygen-to-metal ratio and on gas release. We adopted a gravimetric determination of oxygen similar to that described by Lyon[10] primarily because it has better precision than the NITROX scheme.[11] The precision of the gravimetric oxygen analysis is ±0.005 in the oxygen-to-metal ratio. The gas release measurement, which involves measuring the gas released to a vacuum at 1700°C, has recently been altered by replacing the interior metallic susceptor by an exterior carbon susceptor. This avoids gas being absorbed by the metal.

Table 24.1. Analytical Methods Used on Sol-Gel $(U,Pu)O_2$ Fuel

Constituent	Method
Pu	Coulometric titration
U	Coulometric titration
Isotopic	Mass spectrography
Oxygen-to-metal ratio	Gravimetric oxidation-reduction
C	Combustion-gas chromatography
N	Colorimetric analysis
F	Pyrohydrolysis, spectrophotometry
Cl	Pyrohydrolysis, spectrophotometry
Metallic impurities	Spectrography (carrier distillation)
Gas release	Vacuum heating, mass spectrometry
Density	Mercury porosimetry for microspheres, dimensions and weight for pellets
Surface area	BET analysis

Thermal Conductivity

P. H. Spindler D. L. McElroy
J. P. Moore

We are constructing equipment to determine the physical properties of plutonium-bearing materials. A radial heat flow apparatus for measurements to 10 atm and 1400°K will be used to study solids and powders. Our previous results[12] on packed beds of ThO_2 microspheres were influenced by bed density, gas type and pressure, and temperature, and the new apparatus will extend the range of variables. Other equipment under construction includes: an electrical resistivity apparatus, an absolute heat flow apparatus, and a comparative heat flow apparatus. The measurement capabilities of these were previously described,[13] and we have proof-tested the design of each apparatus.

During this construction period we have obtained results on materials similar to the $(U,Pu)O_2$ fuels that should assist in understanding their behavior. The thermal resistivity of 93%-dense ThO_2 was found to be a linear function of temperature from 400 to 1400°K (see Chap. 9). The lattice conduction in LiF was enhanced by nearly 30% at the melting point by a thermal radiation component.[14] We are attempting to analyze this enhancement from optical quantities (see Chap. 9). This may allow a more realistic evaluation of such phenomena in fuels, since they occur at such high temperatures that they are difficult to assess.

Deformation

C. S. Morgan L. L. Hall

We are studying the compressive deformation of polycrystalline UO_2 specimens prepared from sol-gel-

[10] W. L. Lyon, *The Measurement of Oxygen to Metal Ratio in Solid Solutions of Uranium and Plutonium Dioxides*, GEAP-4271 (May 31, 1963).

[11] W. H. Pechin, *Fuels and Materials Development Program Quart. Progr. Rept. June 30, 1968*, ORNL-4330, pp. 13–17.

[12] D. L. McElroy, J. P. Moore, and P. H. Spindler, *Status and Progress Report for Thorium Fuel Cycle Development 1967–1968*, ORNL-4429, pp. 121–32.

[13] S. C. Weaver and D. L. McElroy, *Fuels and Materials Development Program Quart. Progr. Rept. Dec. 31, 1968*, pp. 54–55.

[14] D. L. McElroy, *Fuels and Materials Development Program Quart. Progr. Rept. March 31, 1969*, ORNL-4420, pp. 16–19.

derived powder. Specimens prepared from ADU powder are tested for comparison. These studies are primarily intended to provide a background for study of the out-of-reactor and in-reactor deformation characteristics of $(U,Pu)O_2$.

The sol-gel specimens were prepared by evaporation of the water from the UO_2 sol, grinding, forming, isostatic pressing at 20,000 psi, and sintering to a density 92% of theoretical. Sintering was done in argon with a rate of temperature rise of 50°C/hr with a 2-day hold at 800°C and 2-hr hold at 1450°C. The specimens were then further sintered at 1750°C for 1 hr in hydrogen. The ADU powder specimens were formed and pressed in the same way but sintered in one operation at 1750°C for 2 hr in hydrogen to a density 97% of theoretical. The oxygen-to-uranium ratio was 2.00 by chemical analysis. The average grain sizes were approximately 15 μ for the ADU and 9 μ for the sol-gel specimens.

In tests at constant strain rate over the 725 to 1525°C range, extensive deformation occurred with both types of specimens, as shown in Fig. 24.3. The sol-gel specimen often exhibited classical metallic yield behavior. The ADU specimens did not exhibit a definite yield stress but deformed at a lower stress. Both materials deformed at lower stress in CO–10 mole % CO_2 than in Ar–4% H_2.

Long-term static-load creep tests at relatively low stresses were made to determine deformation under conditions simulating those occurring in a fuel element.

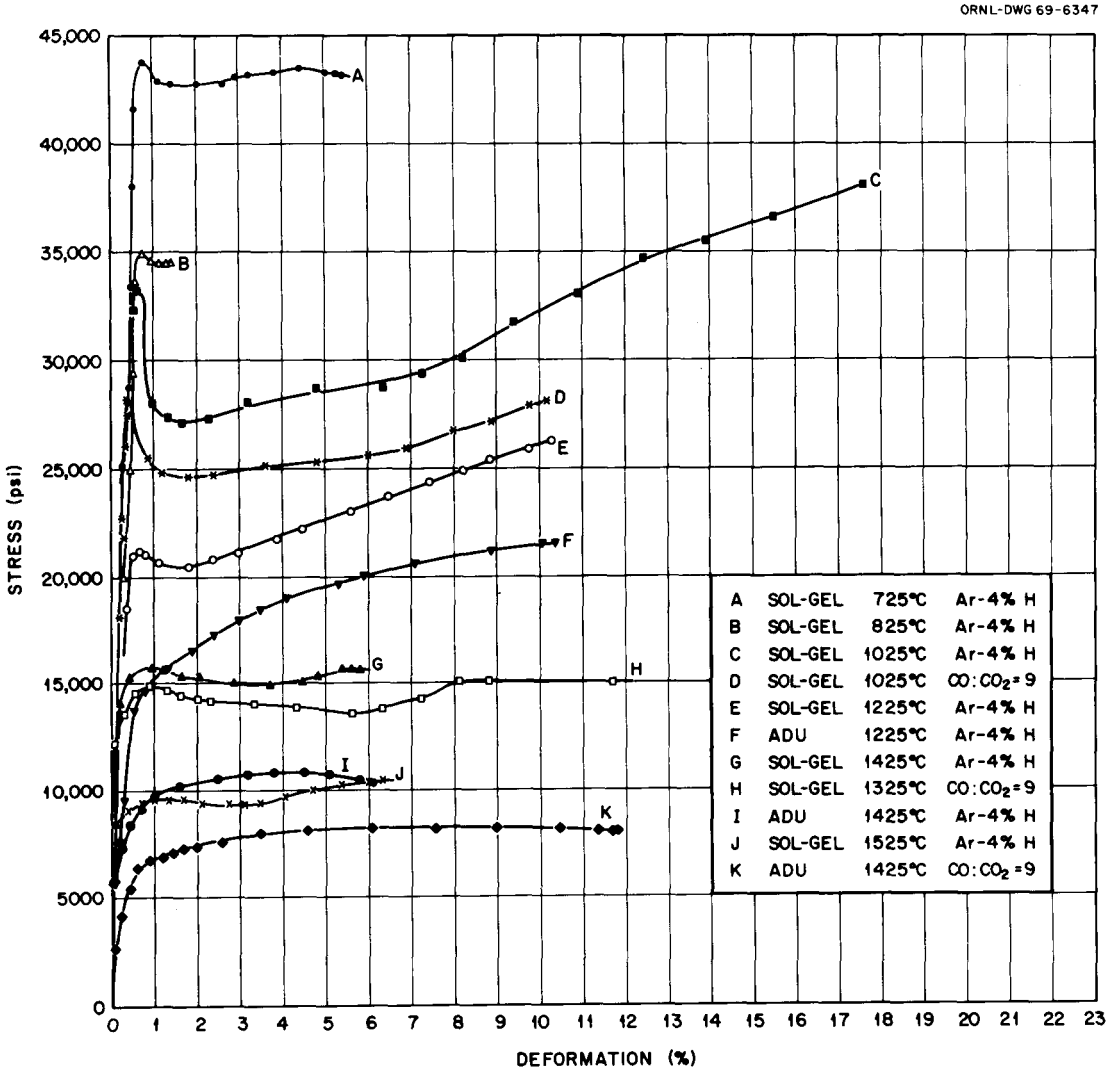

Fig. 24.3 Stress-Strain Curves for UO_2 Specimens Under Constant Compressive Strain Rate of 0.00067/min for Various Testing Temperatures and Environments.

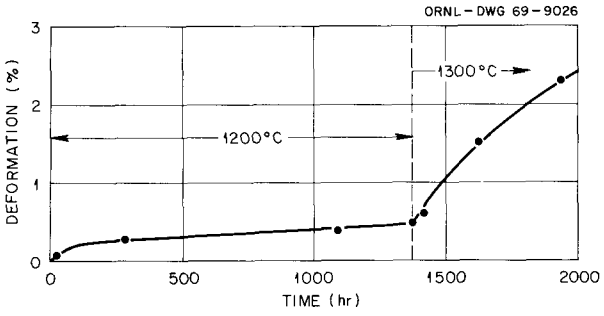

Fig. 24.4. Creep of Sol-Gel UO_2 Under Constant Compressive Stress of 4920 psi.

Results for a specimen under constant stress at 1200°C and then at 1300°C are shown in Fig. 24.4.

These data tend to confirm previous observations[15] that grain size has more effect than density on compressive strength of UO_2. It is not clear why the deformation stress was lower in CO-CO_2, but this may reflect the sensitivity of UO_2 deformation to very small changes in the oxygen-to-uranium ratio. We believe that the deformation mechanism is a complicated mixture of plastic flow and grain boundary sliding.

THERMODYNAMICS OF MIXED OXIDE FUELS

J. M. Leitnaker

Thermodynamics is applicable to several aspects of the overall uranium-plutonium oxide program. For example, the thermodynamic description of the fuel itself provides the basis for a choice of manufacturing conditions. Thermodynamic relationships with other materials can indicate the most likely choices for cladding materials. Furthermore, in-reactor restructuring of the fuel, both physically and chemically, will be determined, at least in part, by the basic thermodynamic properties of the fuel. For these reasons certain thermodynamic aspects of the oxide fuels are being examined.

Thermodynamic Applications to $(U,Pu)O_{2\pm x}$ Fuel Systems

K. E. Spear J. M. Leitnaker

In the large temperature gradients associated with typical reactor operation, mixed oxide fuels show a surprising behavior: initially substoichiometric fuels have a lower-than-initial oxygen-to-metal ratio in the hotter portions of the fuel and a higher-than-initial ratio in the colder portions. On the other hand, initially hyperstoichiometric fuels behave oppositely: the hot center is enriched in oxygen and the cold outside loses oxygen.[16] Obviously, a simple constant-oxygen-potential explanation does not explain the experimental observations.

We have obtained qualitative confirmation of a theory by Rand and Markin[17] to explain this behavior. The theory postulates that a constant CO-to-CO_2 ratio across the fuel determines the oxygen potential. Samples of UO_2 heated in an 800°C/in. gradient in CO–1 mole % CO_2 showed a higher oxygen content at the hot end and a lower oxygen content at the cold end, as determined by x-ray diffraction and shown in Table 24.2. Application of the Rand-Markin theory predicts the observed effect.[18]

A Model for the Low-Temperature Heat Capacity of UO_2

J. M. Leitnaker H. L. Davis[19]
K. E. Spear

A serious uncertainty exists in the entropy of PuO_2 at room temperature. Although Sandenaw[20] has measured the low-temperature heat capacity of PuO_2 from which the room-temperature entropy, S°_{298}, can be derived, his value has not been generally accepted. The reasons for the lack of acceptance are the self-damage and self-heating problems.[21,22]

---

[15] H. D. Sheets and W. H. Duckworth, pp. 199–206 in *Uranium Dioxide Properties and Nuclear Applications*, ed. by J. Belle, U.S. Government Printing Office, Washington, D.C., 1961.

[16] J. A. Christensen, *Stoichiometric Effects in Oxide Nuclear Fuels*, BNWL-536 (December 1967).

[17] M. H. Rand and T. L. Markin, *Some Thermodynamic Aspects of $(U,Pu)O_2$ Solid Solutions and Their Use as Nuclear Fuels*, AERE-R-5560 (August 1967); also pp. 637–50 in *Thermodynamics of Nuclear Materials*, International Atomic Energy Agency, Vienna, 1968.

[18] K. E. Spear, A. R. Olsen, and J. M. Leitnaker, *Thermodynamic Applications to $(U,Pu)O_{2\pm x}$ Fuel Systems*, ORNL-TM-2494 (April 1969).

[19] Now in Solid State Division.

[20] T. A. Sandenaw, "Heat Capacity of Plutonium Dioxide Below 325°K," *J. Nucl. Mater.* **10**, 165–72 (1963).

[21] D. W. Osborne and E. F. Westrum, Jr., "The Heat Capacity of Thorium Dioxide from 10 to 305°K: The Heat Capacity Anomalies in Uranium Dioxide and Neptunium Dioxide," *J. Chem. Phys.* **21**, 1884–87 (1953).

[22] *Thermodynamic and Transport Properties of Uranium Dioxide and Related Phases, Report of the Panel held in Vienna March 16–20, 1964*, Technical Reports Series No. 39, International Atomic Energy Agency, Vienna, 1965.

To attempt to understand the PuO_2 problem, we have "backed up" to examine the case of UO_2. The low-temperature heat capacity of UO_2 shows an antiferromagnetic-paramagnetic transformation at 30.4°K. Osborne and Westrum[21] calculated that the entropy associated with such an effect should be $R \ln 3$ (2.18 e.u.) rather than the 0.87 e.u. observed.[23]

Low-temperature, far-infrared spectroscopic measurements have revealed three electronic transitions in UO_2, implying four levels.[24] If the multiplicities are taken as unity and, above the transition temperature, Boltzmann statistics are assumed, the electronic contribution to the heat capacity and entropy can be calculated by well-known statistical methods.[25]

The calculated electronic heat capacity and entropy are compared with the difference between those quantities for UO_2 and ThO_2 in Table 24.3. Both the heat capacity and entropy comparisons are very close above the transition temperature to about 100°K. If two additional electronic levels are arbitrarily added, agreement can be obtained to 300°K, as also shown in Table 24.3.

The fact that both the heat capacities and the entropies, as calculated, agree so well (particularly just above the transition temperature) is significant. Nevertheless, Allen[26] has questioned the assignment of all the infrared absorption lines to electronic transitions. Further, the model deduced from inelastic neutron scattering experiments at 296°K by Dolling, Cowley, and Woods,[27] although providing agreement with our lattice heat capacity estimates, does not agree nearly so well at low temperatures. Additional information would be desirable on samples in which the magnetic transformation is quenched.

Table 24.2. Lattice Parameters of UO_2 Rod Subjected to a Thermal Gradient

Sample	Temperature[a] (°C)	a_0, Lattice Parameter[b]	O/M[c]
Hot surface	1820	5.47032 ± 0.00016	2.002
Hot center	(1800)	5.47052 ± 0.00016	2.000
Cold surface	950	5.47090 ± 0.00018	1.998
Cold center	(950)	5.47108 ± 0.00017	1.998

[a]Temperatures are observed on surface and may be 100° in error.

[b]The lattice parameter was obtained as described in "The Ideality of the UC-UN Solid Solution," pp. 317–30 in *Thermodynamics of Nuclear Materials, 1967,* International Atomic Energy Agency, Vienna 1968.

[c]The oxygen-to-metal ratio was obtained by extrapolation of data given in TRG-Report-1601 (1968), p. 11.

[23]W. M. Jones, J. Gordon, and E. A. Long, "The Heat Capacities of Uranium, Uranium Trioxide, and Uranium Dioxide," *J. Chem. Phys.* **20**, 695–99 (1952).

[24]K. Aring and A. J. Sievers, "Thermal Conductivity and Far-Infrared Absorption of UO_2," *J. Appl. Phys.* **38**, 1496–98 (1967).

[25]G. N. Lewis and M. Randall, *Thermodynamics,* 2d ed., revised by K. S. Pitzer and L. Brewer, McGraw-Hill, New York, 1961.

[26]S. J. Allen, Jr., "Spin-Lattice Interaction in UO_2. I. Ground-State and Spin Wave Excitations," *Phys. Rev.* **166**, 530–39 (1968).

[27]G. Dolling, R. A. Cowley, and A. D. B. Woods, "The Crystal Dynamics of Uranium Dioxide," *Can. J. Phys.* **43**(8), 1397 (1965).

Table 24.3. Electronic Contributions to the Heat Capacity and Entropy of UO_2

Temperature (°K)	Electronic Heat Capacity (cal mole^{-1} °C^{-1})			Electronic Entropy (cal mole^{-1} °C^{-1})		
	calcd[a]	calcd[b]	measured[c]	calcd[a]	calcd[b]	measured[d]
10	0.872	0.872	0.032	0.521	0.521	0.006
50	0.986	0.986	0.840	1.916	1.912	1.870
100	0.516	0.523	0.584	2.453	2.454	2.356
200	0.162	0.334	0.350	2.670	2.714	2.673
298	0.077	0.448	0.440	2.716	2.869	2.817

[a]Calculated from observed levels at 0, 17.63, 79, and 100 cm^{-1}, all nondegenerate.

[b]Calculated from observed levels and added levels at 650 and 850 cm^{-1}, all nondegenerate.

[c]Difference between C_p of UO_2 (ref. 22) and ThO_2 (ref. 21).

[d]Difference between $\int_0^T (C_p/T)\, dT$ of UO_2 (ref. 22) and ThO_2 (ref. 21).

Standard Samples of UO_2 for Oxygen Determination

J. M. Leitnaker K. E. Spear

Initial oxygen potential in $(U,Pu)O_2$ fuels will, in large part, determine their compatibility with stainless steel cladding materials.[18] Determination of oxygen content requires, if not an absolute value, at least a fixed, easily reproducible reference point. A reference material can be produced in the laboratory by heating routinely available oxygen-rich UO_2 in a ten-to-one CO-CO_2 mixture at 1200°C. Heating 6 hr produces a uniform composition in ¼-in.-diam pressed pellets, as determined by x-ray examination and combustion to constant weight in oxygen at 850°C.

IRRADIATION BEHAVIOR

C. M. Cox A. R. Olsen

We are conducting an irradiation test program to determine the basic in-reactor properties and performance of the sol-gel-derived $(U,Pu)O_2$ as functions of fabrication form, porosity distribution, and irradiation conditions. This program includes both fast and thermal flux irradiations and both steady-state and transient power conditions. The objective is a fundamental understanding of the irradiation behavior of these fuels, and we thus concentrate on detailed postirradiation examinations and analysis in terms of fuel performance models.

Uninstrumented Tests

A. R. Olsen R. B. Fitts
J. Komatsu[28] C. M. Cox

The uninstrumented capsules were designed[29] for irradiations in the X-basket facilities of the ETR. Each capsule contains four test rods with 3-in.-long fuel columns. The status of the first ten capsules in this series is described in Table 24.4. The last four capsules, 43-116 through 43-119, are being irradiated to provide fuel containing short-lived fission products for head-end

[28]Foreign visitor on leave from Power Reactor and Nuclear Fuel Development Corporation, Japan.

[29]D. E. Ferguson *et al.*, *Chem. Technol. Div. Ann. Progr. Rept. May 31, 1968*, ORNL-4272, pp. 41–49.

Table 24.4. Uninstrumented Irradiation Screening Tests of Sol-Gel-Derived Urania-Base Bulk Oxide Fuels

Experiment	Fuel		Number of Rods	Peak Burnup (% FIMA)	Peak Linear Heat Rate (w/cm)	Status May 1969
	Form	Composition				
43-99	Sphere-Pac	$(^{235}U$–20% Pu$)O_2$	2	1.5	1640[a]	Report in preparation
43-100	Sphere-Pac	$(^{235}U$–20% Pu$)O_2$	2	1.4	1470[a]	Report in preparation
43-103	Sphere-Pac Pellet	UO_2 (20% ^{235}U) UO_2 (20% ^{235}U)	3 1	5	690	Being examined
43-112	Sphere-Pac	$(^{238}U$–15% Pu$)O_2$ UO_2 (20% ^{235}U)	3 1	0.7	500	Report in preparation
43-113	Sphere-Pac	$(^{238}U$–15% Pu$)O_2$ UO_2 (20% ^{235}U)	3 1	10[b]	500[b]	In-reactor, ≅7% FIMA
43-115	Sphere-Pac	$(^{238}U$–15% Pu$)O_2$ UO_2 (20% ^{235}U)	3 1	5[b]	600[b]	Being examined
43-116	Sphere-Pac	$(^{238}U$–15% Pu$)O_2$	4	1.5[c]	600[b]	Being examined
43-117	Sphere-Pac	$(^{238}U$–20% Pu$)O_2$	4	1.5[c]	600[b]	In preparation
43-118	Sphere-Pac	$(^{238}U$–20% Pu$)O_2$	4	1.5[c]	600	In preparation
43-119	Sphere-Pac	$(^{238}U$–20% Pu$)O_2$	4	1.5[c]	600	In preparation

[a]Rods failed in-reactor from overpowering.
[b]These are target design values.
[c]This is an approximate level. This test will be irradiated for two ETR cycles to produce fuel for reprocessing studies.

process development by the Chemical Technology Division.[29] No detailed postirradiation examination is planned for these rods, only neutron radiographs. Two experiments, 43-115 and 43-116, completed their scheduled irradiation during the past year.

Details of postirradiation examination of 43-99, 43-100, and 43-112 have been reported previously.[30-33] The comparison of predicted burnup from physics calculations with experimental data for 43-112 has been completed. The method of calculation has been reported elsewhere.[34] The agreement, as shown in Table 24.5 is excellent. Similar calculations for experiments 43-99, 43-100, and 43-103 have shown that the actual unperturbed flux in the ETR irradiation positions was much higher than advertised. For 43-103 this conclusion was verified by subsequent flux measurements as well as the burnup results shown in Table 24.6.

A flux peaking analysis is necessary to understand the test results from experiments 43-103 and 43-115. The gamma scan of 43-103 shown in Fig. 24.5 indicates some penetration of fuel through the upper ThO_2 insulators for both rods 2 and 3. A recently obtained neutron radiograph of 43-115 clearly shows some fuel penetration through the upper ThO_2 insulator for rods 2 and 3 and a localized increase in the fuel central void diameter at both ends of all four rods. Instead of depleted UO_2, ThO_2 insulators are used to avoid the effects of insulator material on isotopic burnup analysis. The postirradiation examination of these two experiments is incomplete. However, Figs. 24.6 and 24.7 show the comparative appearance of pellet and Sphere-Pac UO_2 fuels irradiated to approximately 50,000 Mwd/MT of heavy metal at high linear heat rates in capsule 43-103.

As discussed elsewhere,[33] we are considering several mechanisms of void migration and grain growth in evaluating the microstructural changes in these fuels.

Table 24.5. Comparison of Calculated and Measured Linear Heat Rates and Burnups for ETR Experiment 43-112

Quantity Determined	Fuel Pin Section			
	1B[a]	2B[b]	3B[a]	4B[a]
Linear heat rate, kw/ft				
Design prediction[c]	8.6	12.0	12.2	10.0
Postirradiation measurement				
Isotopic analysis	8.4	10.4	12.6	10.5
Radiochemical analysis[d]	9.2	11.6	12.8	10.2
^{60}Co activity[e]	9.2	11.9	14.3	10.9
Burnup, % FIMA				
Design prediction[c]	0.47	0.71	0.65	0.54
Postirradiation measurement				
Isotopic analysis	0.46	0.61	0.67	0.57
Radiochemical analysis[d]	0.50	0.68	0.68	0.55
^{60}Co activity[e]	0.50	0.70	0.76	0.59

[a](U–15% Pu)O_2.
[b]UO_2 (20% enriched).
[c]Based on advertised unperturbed flux.
[d]Average of ^{137}Cs, ^{89}Sr, and ^{144}Ce determinations.
[e]Renormalization of reactor physics calculations, based on neutron activation of the cladding.

Table 24.6. Burnups and Time-Averaged Linear Heat Rates for Experiment 43-103

Fuel Rod	Fuel Form	Burnup[a] (% FIMA)	Linear Heat Rate[b] (kw/ft)
43-103-1	Sphere-Pac	4.10	15.6
43-103-2	Pellets	4.98	22.0
43-103-3	Sphere-Pac	5.44	20.7
43-103-4	Sphere-Pac	4.34	16.5

[a]Because of erratic and generally high burnup levels obtained from radiochemical analyses, we are using the burnup levels derived from changes in isotopic analysis for these UO_2 fuels (20% ^{235}U).
[b]The linear heat rates are time-averaged over the total exposure time of 126 days of effective full power, assuming 177 Mev/fission.

ORR Instrumented Tests

R. B. Fitts V. A. DeCarlo[35]

The ORR instrumented capsule tests are being used to investigate the basic in-reactor characteristics of $(U,Pu)O_2$ fuels. Since a knowledge of the fuel temperatures is fundamental to the analysis and understanding of fuel behavior, the capsule has been designed[36] to

[30]A. R. Olsen and R. B. Fitts, *Metals and Ceramics Div. Ann. Progr. Rept. June 30, 1967,* ORNL-4170, pp. 125–27.

[31]A. R. Olsen, R. B. Fitts, and J. Komatsu, *Metals and Ceramics Div. Ann. Progr. Rept. June 30, 1968,* ORNL-4370, pp. 144–45.

[32]A. R. Olsen, R. B. Fitts, and J. Komatsu, *Fuels and Materials Development Program Quart. Progr. Rept. June 30, 1968,* ORNL-4330, pp. 18–20.

[33]A. R. Olsen, R. B. Fitts, and J. Komatsu, *Fuels and Materials Development Program Quart. Progr. Rept. Sept. 30, 1968,* ORNL-4350, pp. 22–25.

[34]A. R. Olsen, C. M. Cox, and R. B. Fitts, *Fuels and Materials Development Program Quart. Progr. Rept. Mar. 31, 1969,* ORNL-4420, pp. 25–28.

[35]Reactor Division.

[36]R. B. Fitts and V. A. DeCarlo, *Metals and Ceramics Div. Ann. Progr. Rept. June 30, 1968,* ORNL-4370, pp. 145–49.

monitor fuel-central and cladding-surface temperatures and fuel rod heat generation rates. The primary fuel properties to be investigated are the in-reactor thermal conductivity and the characteristic temperatures for fuel microstructural changes. With the first series of capsules, we are examining these properties for sol-gel (U–20% Pu)O_2 Sphere-Pac[37] and pellet[38] fuels at an oxygen-to-metal ratio of 1.98 and a smear density of about 82%. The influence of such variables as fuel composition, stoichiometry, density, fabrication history, and burnup may be investigated in later tests.

The results of the first capsule in this series, SG-1, were reported last year.[36] In general, this test verified the capsule design and showed that the Sphere-Pac fuels

[37] R. B. Fitts, A. R. Olsen, and J. Komatsu, "Sphere-Pac Fabrication of Sol-Gel Nuclear Fuels," *Am. Ceram. Soc. Bull.* 47(9), 844 (1968).

[38] R. A. Bradley, "Pellet Development," *Fuels and Materials Development Program Quart. Progr. Rept. June 30, 1969*, ORNL-4440 (in preparation).

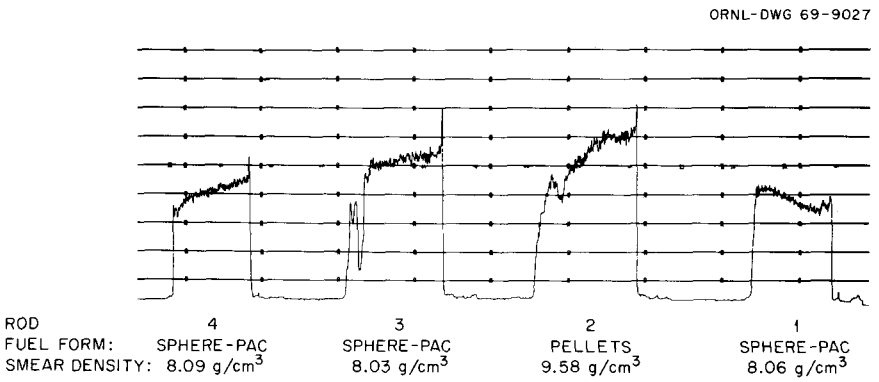

Fig. 24.5. Postirradiation Gamma Scan of Test Capsule 43-103; All Fuel UO_2 (20% ^{235}U).

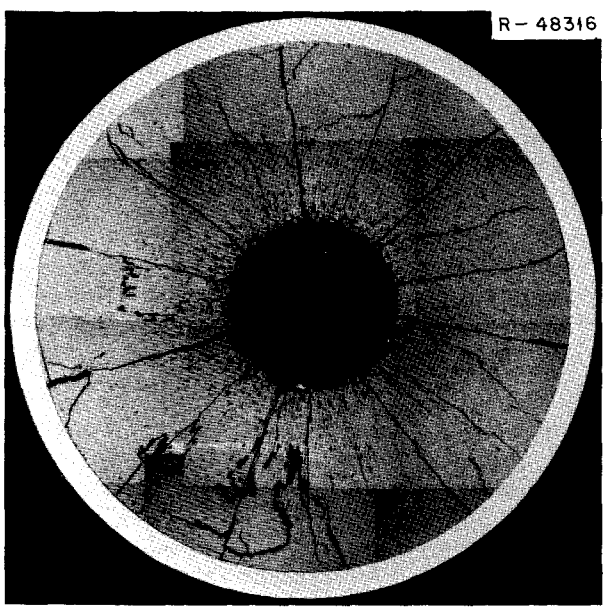

Fig. 24.6. Pellet Fuel of UO_2 (20% ^{235}U) from Rod 43-103-2 Operated at Approximately 22 kw/ft Linear Heat Rate to 50,000 Mwd/MT of U Burnup. Initial smear density 9.58 g/cm^3. Reduced 16%.

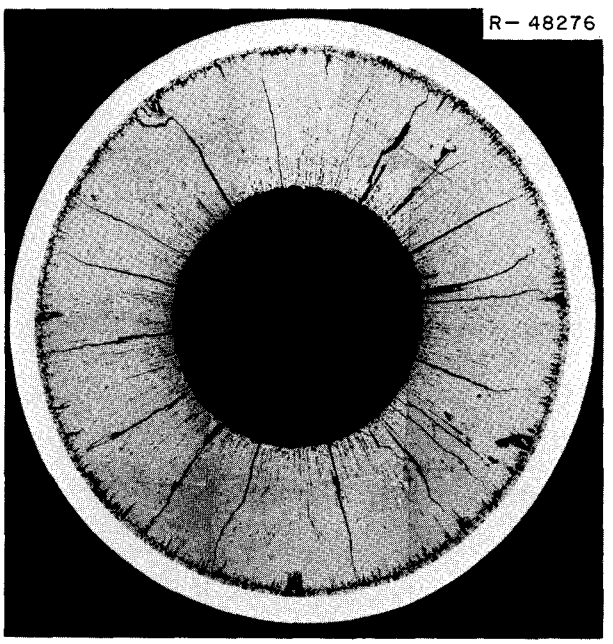

Fig. 24.7. Sphere-Pac UO_2 (20% ^{235}U) Fuel from Rod 43-103-3 Operated at Approximately 20 kw/ft Linear Heat Rate to 50,000 Mwd/MT of U Burnup. Initial smear density 8.03 g/cm^3. Reduced 13.5%.

have thermal conductivities similar to those of pellet fuels of comparable density.

The second capsule is presently in the ORR. It contains two fuel rods of (U–20% Pu)$O_{1.98}$ Sphere-Pac fuel from the batch to be used for the first series of TREAT tests (see below). This test is intended to yield information on the lowest temperature microstructural change and the fuel thermal conductivity up to that temperature. To date, the fuel center-line temperature has been increased from 100 to 1350°C in 50 and 100°C steps.[39] The thermal conductivity is within about 10% of that observed in capsule SG-1. There is as yet no indication that thermal conductivity changes with time at a constant temperature, so we believe no significant microstructural changes have occurred below 1350°C.

Transient Irradiation Tests

C. M. Cox J. D. Jenkins[35]
R. E. Adams

We plan to compare the behavior of pelletized and Sphere-Pac (U–20% Pu)O_2 fuels during power and temperature transients typical of those to be expected from hypothetical accidents. The initial experiments with unirradiated fuel include three capsules containing multiple fuel pins and one containing a single long fuel pin. These will be initiated at the Transient Reactor Test Facility (TREAT) in August 1969.

We performed a detailed series of calculations to investigate the use of B, Cd, and Eu as thermal neutron filters and to compare NaK and Na as the fuel pin-to-capsule bond. Reactor physics calculations predicted that cadmium was the most effective filter for reducing the radial power depression across the fuel.[40] The calculated fuel transient temperature profiles with the cadmium filter indicate somewhat higher fuel temperatures and less surface peaking than predicted with no filter.[41] However, the improvements are too small to warrant the use of neutron filters with the initial experiments.

We also considered NaK rather than Na for the cladding-to-capsule thermal bond. Heat transfer calculations predicted that the substitution of NaK for Na has a negligible effect on the fuel temperatures but causes the peak temperatures in the cladding to increase[41] some 100°C. This would be undesirable in our study of failure thresholds and mechanisms, so we intend to use sodium in all our TREAT capsules.

An additional heat transfer analysis showed that the extent of fuel melting over the range of interest, 25 to 75 vol %, is quite sensitive to changes in the reactor integrated power or pulse period.[42] Since these parameters cannot be closely controlled, we have included both Sphere-Pac and pellet fuels in each of the first three capsules to get directly comparable fuel performance data.

Fast Flux Irradiation Tests

A. R. Olsen C. M. Cox

Five encapsulated rods containing Sphere-Pac (^{235}U–20% Pu)O_2 are being irradiated to a scheduled 7500 Mwd of EBR-II operation. Details of the individual rod loadings are given in Table 24.7. In addition to the sol-gel Sphere-Pac capsules, this subassembly contains two with mixed carbide fuel, four capsules containing samples of structural materials, and eight others containing oxide fuels. This exposure will provide a peak burnup level in excess of 4% FIMA for the highest heat rate Sphere-Pac rod, S-1-C. As of May 28, 1969, the exposure was 2238 Mwd.

The initial hazards analysis[43] is based on the design parameters with an anticipated average burnup level of 5% FIMA in the position of highest heat rating in a row 4 subassembly. However, we have begun preliminary physics calculations for a more detailed operational prediction.

We are currently preparing a proposal for irradiation of unencapsulated pins in a 37-pin subassembly to be shared with Babcock and Wilcox test pins.[44] The special type 316 stainless steel cladding material for these tests will be shipped by Pacific Northwest Laboratories in July 1969. Pin fabrication is to be completed by next spring.

---

[39] R. B. Fitts, V. A. DeCarlo, and K. R. Thoms, "ORR Instrumented Tests," *Fuels and Materials Development Program Quart. Progr. Rept. June 30, 1969,* ORNL-4440 (in preparation).

[40] C. M. Cox and J. D. Jenkins, *Fuels and Materials Development Program Quart. Progr. Rept. June 30, 1968,* ORNL-4330, pp. 23–24.

[41] C. M. Cox, *Fuels and Materials Development Program Quart. Progr. Rept. Sept. 30, 1968,* ORNL-4350, pp. 29–31.

[42] C. M. Cox and R. E. Adams, *Fuels and Materials Development Program Quart. Progr. Rept. Mar. 31, 1969,* ORNL-4420, pp. 30–32.

[43] A. R. Olsen, *Experiment Description and Hazards Evaluation for the Series I ORNL Oxide Fuels Irradiation in EBR-II,* ORNL-TM-2635 (in preparation).

[44] A. R. Olsen, *Metals and Ceramics Div. Ann. Progr. Rept. June 30, 1968,* ORNL-4370, p. 149.

Table 24.7. Series-I ORNL Oxide Fuel Rods for EBR-II Irradiation

Capsule	Rod	Fuel Column Height (in.)	Fuel Weight (g)	Smear Density (g/cm^3)	Smear Density (% of theoretical)[a]	Oxygen-to-Metal Ratio
S-1-A	14-27-E	13.44	76.853	9.096	83.07	1.99
S-1-B	14-23-A	13.05	77.183	9.409	85.93	1.99
S-1-C	17-1	13.50	73.972	9.041	82.57	1.99
S-1-D	17-4-A	13.44	70.755	8.687	79.48	1.98
S-1-E	17-4	13.45	73.089	8.966	81.88	1.99

[a]The theoretical density for the $(U-20\% Pu)O_2$ fuel has been adjusted to account for both isotopic analysis and the oxygen-to-metal ratios. At 1.99 oxygen-to-metal, theoretical density is 10.95 g/cm^3; and at 1.98 oxygen-to-metal, the theoretical density is 10.93 g/cm^3.

MATHEMATICAL ANALYSIS OF IRRADIATION EXPERIMENTS

C. M. Cox

We are continuing the development and verification of numerical models to simulate fuel rod performance as an integral part of the design and interpretation of our irradiation experiments. During the past year, our work has been predominantly oriented toward verifying the accuracy of our reactor physics and heat transfer analyses through comparisons with experimental data.

Reactor Physics Analyses

C. M. Cox J. D. Jenkins[35]
A. R. Olsen

Because of the high fissile concentration of the LMFBR fuels, multigroup neutron transport theory calculations are needed to accurately describe the flux and fission distributions, especially in thermal reactor experiments. Our principal analytical tool is the ANISN discrete ordinates neutron transport code.[45]

Calculations were performed for the graphite-moderated TREAT reactor and the water-moderated ORR and ETR with 36 neutron energy groups, using diffusion theory for the six fast groups (>1.86 ev) and transport theory for the thermal groups. Agreement with experimental burnup and flux monitor analyses (see above under Irradiation Performance) was quite good, generally within ±15%.

Using similar techniques but with a 16-group fast cross section library, we calculated fission rates for the EBR-II within ±10% of experimental data. In addition, we performed a 99-group calculation of the EBR-II with a typical loading to obtain a set of position-dependent cross sections for all of the U, Pu, and Th isotopes of interest. These cross sections are fairly constant in the core but vary rapidly in the reflector.

Heat Transfer Analyses

R. B. Fitts C. M. Cox

To accurately predict temperature distributions in irradiation experiments, one must account for temperature-dependent thermal conductivities, thermal expansion of the capsule components, and restructuring of the oxide fuel, in addition to determining the fission distribution in the fuel. In most steady-state cases, a one-dimensional analysis with the GENGTC[46] and PRØFIL[47] heat transfer codes is sufficient.

Data from the first instrumented capsule[48-50] are included here to compare analytical predictions with results. The fuel was Sphere-Pac $(U-15\% Pu)O_2$ of 8.8

[45]W. W. Engle, Jr., *A User's Manual for ANISN,* K-1693 (March 1967).

[46]H. C. Roland, *GENGTC – A One-Dimensional CEIR Computer Program for Capsule Temperature Calculations in Cylindrical Geometry,* ORNL-TM-1942 (December 1967).

[47]C. M. Cox and F. J. Homan, *PRØFIL – A One-Dimensional FØRTRAN IV Program for Computing Steady-State Temperature Distributions in Cylindrical Ceramic Fuels,* ORNL-TM-2443 (March 1969), and ORNL-TM-2443 addendum, in press.

[48]R. B. Fitts and V. A. DeCarlo, *Fuels and Materials Development Program Quart. Progr. Rept. June 30, 1968,* ORNL-4330, pp. 20–23.

[49]R. B. Fitts and V. A. DeCarlo, *Fuels and Materials Development Program Quart. Progr. Rept. Sept. 30, 1968,* ORNL-4350, pp. 25–29.

[50]R. B. Fitts, *Fuels and Materials Development Program Quart. Progr. Rept. Dec. 31, 1968,* ORNL-4390, pp. 25–26.

g/cm^3 smear density. The capsule was operated at selected linear heat generation rates betwen 5 and 15 kw/ft for about 1200 hr.

Calculated and measured NaK annulus and central fuel temperatures are compared in Fig. 24.8. They compare closely enough to verify the usefulness of this empirical model. Detailed assumptions for these calculations have been reported.[51]

Comparison of Thermal-Flux and Fast-Flux Thermal Gradients

R. B. Fitts

Much of the initial irradiation testing of fast-reactor fuels is being carried out in thermal-flux reactors because of the limited space available for fast-flux testing. Since the two energy distributions produce different distributions of fissioning and temperature for a given rate of heat generation, the validity of testing fast-reactor fuels in the thermal flux is questionable. The two were compared[52] on the basis of the radial fission rate and temperature profiles expected to exist in operating (U–15% Pu)O_2 fuels. The calculations assumed density changes such that all fuel between 1400 and 1750°C became 94% dense, and all above 1750°C became 97% dense. Such restructuring has occurred within the first few hours of irradiation testing.[53] The thermal conductivity of the fuel was assumed to be that given by W. E. Bailey *et al.*[54] Figure 24.9 compares the predicted density, fission rate (heat generation) profiles, and temperature profiles for a fuel initially 80% dense and operating in a thermal and a fast flux.

These calculations predict that fuel temperature profiles are very similar in fast- and thermal-flux tests if the rates of heat generation are properly chosen. No great differences in thermal gradient are expected, and

[51] C. M. Cox, R. B. Fitts, and F. J. Homan, *Fuels and Materials Development Program Quart. Progr. Rept. Mar. 31, 1969*, ORNL-4220, pp. 33–37.

[52] R. B. Fitts, *Fuels and Materials Development Program Quart. Progr. Rept. Dec. 31, 1968*, ORNL-4390, pp. 29–32.

[53] G. Testa *et al.*, *Trans. Am. Nucl. Soc.* 11(2), 494 (1968).

[54] W. E. Bailey *et al.*, "Thermal Conductivity of Uranium-Plutonium Oxide Fuels," *Intern. Symp. Plutonium Fuel Technol., Scottsdale, Ariz. 1967, Nucl. Met.*, vol. 13, 293–308 (1968).

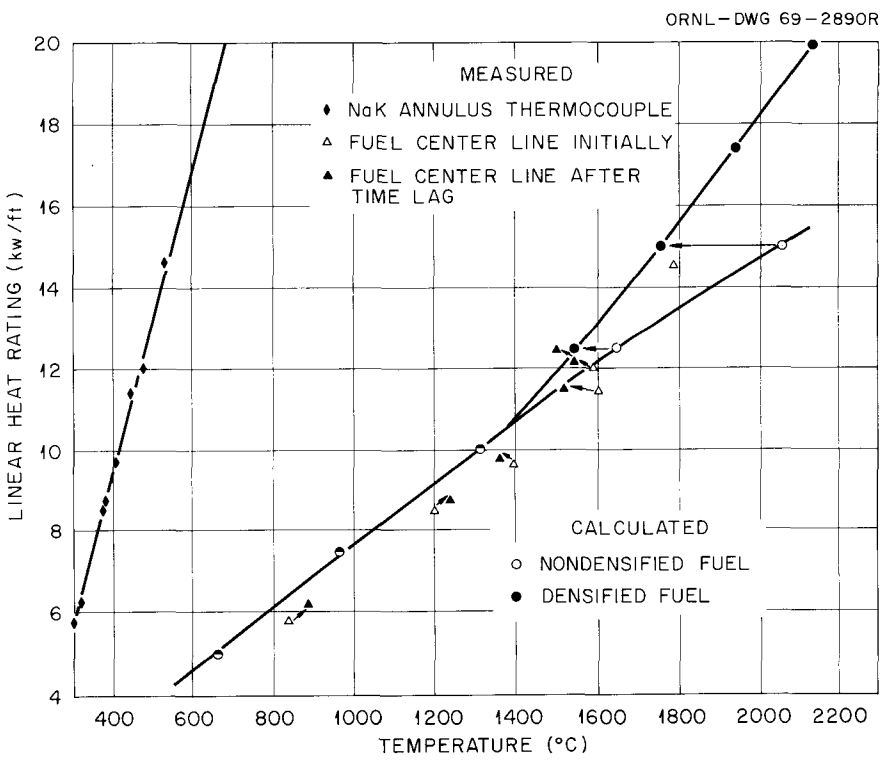

Fig. 24.8. Comparison of Calculated and Observed Temperatures for Instrumented Capsule SG-1.

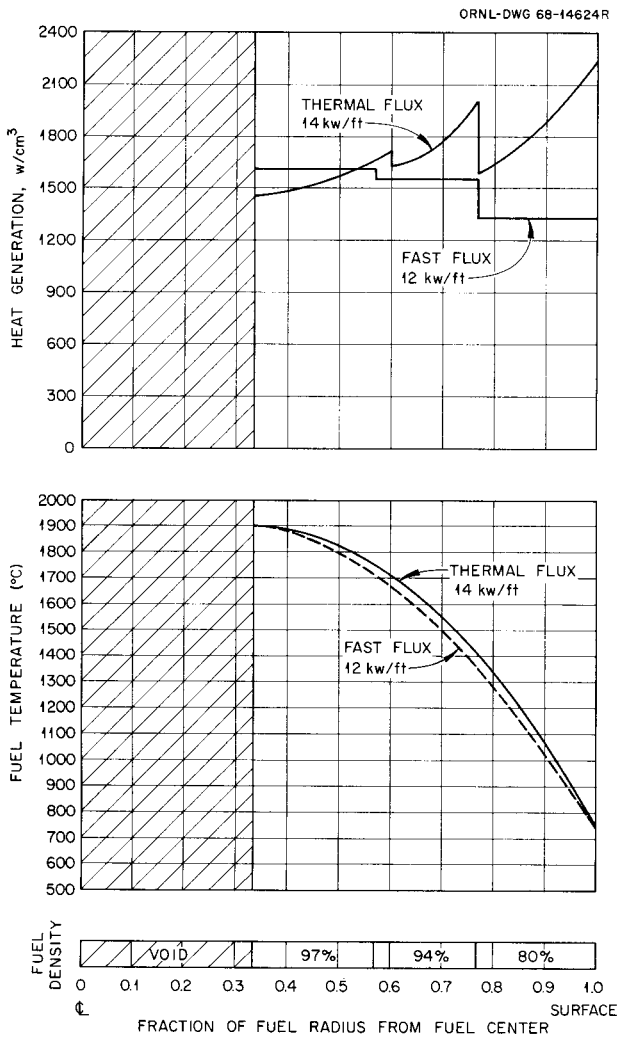

Fig. 24.9. Comparison of Calculated Fuel Temperatures and Heat Generations for Fast- and Thermal-Flux Irradiation of $U_{0.8}Pu_{0.2}O_2$.

the fuel structures will therefore be very similar until significant fission products accumulate to alter the characteristics of the fuel. The most important difference, in terms of fuel behavior, is probably the generation of a much greater portion of the fission products in the cooler regions near the surface during thermal-flux testing. This difference in distribution would be expected to influence the chemical and mechanical interactions between fuel and cladding, although the degree of this effect is not known.

Our analysis, which considers only the fuel behavior and not the effects of fast neutrons on the cladding, indicates that thermal-flux testing of fast-reactor fuels is quite adequate for lower burnup studies of such factors as in-reactor fuel restructuring, thermal conductivity, and basic compatibility of fuel and cladding. Long-term tests to prototypic burnups can be carried out in a thermal flux but are subject to careful interpretation and require confirmation in fast-flux tests.

25. Zirconium Metallurgy

P. L. Rittenhouse

Many of the nuclear power reactors now in operation make use of zirconium alloys as fuel cladding and structural components. These alloys are used primarily because of their desirable nuclear characteristics but also because they possess sufficient strength and corrosion resistance. The major application of these alloys is as cladding for the UO_2 fuel in light-water reactors, and up to 500,000 ft of Zircaloy tubing is used for each core loading. It is desirable to increase the operating temperature of these Zircaloy-clad fuel rods, to decrease the cladding thickness, and to extend the life of the core to achieve higher fuel burnup, better operating efficiency, and lower cost of power produced. This, over and above the difficulties already experienced with fabrication, quality control, and properties of the cladding (especially hydride orientation), places severe demands on the present technology of zirconium alloys. We feel that, not only many of the problems that have been encountered to date, but also the most promising method of permitting these materials to satisfactorily withstand the desired changes in reactor operating parameters is associated with the crystallographic texture developed during fabrication. By control of texture we can ensure quality control in terms of reproducibility of fabricability, hydride orientation, and strength and ductility. In addition, as control of texture is synonymous with control of the anisotropy of properties, it provides a method of tailoring a structure with strength or ductility optimum for a given stress state and application. Careful control of the texture in zirconium alloys should allow them to meet the stringent requirements demanded by increased reactor operating temperatures and core lives and result in not only a more economical but a safer reactor.

EXPERIMENTAL FABRICATION OF ZIRCALOY-4 TUBING

T. M. Nilsson P. L. Rittenhouse

The planning of 12 fabrication schedules for Zircaloy-4 tubing and the manufacture of tubing according to these schedules has been described.[1] This tubing is being used in a study of the influence of fabrication variables on crystallographic texture and anisotropy of mechanical properties. We fabricated extruded tube shells to final size by tube reducing and by combinations of tube reducing and drawing, planetary swaging, and hammer swaging. In the following sections the texture and properties of tubing from these experimental fabrication schedules and commercially produced tubing are described.

TEXTURE DEVELOPMENT AND CONTROL IN ZIRCALOY TUBING

Erich Tenckhoff D. O. Hobson P. L. Rittenhouse

We have completed our studies of texture development and texture gradients in Zircaloy tubing fabricated by various hot and cold deformation processes under different deformation conditions.[2-4] The aim was to find how the texture develops during successive fabrication steps, how it varies across the wall of the tubing, and how the development and variations are influenced by the fabrication method. The results can be summarized as follows:

1. In tubing fabricated to the same final size from extrusion billets of identical size, different processing conditions – a preponderance of reduction in wall

[1] T. M. Nilsson and P. L. Rittenhouse, *Experimental Fabrication of Zircaloy-4 Tubing*, ORNL-TM-2576 (in press).

[2] D. O. Hobson, P. L. Rittenhouse, and E. Tenckhoff, *Metals and Ceramics Div. Ann. Progr. Rept. June 30, 1968*, ORNL-4370, pp. 157–59.

[3] E. Tenckhoff and P. L. Rittenhouse, "Texture Gradients in Thin Walled Zircaloy Tubing," presented at Nov. 5–7, 1968, ASTM Meeting on Applications-Related Phenomena in Zr and Hf and their Alloys, to be published.

[4] D. O. Hobson and E. Tenckhoff, "Effects of Fabrication Parameters on Textures Produced in Zircaloy Cladding," presented at the 15th Annual Meeting of the American Nuclear Society, Seattle, Wash., June 15–19, 1969.

thickness, R_W, or in diameter, R_D – cause markedly different final textures.

2. A preponderance of R_W (i.e., wall reduction greater than diameter reduction) promotes a texture with basal poles parallel to the radial direction, RD. A preponderance of R_D (wall reduction less than diameter reduction) leads to a split of basal poles toward the tangential direction, TD. When $R_W = R_D$ a fiber texture with a random distribution of basal poles is favored. These concepts are illustrated in Fig. 25.1.

3. In actual tubing production practice, the effects of R_W and R_D compete, and the textures formed are intermediate to those described in Fig. 25.1. The appearance of intensity maxima in positions between the RD and TD can be explained by taking into account the entering texture of the material and the rotation of the poles relative to the termination of fabrication.

4. The relative ratio of wall to diameter reduction determines the direction in which the basal poles move, and the total deformation influences how much they move.

5. The concepts described above have been applied to explain the texture gradient in successive layers through the wall of the tubing. As the ratio of R_W to R_D changes from layer to layer, texture gradients develop across the tubing wall.

6. Similar textures are developed by different fabrication methods – extrusion, rocking, drawing, and planetary ball swaging – when the processes are done with identical reductions in area, wall thickness, and diameter.

7. The development of texture in tubing fabrication processes can be controlled. This is facilitated by the use of a newly developed method for graphically interrelating up to seven fabrication parameters on plots as shown in Fig. 25.2. The path followed during the fabrication procedure appears as a curve on the plot, and the instantaneous direction or slope of the curve in relation to the plot determines the texture that will be formed.

8. Finally, the parameter plots are invaluable in designing dies and mandrels for texture control during fabrication. The various tapers of both the die and the mandrel appear as curves on the parameter plot. Conversely, we can represent a fabrication schedule on the plot, derive its effect on texture, and then design the appropriate dies and mandrels.

ANNEALING TEXTURES IN ZIRCALOY TUBING

Erich Tecnkhoff P. L. Rittenhouse

The annealing textures in Zircaloy tubing are more complex than those reported for rolled and annealed Zr or Ti, and different features develop depending on whether the tubing is hot extruded, tube reduced

ORNL-DWG 69-5592

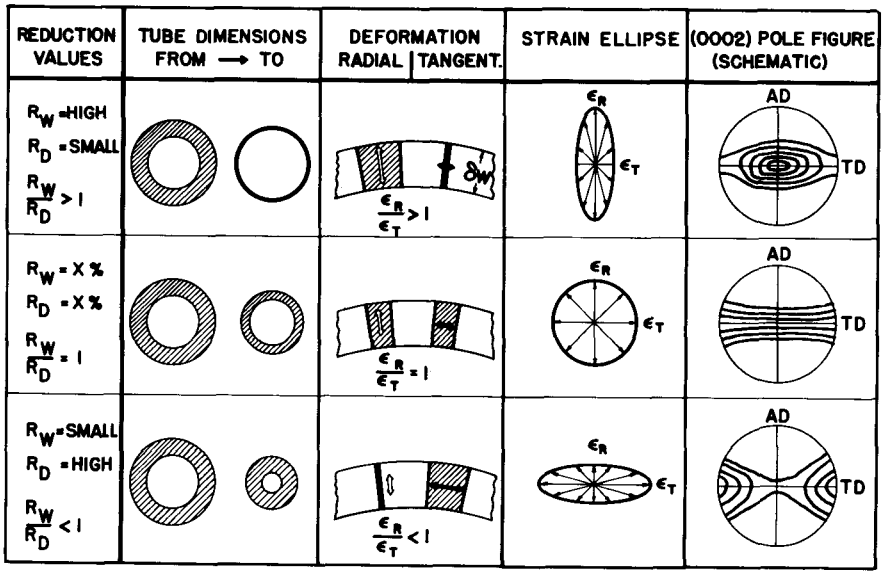

Fig. 25.1. Schematic Demonstration of Texture Development Concepts. The variation of tubing dimensions, deforming stress, its associated strain ellipse, and the resulting texture are illustrated as a function of wall-to-diameter reduction ratio.

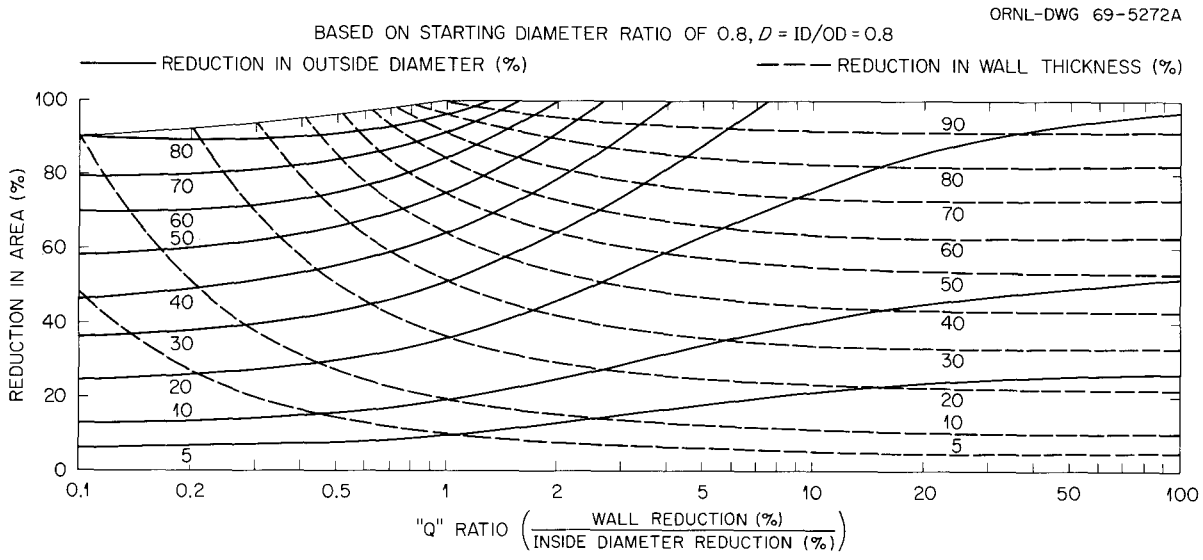

Fig. 25.2. Fabrication Parameter Plot. This chart shows six of the fabrication parameters that can be graphically interrelated. The seventh parameter involves the intersection of constant reduction-in-diameter and wall thickness lines in a particular fashion and is omitted here for graphical clarity.

(rocked), or drawn before it is annealed. Our studies[5] have shown that material extruded at 700°C shows a tilt of basal planes from the radial direction, RD, to the tangential direction, TD, (±40 to 50°), and this tilt remains stable during annealing. The prism planes rotate progressively with increasing annealing temperature to replace the $\langle 10\bar{1}0 \rangle$ by the $\langle 11\bar{2}0 \rangle$ as parallel to the axial direction, AD. However, this replacement is not complete until the annealing temperature exceeds 1000°C. In tubing that we hot extruded and then tube reduced, the position of the basal planes is also stable, but the rotation of basal planes around their poles to replace the $\langle 10\bar{1}0 \rangle$ by the $\langle 11\bar{2}0 \rangle$ is complete after only 1 hr at 700°C. Finally, when we annealed cold drawn tubing the ±40 to 50° tilt of the basal planes was not stable. Instead, the preferred position was parallel to the RD after 1 hr at 700°C. Simultaneously, the basal planes rotated so that the $\langle 10\bar{1}0 \rangle$ direction, parallel to the AD in the drawn condition, became nearly randomly distributed around the basic great circle of the pole figure.

One of the most significant factors in promoting the variations in annealing behavior of Zircaloy tubing is a difference in the starting or deformation texture. Different deformation textures can result from variations in total deformation and deformation method, and these variations are generally greater in tubing fabrication than in rolling. Also, the fabrication temperature influences the texture produced. Finally, differences between the annealing behavior of Zircaloy and zirconium may also depend on the effect of alloying additions and impurities on the active deformation systems, their recrystallization behavior, and the allotropic transformation from close-packed hexagonal α- to body-centered cubic β-zirconium.

One of the most important conclusions of this study is that annealing can alter texture to a larger extent than had been believed. Therefore, with a better understanding of the differences in development of annealing textures, one might use annealing as an additional tool to control texture in Zircaloy.

[5]E. Tenckhoff and P. L. Rittenhouse, "Deformation and Annealing Textures in Drawn Zircaloy Tubing," presented at Fall Meeting of AIME, Detroit, Oct. 13–17, 1968.

PLASTIC YIELDING OF HIGHLY TEXTURED ZIRCALOY TUBING

P. L. Rittenhouse

We have correlated texture with the biaxial yield properties of Zircaloy tubing. Simple relationships between uniaxial yield strength, intensity of basal poles of the texture, and the equivalence of certain stress states allow us to construct biaxial yield surfaces for Zircaloy of any texture. These surfaces suggest that, in certain stress states, differences between the yield strengths of different lots of tubing can exceed 50%. This expectation has been verified by experimentally determining three quadrants of the axial-tangential yield surface for more than a dozen lots of tubing. In addition, these experimental data were used to justify the applicability of the postulated method of yield surface construction. Fig. 25.3 shows the results of two such cross-checks between experiment and theory.

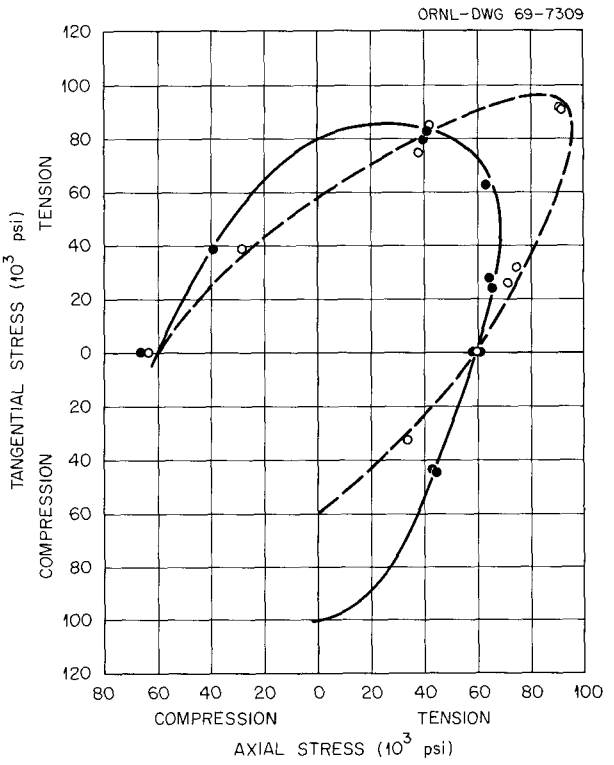

Fig. 25.3. Comparison of Yield Surface Construction Method and Experimental Data. The solid dashed curves represent the biaxial yield surfaces predicted from the textures of two lots of Zircaloy tubing. The filled and open circles are the experimental yield stress data corresponding to the solid and dashed line surfaces respectively.

Part IV. Reactor Development Support

26. Desalination

G. M. Slaughter

Metallurgical assistance for the desalination program concerns two reactor concepts: the Unclad Metal Breeder Reactor (UMBR) and uranium-metal-fueled pressurized water reactor (PWR). Both are proposed as low-cost sources of heat for seawater distillation and power generation.

Work on the UMBR included a literature survey to evaluate the thorium-uranium fuel alloy, the initiation of some basic feasibility studies, and determination of electrical and thermal conductivities of some wrought and powder alloys. A literature survey of the corrosion behavior of the unclad fuel alloy in the sodium coolant was completed and a test program was outlined for determining the corrosion performance. Consulting and liaison services were furnished the Reactor Division in the operation of a sodium loop for preliminary compatibility testing.

Work on the metal-fueled PWR consisted of a literature survey on irradiation performance, fabrication, and potential corrosion problems. An outline of a development program required to produce fuel elements of the required reliability is being written.

EVALUATION OF UMBR FUEL ELEMENT PERFORMANCE AND FABRICATION

G. L. Copeland

The reference UMBR fuel element consists of an array of hexagonal coolant channels in a hexagonal sheath.[1] We surveyed the literature on thorium-uranium alloys with regard to use of a Th–20 wt % U alloy for the UMBR fuel element.[2] The survey indicates that the irradiation performance of the Th–20 wt % U alloy is sufficient to reach the design life of 33,000 Mwd/ton at maximum fuel temperatures up to 650°C.

Several techniques appear practicable for fabricating the fuel element. We have begun small-scale experiments to determine the basic feasibility of (1) casting to shape, (2) casting a billet, and (3) forming from a billet shapes from which the fuel element can be constructed. Since one potential problem in casting appears to be hot tearing due to the low-melting uranium-rich eutectic, we drop cast an H-shaped section into a water-cooled copper mold to determine the extent of hot tearing in this "worst-case" configuration. A cross section of the H is shown in Fig. 26.1. Although some small cracks are in the inside corners, we feel that hot tearing would not be a problem in properly designed

[1] R. P. Hammond *et al.*, *The Unclad-Metal Breeder Reactor (UMBR) for Desalting or Power*, ORNL-4202 (January 1969).

[2] G. L. Copeland, *An Evaluation of Thorium-Uranium Alloys for the UMBR Fuel Element*, ORNL report in preparation.

Y-91484

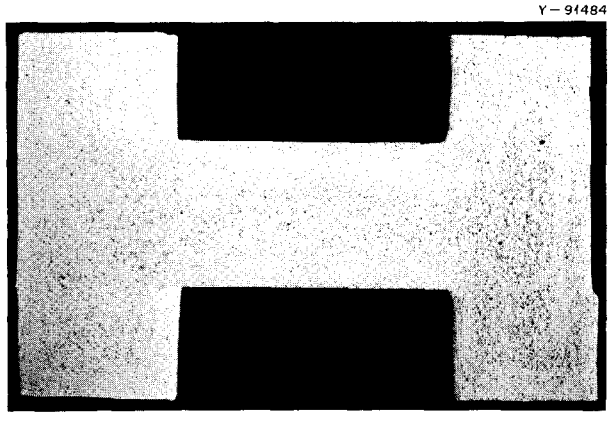

Fig. 26.1. Cross Section of Th–20 wt % U Casting. 5X. As polished. The casting is very sound. Reduced 42%.

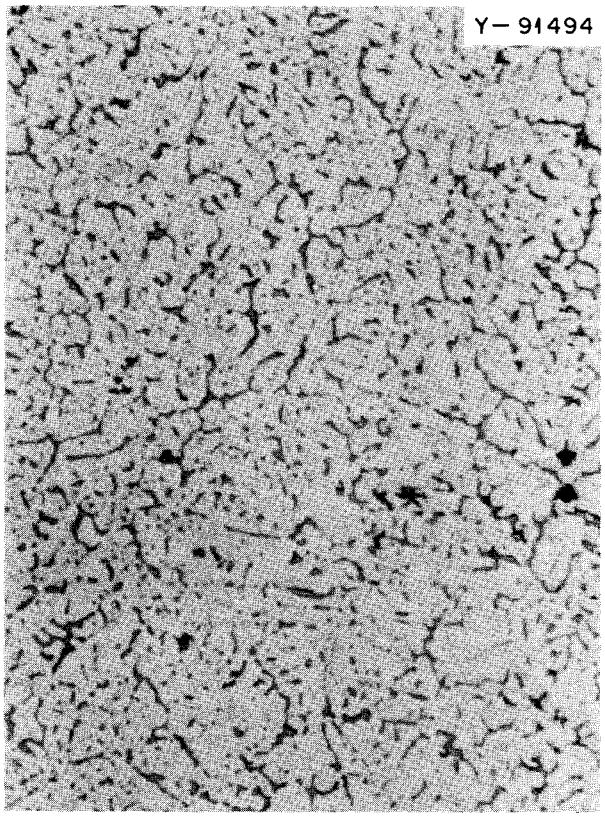

Fig. 26.2. Microstructure of Cast Th–20 wt % U Alloy. The Uranium-rich phase is distributed uniformly through the thorium-rich matrix. As polished. 500X.

castings. The microstructure of this casting is shown in Fig. 26.2. The lightest phase is thorium-rich, the intermediate phase is the uranium-rich eutectic, and the darkest gray particles are oxide. This structure should give good irradiation performance since most of the fission fragments from the uranium will land in the more damage-resistant isotropic thorium phase. After rolling to reductions up to 90%, the uranium phase appears as very small discrete platelets uniformly dispersed in the thorium matrix. This structure should offer the same good irradiation performance.

PHYSICAL PROPERTIES OF THORIUM-URANIUM ALLOYS

R. S. Graves J. P. Moore D. L. McElroy

Physical property determinations within the range 100 to 900°K were completed on samples of Th–20 wt % U produced by a powder metallurgy technique and by arc-casting and hot swaging. Table 26.1 indicates the results obtained using previously described[3,4] measurement methods. The powder-metallurgy-produced samples had densities greater than 90% of that of the

[3] J. P. Moore, D. L. McElroy, and R. S. Graves, *Can. J. Phys.* **45**, 3849–65 (1967).

[4] W. Fulkerson, J. P. Moore, and D. L. McElroy, *J. Appl. Phys.* **37**, 2639–53 (1966).

Table 26.1. Physical Property Results on Th–20 wt % U Alloys

Sample	Density[a] (g/cm^3)	Temperature (°K)	Electrical Resistivity (μohm-cm)	Thermal Conductivity (w cm^{-1} °K^{-1})
Powder metallurgy 1	12.1	298	37.3	
Powder metallurgy 2	12.0	298	30.0	
Powder metallurgy 3	11.6	298	50.1	
Arc-cast, hot-swaged	12.6	100	16.3	0.185
		200	22.1	0.249
		300	27.9	0.289
		400	33.7	0.316
		500	38.5	0.342[b]
		600	43.3	0.366[b]
		700	48.1	0.383[b]
		800	53.0	0.397[b]
		900	57.9	0.408[b]

[a] Bulk density at room temperature, 298°K.
[b] Calculated values; see text.

arc-cast hot-swaged sample, but their room-temperature electrical resistivity varied from 108 to 180% of that of the arc-cast hot-swaged sample. This variation may be due to grain-boundary oxide films in these samples. The electrical resistivity, ρ, of the arc-cast hot-swaged sample could be fit within ±0.4% by

$$\rho = 10.5 + 0.058T, \quad 100 < T < 400°\text{K} ;$$

$$\rho = 14.5 + 0.048T, \quad 400 < T < 900°\text{K} .$$

Thermal conductivity, λ, of the arc-cast hot-swaged sample from 100 to 400°K fits the expression

$$\lambda = 0.0261\ T/\rho + 2.5/T$$

to better than ±1.4%. This expression was used to calculate the λ values given in Table 26.1 from 500 to 900°K. This λ equation indicates a Lorenz constant 6% larger than the Sommerfeld limit and a small lattice component.

METAL-FUELED PWR

G. L. Copeland

The metal-fueled PWR concept is essentially a commercial PWR with the oxide elements replaced by Zircaloy-clad hollow-core, uranium metal fuel elements. The neutronic advantages of uranium metal have long been recognized; however, the low burnup limits imposed by the high swelling and growth have made commercial use impractical. Two significant developments in recent years have increased attainable burnup levels to the point where these fuels are commercially attractive.[5] These developments are (1) the use of low-alloyed uranium (a few hundred parts per million Fe, Si, and Al) to reduce the fuel swelling, and (2) the use of clad, hollow-core elements to allow space for fuel swelling without external cladding strain.

We have surveyed the literature on irradiation performance, fabrication of the fuel elements, and metal-water reactions in the event of a cladding failure. The most pertinent irradiation data is from Pacific Northwest Laboratory, where 6-in.-long test elements of this design have accumulated up to 15,000 Mwd/ton burnup with no significant external swelling.[6,7] The fabrication of hollow-core fuel elements will require extension of the present technology of coextrusion over a mandrel. Extrusions up to 6 ft long have been made; 12-ft-long elements are required for the reactor.

The biggest potential problem appears to be the metal-water reaction if a cladding failure occurs. The reaction is so rapid that the reactor should be shut down immediately upon detection of a failure and the defective element replaced. The most corrosion-resistant alloys of uranium offer some improvement in that the time to shut down could be increased from minutes to hours or days. However, the best solution is to minimize the frequency of cladding failures so that the costs of unscheduled shutdowns do not outweigh the fuel cycle cost advantages of the reactor. Thus, a major part of the development work required on the fuel elements would be directed toward improving reliability and applying nondestructive tests to assure that only reliable fuel elements are accepted for the reactor.

---

[5] T. D. Anderson, J. E. Jones, Jr., and C. M. Podeweltz, *A Study of Metallic-Uranium-Fueled Pressurized Water Reactors for the Production of Process Heat or Electric Power*, ORNL-TM-2451 (in preparation).

[6] R. D. Leggett, Pacific Northwest Laboratory, personal communication.

[7] R. D. Leggett, R. K. Marshall, and J. W. Weber, "Irradiation of Metallic Uranium Hollow Core Fuel Elements to 1 at. % Burnup," *Trans. Am. Nucl. Soc.* 11(1), 153 (June 1968).

27. Gas-Cooled Reactor Program

J. H. Coobs J. L. Scott

Our materials effort in support of the Gas-Cooled Reactor Program is directed primarily toward the development of unclad ceramic fuel elements for high-temperature gas-cooled converter reactors (HTGR's) such as the Fort St. Vrain Reactor being constructed by Gulf General Atomic for Public Services Corporation of Colorado. The reference fuel elements consist of hexagonal graphite blocks containing coated $(Th,U)O_2$ or $(Th,U)C_2$ microspheres and are designed to retain most of the fission-product activity within the fuel element to simplify maintenance.

Our program consists principally of developing techniques for bonding coated particles into fuel elements and preparing, characterizing, and irradiation testing of pyrolytic carbon coatings, coated particles, and simulated bonded fuel elements. Irradiation testing is done principally in HFIR target positions, but a few tests have been run in the Dounreay Fast Reactor (DFR). Fast-neutron exposures approaching the peak HTGR fluence of 8×10^{21} neutrons/cm^2 (>0.18 Mev) have been achieved. Temperatures have spanned the range experienced in an HTGR, 600 to 1200°C.

A significant supporting effort for HTGR's involves the characterization of constituents for use in concretes for prestressed concrete vessels proposed for large power stations. We are also studying the corrosion resistance and other properties of weldments of nickel-base alloys proposed for advanced steam generators and have contributed to the design, fabrication, examination, and interpretation of irradiation experiments on fuel rods proposed for a gas-cooled fast breeder reactor (GCFR).

COATED PARTICLE BONDING DEVELOPMENT FOR HTGR FUELS

J M Robbins

The results from recent irradiation experiments show that the stability of the bonding matrix needs to be improved for use in HTGR fuels.[1] This matrix would minimize spillage of fuel particles if a graphite block were broken. Two possible ways of improving the irradiation stability of the bond are the careful selection of bonding materials and the addition of large amounts of filler material to the matrix or voids among the particles. Materials that are expected to be relatively stable under irradiation are being selected and evaluated as constituents of the bonding mix. Also, a dense matrix produced by the addition of large amounts of filler material is less likely to shrink severely and break up during irradiation.

Poco grade AXM graphite was selected as a prime candidate for the filler material because recent irradiation tests[2] show the relative stability of this material. Additional filler material can be added as carbon black[3] because of the size distribution and wettability of the material. Primarily, prepolymerized furfuryl alcohol has been used as a binder. Specimens have been fabricated containing 40 wt % Poco grade AXM graphite flour (<40 μ) only and containing 29 wt % Poco grade AXM graphite flour with 29 wt % carbon black. The binder was injected with a grease gun.[4] The microstructures of the specimens are compared in Fig. 27.1. The improvement in homogeneity and density of the matrix by the use of carbon black is apparent. Specimens of both types have been fabricated for irradiation testing. Table 27.1 shows the dependence of the carbonized matrix density on the filler content of the binder. The 1.25 g/cm^3 for the mixed filler represents the maximum that can be attained practically with this system.

---

[1] J. H. Coobs *et. al., GCR Program Semiann. Progr. Rept. Sept. 30, 1968,* ORNL-4353, pp. 28–54.

[2] C. R. Kennedy, *MSR Program Semiann. Progr. Rept. Aug. 31, 1968,* ORNL-4344, pp. 233–35.

[3] Thermax from R. T. Vanderbilt Co.

[4] R. L. Hamner, H. Beutler, and J M Robbins, *Metals and Ceramics Div. Ann. Progr. Rept. June 30, 1968,* ORNL-4370, pp. 165–67.

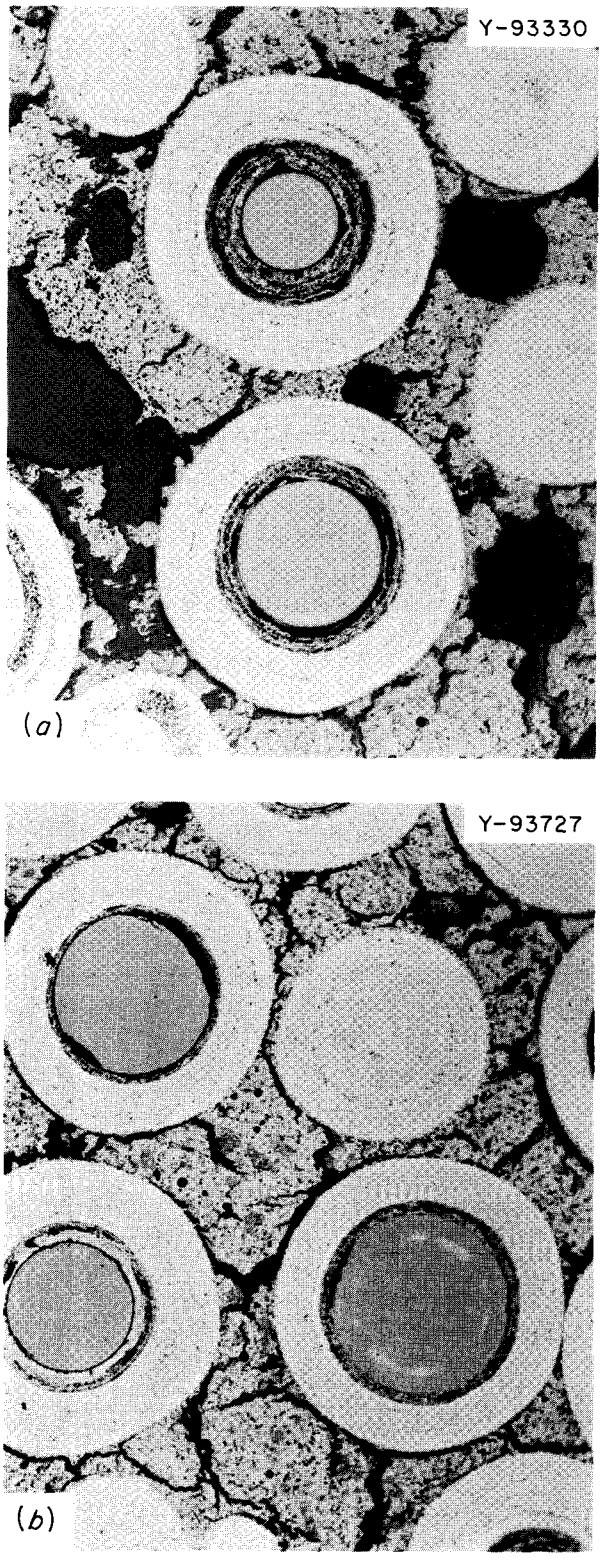

Fig. 27.1. Bonded Beds of Pyrolytic-Carbon-Coated ThO_2 Particles After Carbonizing at 1000°C. Prepolymerized furfuryl alcohol (Varcum 8251) binder. As polished. 100X. (*a*) 40 wt % Poco AXM graphite flour as filler. (*b*) 29 wt % Poco AXM graphite flour and 29 wt % carbon black (Thermax) as fillers.

Table 27.1. Effect of Resin Type and Filler Content on Density of Carbonized Matrix

Resin	Filler		Matrix Density (g/cm^3)
	Type	Content (wt %)	
Phenolic	Graphite flour	15	0.60
Furfuryl alcohol	Graphite flour	15	0.65
Phenolic	Graphite flour	40	0.85
Furfuryl alcohol	Graphite flour	40	0.90
Furfuryl alcohol	Graphite flour Carbon black	29 29 } 58	1.25

Because of the relative ease of fabrication, most bonded-bed fuel specimens have been made with thermosetting binders. A binder that yields a highly graphitizable carbon would, perhaps, be more desirable than the glassy carbons produced from phenolic resin and furfuryl alcohol. Isotruxene, decacyclene, acenaphthylene, and various pitches are examples of such binders. Since these binders are thermoplastic, fabrication of specimens with the high (62–64 vol %) particle loading needed for the Fort St. Vrain Reactor is difficult. Decacyclene is of particular interest because it yields over 85 wt % C under conditions used for bonded-bed fuel fabrication. However, it melts near 400°C and thus is difficult to work with. We are investigating coal tar pitch[5] as a thermoplastic binder because of its relatively low melting point (about 100°C). Small specimens containing grade 15V pitch with 40 wt % Poco grade AXM graphite finer than 40 μ have been fabricated successfully and are being readied for irradiation testing at Dounreay, Scotland.

IRRADIATION OF BONDED BEDS

S. C. Weaver

Two capsules, HFIR-HT1 and HFIR-HT3, were irradiated in the target region of HFIR to test the stability of bonded-bed fuel sticks under irradiation. The test conditions ranged from 660 to 1100°C with a maximum fast-neutron exposure of approximately 8 X 10^{21} neutrons/cm^2 (>0.18 Mev).

The individual test specimens, 0.20 in. in diameter X 0.25 in. long, were made from pyrolytic-carbon-coated microspheres of ZrO_2 by injection bonding. We used ZrO_2 because of excessive fission and gamma heating of UO_2 or ThO_2 kernels. The binder matrix consisted of carbonized phenolic resin and graphite. In addition to the bonded beds, samples containing matrix material only were tested to check the dimensional changes. The samples were contained in Poco grade AXF graphite,

[5] Grade 15V pitch from Allied Chemical Company.

which was selected for its dimensional stability during irradiation.

The bonded beds tested from 660 to 800°C remained relatively strong after exposure. Although the samples were quite friable, they could be handled with manipulators. The bonded beds irradiated from 950 to 1100°C had completely disintegrated to loose particles. Figure 27.2 shows the high-temperature samples after irradiation. These samples probably debonded because of severe shrinkage of the bonding matrix. Measurements on the resin sticks containing no coated particles showed volume shrinkages ranging from 18 to 35% depending on the temperature and neutron exposure.

Dimensions were also measured on some of the bonded beds from the low-temperature region of HFIR-HT3. Beds containing coated particles with high-temperature isotropic outer coatings showed volume shrinkages averaging 5%, while beds containing particles with low-temperature isotropic outer coatings shrank 16%. These shrinkages correlate well with those observed on unbonded coated particles and pyrolytic carbon strips.

Several of the bonded beds from each capsule were examined metallographically for coating failure. The bonded beds irradiated at 660°C to fast neutron doses of 3.6 to 5.0 $\times$ 10^{21} neutrons/cm^2 showed no cracked coatings. However, about 20% of the coatings were cracked in the beds in HFIR-HT1 irradiated at slightly higher temperatures (800°C) and fast-neutron doses (6.5 $\times$ 10^{21} neutrons/cm^2). The specimens irradiated at 1100°C to maximum neutron exposures of 8 $\times$ 10^{21} neutrons/cm^2 showed only a very few cracked coatings (~3%). However, the samples irradiated at 950°C to the same exposure contained a large number of broken particles, from 27 to 100% per sample. This high failure rate was attributed in part to carbon transport by CO-CO_2 in the static capsule. The gas came from reaction between the ZrO_2 kernels and pyrolytic carbon coatings. In future tests ZrC or SiC kernels will be used.

The problems experienced with these bonded-bed irradiations emphasize the need for continuing effort. Additional irradiation tests are under construction with improved bonded beds. These tests required only two months irradiation time because of the high fast fluxes in HFIR. The ability to pinpoint problem areas in a short period of time emphasized the value of HFIR as a testing facility.

IRRADIATION OF PYROLYTIC CARBON COATINGS

D. M. Hewette, II T. G. Godfrey

Fast-neutron damage may induce significant plastic deformation of pyrolytic carbon coatings, sometimes causing cracking. We are testing various types of

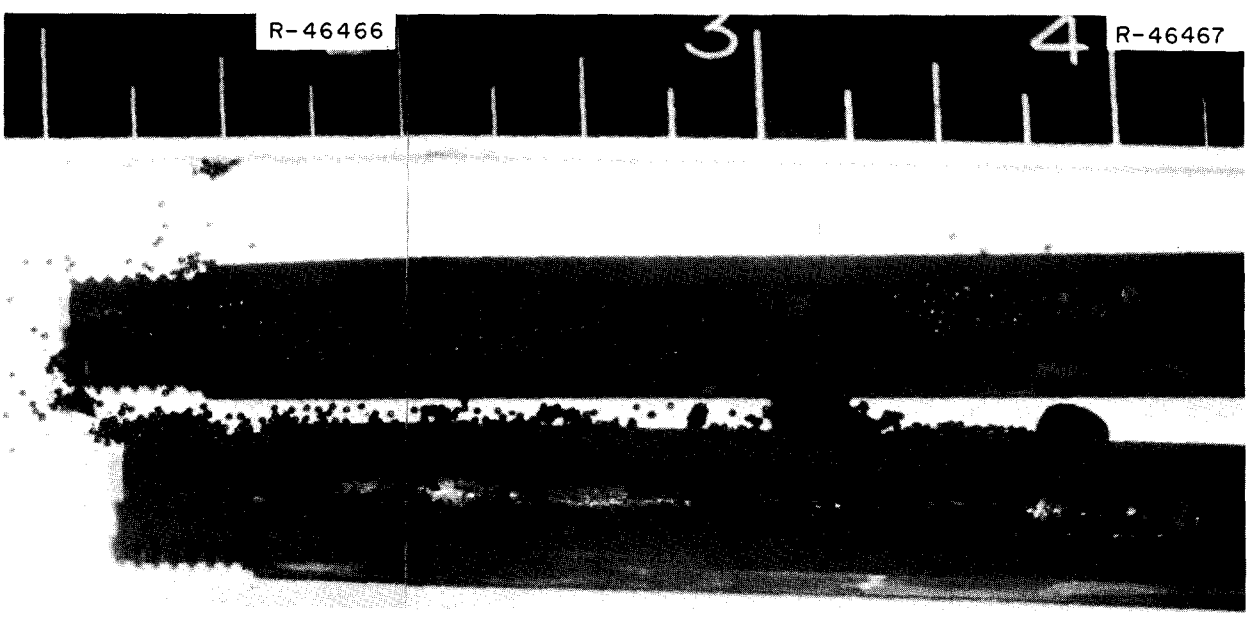

Fig. 27.2. Poco Graphite Specimen Holder Containing Disintegrated Bonded Beds After Irradiation at 950°C to a Fast Neutron Exposure of 8 $\times$ 10^{21} Neutrons/cm^2 (>0.18 Mev). The intact specimens on the right hand were disks of H-327 graphite and bonded matrix specimens with no coated particles.

coatings at temperatures and fast fluences experienced in the HTGR to determine both the magnitudes and mechanisms of these effects. The resulting data are used in mathematical models of coated particle behavior.

Two systematic irradiation tests were completed this year – one in the Dounreay Fast Reactor (DFR) and the other in the High Flux Isotope Reactor (HFIR). In the DFR test we studied the effects of fast-neutron damage alone on four types of spherical pyrolytic carbon coatings. The coatings ranged in density from 1.74 to 2.07 g/cm^3, had Bacon anisotropy factors from 1.0 to 1.4, and were irradiated to 4.5×10^{21} neutrons/cm^2 (>0.18 Mev) at about 1200°C. A porous buffer layer prevented interaction between the coating and the sol-gel ThO_2 kernels. Essentially no fissioning occurred in the ThO_2 in the fast-neutron spectrum.

The properties of the four coating structures and the irradiation results are given at the left in Fig. 27.3. Only the coatings with the highest anisotropy factor failed. Coatings with an initial density of 1.8 g/cm^3 or less densified, while coatings with an initial density of 1.9 g/cm^3 or greater swelled. Metallographic examination

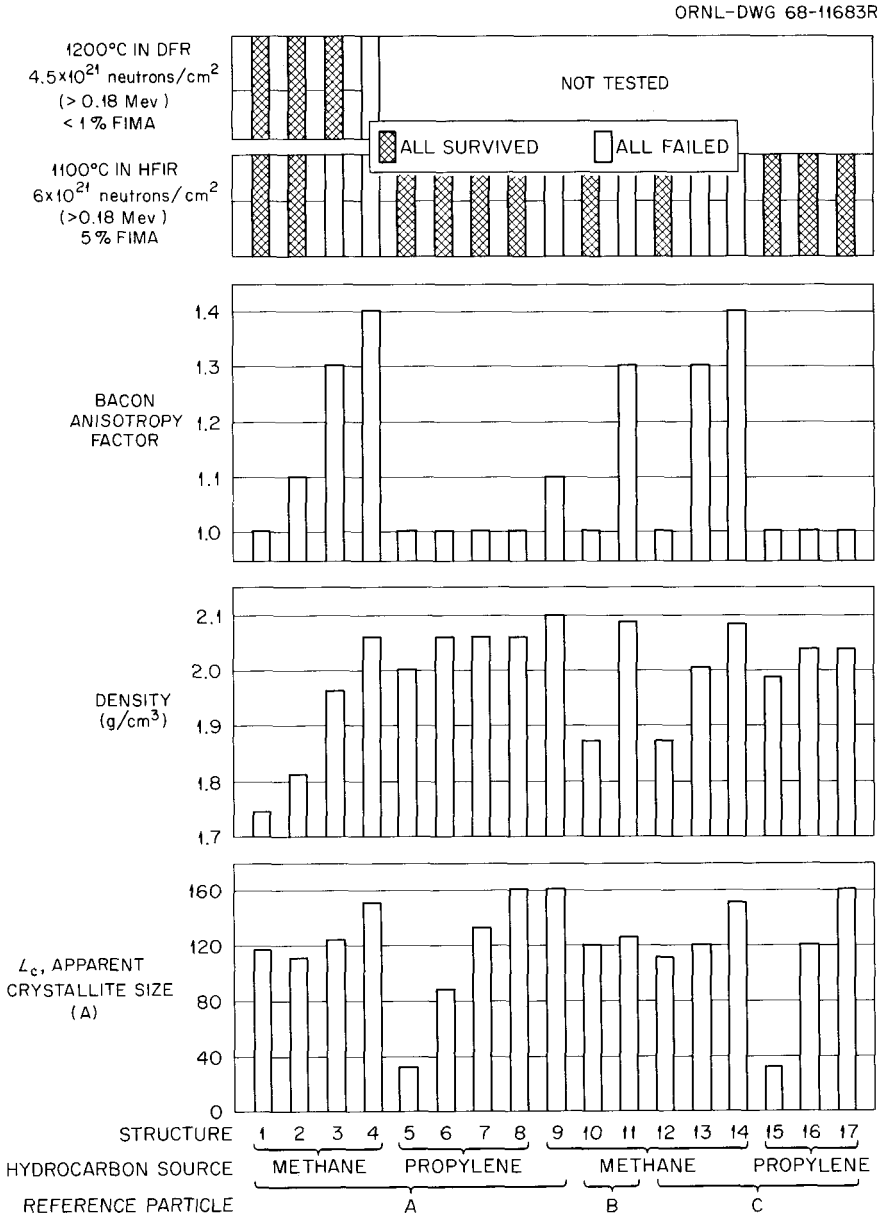

Fig. 27.3. Effect of Outer Coating Properties on Pyrolytic-Carbon-Coated Particle Survival. Particle dimensions are given in Table 27.2.

revealed that the preferred orientation increased in the coatings that densified.

In HFIR we irradiated 17 sample types (including the four types tested in the DFR) consisting of coated ThO_2 particles. One set of each type was tested at either 650 or 700°C and another at 1100°C. Some properties of the samples are given in Table 27.2 and Fig. 27.3. All particle types irradiated at the lower temperatures survived. Here the fluence was 4×10^{21} neutrons/cm^2 and the burnup was about 3%. At the top of Fig. 27.3 we show the survival rate of the samples tested at 1100°C to a fluence of 6×10^{21} neutrons/cm^2 (>0.18 Mev) and a burnup of 5%. All isotropic coatings survived regardless of density and crystallite size in the range tested. An indication of the importance of density was evident from the behavior of two samples (structures 2 and 9) that were nearly isotropic (BAF = 1.1). The sample with a coating density of 1.81 g/cm^3 survived 100%, while all particles failed in the sample that had a density of 2.1 g/cm^3.

Two sample types contained a SiC intermediate barrier layer. At 1100°C this type particle survived with an outer layer having a density of 1.81 g/cm^3 and a BAF = 1 but failed with an outer layer having a density of 2.06 g/cm^3 and a BAF of 1.3.

The results of this test indicate that the pyrolytic-carbon-coated particles of the current HTGR reference (having a SiC barrier layer) will survive fast-neutron exposure and a fuel burnup two-thirds and one-fourth of the current design, respectively.

We compared the performance of some of these coated particles with predictions of the Prados-Scott model[6-10] and found excellent agreement. Two separate subroutines were used. One employed dimensional change data of Bokros *et al.*[11] obtained for a variety of pyrolytic carbon disks irradiated to high fluences. These data yield the results shown in Fig. 27.4 for four of the particle batches irradiated in HFIR. We see that all were predicted to survive at the fluence obtained at the lower temperature and two to fail at the higher fluence, just as observed.

A second subroutine involved the assumption that the anisotropy of the outer coating increases with the creep strain while the density changes exponentially to the

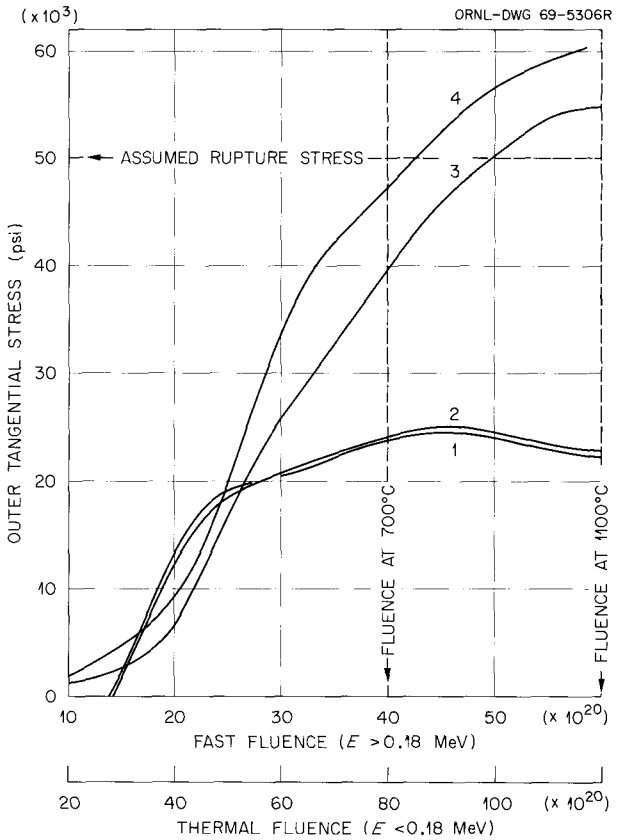

Fig. 27.4. Calculated Stress History for Particles Irradiated in the HFIR HT-1 Test. Creep coefficient of 2.0×10^{-27} psi^{-1} (neutrons/cm^2)$^{-1}$, dimensional change data of Bokros *et al.* (GA-8700). Numbers give structural designation corresponding to Fig. 27.3.

Table 27.2. HFIR HT1 Reference Particles

Designation	Kernel Sol-Gel ThO_2 Microsphere Diameter (μ)	Inner Layer Thickness (μ)	Inner Layer Nature	Outer Layer (μ)
A	275	40	Porous	75
B	275	15	Low density, isotropic	75
		25	SiC	
C	425	100	Porous	150

[6] J. W. Prados and J. L. Scott, *Analysis of Stress and Strain in Spherical Shells of Pyrolytic Carbon,* ORNL-3553 (June 1964).

[7] J. W. Prados and J. L. Scott, "Mathematical Model for Predicting Coated-Particle Behavior," *Nucl. Appl.* 2, 402–14 (1966).

[8] J. W. Prados, "Calculation of Creep in Spherical Pyrolytic-Carbon Shells Under Combined Radiation Damage and Internal Pressure," *Trans. Am. Nucl. Soc.* 9(2), 382–83 (1966).

[9] J. W. Prados and J. L. Scott, "The Influence of Pyrolytic-Carbon Creep on Coated-Particle Fuel Performance," *Nucl. Appl.* 3, 488–94 (1967).

[10] J. W. Prados and T. G. Godfrey, *GCR Program Semiann. Progr. Rept. March 31, 1968,* ORNL-4266, pp. 71–76.

[11] J. C. Bokros *et al., Radiation-Induced Dimensional Changes and Creep in Carbonaceous Materials,* GA-8700 (Aug. 30, 1968).

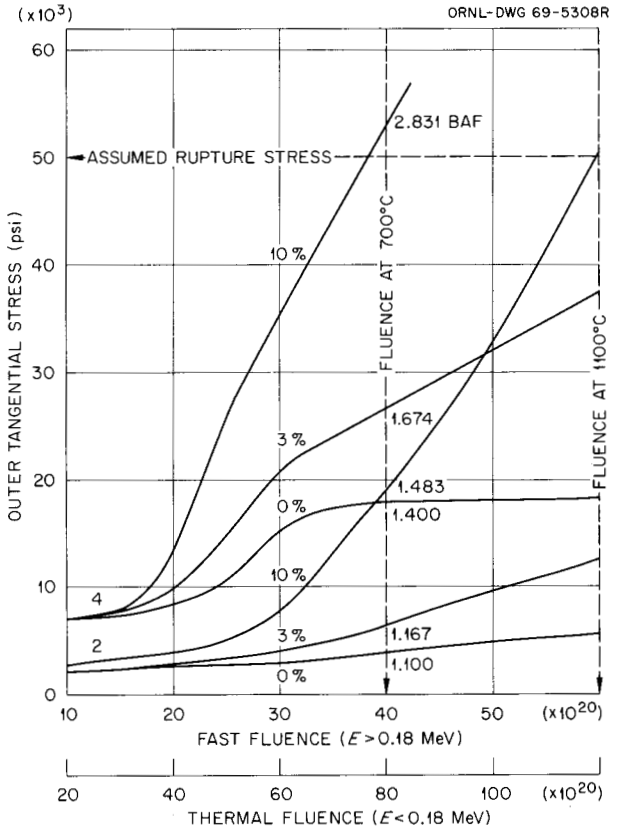

Fig. 27.5. Calculated Stress History for Particles Irradiated in HFIR HT-1 Test. Creep coefficient of 2.0 X 10^{-27} psi^{-1} $(neutrons/cm^2)^{-1}$, exponential change in density to final value. Indicated percent change in BAF per unit creep strain. Numbers give structural designation.

finally observed value. Figure 27.5 shows results obtained for two of the HFIR particle types for 0, 3, and 10% changes in BAF per unit creep strain. A percentage change between 3 and 10 would yield the correct prediction.

CONCRETE FOR REACTOR PRESSURE VESSELS

J. G. Stradley J. P. Moore

The time-dependent deformation behavior and the strength of concrete as affected by the operating environment are among the most important aspects of the design and safety evaluation of a prestressed concrete reactor vessel (PCRV). As discussed last year,[12] the time-dependent deformation behavior or creep and shrinkage are being determined for three different concretes by the Waterways Experiment Station and the University of Texas. We are characterizing the three concretes and their individual constituents so that the deformation data will be more meaningful. These studies are a portion of a larger program[13] directed toward assessing the long-range performance and safety of PCRV structures.

Three different types of aggregate – limestone, graywacke, and chert – are being used with the same type II portland cement to produce the three concretes under study. Property data such as size, shape, surface roughness, mineralogical class, chemical composition, strength, modulus of elasticity, Poisson's ratio, and coefficient of thermal expansion have been determined for the aggregates[14,15] by techniques such as x-ray diffraction, chemical analysis, petrographic examination, differential thermal analysis (DTA), thermal gravimetric analysis (TGA), screen analyses, linear thermal expansion, and compression loading. The three concretes have been characterized[15] at various ages by determining their compressive and splitting tensile strengths, Poisson's ratios, and modulus of elasticity. An apparatus was designed and built for measuring the coefficient of thermal expansion of concrete from room temperature to 350°F (177°C). Coefficients[14] have been determined for the limestone portland cement concrete in an unsealed state. The thermal conductivity, thermal diffusivity, and specific heat were measured for the limestone portland cement concrete.[16]

STEAM CORROSION OF ADVANCED STEAM GENERATOR ALLOYS

J. P. Hammond

The corrosion characteristics of similar- and dissimilar-metal weldments in superheater alloys were determined after exposures of 6000 hr in dynamic steam at 1100 and 1200°F. Fifteen alloy combinations

[12] J. G. Stradley, L. A. Harris, and J. P. Moore, *Metals and Ceramics Div. Ann. Progr. Rept. June 30, 1968,* ORNL-4370, pp. 172–73.

[13] G. D. Whitman, *Prestressed Concrete Reactor Vessel Research and Development Program Summary,* ORNL-TM-2179, April 1, 1968.

[14] J. H. Hannah, M. R. Hansen, L. A. Harris, J. P. Moore, and J. G. Stradley, *GCR Program Semiann. Progr. Rept. Sept. 30, 1968,* ORNL-4353, pp. 210–23.

[15] J. H. Hannah, J. P. Moore, and J. G. Stradley, "Basic Concrete Studies," *GCR Program Semiann. Progr. Rept. March 31, 1969,* ORNL-4424 (in press).

[16] J. P. Moore, R. S. Graves, J. G. Stradley, J. H. Hannah, and D. L. McElroy, *Some Thermal Properties of a Limestone Concrete,* ORNL-TM-2644 (in press).

containing Inconel 625, Hastelloy X, IN 102, Incoloy 800, Inconel 600, 2¼% Cr–1% Mo low-alloy steel, and type 304 stainless steel plate, welded with various recommended filler metals including Inconel 82, Inconel 62, Hastelloy W, and type 308 stainless steel, are being investigated.[17] Both general corrosion and various forms of preferential attack are being investigated. Transverse, strip-type corrosion specimens were used; these were cut from ½-in.-thick weldments prepared by the gas tungsten-arc process using 5/32-in. filler wire.

The corrosion on weldments of 2¼% Cr–1% Mo steel (lower temperature application) joined to Incoloy 800 (intermediate-temperature application) with Inconel 82 filler metal at 1100°F was 100 times that on other dissimilar-metal weldments, and at 1200°F attack of the low-alloy steel in 4000 hr was so great (0.03 in. of scale) as to require stopping tests at this temperature.

Dissimilar-metal joints of Incoloy 800 to Inconel 625, Hastelloy X, and IN 102 (alloys for use at higher temperatures) were welded with Inconel 82 and with wire taken from base metal of the high-temperature alloys. The welds showed very good corrosion behavior at both 1100 and 1200°F aside from an incipient deficiency in the IN 102 alloy. The weight gains for these weldments after 6000 hr at 1200°F was very low (around 0.35 mg/cm^2 and lower), as were their rates of corrosion. The scales that formed on Inconel 625 and Hastelloy X as plate and filler metal and on the Inconel 82 filler metal were uniform, tenacious, and only 2 to 6 μ thick (Fig. 27.6). Whereas corrosion of IN 102 was not great, oxide scale on this alloy tended to spall at 1200°F.

The corrosion of the similar-metal weldments as a function of time at 1100 and 1200°F is illustrated by the weight-gain curves presented in Fig. 27.7. The anomaly of a higher weight gain in the IN 102 weldment at 1100°F than at 1200°F is explained by the spalling tendency of this alloy at the higher temperature.

Corrosion results on both similar- and dissimilar-metal weldments by the weight-gain method of study correlated well with metallographic observations of scaling characteristics and thickness.

No preferential corrosion was uncovered along the fusion lines of any of the dissimilar-metal welds; this had been one of the original major points of concern in this study. Also, preliminary studies of stress corrosion cracking have been conducted on statically stressed U-bend specimens at 1100°F with and without crevices. Indications are that stress corrosion probably does not occur in these weldments in high-quality commerical steam for the amount of moisture present. Future tests are planned in which oxygen and chloride ions will be introduced as contaminants.

GAS-COOLED FAST REACTOR FUEL ELEMENT DEVELOPMENT

R. B. Fitts C. M. Cox
A. L. Lotts

Most of the effort to develop a fast breeder reactor is being applied to the sodium-cooled LMFBR concepts. There is, however, much interest in the development of the gas-cooled fast breeder reactor (GCFR) as an alternate. It has the potential of lower cost power production and would avoid the sodium void coefficient problem and difficulties with maintenance of liquid-metal-cooled systems.[18]

Our GCFR fuel element development work is done on two closely related but separate programs. One is a cooperative program with Gulf General Atomic in which several GGA fuel rod design concepts have been irradiation tested by ORNL. The other is an independent fuel element development effort, which was initiated during the past year. This work is closely coordinated with the GGA GCFR Core Development Program and with the GCFR core design and safety studies under way at ORNL.

GCFR Fuel Development

R. B. Fitts C. M. Cox
J. M. Leitnaker

We began developing a viable fuel element for the Gas-Cooled Fast Reactor. This effort includes the selection of reference fuel rod designs and the necessary in- and out-of-reactor testing to verify and improve these designs. A short-range objective has been the definition and testing of a reference fuel rod for a GCFR to operate at minimum economically competitive conditions. The necessary data will subsequently be obtained to optimize and test a fuel rod and element for a high-performance GCFR. The main areas of research are: (1) fuel element design, (2) irradiation tests in thermal and fast flux reactors, (3) out-of-reactor

[17] J. P. Hammond, "Properties of Nickel Alloy Weldments for Advanced HTGR Steam Generators," *GCR Program Semiann. Progr. Rept. March 31, 1969*, ORNL-4424 (in press).

[18] *An Evaluation of Alternate Coolant Fast Breeder Reactors*, WASH-1090 (April 1969).

PHOTO 96679

Fig. 27.6. Typical Scales Formed on Two Weldments in Steam at 1200°F in 4000 hr. As polished. 2000X. Top sequence shows (left to right) scale on Inconel 625 plate, Inconel 625 filler metal, and Incoloy 800 plate. Bottom sequence similarly shows Hastelloy X plate, Inconel 82 filler metal, and Incoloy 800 plate.

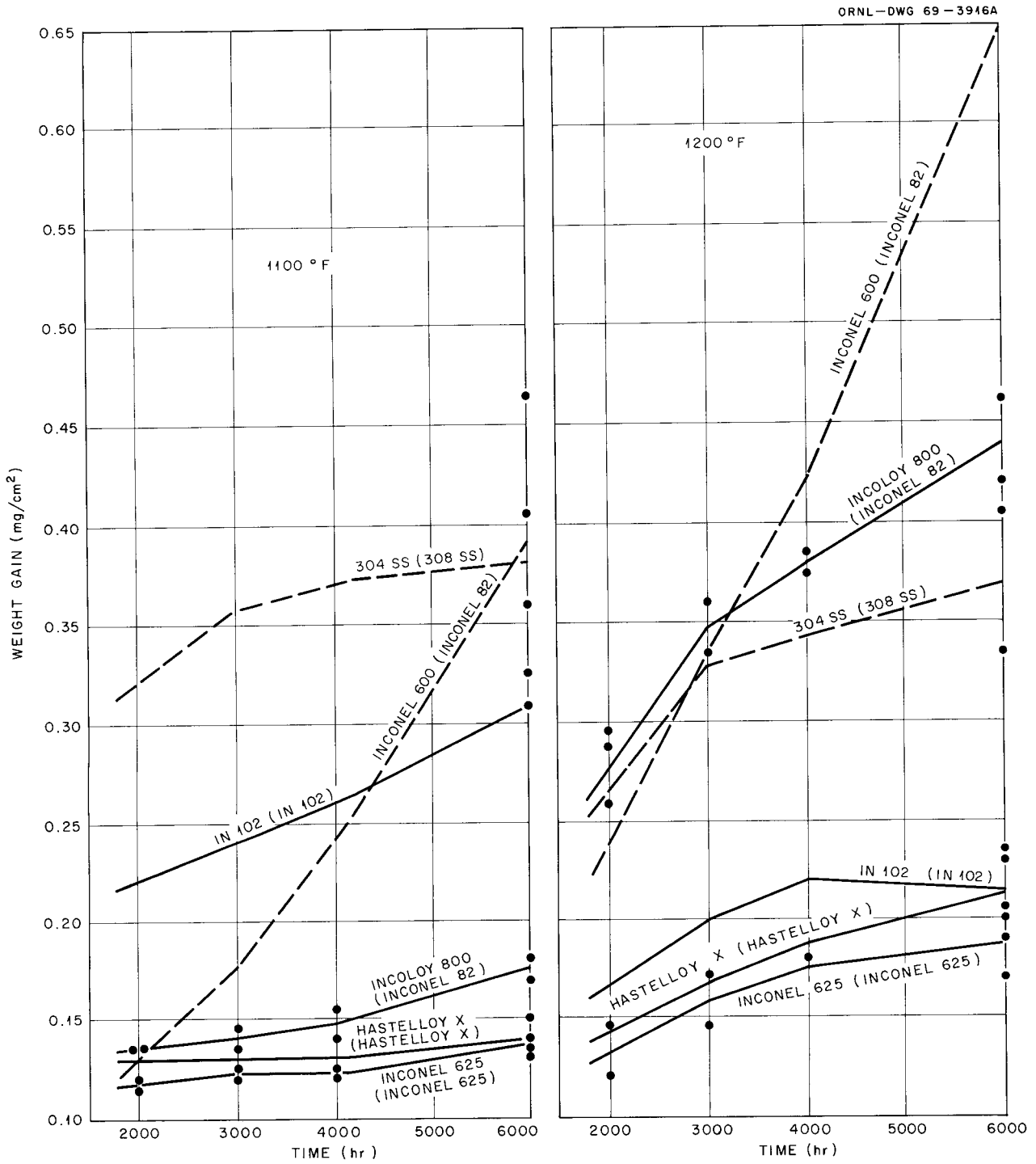

Fig. 27.7. Weight Gain Curves of Superheater Alloy Weldments. Alloy in parentheses is the filler metal.

fuel and cladding compatibility studies, and (4) fast flux testing of cladding materials under GCFR conditions.

The work this year has concentrated on the preparation of a design and irradiation test for the reference GCFR "minimum competitive" fuel rod. This design is based on an attempt to use, to the maximum extent possible, the fuel rod technology developed for the LMFBR system. A review of the existing GGA-ORNL irradiation tests (see below) and of current LMFBR data leads to the initial reference design conditions that follow:

Fuel	$(U,Pu)O_2$
Cladding	Type 316 stainless steel
Cladding temperature	650°C
Heat generation rate	16 kw/ft
Burnup	75,000 Mwd/MT
Coolant pressure	1000 psi
Internal pressure	1050 psi

The significant difference between this design and the present LMFBR designs is the balanced internal and external pressures. These are probably necessary to prevent collapse of the fuel cladding under the high coolant pressures in the GCFR. More detailed design studies, which are under way, may lead to modification of these conditions for later tests.

The out-of-reactor studies of fuel thermodynamics and fuel-cladding compatibility are in their early stages, but they are essential to the development of an optimized GCFR core. This optimization requires the use of higher coolant and cladding temperatures than are presently planned for the LMFBR, and fuel-cladding chemical interactions will be aggravated. Such chemical interactions between cladding and both UO_2 and $(U,Pu)O_2$ fuels have been observed in fuel pins tested in the cooperative ORNL-GGA irradiation program, as shown in Fig. 27.8. A comparison of fuel pins 10 and 11 shows that the reaction zone at 816°C is about twice that observed at 710°C. At equivalent temperatures in fuel pins 11 and 13 we observed that the interaction zone between UO_2 and Hastelloy X is about twice that for $(U,Pu)O_2$ fuel, but the burnup and exposure were also greater. Similar reactions between $(U,Pu)O_2$ fuel and stainless steels have been observed by others.[19,20] These interactions must be studied and understood on engineering and more fundamental bases. These interactions are being investigated in cooperation with similar efforts on the LMFBR fuel system reported in Chapter 24 of this report.

[19] *Sodium-Cooled Reactors, Fast Ceramic Reactor Development Program, Twenty-Sixth Quarterly Report, January-April, 1968,* GEAP-5631.

[20] T. Lauritzen, *Compatibility of Urania-Plutonia Fuels with Stainless Steel and Sodium,* GEAP-5633 (June 1968).

Cooperative Irradiation Test Capsules

R. B. Fitts E. L. Long, Jr.
A. W. Longest[21]

Sixteen fuel rods have been examined in a cooperative program with Gulf General Atomic, aimed at the evaluation of various fuel rod concepts for use in the Gas-Cooled Fast Breeder Reactor. Three additional rods are being examined, and the next irradiation capsule in this series is being assembled.

The 0.350-in.-OD fuel rods are tested in NaK-filled capsules pressurized at about 1000 psig to simulate GCFR coolant pressure. Several thermocouples are used on each fuel rod to monitor cladding temperature. The early rods contained UO_2 fuel clad with Hastelloy X; seven of the last eight rods were $(U,Pu)O_2$ fueled, and one was clad with type 316 stainless steel.

The results from the first 16 test rods[22-24] showed that: (1) fuel pins with thin fuel-supported cladding are not acceptable because of fuel plasticity, (2) prepressurizing of fuel pins to reduce differential pressure will prolong fuel pin life but presents manufacturing difficulties, and (3) chemical reactions between fuel and cladding may affect the strength and integrity of the cladding (as discussed above). As a result of these tests, the primary reference design for the GCFR now includes pressure equalization.[25] In this design, the pressure differential across the cladding, arising in other concepts from the high coolant pressure, is eliminated by a pressure balancing system. Most future tests will employ pressure-equalized fuel rods to study fuel-cladding interactions and fuel rod performance.

[21] Reactor Division.

[22] E. L. Long, Jr. *et al.,* "Irradiation Tests of Fuel Rods Containing UO_2 for GCFR," to be published in *Ceramic Nuclear Fuels,* American Ceramic Society, Inc., Columbus, Ohio.

[23] R. B. Fitts, E. L. Long, Jr., and A. R. Olsen, *GCR Program Semiann. Progr. Rept. Sept. 30, 1968,* ORNL-4353, pp. 118–24.

[24] R. B. Fitts, E. L. Long, Jr., and A. R. Olsen, "Postirradiation Examination of Capsule O3-P7," *GCR Program Semiann. Progr. Rept. March 31, 1969,* ORNL-4424 (in press).

[25] "Manifolded Fuel Rod Concept," *Gas-Cooled Fast Breeder Reactor Quarterly Progress Report for Period Aug. 1, 1967 to July 31, 1968,* GA-8787, pp. 61–62 (Sept. 20, 1968).

R-33965

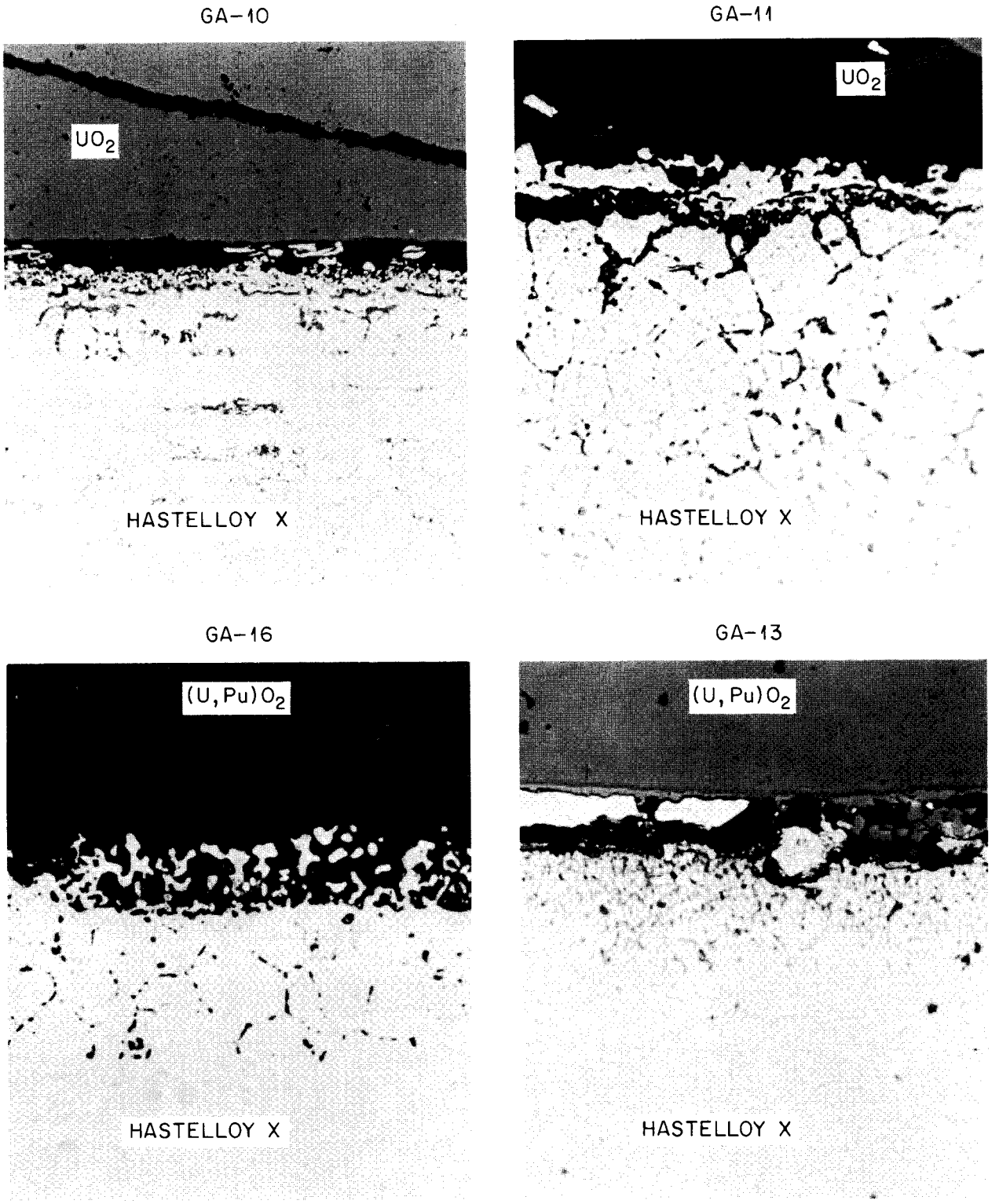

Fig. 27.8. Fuel-Cladding Reaction Zones Observed in Irradiated GCFR Fuel Rods. (*a*) Rod GA-10 irradiated to 11,000 Mwd/MT with a maximum cladding temperature of 710°C. (*b*) Rod GA-11 irradiated to 12,600 Mwd/MT with a maximum cladding temperature of 816°C. (*c*) Rod GA-16 irradiated to 16,100 Mwd/MT with a maximum cladding temperature of 756°C. (*d*) Rod GA-13 irradiated to 4800 Mwd/MT with a maximum cladding temperature of 812°C.

The three fuel rods[26] (GA-17, -18, -19) presently undergoing examination in the HRLEL were of a sealed pin design,[27] which employed initial internal pressurization to minimize the pressure differential across the cladding. Two rods were clad with Hastelloy X, and the third with type 316 stainless steel. They have apparently performed satisfactorily[28] to 50,000 Mwd/MT of $(U,Pu)O_2$ fuel at peak cladding outer surface temperatures of 650°C. This concept is now the basis of the backup GCFR fuel rod design.

The capsule presently under fabrication contains fuel rod GA-20. This is a pressure-equalized, type 316 stainless-steel-clad $(U,Pu)O_2$-fueled rod designed[29] to be tested to 50,000 Mwd/MT at 15 kw/ft. The peak cladding surface temperature will be 700°C, and the integral charcoal fission product trap at the vent end will operate at approximately 300°C. The fuel will be sol-gel pellets produced at 91% of theoretical density, as described in Chapter 24 of this report. This test will yield information on the performance of a true vented fuel rod and on the behavior of fission products in such a system.

---

[26] "Capsule 8," *Gas-Cooled Fast Breeder Reactor Quarterly Progress Report for Period Aug. 1, 1967 to July 31, 1968,* GA-8787, pp. 110–11 (Sept. 20, 1968).

[27] "Fuel-Cladding Interacting Fuel Rod Concept," *Gas-Cooled Fast Breeder Reactor Quarterly Progress Report for Period Aug. 1, 1967 to July 31, 1968,* GA-8787, pp. 38–57 (Sept. 20, 1968).

[28] R. B. Fitts and A. R. Olsen, "Postirradiation Examination of Capsule O4-P8," *GCR Program Semiann. Progr. Rept. March 31, 1969,* ORNL-4424 (in press).

[29] "Irradiation of Capsule 9," *Gas-Cooled Fast Breeder Reactor Quarterly Progress Report for Period Aug. 1, 1967 to July 31, 1968,* GA-8787, pp. 110–16 (Sept. 20, 1968).

28. Heavy Section Steel Technology

D. A. Canonico

The Heavy Section Steel Technology Program is an engineering effort to determine the structural behavior of the thick plates and pressure vessels needed for large light-water nuclear reactors. The overall program emphasizes the effects of flaws, discontinuities, and inhomogeneities on the integrity of the reactor vessel during shutdown as well as during operation. Extensive testing programs are being conducted on weldments and plates. These include the determination of strength and classical fracture toughness properties as well as the development and application of fracture mechanics for those steels currently being used in the fabrication of light-water nuclear pressure vessels.

We participate as both consultants and experimentalists. First, we serve on the staff of the Program Office as metallurgical consultants and are expected to contribute to decisions that require metallurgical knowledge. In addition, we are involved experimentally in those tasks that require the facilities and expertise available within the Division.

CHARACTERIZATION OF HEAVY SECTION STEEL WELDMENTS

D. A. Canonico

Submerged arc, shielded-metal arc, and electroslag weldments in heavy sections are under study. Representative photographs of the various types of weldments are shown in Fig. 28.1. The weld metal in the electroslag weldment is least discernible; however, this is due to the quench-and-temper treatment imposed on the completed weldment. Our initial efforts have concentrated on a submerged arc weld made using multipass welding procedures and parameters that are typical for joining 12-in.-thick A533 grade B Class I steel plates. The weldment was stress relieved at 1150°F for 15 hr.

The weld metal was chemically analyzed and found to be homogeneous. A complete Charpy V (CV) notch weld-metal curve has been determined for the quarter-thickness location; these data are presented in Fig. 28.2. The weld-metal CV energy shelf is similar to that obtained for the base metal, approximately 120 ft-lb; however, the 30 ft-lb temperature is considerably lower, −60°F vs +10°F. The energy variation through the weld at −60°F has been investigated, and differences occurred; however, they are within the anticipated CV notch variations for tests conducted at temperatures within the transition range. The energy values ranged from about 10 to 35 ft-lb at −60°F.

Transverse weld metal tensile properties have been determined. Three diameters of tensile specimens were employed: 0.125, 0.252, and the standard 0.505 in. All possessed 0.2% offset yield strengths considerably in excess of the ASME minimum allowable value of 50,000 psi. They averaged about 63,000 psi. However, the ultimate tensile strength of the 0.125 and 0.252-in.-diam specimens were about 79,500 psi, just below the minimum allowable value of 80,000 psi. The 0.505-in.-diam specimens had average ultimate tensile strengths slightly greater than the minimum allowable value.

EVALUATION OF DISCONTINUITIES IN HSST PLATE 01

D. A. Canonico K. K. Klindt[1]

We determined the nature of discontinuities found during the nondestructive examination (NDE) of HSST plate 01. These areas were cut out of the plate and studied extensively by nondestructive methods. In mapping out the discontinuities, the testing procedure was varied to include the effect of ultrasonic transducer size, testing frequency, and amplifier gain. The back-reflection loss was mapped for each combination of the testing parameters. The test frequency had the major effect on the size of the area defining the complete loss

[1]Inspection Engineering Department.

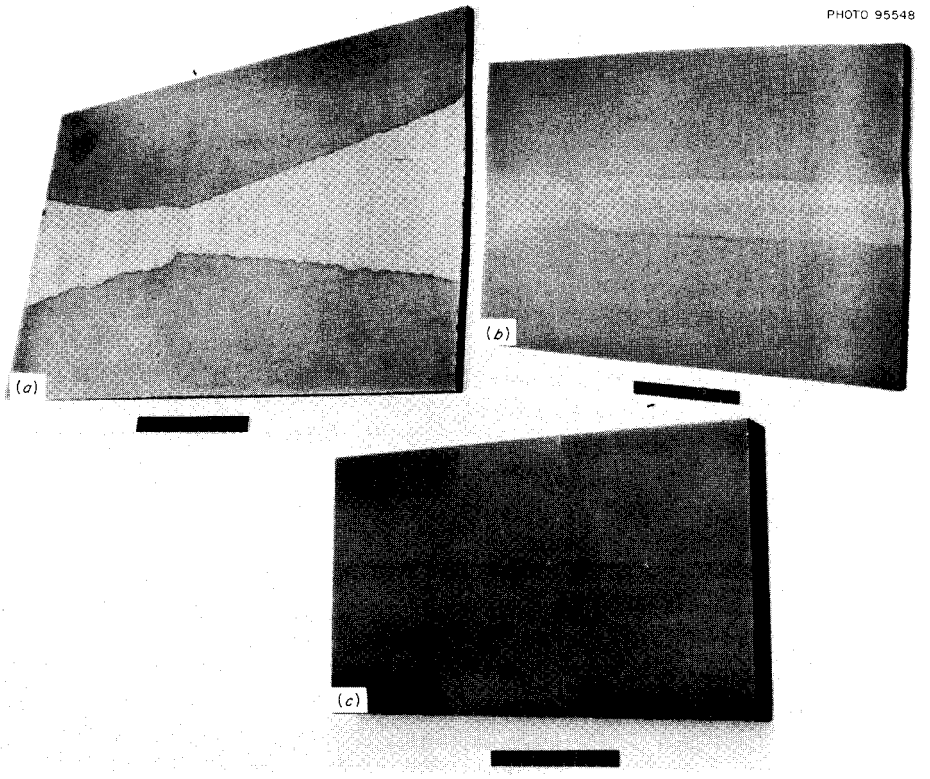

Fig. 28.1. Weldments Made with the Various Processes Employed in the Fabrication of Thick-Sectioned Pressure Vessels. (*a*) Shielded metal arc weld in 12-in. plate. (*b*) Submerged arc weld in 12-in. plate. (*c*) Electroslag weld in 6-in. plate.

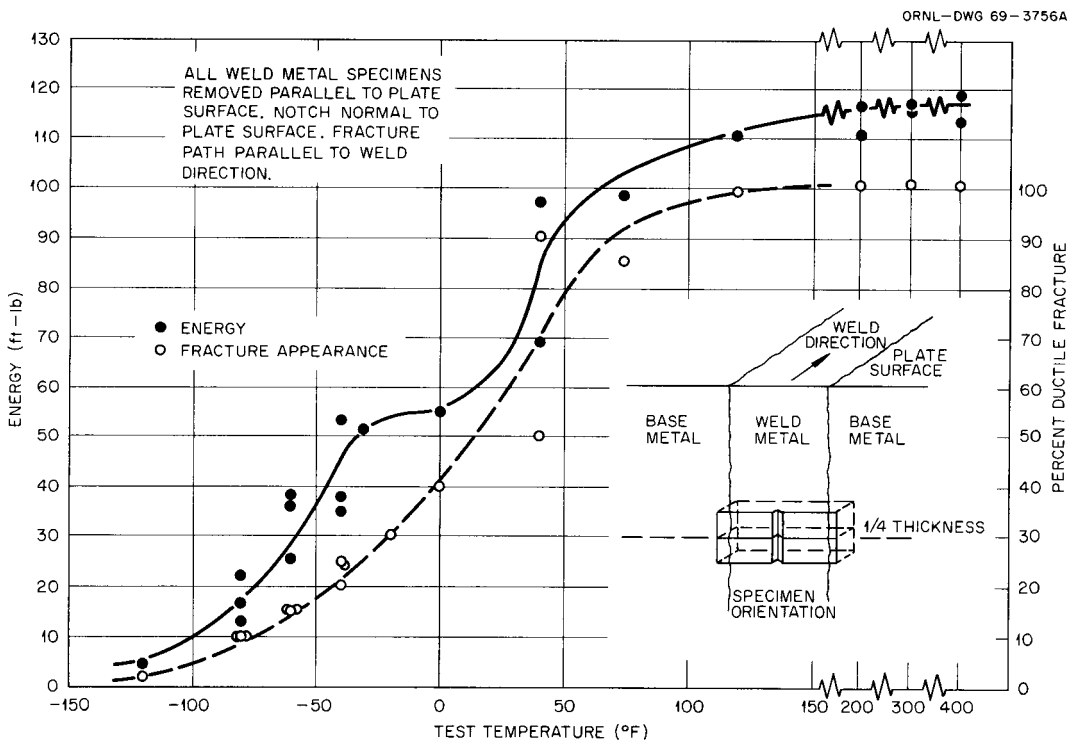

Fig. 28.2. Results of Charpy V Notch Test on HSST Submerged Arc Weldment at Quarter-Thickness Location.

of back reflection. Radiography and magnetic particle inspection of cut surfaces revealed extensive discontinuity areas. After the ultrasonic studies, the specimen was sectioned to expose its interior, and an extensive destructive investigation was conducted. The area contained many lamellar voids filled with foreign inclusions.

An example of the type and shape of the discontinuities is shown in Fig. 28.3. The material found in the inclusions was crystalline. This entrapped material was analyzed for Al, Mn, Fe, Si, and Ca; Table 28.1 lists the contents found. We assumed that the material was a crystalline oxide, considered the amount of oxygen required to stoichiometrically satisfy each element, and calculated the oxide contents, also given in Table 28.1. The material balance is 95.3%, an excellent approximation. The foreign material was extensively analyzed with the electron-beam microprobe. The results of this study are given in Fig. 28.4. It consists of large crystalline fragments rich in aluminum, distributed in a matrix containing Si, Mn, Al, and Ca. The elements, the crystalline character, and the analysis of the foreign material indicate that it is slag entrapped during pouring and contained within the plate during its processing.

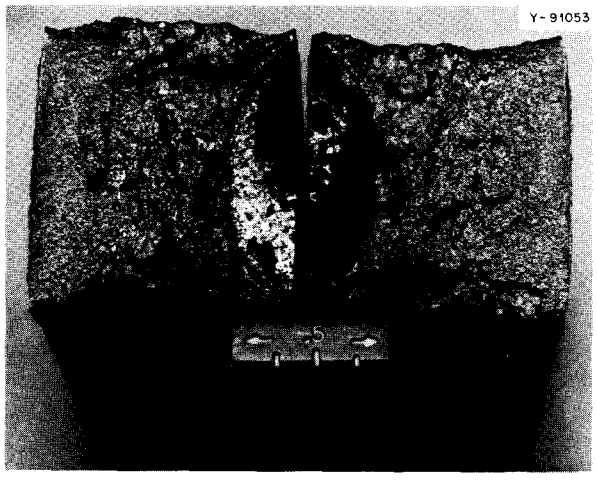

Fig. 28.3. Discontinuities in HSST Plate Section Broken at a Flaw Revealed by a Saw Cut. *The round cavity had contained slag.*

Table 28.1. Content of Foreign Material Entrapped in Discontinuities in Section 01-MP

Foreign Materials		Suggested Oxide	
Element	Content (%)	Formula	Content (%)
Al	31.2	Al_2O_3	59.0
Mn	7.01	MnO_2	11.1
Fe	3.44	Fe_2O_3	4.92
Ca	4.97	CaO	6.95
Si	6.24	SiO_2	13.35

PHOTO 97053

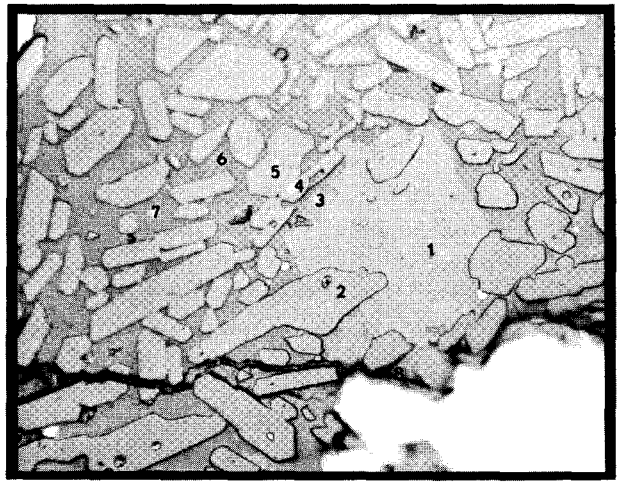

400X

POINT	ELEMENT (wt %)[a]				
	Si	Mn	Al	Fe	Ca
1		16.8	26.3		
2			53.4		
3	15.2	7.6	9.4		1.8
4			52.9		
5			51.3		
6	14.7	15.5	5.6		3.8
7	11.4		34.4		12.5
8	6.1	3.1	16.1		6.2

[a] THESE VALUES ARE NOT CORRECTED FOR ABSORPTION, SECONDARY FLUORESCENCE, OR ATOMIC NUMBER.

Fig. 28.4. Distribution of Metallic Elements in Slag Particles in HSST Plate. Reduced 31.5%.

29. High Flux Isotope Reactor Target Development

A. L. Lotts

The Transuranium Project is producing quantities of the heavier transuranium elements for research by successive neutron captures in ^{239}Pu. The program at ORNL started with primarily ^{242}Pu, ^{243}Am, and ^{244}Cm. Target elements containing principally these three isotopes are fabricated at ORNL and irradiated in the High Flux Isotope Reactor at a flux of approximately 3×10^{15} neutrons cm^{-2} sec^{-1}. In addition, special target elements of higher isotopes are fabricated periodically and irradiated in HFIR. The target elements are removed periodically from the HFIR and reprocessed in the Transuranium Processing Facility (TRU). At TRU the product actinides are separated and the target actinides are recovered and fabricated into recycle target elements. In addition, special targets for irradiation in the HFIR Hydraulic Rabbit Facility are fabricated and special encapsulations are made of the product actinides.

The program at TRU is carried out jointly by the Chemical Technology Division, the Metals and Ceramics Division, and the Analytical Chemistry Division. Our tasks in this program have included the design and evaluation of the original targets, the development of equipment and techniques for fabricating these elements, both in gloved boxes and remotely, the monitoring of the performance of the target elements in HFIR, and the design and fabrication of modified targets that may withstand HFIR service conditions. The principal activities during the past year have been the fabrication of recycle targets and special target elements and sources, improvement of the equipment in the TRU, further investigation of the target failures that were reported previously, and irradiation of targets modified to withstand the HFIR service conditions.

TRU TARGET FABRICATION

E. J. Manthos J. E. Van Cleve, Jr.

The target fabrication production line, used to fabricate target rods containing either $^{242}PuO_2$ or $(Am,Cm)O_2$ as the starting material, has operated as the feed was available. The feed material is transmuted to heavier isotopes and fissioned while in the HFIR core. The targets are removed, the fission products and heavier isotopes are separated, and the americium and curium are reconstituted into the oxide and finally assembled into new targets for additional irradiation.

The remote target fabrication equipment has been in use for approximately 18 months, and its operation has become almost routine. The only persistent trouble encountered was in the weighing systems. The scales used were modified top-loading balances. Because calibration of these scales was prone to drift, the balances were replaced with weigh cells of much sturdier construction and the same sensitivity. We have experienced no trouble with these units after approximately seven months in the hot cell. The target rods fabricated during this reporting period are listed in Table 29.1.

Small amounts of isotopes of special interest are most efficiently produced by exposing the starting material in the HFIR Hydraulic Rabbit Facility. We developed a rabbit design that is compatible with both our fabrication equipment and the requirements of the reactor. The rabbit is shown in Fig. 29.1. The encapsulation welder is used to make the end closure weld, and the unit is helium leak tested. The rabbits fabricated are listed in Table 29.2. The minute quantities of starting

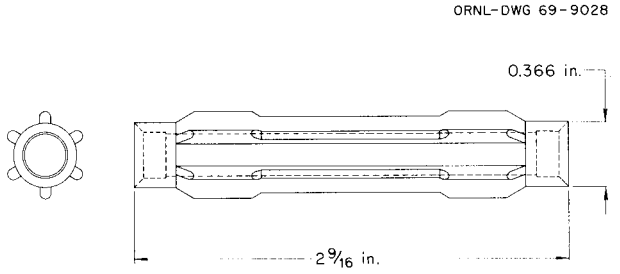

Fig. 29.1. Design of HFIR Hydraulic Rabbit.

Table 29.1. Targets Fabricated at TRU in FY 1969

Target	Oxide Form	Major Isotope	Actinide Weight (g)	Weight of Oxide (g)	Pellet Length Standard Deviation (in.)
					$\times 10^{-3}$
K26	Microspheres and shards	^{244}Cm	6.20	9.00	18
K17	Microspheres and shards	^{244}Cm	2.45	3.85	0.5
K16	Microspheres	^{244}Cm	5.37	8.03	6.3
K23	Shards	^{242}Pu	9.71	11.32	12.4
K24	Shards	^{242}Pu	9.71	11.32	17.8
D70	Shards	^{242}Pu	9.71	11.32	20.7
D75	Shards	^{242}Pu	9.71	11.32	17.8
D73	Shards	^{242}Pu	9.71	11.32	16.1
D74	Shards	^{242}Pu	9.71	11.32	15.2
D79	Shards	^{242}Pu	9.71	11.32	19.1
D77	Shards	^{242}Pu	9.71	11.32	26.4
D78	Shards	^{242}Pu	9.67	11.32	20.0

isotope are loaded into the rabbit by techniques developed jointly with Chemical Technology personnel. We prepare a pellet liner with a 90%-dense bottom cap pressed in place, slurry the isotope in solution with the aluminum core powder, vacuum the slurry through the pellet liner using the bottom cap as a filter frit, and then press it into a pellet. The pellet is loaded into the rabbit, the end closure weld is made and inspected, and the rabbit is sent to the reactor.

Table 29.2. Rabbits and Neutron Sources Fabricated in TRU in FY 1969

Identification	Major Isotope	Actinide Weight (μg)
	HFIR Rabbits	
R02	^{253}Es	0.04
R03	^{252}Cf	10.00
R04	^{253}Es	0.50
R05	^{253}Es	0.50
R06	^{253}Es	0.50
12-68-1	^{252}Cf	10.00
R08	^{252}Cf	10.00
12-68-9	^{252}Cf	1.30
12-68-10	^{252}Cf	1.30
3-69-1	^{249}Bk	0.10
4-69-1	^{253}Es	0.50
5-69-2	^{253}Es	1.50
5-69-3	^{253}Es	0.20
5-69-6	^{253}Es	0.20
5-69-7	^{253}Es	2.50
5-69-8	^{252}Cf	800
5-69-9	^{252}Cf	1800
5-69-10	^{252}Cf	1900
5-69-11	^{252}Cf	1700
6-69-47	^{253}Es	4.00
	Neutron Sources	
NS-2	^{252}Cf	500
NS-3	^{252}Cf	100

Two neutron sources were assembled. We have developed a standard neutron source, Fig. 29.2, which we believe will suit most experimenters. The design requirements satisfied by the container were that it be of the physical dimensions and shape that we could handle it with our standard equipment. The two sources, shown in Table 29.2, were of the standard type made of stainless steel.

HFIR TARGET PERFORMANCE

E. J. Manthos

Status of Targets in HFIR

J. E. Van Cleve

Table 29.3 lists the target rods exposed in HFIR during the previous year. No sign of failure but an increase in the alpha activity of the primary coolant stream has been observed. The failures[1,2] of targets irradiated at SRL and in HFIR occurred at approximately 40% FIMA, and, as may be seen in the table, several of the D series targets have exceeded this value.

[1] A. L. Lotts, J. E. Van Cleve, E. J. Manthos, R. T. King, and E. L. Long, Jr., *Metals and Ceramics Div. Ann. Progr. Rept. June 30, 1968,* ORNL-4370, pp. 193–97.

[2] A. L. Lotts, E. J. Manthos, J. E. Van Cleve, E. L. Long, Jr., J. R. Weir, and R. E. Adams, *Metals and Ceramics Div. Ann. Progr. Rept. June 30, 1967,* ORNL-4170, pp. 187–91.

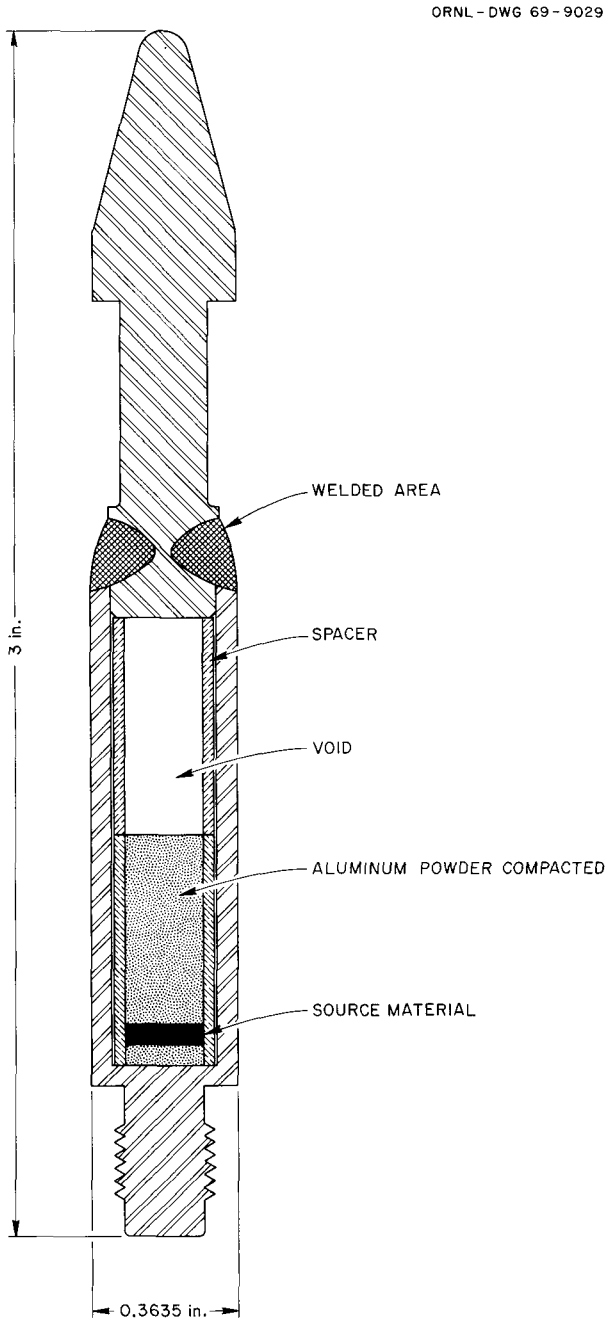

Fig. 29.2. Design of ^{252}Cf Neutron Sources Made in TRU.

Table 29.3. HFIR Target Element Performance

Rod	Burnup (% FIMA)	Fluence (neutrons/cm^2) <0.41 ev	Fluence (neutrons/cm^2) >0.81 Mev
		$\times 10^{22}$	$\times 10^{22}$
D67	27.1	6.02	1.85
D37	42.4	8.48	2.64
D35	51.9	10.13	2.59
D31	52.0	10.16	2.54
D14	58.1	11.28	3.08
D19	58.1	11.28	3.08
D21	58.1	11.28	3.08
E22	56.0	10.85	3.31
E70	62.0	12.09	2.98
E71	62.0	12.09	2.98
E72	62.0	12.09	2.98
E73	62.0	12.09	2.98
E74	62.0	12.09	2.98
E75	62.0	12.09	2.98
D12	70.5	14.07	3.54
K11[a]	42.4	4.40	1.41
K12[a]	42.4	4.40	1.41
K14[a]	42.4	4.40	1.41
K19[a]	42.4	4.40	1.41
K20[a]	42.4	4.40	1.41
K21[a]	42.4	4.40	1.41
D63	18.3	4.62	1.39
D68	33.0	7.03	2.17
E13	38.7	7.93	1.65
E30	38.7	7.93	1.65
E47	38.7	7.93	1.65
E49	38.7	7.93	1.65
E66	38.7	7.93	1.65
D69	38.7	7.93	1.65
D66	24.1	5.58	1.70
K16	25.5	2.63	0.76
K17	25.5	2.63	0.76
K23	8.57	2.63	0.76
K26	25.5	2.63	0.76

[a]Removed from HFIR and processed in TRU.

Analysis of Target Performance

E. J. Manthos

Two groups of targets were removed from the HFIR and chemically processed at TRU to recover the contained transplutonium elements. One group consisted of 13 "virgin" plutonium targets that had been irradiated only in HFIR for 17 cycles. At the time of removal, June 12, 1968, they had accumulated fluences ranging from 8.19 to 9.09 $\times 10^{22}$ fast neutrons/cm^2 (>0.81 Mev) and 42 to 46% FIMA at the target midplane without any indications of failure. In comparison, the SRL-HFIR targets first failed at 39% FIMA and fluences of 6.36 $\times 10^{22}$ thermal neutrons/cm^2 and 1.04 $\times 10^{22}$ fast neutrons/cm^2 (>0.81 Mev).

There were at least two differences between the "virgin" and SRL targets. The "virgin" targets had been irradiated in HFIR only, whereas the SRL-HFIR targets

had been irradiated both at SRL and in HFIR. The plutonium loading was different: the "virgin" targets each contained 8 g ^{242}Pu and the SRL-HFIR targets contained 10 g of ^{242}Pu, both in pellets pressed to 90% of theoretical density.

According to a model developed, failure should have occurred in the virgin targets at 46% FIMA. Since none of these targets had failed at the scheduled removal time, one (D-12) was left in the reactor until failure. When D-12 fails, it will be sectioned and examined metallographically to see if the mode of failure is the same as for the SRL-HFIR targets. As of June 12, 1969, D-12 had been irradiated to 70.5% FIMA, 14.07 $\times$ 10^{22} thermal neutrons/cm^2, and 3.54 $\times$ 10^{22} fast neutrons/cm^2 (>0.81 Mev) without any indication of failure.

The 13 "virgin" targets were visually examined at TRU before they were processed, and we saw no evidences of failure on any of the targets. They were normal in appearance and covered with a light-colored oxide deposit. A section of the target tube and pellet was obtained from the midplane of target D-65 and submitted for metallographic examination. In addition, several cover sheath sections were also obtained and transferred to the HRLEL for further examinations.

The other group that was removed for processing comprised six curium recycle targets. They were removed from HFIR in February 1969 and had accumulated 4.40 $\times$ 10^{22} thermal neutrons/cm^2, 1.41 $\times$ 10^{22} fast neutrons/cm^2 (>0.81 Mev), and 44.4% FIMA. Each contained 4.5 g of curium, mainly ^{244}Cm, in pellets pressed to a density 80% of theoretical.

These six targets were the first curium recycle targets that had been fabricated in TRU. Each target was thoroughly examined after it was returned from HFIR. We saw no evidence of failure, and the targets were covered with a light-colored oxide deposit typical of targets that have been irradiated in HFIR.

As of June 1969, no target has failed for over two years since irradiations of the 10-g-Pu SRL-HFIR targets were terminated. At present seven targets in the HFIR have been irradiated for over two years. The six low-density targets[1,2] have achieved a burnup of 62% FIMA and target D-12 70.5% FIMA. Planned exposure of future plutonium targets will be limited to twelve 23-day HFIR cycles and approximately 29% FIMA. Curium targets will be exposed for nine cycles and 40% FIMA.

All targets that have been fabricated since the SRL-HFIR target failures and all future targets will contain pellets pressed to 80% theoretical density instead of 90%. The failure model[1] predicts that target life will be extended if more porosity is available in the pellets. Since all future targets will contain pellets with more porosity and irradiation time will be 12 cycles or less, we believe that the probability of target failures in HFIR has been reduced, if not eliminated. Surveillance of all HFIR targets will continue, and each target removed from HFIR will be carefully examined for any evidence of failure before it is chemically processed.

IRRADIATION EFFECTS ON MECHANICAL PROPERTIES OF CLADDING

R. T. King

The failure of the 8001 aluminum TRU target rod cladding has been investigated and ascribed to neutron irradiation effects, as described in Chap. 5 of this report. Our present work is directed toward understanding the causes of low-ductility failures in neutron-irradiated aluminum and determining which alloys are suitable for cladding use in the HFIR environment. We have found several neutron-irradiation effects that might increase the strength of irradiated aluminum and decrease its ductility: (1) the production of helium by ^{27}Al(n,α) reactions with fast neutrons; (2) the production of hydrogen by ^{27}Al(n,p) reaction with fast neutrons and introduction of hydrogen from the aqueous reactor environment; (3) the production of silicon in supersaturated solid solution by thermal neutron reactions with aluminum, and the subsequent precipitation of silicon-rich precipitates; (4) the production of displacement damage and subsequent formation of high concentrations of voids in the material.

Cyclotron-injected uniform concentrations of hydrogen and helium have been used to discriminate between the effects of these gases and other irradiation effects. Above half the absolute melting point 5 ppm He reduces the short-time tensile ductility of 1100 and 8001 aluminum but not of 6061 and SAP alloys. The creep ductility of 1100 aluminum and high-purity aluminum was significantly lowered at 300°F by 3 ppm He in preliminary tests, but strains at failure still exceeded 30%. Up to 10 ppm of injected hydrogen had no significant effects on the creep properties of these alloys at 300°F.

Specimens of 6061, 1100, and 8001 aluminum alloys have been irradiated in special HFIR capsules, out of contact with the coolant. Irradiation for 3 and 5 cycles in HFIR produces fluences of 2 to 5 $\times$ 10^{21} neutrons/cm^2 (>0.81 Mev). These alloys exhibit reduced elevated-temperature tensile ductility and increased strength at 300°F and above, similar to the property changes observed in previous tests on ring and sheet

specimens irradiated in contact with the coolant. These results verify that irradiation damage is the source of the problem and have been used as a guide in designing reactor irradiation experiments aimed at developing damage-resistant aluminum cladding alloys.

DENSITY CHANGES IN ALUMINUM ALLOYS AS A RESULT OF IRRADIATION

E. L. Long, Jr.

Immersion densities have been measured on type 1100 aluminum specimens that were sectioned from an ORR N_f tray.[3] The aluminum was irradiated at about 45°C and received a maximum fluence of 1.5×10^{22} neutrons/cm^2 (>1 Mev); a 1.5% decrease in density was measured at the region of maximum fluence. As expected, the measured decrease in density of the aluminum could be correlated with the flux profile along the N_f tray. Density changes were measured for type 1100 aluminum after postirradiation heat treatment between 90 and 620°C. In addition, densities have been determined by immersion on type 8001 aluminum specimens from target hex cans that had reached fluence levels up to 2.7×10^{22} neutrons/cm^2 (>0.81 Mev).

Specimens from the maximum-flux region of the ORR N_f tray were heat treated in air for 20 hr at various temperatures up to 620°C and air cooled; the results are shown in Fig. 29.3. Maxima in the decreases in density occurred at about 130 and 565°C; a minimum existed at 315°C (about $0.6T_m$). Transmission electron microscopy disclosed polyhedral voids about 800 A across that had been formed during irradiation; a higher concentration of voids existed adjacent to the grain boundaries. A specimen heat treated at 200°C showed a decrease in void concentration and a coarsening of the silicon precipitate. A specimen heat treated at 315°C disclosed additional coarsening of the precipitate and no evidence of voids. The reversal of the slope of the curve from 315 to 565°C probably results from the formation of gas bubbles within the aluminum.

Density changes were determined on sections of hex cans that had received fluences ranging from 2.8×10^{21} to 2.7×10^{22} neutrons/cm^2 (>0.81 Mev). Specimens were taken from near maximum and minimum flux regions of several hex cans; the average operating temperatures of these sections were approximately 66 and 58°C respectively. The changes in density with fluence are shown in Fig. 29.4, along with those of type 1100 aluminum from the ORR N_f tray. The type 1100 aluminum decreased 1.5% in density at a fast-fluence level of 1.5×10^{22} neutrons/cm^2; at slightly less than twice that fluence the density of the type 8001 aluminum decreased about 5%. The two curves shown imply that a family of curves may exist for various aluminum alloys, but factors such as operating temperatures and neutron spectra also can influence the changes in density during irradiation.

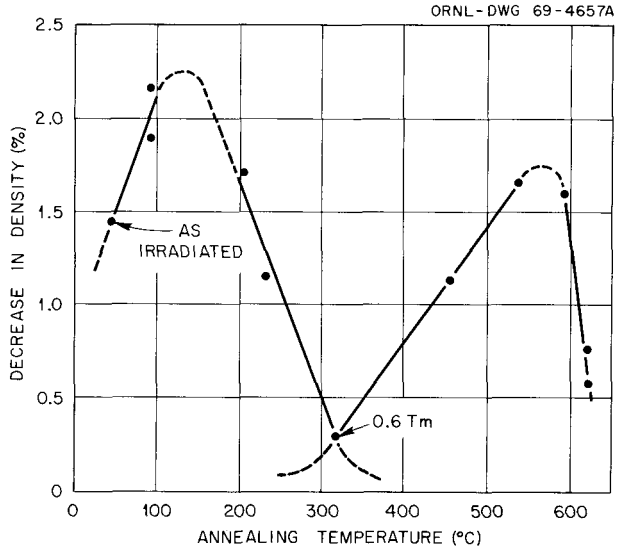

Fig. 29.3. Density Changes in Specimens from the Maximum Fluence Region of an ORR N_f Tray After Heat Treatment at Various Temperatures for 20 hr. The fluence level of these specimens ranged from 1.4 to 1.5×10^{22} neutrons/cm^2 (>1 Mev).

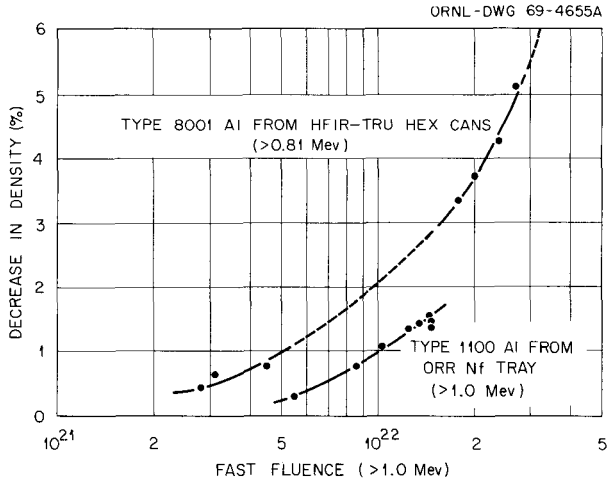

Fig. 29.4. Density Changes in Irradiated Type 1100 and Type 8001 Aluminum Alloys from an ORR N_f Tray and HFIR Hex Cans. The type 1100 aluminum was irradiated at 45°C and the 8001 was irradiated at higher average temperatures from 58 to 66°C.

[3] S. S. Hurt, III, "Experience with Neutron Damage to Beryllium and Aluminum Lattice Components at the ORR," *Trans. Am. Nucl. Soc.* 10 (Supplement), 11–12 (July 1967).

30. LMFBR Cladding and Structural Materials

G. M. Adamson, Jr. J. R. Weir, Jr.
W. O. Harms

The development work covered in this chapter is directed at both short- and long-term Liquid-Metal Fast Breeder Reactor (LMFBR) applications. Support for the programs described derives from both LMFBR Project and General Reactor Technology funds, the latter directed toward the long term. The section on fabrication deals with fuel cladding and, in part, represents a joint effort with the Fast Flux Test Facility (FFTF) Division at the Batelle Northwest Laboratory. The principal aim in this area is to establish the optimum fabrication schedule, including intermediate heat treatments, for the quality of tubing required for LMFBR fuel cladding. The section on irradiation effects applies to both cladding and core structural materials, the former including nickel-base alloys, vanadium, and vanadium alloys as well as austenitic stainless steels. The evaluation of titanium-modified austenitic stainless steels developed by ORNL has been emphasized in both the fabrication and irradiation effects programs. The compositions and geometries of austenitic stainless steel pressure vessels for both FFTF and long-term LMFBR applications form the basis for the welding development program.

FABRICATION DEVELOPMENT FOR LMFBR FUEL CLADDING

W. R. Martin H. E. McCoy R. W. McClung

Fabrication of Small-Diameter Stainless Steel Tubing

G. A. Reimann

Our program on stainless steel tubing fabrication has shifted from titanium-modified type 304 stainless steel[1] to type 316 stainless steel, with emphasis on dimensional precision, product reproducibility, and quality assurance.

Seamless tube hollows of type 316 stainless steel were obtained for redrawing into 0.250 in. OD X 0.016 in. wall thickness FFTF-type fuel cladding. Several closely controlled drawing and annealing schedules, including one that closely resembled commercial drawing practice, were employed to achieve the desired size. We found that a 40% reduction in area (RA) can be achieved for type 316 stainless steel in a single pass with appropriate heat treatment after each pass. In a second processing route, 50% RA was achieved in three passes of approximately equal magnitude between heat treatments. Both routes usually produced apparently satisfactory tubing; detailed nondestructive testing and mechanical property measurement are in progress.

Efforts have begun to produce tubing with the FFTF cladding dimensions of 0.230 in. OD X 0.015 in. wall thickness, and we are examining variations in drawing schedule and interpass annealing temperature to obtain a microstructure with improved properties. A grain size of ASTM 12 (average grain diameter of 5.5 μ) has been produced in type 316 stainless steel tubing by proper choice of the interpass annealing temperature. Preliminary nondestructive testing results indicate that about 75% of the tubing produced by this schedule meets the specifications.

Effect of Process Variation on the Texture of Titanium-Modified Type 304L Stainless Steel Tubing[2]

T. M. Nilsson G. A. Reimann

Small-diameter, thin-walled tubing of titanium-modified type 304L stainless steel was produced by vacuum melting, casting, hot forging, hot extrusion,

[1]G. A. Reimann, *Metals and Ceramics Div. Ann. Progr. Rept. June 30, 1968,* ORNL-4370, pp. 120–21.

[2]T. M. Nilsson and G. A. Reimann, "Evaluation of Titanium-Modified Type 304L Stainless-Steel Tubing," (summary) *Trans. Am. Nucl. Soc.* 12(1), 134–35 (June 1969).

swaging, and mandrel drawing with a final 5% cold work by plug drawing. The purpose was to determine the effect of drawing schedule on the texture of the finished tubing. Two schedules were used to draw the tubes from the swaged size of 1.40 in. OD X 0.85 in. ID to the final size of 0.250 in. OD X 0.016 in. wall thickness. In schedule I, the material was annealed for 0.5 hr at 1200°C between successive passes of 10 to 15% reduction in area; in schedule II the same heat treatment was used but after each two passes (i.e., after 20 to 30% reduction). The relatively high annealing temperature and low amount of cold work between anneals was necessary to prevent cracking of the tubing caused during drawing by a titanium-containing precipitate. In both schedules, the last heat treatment at 925°C for 1 hr produced a grain size of ASTM 7 to 9 (average grain diameter of 32 to 16 μ).

Evaluation of these tubes reported in the next two sections consisted of optical and electron microscopy and texture measurements by x-ray diffraction on chemically thinned specimens. After the last 20% cold working operation in schedule II, the texture with respect to the radial direction (R.D.) and the axial direction (A.D.) was composed of two components about equally strong. These components were $[011]_{R.D.}[100]_{A.D.}$ and $[322]_{R.D.}[\bar{4}33]_{A.D.}$. The 20% cold work condition (schedule II) was achieved through two steps of 12 and 10% reductions. The first step was primarily a sinking operation and the second was primarily wall thinning. In schedule I the final 10% cold work was achieved primarily by ironing through mandrel drawing. In this case the component $[322]_{R.D.}[\bar{4}33]_{A.D.}$ was virtually absent. Annealing decreased the preferred orientation (i.e., maximum intensity). Tubes fabricated by schedule I, with the lower amount of cold work between anneals, exhibited less preferred orientation than those fabricated by schedule II.

Texture of Drawn and Planetary-Swaged Tubes of Titanium-Modified Type 304L Stainless Steel

T. M. Nilsson

Planetary-swaged austenitic stainless steel tubes have higher creep ductilities than tubes of this material produced by drawing.[3] Because this difference in behavior may be associated with differences in texture, we measured the texture of 0.2%-Ti-modified type 304L stainless steel tubes manufactured by planetary swaging and drawing in both the cold worked and annealed conditions. Figure 30.1 shows $(111)_\gamma$ pole figures of tubes cold worked 40 and 45% by planetary swaging and drawing respectively. Except for the last 5% deformation by plug drawing, the reduction sched-

[3] M. M. Haberlin, H. Lloyd, and A. McLean-Elrick, *Improvements in the Treatment of Stainless Steel Tubes,* British Patent 1,124,287, Aug. 21, 1968.

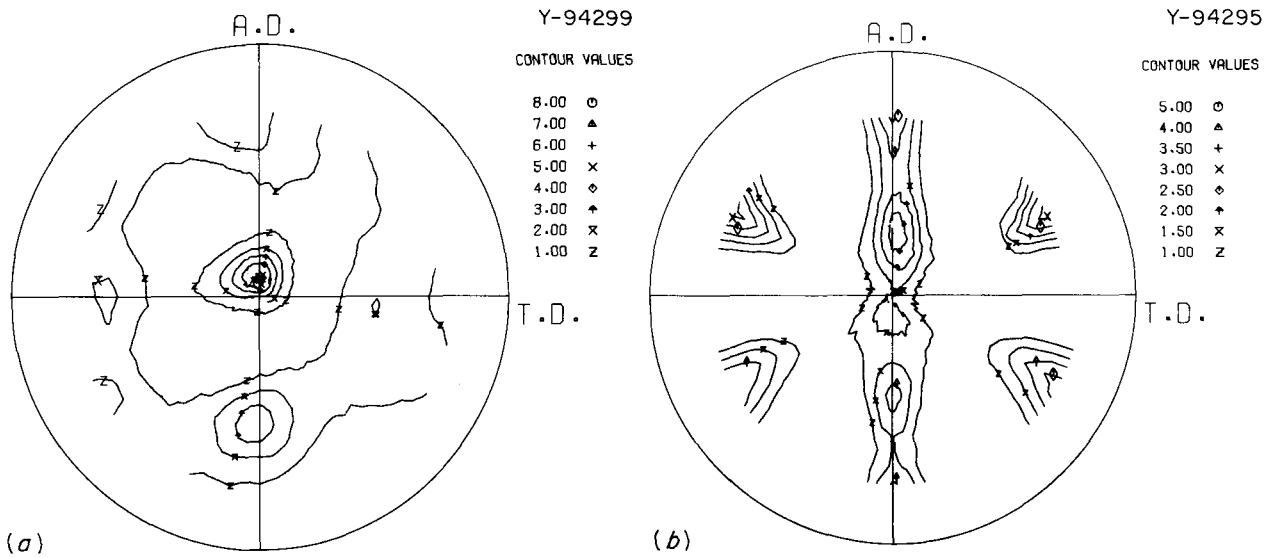

Fig. 30.1. Pole Figures of 0.2%-Ti-Modified Type 304L Stainless Steel Tubes After (*a*) 40% Cold Planetary Swaging and (*b*) 45% Cold Drawing. The pole figures show the density of the $[111]_\gamma$ poles. A.D. and T.D. correspond to the axial and tangential directions, respectively; the radial direction is perpendicular to the plane of the pole figure in the center. Notice the high density of $[111]_\gamma$ poles near the radial direction after planetary swaging.

ules were identical. The reduction process consisted primarily of diameter reduction with very little wall thinning. The textures are clearly quite different: After planetary swaging the intensities are higher and there is a high density of $[111]_\gamma$ poles in the radial direction corresponding to a large number of circumferential $(111)_\gamma$ planes.

Texture analysis, including $(200)_\gamma$ pole figures, has shown that the textures in both cases are composed of three components: two (nearly identical) close to $[111]_{R.D.}[\bar{1}2\bar{1}]_{A.D.}$ and the symmetrical $[111]_{R.D.}[1\bar{2}1]_{A.D.}$. After drawing, a third and the strongest component is $[011]_{R.D.}[100]_{A.D.}$. After planetary swaging, the third component is $[001]_{R.D.}$-$[110]_{A.D.}$.

We also measured the textures of tubes with intermediate levels of cold work after the reduction schedules described above. After about 10% cold work, the texture consisted of the three components characteristic of the working technique, and the peaks were of the same intensity as those shown in Fig. 30.1. The sharpness of the peaks, however, increased with increasing amount of cold work. That the intensities did not increase accordingly, as would be expected, is probably due to the decrease in total volume of the austenite phase owing to the formation of the ϵ and α' phases, as described in the next section. After annealing, the cold-worked tubes showed less preferred orientation (i.e., the peaks were lower in intensity and broader).

Electron Microscopy of Cold-Worked Tubes of Titanium-Modified Type 304L Stainless Steel

T. M. Nilsson

We have investigated the effect of cold work on the microstructure of titanium-modified type 304L stain-

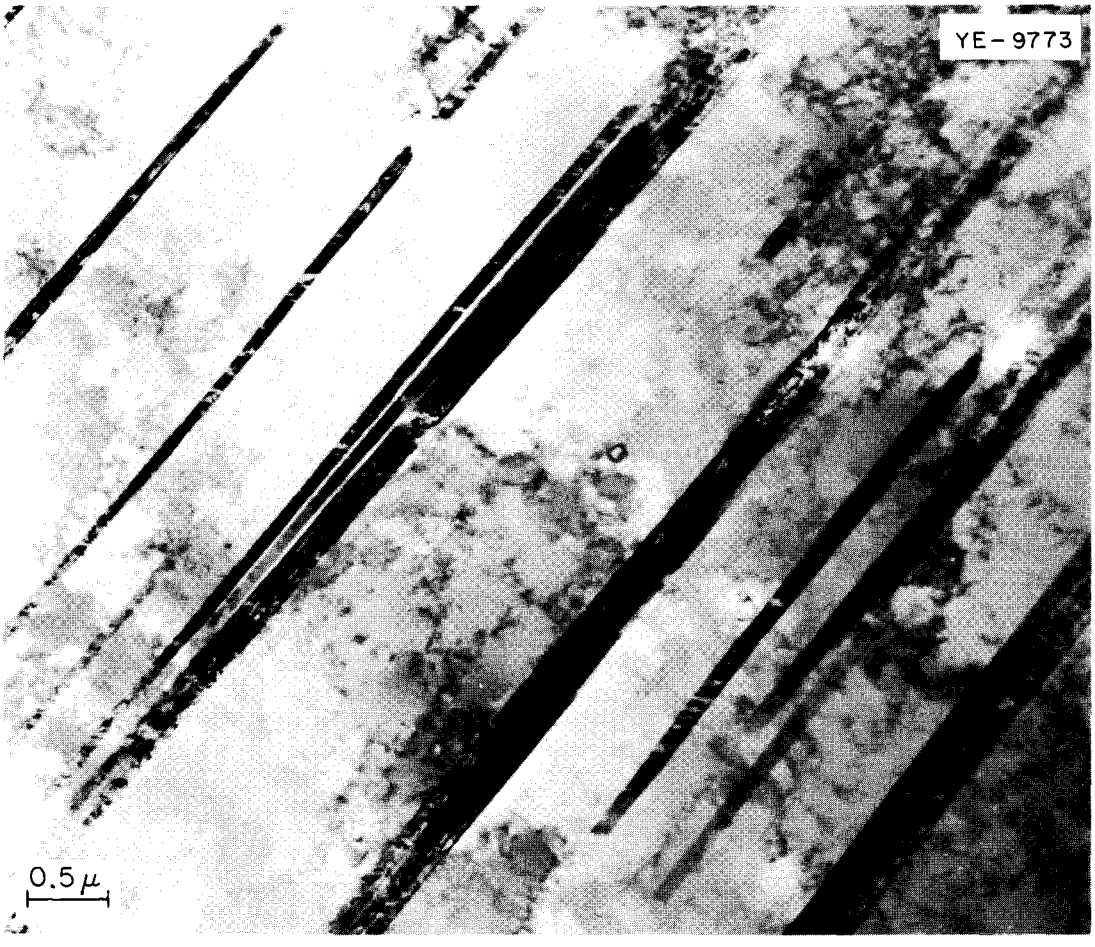

Fig. 30.2. Microstructure of Titanium-Modified Type 304L Stainless Steel After 5% Cold Work by Plug Drawing. The micrograph shows a faulted ϵ phase formed on one set of $(111)_\gamma$ planes. Inside the ϵ phase many small martensitically formed α' needles are visible, and a dislocation network exists in the austenite matrix.

less steel tubes. The effects of both mandrel drawing and planetary swaging were similar.

During cold working, two products were formed from the deformation-induced decomposition of the austenitic phase: a hexagonal close-packed phase, ϵ, and a martensitic (ferrite) phase, α'. After relatively small amounts of deformation the ϵ-phase appears as thin disks on one set of $(111)_\gamma$ planes, as shown in Fig. 30.2. This phase can be formed by the movement of $^a/_6\,[112]$ partial dislocations on every second slip plane. The ϵ-phase contains stacking faults, showing that the transformation is not completely regular. The martensitic phase (α') usually forms inside the ϵ-phase as needles (Fig. 30.2). After further deformation, faulting starts on other sets of $(111)_\gamma$ planes, and the number and length of martensite needles increase. After about 20% deformation the α' needles are about 150 A wide X 2000 A long.

In some cases α' forms independently of the ϵ-phase (Fig. 30.3). This observation is not consistent with mechanisms that have been proposed[4] for the formation of martensite in stainless steels with low stacking-fault energies.

Selected-area diffraction shows that the orientation relationship between the austenite and martensite is always close to that of Kurdjumov and Sachs;[5] that is, $(111)_\gamma \parallel (110)_{\alpha'}$, $[\bar{1}01]_\gamma \parallel [\bar{1}11]_{\alpha'}$, although a precise analysis is not possible due to the attendant distortion of the austenitic crystal structure. The growth direction of the α' needles is usually close to $[110]_\gamma$, and the habit plane is close to $(111)_\gamma$.

[4] R. Lagneborg, *Acta Met.* **12**, 823–43 (July 1964).

[5] G. V. Kurdjumov and G. Sachs, *Z. Phys.* **64**, 325 (1930).

Fig. 30.3. Microstructure of Titanium-Modified Type 304L Stainless Steel After 13% Mandrel Drawing. Two sets of α' needles are apparent. In this case, the generation of the α' needles appears to be independent of the ϵ phase.

Effect of Boron on the Hot Ductility of Type 316 Stainless Steel

A. K. Chakraborty[6]

The effect of boron on the hot ductility of type 316 stainless steel was investigated from 900 to 1300°C. Boron concentrations should be low in fuel cladding materials because of irradiation damage due to the $^{10}B(n,\alpha)^{7}Li$ reaction. Boron is commonly added to nickel-base alloys and less commonly to type 316 stainless steel to improve fabricability at high temperatures. In certain iron-base alloys, boron is added to improve hardenability. We selected the nickel-base alloy Inconel 600 for comparison with stainless steel.

Commercial Inconel 600 and type 316 stainless steel were remelted, and from 5 to 200 ppm B was added to each. These alloys were drop cast in a 1-in.-diam mold, hot swaged at 1000°C to slightly more than ¼ in. in diameter, and annealed for 1 hr at 1050°C in hydrogen.

The high-temperature mechanical properties of these alloys were examined by testing 0.250-in.-diam X 3-in.-long specimens in a Gleeble apparatus.[7] The effect of deformation temperature and boron content on the Gleeble-test reduction in area of type 316 stainless steel is shown in Fig. 30.4. From 900 to 1100°C, the reduction in area apparently is not affected by boron content. At higher temperatures, however, the ductility drops rapidly with boron content at the high boron levels; at 1300°C, the ductility is reduced even with relatively low boron contents. The Inconel 600 shows better ductility than does type 316 stainless steel at 1300°C; its ductility otherwise remains fairly constant with increasing boron content and increases with increasing temperature. We conclude that boron contents above approximately 10 ppm can have a detrimental effect on the high-temperature ductility of type 316 stainless steel.

Inspection of Tubing for LMFBR Fuel Cladding

K. V. Cook

We have modified our tube-scanning tank for the ultrasonic inspection of small-diameter stainless steel tubing for both longitudinal and transverse flaws at a sensitivity established on 0.001-in.-deep X 0.002-in.-to-0.005-in.-wide X 0.030-in.-long electrical discharge machined reference notches. We can also measure the wall thickness of these tubes by a resonance ultrasonic method and record the results of each of the three tests. The relatively small quantities of tubing prepared in the ORNL cladding fabrication program described above have been inspected successfully with the existing facility. For the larger amounts of tubing required in the longer range development program for LMFBR tubing fabrication, we are acquiring a scanning mechanism that will allow simultaneous evaluation by all three ultrasonic examinations.

We have also developed methods for applying the fluorescent penetrant technique to the inspection of the inner surface of tubing with inside diameters as small as 0.5 in. and with lengths up to approximately 4.5 ft. For this application we use a black-light borescope and a small lathe for scanning the tubes.

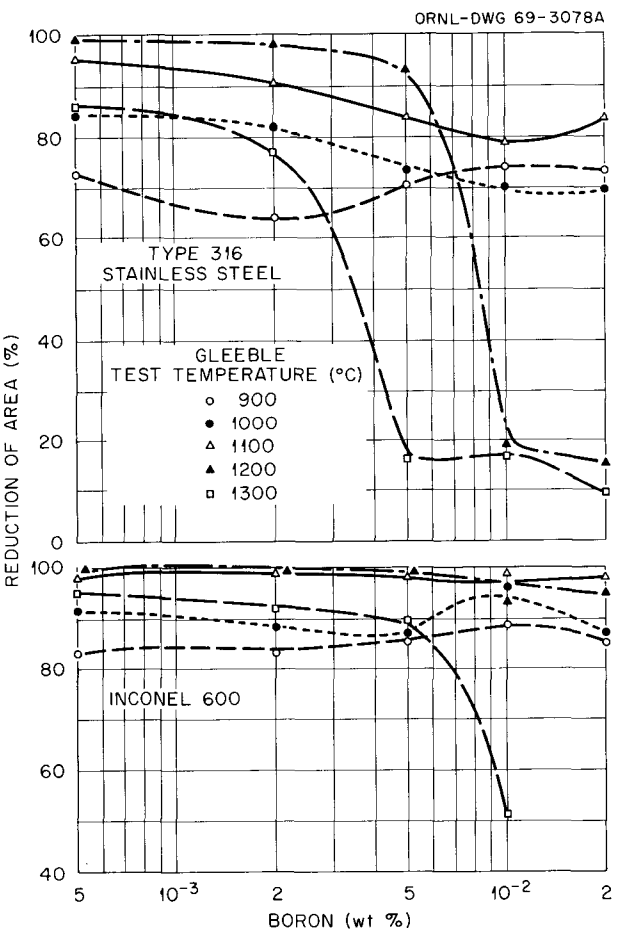

Fig. 30.4. Hot Ductility of Type 316 Stainless Steel and Inconel 600 as a Function of Boron Content.

[6]Consultant from University of Tennessee; now with Argonne National Laboratory, Idaho Falls, Idaho.

[7]E. F. Nippes and W. F. Savage, "Development of Specimens Simulating Welding Heat Affected Zones," *Welding J.* 28, 534-s–546-s (1949).

Biaxial Creep-Rupture Properties of Titanium-Modified Type 304L Stainless Steel Tubing

R. T. King

We are studying the effects of fabrication variables on mechanical properties. The biaxial creep-rupture characteristics of ultrasonically inspected tubing of type 304L stainless steel modified with 0.2% Ti were examined in several cold-worked and annealed conditions at 600 and 700°C. The test results showed that the properties of unirradiated, annealed, nondefective tubing compare favorably with those of commercially available, nonmodified stainless steel tubing. Discontinuities detectable by the nondestructive techniques appeared to reduce rupture life and ductility. However, cold-worked tubing frequently exhibited low-ductility failures that initiate at bore defects that cannot be detected nondestructively.

EFFECTS OF IRRADIATION ON LMFBR CLADDING AND STRUCTURAL ALLOYS

H. E. McCoy

The high-temperature mechanical properties of candidate LMFBR cladding and structural alloys are influenced by neutron-induced atomic displacements and transmutations. The displacements are caused by the fast neutrons and can result in the formation of such defects as dislocation loops and microscopic voids. The transmutations of concern involve the formation of grain-boundary helium bubbles that result from the thermal $^{10}B(n,\alpha)^{7}Li$ reaction and the fast (n,α) reactions with the components of stainless steels and nickel-base alloys.

In LMFBR's, cladding and structural alloys will be exposed to a high flux of fast neutrons and a low flux of thermal neutrons. For experimental purposes, however, the fast flux in thermal reactors such as the Oak Ridge Research Reactor (ORR) and the High Flux Isotope Reactor (HFIR) is high enough to obtain useful information. In this program, experiments are performed in these reactors as well as in EBR-II, where the neutron spectrum is more representative of fast reactors. Cyclotrons are being used to study the intrinsic effects of the production of helium and hydrogen and of atomic displacements.

We have emphasized the austenitic stainless steels, which are included in reference designs for the FFTF and for first-round LMFBR demonstration reactors. More advanced alloys, such as those based on vanadium, have also been investigated because they may be used as cladding in later systems. Incoloy 800 has been included as a candidate structural alloy, and nickel 270 was included for comparison.

Irradiation Damage to Annealed Type 316 Stainless Steel

E. E. Bloom

The tensile properties from 550 to 750°C and the creep-rupture properties at 650°C have been determined for type 316 stainless steel irradiated in the ORR at 550, 650, and 750°C. The composition of the alloy was (by weight percent): C, 0.07; Cr, 17.2; Ni, 12.5; Mo, 2.1; Mn, 1.9; Si, 0.5; P, 0.039; S, 0.004; B, 0.0008; total N, 0.018; soluble N, 0.011. Before irradiation the test specimens were solution annealed 1 hr at 1050°C, producing an ASTM grain size of 12 (average grain diameter of 5.5 μ). The irradiation was conducted for approximately 2200 hr, during which the specimens accumulated neutron fluences of 9×10^{20} neutrons/cm^2 (thermal) and 7×10^{20} neutrons/cm^2 (>1 Mev). Similar mechanical properties tests were conducted on annealed specimens and specimens that had been annealed and aged 2000 hr at 550 and 650°C.

Irradiation at 550°C did not significantly change either the yield strength (σ_{ys}) or ultimate tensile strength (σ_{uts}). After irradiation at either 650 or 750°C, σ_{uts} was unchanged but σ_{ys} was increased by approximately 5000 psi over the value of 15,000 psi for annealed material. Specimens aged 2000 hr at 550 and 650°C exhibited σ_{ys} values comparable to those of specimens irradiated at 550 and 650°C respectively. Thus, the increase in yield strength after irradiation at 650 or 750°C appears to result from thermal rather than irradiation effects. Irradiation at each temperature reduced tensile ductility, and the ductility decreased with increasing test temperature.

These irradiations reduced rupture life by an amount that depended on the irradiation temperature, as shown in Fig. 30.5. The shortest rupture life occurred after irradiation at 750°C and the longest after irradiation at 650°C, in general agreement with the observed minimum creep rate and ductility values. Irradiation at 550°C caused a slight increase in creep rate but a very large reduction in ductility; however, irradiation at 650°C resulted in somewhat higher creep rates and significantly higher ductilities than did the 550°C irradiation. Finally, irradiation at 750°C resulted in a significant increase in creep rate and a reduction in ductility comparable to that observed for specimens irradiated at 650°C. Thus, both the reduction in ductility and increase in creep rate act to reduce the rup-

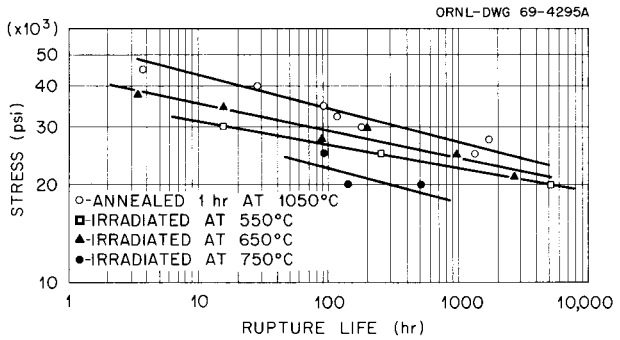

Fig. 30.5. Effect of Irradiation Temperature on the Stress-Rupture Properties of Type 316 Stainless Steel at 650°C. Specimens were irradiated for approximately 2200 hr at the indicated temperatures to 9×10^{20} neutrons/cm^2 (thermal) and 7×10^{20} neutrons/cm^2 (>1 Mev).

ture life. Results of tests on specimens aged 2000 hr at 550 and 650°C indicate that the higher creep rates observed in the irradiated specimens resulted from thermal aging, whereas the reduced ductility resulted from the irradiation.

Transmission Electron Microscopy of Irradiated Austenitic Stainless Steel and Nickel 270

E. E. Bloom J. O. Stiegler

Specimens of type 304L stainless steel taken from various EBR-II components and specimens from an irradiation experiment in the EBR-II were examined by transmission electron microscopy. The reactor components had been irradiated at temperatures between 370 and 470°C and to maximum fast neutron fluences of approximately 9×10^{22} neutrons/cm^2 (>0.1 Mev).

Specimens of type 304 stainless steel and nickel 270 (99.9% pure) were irradiated in a row 2 position in the EBR-II at temperatures between 370 and 525°C and neutron fluences to 1.4×10^{20} neutrons/cm^2 (>0.1 Mev). Figure 30.6 compares the microstructures after irradiation at 385°C. The type 304 stainless steel contained approximately 1×10^{15} defect clusters/cm^3, which ranged in size from the smallest observable, approximately 25 A in diameter, to a maximum of approximately 150 A. As the irradiation temperature was increased, the defect concentration decreased. After irradiation at 525°C, the stainless steel contained fewer than 10^{12} defect clusters/cm^3. In a specimen irradiated at 465°C, three types of defects were identified by analysis of their diffraction contrast: (1) interstitial dislocation loops having an $a/3\langle 111\rangle$ Burgers vector; (2) dislocation loops having an $a/2\langle 110\rangle$ Burgers vector; and (3) clusters with associated three-dimensional strain fields, and, therefore probably vacancy clusters.

In comparison, nickel 270 irradiated between 385 and 525°C contained a complicated dislocation structure and octahedral voids. The dislocation structure apparently consisted of dislocation lines (possibly very large loops) in addition to much smaller loops. The smaller loops were perfect (i.e., they had no stacking fault associated with them) and were not distributed randomly but rather appeared to be associated with the dislocation lines. After irradiation at 385°C, the nickel 270 contained octahedral voids having diameters ranging from the smallest observable, approximately 50 A, up to 175 A, with a mean of 110 A. As the irradiation temperature was increased, both the maximum and the mean void sizes increased and the dislocation density decreased.

Significant differences in the nature of the irradiation damage were also observed in regions adjacent to grain boundaries, as shown in Fig. 30.6. In the stainless steel irradiated at 385°C, a zone approximately 1000 A wide adjacent to the boundary contained no visible damage. In nickel 270 irradiated at the same temperature, the dislocation structure was absent over a distance of approximately 10,000 A from the boundary, and the region denuded of voids was only about 1000 A wide.

A defect structure consisting of voids and dislocation loops was observed in type 304L stainless steel irradiated to fast neutron fluences as low as 4×10^{21} neutrons/cm^2 (>0.1 Mev). Quantitative measurements of loop and void densities indicate that the loop density saturates at fluences about 10^{21} neutrons/cm^2 (>0.1 Mev), whereas the void density increases monotonically with fluence. At a given irradiation temperature the mean void diameter increases with increasing fluence but the maximum void diameter appears to reach a limiting size after irradiation to about 1×10^{22} neutrons/cm^2 (>0.1 Mev). This is illustrated by a comparison of the microstructures shown in Fig. 30.7. Figure 30.7(*a*) shows the voids present in a type 304L stainless steel specimen irradiated to 1.4×10^{22} neutrons/cm^2 (>0.1 Mev) at 430°C. The void density in this specimen was 1.3×10^{15}/cm^3, the mean void diameter was 151 A, and the maximum void diameter was 325 A. In contrast, Fig. 30.7(*b*) shows the voids present in a specimen irradiated at approximately 410°C to 9×10^{22} neutrons/cm^2 (>0.1 Mev). In this specimen the void density was 1.2×10^{16}/cm^3, the mean void diameter was 172 A, and the maximum void diameter was 325 A. Similarly, specimens irradiated at 370°C to fluences of 0.8×10^{22} and 5.0×10^{22}

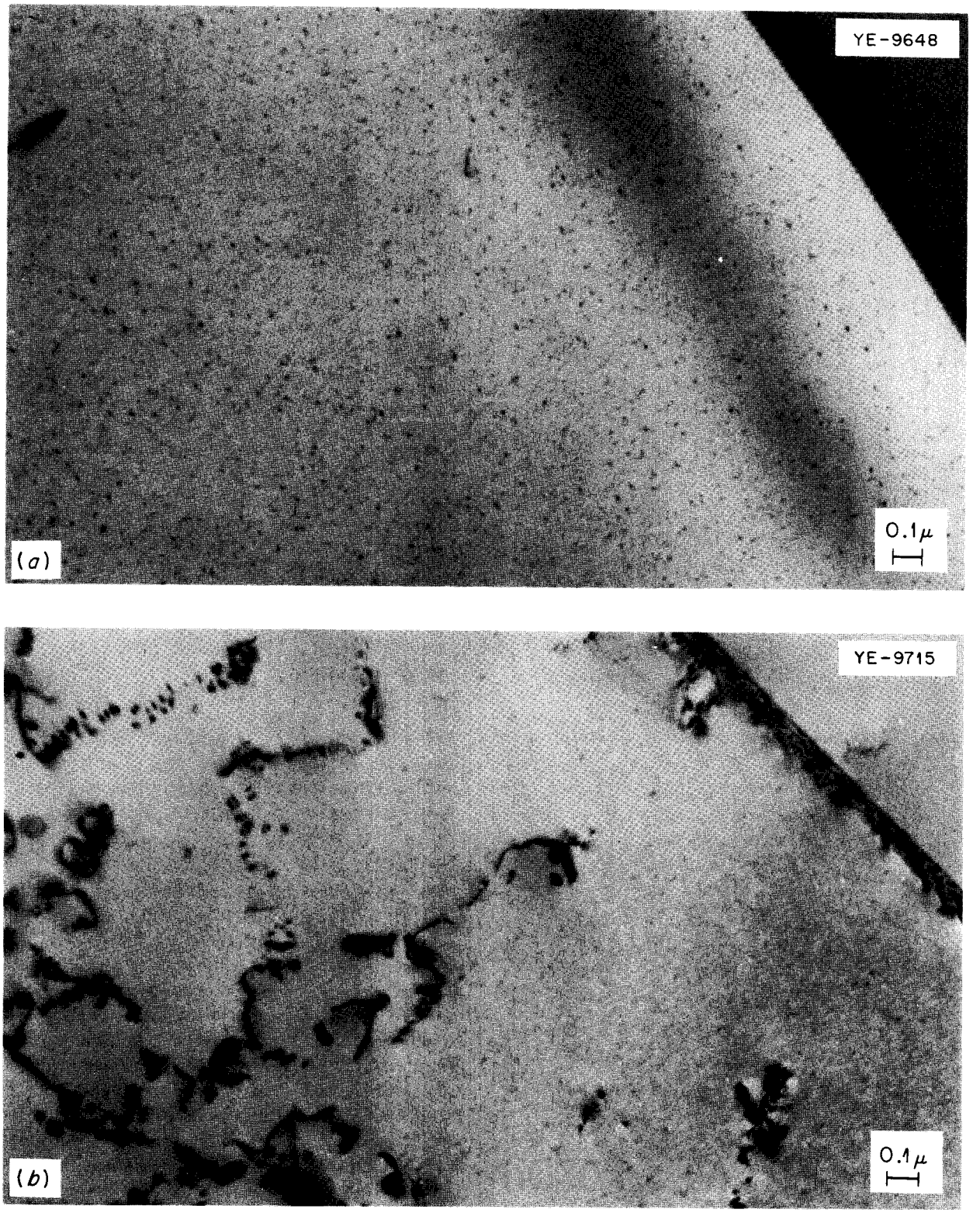

Fig. 30.6. Comparison of Damage Structures in (*a*) Type 304 Stainless Steel and (*b*) Nickel 270 Irradiated in the EBR-II at 385°C to 1.4 × 10^{20} neutrons/cm^2 (>0.1 Mev).

neutrons/cm^2 (>0.1 Mev) exhibited approximately the same maximum void size. This limiting size increases with the irradiation temperature.

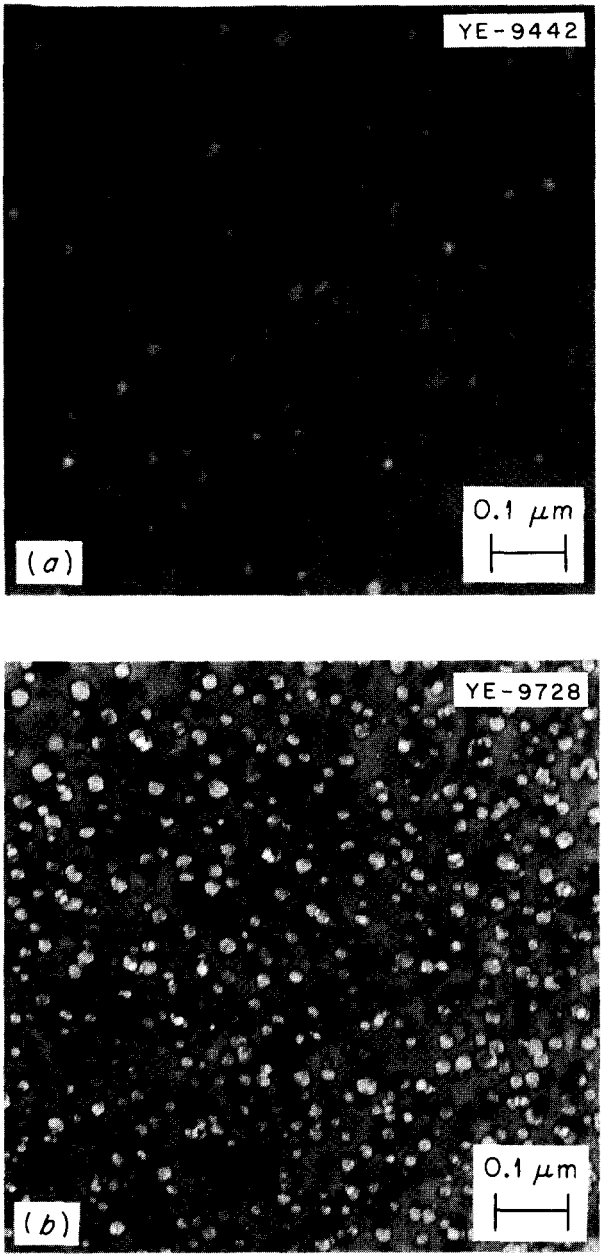

Fig. 30.7. Voids in Type 304L Stainless Steel. (*a*) Irradiated at 430°C to 1.4 × 10^{22} neutrons/cm^2 (>0.1 Mev). (*b*) Irradiated at 410°C to approximately 7 × 10^{22} neutrons/cm^2 (>0.1 Mev).

Creep-Rupture of Aged Titanium-Modified Type 304L Stainless Steel Containing Cyclotron-Injected Helium

R. T. King

Specimens of modified type 304L stainless steel containing 0.2% Ti and 20 ppm of cyclotron-injected helium have been shown to have significantly higher creep ductility than a helium-injected standard stainless steel. To determine whether thermally produced structural modifications might improve the ductility and creep strength of this alloy at 600°C, we tested annealed specimens, specimens having carbide-decorated dislocations and grain boundaries after aging 10 hr at 750°C, and specimens having a duplex structure with a fine matrix and grain-boundary precipitate produced by multiple aging. The multiply aged specimens had slightly longer rupture times than the annealed specimens; the 750°C aging treatment produced a weaker matrix and shortened rupture times. However, these thermal treatments did not significantly alter the ductility of the alloy, as shown in Fig. 30.8. Although 20 ppm He slightly reduced ductility (from about 50% to 40%) for tests lasting from 10 to 100 hr, the measured creep ductility for both longer- and shorter-term tests was not seriously affected. Standard type 304L stainless steel containing 20 ppm He fractures after 12 to 25% strain under similar conditions.

Production of Displacement Damage by Light Ions

R. T. King

The rate at which displacement damage is produced in type 304 stainless steel by bombardment with alpha particles and protons was calculated. The damage rates are given in Fig. 30.9 as a function of particle energy between 150 kev and 80 Mev. Damage production rates up to 10^5 times those possible in nuclear reactors may be obtained with existing particle accelerators. This information is being used to design experiments to assist in more rapid development and confirmation of theories for void growth in neutron-irradiated materials than present neutron irradiation techniques will allow. By this approach, specimens can be prepared cheaply and tested with relative ease since they are not highly radioactive.

It is important to note, however, that precisely simulated neutron irradiation conditions cannot be achieved in cyclotron experiments. The transmutation-

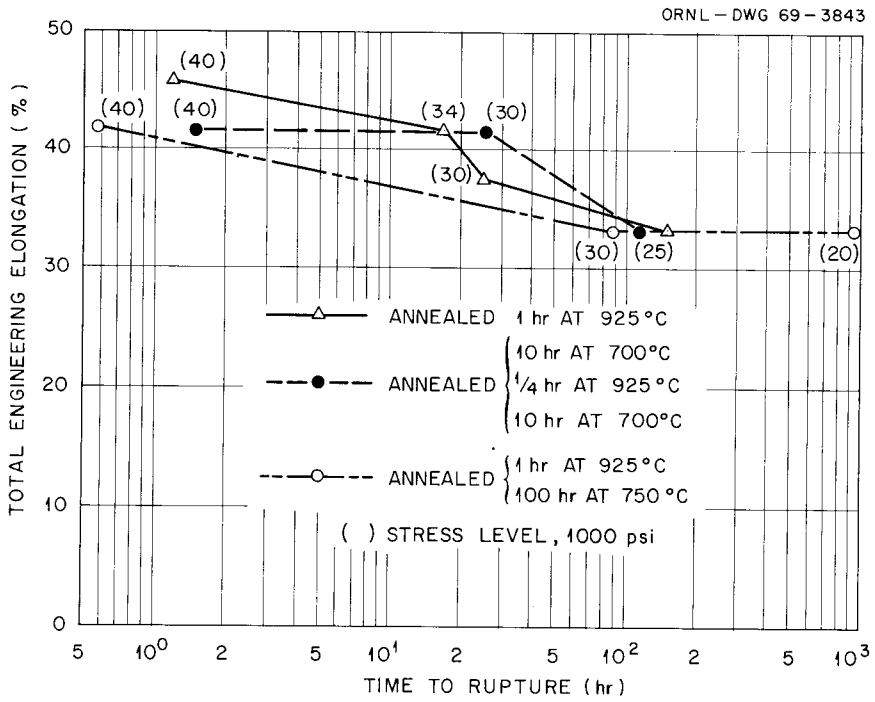

Fig. 30.8. Strain Plotted Against Rupture Life at 600°C for Type 304L Stainless Steel Modified with 0.2% Ti and Containing 20 ppm He.

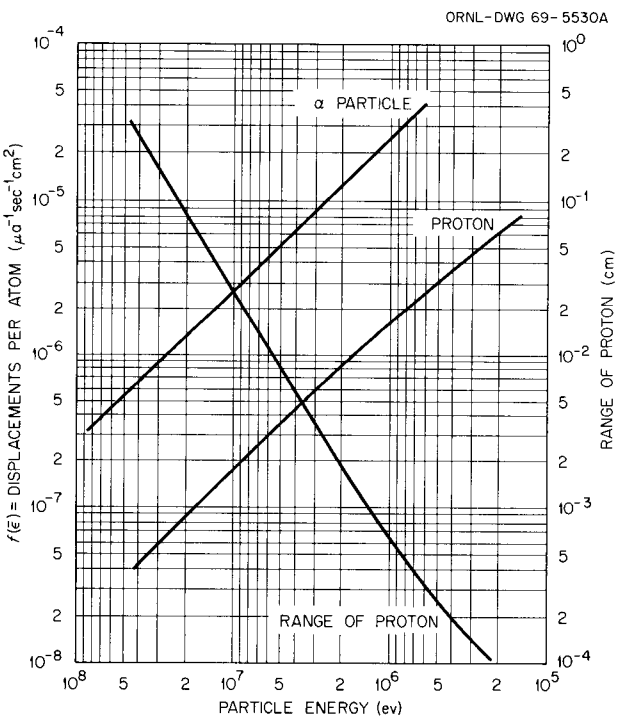

Fig. 30.9. Displacement Damage Production Rates and Proton Range in Type 304 Stainless Steel.

produced gases, helium and hydrogen, cannot be simultaneously injected into a region in which a constant rate of displacement damage is being produced. Furthermore, the spectrum of energies transferred in a primary knock-on event and the resulting displacement cascade structures produced by ions are probably not identical to those produced during neutron irradiation. Nevertheless, ion bombardment experiments are felt to be an important supplement to neutron irradiation damage studies.

Irradiation Effects in Incoloy 800

D. G. Harman

Our previous annual report[8] showed that the postirradiation creep ductility of Incoloy 800, irradiated and tested at 700 or 760°C, is enhanced by incorporation of 0.1% Ti. Further ductility increases were shown for material with finer grain sizes or tested at lower stress levels. The ductility was unaffected by carbon contents ranging from 0.03 to 0.12%.

[8] D. G. Harman, *Metals and Ceramics Div. Ann. Progr. Rept. June 30, 1968*, ORNL-4370, pp. 121–22.

As shown in Fig. 30.10, lowering the postirradiation test temperature to 650°C lowered the tensile and creep ductility of the alloy containing 0.1% Ti and 0.12% C to about half that previously reported for 700 and 760°C. The ductility at 650°C is further reduced if the irradiation temperature is reduced to 500°C from 700°C, the minimum creep rate is lower, and the yield strength is higher. Similar but smaller trends were found for the thermal control specimens, indicating that this composition is unstable at 500°C after the material has been solution annealed at 1150°C.

Electron microscopy showed near-continuous, grain-boundary films of $M_{23}C_6$ after the 500°C exposure; the presence of this type carbide would lead to the observed premature intergranular fracture at 650°C. Furthermore, we tested specimens that had been held 100 hr at 800°C before the neutron or thermal exposure at 500°C to agglomerate any precipitating carbides; the ductility at 650°C returned to the high values.

We irradiated several high-purity Incoloy 800 ternary alloys with only 0.007% C and found the same postirradiation ductility enhancement at the 0.1% Ti level. For material with similar grain sizes at stresses providing similar minimum creep rates, the carbon content (over the range of 0.007 to 0.12%) had no effect on the postirradiation ductility of Incoloy 800 irradiated at 700°C.

Electron Microscopy of Vanadium and V–20% Ti Irradiated in EBR-II

F. W. Wiffen J. O. Stiegler

Unalloyed vanadium irradiated in the EBR-II by United Nuclear Corporation as part of a carbide fuel irradiation experiment has been examined by transmission electron microscopy. It was irradiated at a temperature near 600°C to a peak fast neutron fluence of 1.7×10^{22} neutrons/cm^2 and has been examined as irradiated and as annealed after irradiation. The irradiated material showed a void density greater than 10^{15}/cm^3 and a high density of ribbon-like precipitate particles. The void distribution, shown in Fig. 30.11(*a*), is similar to that of other metals. Stereographic microscopy showed the voids to be uniformly distributed through the depth of the foils. Grain boundaries and adjacent zones were free of voids.

The void density was near 5×10^{15}/cm^3, the average diameter was near 120 A, and the maximum diameter

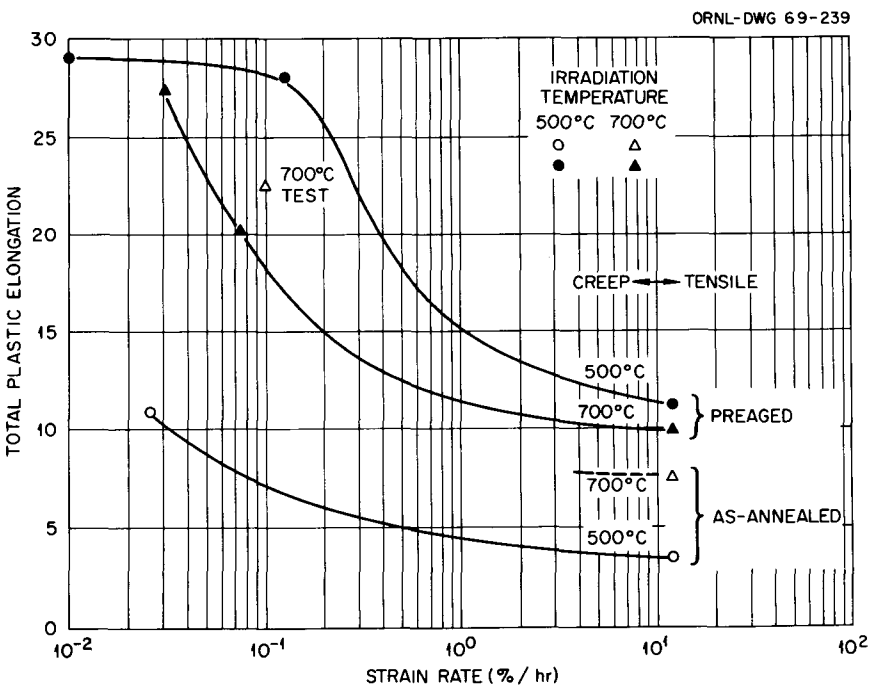

Fig. 30.10. Effect of Preirradiation Aging on Ductility of Incoloy 800 at 650°C After Irradiation at the Temperatures Indicated to About 0.8 × 10^{21} Neutrons/cm^2 (Thermal and Fast). All specimens contained 0.1% Ti and 0.12% C and were annealed at 1150°C. Some specimens were then aged 100 hr at 800°C before being irradiated.

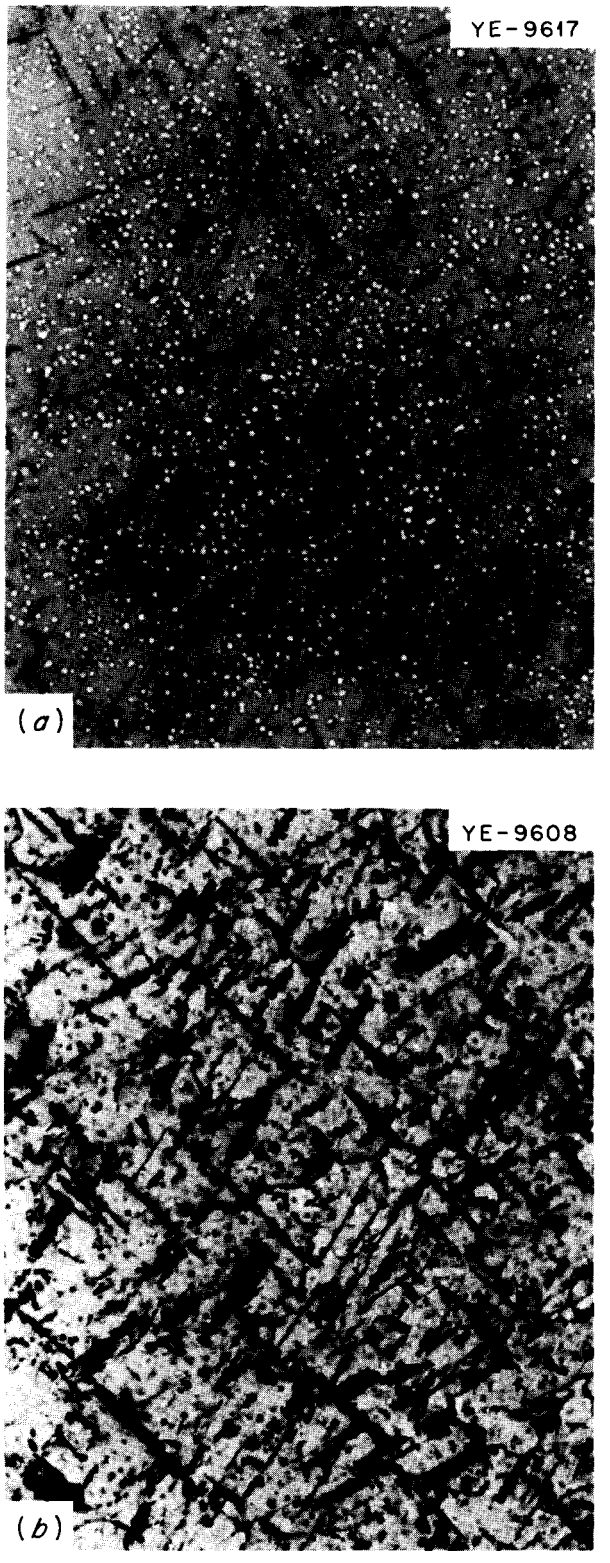

Fig. 30.11. Microstructure of Unalloyed Vanadium Irradiated to a Fluence of 1.7 × 10^{22} Neutrons/cm^2 (>0.1 Mev) in Row 4 of EBR-II at Approximately 600°C. (*a*) Foil oriented to show voids as white dots. (*b*) Foil oriented for diffraction from the ribbon-like precipitate structure. 50,000X.

was 230 A. This distribution corresponds to a calculated volume increase of approximately 0.5%.

The irradiation-produced precipitate, shown in Fig. 30.11(*b*), is distinctly different from the black-spot and loop-type damage seen in other metals and in unalloyed vanadium irradiated at 50 to 100°C and then annealed.[9,10] This platelet structure formed on planes with a zone axis of ⟨001⟩ and probably resulted from an interaction between irradiation-produced self-interstitials and interstitial impurity atoms. On post-irradiation annealing for 1 hr at 650°C the ribbon-like precipitate transformed to an interconnected dislocation network. At higher temperature the dislocation density decreased, presumably through dislocation annihilation reactions.

After 1 hr at 900°C all dislocations were in a stable, polygonized network. Voids were relatively stable after annealing at temperatures up to and including 750°C. Annealing at 800°C and higher, however, reduced the void population without large changes in the size distribution. After 1 hr at 850°C very few voids could be found; 1 hr at 900°C removed all voids.

A segment of the same cladding that had been irradiated to no more than half the fluence near 500°C showed a void density of 1 × 10^{16}/cm^3 with a maximum void diameter of 100 A.

A tube of V–20% Ti was also irradiated in the same experiment and, therefore, under similar conditions. Examination of several segments of this material failed to reveal any voids. The only structural effect was a high density of dislocations. The character of these dislocations suggests that they were formed at the irradiation temperature and are not a result of handling or working the material at room temperature. The effect of any stresses caused by fuel swelling in the experiment cannot be separated from the irradiation effects in determining the origin of these dislocations.

WELDING DEVELOPMENT FOR LMFBR VESSELS AND COMPONENTS

G. M. Goodwin G. M. Slaughter
N. C. Cole

In direct support of the FFTF Program, we prepared weldments in 1-in.-thick type 304 stainless steel to be evaluated in an irradiation test program.

[9] J. D. Elen, *Direct Observation of Damage in Neutron Irradiated Vanadium,* RCN-96 (December 1967).

[10] R. C. Rau, F. Secco d'Aragona, and R. L. Ladd, *AEC Fuels and Materials Development Program Progress Report No. 74,* GEMP-1006 (June 29, 1968), pp. 54–71.

Weldments were produced by the submerged-arc, gas-metal arc, and shielded metal-arc processes, in each case using filler metals and welding input conditions typical of industrial practice. Weld cross sections representative of the different processes are shown in Fig. 30.12. All welding was performed under carefully controlled conditions, automated where possible, to ensure integrity and reproducibility. The submerged-arc equipment is shown in Fig. 30.13.

Approximately 400 $\frac{1}{8}$-in.-diam button-heat weld-metal tensile specimens were prepared for testing. Preliminary out-of-reactor mechanical properties tests showed substantial variations in yield strength, elongation, and reduction in area in specimens prepared by three different processes.

Transverse cross sections from each of the weldments were examined macroscopically and microscopically, and ferrite contents were measured with a quantitative television microscope. Average ferrite contents ranged from 3.1 vol % for the shielded metal-arc specimens to 8.2 vol % for the gas-metal arc specimens.

A preliminary study of the amount and distribution of ferrite in the weldments (which is considered to have a significant effect on mechanical properties) has shown that the situation is very complex. Extreme variations occur, even within a particular cross section, and we doubt that any simple expression can unequivocally define the amount and distribution of ferrite in a weldment.

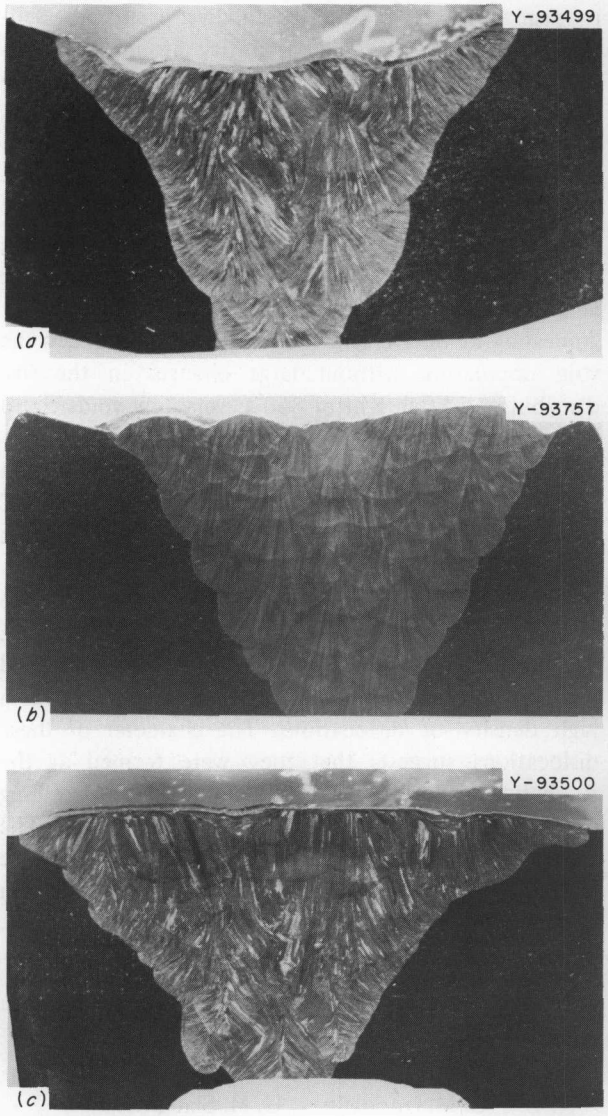

Fig. 30.12. Cross Sections of FFTF Weldments Prepared with (*a*) Submerged-Arc, (*b*) Shielded Metal-Arc, and (*c*) Gas-Metal Arc Processes. Lactic-hydrochloric-nitric acid etch. 2.5X. Reduced 40.5%.

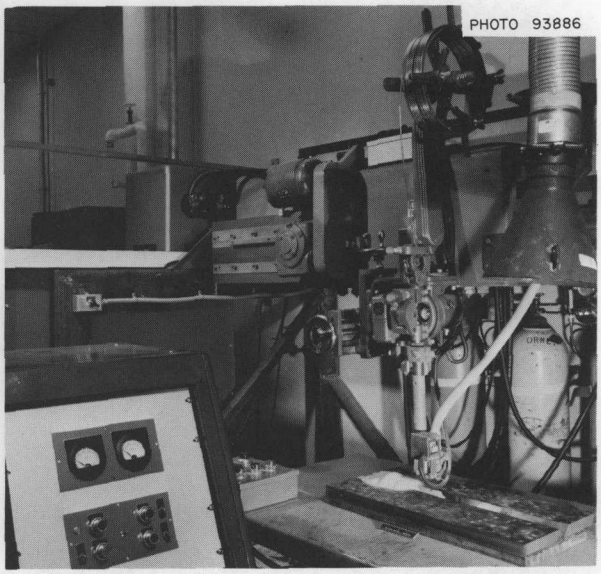

Fig. 30.13. Submerged-Arc Welding Equipment Used in FFTF Program.

31. Military Reactor Fuel Element Procurement Assistance

R. J. Beaver

This task includes standardization of specifications, review of technical requirements for procurement packages, and participation in fuel procurement as well as quality control audits of fuel fabricators.

Two PM type-4 cores for the Navy's reactor in Antarctica were procured by the AEC New York Operations Office (NYO) with our assistance in surveillance and inspection. The type-4 core is significantly different from the previous types but was procured without benefit of prototype development. Delivery of the first core in December was an outstanding achievement because of the limited time involved and the complexity of the job. It was made possible by the excellent cooperation on the part of the vendor (NUMEC) and our aggressive surveillance and inspection. This delivery was stimulated by our prompt review and processing for approval by the AEC of 450 submittals by NUMEC involving process and inspection procedures, engineering change requests, and requests for waivers.

We also prevented delivery of control rod assemblies made by NUMEC's subvendor by our discovery of cracks in welds and improper heat treatment of the 17-4 PH stainless steel caps attached to these assemblies.

A program was started to upgrade the UO_2 pellet–stainless steel tubular fuel element assembly specification for the MH1A floating nuclear power plant, the "Sturgis," and procurement of two half cores to this specification. Many undefined requirements of the previous specification were clarified. Kerr-McGee was the successful bidder on this 32-fuel-element order to this revised specification. We assisted the AEC in its initial surveillance of the Kerr-McGee facilities and discussion of the specification requirements.

Procurement of 116 ETR-type, aluminum-base, plate-type fuel elements for the Air Force Nuclear Engineering Test Reactor (AFNETR) at Wright-Patterson Air Force Base was initiated in September 1968 by the AEC-NYO. Using the previously revised specifications as a base, we encouraged interested vendors to develop functional fit gages in an effort to reduce the costs of dimensional inspection. Significant cost reductions were achieved by these efforts. United Nuclear Corporation was the successful bidder. They developed engineering functional fit gages, which we have reviewed in detail and which appear reasonable. Final acceptance will depend on demonstration at qualification of fuel assemblies to be accomplished early next fiscal year.

32. Molten-Salt Reactor Program

J. R. Weir, Jr. H. E. McCoy, Jr.

The Molten-Salt Reactor Program is an ORNL program for the development of a thermal breeder. The program presently has a small experimental converter reactor (MSRE) in operation. This reactor uses the liquid fuel ^{7}LiF–29.1 mole % BeF_2–5 mole % ZrF_4–0.9 mole % UF_4, a graphite moderator, and Hastelloy N as the metallic structural material. This reactor went critical on June 1, 1965, had been critical for 15,425 hr by June 1, 1969, and recently demonstrated stable operation with ^{233}U. Future thermal breeders will breed by the ^{232}Th-^{233}U cycle. The uranium (predominantly ^{235}U) was stripped from the entire fuel charge and replaced by uranium highly enriched in the ^{233}U isotope. This first operation of a reactor with ^{233}U has been satisfactory and very close to that calculated by physicists. This period of operation will be used to obtain a more accurate value of η, the net number of neutrons produced from ^{233}U per fission. This quantity is very important in predicting the rate of breeding in these reactors.

Our main involvement with the operation of the MSRE has been a surveillance program in which we follow the property changes of the graphite and the Hastelloy N. The same samples are used by the Reactor Chemistry Division to study the behavior of the fission products.

The next goal of this program is to design and construct a small breeder demonstration reactor. We anticipate that this reactor, called the MSBE, will be about 150 Mw (thermal) and that fabrication will begin in 1974. Our work in support of this reactor includes:

1. the development of a modified Hastelloy N with improved resistance to irradiation damage;
2. the evaluation of a new coolant salt, sodium fluoroborate, for use in the MSBE;
3. the demonstration that some commercial graphites can be exposed to fast neutron fluences of 3×10^{22} neutrons/cm^2 and maintain reasonable dimensional and mechanical integrity;
4. the development of graphites for future reactors with stability better than that of current graphite;
5. the development of a sealing technique for reducing the surface diffusivity of gaseous fission products on graphite.

MSRE SURVEILLANCE

Specimen Removal and General Observations

W. H. Cook

The reactor core surveillance specimens of graphite and Hastelloy N were removed from the MSRE on June 5, 1969, as part of the fourth group of specimens removed since the reactor attained critical operation on June 1, 1965. We have disassembled all three stringers and have just started our detailed examination of them. One stringer has been at 650 ± 10°C for a total of 2.6 years and has accumulated fast (>50 kev) and thermal (<0.876 ev) fluences of 1.1×10^{21} and 1.5×10^{21} neutrons/cm^2 respectively.[1] The other two stringers were at temperature for 0.8 year and accumulated fast and thermal fluences of 2.8×10^{20} and 5.1×10^{20} neutrons/cm^2 respectively.[1]

The specimens appear mechanically sound by visual examination. As usual, the fuel salt drained well, so the surfaces of the specimens are essentially free of salt. The graphite appears unaltered; however, the Hastelloy N is a slightly darker gray than observed on the previous specimens. Since this is true for specimens with both short and long exposure, the darkening is related to some characteristic of recent MSRE operation or to the current sampling operations.

[1] All fluence values given are calculated estimates, private communication from R. C. Steffy of the Reactor Division.

The graphite samples removed previously had surface films that could be seen in special lighting and also flow patterns near protrusions on the surveillance assembly.[2] These films were still visible on the samples just removed that had been at temperature for 2.6 years (installed in the MSRE on September 13, 1966). However, the flow patterns were absent or modified by the conditions that produced the darker gray appearance of the Hastelloy N. The film on the graphite appears to be approximately the same thickness as previously observed. We have been unable to acquire enough of the film material to identify it. We could not find any films on the graphite from the other two stringers that had been in the MSRE for a little less than a year.

The surveillance samples were contained in a perforated Hastelloy N basket. The sample basket was used for about 2 years at 650°C and accumulated a thermal fluence of 1×10^{21} neutrons/cm^2 (<0.876 ev). A portion of the section of the basket was sharply bent double (~180°) at ambient temperature during handling in the hot cells. No visible cracks were formed in the tension side of the bend, indicating the retention of reasonable ductility.

Properties of Hastelloy N Surveillance Samples

H. E. McCoy

The standard Hastelloy samples from the first three groups of surveillance samples removed from the MSRE have been tested under tensile and creep-rupture conditions.[3-5] The changes in the tensile properties are shown in Fig. 32.1. The fracture strain at low temperatures is reduced but still quite high. We attribute this embrittlement to the precipitation of grain boundary carbides, since the original ductility can be restored by a postirradiation carbide-coarsening anneal of 8 hr at 871°C. This precipitation seems to be related to the time at temperature as well as the neutron fluence. The reduction in ductility above 500°C is attributed to the presence of helium from the thermal-neutron transmutation of ^{10}B to ^{4}He and ^{7}Li. This embrittlement depends primarily upon the thermal neutron fluence and is not recoverable by postirradiation annealing.

The rupture life at a given stress level is reduced by irradiation, but the minimum creep rate is not altered. However, the change of most concern is the reduction in the fracture strain, which is very dependent upon the strain rate as well as the thermal neutron fluence. The

[2] W. H. Cook, *MSR Program Semiann. Progr. Rept. Aug. 31, 1968*, ORNL-4344, p. 214.

[3] H. E. McCoy, *An Evaluation of the Molten-Salt Reactor Experiment Hastelloy N Surveillance Specimens – First Group*, ORNL-TM-1997 (November 1967).

[4] H. E. McCoy, *An Evaluation of the Molten-Salt Reactor Experiment Hastelloy N Surveillance Specimens – Second Group*, ORNL-TM-2359 (February 1969).

[5] H. E. McCoy, *An Evaluation of the Molten-Salt Reactor Experiment Hastelloy N Surveillance Specimens – Third Group*, ORNL-TM-2647 (in press).

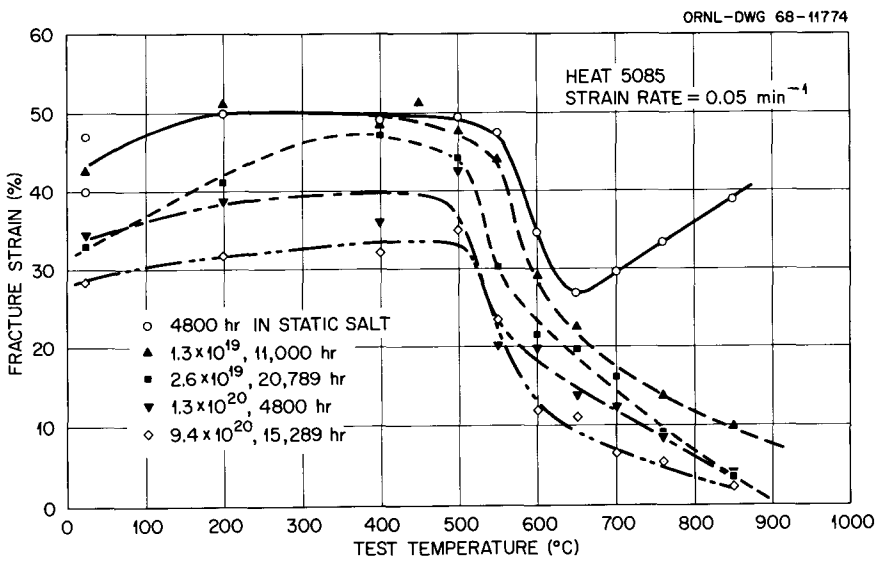

Fig. 32.1. Postirradiation Tensile Properties of MSRE Surveillance Samples.

interdependence of these factors is shown in Fig. 32.2. The strain rate of 0.1%/hr results in the minimum fracture strain of irradiated Hastelloy N. The fraction of the strain remaining is based on the number shown in parentheses, which is the value measured in the unirradiated starting material after a 2-hr anneal at 900°C. The corresponding curve for the burnup of ^{10}B based on a cross section of 1930 barns for the MSRE spectrum is shown for comparison. Since the thermal flux in the core is about 40 times that at the vessel wall, the fluences on many of the surveillance samples already exceed that anticipated for the vessel (likely about 5×10^{19} neutrons/cm^2). The control rod thimbles are the only metallic components exposed to higher fluences, and they are under a very small compressive stress and are not likely to fail.

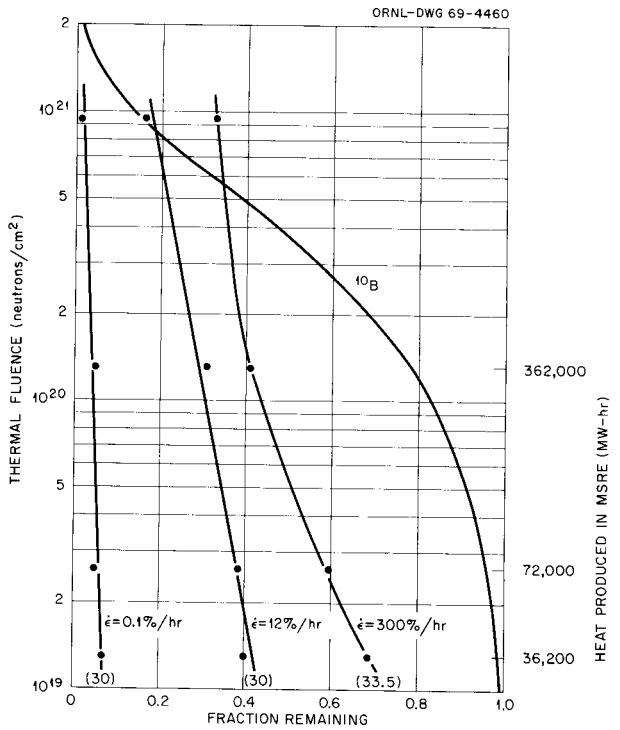

Fig. 32.2. Variation of Fracture Strain of Hastelloy N Surveillance Specimens with Thermal Fluence for Various Strain Rates.

Postirradiation Welding of Hastelloy N

H. E. McCoy R. W. Gunkel

The maintenance of molten-salt breeder reactors requires that we be able to weld irradiated Hastelloy N. To get some idea of the difficulty of this task, we made fusion welds covering 75% of the cross section in small tensile samples (0.125 in. in diameter) of Hastelloy N irradiated to thermal fluences up to 2.4×10^{20} neutrons/cm^2. The welding technique worked well for unirradiated samples, but only two-thirds of the welds were satisfactory in the irradiated samples.[6,7] The successfully welded irradiated samples generally had as good tensile properties at 25 and 650°C as the irradiated base metal. At 650°C the welded samples had higher fracture strains since the weld metal deformed appreciably and contributed to the overall fracture strain. Some porosity was noted near the fusion line of the irradiated samples, but this did not seem to affect the location of the fracture.

The problem involved with welding the irradiated specimens was apparently related to a small amount of subsurface contaminant introduced during exposure to the fuel salts. Even though very small voids were evident throughout several of the welds, failure frequently occurred in the base metal. Figure 32.3 indicates the appearance of such a weld.

[6]R. W. Gunkel and T. E. Scott, *MSR Program Semiann. Progr. Rept. Aug. 31, 1968,* ORNL-4344, p. 278.

[7]H. E. McCoy, *MSR Program Semiann. Progr. Rept. Aug. 31, 1968,* ORNL-4344, pp. 278–82.

MSBR DEVELOPMENT

Effect of Titanium and Carbon on Fracture of Nickel Alloys[8]

C. E. Sessions

The influences of titanium and carbon interactions on the mechanical behavior of nickel and nickel-base alloys are being studied to define the conditions that promote low-ductility intergranular fractures. An understanding of these alloying effects in unirradiated materials would give us a better understanding of the radiation embrittlement of structural alloys. The factors that favor high ductility appear to be (1) grain boundary mobility at the test temperature so that stress concentrations along grain boundaries can be relieved, (2) an optimum spacing of precipitate particles to inhibit the growth of wedge-type cracking along grain boundaries, and (3) an optimum morphology of precipitate that allows grain boundary deformation processes to take place without initiating grain boundary cracks. The importance of

[8]This work is supported by the Fuels and Materials Branch of RDT.

Fig. 32.3. Irradiated and Then Welded Hastelloy N. The material was irradiated for 15,289 hr in fuel salt in the MSRE at 650°C to a thermal fluence of 9.4 X 10^{20} neutrons/cm^2, welded in a hot cell, and tested at 650°C. Fracture occurred in the base metal. Etchant: Aqua regia. 35X.

these factors depends on the testing conditions (temperature, strain rate, etc.) and on the relative contribution of grain boundary sliding to bulk deformation within the grain. We are comparing alloying effects in high-purity material and in nickel alloys to contrast the important effects of gross precipitation on fracture processes.

Titanium additions to pure nickel promote both strengthening and ductilizing at elevated temperatures, as measured in both creep and tensile tests. The fracture mode at a given temperature is changed from intergranular to transgranular by small titanium additions, and the ductility enhancement is virtually the same as achieved by zone refining. In this case, titanium is probably gettering an impurity element that promotes low-ductility, intergranular failures. Another possible mechanism is that titanium retards or eliminates some detrimental aging process due to trace impurities. We can not yet decide between these possibilities.

Titanium has been added to more complex nickel-base alloys and found to have large effects on the mechanical properties. One major effect is that of promoting the formation of MC-type carbides that are stable to higher aging temperatures. In solution-annealed Ni-Mo-Cr alloys containing up to 1.2% Ti the creep fractures are intergranular regardless of the titanium content, but aged alloys with high titanium concentrations fracture transgranularly and aged low-titanium alloys fracture intergranularly.

The presence of titanium and carbon is very important in the creep deformation of unirradiated Hastelloy N, as shown in Fig. 32.4. The presence of 0.5% Ti in alloys 195 and 196 significantly enhanced the ductility. This benefit of titanium is also evident

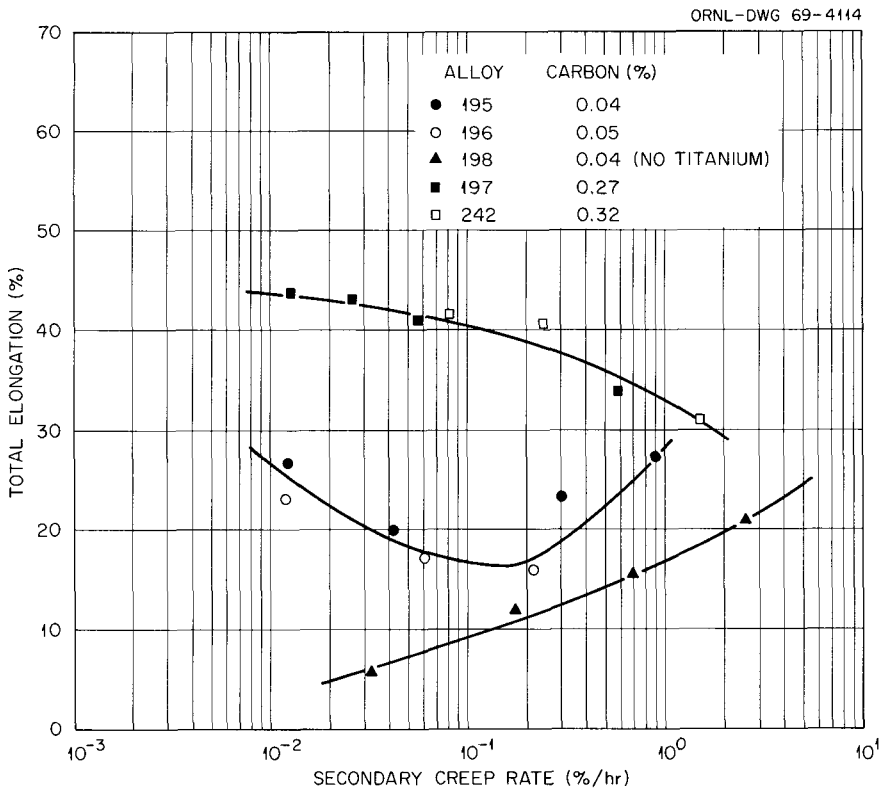

Fig. 32.4. Change in Strain Rate Sensitivity of the Creep Deformation with Titanium and Carbon Contents in Hastelloy N.

after irradiation[9,10] and is likely the result of the favorable carbide morphology. Figure 32.4 shows that high carbon levels of about 0.3% further improve the fracture strain. Much of this improvement is likely associated with the extremely fine grain size of these alloys.

Comparison of the Thermal Stability of Titanium-Modified Hastelloy N at 650 and 760°C

C. E. Sessions

A modified Hastelloy N containing small additions of titanium is being evaluated for use in advanced molten-salt reactors. Titanium additions up to about 1% are contemplated, and the service temperature range is 550 to 700°C. The aging response of these alloys is of extreme importance, since the design lifetime of these systems is 30 years. Our present studies include alloys with 0.1 to 1.2% Ti, aging temperatures of 650 and 760°C, and various preaging heat treatments. We used as our criteria of aging the change in mechanical properties measured by a tensile test (strain rate of 0.002/min) and a creep test (40,000 psi) at 650°C. Our conclusions based on samples aged up to 10,000 hr follow.

1. The susceptibility to aging in this alloy does not uniquely correlate with the titanium content. The alloy containing an intermediate titanium level (0.5% Ti) was most stable.
2. The most severe aging occurs for the alloys containing only 0.15 and 0.30% Ti.
3. Ductility losses increase with increasing aging time (1500, 3000, and 10,000 hr), aging temperature (650 and 760°C), and preage annealing temperature (1177 and 1260°C).
4. For samples aged in the solution-annealed condition, the yield and ultimate tensile strengths increase on

[9] J. R. Weir, Jr., H. E. McCoy, Jr., and D. G. Harman, *Metals and Ceramics Div. Ann. Progr. Rept. June 30, 1968,* ORNL-4370, pp. 198–99.

[10] H. E. McCoy, Jr., and J. R. Weir, Jr., "Development of a Titanium-Modified Hastelloy with Improved Resistance to Radiation Damage," paper presented at the Symposium on Effects of Radiation on Structural Metals, San Francisco, Calif. June 23–28, 1968 (to be published in proceedings).

aging at 650°C, whereas aging at 760°C increases the yield strength and generally decreases the ultimate strength.

5. Prestraining these alloys 10% at room temperature before aging raises the yield strength from 30,000 to 45,000 psi and reduces the uniform elongation from 30 to about 20%.
6. Prestraining increases the ductility loss on aging for the lower titanium levels but has no effect on the ductility change for the higher titanium levels.
7. No significant loss in creep strength or ductility occurs for higher titanium levels after 3000 hr of aging (at 650 and 760°C); however, the strength and ductility decrease for the lower titanium levels after 3000 hr at 760°C.

Microstructural examination of the tested samples shows large differences in the precipitate distribution after aging at 760 and 650°C. At 650°C a heavy, nearly continuous grain-boundary precipitate of the MC type was found; however, at 760°C we identified fewer but larger particles of the M_2C type for the low titanium contents and some MC carbide for the 1.2%-Ti heat.

Electron Microscopy

R. E. Gehlbach S. W. Cook

Our electron microscopy studies of Hastelloy N are directed toward ascertaining the microstructural behavior of the various alloys as a function of thermal and mechanical behavior and the role of various alloying additions in changing the microstructures. We found significant relationships between certain types of microstructures and changes in mechanical behavior of both irradiated and unirradiated material.

Standard Hastelloy N. – The types and behavior of precipitated phases in Hastelloy N are closely related to the concentration of silicon in the alloy. More than about 0.2% Si in the melt increases the concentration of silicon in the M_6C or $(Ni,Mo,Cr)_6C$ type precipitate, the only type found in the standard air-melted version of the alloy. Silicon promotes the formation and stability of "M_6C" at high temperatures. Above about 1300°C a lamellar silicide phase of the M_6C type is formed. At temperatures above 1350°C the lamellar silicide phase transforms to the hexagonal Mo_2Ni_3Si Laves-type intermetallic, which reacts to form M_6C and M_2C at lower temperatures.[11] We feel that the silicides are probably responsible for increased embrittlement after high annealing temperatures or welding.

In alloys containing about 0.2% Si some true M_6C is formed, which can be put into solid solution at high annealing temperatures. The high-temperature silicide phase is nor formed. Decreasing either the silicon or molybdenum content causes the precipitation of M_2C as well as M_6C. Alloys with trace levels of silicon precipitate only M_2C after extended exposure at elevated temperatures.

Modified Hastelloy N. – The microstructures of the modified alloys are quite different from that of the standard material. Two of the major composition changes that affect the microstructure and precipitates that form are a decrease in molybdenum from 16 to 12% and a decrease in silicon from 0.6 to below 0.1%. As a result, the M_6C-type precipitate is absent. Unlike the behavior in the standard alloy, most precipitate particles in the modified Hastelloy N are put into solid solution at normal annealing temperatures (1177 or 1260°C). Exposure at temperatures similar to those expected in service results in precipitation both at grain boundaries and in the matrix.

In the modified alloys without additions of the titanium-group elements,[12] only M_2C precipitates at aging temperatures of 650 and 760°C. The additions of the titanium-group elements promote the formation and stability of cubic carbides of the MC type. Higher concentrations of the titanium-group elements are required to stabilize the MC types at 760°C than at 650°C. These trends are shown in Table 32.1.

The compositions of the MC types depend on the amount of the particular elements from the titanium group present in the material. At low titanium concentrations, (Mo,Cr)C is formed. Increasing the concentration of titanium in the alloy results in some titanium substituting for chromium in the carbides, increasing the lattice parameter from 4.21 to 4.28 A. Adding hafnium or zirconium promotes the stability of the carbides of that group, such as HfC. In general, the MC carbide is finer than the M_2C type, and its distribution in the bulk material appears to result in superior postirradiation mechanical properties than that of the M_2C precipitate.

The distribution of MC, or (Mo,Cr,Ti)C, in heat 66-548 (a commercial alloy with 0.45% Ti) after aging at 650°C is shown in Fig. 32.5. The characteristic feature is the many fine precipitate particles adjacent to the grain boundaries and extending into the matrix. In contrast, aging this material at 760°C precipitates larger particles in both the matrix and grain boundaries. The

[11] The M_2C carbide has a Mo_2C structure but contains some chromium and thus is actually $(Mo,Cr)_2C$.

[12] The alloying elements Ti, Nb, Zr, and Hf will be referred to as the titanium-group elements.

Table 32.1. Phases Present in Various Hastelloy N-Type Alloys After Aging (>1000 hr) at the Indicated Temperature

Alloy[a]	Precipitate Observed	
	at 650°C	at 760°C
Std Hastelloy N (0.5 Si)	M_6C	M_6C
Std Hastelloy N (<0.1 Si)	M_2C	M_2C
198 (modified)	M_2C	
66-535 (0.12 Ti)	MC + M_2C	M_2C
196 (0.5 Ti)	MC + $(M_2C)^b$	
66-548 (0.45 Ti)	MC	$(MC)^b + M_2C$
107 (1.0 Ti)	MC	
67-548 (1.2 Ti)	MC	MC
112 (1.0 Zr)	MC	
181 (0.5 Ti–2 Nb)	MC	MC
184 (1 Ti–1 Hf)		MC

[a]Alloys with heat numbers are Ni–12% Mo–7% Cr–0.2% Mn–0.05% C plus the indicated addition, except that 184 also contains 4% Fe and 0.2% Si.
[b]Present in minor amounts.

distribution of MC in heat 67-548 (1.2% Ti) depends on both the annealing and aging temperatures. Annealing at 1260°C dissolves more of the precipitate than annealing at 1177°C and enhances precipitation during subsequent aging. This precipitation of (Mo,Ti,Cr)C has the form of thin massive films containing many fine (<200 A) particles, giving rise to stacking fault contrast, as shown in Fig. 32.6. The sheets of precipitate creating the stacking faults are more extensive after aging at 760°C than at 650°C, being approximately 6 to 8 μ and 4 to 6 μ, respectively, after 3000 hr. We will determine the effects of this structure on postirradiation mechanical properties.

Examination of irradiated specimens from several different modified heats has shown a close correlation between a fine precipitate structure and good mechanical properties. We are determining the effects of various alloying elements on the precipitate distribution and will be irradiating samples with these microstructures to determine their postirradiation mechanical properties.

Development of a Modified Hastelloy N for Future MSBR's

H. E. McCoy

The metallic structural material in MSBR's will be exposed to a large fluence of thermal neutrons and must retain reasonable mechanical properties. Under these irradiation conditions the mechanical properties are altered by helium produced from the transmutation of ^{10}B. The problem is aggravated by the tendency of boron to segregate to the grain boundaries. We have sought to reduce the property changes by adding elements that form borides and hence disperse the boron more uniformly. The elements added to date include Ti, Zr, Hf, and Nb.

Much of our work has involved alloys modified with titanium. An alloy containing only 0.5% Ti had excellent properties when irradiated at 650°C, but had very poor properties when irradiated at 700°C and higher. This strong temperature dependence appears related to the types of carbides formed at 650 and 760°C. The desired properties are favored by the formation of finely dispersed MC-type carbide and the

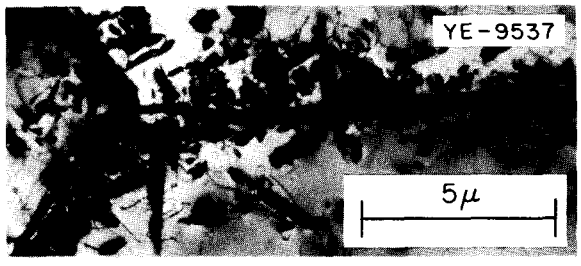

Fig. 32.5. Morphology and Distribution of (Mo,Cr,Ti)C in Hastelloy N, Heat 66-548 (0.45% Ti), Annealed at 1177°C and Aged 1500 hr at 650°C. Transmission electron micrograph, 5000X.

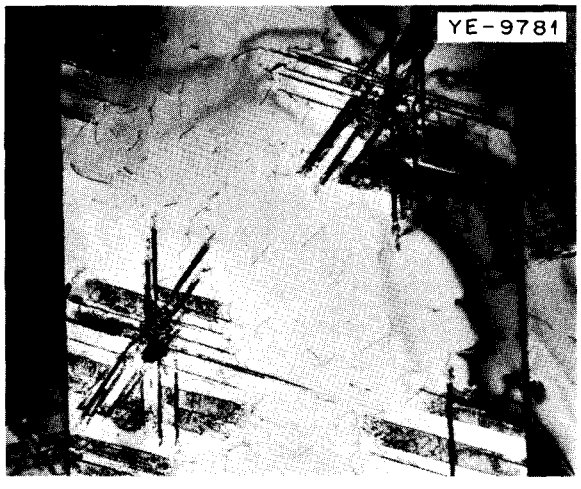

Fig. 32.6. Precipitation of (Mo,Ti,Cr)C Causing Stacking Faults in Heat 67-548 (1.2% Ti), Annealed at 1260°C and Aged 3000 hr at 650°C. Transmission electron micrograph, 5000X.

poor properties result from the formation of coarse M_2C carbide.

Additions of Ti, Zr, Hf, and Nb favored the formation of the desired MC-type carbide, and alloys containing sufficient amounts of these elements have good post-irradiation properties, even when irradiated at 760°C. Specific alloys noted to have good properties are modified with 1.2% Ti, 1% Hf, 0.5% Ti + 2% Nb, and 1% Ti + 1% Hf. An alloy modified with 1% Zr had excellent postirradiation properties but very poor weldability. Our work presently centers on determining the concentrations of these elements required to obtain the desired properties.

Corrosion Studies

J. W. Koger A. P. Litman

We are studying the compatibility of fused fluoride salts with structural materials of interest to the Molten-Salt Reactor Project.[13–16] The alloys under investigation are standard Hastelloy N, the more radiation resistant titanium-modified Hastelloy N (0.5% Ti), and type 304L stainless steel with fuel, blanket, fertile-fissile, and coolant salts. The fuel and blanket salts are germane to the older two-fluid concept, while the fertile-fissile salt is proposed for the more recent one-fluid MSBR system. The active salts are mixtures of LiF and BeF_2 with additions of UF_4 (fuel salt), ThF_4 (blanket salt), and both (fertile-fissile salt). A sodium fluoroborate mixture, $NaBF_4$–8 mole % NaF, is proposed as the coolant for both MSBR concepts. The following significant observations have been made this year.

Fuel, Blanket, and Fertile-Fissile Salts. – 1. The standard Hastelloy N loop containing an old type fuel salt has operated over 7.2 years at a maximum temperature of 705°C with no evidence of plugging. No removable specimens are in this loop.

2. We have operated a type 304L stainless steel loop with the same salt for 6 years at a maximum temperature of 688°C. The removable specimen at the highest temperature has lost 48.9 mg/cm^2 in 16,500 hr, equivalent to about 0.001 in./year uniform corrosion. Thus, stainless steel remains an inferior replacement for Hastelloy N in fused fluorides.

3. Removable specimens in more recently fabricated standard Hastelloy N loops containing fuel, blanket, and fertile-fissile salts operating at a maximum temperature of 700°C have lost a maximum of 0.8 mg/cm^2 in 5000 hr (4×10^{-5} in./year). These salts continue to show excellent compatibility with both titanium-modified and standard Hastelloy N. The fertile-fissile salt in one loop contacted liquid bismuth during operation. No detrimental pickup of bismuth by the salt or change in the corrosion rate was noted.

4. We operated a TZM capsule containing fertile-fissile salt for 1000 hr at 1100°C in support of the vacuum distillation method of salt purification. Removal of titanium and zirconium with resulting recrystallization was noted in the alloy. Weight changes of removable specimens were small, and the general compatibility of the system was considered to be good.

Coolant Salt. – 1. The corrosion of materials exposed to the fluoroborate salt is highly dependent on the water and oxygen-containing impurities in the salt.[14,15,17]

2. Natural circulation loops, fabricated from Hastelloy N and Croloy 9M, that circulated impure (>3000 ppm impurities) $NaBF_4$–4 mole % NaF–6 mole % KBF_4 at a maximum temperature of 605°C with a temperature difference of 145° evidenced serious temperature-gradient mass transfer. All major constituents of the container materials migrated, restricting flow in the Hastelloy N loop by deposition of Na_3CrF_6 crystals and completely plugging the Croloy 9M loop with iron dendrites.[17]

3. Removable titanium-modified Hastelloy N specimens in a standard Hastelloy N coolant salt loop operating at a maximum temperature of 607°C lost a maximum of 16.0 mg/cm^2 in 11,000 hr (6×10^{-4} in./year uniform corrosion). The impurity content (analyzed water and oxygen concentration) has cycled from 500 to 2000 to 1000 ppm as operating conditions varied.[13–16]

4. Standard Hastelloy N specimens in a standard Hastelloy N coolant salt loop operating at a maximum temperature of 607°C have lost a maximum of 7.0 mg/cm^2 in 3500 hr (8×10^{-4} in./year uniform corrosion).

5. A standard Hastelloy N coolant salt pump loop MSR-FCL-1 (10 ft/sec) has operated for 2082 hr at a

[13] J. W. Koger and A. P. Litman, *MSR Program Semiann. Progr. Rept. Feb. 29, 1968,* ORNL-4354, pp. 218–25.

[14] J. W. Koger and A. P. Litman, *MSR Program Semiann. Progr. Rept. Aug. 31, 1968,* ORNL-4344, pp. 257–66.

[15] J. W. Koger and A. P. Litman, *MSR Program Semiann. Progr. Rept. Feb. 28, 1969,* ORNL-4396, pp. 243–53.

[16] J. W. Koger and A. P. Litman, *Metals and Ceramics Div. Ann. Progr. Rept. June 30, 1968,* ORNL-4370, p. 207.

[17] J. W. Koger and A. P. Litman, *Compatibility of Hastelloy N and Croloy 9M with $NaBF_4$–NaF–KBF_4 (90-4-6 mole %) Fluoroborate Salt,* ORNL-TM-2490 (April 1969).

maximum salt temperature of 587°C. Maximum weight loss from a tab specimen in the loop was 11.0 mg/cm^2. The salt contained about 1000 ppm each of water and oxygen. The corrosion mechanism in the salts with high water and oxygen contents was shown to be impurity controlled with uniform removal of material from the alloys. Higher corrosion in the pump loop is partly due to the increased velocity.

6. We operated standard Hastelloy N coolant salt capsules with varying overpressures of BF_3 gas. The salt contained about 400 ppm H_2O before and after test, and the corrosion was nil.

Status of Fused Fluoride Corrosion. – The results of the past year have continued to confirm that the temperature-gradient mass-transfer corrosion mechanism in pure fluoride salts involves the formation of the most stable structural metal fluoride (usually chromium) in a hot section, followed by deposition of a portion of the corrosion products, as reduced metal, in a cool region. It is clear that below the solubility limit of the fluorides of the structural metal constituents in the fluid, the balance of the corrosion products remains in the salt. The presence of impurities leads to more oxidizing conditions (the worst case being ultimate formation of HF), which permit all constituents in the container alloy to be attacked. Our program has advanced to the point where we can now distinguish the individual and collective roles of the alloy constituents in the overall corrosion scheme. In all cases where the titanium-modified Hastelloy N and standard Hastelloy N specimens were tested under comparable conditions, the titanium-modified alloy corroded more slowly. We attribute this reduction primarily to the lower iron content of the modified alloy.

The general picture that we have developed for the corrosion of structural materials in fluoride salts is summarized in Table 32.2. The rates for Hastelloy N in the fuel, blanket, and fertile-fissile salts are extremely low and acceptable for indefinite operation. We feel that the higher corrosion rates in the sodium fluoroborate are associated with impurities, but further experiments will be necessary to determine (1) whether the corrosion rates are too high in salt of the present purity and (2) whether techniques can be developed for further reducing the impurity levels.

Residual Stress Measurements in Hastelloy N Welds

A. G. Cepolina[18] D. A. Canonico

We found previously[19] that gas tungsten-arc (GTA) welds made in ½-in.-thick Hastelloy N plate with argon shielding gas and 15,000 joules/in. bead produced peak tangential and radial residual stresses of 50,000 and 17,000 psi, respectively. Postweld heat treating these weldments at 870°C for 6 hr or 1177°C for 1 hr lowered the tangential and radial stresses to 5000 and

[18] Now with Italian Institute of Welding, Genoa.

[19] A. G. Cepolina and D. A. Canonico, *Metals and Ceramics Div. Ann. Progr. Rept. June 30, 1968,* ORNL-4370, pp. 205–6.

Table 32.2. Maximum Weight Loss of Container Materials Exposed to Fused Fluorides Flowing at 5 to 7 ft/min During First 5000 hr of Operation

Alloy	Salt Type	Max Temp (°C)	ΔT (°C)	Wt Loss (mg/cm^2)
Titanium-modified Hastelloy N	Fuel	705	170	0.3
	Blanket	675	55	0.2
	Fertile-fissile	705	170	0.5
	Fluoroborate[a]	605	150	3.0
Standard Hastelloy N	Fuel	705	170	0.6
	Blanket	675	55	0.4
	Fertile-fissile	705	170	0.7
	Fluoroborate[a]	605	150	4.0
Type 304L stainless steel	Fuel	688	100	25.0
	Fluoroborate[b]	Cycled 538–690		~175[c]

[a] 500 to 1000 ppm analyzed water and oxygen impurities.
[b] 1000 to 2000 ppm analyzed water and oxygen impurities.
[c] Extrapolated.

1000 psi, respectively. More recently we determined the effect of (1) postweld heat treatments at lower temperatures, (2) shielding gas, and (3) heat input.

Table 32.3 contains a synopsis of the effects of postweld heat treatment temperature on the maximum tangential and radial residual stresses of welds made with argon shielding gas. Included for comparison are data for welds made with helium. Substantial stress relief did not occur at 650°C, and the 870°C treatment is about optimum. If a temperature limitation is necessary, Hastelloy N weldments can probably be satisfactorily stress relieved at 760°C. Extending the time at temperature beyond 6 hr should decrease the listed peak stress values somewhat. The use of helium shielding gas had essentially no effect on the radial residual stress; however, it did increase the peak tangential residual stress by about 20% (50,000 to 60,000 psi).

Decreasing the heat input from 15,000 to 7500 joules/in. bead reduced the peak tangential residual stress from 51,000 to 44,000 psi but did not change the stress distribution appreciably.

Evaluation of New Materials

W. H. Cook

The graphite for future molten-salt breeder reactors must have (1) maximum pore entrance diameters less than 1 μ to prevent salt absorption and to simplify the problems of sealing these against gas permeation, (2) a surface diffusivity of less than 10^{-8} cm^2/sec for fission gases such as ^{135}Xe, and (3) reasonable dimensional stability to a neutron fluence of at least 3×10^{22} neutrons/cm^2 (>50 kev) at 700°C. These requirements are not independent, and we are finding that some work will be required for commercial vendors to produce the desired graphite in suitable shapes. Extruded shapes approximately 4 in. sq. × 8 ft long will be required for the MSBE, and future reactors will require similar cross sections in lengths to 16 ft.

Several commercial grades of graphite are available that have high density, greater than 1.85 g/cm^3, and mechanical properties that meet the MSBR requirements. The small pore entrance diameters, the low gas permeability, and the irradiation stability are more difficult to obtain, but some graphites satisfy the first and third requirements adequately.[20] Some factors that contribute to irradiation stability and our results on some grades of graphite are discussed in the later sections on X-Ray Studies and Irradiation Damage. The helium gas permeabilities of these premium grades of graphite range from 3×10^{-5} to 0.1 cm^2/sec at room temperature. These data emphasize the necessity for sealing the graphite to attain the surface gas diffusivity below 10^{-8} cm^2/sec, and this work is discussed later in this chapter.

We have had a cooperative program with the Chemical Engineering Development Department (CEDD) of the Y-12 Plant[21] for several years for the production of small pieces of research graphite directed toward the development and understanding of an irradiation-resistant graphite. Their fabrication facilities, our irradiation facilities, and the facilities for characterization at both installations are uniquely complementary. One of the products of this joint effort presently being studied is reconstituted graphite. Some of the isotropic grades of graphite that have good resistance to irradiation damage are formed by molding, a process that is unsuited for forming the large shapes required for MSBR's. Pieces of these isotropic products were crushed to form filler material for bodies that were blended with a polymerized furfuryl alcohol, formed by extrusion, and fired at a graphitizing temperature. These are referred to as reconstituted graphite. The physical properties of these "reconstituted" isotropic grades of graphite formed by the classical extrusion process were essentially as good as those of the starting

Table 32.3. Effect of Postweld Heat Treatments on the Peak Residual Stresses in Hastelloy N Weldments[a]

Shielding Gas	Postweld Heat Treatment		Maximum Stress (psi)	
	Temp (°C)	Time (hr)	Tangential	Radial
			$\times 10^3$	$\times 10^3$
Argon			50	16.8
Argon	870	6	~5	~1
Argon	1177	1	~5	~2
Helium			60	17.3
Helium	870	4.5	5.2	1
Argon	870	4.5	5.0	1.6
Argon	760	6	10	4
Argon	650	100	36.8	12.6

[a]Heat input, 15,000 joules/in. bead.

[20]W. H. Cook, *MSR Program Semiann. Progr. Rept. Aug. 31, 1967*, ORNL-4191, pp. 208–9.

[21]Y-12 Plant, operated by the Union Carbide Corporation for the U.S. Atomic Energy Commission, P.O. Box Y, Oak Ridge, Tenn. 37830.

materials.[22] The irradiation damage resistance of these reconstituted graphites must be determined, and then the scale-up without serious degradation of properties must be demonstrated.

Some graphite samples have been produced in which the starting material(s) have been synthesized or a commercial high-melting, high-carbon binder material is used.[22] The first of these is a reconstituted isotropic graphite, grade AXM, bonded with synthesized isotruxene, $C_6H_3(C_6H_5)_3$, or a hard pitch in a molding process[23] before firing at 2800°C. The physical properties of these first trial productions did not meet the MSBR graphite requirements,[22] but optimization of the processing parameters should yield a useful product. The carbon yields are 10 to 30% better than those obtained by commercial practice and should lead to less shrinkage during processing. These materials are being included in all phases of our program.

X-Ray Studies

O. B. Cavin

The dimensional stability of polycrystalline graphite during neutron irradiation is strongly influenced by the relative orientation of the crystallites in the fabricated material. Accordingly, we are using x-ray diffraction techniques to determine the crystalline anisotropy of several graphites of interest to the Molten-Salt Reactor Program before they are irradiated.

We are using two well-known preferred orientation techniques for ascertaining the diffracted x-ray intensity distribution and thus the relative number of c axes in various directions in the material. The first approach uses the Schulz arrangement and has been described previously.[24] A second extensively used technique[25] uses a 0.2-in.-diam spherical sample that is machined on the end of a 0.25-in.-diam × 1.0-in.-long cylinder. A value for the anisotropy factor, R, can be determined from data on the x-ray intensity vs angular position by using a slight modification of a technique developed by Price and Bokros.[26] The value of R measured in a direction parallel to the extrusion direction, $R_{\|}$, is defined as

$$R_{\|} = \frac{\int_0^{\pi/2}\int_0^{2\pi} I(\phi,\beta)\sin^3\phi\, d\phi\, d\beta}{\int_0^{\pi/2}\int_0^{2\pi} I(\phi,\beta)\sin\phi\, d\phi\, d\beta},$$

where

ϕ = angle between normals to sample surface and diffracting planes,

β = rotational angle about surface normal,

$I(\phi,\beta)$ = x-ray intensity at direction (ϕ,β).

This equation reduces to a single integration through ϕ for data taken from a sphere because the integration through β is approximated by rapid rotation about the stem axis. If we assume symmetry about the axis of rotation, the anisotropy factor in the perpendicular direction, $R_{\perp}$, is given by $R_{\perp} = 1 - R_{\|}/2$.

If we then assume that graphite is a single phase, the R values can be used to describe the irradiation-induced growth rate ($\dot{G}$'s) in the two directions:

$$\dot{G}_{\|} = R_{\|}\dot{G}_a + (1 - R_{\|})\dot{G}_c ,$$

$$\dot{G}_{\perp} = R_{\perp}\dot{G}_a + (1 - R_{\perp})\dot{G}_c .$$

The crystallite growth rates in the a and c directions are $\dot{G}_a$ and $\dot{G}_c$ respectively. Values of R can range from 0 to 1, and an isotropic material has an R of 0.667. The equations predict that the growth rates in a particular direction are determined by the crystallite growth rates in the a and c directions and the anisotropy factor measured in the direction of interest. The irradiation-induced growth rates in the two orthogonal directions at constant volume are measured on irradiated samples, and the anisotropy factors are determined by x-ray measurements. The various observations are plotted in Fig. 32.7. Not only are these equations satisfied for each grade of graphite, but all lines superimpose to give one straight line, which passes through the R value of 0.667 at a zero growth rate. By extrapolation, the crystallite growth rates in the a and c directions are -11×10^{-22} %/(neutron/cm^2) and 22×10^{-22} %/(neutron/cm^2) respectively.

This correlation shows that the single-phase model is adequate for describing the radiation-induced growth rates, which are dependent primarily upon the anisotropy of the coke particles and not on the binder or impregnants.

---

[22] W. H. Cook, *MSR Program Semiann. Progr. Rept. Feb. 28, 1969*, ORNL-4396, pp. 217–19.

[23] The relatively small quantities of starting materials available dictated the molding technique for the initial work.

[24] O. B. Cavin, *MSR Program Semiann. Progr. Rept. Feb. 28, 1969*, ORNL-4396, pp. 219–21.

[25] L. K. Jetter and B. S. Borie, Jr., *J. Appl. Phys.* **24**, 532–35 (1953).

[26] R. J. Price and J. C. Bokros, *J. Appl. Phys.* **36**, 1897 (1965).

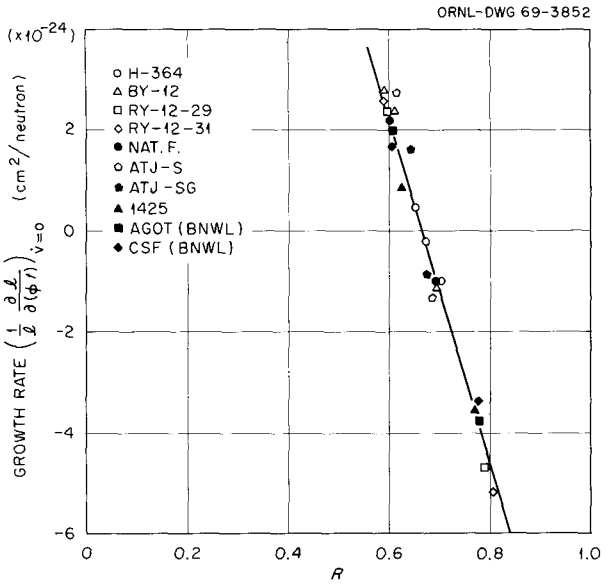

Fig. 32.7. Growth Rate of Graphites at 715°C as a Function of Orientation Parameter *R*.

These anisotropy factors are important parameters for characterizing graphites without expensive and time-consuming long-term irradiation experiments. The two experimental approaches that we mentioned give comparable results, but we will likely use the spherical samples more often since the results are obtained more rapidly.

Graphite Irradiation in HFIR

C. R. Kennedy

Graphite samples have received exposures in HFIR up to 2.5 X 10^{22} neutrons/cm^2 (>50 kev) and will accumulate up to 3.8 X 10^{22} neutrons/cm^2 when they are removed from HFIR in June 1969. The linear dimensional changes resulting from the irradiation were least-squares fitted to a quadratic expression. The volumetric changes were calculated from the linear dimensional change data and the curves are given in Fig. 32.8. Several significant behavioral characteristics, which are important to the development of a more irradiation-resistant graphite, are apparent. The first is that the maximum densification of the graphite is a linear function of the original density, as shown in Fig. 32.9.

The three grades, ATJ-S, ATJ-SG, and 1225, which do not fall on the curve, are very heavily impregnated, and the impregnant is not fully integrated with the structure. The behavior shown in Fig. 32.9 is strong evidence that density changes are a result of closure and opening of the open porosity.

If the densification rate is common for the graphites, then the fluence required to obtain the maximum density will also be a linear function of the original density. This relationship is shown in Fig. 32.10. This means that the more dense conventional materials will achieve their maximum density more quickly, begin to expand, and have a shorter lifetime.[27] Two materials, H364 and Natural Flake, do not fall on the curve, and obviously the unplotted Poco grades would not follow this correlation. The initial structure of the natural flake grade is probably the most highly graphitic of the group. Thus, the initial crystallite growth rates and the initial densification rate would be lower and the fluence required for maximum densification would be extended. The lower crystallite growth rate can only be hypothesized, since the separation of volume change effects from crystallographic growth rates is virtually impossible at low exposure.

The H364 and Poco grades do not fall on the curve in Fig. 32.10 because of a delayed densification. This factor is very significant since it results in an extension of the lifetime of the graphite. This delay in densification is a result of the isotropy and the high continuity of *c* axis in the structure. The high continuity of *c* axis is reflected by the very high coefficient of thermal expansion for these materials, 7 to 7.5 X 10^{-6} for H337 and H364 grades. Although the Poco grades have not reached their maximum density and could not be included in Fig. 32.10, they do exhibit an initial delay period and will likely fall above the line. We do not understand why these graphites begin to densify after a significant period of irradiation. The *c* axis continuity appears to be reduced, as evidenced by the decrease in the coefficient of thermal expansion as the material begins to densify.[28] The internal stresses created by the differential growth should be compressive in the *c* axis direction, so it is difficult to understand how this could cause separations along the *c* axis. However, these graphites (H364, Poco grades) have begun to densify

[27]The "lifetime" of the graphite is defined as that exposure at which void generation, as evidenced by volume expansion, is sufficient to increase the open pore size to allow excessive fission product and poison accumulation. We have arbitrarily chosen the fluence required to return the material to its initial volume after some densification. This is a conservative approach and may be particularly conservative for graphites that densify only 1 to 2% before expansion. The actual limitation in lifetime will have to be determined by experiment.

[28]A. L. Pitner, *Irradiation Behavior of POCO Graphites*, BNWL-CC-1930 (November 1968).

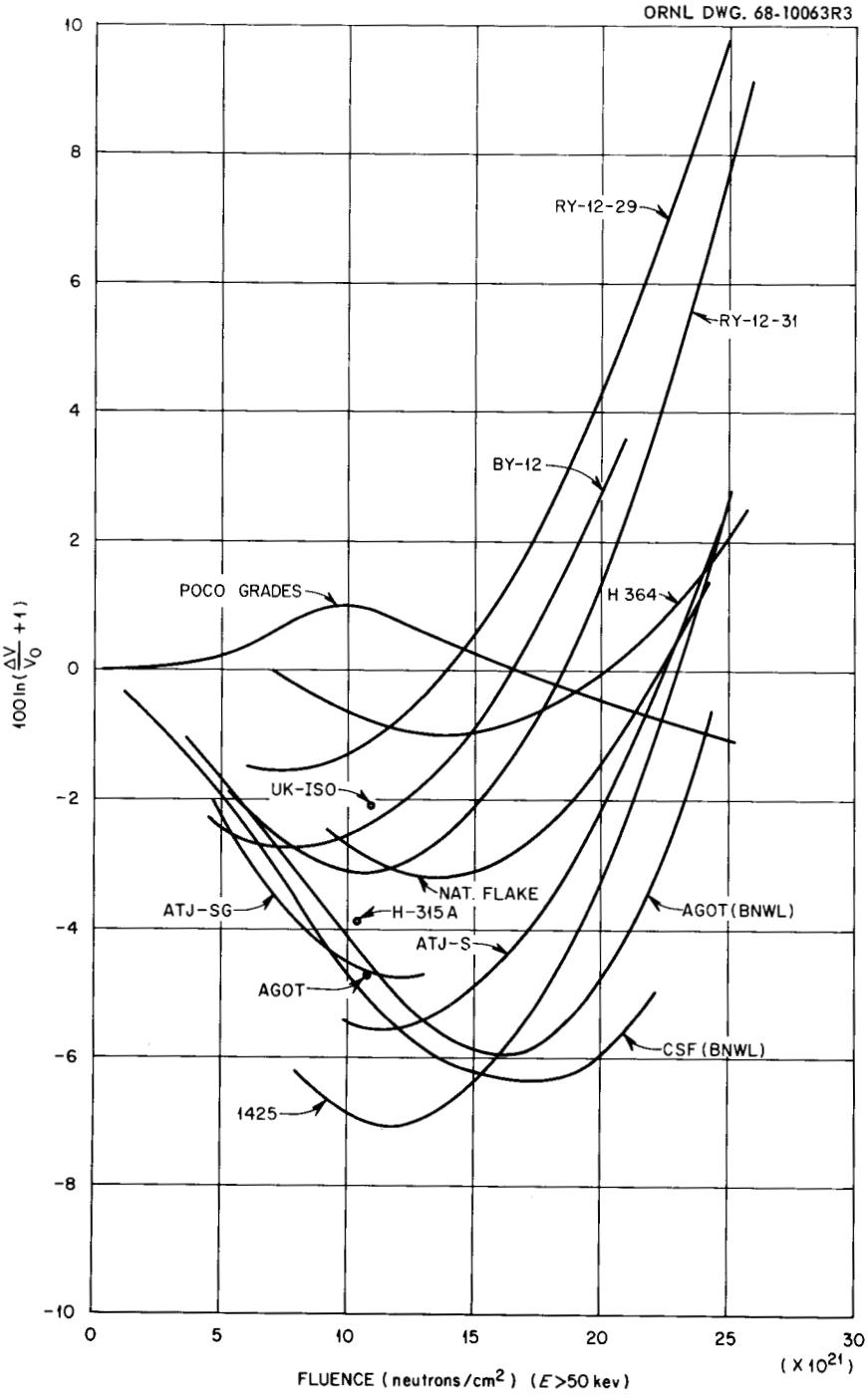

Fig. 32.8. Volume Changes in Graphites at 715°C.

after an initial delay, and the H364 has already achieved maximum density and experienced some volume expansion. In general, these results and the analysis of the results lead to several conclusions.

1. Linear dimensional stability is obtainable only with isotropic or near-isotropic materials.

2. Volumetric changes also contribute to linear dimensional changes, and the magnitude of their contribution is reduced by increasing the original structural density.

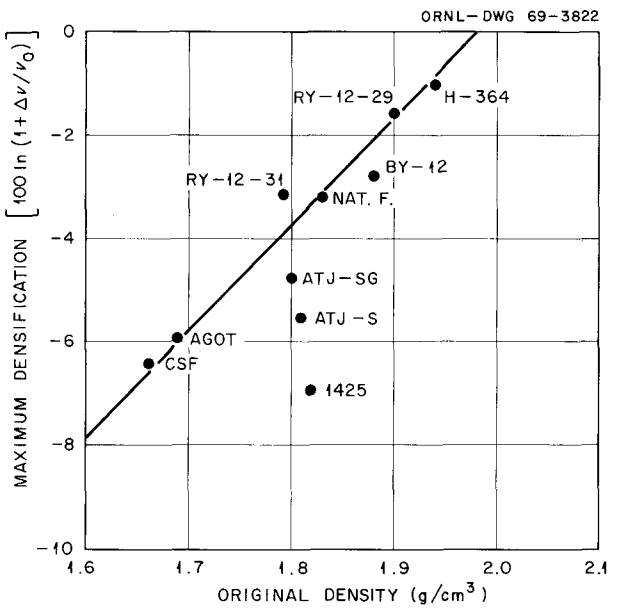

Fig. 32.9. Maximum Densification at 715°C as a Function of Original Density.

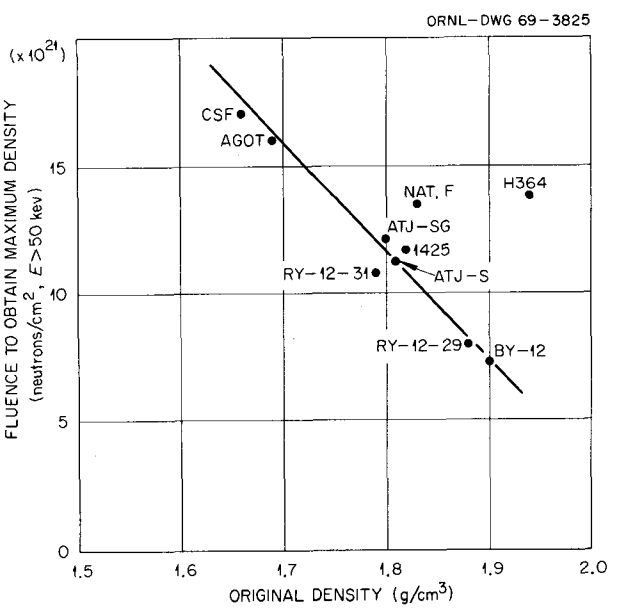

Fig. 32.10. Fluence to Obtain Maximum Density as a Function of Original Density.

3. The major characteristic that separates grades H364 and Poco graphites from the conventional graphites is a delayed densification. This is the only process observed that appears to extend the useful life of the graphite. The origin of this desirable characteristic is not clear, but we have observed it only in the two types of materials having isotropic structures with very high coefficients of thermal expansion.

Microstructure of Graphite

C. S. Yust C. S. Morgan

The microstructures of polycrystalline graphites are being studied by transmission electron microscopy. Although a substantial amount has been done on single-crystal graphite, the transmission work on polycrystalline graphite is quite limited. In fact, the first requirement in this study was the development of a suitable thinning technique. We modified a technique for thinning by mechanical polishing to prepare suitable specimens of many graphites. Smaller thinned areas of several graphites have been prepared by flame and chemical thinning.

A typical microstructure observed in AXF graphite is seen in Fig. 32.11. The ribbon-like structure so evident in this micrograph occurred frequently in each of the eight or so graphites examined. In some specimens specific features such as moiré patterns or rosettes were observed. Small angle tilt of the specimens would change some dark areas to light and vice versa. Analysis of the electron diffraction patterns from areas of aligned ribbons suggests that the ribbons consist of closely aligned layers of graphite with the basal planes oblique to the plane of the foil.

Figure 32.12 shows the microstructure of a piece of AXF graphite that was irradiated to a fluence of 1.2×10^{22} neutrons/cm^2. The transmitting areas of the irradiated material appear to be denser and have fewer cracks than those in the unirradiated material in Fig. 32.11. Ribbons of material remain but in general are less evident. Electron diffraction spots representing small individual diffracting units appear more numerous and distinct. These spots have sizes roughly equal to the 250-A crystallite size measured by x-ray diffraction line broadening.

Gas Impregnation of Graphite with Carbon

R. L. Beatty

Graphite for molten-salt reactors should have a permeability low enough to prevent xenon absorption

until the xenon can be sparged from the salt by gas. This permeability is currently specified as less than 10^{-8} cm^2/sec for helium at room temperature and requires a permeability reduction in high-quality commercial graphite of four to six orders of magnitude. For neutron economy and salt compatibility, the only sealant material being considered is carbon.

Pyrolytic carbon impregnation of graphite by gas pulsing continues to look very promising. The process is adaptable to graphites of widely different pore structures, although processing conditions must be optimized for each basic pore size spectrum. Principal conditions to be optimized are deposition temperature and periods of evacuation and hydrocarbon gas pulses.

Fig. 32.11. Transmission Electron Micrograph of a Highly Isotropic Graphite, Poco Grade AXF. The material has regions containing closely aligned lamellae or ribbons. Some pores and cracks between ribbons are visible. 14,500X. Reduced 11%.

Fig. 32.12. Transmission Electron Micrograph of AXF Graphite After Irradiation to a Fluence of 1.24 × 10^{22} Neutrons/cm^2. Lamellae or ribbons are still present but less distinct. Cracks between individual ribbons have been partially closed. Voids or pores are still present but are not seen in this field. 55,000×. Reduced 57.5%.

We have studied three graphites of potential interest for MSBR's: Union Carbide grade ATJ-SG, Poco grade AXF, and Great Lakes grade H337. Near-optimum conditions for gas impregnation of these graphites are, respectively, temperatures of 900, 800, and 700°C, evacuation periods of 4, 8, and 15 sec, and hydrocarbon (1,3-butadiene at 10 psig) exposure periods of 1, 2, and 4 sec. In general, as graphite pore size is reduced, reducing temperature and increasing evacuation and pressurization periods maintain the optimum (maximum) rate and depth of penetration. All of these graphites can be sealed to well below the specified 10^{-8} cm^2/sec of helium permeability in from 2 to 50 hr, with the longer times being employed for maximum penetration.

We have irradiated gas-impregnated Poco AXF specimens to a fast neutron fluence of about 1 × 10^{22} neutrons/cm^2 (>50 kev), and initial results were encouraging. Despite experimental uncertainties that make conclusions difficult, one specimen retained a near-surface permeability well within the present specification. The neutron fluence received by the impregnated graphite in this first test was about one third of the design fluence for an MSBE. Further irradiation tests are in progress.

The gas pulse impregnation process as currently employed should be suitable for scale-up, and work in this direction will follow.

Graphite-to-Hastelloy N Transition Joints

J. P. Hammond

Graphite and Hastelloy N have widely differing coefficients of thermal expansion; that is, 4 to 5 and 12.3 × 10^{-6}/°C respectively. To eliminate damaging thermal strain in joints between these materials for applications in the Molten-Salt Breeder Reactor, we developed a graded transition joint.[29] The joint consists of a series of tungsten-rich, nickel-matrix dispersions fabricated individually by liquid-phase sintering; these are brazed together with copper to form an insert spanning the large gap in expansion coefficient between nuclear graphite and Hastelloy N. Premium grades of graphite are also introduced adjacent to the nuclear graphite to reduce the dimensional instability associated with irradiation of graphite.

Using processes and materials previously developed,[30,31] transition joints of several designs were fabricated. One joint, designed to eliminate plastic deformation during thermal cycling, contained seven intervening heavy-metal alloy segments. However, the most economical joint contained only three segments, and this is shown in Fig. 32.13.

The coefficients of thermal expansion of the segments of this joint in relation to those for the materials being joined are shown in Fig. 32.14. Observe that the Poco graphite segment, inserted to impart irradiation stability to the joint, has an expansion coefficient about midway between those of nuclear graphite and Hastelloy N. This large change in coefficient between the two graphite members is accommodated by the very low modulus of elasticity of graphite. The remaining gap in coefficient is bridged with two heavy-metal segments, one containing 80% W (matching the Poco graphite) and the other containing 60% W (intermediate between the 80% W

[29] J. P. Hammond, *Metals and Ceramics Div. Ann. Progr. Rept. June 30, 1968,* ORNL-4370, pp. 208–9.

[30] J. P. Hammond, *MSR Program Semiann. Progr. Rept. Feb. 29, 1968,* ORNL-4254, pp. 235–38.

[31] J. P. Hammond, *MSR Program Semiann. Progr. Rept. Aug. 31, 1968,* ORNL-4344, pp. 272–76.

segment and the Hastelloy N terminal piece). We decided to match the expansion coefficients of Poco graphite and the heavy metal adjoining it because failures have usually occurred at this interface.

Calculations indicate that, as a result of the very low elastic modulus of graphites (approximately two orders below that of heavy-metal alloys), joints between nuclear graphite and Poco graphite could be cycled between 700°C and room temperature without straining beyond their elastic ranges. Couplings between the metallic components of this joint, on the other hand, should undergo moderate plastic strain with such cycling; however, we anticipate that they might sustain it without failure because of the good ductility of these materials.

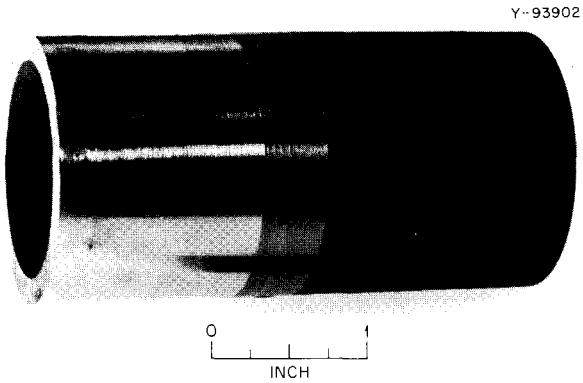

Fig. 32.13. The Compositions of the Three Segments Introduced Between the Hastelloy N and Nuclear Graphite Are (Left to Right) W–28% Ni–12% Fe, W–14% Ni–6% Fe, and Poco Graphite. The two tungsten alloys are not distinguishable in the photograph.

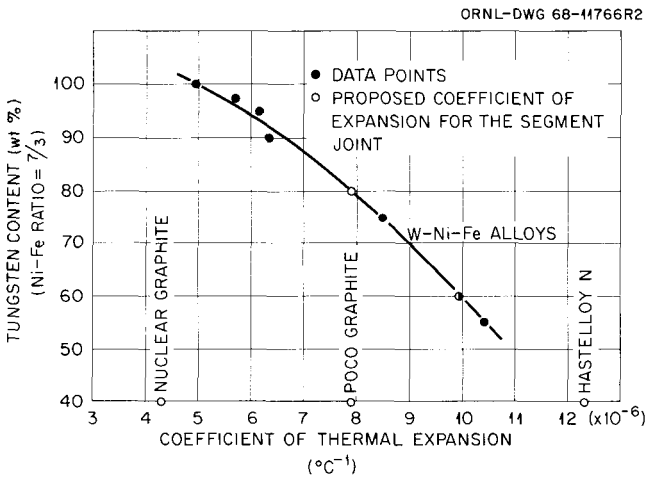

Fig. 32.14. Expansion Coefficients of Three-Segment Joint Materials as a Function of Composition. Coefficients are mean values between room temperature and 600°C and were determined on an optical interferometer.

Two three-segment joints of this design were subjected to twenty-four 20-min cycles of heating and cooling between 750°C and room temperature without suffering any detectable cracks. Also, metallurgical compatibility between the materials composing the joint was demonstrated by a stabilizing heat treatment of eight weeks at 750°C. Tests of compatibility of this joint with the molten salt fuel are under way, although earlier tests on the basic materials composing the joint indicated good compatibility. These results are encouraging and indicate that joints of this general design should show excellent behavior under service conditions.

Physical Properties of Graphites

R. S. Graves J. P. Moore D. L. McElroy

We are concerned with the influence of temperature, anisotropy, and irradiation on the thermal conductivity of several potential MSBR graphites. Within the range 300 to 475°K the thermal conductivity of unirradiated ATJ-S, ATJ-SG, and H337 graphites in the parallel and perpendicular directions decreased and constant anisotropy ratios of 1.3, 1.1, and 1.05, respectively, were noted. Similar ratios exist for electrical conductivity.

ATJ-SG graphite was irradiated at 1000°K to 4.8 X 10^{19} neutrons/cm^2, and the thermal conductivity at 300°K decreased from 1.21 to 0.62 w cm^{-1} °K^{-1}. An extrapolation parallel to previous graphite data projects this 50% reduction at 300°K into a 25% reduction at 1000°K. Comparative heat flow measurements below 400°K are planned for other irradiated graphites. A linear heat flow apparatus for thermal conductivity measurements to 1000°K is being constructed to measure the effects of irradiation on this very important property.

33. Reactor Evaluation

A. L. Lotts

A number of components such as reactor capital costs, reactor operating costs, and fuel cycle costs make up the total cost for producing heat or power by nuclear energy. For several years ORNL has been evaluating various new reactor concepts, pointing out which reactor concepts are most economical and indicating areas of technology in which research and development might be profitable. Such evaluations require a number of interacting variables to be evaluated. Our role in this effort has been to evaluate fuel cycle costs and, more particularly, the effect of fuel performance and fuel fabrication costs on the fuel cycle. Thus the work is done in cooperation with chemical engineers of the Chemical Technology Division on the fuel cycle studies and with the physicists and reactor design engineers in the Reactor Division on both fuel fabrication cost studies and fuel performance evaluation.

The primary effort this year has been the development of a computer code for analysis of fuel performance and the continued development of codes for economic analyses involved in fuel cycle cost determination. The development of a fuel performance model and computer code for pin-type fuel elements is being done to more effectively coordinate our present performance evaluations with irradiation experiments being conducted at ORNL and elsewhere. Also the model will assist in determining which areas of fuel development might be fruitful for research. The computer code development for economic analyses is an attempt to incorporate more detailed analysis of the individual steps involved in fuel element fabrication and to model the management decisions required in a growing nuclear economy. In particular we are interested in scheduling expansion of fuel fabrication plants. In addition to these efforts applied to the development of tools for analysis, we have assisted in the evaluation of several reactor concepts during the year.

COMPUTER PROGRAM DEVELOPMENT FOR COST ANALYSIS

A. L. Lotts

For several years we have had in operation a number of computer codes for estimating fuel element fabrication costs for a variety of fuel element concepts. We have continued to update and improve these as required. However, the basic methods and structure of the codes have not changed during the past year. Primarily we have continued the development of new models and codes required for the determination of (1) the economically optimum schedule for building fuel fabrication plants in a growing nuclear economy and (2) to determine the optimum time to start recycle of ^{233}U in a high-temperature gas-cooled reactor economy.

Fuel Fabrication Costs

R. B. Pratt

During the year we started the development of a computer-based HTGR fuel fabrication model (FABCØST 11). Its purpose is to simulate the process and to calculate capital, operating, and hardware costs for a variety of HTGR elements fueled with stick-bonded coated particles. The program is divided into three major subtasks: (1) particle preparation and coating, (2) fuel stick fabrication, and (3) element loading and assembly. Provision was made for preprogrammed selections of manual or automatic process equipment. Selection is based on the type of equipment employed, the processing rate, and type of fabrication plant used for the calculation.

In developing this code, we tried to provide for observing the effect of criticality on the process. Equipment capacities were limited by criticality considerations of geometry, type, form, and enrichment of

fissile material. Future additions to the program will consider equipment layout, interactions, and the use of nuclear poisons.

A by-product of criticality considerations is information suitable for in-process nuclear material accountability. Output will show the amount of fissile metal, heavy metal, and total compound for each process step per batch and per unit time.

The subroutines concerned with particle coating will provide process information in addition to economic and accountability information. Input of data concerning the number, type, and physical properties of the desired coatings will determine operating parameter values, such as coating time, gas flow rates, and temperature requirements for each coating.

To date, the overall plan for the FABCØST 11 program has been developed and subroutines for most equipment items used in the particle preparations and coating subtask have been drafted.

Optimization of Fabrication Capacity Expansion

F. J. Homan

The subject of optimizing nuclear fuel fabrication capacity was first introduced last year.[1] A preliminary report was published,[2] and our method has been developed further to permit study of the various economic parameters involved in fuel fabrication and their influence on fabrication costs and optimum expansion schedules. A flexible computer program (XSTART) is now available to determine actual fabrication costs in a rapidly growing industry, using fixed economic data available through the FABCØST 9 code.[3] XSTART can also select optimum expansion schedules by minimizing the levelized unit cost of fabricated fuel over the period of study. The code user can input his own economic assumptions, such as rate of return on investment, underproduction penalty, use of overtime, and demand curve. This work is now nearing completion and was recently presented.[4]

[1] A. L. Lotts, *Metals and Ceramics Div. Ann. Progr. Rept. June 30, 1968,* ORNL-4370, p. 213.

[2] F. J. Homan, *Plant Size Optimization in a Growing Nuclear Fuel Fabrication Industry,* ORNL-TM-2346 (December 1968).

[3] A. L. Lotts, T. N. Washburn, and F. J. Homan, *FABCØST 9, A Computer Code for Estimating Fabrication Costs for Rod-Bundle Fuel Elements,* ORNL-4287 (August 1968).

[4] F. J. Homan and T. N. Washburn, "Capacity Expansion Optimization in a Growing Nuclear Fuel Fabrication Industry," *Trans. Am. Nucl. Soc.* 12(1), 25 (June 1969).

Recycle DELAY Code

F. J. Furman

Considerable economy, both in cost and preservation of resources, may be achieved by advanced converter and breeder reactors, as compared with present-day reactors, by recycling the converted or bred fuel. However, fuel must be recycled in large, highly automatic reprocessing and refabrication plants to obtain these economies. Thus, when a power reactor system is in the early stages of growth, recycle operation may not be economical.

We calculated the economically optimum time for the start of recycle operations in a high-temperature gas-cooled reactor industry using computer code DELAY. Capital and operating costs as functions of plant size were calculated for facilities to fabricate ^{235}U-Th fuel, to store spent fuel, to reprocess and refabricate ^{233}U-Th, and to store reprocessing waste. The fuel requirements for an HTGR operating both with and without recycle were calculated. Using these results and estimated growth curves for the HTGR industry, the optimum start date for recycle was found to be five to eight years after the initial 1000 Mw (electrical) HTGR is built.[5]

FUEL FABRICATION COST ANALYSIS

As a part of the overall approach to reducing power costs, we evaluate fuel element fabrication costs as they relate to the fuel cycle component of total power costs, using computer codes to perform the many calculations required. Fabrication procedures and flowsheets are selected and analyzed for capital and operating increments at each point in the processes, and the results are stored in the computer program along with estimated hardware costs for a wide range of production rates. The input parameters for the computer code for each concept to be estimated are based upon the specific design, the fabrication process desired, and the financial data and requirements in the ground rules for the particular study.

During the past year we concentrated on the analysis of a metal-fueled PWR and a comparative cost study for

[5] A. L. Lotts and R. G. Wymer, "Economics and Technology of HTGR Fuel Recycle," pp. 789–813 in *Advanced and High-Temperature Gas-Cooled Reactors, Proceedings of a Symposium on Advanced and High-Temperature Gas-Cooled Reactors Held by the International Atomic Energy Agency in Jülich, 21–25 October, 1968,* International Atomic Energy Agency, Vienna, 1969.

Sphere-Pac fuel rods. We also continued to assist the Fuel Recycle Task Force and to assist in the preparation of a guide for economic evaluations of nuclear reactor plant designs.

Fuel Recycle Task Force

A. L. Lotts

We have continued to participate in the AEC Fuel Recycle Task Force (FRTF) activities as a part of their contribution toward updating *Civilian Nuclear Power, A Report to the President – 1962.* Previously we had developed fuel fabrication cost estimates for approximately 40 reactor concepts considered in the FRTF study. These concepts were for a wide range of reactor designs, as reported previously.[6]

The primary effort this year has been to continue to check the calculated results against available data and to revise the manuscript of the FRTF report.[7] A final draft of this report has been transmitted to the AEC and members of the FRTF for review.

Guide for Reactor Evaluation

A. L. Lotts

Technical assistance was provided to the NUS Corporation, which has prepared a guide for economic evaluation of nuclear reactor plant designs.[8] Basically, the NUS report uses ORNL-developed methods for calculation of fabrication costs in cases where specific information from existing or potential suppliers of fuel elements is not available.

Fuel Fabrication Costs for a Conceptual (U,Pu) Metallic-Fueled PWR

R. B. Pratt

Fuel fabrication costs were calculated for a conceptual (U,Pu) metallic fueled PWR using the Diablo Canyon Reactor core as reference.[9,10] These costs were part of an overall physics, thermal-hydraulic, and fuel cycle analysis.[11] The metallic uranium core was considered as a direct replacement for an oxide PWR core. A comparison of a direct replacement metal core with the oxide core has the disadvantage that the core lattice is optimized for oxide fuel, not metal fuel.

Coextrusion of clad uranium metal fuel slugs is a well-developed process. Workers at PNWL have coextruded 6-ft-long hollow-core fuel rods containing adjusted uranium and clad with a zirconium alloy.[12] Fabrication of 12-ft-long rods, as was assumed in the present evaluation, appears to be a reasonable extension of technology.

Our part of this analysis concerned fuel fabrication costs. Advanced converter ground rules were used for this analysis. Costs for the fuel rod designs were evaluated at plant throughputs of 0.5 and 10 metric tons/day heavy metal and combined with other fuel cycle costs. The optimum case was thus evaluated for a near-equilibrium recycle case. As a result, the metal-fueled direct replacement core showed a fuel cycle cost advantage over the oxide system of up to 0.3 mill/kwhr. However this relative advantage could not be determined precisely because of possible inconsistencies in the physics analyses of oxide and metal cores.

Comparative Cost Evaluation for Sphere-Pac Fuel Rods

R. B. Pratt

A comparative cost evaluation for Sphere-Pac fuel rods was begun to determine if cost can be saved by loading coarse microspheres of UO_2 and fine microspheres of $(U,Pu)O_2$ rather than loading both coarse and fine microspheres containing $(U,Pu)O_2$. Reasoning supporting this concept emphasizes that UO_2 fuel can be fabricated in a hooded facility at a lower cost than the $(U,Pu)O_2$, which must be fabricated remotely.

Costs for the coarse and fine microsphere loading steps represented the area of most uncertainty. Consequently, equipment designs for these steps were conceived and nonmachine unit times were derived. It became obvious early in the analysis that the loading time for the fine microspheres could have a large effect on the fuel fabrication costs by determining the number of loading machines and amount of manpower required.

---

[6] A. Goldman, *Metals and Ceramics Div. Ann. Progr. Rept. June 30, 1968,* ORNL-4370, p. 214.

[7] *Reactor Fuel Cycle Costs for Nuclear Power Evaluation,* WASH-1099 (draft, to be published).

[8] *Guide for Economic Evaluation of Nuclear Reactor Plant Designs,* NUS-531 (January 1969).

[9] Pacific Gas and Electric Co., *Nuclear Plant, Diablo Canyon Site. Preliminary Safety Analysis Report, Vol. 1,* DOCKET-50275-2 (Jan. 18, 1967).

[10] Pacific Gas and Electric Co., *Nuclear Plant, Diablo Canyon Site. Preliminary Safety Analysis Report, Vol. 2,* DOCKET-50275-3 (Jan. 18, 1967).

[11] F. G. Welfore and J. E. Jones, *Physics, Thermal-Hydraulic and Fuel Cycle Cost Analyses of a Metallic Uranium Direct Replacement Core for PWR's,* ORNL-TM-2493 (in press).

[12] W. E. Gurwell, private communication to J. E. Jones and G. L. Copeland, October 1968.

To complicate the picture, experience has shown a wide divergence between times observed for loading ThO_2 microspheres under ideal conditions and actual times recorded for loading EBR-II fuel rods with $(U,Pu)O_2$. To resolve conflicting information, we set up an empirical model to relate loading times for various rod diameters, lengths, and particle shapes. Model results for the case of interest gave loading times in the middle of the two extremes. Using this information, costs for loading fine microspheres were calculated.

Costs for the two overall loading schemes were calculated. The scheme using discrete UO_2 coarse particles and $(U,Pu)O_2$ fine particles has a 5% cost advantage. However, the practicality of this scheme is questionable, since there is little or no successful experience in producing $(U,Pu)O_2$ microspheres with a high percentage of plutonium (80%). A possible alternative is to use a three-particle system to obtain the required 82% of theoretical fuel density used in the study. The cost of this scheme would probably more than offset any advantage claimed for the discrete particle system. Additional laboratory studies of conditions that affect microsphere loading times were recommended.

FUEL PERFORMANCE MODEL DEVELOPMENT

F. J. Homan C. M. Cox

Fuel performance modeling work in the form of a computer simulation of a single fuel pin has been in progress at ORNL for about a year. The simulation employs an iterative calculational technique between the thermal characteristics of fuel and cladding and mechanical interactions due to thermal stresses and fission product swelling. The fuel pin is divided into radial increments and axial regions so as to adequately account for changes in environment and properties that occur with changes in axial and radial position. The fuel pin lifetime is subdivided into arbitrary time intervals. Temperature profiles and stress-strain distributions are calculated for each time interval, and fuel and cladding creep calculated from these conditions. Thus, a running account of dimensional changes can be kept over the fuel pin lifetime. Using this simulation we hope to predict the following as functions of axial position and burnup:

1. temperature profiles,
2. fuel-cladding dimension,
3. central void dimension,
4. fission-gas pressure (as a function of burnup only), and
5. stress-strain distribution in cladding and fuel.

The thermal analysis portion of our simulation is based on work by Cox and Homan.[13] Using the PRØFIL code one can calculate the radial temperature distribution across a fuel pellet, knowing the temperature at the outside of the pellet, the pellet dimensions, the pellet density, and the fission rate as a function of radial position. Three thermal conductivity functions are available to code users; they are described in detail.[13] Fuel restructuring is considered in the code and is based on postirradiation observations of fuel densities.

The mechanical interaction analysis we use for our computer simulation is modeled after the method developed by Puthoff.[14] The stress-strain distribution at zero burnup is determined for fuel and cladding. This provides a starting point for later creep calculations. If there is an initial fuel-cladding gap the fuel and cladding are considered as separate cylinders. Boundary conditions are the pressures existing in the central void, in the fuel-cladding gap, and on the outside of the cladding. As burnup proceeds additional stress will develop within the fuel lattice (in addition to the thermal stresses already present) due to the introduction of fission products. Release of fission product gases with increasing burnup will increase the internal gas pressure, increasing cladding stresses. Eventually the fuel-cladding gap (if any) will close and fuel swelling stresses will be transmitted directly to the cladding.

---

[13] C. M. Cox and F. J. Homan, *PRØFIL, A One-Dimensional FØRTRAN IV Program for Computing Steady-State Temperature Distributions in Cylindrical Ceramic Fuels,* ORNL-TM-2443 (March 1969); and Addendum (in press).

[14] R. L. Puthoff, *A Digital Computer Program for Determining the Elastic-Plastic Deformation and Creep Strains in Cylindrical Rods, Tubes and Vessels,* NASA-TM X-1723 (January 1969).

FISSION-GAS RELEASE FROM $(U,Pu)O_2$ FUEL DURING FAST FLUX IRRADIATION

C. M. Cox F. J. Homan

We have begun a correlation of fission-gas release from $(U,Pu)O_2$ as a function of temperature and burnup in fast flux irradiation experiments. Data were taken from a review by Cox,[15] and the FMØDEL code was used to calculate the volume-average temperature listed for the fuel in all cases where enough information was available. The temperature dependence of fission-gas release in the burnup range of 5 to 6% FIMA was examined. Data from many more pins must be examined to establish a meaningful correlation; however, the data analyzed thus far suggest that Vi-Pac fuels have higher gas release than pellets and that fission-gas release data can be consistently estimated from fuel average temperature, burnup, and fabrication form.[16]

---

[15] C. M. Cox, "The Irradiation Performance of Uranium-Plutonium Mixed Oxide Fuel Pins," to be published in *Nuclear Safety*.

[16] C. M. Cox, R. B. Fitts, and F. J. Homan, *Fuels and Materials Development Program Quart. Progr. Rept. March 31, 1969*, ORNL-4420, pp. 33–39.

34. Thorium Utilization

A. L. Lotts

The objective of the Th-^{233}U fuel cycle development, currently in progress in the Chemical Technology and Metals and Ceramics Divisions, is the demonstration of economic fuel recycle for high-temperature gas-cooled reactors in a pilot facility. The pilot facility will be the recently completed Thorium Uranium Recycle Facility, which has already been used for the production of the ^{233}U-containing salt that was used to refuel the Molten Salt Reactor Experiment. The refabrication development is concentrated on a fuel design similar to that being employedby Gulf General Atomic, Inc. on the Ft. St. Vrain power reactor. Equipment and processes are being developed to enable us to fabricate 10 kg/day of oxide fuel into prismatic graphite fuel blocks used in this reactor type. During the past year we concentrated on handling the particulate fuel used in this reactor type, coating of the fuel particles, and bonding these particles into fuel sticks. As a demonstration of the processes developed for particle handling and coating, we fabricated 32 kg of oxide fuel for use in High-Temperature Lattice Test Reactor experiments. Also a limited number of irradiation tests on thorium fuels have been performed and are currently being examined.

THORIUM-URANIUM RECYCLE FACILITY

J. M. Chandler[1]

The Thorium-Uranium Recycle Facility was constructed to enable processing of thorium fuels containing, as an impurity, high quantities of ^{232}U, a material necessitating heavy shielding. The facility is of sufficient size that a number of processes can be developed and evaluated at pilot-scale level. During the past year the ^{233}U-bearing salt for refueling the Molten Salt Reactor Experiment was prepared in this facility.

Status of TURF

The safety analysis was published.[2] It describes the plant and was written and submitted to the AEC-ORO preoperational review committee for use in their consideration of acceptance of the TURF for use in performing a broad spectrum of research activities. Acceptance by the AEC was received in January 1969.

The facility maintenance manual was completed. It gives procedures for conducting the preventive maintenance program, maintaining process equipment, and testing safety equipment such as hoists, slings, air filters, and radiation monitoring and alarm equipment. This is probably the most complete up-to-date manual of its kind and exemplifies laboratory practice of quality assurance standards.

Cell G was cleaned and decontaminated after use for the $^{233}UF_4-^{7}LiF$ (MSRE) fuel preparation and removal of the ^{233}U product. The cell is being cleaned preparatory to installation of equipment for isolating isotopically pure ^{248}Cm after separation from the ^{252}Cf precursor. The cell was cleaned out in three phases according to detailed written procedures. Successful completion without spread of contamination outside the highly contaminated cell is an example of the effectiveness of written operational procedures for such work.

We continued the efforts to place the in-cell CO_2 fire protection system in condition for acceptance test by the Factory Mutual Company. This is a rather extensive job, requiring modification of the CO_2 piping and to some structural parts in Cell A and the ventilation control system of Cells A and E. The fire protection system is unique in that gaseous rather than liquid CO_2 is supplied to the cell on fire. This type system places added burden on the cell ventilation flow and pressure control equipment.

---

[1] On loan from the Chemical Technology Division.

[2] J. W. Anderson, S. E. Bolt, and J. M. Chandler, *Safety Analysis for The Thorium-Uranium Recycle Facility (TURF)*, ORNL-4278 (May 1969).

Work was conducted to get the TURF equipment ready in support of a heavily shielded cell bank designed for the remote maintenance and operation of the in-cell process equipment. To do this we altered or replaced some faulty electrical motors, revised some ventilation control instrumentation, and added some equipment to better fit the expected needs. All changes were based on the results of tests on the existing equipment piece or a functional group of equipment pieces. For example, the diesel-electric emergency power generator fuel system was replaced.

One area of the TURF, the Cell G pump room, has been altered to provide work space and off-gas and waste handling equipment for a glove box installation there.

Preparation of ^{233}U Fuel for the MSRE

We prepared 63 kg of ^{7}LiF–27 mole % $^{233}UF_4$ salt containing 39 kg of uranium (91.4% ^{233}U, 222 ppm ^{232}U) to refuel the Molten Salt Reactor Experiment. The uranium oxide was converted to $LiF\text{-}UF_4$ in nickel-lined equipment in Cell G. The product salt was packaged in containers of varied capacity and shipped in shielded casks to the MSRE site. Details are in the project report.[3] Four product cans containing 1.7 kg U were not required by the MSRE and were packaged and shipped to the Building 3019 long-term storage facility. Fifteen enrichment capsules containing 1.6 kg ^{233}U as the UF_4-LiF eutectic salt are stored in Cell B of TURF.

FUELED-GRAPHITE DEVELOPMENT

F. J. Furman J. D. Sease

Our objective is to provide economical processes for remote refabrication of Th-^{233}U-bearing HTGR fuels. Presently, our main concern is with processes dealing with the fuel particles. This work is divided into four parts: particle handling, particle coating, particle inspection, and bonding of fuel particles.

Particle Handling

In TURF, over 10 kg/day of particles will have to be remotely sized, shape separated, sampled, and transferred. Recently, we have concentrated on developing the sizing and shape separation steps, since these operations must be routinely used in our other programs.

For sizing, we are currently modifying commercial gyratory, self-cleaning screens[4] for remote use. The modifications will allow modular assembly with manipulators.

Shape separation and the removal of nonspherical microspheres by a combination of vibration and gravity requires a microsphere feed of 200 to 500 g/hr. To achieve these feed rates, we developed a small adjustable-orifice feeder, which has only one movable part to minimize maintenance and fabrication problems.

Particle Coating

Deposition of pyrolytic carbon and silicon carbide coatings on nuclear fuels is a key operation in fabrication of HTGR fuel elements. Thus, we have directed condiderable effort to development of pilot-scale equipment[5] to coat sol-gel microspheres in quantities of 10 kg/day. The design of the currently used 5-in.-diam cone furnace was modified to permit remote operation and maintenance. The construction of this modified furnace, shown in Fig. 34.1, is now complete. Incorporated in the design of this furnace is the capability of coating with pyrolytic carbon at high and low temperatures and with silicon carbide. The off-gas system consists of a bag filter for soot formed during pyrolytic carbon coating and a scrubbing system for acidic gas formed during silicon carbide coating, in addition to roughing and absolute filters. The off-gas flow is assisted by a water-sealed vane pump. All controls for the equipment are located on a panel board remote from the furnace, as will be done in the TURF.

Particle Inspection

A large facility producing HTGR fuels must have rapid inspection of coated and uncoated particle size to control the coating process and assure quality. We made a light blockage particle-size analyzer, capable of giving these results and calibrated it to measure particles between 150 and 850 μ in diameter. To calibrate it we developed a device to continuously cycle a single particle through the measuring cell. With this device, we used a carefully sized particle to set the thresholds of

[3] John M. Chandler and S. E. Bolt, *Preparation of Enriching Salt ^{7}LiF–$^{233}UF_4$ for Refueling the Molten Salt Reactor*, ORNL-4371 (March 1969).

[4] SWECO, Inc., 6111 East Bandine Blvd., Los Angeles, Calif. 90054.

[5] R. B. Pratt, J. D. Sease, W. H. Pechin, and A. L. Lotts, "Pyrolytic Carbon Coating in an Engineering-Scale System," *Nucl. Appl.* 6, 241–55 (March 1969).

the analyzer. Besides giving a mean size for a batch of particles, the instrument gives a size distribution and counts the particles, so a density can be calculated when the weight of the counted batch is known.

Bonding of Fuel Particles

The reference HTGR design has the coated fuel particles bonded into fuel sticks to allow inspection of the mixed fuel before insertion into the graphite blocks and to prevent spilling of the particles if the block breaks. The particles are currently bonded with a mixture of phenolic resin, maleic anhydride accelerator, and carbon flour filler.

Over 500 fuel sticks, 13 in. long and approximately 0.5 in. in diameter were produced for scoping studies in head-end reprocessing development. These fuel sticks were produced in swaged stainless steel molds which were filled with two types of particles blended by simultaneous pouring directly into the molds. After the molds were filled with particles, the bonding mixture was injected into the molds and thermally polymerized. After cooling, the fuel sticks were ejected by hydraulic pressure, inspected, and inserted into graphite blocks.

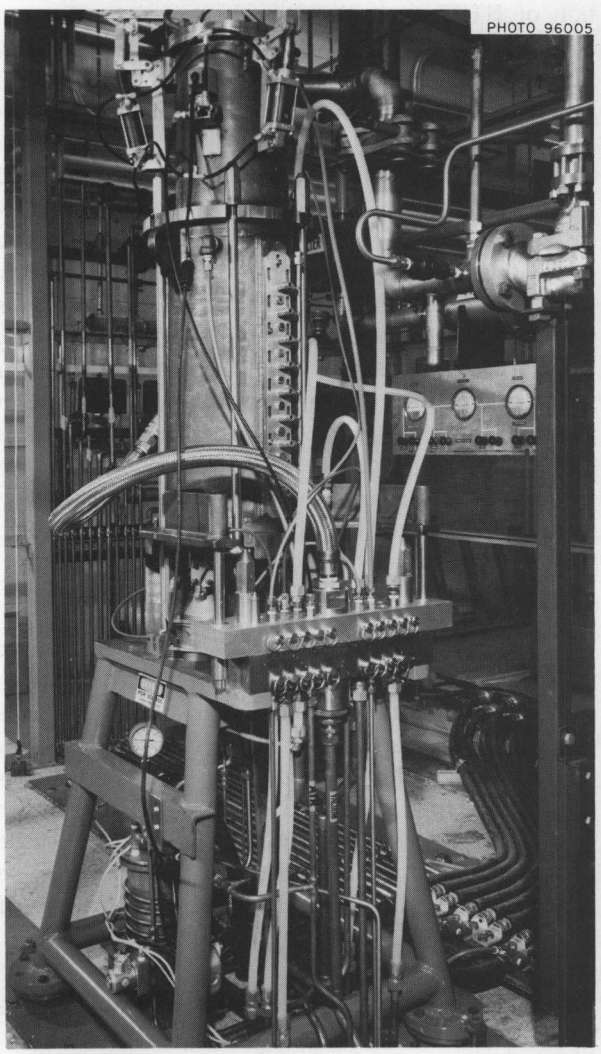

Fig. 34.1. Coating Furnace for Remote Operation and Maintenance.

COATING OF (^{233}U-Th)O_2 FUEL

F. J. Furman

The High-Temperature Gas-Cooled Reactor being developed by Gulf General Atomics operates with the Th-^{233}U cycle at 1200°C and higher. Operation at high temperature will affect the reactor reactivity by Doppler broadening of the neutron spectrum. Battelle Memorial Institute, Pacific Northwest Laboratory, Richland, Washington, will perform Doppler broadening studies in the High-Temperature Lattice Test Reactor using simulated HTGR fuel. This fuel consists of 32 kg of approximately 300-μ-diam (^{233}U,Th)O_2 microspheres prepared by the Chemical Technology Division and coated by us with approximately 100 μ of pyrolytic carbon in the 5-in.-diam cone furnace in the Coated Particle Development Laboratory.

The material was prepared for coating by eliminating over- and undersized and nonspherical microspheres and batching in 1000-g lots, which is all done in glove box facilities. The coating furnace was modified to contain all potential radioactive contamination. Coating was done by decomposing propylene at 1250°C. Following the coating, the material was screened to remove carbon chunks or undersized material, sampled for tests, and packaged for shipment. The coated material was analyzed for chemical composition, size, density, and thermal stability.

IRRADIATION OF THORIA-BASE OXIDE FUELS

A. R. Olsen

The limited funding and concentration on coated particle fuels has forced the suspension of all tests of metal-clad thoria-base bulk oxide fuels. The detailed status of the various tests in progress at the time of this suspension has been reported elsewhere.[6] The status of the various tests is summarized in Table 34.1.

[6] A. R. Olsen, "Irradiation of Bulk Oxide Fuels," *Status and Progress Report for Thorium Fuel Cycle Development 1967–1968,* ORNL-4429, pp. 137–51.

Table 34.1. Thorium Fuel Cycle Program Powder-Packed Rods Current Status[a]

Designation	Number of Rods	Type of Oxide	Density (% of Theoretical)	Fuel Rod Dimensions (cm)			Linear Heat Rating (w/cm)	Peak Burnup (Mwd/MT metal)	Objective	Status
				Length	OD	Wall				
MTR-II	2	Sol-Gel S ThO_2–4.5% UO_2 Vi-Pac	88 to 89	57	0.8	0.06	600	100,000	Obtain higher heat rating by increasing enrichment	Being examined
MTR-III	6	Sol-Gel 35 ThO_2–4.5% UO_2 Vi-Pac	86 to 89	30	1.1	0.06	820	100,000	Compare oxide calcining atmospheres and higher heat ratings obtained by increasing diameter	Being examined
ETR-II	6	BNL Sol-Gel ThO_2–4% $^{233}UO_2$ Vi-Pac	90	48	1.3	0.09	630	30,000 to 100,000	Study effects of remote fabrication and oxide recalcining	2 being examined. 4 stored in ETR canal since June 20, 1968
ETR-III	7	Sol-Gel ThO_2 Vi-Pac	88	48	1.3	0.09	770	10,000 to 70,000	Study ThO_2 blanket material with gradually increasing heat rating and provide high-protactinium low-fission-product material for chemical processing	3 rods processed 2 rods being examined 2 rods stored at ORNL
ETR-IV	6	Sol-Gel ThO_2–5% PuO_2 Sphere-Pac	84	24	1.3	0.09	650 to 1000	20,000 to 100,000	Study sol-gel ThO_2-PuO_2 microsphere performance as vibratorily compacted beds at various heat ratings and burnup levels	1 rod being examined 5 rods stored in ETR canal since June 20, 1968
Sphere-Pac	4	Sol-Gel ThO_2–5% PuO_2 Sphere-Pac	84	19	0.64	0.025	650 to 1000	10,000	Test sol-gel ThO_2-PuO_2 microspheres with high cladding temperatures	Being examined
Pellet Rods	3	ThO_2–4.5% UO_2	91	11.4	0.79	0.06	400	150,000	Investigate swelling and gas release of ThO_2-base fuels at very high burnup	Being examined

[a]ETR-II, ETR-III, and ETR-IV rods are clad with Zircaloy-2; all other fuel rods are clad with type 304 stainless steel.

[b]The linear heat rating listed here is the peak linear heat rating proposed for test operation.

35. Water Reactor Safety

P. L. Rittenhouse

The 100 to 200 tons of Zircaloy-clad UO_2 fuel in a modern 1000-Mw (electric) light-water reactor is contained in about 40,000 rods nominally 12 ft in length × ½ in. in diameter. During the loss-of-coolant accident (LOCA) postulated for reactors of this type, the Zircaloy cladding of the fuel rods is heated very rapidly to temperatures far above its designed operational temperature. At first, from about 700 to 1800°F, the heating is the result of redistribution of the energy stored in the fuel. Continued heating is effected by the decay heat of the fission products and, above 2100°F, by the exothermic reaction between the Zircaloy cladding and steam. This thermal transient, unterminated, would destroy the reactor core, primary vessel, and containment and result in the release of accumulated fission products to the surrounding population. Because of this possibility, emergency core cooling systems (ECCS) are provided in these reactors to remove the stored energy and decay heat of the fuel rods and to terminate the transient before significant metal-water reaction can occur. These systems are designed and sized on the assumption that the accident will not change the geometry of the core. This assumption, however, bears directly on the behavior of the Zircaloy-clad fuel rods. There is concern that the failure of the fuel cladding may result in dimensional changes sufficient to alter the thermal response of the core to the ECCS. The Atomic Energy Commission recognized that a coordinated effort of research and testing was required to solve this potentially important and timely question on fuel rod failure behavior and its effect on the outcome of an LOCA. This recognition led to the undertaking of the coordination of all work in the area of Zircaloy-clad fuel rod failure at the Oak Ridge National Laboratory.

FUEL ROD FAILURE PROGRAM COORDINATION

P. L. Rittenhouse

Coordination of all AEC-sponsored research and testing programs on the behavior and failure of Zircaloy-clad UO_2 fuel rods during an LOCA and of the effect of this behavior on emergency cooling effectiveness is being provided by the Metals and Ceramics Division at the Oak Ridge National Laboratory. In addition, studies of the high-temperature properties of Zircaloy cladding are conducted in the Metals and Ceramics Division. Other AEC-sponsored work on fuel rod failure is being performed at Phillips Petroleum Company (Idaho Falls, Idaho), General Electric–Nuclear Systems Programs (Cincinnati, Ohio), Battelle Memorial Institute (Columbus, Ohio), and in the Reactor and Reactor Chemistry Divisions at the Oak Ridge National Laboratory. Close contact is also maintained with the progress of related programs being carried out by the light-water reactor manufacturers. This latter feature of coordination is essential in ensuring that both the AEC and privately funded testing and research are best directed to obtain intelligent and timely answers to the questions on fuel rod behavior during an LOCA.

In the role of coordinator of fuel rod failure studies, ORNL has prepared two program documents[1,2] to identify the potential problems and to suggest work that must be done to negate or affirm their importance.

[1] P. L. Rittenhouse, *Failure Modes of Zircaloy-Clad Fuel Rods,* ORNL-TM-2347 (September 1968).

[2] P. L. Rittenhouse, *Failure Modes of Zircaloy-Clad Fuel Rods. Part 2: Program Revisions,* ORNL-TM-2548 (May 1969).

Communication and coordination among the sites mentioned above has been effected by scheduled Fuel Rod Failure Program meetings, interchange of progress reports, and extensive correspondence and travel.

HIGH-TEMPERATURE PROPERTIES OF ZIRCALOY CLADDING

R. D. Waddell, Jr.

During the LOCA the Zircaloy cladding of the fuel rods will reach temperatures at which its strength is very low. This low strength, combined with the internal pressure of the fission gases, will result in expansion and then rupture of the cladding. Expansion exceeding 30% will cause contact between adjacent rods and reduce the area of the coolant channel by 60%. If expansion reaches 60%, the entire coolant channel will be blocked. Cladding expansion, then, is certainly a failure mode with which we must be concerned.

Because of this we started a study of the high-temperature properties of Zircaloy cladding. Our primary intent is to determine ductility, strength, and mode of failure over the temperature range associated with an LOCA (600°F and higher). To scope the range of behavior quickly we are concentrating our attention on temperatures between 1100 and 2100°F. The lower temperature is that at which the first of the fuel rods is expected to fail because of internal pressure, and the higher is the upper limit that should be reached before the ECCS reverses the temperature excursion. The property of greatest concern to us is the ductility of the cladding (i.e., how much it will expand before rupture). Many factors may affect this expansion, including the conditions existing during the accident – rate of temperature rise, composition of the surrounding atmosphere, maximum temperature, etc. – and the metallurgical history of the cladding – microstructure, fabrication, and imperfections.

Isothermal and temperature-transient burst tests are being used to obtain the required mechanical property data. The purpose of the isothermal tests is to determine the metallurgical variables that significantly affect high-temperature properties. These variables will be incorporated into the transient tests designed to study the effects of heating rate, internal pressure, and environment. In both types of tests the free volume typical of real fuel rods is simulated by filling the fuel space with ceramic pellets. Also, in the transient tests the plenum volume will be sized so that we can realistically determine the effects of pressure buildup and gas transfer within the fuel rods.

Zircaloy tubing typical of both BWR and PWR cladding has been tested isothermally in the normal (stress relieved) condition at five selected temperatures between 1100 and 2100°F. The expansions measured at fracture in these tests are shown in Fig. 35.1. The smallest range of expansions was observed at 2100°F and the greatest at 1450°F. The lower bound of the range, ~50% expansion, does not vary appreciably with

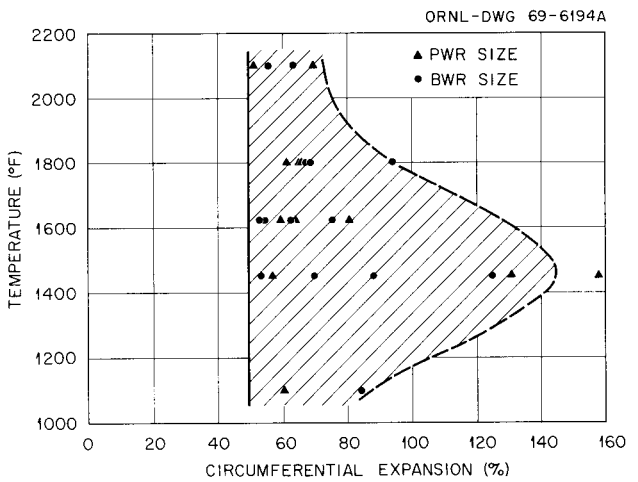

Fig. 35.1. High-Temperature Fracture Expansion for Zircaloy Tubing. Circumferential expansion at fracture is shown as a function of test temperature from 1100 to 2100°F. Minimum expansion observed was about 50% at all temperatures, but note the very wide variation in expansion values at 1450°F.

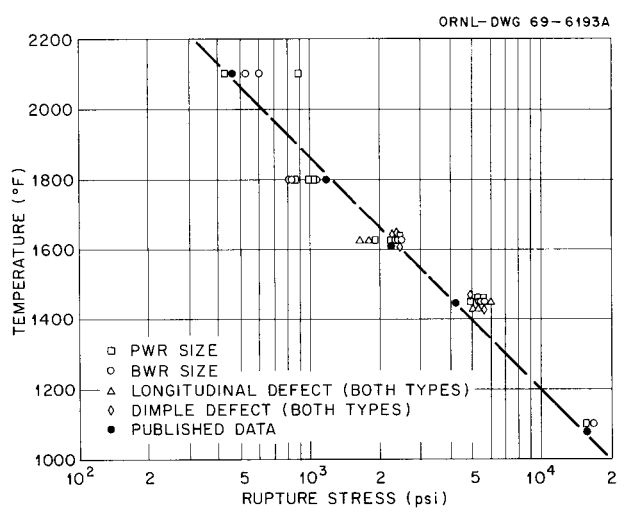

Fig. 35.2. Rupture Stress of Zircaloy Tubing. The rupture stresses of tubing representative of both BWR and PWR fuel cladding are essentially identical and agree with published tensile data. The data on this plot also show that the effect of the defects introduced on rupture stress is minimal in this temperature range.

temperature. Points of local maximum expansion have been seen along the 6-in. flat hot zone in tests of both BWR and PWR cladding. These may be due to nonhomogeneity of the material and/or variations in wall thickness along the tubing.

Samples with carefully introduced and calibrated defects, longitudinal line defects about 0.020-in. wide × 10% of the wall thickness, and dimple defects about 0.030 in. in diameter × 10% of wall thickness, have also been tested. The line defects simulate damage that might occur during handling, loading, and operation of the fuel rods, and the dimple defects simulate corrosion pitting. Five of the six specimens tested with these latter defects did not fail in the defect area, and the single specimen that did failed only after 117% expansion at 1450°F. All six of the specimens had fracture expansions consistent with those of undefected material. Therefore, it seems clear that dimple defects will not limit expansion. However, four of the five specimens tested with longitudinal line defects failed in the defect at expansions from 20 to 38%. This is substantially lower than the ductility of nondefective tubing.

Figure 35.2 shows rupture stress of Zircaloy tubing as a function of temperature for both the defective and nondefective tubing as well as values calculated from published tensile data.[3] It is clear that the defects have had little effect on rupture stress.

Data that we have collected to date show that the expansion of Zircaloy cladding certainly has the potential to seriously interfere with the flow of emergency coolant in an LOCA. However, these experimental data should be considered only as the maximum expansions possible and not necessarily those that will occur during an accident. Many other factors, including heating rate, internal pressure, and environment, must be considered before the extent and degree of expansion and associated flow blockage can be predicted.

---

[3] H. C. Brassfield *et al.*, *Recommended Property and Reaction Kinetics Data for Use in Evaluating a Light-Water-Cooled Reactor Loss-of-Coolant Incident Involving Zircaloy-4- or 304-SS-Clad* UO_2, GEMP-482 (April 1968).

Part V. Other Program Activities

36. Absorber Materials for SO_2 from Flue Gas

W. S. Ernst, Jr.

The National Air Pollution Control Administration of the Department of Health, Education, and Welfare is evaluating processes to remove SO_2 from flue gases. In one process the SO_2 is removed by contact with sodium aluminate particles. When saturated, these particles are regenerated in hydrogen, and H_2S is driven off. The sulfur recovered from the H_2S should more than pay for the cost of operating such a process. However, in pilot plant runs, the attrition losses of the sodium aluminate particles are sufficiently high that this process does not appear to be economical. In addition to the stresses caused by impacting the stack wall, some other fundamental reason, such as the crystallographic incompatibility of Na_2SO_4 and Al_2O_3, may also contribute to the attrition.

We are studying the physical aspects of the reactions that take place when sodium aluminate is sulfatized and desulfatized cyclicly. Our primary objective is to find out if the concomitant changes in crystal structure limit the usefulness of the sodium aluminate particles. In our experiments, sodium aluminate was exposed cyclicly in static beds to pure SO_2 and then to H_2. No degradation of the particles was found. However, metallographic examination of the starting material revealed large internal cracks in a large fraction of the particles. These cracks, which form during manufacturing, probably contribute to the attrition. Further tests showed that the particles are hygroscopic and also absorb CO_2. Exposure to open atmosphere for several days will convert the particles into $Na_2CO_3 \cdot H_2O$ and $Al_2O_3 \cdot 3H_2O$. If these converted particles are exposed suddenly to hot gases (625°F), they blow apart because of the very fast steam generation. Thus the crystallographic changes and their effects seem unimportant relative to the contribution from the internal cracks and hygroscopic nature of the particles.

37. Army Pulsed Radiation Facility Reactor Assistance

A. P. Litman

The Army Pulsed Radiation Facility Reactor (APRFR) is the most recent in the first generation of fast burst reactors that have core and control element components constructed of gamma-stabilized enriched U–10% Mo alloy. The fast burst reactor operates from prompt neutrons and is a laboratory facility that most nearly simulates the radiation environment of an atomic weapon explosion. Its primary usefulness is to study the transient effects of interaction of radiation with matter. These reactors, including the APRFR, have been and will be used in basic studies of the fission process, radiation dosimetry, shielding studies, calibration of radiation alarms for criticality accidents, and radiobiology.

Last year we reported on the fabrication and testing of the APRFR core.[1] We are now coordinating a core-alloy development program to select a better alloy than U–10% Mo for pulse reactor fuel. This work is sponsored by the U.S. Army Ballistic Research Laboratories through interagency agreement with the USAEC.[2]

CORE ALLOY DEVELOPMENT

C. W. Dean[3] A. P. Litman

Service conditions for fast burst reactors demand that the core material withstand unusually high stress levels resulting from rapid thermal expansion and inertia loads. As an example, rapid additions of reactivity above prompt criticality during the APRFR core test program resulted in temperature increases as large as 880°C in a fraction of a millisecond.[4]

Early in the report period we anticipated that uranium-niobium alloys, due to their strength characteristics, might prove of interest for pulse reactor service. Studies at the Y-12 Plant, however, indicated that the niobium-containing alloys did not have sufficient gamma stability. At about the same time a consolidation of considerations indicated that the limit of useful service for APRFR core alloys hinged on their ability to resist propagation of surface fissures resulting from stress-corrosion cracking. Thus, we proceeded on the basis that toughness, rather than strength alone, was a controlling mechanical property.

Based on the above our program was redirected for the near term to comparing toughness properties of some low-dilution, uranium-molybdenum alloys.

ALLOY EVALUATION

C. W. Dean[3] A. P. Litman

Ingots of the selected compositions were vacuum induction melted, cast, vacuum heat treated at 900°C for 16 hr, and water quenched. Examination showed that the ingots were homogeneous and, with the possible exception of the tantalum-containing alloy, single phase. The castings were then machined into standard Charpy V-notch impact specimens and aged at 475°C (estimated maximum embrittlement temperature) for times to 64 hr. All specimens were impact loaded at 200°C in air. At least one alloy showed a clear superiority in notch toughness. A U–10% Mo alloy containing the tantalum addition also appears promising because of its relatively constant toughness after aging 1 hr. This program is continuing.

---

[1] A. P. Litman, *Metals and Ceramics Div. Ann. Progr. Rept. June 30, 1968,* ORNL-4370, pp. 241–42.

[2] M. I. Lundin, Reactor Division, serves as Program Director at ORNL.

[3] Y-12 Metallurgical Development Department.

[4] J. T. Mihalczo, *Static and Dynamic Measurements with the Army Pulse Radiation Facility Reactor,* ORNL-TM-2330 (June 1969).

38. Metallography

R. J. Gray

The Metallography Group continues to provide service to the various programs of the Metals and Ceramics Division and to other divisions of this Laboratory. This service applies to both nonradioactive and radioactive materials. Assistance in the interpretation of microstructures is provided or, if the requester is unfamiliar with metallography, the complete interpretation is provided. Equipment development and the general upgrading of metallographic techniques have continued.

ALPHA METALLOGRAPHY FACILITY

R. J. Gray H. R. Gaddis
B. C. Leslie J. W. Chumley

We have continued to improve the alpha metallography glove box line reported previously.[1] High alpha emitting specimens of plutonium and plutonium compounds have been prepared since August 1968, and the entire facility has been very satisfactory. The glove box line has been equipped for argon atmosphere with a monitoring station to analyze the argon purity in each box. We have been particularly impressed with the performance of our metallograph enclosed in a glove box. The glove box metallograph[2] (Fig. 38.1) which was designed, modified, and installed at ORNL, has functioned extremely well. The optical relays[3] have been flawless. Microscopy and photomicrography of the metallograph with the optical relays is equal in quality to the results from the original equipment. Exposure periods have increased 15 to 20% because of light loss through the optical relays; however, the exposure generally is less than 2 sec with bright field. Microspheres of UO_2-PuO_2 photographed with the alpha metallograph are shown in Fig. 38.2. An additional feature has been the adaptability of a Zeiss 63-mm lens for photomacrography and a substage lamp for photomacrography illumination, shown in Fig. 38.3. The lamp and lens are shown installed on a conventional Bausch & Lomb Research I metallograph. Magnifications vary according to the projection lens as shown in Table 38.1. An example of a photomacrograph with this equipment is shown in Fig. 38.4.

Glove boxes for photomacrography and microhardness testing have been completed and installed. The photomacrography box is equipped with external electronic flash for illuminating the specimen. The satin finish of the internal surface of the stainless steel box serves as an excellent light reflector and diffuser. The microhardness tester is a conventional Service Diamond hardness tester. The microscope is equipped with an optical relay designed and fabricated at ORNL.

ELECTRON MICROPROBE ANALYSIS

H. V. Mateer R. S. Crouse

The electron-beam microprobe analyzer adds a new dimension to analytical metallography by making possible in situ chemical analysis of metallographic speci-

Table 38.1. Magnifications Obtained with Glove Box Metallograph

Projection Lens	Magnification for Various Image Sizes		
	<4 × 5	4 × 5	5 × 7
5X	6–20	21–30	31–50
7.5X	10–17	18–25	26–70
10X	12–21	22–31	32–100

[1] R. J. Gray and B. C. Leslie, *Metals and Ceramics Div. Ann. Progr. Rept. June 30, 1968,* ORNL-4370, pp. 230–31.

[2] R. J. Gray and B. C. Leslie, "A Metallograph for Glove Box Operations," *Proceedings, First Annual Technical Meeting, International Metallographic Society, Inc., November 11, 12 and 13, 1968 – Denver, Colorado,* ed. by K. A. Johnson and J. H. Bender, International Metallographic Society, Inc., Los Alamos, N.M., 1969.

[3] Designed and fabricated by N. E. Wilkins and W. C. Carothers, Plant and Equipment Division, ORNL.

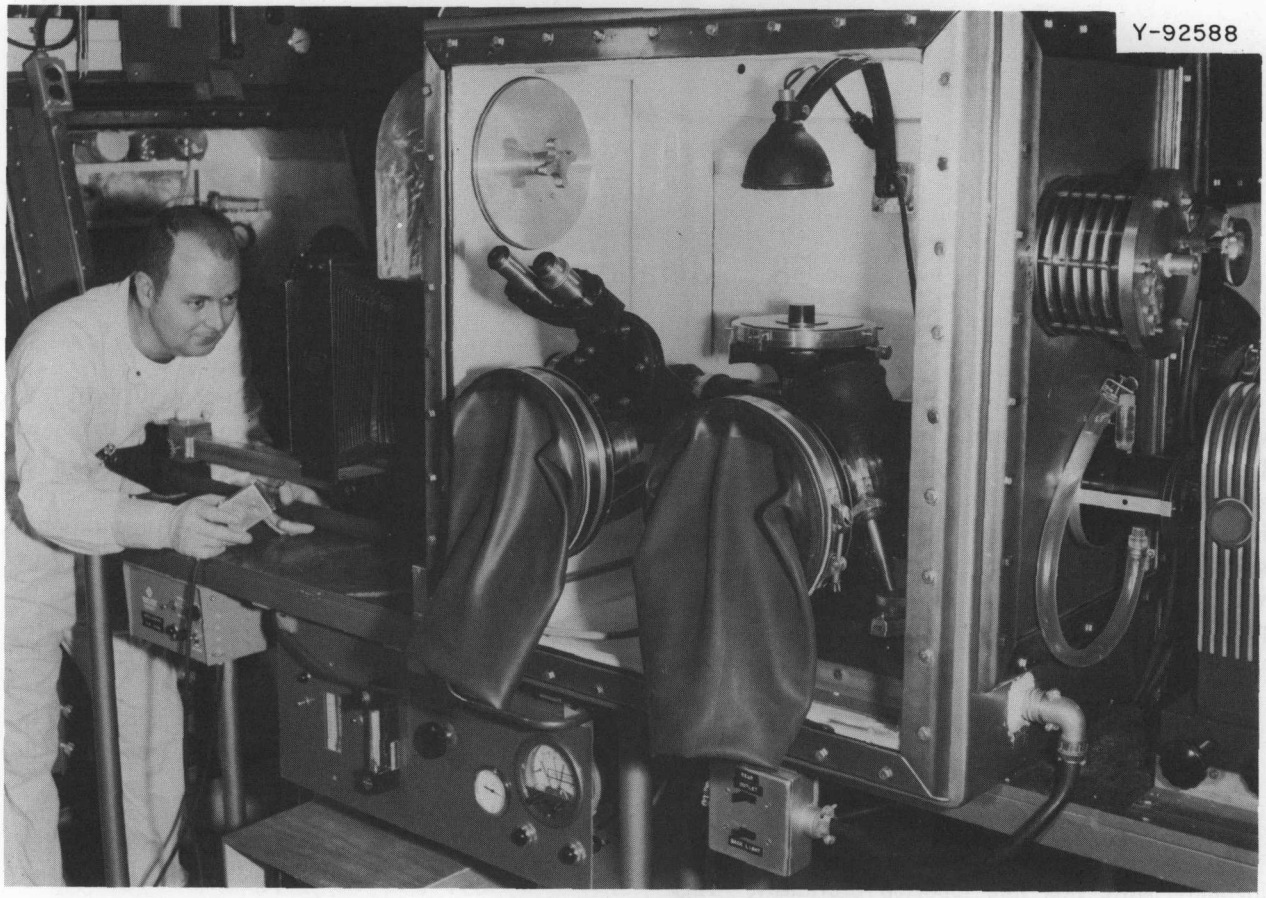

Fig. 38.1. Glove Box Metallograph.

mens. A variety of problems came under the scrutiny of the microprobe in the past year.

Two samples of heat treated Hastelloy N, one containing 0.5 wt % Si nominally and one with no silicon, were examined metallographically; and the silicon-bearing alloy was found to have a finely dispersed precipitate. Microprobe examination confirmed that the precipitate was rich in silicon by showing the matrix to have only 0.05 wt % Si and the precipitate to contain over 2.1 wt %.

In the loop testing program of the Molten Salt Reactor Project, a plug was found in a Hastelloy N loop. The plug contained metal crystals that were identified by the microprobe as almost pure nickel. None of the other possible metallic elements of the system were found.

In many stainless steel and nickel-base alloys a massive yellow angular phase is often found. This phase has long been accepted as a titanium nitride. It has also been noted that in some alloy systems aluminum can be substituted for titanium. The question was raised concerning type 406 stainless steel, which contains an appreciable amount of aluminum, whether the observed yellow phases were nitrides of titanium or aluminum. The microprobe examination revealed a total absence of aluminum in the nitride, so aluminum does not substitute for titanium in these nitrides.

The microprobe was used to assist in the study of swelling in UAl_3-Al fuel core material. The addition of some elements, such as Si, Ge, and Zr, inhibits the swelling, while others such as tin have no effect. Samples in which the UAl_3 had been doped with each of these four elements and heated to 600°C were examined, and cathode ray tube displays pinpointing the elements were made. We found that UAl_4 has a very low solubility for tin and seems to reject it to the surrounding UAl_3 as transformation occurs.

An instrument modification was completed that transformed the Materials Analysis Company model 400 to the model 400S, which is the latest model

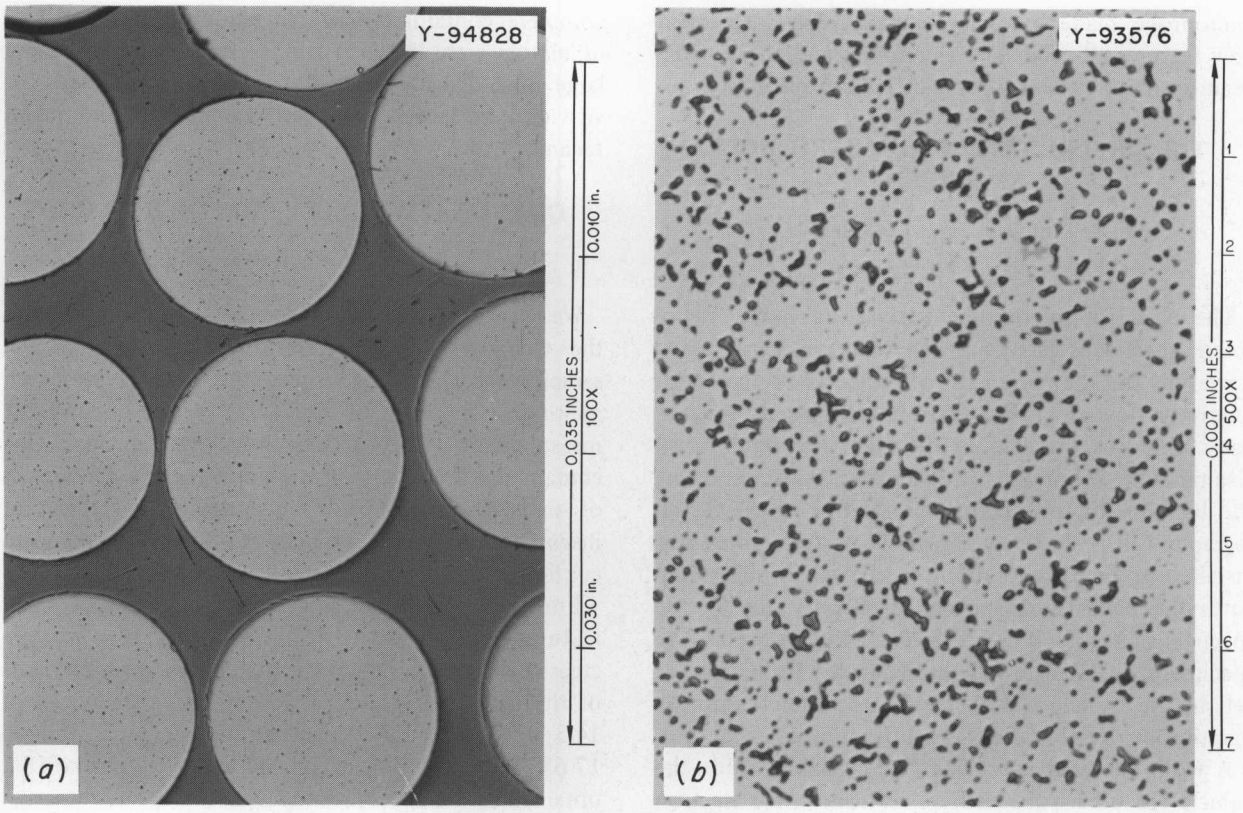

Fig. 38.2. Microspheres of UO_2-PuO_2. (*a*) Median plane view. (*b*) Microstructure.

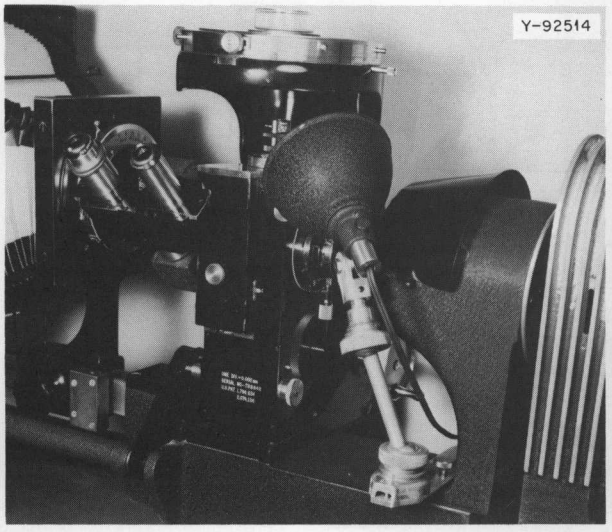

Fig. 38.3. Substage Lamp and Zeiss 63-mm Lens for Photomacrography.

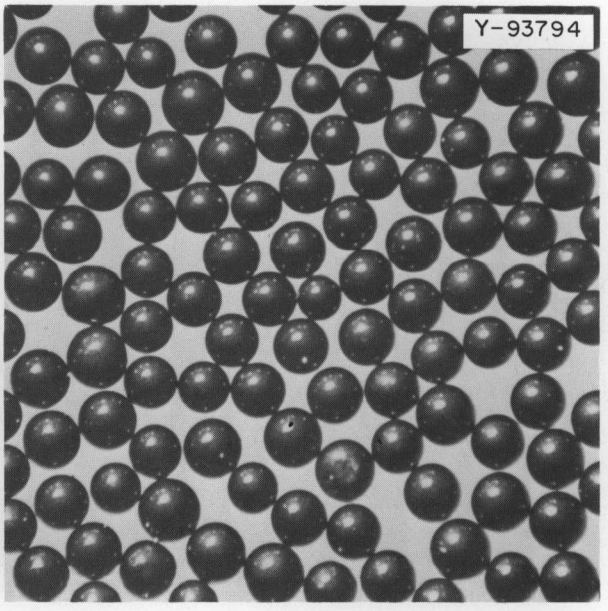

Fig. 38.4. Microspheres of UO_2-PuO_2. 17X.

microprobe made by that company. The instrument now features all solid-state electronics and an electron-beam scanning system capable of 1000-A resolution.

THE SHIELDED ELECTRON MICROPROBE ANALYZER

E. L. Long, Jr. J. L. Miller, Jr.
R. J. Gray

The need for microprobe analyses of highly radioactive specimens has been apparent for many years; however, the development of equipment has been relatively slow. A model 450 Materials Analysis Company unit was installed in the High Radiation Level Examination Laboratory. A schematic drawing showing the location of the microprobe relative to the metallography cell is shown in Fig. 38.5. A steel cubicle was installed juxtaposed to the hot cell wall, which eliminates the need for a shielded carrier to transfer the specimens from a hot cell to a shielded microprobe. The specimens are transferred mechanically from the hot cell to the cubicle and then from the cubicle into the microprobe or a shielded x-ray diffraction unit.

A work space of over 18 ft^2 is available within the cubicle for other jobs such as replication for electron microscopy and autoradiography. The cubicle provides biological shielding by 8 in. of steel or equivalent and complete containment of radioactivity. Model 7 manipulators were installed for specimen handling, and a large high-density glass door was incorporated for viewing and access for decontamination and maintenance.

QUANTITATIVE TELEVISION MICROSCOPY

T. M. Kegley, Jr.

We compared area fraction measurements, made with the Quantimet Image Analyzing Computer, on the samples in which the detected features represented approximately 20% of the area. We contrasted the measurement of test charts shown in Fig. 38.6. One contained a single large feature and the other hundreds of small features. We also investigated the effect of magnification on the area analysis of a bakelite compact containing nickel particles.

For a sample containing a large number of small features, the apparent fraction of the total area increased with magnification. For example, measurements of the chart in Fig. 38.6 indicated area percentages of 14.3, 18.0, and 18.7 at magnifications of 4.2, 8.5, and 17.6X, respectively, as compared with the value of 18.6 obtained by a manual lineal analysis.

A proper setting of the threshold control, which controls the threshold of detection relative to the

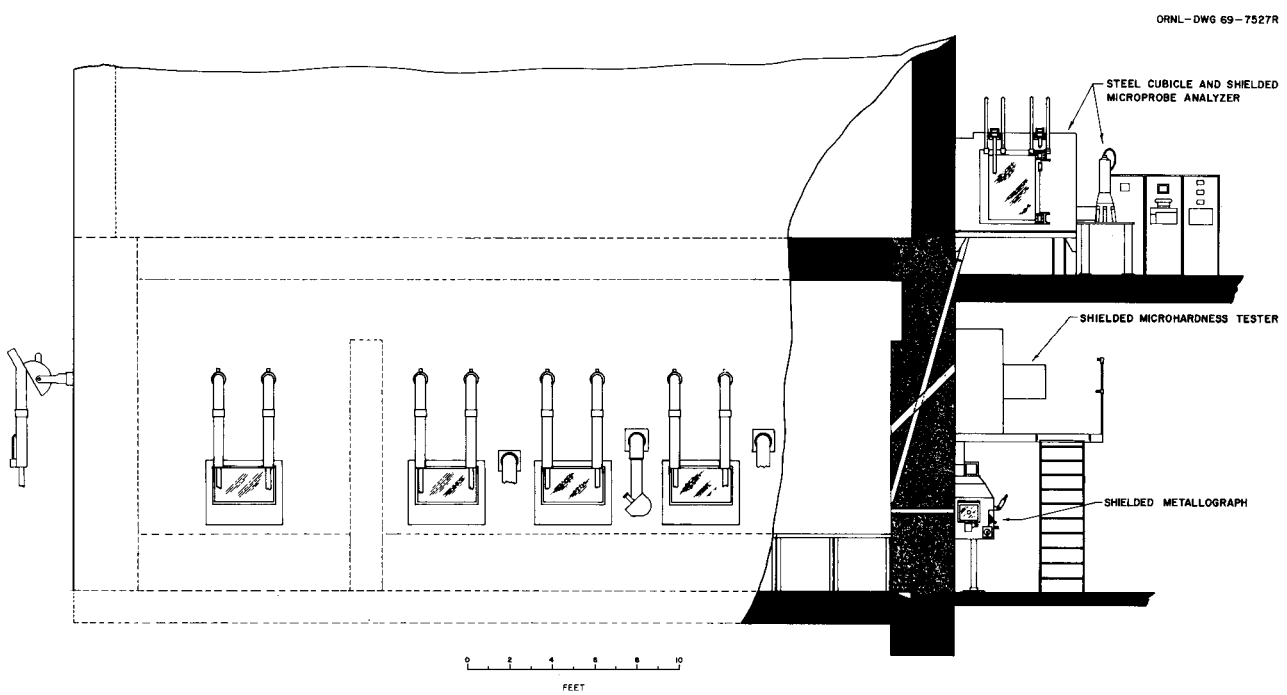

Fig. 38.5. Metallography Cell and Related Equipment in the High Radiation Level Examination Laboratory.

ORNL-DWG 69-9031

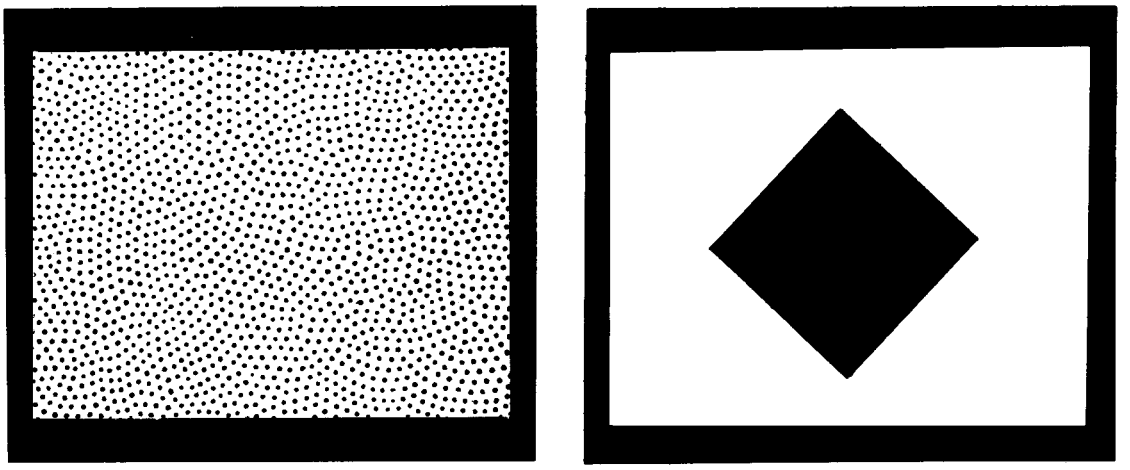

Fig. 38.6. Area Charts Employed in Quantimet Area Measurements Using the Epidiascope Attachment. (*a*) Dot feature, which analyzes 18.6 by lineal analysis. (*b*) Diamond feature chart, which analyzes 19.9 by area analysis.

optical intensity of the detected feature, was much more critical for the detection of samples containing many small features than for samples containing a single feature, as may be seen from Fig. 38.7, which compares threshold area curves for the dot and diamond features of Fig. 38.6. A different threshold was needed for each magnification.

We concluded that accurate Quantimet measurement of samples containing many small features requires (1) sufficient magnification, (2) a proper setting of the visual threshold, and (3) analysis of a sufficient number of fields to obtain an acceptable standard error.

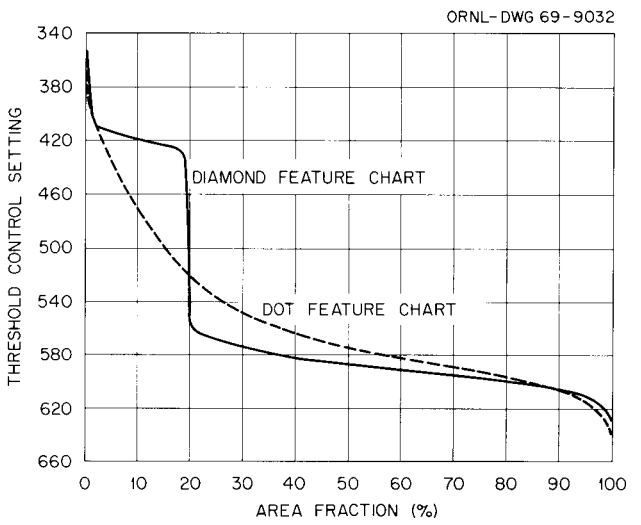

Fig. 38.7. Threshold-Area Curves Obtained from Quantimet for Dot and Diamond Features.

HEATING STAGE MICROSCOPY

R. S. Crouse G. Hadder[4]

Techniques for the use of the Reichert heating-state metallograph were investigated. High-temperature microstructural observations were made on a series of materials including aluminum-uranium alloys, weld-deposited stainless steels, cold swaged copper and aluminum, annealed titanium, and arc castings of Al, Cu, Fe, Ni, and hypereutectoid steels. Temperature-dependent structural changes were recorded by Polaroid camera, 35-mm camera, and time-lapse motion pictures. Exposure and lighting variables were investigated.

Assistance was given in the study of the swelling of UAl_3-Al fuel cores. Direct observation of the UAl_3-UAl_4 transformation was possible by viewing the polished surface of a UAl_3-Al compact while heating it to almost 600°C.

[4]Graduate summer student.

EQUIPMENT AND TECHNIQUES IN METALLOGRAPHY

R. J. Gray

The developments in specimen preparation, examination, and recording have been reviewed.[5] New procedures for cutting, mounting, polishing the specimen, and revealing the microstructure were described. The use of color metallography and microanalysis and the important position of metallography in the examination of radioactive materials were included.

[5]R. J. Gray, "New Methods Point the Way," *Metal Progress* 94(2), 133–43 (August 1968).

39. NERVA Program Metallurgical Support

R. E. Clausing

We continue to provide support for the Materials and Structures Branch of the AEC-NASA Space Nuclear Propulsion Office on the NERVA program.[1] We provide technical consultation for NASA and some of its contractors and also perform experimental work in certain areas.

The final reports on the thermal fatigue testing of nozzle tube configurations have been written.[2,3] Work presently in progress includes (1) the development of nondestructive inspection techniques for coolant channels in beryllium and (2) an investigation of the materials problems that may arise as the result of exposure of the nuclear rocket engine to the space environment.

NONDESTRUCTIVE INSPECTION OF COOLANT CHANNELS IN BERYLLIUM REFLECTOR COMPONENTS

C. V. Dodd R. W. McClung

Two eddy-current techniques were developed for inspecting coolant channels in a beryllium sector. The sector contained $^3/_{16}$-in.-diam channels, which were inspected for longitudinal cracks. In addition, since the channels were produced by drilling from each end of the sector, a small amount of misalignment is present where the two halves of the holes meet in the center. Eddy-current probes and circuits were designed and used both to detect defects and to measure misalignment.

Detection of Defects

The defects were detected with a differential probe consisting of two coils, wound coaxial with the hole. The coils were wound in opposite directions and driven from opposite ends so that the induced electromagnetic fields of the two coils would add. The signal measured is the voltage difference between the two coils. If the coils sense identical conditions in the hole there will be no signal. However, the presence of a localized flaw within the influence of one of the coils will produce a signal.

The probe design and operating frequency were chosen to optimize the signal from a small defect located 0.010 in. under the metal surface of the channel. The probe was manually inserted through a Micarta template containing the pattern of holes to serve as a guide into each hole. The probe was then pulled along the channel at a constant speed with a bead chain driven by a synchronous motor. The coils were driven by a standard bridge circuit with a frequency of 50 kHz. The difference signal was amplified and fed to a strip-chart recorder.

Preliminary scans were made of all the holes. The holes containing the fewest indications were selected, and a series of notches 0.080 in. long × 0.002 in. wide were electroetched in these holes to depths ranging from 0.0048 to 0.012 in. The 0.0048-in. notch was barely visible and represents the minimum detectable notch at the test conditions. The standard notches and relatively short defects produce a double pulse – one pulse as each coil passes over the defect. A single indication is produced by an abrupt change in hole diameter. Such an indication was present in most of the holes about 6 in. from the ends. Some other indications were observed but in some cases could not be separated into discrete signals.

Additional work is in progress to improve the detection of defects and to identify the types of defects causing the unidentified indications. A Hall probe is

[1] R. E. Clausing, *Metals and Ceramics Div. Ann. Progr. Rept. June 30, 1968*, ORNL-4370, pp. 235–37.

[2] D. G. Harman, *Thermal Fatigue of Rocket Nozzle Cooling Tubes*, ORNL-TM-2089 (February 1969).

[3] D. G. Harman, "Thermal Fatigue of Rocket Nozzle Cooling Tubes," to be submitted for publication.

being constructed to identify ferromagnetic discontinuities, and we are attempting to replicate some of the observed defects.

Measurement of Misalignment

An eddy-current spacing probe was constructed and used to measure the misalignment in the coolant channels. The probe head consists of two spring-steel leaves with a coil attached to one leaf. The coil impedance is sensitive to changes in the spacing between the coil and the opposite leaf. Drill bit sections soldered to the leaves contact the edges of the holes and limit the expansion of the springs. When the probe head is inserted into the hole and longitudinally centered where the two drilled sections of the holes meet to form the complete coolant channel, each section will limit the expansion of the spring on one side of the probe. When the probe is rotated, the minimum spacing of the springs is equal to the hole diameter minus the offset between the axes of the two holes. The misalignment was measured to within ±0.002 in. over a range of 0 to 0.037 in.

EFFECTS OF SPACE ENVIRONMENT ON NERVA MATERIALS

R. E. Clausing

Exposure of the NERVA engine to the environment of space may produce some materials problems not encountered in ground tests. A committee composed of representatives from the NASA Space Nuclear Propulsion Office at Cleveland, Aerojet General Corporation, Westinghouse Astronuclear Laboratory, Oak Ridge National Laboratory, and TRW Inc. attempts to define such problem areas and to ensure that the NERVA design and fabrication are consistent with reliable operation in the space environment.

The tendency of atomically clean surfaces to adhere is one of the important space-related phenomena to be considered. Adhesion and friction of clean surfaces are not well understood, but it has been demonstrated that the presence or absence of adsorbed gases on otherwise atomically clean surfaces can completely alter adhesional and frictional properties of both pure materials and engineering alloys. To assess the importance of these effects on the materials in the NERVA system it is necessary to know (1) the specific environment at the location of particular components in the engine and (2) how this environment will influence adhesion and friction. We are providing information on both of these subjects through the two experimental studies described briefly below.

Outgassing of NERVA Fuel Elements

R. E. Clausing D. S. Easton

The gaseous atmosphere at any point in the NERVA engine will depend upon the temperature and history of the entire engine system; in the present design it will be determined primarily by the outgassing of the graphite reactor components. This outgassing cannot be accurately estimated because of the special nature of the core material, its configuration, and its coating. Experimental data must be sought for the actual core elements at temperatures and pressures similar to those expected in space operation. A facility to provide such information has been designed, built, tested, and put into operation.

We are now collecting outgassing data from quarter-length XE-II fuel elements. Full-length single elements and quarter-length clusters of seven elements are also to be tested in the present series. Quarter-length elements can be tested as received or they can be fired in hydrogen and transferred to the outgassing apparatus without exposure to air. Reactor pulse cooling can also be simulated, and elements that have been corrosion tested in hot gases can be studied. The facility can be shielded so that irradiated elements can be tested if necessary.

A schematic drawing of the experimental concept is shown in Fig. 39.1. Both the quantity and species of the gases released from the fuel elements are obtained by combining data from the mass spectrometer and the pressure drop across the orifice. At present 18 mass spectrometer peaks are monitored to give outgassing data for 11 gases. The equipment was designed to

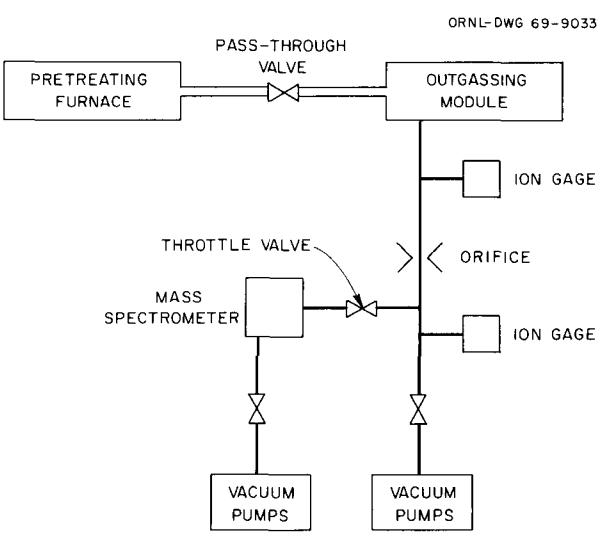

Fig. 39.1. Schematic Diagram of the Outgassing Facility for NERVA Fuel Elements.

obtain outgassing data from room temperature to 1600°F in the pressure range from 10^{-3} to 10^{-9} torr. Test times can be extended to thousands of hours if necessary. Data have been obtained on XE-II elements over these full ranges of temperature and pressure. Tests as long as 350 hr have been made.

The testing thus far has concentrated on development of the optimum test procedures. It has established the capabilities of the equipment and techniques and determined that reproducible data are obtained and that the outgassing data are sensitive to the composition and handling history of the samples. The acquisition and processing of the data require computer techniques. Computer programs have been developed to process the data from the facility and to give both analytical and graphical output of the processed outgassing rates as functions of either time or temperature.

Typical data for the 50°C outgassing of a quarter-length XE-II fuel element (tested as received) are shown in Fig. 39.2. The data for individual gases fit the relation

$$q = At^B , \qquad (1)$$

where q is the outgassing rate in torr-liters per second, t is the time in hours, and A and B are empirical constants. For most gases B is approximately -1, which is typical for outgassing processes controlled by surface phenomena. For hydrogen B is approximately $-\frac{1}{2}$, which would be expected if volume diffusion were the rate controlling step. For water vapor the slope is nearly -2; this simply indicates that the supply of water is rapidly exhausted under these conditions. Values of A and B are given in Table 39.1 for the most plentiful gases. Although Eq. (1) describes the present results and many other published outgassing data reasonably well, it should be remembered that it is empirically derived and that no attempt has been made to justify its application to these results on a theoretical basis.

Techniques for extrapolating the data to times and temperatures not easily accessible to equipment are being explored. Extrapolation in time at a given temperature seems practical. Extrapolation in temperature is much more complex and has not been seriously attempted. We plan to attempt this when more experimental results are available.

Table 39.1. Outgassing Rates for NERVA Fuel Element at 48°C[a]

Gas Evolved	A	B
	$\times 10^{-4}$	
Hydrogen	0.37	−0.61
Water vapor	12.	−1.90
Carbon monoxide	0.29	−1.00
Carbon dioxide	0.23	−1.03
Nitrogen	0.017	−1.14
Oxygen	0.059	−1.48
Argon	0.001	−1.24
Hydrocarbons	0.017	−1.00

[a]Least-squares fit to Eq. (1).

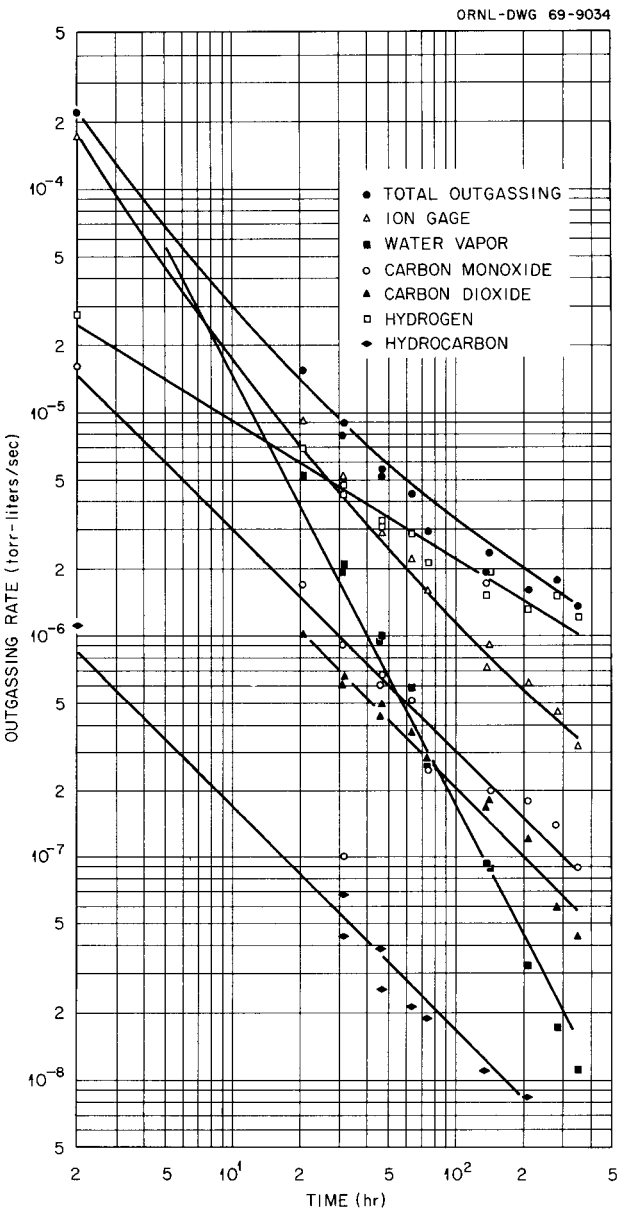

Fig. 39.2. Example of Outgassing Rates as Functions of Time at 50°C.

Observations based on XE-II fuel elements tested in the as-received condition reveal the following. (1) The initial outgassing at 50°C yields mainly water vapor at rates of about 10^{-1} torr-liters/sec per fuel element at 0.1 hr after evacuation but decreases rapidly to 10^{-4} torr-liters/sec per element at 10 hr. (2) At 100 hr the outgassing species becomes predominantly hydrogen (about 1×10^{-5} torr-liters/sec per element). Hydrogen continues to dominate the outgassing at this temperature at a rate described approximately by the relation $q = 1.5 \times 10^{-4}\ t^{-0.6}$. (3) Above about 600°C the outgassing species is mostly CO, and the rate decreases surprisingly slowly with time.

The systematic investigation of the outgassing of the NERVA fuel elements and correlation with the effects of manufacturing, storage, and pretreatment variables will continue.

Adhesion of NERVA Materials

This program is being conducted through an ORNL subcontract with Syracuse University Research Corporation. R. G. Aldrich is the principal investigator, and R. E. Clausing of the ORNL Metals and Ceramics Division is the project monitor. Special emphasis has been placed on determining the roles of surface contamination and shear motion in the adhesion of engineering materials of interest to NERVA. The experiment is providing both a preliminary evaluation of possible adhesion problems with NERVA materials and is guiding the design of future materials and component qualification tests. Adhesion couples of NERVA materials, both metals and graphites, have been tested from 77°K to 2000°C by a contact resistance measuring technique.[4] Several surface cleaning methods were used, and various gases were permitted to contaminate the cleaned surfaces before and during the adhesion testing. Adhesion was obtained for these engineering materials only after severe cleaning and high normal force loading, by impact, or by surface shearing motions. None of the combinations tested showed significant adhesion under static normal-force loading until the loads were well above the usual design limits. The results of the first portion of these tests, which emphasized normal force loading, have been reported.[5,6]

Exposure to oxygen at 10^{-6} torr for approximately 10 sec resulted in a nearly complete loss of adhesion for the materials that otherwise exhibited adhesion. The effect is irreversible, as one would expect. Hydrogen, on the other hand, shows a reversible effect for materials that exhibited adhesion and is much less effective. An exposure to 10^{-3} torr of H_2 for approximately 1 hr is required to produce a nearly complete loss of adhesion.

Impact loading within the Hertzian elastic range resulted in significantly greater amounts of adhesion, and the observed adhesion is less sensitive to surface cleanliness. There was strong adhesion after gross plastic deformation by impact. The strongest tendency for mutual adhesion, however, was induced by rubbing (shear displacements), and this effect is least sensitive to surface cleanliness.

All results so far indicate that the tendency for adhesion is measurable in terms of contact resistance. All of the NERVA materials demonstrated sharp drops in contact resistance as a result of cleaning. However, a definite threshold value for each material combination, corresponding to surfaces of almost atomic cleanliness, was required for substantial normal force adhesion at slow loading rates. This threshold value is difficult to obtain for two reasons: (1) these are engineering materials and hence inherently very dirty and (2) minor alloying elements (e.g., C in Fe), particularly surface active ones, may be providing a barrier to adhesion (e.g., brittle intermetallics).

The abrupt drop in contact resistance due to surface cleaning of the engineering materials may be significant even though no adhesion under static loads was observed. For each particular mode of deformation there may be a corresponding threshold for adhesion relatable to contact resistance. Materials that exhibit no significant tendency to cold weld under static loads may do so rather abruptly under more severe conditions of deformation (e.g., impact and rubbing). This is being investigated at present for the following adhesion couples: (1) type 440C stainless steel vs itself, (2) pyrolytic graphite vs ZTA graphite, (3) NbC on graphite vs itself, (4) electrolyzed Inconel 718 vs gold-plated type 302 stainless steel.

---

[4] K. I. Johnson and D. V. Keller, *J. Appl. Phys.* 38, 1896–1904 (1967).

[5] R. E. Clausing, *Metals and Ceramics Div. Ann. Progr. Rept. June 30, 1968,* ORNL-4370, p. 237.

[6] R. G. Aldrich, *Ultra High Vacuum Adhesion Testing of NERVA Engine Materials,* TID-25088 (July 1968).

40. Miscellaneous Studies

We are occasionally called upon to do limited studies for the Y-12 plant. Two such recent studies are reported below.

LOW-TEMPERATURE DUCTILITY AND HYDROGEN EMBRITTLEMENT OF URANIUM – A LITERATURE REVIEW[1]

H. Inouye A. C. Schaffhauser

The ductile-to-brittle transition temperature of uranium, which ranges between 100 and −50°C, is influenced by the grain size, strain rate, and the grain structure. Thus, the ductility of uranium at room temperature depends upon the heat treatment, fabrication procedures, and the testing conditions. Aluminum, silicon, and carbon impurities in concentrations below 1000 ppm impair the ductility.

A literature review of the hydrogen embrittlement of uranium was made. Threshold concentrations between 0.2 and 0.5 ppm H present as β-UH_3 are the probable causes of the severe impairment of the ductility at room temperature. The morphology of UH_3 and microcracks associated with this phase also influence the degree of embrittlement. The hydrogen in heat-treated uranium is derived from the reaction of uranium with water vapor in the annealing media.

[1] Abstract of ORNL-TM-2563 (in press).

[2] Abstract of ORNL-TM-2482 (February 1969).

THE EFFECT OF ALLOY ADDITIONS AND HEAT TREATMENTS ON THE MECHANICAL PROPERTIES OF U–0.5% Ti ALLOY[2]

J. I. Federer

Specific amounts of C, Fe, Ni, Si, Y, and H were added to a base U–0.5 wt % Ti alloy. The tensile properties of the alloys in various heat-treated conditions were then compared to the properties of the base alloy in a similar condition. In gamma-quenched alloys tested at 25 and 600°C, carbon contents of 0.014 and 0.028% did not substantially affect properties, although the effects were mostly detrimental. Silicon contents of 300 and 400 ppm caused small changes in properties similar to those caused by carbon, except that the elongation at 600°C was greatly increased. Iron, nickel, and yttrium each increased the yield and tensile strengths of gamma-quenched alloys; however, iron (340 ppm) was effective at both 25 and 600°C, while nickel (700 ppm) was mostly effective at 25°C, and yttrium (0.10%) was mostly effective at 600°C. Each of these elements decreased elongation at 600°C. Aging the base alloy and alloys containing iron and nickel additions within the alpha range resulted in a further increase in strength at test temperatures of 25 and 400°C. Hydrogen in the range 8 to 14 ppm weakened and embrittled alloys tested at 25°C.

Bend testing at 25°C of the base alloy containing an electron-beam weld-fusion zone showed that cracking originated in the weld at much lower strains than had occurred prior to failure in tensile tests of unwelded specimens having the base alloy composition.

Papers and Publications

Papers and Oral Presentations

Compiled by Frances A. Scarboro

American Crystallographic Association Summer Meeting, Buffalo, N.Y., Aug. 12–16, 1968

Robert W. Hendricks,* "Application of Small-Angle X-Ray Scattering to Metals"

Conference on Application of X-Ray Analysis, Denver, Colo., Aug. 21–23, 1968

E. A. Starke,* J. C. Ogle, and C. J. Sparks, Jr., "Deformation Textures of Ordered and Disordered Cu_3Au"

American Nuclear Society National Topical Meeting, Schenectady, N.Y., Aug. 22–23, 1968

J. H Frye, Jr.,* "An Assessment of Current Materials Research Programs and Their Impact on Future Reactor Designs"

P. L. Rittenhouse, "Yielding and Plastic Flow Phenomena in Zirconium Alloys" (presented by D. O. Hobson)

11th International Conference on Low Temperature Physics, St. Andrews, Scotland, Aug. 21–28, 1968

F. E. Obenshain,* J. C. Love, and G. Czjzek, "Mössbauer Measurements with ^{61}Ni in 3*d* Transition Metal Alloys"

International Symposium on Structural Stability in Superalloys, Seven Springs, Pa., Sept. 4–6, 1968

R. E. Gehlbach* and H. E. McCoy, "Phase Instability in Hastelloy N"

156th National American Chemical Society Meeting, Atlantic City, N.J., Sept. 8–13, 1968

G. Pedro Smith,* Jorulf Brynestad, Charles R. Boston, and W. Ewen Smith, "Coordination Equilibria of Nickel(II) in Molten Chloride Salts"

11th International Conference on Coordination Chemistry, Jerusalem, Israel, Sept. 16–18, 1968

Niels J. Bjerrum* and G. Pedro Smith, "Lower Oxidation States in Polynuclear Tellurium Complexes"

American Ceramic Society Meeting, Basic Science and Electronics Divisions Joint Fall Meeting, St. Paul, Minn., Sept. 17–20, 1968

C. S. Morgan,* "Comments on Sintering Activation Energy"

8th Symposium on Physics and Nondestructive Testing, Schiller Park, Ill., Sept. 24–26, 1968

C. V. Dodd, W. E. Deeds,* and J. W. Luquire, "Integral Solutions to Some Eddy Current Problems"

Fall Meeting of the American Society for Testing and Materials, Atlanta, Ga., Sept. 30–Oct. 4, 1968

J. V. Cathcart* and G. F. Petersen, "The Role of Short Circuit Diffusion Paths in the Oxidation of Copper and Nickel"

*Speaker.

American Institute of Mining, Metallurgical, and Petroleum Engineers Metallurgy Symposium on Materials for Radioisotope Heat Sources, Gatlinburg, Tenn., Oct. 2–4, 1968

D. T. Bourgette,* "Evaporation of Radioisotope Capsule Materials in Vacuum"

J. H. DeVan,* "Basic Consideration in Selecting Compatible Materials"

J. R. DiStefano,* "Compatibility of Strontium and Curium Fuels with Capsule Materials"

R. G. Donnelly* and R. W. Gunkel, "Remote Encapsulation Techniques for Strontium and Curium Fuel Forms"

Symposium on Preparation and Purification of Ultrapure Metals, Electrochemical Society, Montreal, Canada, Oct. 6–11, 1968

D. S. Easton* and J. O. Betterton, "Zone Purification of Hafnium"

1968 Fall Meeting of the Nuclear Division of the American Ceramic Society, Pittsburgh, Pa., Oct. 6–9, 1968

R. B. Fitts,* A. R. Olsen, and J. Komatsu, "Sphere-Pac Fabrication of Sol-Gel Nuclear Fuels"

J. P. Moore,* R. S. Graves, and D. L. McElroy, "The Thermal Conductivity of ThO_2 and UO_2 from 77 to 1300 K"

American Welding Society National Fall Meeting, Cincinnati, Ohio, Oct. 7–10, 1968

R. W. Gunkel,* R. G. Donnelly, and G. M. Slaughter, "Electron-Beam Welding of SNAP-21 and SNAP-23 Isotopic Fuel Capsules"

W. J. Werner and G. M. Slaughter,* "Brazing of Graphite for Critical Nuclear Application"

Eighth Conference on Thermal Conductivity, Purdue University, Lafayette, Ind., Oct. 7–10, 1968

K.-H. Bode,* "Possibilities to Determine Thermal Conductivity Using New Solutions for Current-Carrying Electrical Conductors"

J. P. Moore, R. K. Williams, and D. L. McElroy,* "Further Comments on Transport Properties of Chromium"

R. K. Williams,* J. P. Moore, R. S. Graves, T. E. Banks, and D. L. McElroy, "Physical Properties of Molybdenum from 80 to 1300 K"

1968 Fall Meeting of the Institute of Metals Division, The Metallurgical Society, Detroit, Mich., Oct. 13–17, 1968

E. E. Bloom* and J. O. Stiegler, "Void Formation in Stainless Steel Irradiated to High Fast Neutron Fluences"

R. W. Carpenter,* "Defect Substructure in Strained Single-Crystal Rhenium"

K. Farrell,* C. K. H. DuBose, and J. O. Stiegler, "Metallography of an Aluminum Alloy Subjected to a High Neutron Fluence"

D. G. Harman,* "Enhanced Postirradiation Ductility of Incoloy 800"

R. W. Hendricks,* C. C. Koch, and G. R. Love, "Kinetics of the Omega Transformation in Ti-23 a/o Nb"

D. O. Hobson,* "Examination of Orientation Factors for the Deformation Systems of Zirconium under Biaxial Stress Conditions"

R. T. King* and E. L. Long, Jr., "Irradiation Damage to 1100 Aluminum at High Fast Neutron Fluences"

R. T. King* and J. R. Weir, Jr., "The Effects of Cyclotron-Injected Helium on the Creep-Rupture Properties of Type 304 and 0.2% Ti Type 304L Stainless Steel"

C. C. Koch* and G. R. Love, "Superconductivity in the System Niobium-Gadolinium"

B. T. M. Loh, E. E. Bloom, and J. O. Stiegler,* "Annealing Behavior of Voids in Irradiated Stainless Steel"

G. R. Love* and C. C. Koch, "On the Scale of Significant Flux-Pinning Defects in Superconductors"

T. S. Lundy* and R. E. Pawel, "Short-Circuiting Diffusion in Body-Centered Cubic Metals"

G. T. Newman* and D. W. Short, "The Effect of Prestrain on the Creep Properties of Irradiated and Unirradiated Type 304L Modified Stainless Steel"

D. K. Reimann* and T. S. Lundy, "Diffusion of U-233 in UN and UO_2 Single Crystals"

P. L. Rittenhouse,* "Plastic Yielding of Highly Textured Zircaloy Tubing"

C. E. Sessions* and H. E. McCoy, "High-Temperature Irradiation Damage in the Nickel-Base Alloy, Hastelloy N"

R. L. Stephenson,* "The Effect of Fabrication Variables on the Creep-Rupture Properties of Molybdenum-Base Alloys"

E. Tenckhoff* and P. L. Rittenhouse, "Deformation and Annealing Textures in Drawn Zircaloy Tubing"

R. A. Vandermeer* and J. C. Ogle, "Possible Causes for Texture Inhomogeneities in Cold-Rolled Niobium"

F. W. Wiffen* and J. O. Stiegler, "Voids in Neutron-Irradiated Vanadium"

R. O. Williams,* "The Representation of Thermodynamic Functions for Binary Solutions as Fourier Series"

Alan Wolfenden,* "The Energy Stored During the Low-Temperature Tensile Deformation of Copper and Aluminum"

Alan Wolfenden,* "The Ratio of Stored to Expended Energy During the Low-Temperature Deformation of Copper and Aluminum Single Crystals"

M. H. Yoo,* "Dislocation Reactions in H.C.P. Metals"

C. S. Yust* and C. J. McHargue, "Dislocation Substructures in Deformed UO_2 Single Crystals"

American Society for Testing and Materials Meeting, New York, Oct. 13–17, 1968

G. L. Copeland,* M. M. Martin, R. T. King, and W. R. Martin, "Observations on Hydrogen in Aluminum for Nuclear Applications"

American Society for Metals, Materials Engineering Exposition and Congress, Detroit, Oct. 14–17, 1968

R. T. King,* E. M. Thomas, and H. E. McCoy, "The Computer – An Aid for Analyzing and Processing Creep-Rupture Data"

28th Annual Conference of the American Society for Nondestructive Testing, Detroit, Oct. 14–17, 1968

C. V. Dodd,* "Analysis of Eddy-Current Problems with a Time-Sharing Computer"

Symposium on Advanced and High-Temperature Gas Cooled Reactors, sponsored by IAEA, Jülich, Germany, Oct. 21–25, 1968

A. L. Lotts and R. G. Wymer, "Economics and Technology of HTGR Fuel Recycle," (presented by D. B. Trauger)

US/Japan Information Exchange Meeting on Ceramic Nuclear Fuels, Tokyo, Japan, Oct. 22–25, 1968

R. B. Fitts and A. L. Lotts,* (compilers) "Nuclear Fuels Development at the Oak Ridge National Laboratory"

Radioisotope and Reactor Thermionics Classified Meeting, U.S. Army Natick Laboratory, Boston, Oct. 23–24, 1968

J. R. DiStefano,* "Compatibility of Refractory Metals with $^{244}Cm_2O_3$"

AEC/RDT Meeting on Vanadium and Vanadium Alloys, Ames, Iowa, Oct. 24–25, 1968

J. H. DeVan,* R. L. Klueh, D. H. Jansen, and R. L. Wagner, "Mass Transfer of Interstitial Impurities Between Vanadium Alloys and Sodium"

K. E. Spear* and J. D. L. Harrison, "Compatibility of Vanadium Alloys with Nitride Fuels"

F. W. Wiffen* and J. O. Stiegler, "Void Formation in Irradiated Vanadium and Vanadium Alloys"

Seventh Rare Earth Research Conference, Coronado, Calif., Oct. 28–30, 1968

C. B. Finch,* L. J. Nugent, G. K. Werner, and M. M. Abraham, "Self-Activated Thermoluminescence in Several Lanthanide- and Actinide-Doped Thorium Dioxide Crystals"

C. C. Koch* and C. J. McHargue, "Phase Transformations Associated with the Sm-Type Structure in the Gd-Ce System"

American Society for Testing and Materials (Symposium title: "Applications Related Phenomena in Zirconium and Hafnium and Their Alloys"), Philadelphia, Nov. 5–6, 1968

D. O. Hobson,* "Texture Changes Produced During Zircaloy-4 Tubing Fabrication: From Forged Billet to Finished Tubing"

P. L. Rittenhouse,* "The Effect of Texture on the Torsional Yielding of Zircaloy Tubing"

E. Tenckhoff* and P. L. Rittenhouse, "Texture Gradients in Thin-Walled Zircaloy Tubing"

American Nuclear Society Winter Meeting, Washington, D.C., Nov. 10–15, 1968

R. L. Beatty* and D. V. Kiplinger, "Gas Impregnation of Graphite with Carbon"

W. H. Cook* and A. Taboada, "MSRE Surveillance Program"

J. H. Erwin, M. M. Martin,* and W. R. Martin, "The Effect of Fuel Concentration on the Compressive Strength of Core Materials Used in Research Reactor Fuel Plates"

A. E. Goldman* and A. L. Lotts, "Parametric Studies of LMFBR Fuel Fabrication Costs"

D. G. Harman,* "Improved Resistance to Radiation Damage in Incoloy 800"

C. R. Kennedy,* "Irradiation of Graphite in HFIR"

W. R. Martin,* "Application of Today's Materials Studies to Tomorrow's Operation of Research Reactors"

C. E. Sessions* and H. E. McCoy, "Development of Hastelloy N with Improved Resistance to Irradiation Damage"

W. J. Werner and G. M. Slaughter,* "Brazing of Graphite for Molten-Salt Applications"

C. S. Yust* and C. J. McHargue, "Deformation of Uranium Dioxide Single Crystals"

AEC-Argonne National Laboratory International Conference on Sodium Technology and Large Fast Reactor Design, Argonne National Laboratory, Nov. 7, 1968

R. L. Klueh,* "The Effect of Oxygen in Sodium on the Compatibility of Sodium with Niobium"

European Conference on Thermophysical Properties of Solid Materials at High Temperature, Baden-Baden, Germany, Nov. 11–13, 1968

T. G. Kollie, M. Barisoni, D. L. McElroy, and C. R. Brooks,* "Pulse Calorimetry Using a Digital Voltmeter for Transient Data Acquisition"

1st Annual Technical Meeting of the International Metallographic Society, Denver, Colo., Nov. 11–13, 1968

R. E. Gehlbach,* M. D. Allen, and J. D. Braun, "Autoradiographic Study of Carbon-14 in Hastelloy N"

R. J. Gray* and B. C. Leslie, "A Metallograph for Glove Box Operation"

American Physical Society Meeting, Miami, Fla., Nov. 25–27, 1968

Harold L. Davis,* "Calculation of the Hyperfine Field in Metallic Copper Appropriate to a Fermi-Surface Electron"

Fourteenth AEC Coated-Particle Fuels Working Group Meeting, Oak Ridge National Laboratory, Nov. 20–21, 1968

J. H. Coobs and O. Sisman (compilers) "Coated-Particle Fuels Development at Oak Ridge National Laboratory"

D. R. Cuneo,* "High Burnup Irradiation Test of Bonded Beds"

F. J. Furman,* "Particle Coating and Fuel Stick Preparation"

D. M. Hewette II,* "Irradiation of Loose Coated Particles in HFIR Target"

T. N. Washburn,* "Dragon Project Experience"

S. C. Weaver,* "Bonded-Bed Irradiations in HFIR Target"

American Chemical Society Meeting, Tallahassee, Fla., Dec. 4–6, 1968

George E. Shankle and G. Pedro Smith,* "Crystal Field Splittings and Vibronic Interactions of Nickel(II) Electronic States in $CdCl_2:Ni^{2+}$ and $LiCl:Ni^{2+}$"

G. Pedro Smith,* Jorulf Brynestad, and W. Ewen Smith, "Coordination Distribution Equilibria of Ni(II) Ions in Binary Molten Salt Systems at High Temperatures"

Southeastern Electron Microscopy Society, the University of Tennessee, Knoxville, Dec. 6–7, 1968

R. E. Gehlbach,* "Electron Microscope Microprobe Analysis"

27th High Temperature Fuels Committee Meeting, Canoga Park, Calif., Dec. 10–12, 1968

W. Fulkerson, "Summary of Recent ORNL Work on Uranium Nitride," (presented by J. L. Scott)

J. L. Scott,* (compiler) "Summary of Recent ORNL Work on Fuels and Cladding Materials"

High Temperature Defect Configurations, AEC Headquarters, Germantown, Md., Jan. 9–10, 1969

J. O. Stiegler,* (compiler) "Summary of Recent Research on High-Temperature Defect Configurations"

98th Annual Meeting of the Metallurgical Society of the American Institute of Mining, Metallurgical, and Petroleum Engineers, Washington, D.C., Feb. 17–20, 1969

J. W. Koger* and A. P. Litman, "Kinetic Behavior of Chromium and Iron in Some Iron- and Nickel-Base Alloys Exposed to Fluoride Salts"

Spring Meeting of the American Society for Nondestructive Testing, Los Angeles, March 10–13, 1969

C. V. Dodd, "An Infrared Microscope System for the Detection of Internal Flaws in Solids" (presented by W. E. Deeds)

American Physical Society, Philadelphia, March 24–27, 1969

Gordon Czjzek* and Wolfram G. Berger, "Studies of Recoil Atom Positions by the Mössbauer Effect in Fe-Al Alloys"

J. C. Love,* Felix E. Obenshain, and Gordon Czjzek, "Mössbauer Studies of ^{61}Ni in *3d* Alloys and Ni^{2+} Compounds"

American Society for Testing and Materials, Technical Session on Fractography, Philadelphia, March 27, 1969

K. Farrell* and J. O. Stiegler, "Application of Fractography to the Study of High Temperature Processes"

American Chemical Society Meeting, Minneapolis, Minn., April 13–18, 1969

R. W. Hendricks* and S. Lindenbaum, "A Small-Angle X-Ray Scattering Investigation of Aqueous Solutions of Tetra-Alkylammonium Halides"

G. Love,* "The Metallurgy of Technetium and Its Alloys"

Seventh Symposium on Nondestructive Evaluation of Components and Materials in Aerospace, Weapons Systems, and Nuclear Applications, San Antonio, Texas, April 23–25, 1969

K. V. Cook,* "Remote Ultrasonic Examination of Closure Welds on Isotope Capsules"

B. E. Foster* and S. D. Snyder, "An X-Ray Technique for Measuring Thickness of Tungsten on Copper"

K. K. Klindt* and D. A. Canonico, "Evaluation of Discontinuities in HSST Twelve Inch Thick Plate"

50th Annual Meeting of the American Welding Society, Philadelphia, April 28–May 2, 1969

D. A. Canonico,* N. C. Cole, and G. M. Slaughter, "Development of High-Temperature Brazing Filler Metals"

International Conference on Fundamental Aspects of Dislocation Theory, Gaithersburg, Md., April 21–25, 1969

M. H. Yoo* and B. T. M. Loh, "Structural and Elastic Properties of Zonal Twin Dislocations in Anisotropic Crystals"

71st Annual Meeting of the American Ceramic Society, Washington, D.C., May 3–8, 1969

A. T. Chapman,* G. W. Clark, and D. E. Hendrix, "UO_2-W Cermets Produced by Unidirectional Solidification"

J. M. Leitnaker,* R. A. Potter, K. E. Spear, and W. R. Laing, "The Lattice Parameter of U(C,N) as a Function of Composition"

R. W. McClung,* "Nondestructive Testing Aids the Development of Ceramic Materials at the Oak Ridge National Laboratory"

Karl E. Spear* and James M. Leitnaker, "The Formation of Active Carbon in Twin Crucible Studies of Vanadium Carbonitride Solutions"

International Symposium on Ceramic Nuclear Fuels (sponsored by the Nuclear Division of the American Ceramic Society), Washington, D.C., May 3–8, 1969

E. L. Long, Jr.,* F. R. McQuilkin, D. R. Cuneo, J. R. Lindgren, and J. N. Siltanen, "Irradiation Tests of Fuel Rods Containing UO_2 and $(U,Pu)O_2$ for GCFR"

Spring Meeting of the Electrochemical Society, New York, May 4–9, 1969

R. E. Pawel* and T. S. Lundy, "Diffusion Studies and Electrochemical Sectioning"

EURATOM Meeting "The Effect of Fast Neutron Irradiation at Temperature above 600°C on the Physical and Mechanical Properties of Graphite and Pyrocarbons," Brussels, Belgium, May 5–6, 1969

R. L. Beatty and D. V. Kiplinger, "Gas Impregnation of Graphite with Carbon," presented by C. R. Kennedy

O. B. Cavin, "Preferred Orientation and Its Effect on Radiation Stability," presented by C. R. Kennedy

D. M. Hewette II, "Irradiation of Pyrolytic-Carbon-Coated ThO_2 Particles to Significant HTGR Fast Fluences," presented by C. R. Kennedy

C. R. Kennedy,* "The Irradiation of Graphite in HFIR"

23rd Annual Technical Conference of the American Society for Quality Control, Los Angeles, May 5–7, 1969

B. E. Foster, S. D. Snyder,* and R. W. Knight, "X-Ray Attenuation Scanning of Nuclear Fuel Plates"

Libby-Cockcroft Meeting, Harwell, England, May 12–13, 1969

R. L. Beatty and D. V. Kiplinger, "Gas Impregnation of Graphite with Carbon," presented by C. R. Kennedy

O. B. Cavin, "Preferred Orientation and Its Effect on Radiation Stability," presented by C. R. Kennedy

D. M. Hewette II, "Irradiation of Pyrolytic-Carbon-Coated ThO_2 Particles to Significant HTGR Fast Fluences," presented by C. R. Kennedy

C. R. Kennedy,* "The Irradiation of Graphite in HFIR"

Spring Meeting of the Metallurgical Society of the American Institute of Mining, Metallurgical, and Petroleum Engineers, Pittsburgh, Pa., May 11–15, 1969

R. W. Carpenter* and C. T. Liu, "Deformation Behavior of Niobium-Hafnium Alloys"

J. P. Hammond* and G. M. Slaughter, "Powder Metallurgy Transition Joint for Joining Graphite to Metals"

R. W. Hendricks, C. C. Koch, and G. R. Love,* "On the Mechanism and Kinetics of the Omega Transformation in Ti–25 at. % Nb"

R. L. Klueh* and J. H. DeVan, "The Effect of Oxygen on the Compatibility of Vanadium and Vanadium Alloys with Sodium"

C. C. Koch* and C. J. McHargue, "Phase Transformations Associated with the Samarium-Type Structure in Intra-Rare-Earth Alloys"

C. T. Liu,* R. W. Carpenter, and H. Inouye, "Precipitation in Niobium-Hafnium Alloys"

T. S. Lundy* and R. E. Pawel, "Residual Activity Methods for Determination of Lattice Diffusion Coefficients"

R. L. Wagner,* "Nitrogen Diffusion and Solubility in Tungsten"

W. J. Werner* and J. E. Spruiell, "An Investigation of the Effect of Certain Minor Elements on the Elevated Temperature Ductility of Incoloy 800"

A. Wolfenden,* "The Energy Stored in a Gold-Silver Alloy"

A. Wolfenden,* "The Energy Stored in Silver Single Crystals"

AEC/RDT Meeting on Vanadium and Vanadium Alloys, Pittsburgh, Pa., May 13, 1969

J. H. DeVan,* "Summary Status of Vanadium Corrosion Program at ORNL"

28th Meeting of the High Temperature Fuels Committee, Oak Ridge National Laboratory, May 13–15, 1969

T. N. Washburn (compiler) "Summaries of Recent ORNL Work on Fuels and Cladding Materials"

E. E. Bloom* and J. R. Weir, "Review of Irradiation Testing of Stainless Steel Cladding"

G. W. Clark,* "Eutectic Melting of UO_2-W"

J. H. Coobs,* "Irradiation of HTGR Fuel Particles in HFIR"

C. M. Cox,* "Fuel Performance Models"

R. B. Fitts and A. R. Olsen,* "Irradiation Testing of $(U,Pu)O_2$"

W. Fulkerson,* "Fundamental Studies of UN System"

J. M. Leitnaker,* "Physical Chemistry of Mixed Oxides"

T. B. Lindemer,* "Kinetic Studies in the U-C-O-N System"

S. C. Weaver,* "Irradiation Behavior of UN"

International Atomic Energy Agency Symposium on Radiation Damage in Reactor Materials, Vienna, Austria, June 2–6, 1969

J. O. Stiegler,* K. Farrell, C. K. H. DuBose, and R. T. King, "High Fluence Neutron Irradiation Damage in Aluminum"

15th Annual Meeting of the American Nuclear Society, Seattle, Wash., June 15–19, 1969

E. E. Bloom,* "Irradiation Damage to Annealed Type 316 Stainless Steel"

E. E. Bloom* and J. O. Stiegler, "Comparison of Defect Structures in Nickel and Stainless Steel After Irradiation at Intermediate Temperatures"

John M. Chandler and Samuel E. Bolt,* "^{233}U-Bearing Salt Preparation for the Molten Salt Reactor Experiment"

G. L. Copeland,* "An Improved Crushing Method for UAl_x Fuel Particles"

D. O. Hobson* and E. Tenckhoff, "Effects of Fabrication Parameters on Textures Produced in Zircaloy Cladding"

F. J. Homan* and T. N. Washburn, "Capacity Expansion Optimization in a Growing Nuclear Fuel Fabrication Industry"

R. T. King,* "Biaxial Creep Rupture of 0.2% Ti-Modified Type 304L Stainless Steel Tubing"

J. M. Leitnaker,* R. L. Beatty, and K. E. Spear, "Possible Stabilization of Nitride Fuel by Oxygen"

M. M. Martin* and A. E. Richt, "Effect of Void Volume on the Irradiation Performance of Aluminum-Base Dispersion-Type Fuel Plates"

T. M. Nilsson* and G. A. Reimann, "Evaluation of Titanium-Modified Type 304L Stainless Steel Tubing"

J. R. Parrott,* F. L. Daley, F. J. Furman, and J. W. Snider, "Pilot Scale Preparation of Pyrocarbon Coated Uranium(IV)^{233} Oxide-Thorium Dioxide Microspheres for High Temperature Lattice Test Reactor"

C. E. Sessions* and E. E. Stansbury, "Comparison of the Thermal Stability of Titanium-Modified Hastelloy N at 650 and 760°C"

T. N. Washburn,* "Porous UO_2 Bodies Produced by Reduction of U_3O_8"

F. W. Wiffen* and J. O. Stiegler, "Irradiation Damage in Vanadium at 600°C"

1969 Vacuum Metallurgy Conference, Pittsburgh, Pa., June 16–19, 1969

H. Inouye,* "The Effect of Low Pressure Oxygen on the Creep Properties of Tungsten and a Tungsten-Molybdenum Alloy"

American Carbon Committee Ninth Biennial Conference on Carbon, Boston, June 16–20, 1969

O. B. Cavin,* "Anisotropy Determinations of Potential Nuclear Graphites"

C. R. Kennedy,* "Irradiation of Graphite in HFIR"

Cullie J. Sparks, Jr.,* and Ernest Epperson, "Thermal Motion in Highly Oriented Graphite"

Publications

Compiled by Meredith R. Hill

Abraham, M. M., G. W. Clark, C. B. Finch, R. W. Reynolds, and H. Zeldes, "Ground-State Splitting of Trivalent Gd and Cm in $ZrSiO_4$, $HfSiO_4$, and $ThSiO_4$, Determined by ESR," *J. Chem. Phys.* **50**(5), 2057–62 (March 1969).

Adamson, G. M., Jr., *Fabrication Procedures for the Initial High Flux Isotope Reactor Fuel Elements,* ORNL-4342 (February 1969).

Anderson, J. W., S. E. Bolt, and J. M. Chandler, *Safety Analysis for the Thorium-Uranium Recycle Facility,* ORNL-4278 (May 1969).

Askill, John, "A Preliminary Investigation of Self Diffusion in Manganese," *Phys. Status Solidi* **33**(2), K105–K107 (June 1969).

Barisoni, M., R. K. Williams, and D. L. McElroy, "Physical Properties of Indium from 77 to 350°K," pp. 279–92 in *Thermal Conductivity, Proc. 7th Conf. Gaithersburg, Maryland, Nov. 13–16, 1967, Nat. Bur. Std. Spec. Publ.* **302**, ed. by D. R. Flynn and B. A. Peavy, Jr., National Bureau of Standards, Washington, D.C., September 1968.

Barrett, Lida K., and C. S. Yust, *Some Fundamental Ideas in Topology and Their Application to Problems in Metallurgy,* ORNL-4411 (June 1969).

Beatty, R. L., and D. V. Kiplinger, "Gas Impregnation of Graphite with Carbon," (Summary) *Trans. Am. Nucl. Soc.* **11**(2), 622–23 (November 1968).

Beaver, R. J., and M. M. Martin, *The Status of Europium Compounds for Reactivity Control in Nuclear Reactors,* ORNL-4368 (February 1969).

Berger, W. G., and G. Czjzek, "Radiation Effects in Ordered Fe-Al Alloys: Mössbauer Experiments Following Neutron Capture," pp. 504–13 in *International Conference on Vacancies and Interstitials in Metals, Jülich, 1968,* Vol. II, KFA-Jül-Conf-2, Kernforschungsanlage, Jülich (September 28, 1968).

Bjerrum, N. J., and G. P. Smith, "Tellurium in the Formal Electropositive Oxidation State One-Half in Acidic Chloride Media," *J. Am. Chem. Soc.* **90**(16), 4472 (July 1968).

Bloom, E. E., and J. O. Stiegler, "Void Formation in Stainless Steel Irradiated to High Fast Neutron Fluences," (Abstract) *J. Metals* **20**(8), 114A–15A (August 1968).

Bloom, E. E., and J. R. Weir, Jr., *Development of Austenitic Stainless Steels with Improved Resistance to Elevated-Temperature Irradiation Embrittlement,* ORNL-TM-2328 (December 1968).

Bloom, E. E., "Irradiation Damage to Annealed Type 316 Stainless Steel," (Summary) *Trans. Am. Nucl. Soc.* **12**(1), 129–30 (June 1969).

Bloom, E. E., and J. O. Stiegler, "Comparison of Defect Structures in Nickel and Stainless Steel after Irradiation at Intermediate Temperatures," (Summary) *Trans. Am. Nucl. Soc.* **12**(1), 116–17 (June 1969).

Bode, K.-H., "Possibilities to Determine Thermal Conductivity Using New Solutions for Current-Carrying Electrical Conductors," *Thermal Conductivity, Proc. 8th Conf.,* ed. by C. Y. Ho and R. E. Taylor, Plenum Press, New York, 1969.

Boston, C. R., C. H. Liu, and G. P. Smith, "Coordination of Nickel(II) in Molten Lithium Bromide–Potassium Bromide and Lithium Iodide–Potassium Iodide Mixtures," *Inorg. Chem.* **7**(9), 1938–40 (September 1968).

Boston, C. R., and G. P. Smith, "Furnaces with low thermal gradients for molten salt spectrophotometry," *J. Sci. Instr. (J. Phys. E) 1969 Series 2,* **2**, 543–546 (June 1969).

Bourgette, D. T., "Evaporation of Radioisotope Capsule Materials In Vacuum," pp. 248–70 in *Symposium on Materials for Radio-Isotope Heat Sources, Nucl. Met.* **14**, ed. by D. E. Thomas, W. O. Harms, and R. T. Huntoon, American Institute of Mining, Metallurgical and Petroleum Engineers, New York, 1969.

Box, W. D., and R. S. Crouse, *Compatibility Screening Tests for Selection of Radioisotope Heat Source Compounds,* ORNL-4298 (December 1968). CLASSIFIED

Burkett, M. N., W. P. Eatherly, and W. O. Harms, "Fueled-Graphite Elements for the German Pebble-Bed Reactor (AVR)," pp. 45–64 in *High Temperature Nuclear Fuels (Symposium held in Delavan, Wisconsin, October 1966) Met. Soc. Conf.* **42**, ed. by A. N. Holden, Gordon & Breach, New York, 1968.

Canonico, D. A., "Technical Note: Depth of Heat-Affected Zone in Thick Pressure Vessel Steel Plate Due to Flame Cutting," *Welding J. (N.Y.)* **47**(9), 410-s and 419-s (September 1968).

Carpenter, R. W., "Defect Substructure in Strained Single-Crystal Rhenium," (Abstract) *J. Metals* **20**(8), 13A (August 1968).

Carpenter, R. W., and H. G. Paris, "Preparation of Rhenium for Transmission Electron Microscopy," *J. Appl. Phys.* **39**(12), 5809–10 (November 1968).

Carpenter, R. W., and J. C. Ogle, "Deformation Substructure and Fracture in Very Thin Pack-Rolled Metal Foils," *Trans. Met. Soc. AIME* **245**(4), 613–18 (April 1969).

Cathcart, J. V., G. F. Petersen, and C. J. Sparks, Jr., "The Structure of Thin Oxide Films Formed on Nickel Crystals," *J. Electrochem. Soc.* **116**(5), 664–68 (May 1969).

Chandler, J. M., and S. E. Bolt, "^{233}U-Bearing Salt Preparation for the Molten Salt Reactor Experiment," (Summary) *Trans. Am. Nucl. Soc.* **12**(1), 25–26 (June 1969).

Clausing, R. E., *Desorption of Carbon Monoxide from Tungsten by Bombardment with Electrons,* ORNL-TM-2307 (April 1969), D.Sc. Thesis, the University of Virginia.

Cook, W. H., and A. Taboada, "MSRE Surveillance Program," (Summary) *Trans. Am. Nucl. Soc.* **11**(2), 621–22 (November 1968).

Copeland, G. L., "An Improved Crushing Method for UAl_x Fuel Particles," (Summary) *Trans. Am. Nucl. Soc.* **12**(1), 97–98 (June 1969).

Cox, C. M., and F. J. Homan, *PRØFIL – A One-Dimensional FØRTRAN IV Program for Computing Steady-State Temperature Distributions in Cylindrical Ceramic Fuels,* ORNL-TM-2443 (March 1969).

Cuneo, D. R., and H. E. Robertson, "Fission Product Profiles in Graphite Exposed to Fissioning ^{7}LiF-BeF_2-ZrF_4-UF_4," (Summary) *Trans. Am. Nucl. Soc.* **12**(1), 80–81 (June 1969).

Czjzek, Gordon, J. L. C. Ford, Jr., J. C. Love, F. E. Obenshain, and H. H. F. Wegener, "Coulomb-Recoil-Implantation Mössbauer Experiments with ^{73}Ge," *Phys. Rev.* **174**(2), 331–45 (October 1968).

Davis, H. L., "The Hyperfine Field in Metallic Copper Appropriate to a Fermi-Surface Electron," *Phys. Letters* **28A**(2), 85–87 (November 1968).

DeCarlo, V. A., F. R. McQuilkin, R. L. Senn, K. R. Thoms, and S. C. Weaver, *Design of a Capsule for Irradiation Testing of Uranium Nitride Fuel,* ORNL-TM-2363 (February 1969).

DeVan, J. H., *Effect of Alloying Additions on Corrosion Behavior of Nickel-Molybdenum Alloys in Fused Fluoride Mixtures,* ORNL-TM-2021, Vol. I, M.S. Thesis, the University of Tennessee.

DiStefano, J. R., "Compatibility of Refractory Metals with $^{244}Cm_2O_3$," pp. 352–64 in *Proceedings of the Thermionic Conversion Specialist Conference, Natick, Massachusetts, October 23–24, 1968,* TID-24818. CLASSIFIED

DiStefano, J. R., *Refluxing Capsule Experiments with Refractory Metals in Boiling Alkali Metals,* ORNL-4323 (February 1969).

Dodd, C. V., and W. E. Deeds, "Computer Design of Eddy-Current Tests," pp. 199–203 in *Proceedings of the Fifth International Conference on Nondestructive Testing, Canada, 1967,* The Queen's Printer, Ottawa, Canada, 1969.

Dodd, C. V., W. E. Deeds, J. W. Luquire, and W. G. Spoeri, *Some Eddy-Current Problems and Their Integral Solutions,* ORNL-4384 (April 1969).

Dodd, C. V., W. E. Deeds, and J. W. Luquire, "Integral Solutions to Some Eddy Current Problems," *Intern. J. Nondestructive Testing* **1**(1), 29–90 (June 1969).

Donnelly, R. G., and R. W. Gunkel, "Remote Encapsulation Techniques for Strontium and Curium Fuel Forms," pp. 211–22 in *Symposium on Materials for Radio-Isotope Heat Sources, Nucl. Met.* **14**, ed. by D. E. Thomas, W. O. Harms, and R. T. Huntoon, American Institute of Mining, Metallurgical and Petroleum Engineers, New York, 1969.

DuBose, C. K. H., and C. Jones, *Techniques for the Preparation of Transmission Electron Microscopy Specimens from Tubing,* ORNL-TM-2408 (January 1969).

Easton, D. S., and J. O. Betterton, Jr., *Ultrahigh-Vacuum Zone Purification of Zirconium with Analysis of Partial Pressures,* ORNL-4309 (December 1968); also pp. 469–500 in *Electron and Ion Beam Science and Technology, Proc. 3rd Intern. Conf. Boston, 1968,* ed. by R. A. Bakish, Electrochemical Society, New York, 1968.

Erwin, J. H., W. J. Werner, and M. M. Martin, *Development and Fabrication of Instrumented-Plate Advanced Test Reactor Fuel Elements,* ORNL-4268 (October 1968).

Erwin, J. H., M. M. Martin, and W. R. Martin, "The Effect of Fuel Concentration on the Compressive Strength of Core Materials Used in Research Reactor Fuel Plates," (Summary) *Trans. Am. Nucl. Soc.* **11**(2), 490 (November 1968).

Farrell, K., C. K. H. DuBose, and J. O. Stiegler, "Metallography of an Aluminum Alloy Subjected to a High Neutron Fluence," (Abstract) *J. Metals* **20**(8), 116A (August 1968).

Farrell, K., and J. O. Stiegler, "Electron Fractography for Studying Cavities," *Metallurgia* **79**(471), 35–38 (January 1969).

Faulkner, J. S., "Calculation of Constant-Energy Surfaces for Aluminum by the Korringa-Kohn-Rostoker Method," *Phys. Rev.* **178**(3), 914–18 (February 1969).

Federer, J. I., W. C. Robinson, Jr., and F. H. Patterson, *Conversion of UF_6 to UO_2 in a Flame Reactor,* ORNL-TM-2327 (October 1968); also *Nucl. Appl.* **6**(4), 298–306 (April 1969).

Federer, J. I., *The Effect of Alloy Additions and Heat Treatments on the Mechanical Properties of U–0.5 % Ti Alloy,* ORNL-TM-2482 (February 1969).

Finch, C. B., and G. W. Clark, "Flux Growth and Characterization of Hexagonal Germanium Dioxide Single Crystals," *Am. Mineralogist* **53**(7,8), 1394–98 (July–August 1968).

Finch, C. B., L. J. Nugent, G. K. Werner, and M. M. Abraham, "Self-Activated Thermoluminescence in Several Lanthanide- and Actinide-Doped Thorium Dioxide Crystals," (Abstract) p. 637 in *Rare Earth Research Conf., 7th, Coronado, Calif., October 28–30, 1968,* Vol. II, Solar Division of International Harvester Company and the National Science Foundation, San Diego, Calif., 1968.

Fitts, R. B., A. R. Olsen, and J. Komatsu, "Sphere-Pac Fabrication of Sol-Gel Nuclear Fuels," (Abstract) *Am. Ceram. Soc. Bull.* **47**(9), 844 (September 1968).

Fitts, R. B., H. G. Moore, A. R. Olsen, and J. D. Sease, *Sol-Gel Thoria Extrusion,* ORNL-4311 (September 1968).

Fitzpatrick, C. M., and J. M. Leitnaker, *System for Vacuum Treatment and Nitrogen Equilibration at 1200 to 2000°C,* ORNL-TM-2429 (March 1969).

Foster, B. E., S. D. Snyder, and R. W. Knight, "X-Ray Attenuation Scanning of Nuclear Fuel Plates," pp. 459–66 in *Twenty-Third Annual Technical Conference, May 5–7, 1969, Los Angeles, California,* American Society for Quality Control, Milwaukee; also ORNL-TM-2525 (June 1969).

Foster, B. E., and S. D. Snyder, *An X-Ray Technique for Measuring Thickness of Tungsten on Copper,* ORNL-TM-2524 (June 1969).

Freid, S. H., J. A. Conlin, H. J. De Nordwall, C. L. Segaser, D. R. Cuneo, and E. L. Long, Jr., *Fission Product Release from an Overheated HTGR Fuel (ORR Poolside Capsule 06-11)*, ORNL-TM-2388 (February 1969).

Gehlbach, R. E., and H. E. McCoy, Jr., "Phase Instability in Hastelloy N," pp. 346–66 in *International Symposium on Structural Stability in Superalloys, Seven Springs, Pennsylvania, September 4–6, 1968*, Vol. II. Available from Dr. John Radavich, AIME High-Temperature Alloys Committee, Micromet Laboratories, West Lafayette, Ind.

Gehlbach, R. E., M. D. Allen, and J. D. Braun, "Autoradiographic Study of Carbon-14 in Hastelloy N," pp. 113–18 in *Proceedings, First Annual Technical Meeting, International Metallographic Society, Inc., November 11, 12, and 13, 1968 – Denver, Colorado, U.S.A.*, ed. by K. A. Johnson and J. H. Bender, International Metallographic Society, Inc., Los Alamos, N.M., 1969.

Godfrey, T. G., J. L. Scott, R. L. Beatty, J. H. Coobs, J. W. Prados, L. G. Overholser, and L. M. Ferris, *Coated-Particle Fuels*, ORNL-4324 (November 1968).

Goldman, A. E., and A. L. Lotts, "Parametric Studies of LMFBR Fuel Fabrication Costs," (Summary) *Trans. Am. Nucl. Soc.* **11**(2), 443 (November 1968).

Goldman, A. E., *Fuel Fabrication Cost Estimate for the GE-LMFBR Concept Presented in GEAP-4939*, ORNL-TM-2344 (November 1968).

Gould, R. W., S. R. Bates, and C. J. Sparks, "Application of the Graphite Monochromator to Light Element X-Ray Spectroscopy," *Appl. Spectry.* **22**(5), Part 1, 549–51 (September/October 1968).

Gray, R. J., "New Methods Point the Way," *Metal Progr.* **94**(2), 133–43 (August 1968).

Gray, R. J., "Testing and Inspection," *Metal Progr.* **95**(1), 27–28 (January 1969).

Gray, R. J., and B. C. Leslie, "A Metallograph for Glove Box Operations," pp. 119–25 in *Proceedings, First Annual Technical Meeting, International Metallographic Society, Inc., November 11, 12, and 13, 1968 – Denver, Colorado, U.S.A.*, ed. by K. A. Johnson and J. H. Bender, International Metallographic Society, Inc., Los Alamos, N.M., 1969.

Hammond, J. P., and G. M. Slaughter, "Powder Metallurgy Transition Joint for Joining Graphite to Metals," (Abstract) *P/M Newsletter* **3**(2), 3 (April 1969).

Hammond, R. P., C. C. Burwell, R. S. Carlsmith, J. G. Delene, L. C. Fuller, A. E. Goldman, D. B. Lloyd, J. T. Roberts, J. E. Savolainen, and R. P. Wichner, *The Unclad-Metal Breeder Reactor (UMBR) for Desalting or Power*, ORNL-4202 (January 1969).

Harman, D. G., "Improved Resistance to Radiation Damage in Incoloy 800," (Summary) *Trans. Am. Nucl. Soc.* **11**(2), 500–01 (November 1968).

Harman, D. G., "Enhanced Postirradiation Ductility of Incoloy 800," (Abstract) *J. Metals* **20**(8), 117A (August 1968).

Harman, D. G., *Postirradiation Tensile and Creep-Rupture Properties of Several Experimental Heats of Incoloy 800 at 700 and 760°C*, ORNL-TM-2305 (December 1968).

Harman, D. G., and T. A. Nolan, *Fracture Initiation in XAP-001 SAP Alloy*, ORNL-TM-2324 (February 1969).

Harman, D. G., *Thermal Fatigue of Rocket Nozzle Cooling Tubes*, ORNL-TM-2089 (February 1969).

Harms, W. O., and A. P. Litman, "Compatibility of Materials with Alkali Metals for Space Nuclear Power Systems," *Nucl. Appl.* **5**(3), 156–72 (September 1968).

Hendricks, R. W., J. S. Arrington, Jr., and W. J. Mason, "An automatic balanced filter device for X-ray diffraction experiments," *J. Appl. Cryst.* **1**(Part 2), 128–29 (June 1968).

Hendricks, R. W., C. C. Koch, and G. R. Love, "Kinetics of the Omega Transformation in Ti-23 a/o Nb," (Abstract) *J. Metals* **20**(8), 121A–22A (August 1968).

Hewette, D. M., II, *High-Temperature Fast-Neutron Irradiation of Pyrolytic-Carbon-Coated ThO_2 Microspheres*, ORNL-TM-2475 (March 1969); also *Carbon* **7**(3), 373–78 (June 1969).

Hobson, D. O., "Examination of Orientation Factors for the Deformation Systems of Zirconium Under Biaxial Stress Conditions," (Abstract) *J. Metals* **20**(8), 34A (August 1968).

Hobson, D. O., and P. L. Rittenhouse, "Nonhomogeneous Deformation in Zircaloy Tubing," *Trans. Met. Soc. AIME* **245**(4), 797–800 (April 1969).

Hobson, D. O., and E. Tenckhoff, "Effects of Fabrication Parameters on Textures Produced in Zircaloy Cladding," (Summary) *Trans. Am. Nucl. Soc.* **12**(1), 134 (June 1969).

Homan, F. J., *Plant Size Optimization in a Growing Nuclear Fuel Fabrication Industry,* ORNL-TM-2346 (December 1968).

Homan, F. J., and T. N. Washburn, "Capacity Expansion Optimization in a Growing Nuclear Fuel Fabrication Industry," (Summary) *Trans. Am. Nucl. Soc.* **12**(1), 25 (June 1969).

Houston, J. T., and K. Farrell, "Correlation of Hardness with Microstructure in X8001 Aluminum Alloy," *Metallography* **1**(2), 243–47 (November 1968).

Inouye, H., "Interactions of Refractory Metals with Active Gases in Vacua and Inert Gas Environments," pp. 165–95 in *Refractory Metal Alloys Metallurgy and Technology,* ed. by I. Machlin, R. T. Begley, and E. D. Weisert, Plenum Press, New York, 1968; also ORNL-4312 (October 1968).

Inouye, H., "Equilibrium Solid Solutions of Nitrogen in Cb-1% Zr Between 1200 and 1800°C," pp. 301–15 in *Refractory Metals and Alloys IV, Research and Development, Vol. 1, Met. Soc. Conf.* **41**, ed. by R. I. Jaffee, C. M. Ault, J. Maltz, and M. Semchyshen, Gordon & Breach, New York, 1967.

Inouye, H., "Heat-Resisting Metals and Alloys," *Metal Progr.* **95**(1), 20–21 (January 1969).

Inouye, H., *High-Temperature Sorption of Nitrogen by Nb–1% Zr in Ultrahigh Vacuum,* ORNL-4403 (May 1969).

Jansen, D. H., J. H. DeVan, C. W. Cunningham, L. C. Fuller, and R. E. MacPherson, *Niobium–1% Zirconium Boiling-Potassium Forced-Circulation Loop Test,* ORNL-4301 (December 1968).

Kasten, P. R., E. S. Bettis, W. H. Cook, W. P. Eatherly, D. K. Holmes, R. J. Kedl, C. R. Kennedy, S. S. Kirslis, H. E. McCoy, A. M. Perry, R. C. Robertson, D. Scott, and R. A. Strehlow, *Graphite Behavior and Its Effects on MSBR Performance,* ORNL-TM-2136 (February 1969).

Kegley, T. M., Jr., *Metallographic Preparation of Cerium Carbides,* ORNL-TM-2239 (July 1968).

Kegley, T. M., Jr., D. M. Hewette II, and B. C. Leslie, "Effect of Vibratory Polishing on the Appearance of Pyrolytic-Carbon Coatings," *Metallography* **1**(2), 237–41 (November 1968).

Kegley, T. M., Jr., and F. M. Empson, *Examination of Modified Pillar and Simulated Waste Container Test Heaters,* ORNL-TM-2422 (January 1969).

Kennedy, C. R., "Irradiation of Graphite in HFIR," (Summary) *Trans. Am. Nucl. Soc.* **11**(2), 623–24 (November 1968).

King, R. T., and E. L. Long, Jr., "Irradiation Damage to 1100 Aluminum at High Fast Neutron Fluences," (Abstract) *J. Metals* **20**(8), 116A (August 1968).

King, R. T., and J. R. Weir, Jr., "The Effects of Cyclotron-Injected Helium on the Creep-Rupture Properties of Type 304 and 0.2% Ti Type 304L Stainless Steel," (Abstract) *J. Metals* **20**(8), 64A (August 1968).

King, R. T., "Biaxial Creep Rupture of 0.2% Ti-Modified Type 304L Stainless Steel Tubing," (Summary) *Trans. Am. Nucl. Soc.* **12**(1), 135 (June 1969).

Klueh, R. L., "The Effect of Oxygen in Sodium on the Compatibility of Sodium with Niobium," pp. 171–76 in *Proceedings of the International Conference on Sodium Technology and Large Fast Reactor Design, November 7–9, 1968,* ANL-7520, Part 1.

Klueh, R. L., *Interactions in Alkali Metal Solutions Containing Oxygen I. The Niobium-Oxygen-Potassium System,* ORNL-TM-2476 (February 1969).

Klueh, R. L., *Oxygen Determination and Purification of Liquid Alkali Metals by Zirconium Gettering,* ORNL-TM-2473 (March 1969).

Koch, C. C., and G. R. Love, "Superconductivity in the System Niobium-Gadolinium," (Abstract) *J. Metals* **20**(8), 99A–100A (August 1968).

Koch, C. C., and C. J. McHargue, "The Influence of Plastic Deformation on the F.C.C. ⇌ D.H.C.P. Transformation in Cerium," *Acta Met.* **16**(9), 1105–15 (September 1968).

Koch, C. C., and C. J. McHargue, "Phase Transformations Associated with Sm-Type Structure in the Gd-Ce System," pp. 541–49 in *Rare Earth Research Conf., 7th, Coronado, Calif., October 28–30, 1968,* Vol. II, Solar Division of International Harvester Company and the National Science Foundation, San Diego, California, 1968.

Koger, J. W., and A. P. Litman, *Compatibility of Hastelloy N and Croloy 9M with $NaBF_4$-NaF-KBF_4 (90-4-6 mole %) Fluoroborate Salt,* ORNL-TM-2490 (April 1969).

Koger, J. W., and A. P. Litman, "Kinetic Behavior of Chromium and Iron in Some Iron- and Nickel-Base Alloys Exposed to Fluoride Salts," *J. Metals* **20**(12), 206A–207A (December 1968).

Kollie, T. G., D. L. McElroy, M. Barisoni, and C. R. Brooks, *Pulse Calorimetry Using a Digital Voltmeter for Transient Data Acquisition,* ORNL-4380 (February 1969).

Kollie, T. G., D. L. McElroy, and C. R. Brooks, *Convolute Method of Smoothing or Calculating the Time Derivatives of a Signal Recorded in Digital Form at Equal Time Intervals,* ORNL-TM-2517 (April 1969).

Kopp, O. C., and G. W. Clark, "Hydrothermal Synthesis, Optical Perfection, and Surface Topography of Quartz Grown in RbOH and Other Alkali Hydroxides," *J. Cryst. Growth* **2**(5), 308–12 (September–October 1968).

Leitnaker, J. M., R. L. Beatty, and K. E. Spear, "Oxygen Contamination – A Possible Advantage in Mixed (U,Pu)N," (Summary) *Trans. Am. Nucl. Soc.* **12**(1), 86–87 (June 1969).

Lindemer, T. B., M. D. Allen, and J. M. Leitnaker, "Kinetics of the Graphite-Uranium Dioxide Reaction from 1400° to 1756°C," *J. Am. Ceram. Soc.* **52**(5), 233–37 (May 1969).

Lindemer, T. B., and M. D. Allen, "A Metallographic Method for Studying Reaction Kinetics in Spheres," *ASM (Am. Soc. Metals) Trans. Quart.* **62**(2), 547–48 (June 1969).

Liu, C. H., John Hasson, and G. P. Smith, "Potentiometric and Spectrophotometric Studies of Nickel(II)–Nitrate Complexes in Molten Dimethyl Sulfone and in the Molten $LiNO_3$–$NaNO_3$–KNO_3 Eutectic," *Inorg. Chem.* **7**(11), 2244–47 (November 1968).

Liu, C. H., and L. R. Lieto, "Phase Diagram of the Lithium Iodide–Potassium Iodide System and Densities of the Lithium Iodide–Potassium Iodide and Lithium Bromide–Potassium Bromide Eutectics," *J. Chem. Eng. Data* **14**(1), 83–84 (January 1969).

Loh, B. T. M., E. E. Bloom, and J. O. Stiegler, "Annealing Behavior of Voids in Irradiated Stainless Steel," (Abstract) *J. Metals* **20**(8), 115A (August 1968).

Loh, B. T. M., "Dynamics of Slip Band Formation," pp. 13–20 in *Proc. Intern. Conf. Strength of Metals and Alloys, Tokyo, 1967,* Supplement to *Trans. Japan Inst. Metals* **9** (1968).

Lotts, A. L., T. N. Washburn, and F. J. Homan, *FABCØST 9, A Computer Code for Estimating Fabrication Costs for Rod-Bundle Fuel Elements,* ORNL-4287 (August 1968).

Lotts, A. L., and R. G. Wymer, *Economics and Technology of HTGR Fuel Recycle,* ORNL-TM-2377 (October 1968); also pp. 789–813 in *Advanced and High-Temperature Gas-Cooled Reactors* (Proceedings of a Symposium on Advanced and High-Temperature Gas-Cooled Reactors Held by the International Atomic Energy Agency in Jülich, 21–25 October, 1968) International Atomic Energy Agency, Vienna, 1969.

Love, G. R., and C. C. Koch, "On the Scale of Significant Flux-Pinning Defects in Superconductors," (Abstract) *J. Metals* **20**(8), 99A (August 1968).

Love, G. R., and C. C. Koch, "Flux Pinning by Grain Boundaries in Superconducting Niobium-Zirconium Alloys," *Appl. Phys. Letters* **14**(8), 250–52 (April 1969).

Lundy, T. S., and R. E. Pawel, "Short-Circuiting Diffusion in Body-Centered Cubic Metals," (Abstract) *J. Metals* **20**(8), 52A–53A (August 1968).

Lundy, T. S., and R. A. Padgett, "The Near-Surface Effect for Diffusion in Silver," *Trans. Met. Soc. AIME* **242**(9), 1897–1900 (September 1968).

Lundy, T. S., and R. E. Pawel, "Effects of Short-Circuiting Paths on Diffusion Coefficient Measurements," *Trans. Met. Soc. AIME* **245**(2), 283–86 (February 1969).

Martin, M. M., and A. E. Richt, "Effect of Void Volume on the Irradiation Performance of Aluminum-Base Dispersion-Type Fuel Plates," (Summary) *Trans. Am. Nucl. Soc.* **12**(1), 98–99 (June 1969).

Martin, W. R., "Application of Today's Materials Studies to Tomorrow's Operation of Research Reactors," (Summary) *Trans. Am. Nucl. Soc.* **11**(2), 626–27 (November 1968).

Martin, W. R., and J. M. Jones, *Performance and Stability of Borosilicate Glasses During Rolling of Stainless Steel UO_2 Fuel Coupons,* ORNL-TM-2417 (February 1969).

McClung, R. W., R. B. Oliver, and R. R. Rowand, "Technical Problem Areas," Sect. IV in *Nondestructive Evaluation,* NMAB-252, National Academy of Sciences-National Academy of Engineering, Washington, D.C. (June 1969).

McClung, R. W., "Low Voltage Radiographic and Microradiographic Techniques for Graphite," pp. 97–108 in *Nondestructive Testing of Nuclear Graphite* (A symposium presented at the Seventieth Annual Meeting, American Society for Testing and Materials, Boston, Mass., 25–30 June, 1967), *Am. Soc. Testing Mater. Spec. Tech. Publ.* **439**, American Society for Testing and Materials, Philadelphia, Pa., July 1968.

McCoy, H. E., Jr., *Physical and Mechanical Properties of Type 406 Stainless Steel,* ORNL-TM-2263 (October 1968).

McCoy, H. E., Jr., and D. L. McElroy, "Electrical Resistivity Anomaly in Nickel-Base Alloys," *ASM (Am. Soc. Metals) Trans. Quart.* **61**(4), 730–41 (December 1968).

McCoy, H. E., Jr., *An Evaluation of the Molten-Salt Reactor Experiment Hastelloy N Surveillance Specimens – Second Group,* ORNL-TM-2359 (February 1969).

McCoy, H. E., "Variation of the Mechanical Properties of Irradiated Hastelloy N with Strain Rate," *J. Nucl. Mater.* **31**(1), 67–85 (May 1969).

McCoy, H. E., and D. A. Canonico, *Preirradiation and Postirradiation Mechanical Properties of Hastelloy N Welds,* ORNL-TM-2483 (March 1969); also *Welding J. (N.Y.)* **48**(5), 203-s–211-s (May 1969).

McCoy, H. E., J. R. Weir, Jr., R. L. Beatty, W. H. Cook, C. R. Kennedy, A. P. Litman, R. E. Gehlbach, C. E. Sessions, and J. W. Koger, *Materials for Molten-Salt Reactors,* ORNL-TM-2511 (May 1969).

Miller, J. L., Jr., "Replication of Irradiated Materials," *Metallography* **1**(3-4), 443–47 (January 1969).

Moore, J. P., R. K. Williams, and D. L. McElroy, "Physical Properties of Chromium from 77 to 400°K," pp. 297–310 in *Thermal Conductivity, Proc. 7th Conf. Gaithersburg, Maryland, Nov. 13–16, 1967, Nat. Bur. Std. Spec. Publ.* **302**, ed. by D. R. Flynn and B. A. Peavy, Jr., National Bureau of Standards, Washington, D.C., September 1968.

Moore, J. P., D. L. McElroy, and R. S. Graves, "Thermal Conductivity of a 58% Dense MgO Powder in Nitrogen," (Abstract) p. 711 in *Thermal Conductivity, Proc. 7th Conf. Gaithersburg, Maryland, Nov. 13–16, 1967, Nat. Bur. Std. Spec. Publ.* **302**, ed. by D. R. Flynn and B. A. Peavy, Jr., National Bureau of Standards, Washington, D.C., September 1968.

Moore, J. P., R. K. Williams, and D. L. McElroy, "Further Comments on Transport Properties of Chromium," pp. 303–13 in *Thermal Conductivity, Proc. 8th Conf.,* ed. by C. Y. Ho and R. E. Taylor, Plenum Press, New York, 1969.

Morgan, C. S., "Densification Kinetics During Nonisothermal Sintering of Oxides," Chap. 19, pp. 349–61 in *Materials Science Research,* Vol. 4, Plenum Press, New York, 1969.

Morgan, C. S., "Comment on 'Dorn Method in the Study of Initial Phase of Uranium Dioxide Sintering,' " *J. Am. Ceram. Soc.* **51**(12), 724 (December 1968).

Morgan, C. S., "Activation Energy in Sintering," (Abstract) *P/M Newsletter* **2**(4), 2 (November 1968).

Mortlock, A. J., "The Near-Surface Diffusion Anomaly in Gold," *Trans. Met. Soc. AIME* **242**(9), 1963–67 (September 1968).

Newman, G. T., and D. W. Short, "The Effect of Prestrain on the Creep Properties of Irradiated and Unirradiated Type 304L Modified Stainless Steel," (Abstract) *J. Metals* **20**(8), 115A–16A (August 1968).

Nilsson, T. M., *On the Anisotropy in Mechanical Properties of Extruded Commercial SAP Materials,* ORNL-TM-2322 (October 1968); also *J. Nucl. Mater.* **28**(2), 220–24 (November 1968).

Nilsson, T. M., *Effect of Working Direction on the Microstructure and Mechanical Properties of an Extruded SAP Alloy,* ORNL-TM-2355 (December 1968).

Nilsson, T. M., and G. A. Reimann, "Evaluation of Titanium-Modified Type 304L Stainless Steel Tubing," (Summary) *Trans. Am. Nucl. Soc.* **12**(1), 134–35 (June 1969).

Patriarca, P., and W. O. Harms, *Fuels and Materials Development Program Quart. Progr. Rept. June 30, 1968,* ORNL-4330.

Patriarca, P., and W. O. Harms, *Fuels and Materials Development Program Quart. Progr. Rept. Sept. 30, 1968,* ORNL-4350.

Patriarca, P., *Fuels and Materials Development Program Quart. Progr. Rept. Dec. 31, 1968,* ORNL-4390.

Patriarca, P., *Fuels and Materials Development Program Quart. Progr. Rept. Mar. 31, 1969,* ORNL-4420.

Pawel, R. E., and J. J. Campbell, "Stress Generation during High-Temperature Oxidation I. Oxygen Solution Effects," *J. Electrochem. Soc.* **116**(6), 828–32 (June 1969).

Picklesimer, M. L., "Theory and Practice of the Selection of the Plans of Examination," pp. 326–35 in *Quantitative Microscopy,* ed. by R. T. DeHoff and F. N. Rhines, McGraw-Hill Book Company, New York, 1968.

Pih, Hui, and L. S. Snyders, "Photoelastic Studies of Ultrasonic Waves in a Large Plate," *Exp. Mech.* **9**(4), 1–7, (April 1969).

Pratt, R. B., and A. E. Goldman, *Fuel Element Fabrication Costs for Dragon Project Low-Enrichment, High-Temperature Gas-Cooled Reactor Concept,* ORNL-TM-2241 (September 1968).

Pratt, R. B., J. D. Sease, and A. L. Lotts, *Pilot-Scale Equipment Development for Pyrolytic-Carbon Coating,* ORNL-4302 (December 1968).

Pratt, R. B., *Conceptual Economic Analysis of Flame Reactor Conversion of UF_6 to UO_2,* ORNL-TM-2409 (February 1969).

Pratt, R. B., J. D. Sease, W. H. Pechin, and A. L. Lotts, "Pyrolytic Carbon Coating in an Engineering-Scale System," *Nucl. Appl.* **6**(3), 241–55 (March 1969).

Reagan, P. E., D. M. Hewette II, and J. G. Morgan, *Comparison of Observed and Predicted Irradiation Performance of Pyrolytic-Carbon-Coated Uranium Dioxide Particles,* ORNL-TM-2336 (December 1968).

Reed, R. E., C. W. Dean, R. E. McDonald, and J. F. Emery, *Sources of Contamination During Electron-Beam Melting,* ORNL-TM-2208 (July 1968); also pp. 516–29 in *Electron and Ion Beam Science and Technology, Proc. 3rd Intern. Conf. Boston, 1968,* ed. by R. A. Bakish, Electrochemical Society, New York, 1968.

Reed, R. E., and J. C. Wilson, "Purification of a Metal by Electron-Beam Heating," Chap. 24, pp. 235–47 in *Purification of Inorganic and Organic Materials,* ed. by Morris Zief, Marcel Dekker, Inc., New York, 1969.

Reimann, D. K., and T. S. Lundy, "Diffusion of U-233 in UN and UO_2 Single Crystals," (Abstract) *J. Metals* **20**(8), 54A–55A (August 1968).

Reimann, D. K., and T. S. Lundy, "Cation Self-Diffusion in UO_2," *J. Nucl. Mater.* **28**(2), 218–19 (November 1968).

Richt, A. E., and V. O. Haynes, *Inspection of Europium-Bearing Control Rods from the Army SM-1A Stationary Medium Power Reactor,* ORNL-TM-2349 (January 1969).

Richt, A. E., and V. O. Haynes, *Postirradiation Nondestructive Examination of a Silver-Cadmium-Indium Control Rod from the Army SM-1 Power Reactor,* ORNL-TM-2506 (June 1969).

Rittenhouse, P. L., *Failure Modes of Zircaloy-Clad Fuel Rods,* ORNL-TM-2347 (Sept. 13, 1968); *Part 2: Program Revisions,* ORNL-TM-2548 (May 1969).

Rittenhouse, P. L., "Plastic Yielding of Highly Textured Zircaloy Tubing," (Abstract) *J. Metals* **20**(8), 34A (August 1968).

Robinson, W. C., Jr., and W. R. Martin, *A Feasibility Study of the Conversion of PuF_6 to PuO_2 by Chemical Vapor Deposition,* ORNL-TM-2306 (August 1968).

Robinson, W. C., Jr., J. I. Federer, and W. R. Martin, "Use of Chemical Vapor Deposition to Convert Halides to Fissionable Fuel Compounds," pp. 51–62 in *Fluoride Volatility 1968, Proc. Rocky Flats Fluoride Volatility Conf., June 24–25, 1968,* ed. by J. M. Cleveland and M. A. Thompson, CONF-680610.

Scarbrough, J. O., H. L. Davis, W. Fulkerson, and J. O. Betterton, Jr., "Specific Heat of Uranium Mononitride from 1.3 to 4.6°K," *Phys. Rev.* **176**(2), 666–71 (December 1968).

Scott, J. L., and S. C. Weaver, *Fuels for Water Reactors,* ORNL-TM-2357 (December 1968).

Sears, M. B., R. J. Gray, L. M. Ferris, and B. C. Leslie, *Correlation of Composition and Heat-Treatment with the Microstructures of Uranium Carbides,* ORNL-3515 (July 1968).

Sears, M. B., T. M. Kegley, Jr., L. M. Ferris, and B. C. Leslie, *Metallographic Preparation of Arc-Cast Thorium Carbides and Correlation of Their Microstructures with Composition,* ORNL-4354 (March 1969).

Sessions, C. E., and H. E. McCoy, "High-Temperature Irradiation Damage in the Nickel-Base Alloy, Hastelloy N," (Abstract) *J. Metals* **20**(8), 117A (August 1968).

Sessions, C. E., and H. E. McCoy, "Development of Hastelloy-N with Improved Resistance to Irradiation Damage," (Summary) *Trans. Am. Nucl. Soc.* **11**(2), 621 (November 1968).

Sessions, C. E., and T. S. Lundy, *Diffusion of Titanium in Modified Hastelloy N,* ORNL-TM-2392 (January 1969).

Sessions, C. E., and E. E. Stansbury, "Comparison of the Thermal Stability of Titanium-Modified Hastelloy N at 650 and 760°C," (Summary) *Trans. Am. Nucl. Soc.* **12**(1), 136–37 (June 1969).

Slaughter, G. M., E. A. Franco-Ferreira, E. L. Long, Jr., and G. Hallerman, "Technical Note: Unusual Weld Cracking Problem in Inconel," *Welding J. (N.Y.)* **47**(10), 479-s–480-s (October 1968).

Spear, K. E., and J. M. Leitnaker, "A Consistent Set of Thermodynamic Values for Plutonium Mononitride," *J. Am. Ceram. Soc.* **51**(12), 706–9 (December 1968).

Spear, K. E., A. R. Olsen, and J. M. Leitnaker, *Thermodynamic Applications to $(U,Pu)O_{2\pm x}$ Fuel Systems,* ORNL-TM-2494 (April 1969).

Spear, K. E., and J. M. Leitnaker, "Formation of Active Carbon in Twin-Crucible Studies of Vanadium Carbonitride Solutions," *J. Am. Ceram. Soc.* **52**(5), 257–62 (May 1969).

Spruiell, J. E., *Chemical Vapor Deposition of Silicon Carbide from Silicon Tetrachloride-Methane-Hydrogen Mixtures,* ORNL-4326 (December 1968).

Starke, E. A., Jr., J. C. Ogle, and C. J. Sparks, Jr., "Texture Transition in Ordered Cu_3Au," *Trans. Met. Soc. AIME* **245**(1), 169–70 (January 1969).

Stephenson, R. L., "The Creep-Rupture Properties of Some Refractory Metal Alloys, I. Effect of Heat Treatment on the Properties of the Niobium-Base Alloy D-43," *J. Less-Common Metals* **15**(4), 395–402 (August 1968).

Stephenson, R. L., "The Creep-Rupture Properties of Some Refractory Metal Alloys, II. The Properties of the Niobium-Base Alloys FS-85 and Cb-752 and Their Response to Heat Treatment," *J. Less-Common Metals* **15**(4), 403–14 (August 1968).

Stephenson, R. L., and H. E. McCoy, Jr., "The Creep-Rupture Properties of Some Refractory Metal Alloys, III. Comparative Mechanical Behavior of Some Tantalum-Base Alloys," *J. Less-Common Metals* **15**(4), 415–24 (August 1968).

Stephenson, R. L., "The Effect of Fabrication Variables on the Creep-Rupture Properties of Molybdenum-Base Alloys," (Abstract) *J. Metals* **20**(8), 65A (August 1968).

Stephenson, R. L., "The Effect of Fabrication Variables on the Creep-Rupture Properties of Molybdenum-Base Alloys," *Trans. Met. Soc. AIME* **245**(5), 997–1001 (May 1969).

Stephenson, R. L., "Comparative Creep-Rupture Properties of D-43 and B-66 Columbium Alloys," pp. 789–806 in *Refractory Metals and Alloys IV, Research and Development, Vol. 2, Met. Soc. Conf.* **41**, ed. by R. I. Jaffee *et al.*, Gordon & Breach, New York, 1967.

Stiegler, J. O., and J. R. Weir, Jr., "Effects of Irradiation on Ductility," pp. 311–42 in *Ductility* (Papers presented at a Seminar of the American Society for Metals, October 14 and 15, 1967), American Society for Metals, Metals Park, Ohio, 1968.

Tenckhoff, E., and P. L. Rittenhouse, "Deformation and Annealing Textures in Drawn Zircaloy Tubing," (Abstract) *J. Metals* **20**(8), 30A (August 1968).

Vandermeer, R. A., and J. C. Ogle, "The Development of Preferred Orientations in Cold-Rolled Niobium (Columbium)," *Trans. Met. Soc. AIME* **242**(7), 1317–26 (July 1968).

Vandermeer, R. A., and J. C. Ogle, "Possible Causes for Texture Inhomogeneities in Cold-Rolled Niobium," (Abstract) *J. Metals* **20**(8), 30A (August 1968).

Wamorkar, R. R., and R. W. McClung, *Intensifying Screens for Radiography with Energies Between 70 and 140 Kilovolts Constant Potential,* ORNL-TM-2488 (March 1969).

Washburn, T. N., "Porous UO_2 Bodies Produced by Reduction of U_3O_8," (Summary) *Trans. Am. Nucl. Soc.* **12**(1), 206–7 (June 1969).

Weir, J. R., J. O. Stiegler, and E. E. Bloom, *Irradiation Behavior of Cladding and Structural Materials,* ORNL-TM-2258 (September 1968); also pp. 189–224 in *Proceedings of the National Topical Meeting on Fast Reactor Systems, Materials and Components, Cincinnati, Ohio, April 2–4, 1968,* ed. by W. E. Niemuth and J. F. Weissenberg, CONF-680419.

Werner, W. J., and G. M. Slaughter, "Brazing of Graphite for Molten-Salt Applications," (Summary) *Trans. Am. Nucl. Soc.* **11**(2), 623 (November 1968).

Whaley, H. L., K. V. Cook, R. W. McClung, and L. S. Snyders, "Optical Methods for Studying Ultrasonic Propagation in Transparent Media," pp. 125–31 in *Proceedings of the Fifth International Conference on Nondestructive Testing Canada, 1967,"* The Queen's Printer, Ottawa, Canada, 1969.

Whaley, H. L., *Development of Nondestructive Tests for Intermediate Fabrication of Sintered Aluminum Products,* ORNL-4352 (February 1969).

Wiffen, F. W., and J. O. Stiegler, "Voids in Neutron-Irradiated Vanadium," (Abstract) *J. Metals* **20**(8), 117A–18A (August 1968).

Wiffen, F. W., and J. O. Stiegler, "Irradiation Damage in Vanadium at 600°C," (Summary) *Trans. Am. Nucl. Soc.* **12**(1), 119–20 (June 1969).

Williams, R. K., J. P. Moore, R. S. Graves, T. E. Banks, and D. L. McElroy, "Physical Properties of Molybdenum from 80 to 1300 K," (Abstract) p. 301 in *Thermal Conductivity, Proc. 8th Conf.,* ed. by C. Y. Ho and R. E. Taylor, Plenum Press, New York, 1969.

Williams, R. K. and W. Fulkerson, "Separation of the Electronic and Lattice Contributions to the Thermal Conductivity of Metals and Alloys," pp. 389–456 in *Thermal Conductivity, Proc. 8th Conf.,* ed. by C. Y. Ho and R. E. Taylor, Plenum Press, New York, 1969.

Williams, Ralph O., and R. W. Hendricks, *Program Tape: A General Purpose Program for Converting ASCII Coded Punched Paper Tapes to 7-Level BCD or EBCDIC Magnetic Tapes in the CDC 160-A Computer,* ORNL-TM-2269 (September 1968).

Williams, R. O., "Analytical Methods for Representing Complex Textures by Biaxial Pole Figures," *J. Appl. Phys.* **39**(9), 4329–35 (August 1968).

Williams, R. O., "The Representation of Thermodynamic Functions for Binary Solutions as Fourier Series," (Abstract) *J. Metals* **20**(8), 7A (August 1968).

Williams, R. W., and H. L. Davis, "Calculations Pertaining to the Thermopower of Copper," *Phys. Letters* **28A**(6), 412–13 (December 1968).

Wilson, J. C., "Advantages of Electron-Beam Heating in a Metallurgical Heat-Treating Furnace," (Abstract No. 138) Sect. 4 in *Electron and Ion Beam Science and Technology, Proc. 3rd Intern. Conf. Boston, 1968,* ed. by R. A. Bakish, Electrochemical Society, New York, 1968.

Wolfenden, A., "The Energy Stored During the Low-Temperature Tensile Deformation of Copper and Aluminum," (Abstract) *J. Metals* **20**(8), 43A (August 1968).

Wolfenden, A., "The Ratio of Stored to Expended Energy During the Low-Temperature Deformation of Copper and Aluminum Single Crystals," (Abstract) *J. Metals* **20**(8), 112A (August 1968).

Wolfenden, A., "The New Formulation of the Kuhlmann-Wilsdorf Theory of Work Hardening Analyzed in Terms of Stored Energy Data," *Scripta Met.* **2**(11), 621–24 (November 1968).

Wolfenden, A., "Calibration Heater for a Liquid-Vapor Deformation Calorimeter," *Rev. Sci. Instr.* **40**(5), 712–14 (May 1969).

Wolfenden, A., "The Energy Stored in Silver Single Crystals," *Acta Met.* **17**(5), 585–93 (May 1969).

Wolfenden, A., and K. Farrell, "Bubble Growth Processes at Grain Boundaries in CVD Tungsten," *J. Nucl. Mater.* **29**(2), 133–43 (February 1969).

Wymer, R. G., and A. L. Lotts, *Status and Progress Report for Thorium Fuel Cycle Development for Period Ending December 31, 1966,* ORNL-4275.

Wymer, R. G., and A. L. Lotts, *Status and Progress Report for Thorium Fuel Cycle Development for 1967 and 1968,* ORNL-4429.

Yakel, H. L., "Crystal Structures of Transition Phases Formed in Uranium–16.60 at. % Niobium–5.64 at. % Zirconium Alloys," *Acta Cryst.* **A25**(Abstract III-8), s-16 (Supplement May 1, 1969).

Yakel, H. L., *Program STEREO: A FORTRAN-Language Program for Plotting Stereographic Projections of Lattice Plane Normals and Directions,* ORNL-TM-2461 (March 1969).

Yoo, M. H., "Dislocation Reactions In H.C.P. Metals," (Abstract) *J. Metals* **20**(8), 12A (August 1968).

Yoo, M. H., "$\vec{c} + \vec{a}$ Dislocation Reactions in H.C.P. Metals," *Scripta Met.* **2**(10), 537–40 (October 1968).

Yust, C. S., and C. J. McHargue, "Dislocation Substructures in Deformed UO_2 Single Crystals," (Abstract) *J. Metals* **20**(8), 111A–12A (August 1968).

Yust, C. S., and C. J. McHargue, "Deformation of UO_2 Single Crystals," (Summary) *Trans. Am. Nucl. Soc.* **11**(2), 487 (November 1968).

Yust, C. S., and C. J. McHargue, "Dislocation Substructures in Deformed Uranium Dioxide Single Crystals," *J. Nucl. Mater.* **31**(2), 121–37 (June 1969).

Bibliography of the Technical Literature of the Metals and Ceramics Division for the Period 1948 Through June 30, 1967, ORNL-4270 (October 1968).

METALS AND CERAMICS DIVISION

DIRECTOR J. H. FRYE, JR.
BERTIE BYRUM

ASSOCIATE DIRECTOR J. E. CUNNINGHAM
MARGE WHITE

SECTION CHIEF G. M. ADAMSON, JR.[2]
FREDA FINN
BETTE THOMAS

PROJECT COORDINATION
HFIR – G. M. ADAMSON, JR.[2]
ALUMINUM COORDINATION – W. R. MARTIN[2]
DESALINATION – G. M. SLAUGHTER[2]

MATERIALS PROCESSING
W. R. MARTIN[2]
A. K. CHAKRABORTY
G. L. COPELAND
J. H. ERWIN
J. I. FEDERER
R. W. KNIGHT
M. M. MARTIN
R. E. McDONALD
T. NILSSON
G. A. REIMANN
A. C. SCHAFFHAUSER
L. L. ALLEN
J. K. ALLEY
G. E. ANGEL
T. W. COFFEY
C. E. DUNN
J. B. FLYNN
L. L. FRANCIS
D. G. GATES
J. W. GEER
G. D. GOLDSTON
J. N. HIX
C. W. HOLLAND
W. R. JOHNSON
R. S. PULLIAM
L. QUEENER
H. E. REESOR
E. R. TURNBILL
H. J. WALLACE

METALLOGRAPHY
R. J. GRAY
R. S. CROUSE
E. L. LONG, JR.
D. R. CUNEO[3]
T. M. KEGLEY, JR.
B. C. LESLIE
H. HATTER
J. L. MILLER, JR.
A. E. RICHT
M. D. ALLEN
N. M. ATCHLEY
E. R. BOYD
J. W. CHUMLEY
M. A. COMBS
W. E. DENNY
W. H. FARMER
H. R. GADDIS
W. D. GHORMLEY, JR.
J. C. GOWER
E. P. GRIGGS
C. P. HALTOM
T. J. HENSON
E. H. LEE
K. RUSSELL
L. G. SHRADER
E. D. SIMS
G. D. STOHLER
S. E. SPENCER
H. R. TINCH
P. M. WALLACE
W. H. WARRICK
C. E. ZACHARY

WELDING AND BRAZING
G. M. SLAUGHTER
D. CANONICO
N. C. COLE
G. M. GOODWIN
R. W. GUNKEL
J. P. HAMMOND
W. J. WERNER
S. W. BROYLES
C. W. HOUCK
J. D. HUDSON
L. C. WILLIAMS
J. J. WOODHOUSE

FUEL ELEMENT PROCUREMENT
R. J. BEAVER
W. J. LEONARD

SPECIAL ASSIGNMENT
R. G. STARK
C. H. WODTKE

SECTION CHIEF R. S. BORIE[2]
FRANCES LOVING
WILMA MASON

THEORY
J. S. FAULKNER
H. W. JOY

CRYSTAL PHYSICS
G. W. CLARK
C. B. FINCH
H. M. SMITH
J. C. WILSON

FUNDAMENTAL CERAMICS STUDIES
W. FULKERSON[2]

PHYSICAL PROPERTIES
D. L. McELROY
KARL-HEINZ BODE
W. FULKERSON[2]
T. G. KOLLIE
J. P. MOORE
P. SPINDLER
R. K. WILLIAMS
R. W. WILLIAMS
R. S. GRAVES

REACTIONS AT METAL SURFACES
J. V. CATHCART
R. E. PAWEL
G. F. PETERSEN
J. J. CAMPBELL

SPECTROSCOPY OF IONIC MEDIA
G. P. SMITH, JR.
C. R. BOSTON
J. BRYNESTAD
L. R. LIETO[4]
G. SHANKLE[4]
K. S. TOTH[5]
W. M. EWING

X-RAY DIFFRACTION
H. L. YAKEL, JR.
B. S. BORIE[1]
J. E. EPPERSON
R. W. HENDRICKS
C. J. SPARKS, JR.
R. M. STEELE

SPECIAL ASSIGNMENT
G. V. CZUZEK
L. A. HARRIS

SECTION CHIEF W. O. HARMS[2]
EDITH JONES

ASSISTANT J. R. WEIR, JR.
JANE MORRISON

PROJECT COORDINATION
LMFBR, HTM – W. O. HARMS[2]
MSRP, H. E. McCOY, JR.[2]

MATERIALS COMPATIBILITY
J. H. DEVAN
O. B. CAVIN
W. H. COOK
J. R. DISTEFANO
R. B. EVANS III
D. H. JANSEN
R. L. KLUEH
J. L. GRIFFITH
J. W. HENDRICKS
D. E. MAHAFFEY
B. W. McCOLLUM
L. R. TROTTER

MECHANICAL PROPERTIES
H. E. McCOY, JR.[2]
E. E. BLOOM
W. W. DAVIS
C. W. DOLLINS
D. G. HARMAN
C. R. KENNEDY
R. T. KING
N. H. PACKEN[3]
C. E. SESSIONS
R. L. STEPHENSON
R. W. SWINDEMAN
R. D. WADDELL, JR.
F. W. WIFFEN
J. W. WOODS
F. L. BEELER
K. W. BOLING
E. BOLLING
T. T. BRIGHTWELL
V. R. BULLINGTON
J. FELTNER
P. F. HUBER
H. W. KLINE
V. G. LANE
B. McNABB, JR.
E. B. PATTON, JR.
N. O. PLEASANT
L. G. RARDON
C. K. THOMAS
E. M. THOMAS
L. J. TURNER
C. W. WALKER
B. C. WILLIAMS

NONDESTRUCTIVE TESTING
R. W. McCLUNG
K. V. COOK
C. V. DODD
B. E. FOSTER[3]
S. D. SNYDER
W. G. SPOFFORD III[12]
H. L. WHALEY, JR.
L. D. CHITWOOD
O. E. CONNER
R. A. CUNNINGHAM, JR.
E. V. DAVIS
R. L. FITZGERALD
D. P. GOODSEY
W. J. MASON

ZIRCONIUM ALLOY DEVELOPMENT
P. L. RITTENHOUSE
D. O. HOBSON
E. J. TENCKHOFF
P. J. JONES
G. C. NELSON

REACTOR MATERIALS ENGINEERING
A. F. LITMAN
C. D. BOPP[3]
B. FLEISCHER
J. W. KOGER
F. D. HARVEY
E. J. LAWRENCE
J. B. PHILLIPS

SPECIAL ASSIGNMENT
A. TABOADA

SECTION CHIEF C. J. McHARGUE
LOUIE MAE PYATT

DEFORMATION OF CRYSTALLINE SOLIDS
R. O. WILLIAMS
R. W. CARPENTER
M. H. YOO

DIFFUSION IN SOLIDS
T. S. LUNDY
D. K. REIMANN
L. C. MANLEY
R. A. PADGETT, JR.

ELECTRON MICROSCOPY
J. O. STIEGLER
K. FARRELL
R. E. GEHLBACH
B. T. M. LOH
A. WOLFENDEN
S. W. COOK
C. K. H. DuBOSE
J. T. HOUSTON
C. JONES

PHYSICAL CERAMIC STUDIES
C. S. MORGAN, JR.
C. S. YUST
L. L. HALL

STRUCTURE OF METALS
R. A. VANDERMEER
P. V. GUTHRIE[4]
J. C. OGLE

PHYSICAL METALLURGY
H. INOUYE
D. T. BOURGETTE
C. T. LIU
R. L. WAGNER
J. F. NEMSOME
S. H. WHEELER

METALLURGY OF SUPERCONDUCTING MATERIALS
G. R. LOVE
C. C. KOCH
Z. R. MCNITT
J. O. SCARBOROUGH

SNPO-C DEVELOPMENT
R. E. CLAUSING
D. S. EASTON

SECTION CHIEF P. PATRIARCA
MARJORIE CLARY
VERNELL MOORE
EDITH TAYLOR

PROJECT COORDINATION
GCR, J. H. COOBS[8]
THU, TRU, A. L. LOTTS[2]
ISOTOPIC POWER – R. G. DONNELLY

CERAMICS TECHNOLOGY
J. L. SCOTT
R. L. BEATTY
E. S. BOMAR, JR.[2]
J. Y. CHANG
W. S. ERNST, JR.
T. G. GODFREY, JR.
R. L. HAMNER
J. D. L. HARRISON[4]
D. M. HEWETTE II
J. M. LEITNAKER
T. B. LINDEMER
R. A. POTTER
J. M. ROBBINS
K. E. SPEAR II
J. G. STRADLEY
V. J. TENNERY
S. C. WEAVER
B. R. CHILCOAT
C. M. FITZPATRICK
F. P. JEFFERS
C. HAMBY, JR.
J. H. HANNAH
H. KEATING
D. V. KIPLINGER
J. E. POPE
C. L. ROBERTS[10]
D. E. RUSSON
W. W. PROAPS
W. H. SMITH, JR.
J. F. WILLMERING, JR.

FUEL CYCLE TECHNOLOGY
A. L. LOTTS[2]
S. BOLT[7,10]
R. A. BRADLEY
J. M. CHANDLER[11]
C. M. COX
R. B. FITTS
F. J. FURMAN, JR.
J. KOMATSU
E. J. MANTHOS
W. L. MOORE
A. R. OLSEN
W. H. PECHIN
M. K. PRESTON[8]
J. D. SEASE
D. M. SHEPHERD[9]
B. J. STRADER
J. E. VAN CLEVE, JR.
K. P. BAYNE
W. T. BOSTIC[11]
R. A. BOWMAN
R. A. BUHL
W. L. CLEMENTS
J. T. EAST
J. E. EVE
C. E. FENDER
G. HICKEY, JR.[13]
J. C. HILL
C. L. JOHNSON
H. R. LIVESEY
W. H. MILLER
R. E. POTTER
C. F. SANDERS
J. R. SLAVEN
W. G. STERLING
W. B. STINES
R. J. UNDERWOOD[13]
C. M. WILSON[13]

STUDIES AND EVALUATION
T. N. WASHBURN[4]
R. E. ADAMS
W. H. BRIDGES
F. J. HOMAN
R. B. PRATT

SPECIAL ASSIGNMENT
J. J. PRISLINGER
T. N. WASHBURN[2]
C. E. DeVORE

TECHNICAL OPERATIONS CONTROL
G. M. ADAMSON, JR.[2]

PERSONNEL, LABOR RELATIONS, AND SAFETY
L. E. BANKER, ADMINISTRATIVE ASSISTANT
ANN HOBBS

FINANCE AND MATERIALS
R. G. CARDWELL

PROCUREMENT, MAINTENANCE, ENGINEERING, AND NUCLEAR MATERIALS
R. M. EVANS
RUTH HENGSTLER
H. W. HOOVER
R. G. SHOOSTER
M. A. WHEELER

REPORTS AND PUBLICATIONS
M. R. HILL
THELMA REELY
FRANCES SCARBORO
PATRICIA VILES
SHARON WOODS

EDITORS AND INDUSTRIAL COOPERATION
S. PETERSON D. J. RUCKER

RADIATION CONTROL
B. E. FOSTER[2] E. S. BOMAR[2]

[1]CONSULTANT
[2]DUAL CAPACITY
[3]GRADUATE RESEARCH STUDENT
[4]ORAU GRADUATE FELLOW
[5]ON LOAN FROM REACTOR CHEMISTRY DIVISION
[6]NONCITIZEN VISITOR
[7]RESEARCH PARTICIPANT FROM THE UNIVERSITY OF OKLAHOMA
[8]ASSISTANT DIRECTOR, GAS-COOLED REACTOR PROJECT
[9]ON LOAN FROM GENERAL ENGINEERING DIVISION
[10]ON LOAN FROM REACTOR DIVISION
[11]ON LOAN FROM CHEMICAL TECHNOLOGY DIVISION
[12]PART-TIME EMPLOYEE
[13]ON LOAN FROM ANALYTICAL CHEMISTRY DIVISION

ORNL-4470
UC-25 — Metals, Ceramics, and Materials

INTERNAL DISTRIBUTION

1–3. Central Research Library
4–5. ORNL – Y-12 Technical Library, Document Reference Section
6–60. Laboratory Records Department
61. Laboratory Records, ORNL R.C.
62. MIT Practice School
63. ORNL Patent Office
64. Laboratory Shift Supervisor
65. G. M. Adamson, Jr.
66. L. G. Alexander
67. R. J. Beaver
68. D. S. Billington
69. A. L. Boch
70. E. G. Bohlmann
71. E. S. Bomar
72. B. S. Borie
73. G. E. Boyd
74. R. B. Briggs
75. J. V. Cathcart
76. J. M. Chandler
77. G. W. Clark
78. R. E. Clausing
79. W. C. Colwell
80. J. H. Coobs
81. C. M. Cox
82. J. A. Cox
83. F. L. Culler
84. J. E. Cunningham
85. G. V. Czjzek
86. J. H. DeVan
87. R. G. Donnelly
88. J. H. Erwin
89. J. S. Faulkner
90. J. I. Federer
91. D. E. Ferguson
92. G. W. Flack
93. A. P. Fraas
94. J. H Frye, Jr.
95. W. Fulkerson
96. J. H. Gillette
97. R. J. Gray
98. J. L. Gregg
99. W. R. Grimes
100. J. P. Hammond
101. W. O. Harms
102. C. S. Harrill
103. R. F. Hibbs
104–118. M. R. Hill
119. A. P. Huber (K-25)
120. H. Inouye
121. R. G. Jordan (K-25)
122. H. W. Joy
123. M. A. Kastenbaum
124. M. T. Kelley
125. E. M. King
126. R. B. Korsmeyer
127. W. J. Lackey
128. J. A. Lane
129. J. M. Leitnaker
130. A. P. Litman
131. A. L. Lotts
132. G. R. Love
133. T. S. Lundy
134. H. G. MacPherson
135. W. R. Martin
136. R. W. McClung
137. H. E. McCoy
138. H. C. McCurdy
139. D. L. McElroy
140. C. J. McHargue
141. A. J. Miller
142. E. C. Miller
143. C. S. Morgan
144. A. R. Olsen
145–146. R. B. Parker
147. P. Patriarca
148. S. Peterson
149. J. W. Prados
150. H. P. Raaen
151. P. L. Rittenhouse
152. A. W. Savolainen
153. A. C. Schaffhauser
154. O. Sisman
155. J. L. Scott
156. H. E. Seagren
157. J. D. Sease
158. G. M. Slaughter
159. G. P. Smith, Jr.
160. P. E. Stein (K-25)
161. J. O. Stiegler
162. D. A. Sundberg
163. V. J. Tennery

164. D. B. Trauger
165. J. E. Van Cleve, Jr.
166. R. A. Vandermeer
167. T. N. Washburn
168. M. S. Wechsler
169. A. M. Weinberg
170. J. R. Weir, Jr.
171. W. J. Werner
172. G. D. Whitman
173. R. O. Williams
174. H. L. Yakel
175. C. M. Adam, Jr. (consultant)
176. Leo Brewer (consultant)
177. L. S. Darken (consultant)

EXTERNAL DISTRIBUTION

178–179. D. F. Cope, RDT, SSR, AEC, Oak Ridge National Laboratory
180. N. Engel, Georgia Institute of Technology
181. V. D. Frechette, Alfred University
182. Angelo Giambusso, AEC, Washington
183. W. W. Grigorieff, Assistant to the Executive Director, Oak Ridge Associated Universities
184. R. F. Hehemann, Case Institute of Technology
185. E. E. Hoffman, GE, Cincinnati
186. L. C. Ianniello, AEC, Washington
187. O. C. Kopp, University of Tennessee
188. J. Korringa, Ohio State University
189. C. F. Leitten, Jr., Linde Division, Union Carbide Corporation
190. J. J. Lombardo, NASA, Lewis Research Center
191. W. D. Manly, Union Carbide Corporation, Materials Systems Div., Kokomo, Indiana
192. C. L. Matthews, RDT, AEC, Oak Ridge National Laboratory
193. P. W. McDaniel, AEC, Washington
194. T. W. McIntosh, AEC, Washington
195. R. R. Nash, NASA, Washington
196. E. F. Nippes, Rensselaer Polytechnic Institute
197. R. E. Pahler, AEC, Washington
198. R. M. Parke, MAB, National Academy of Science, Washington
199. H. B. Rahner, Savannah River Operations
200. R. H. Rein, Union Carbide Corp., Linde Div.
201. F. N. Rhines, University of Florida
202. F. C. Schwenk, AEC, Washington
203. J. M. Simmons, AEC, Washington
204. E. E. Sinclair, AEC, Washington
205. L. M. Slifkin, University of North Carolina
206. E. E. Stansbury, University of Tennessee
207. D. K. Stevens, AEC, Washington
208. Dorothy Smith, AEC, Washington
209. J. A. Swartout, Union Carbide Corporation, New York
210. A. Van Echo, AEC, Washington
211. J. Weertman, Northwestern University
212. G. W. Wench, AEC, Washington
213. M. J. Whitman, AEC, Washington
214. C.H.T. Wilkins, University of Alabama
215. Laboratory and University Division, AEC, Oak Ridge Operations
216–432. Given distribution as shown in TID-4500 under Metals, Ceramics, and Materials category (25 copies – CFSTI)